THE MICROSTRUCTURE OF SYNTHETIC AGGREGATE PRODUCED FROM WASTE MATERIALS AND ITS INFLUENCE ON THE PROPERTIES OF CONCRETE

By

SARANAGON HEMAVIBOOL

Submitted in accordance with the requirements for the degree of

Doctor of Philosophy

University of Leeds

School of Civil Engineering

October, 2007

ABSTRACT

This thesis examines the influence of the firing conditions on the properties and microstructure of synthetic aggregate produced using granite quarry fine waste blended with low grade ball clay as the binder. The investigation involved the use of various engineering tests and microstructural characterization techniques with special attention on the evolution of the microstructure of the aggregate pellets upon firing.

The raw materials were extruded and fired in a small bench top model Trefoil rotary kiln. Various temperature profiles were simulated and the effects of firing condition on the water absorption, relative density and mineralogical and microstructural evolution of the synthetic aggregate were investigated.

Powder X-ray diffraction (XRD) and electron microprobe analysis were used to study the phase transformation of the fired pellets produced using different firing conditions. Mercury intrusion porosimetry (MIP) and quantitative image analysis of backscattered electron (BSE) were employed to assess the pore structure of the synthetic aggregate. The main variables considered were the firing temperature and the duration at the highest temperature.

An assessment of the microstructure at the coarse aggregate-cement paste interface is presented in the second part of this thesis. Concretes were cast with two different initial conditions of synthetic aggregate, i.e. dry and pre-wetted aggregate, and the results were compared with those obtained for the natural and Lytag lightweight aggregate concrete. This investigation was done with respect to the variables of hydration time, moisture condition of the aggregate particles and the type of coarse aggregate. Image analysis of backscattered electron image of flat and well-polished concrete samples was employed to provide quantitative information about the microstructural gradients at the coarse aggregate-cement paste interfaces.

Finally, the influence of three different types of coarse aggregate on the permeability, compressive strength and elastic behavior of concrete was studied; the three aggregates were natural quartz, Lytag and the synthetic aggregate produced during this research.

The results of the investigation show the significant influence of firing condition on the properties and mineralogical evolution of the synthetic aggregate. The microstructure of

the synthetic aggregate was primarily controlled by two competing processes, i.e. pore growth and densification. Pore growth was observed when the aggregate was fired between 900° and 1,110°C, while densification started to overcome pore growth at about 1,110°C with a sintering time between 0 to 5 minutes. Densification of the synthetic aggregate depended on the amount of liquid phase that was associated with the melting of the feldspar mineral.

The microstructural study shows that the moisture condition and type of coarse aggregate affects the microstructure of the interfacial transition zone (ITZ) between coarse aggregate and cement paste matrix. The results confirm the benefit of absorbing water from the surrounding paste by the porous aggregate on the ITZ microstructure unless too much and/or too rapid absorption of water occurs. Preferential deposition of calcium hydroxide was observed at the region close to the interface of quartz and synthetic aggregate that had a dense microstructure but very little deposition or build up was found for the porous synthetic aggregate.

The Lytag and synthetic aggregate concretes showed a higher permeability than the natural quartz aggregate concrete. These results indicate the negative influence of the oven-dried technique that is commonly used in sample preparation, which might generate microcracks inside the tested samples.

The 28-day compressive strengths achieved ranged from 37 to 44 N mm^{-2} and compared favourably with control concretes made with the natural quartz or Lytag lightweight aggregates. The elastic modulus of the synthetic and Lytag lightweight aggregate concrete appeared to be about 30 to 40 percent lower than the natural aggregate concrete.

ACKNOWLEDGEMENTS

I wish to acknowledge the Royal Thai government for the supporting scholarship of the author's PhD study.

I would like to gratefully thank Dr. P J Wainwright and Dr. I G Richardsons for their help and assistance.

I would like to thank Dr. Adrian Brough, Dr. Catherine A love and Dr. H Dyson for their scanning electron microscope (SEM) and SEM-sample preparation training. Thanks to Stuart Shaw for his MIP demonstration. I am also very thankful to Dr. Eric Condliffe for performing the electron microprobe session for my specimens.

I am very thankful to Dr. Cyril Lynsdale for showing me how to perform the permeability test and allowing me to use his equipments at the University of Sheffield.

I deeply thank to my family for their love, support and encouragement throughout my study. This thesis is dedicated to them.

Table of contents

List of Tables

List of Figures

Chapter 1

Introduction and objectives

1.1 Introduction

The generation of solid waste across Europe every year was conservatively estimated to a figure of 4,000 million tones (EEA, 1998). This figure tends to increase every year. In OECD Europe, total waste generation between 1990 and 1995 increased by nearly 10%. There are two important points of view that relate to the waste production in that it can give rise to environmental and human health problems, and it is a reflection of the inefficient way societies use resources. At present there is an increasing interest in developing a simple and economic method to turn waste materials into a substitute for primary materials. The reason for increasing recycling activities originates from the well recognized situation in Europe, where many countries have to cope with the decreasing capacities of landfill sites and the stricter requirements for opening new sites (EEA, 1998). Many methodologies have been launched in order to reduce the level of waste generation and encourage a greater proportion of recycling and re-use of these waste materials. For example, taxation for primary aggregates based on the environmental impact of the aggregate quarrying and supplying were introduced (Wainwright et. al., 2001). The introduction of a landfill tax is another way that has been used to support the environmental target in many countries. The taxation on all waste disposed in landfill sites which are subject to the licensing requirements under the Environmental Protection Act 1990 was introduced by the UK government in 1996. It was set at two rates, i.e. a reduced rate of £2 per tonne for inactive (or inert) wastes and a standard rate of £7 per tonne (rising to £15 per ton by 2004) for all other taxable wastes (DoE, 1995; Hill et. al., 2001). An increasing of the waste disposal and the primary material production cost are one of the economic instruments that are normally used to encourage business and consumers to produce less waste and make re-use and recycling potentially more economically viable.

The use of inert waste material as lightweight aggregate in the construction industry is a subject of interest at present. Lightweight aggregate is usually defined as an any aggregate with a particle density of less than 2000 kg/m^3 or dry loose bulk density of less than 1200 kg/m^3 (Owens, 1993). Most manufacturing processes for

lightweight aggregates are carried out in the conventional rotary kiln, sinter strand or foaming beds (FIP, 1983). The principal artificially produced lightweight aggregates are generally made of clay, shale or pulverized-fuel ash (read Owens, 1993, for more detailed information). Using lightweight aggregate for structural concrete has many benefits, e.g. saving of the construction cost due to the reduction of deadweight of a structure, greater fire resistance and low thermal conductivity etc. However, the application of this material is still limited by the requirement from the market, together with the limitation of the raw material and the method of processing. Therefore, to overcome these limitations, a study of a process to take waste materials and convert them to a useful concrete aggregate, and the demonstrable proof of long-term performance of concrete made of these artificial aggregates is necessary.

There is a lot of information that has been published in the past related to the utilization of waste materials in construction, notably the conference organized by WASCON (WASCON 91; WASCON 94; WASCON 97; WASCON 2000; WASCON 2003). Many of the studies in these conferences focus on the unbound or bituminous bound applications of waste materials and in particular on the leaching characteristics in relation to ground water pollution. In addition, many of the applications studied involve the use of unprocessed waste. Little work has been published on the use of processing the waste into a synthetic aggregate and that which has been done has tended to focus on the macroproperties of the materials. Therefore, most of the information available did not influence the development of this work.

A study under the framework of EU project of aggregate demand and consumption as well as the processing for turning waste materials into the synthetic lightweight aggregate by using the innovative design of the Trefoil kiln (see Figure 3.7) has recently been undertaken (Wainwright et al., 2001). A wide range of waste materials were investigated and the full engineering process that was required for these materials were studied. Large amounts of valuable information, involving the processing of waste materials, synthetic aggregate production, physical and environmental performance of these aggregates, were obtained in this study. However, due to the broad scope of their study, only preliminary investigation was done. There are still a number of issues related to the quality of the aggregate and its performance in concrete that need to be addressed.

1.2 Objectives of the investigation

The present work is a continuation of the EU project mentioned earlier and has three main objectives. The first objective is to provide a better understanding of the effect of firing condition on the synthetic aggregate properties. This knowledge is very important for the manufacturer in order to improve and control the product properties. A small bench top model Trefoil kiln (see Figure 3.8) was, therefore, built to serve this purpose. This kiln was specially designed to simulate the temperature profile which pellets experience when they move along the Trefoil kiln during the firing process. Various temperature profiles were simulated and many techniques were used to investigate the engineering properties and microstructure of the synthetic aggregate produced from these firing conditions.

The granite washing produced from the Glensanda quarry in Scotland, UK, was chosen as a raw material to produce the synthetic aggregate in this study. Based on the earlier work of Wainwright et. al. (2001), it was identified as being suitable for producing a good quality aggregate and was also available in large quantity. This material is generated during the production of crushed granite aggregate. The amount of this quarry waste generally depends on the geology of the natural resource and the method used for extraction and processing. A figure of 30 million tones was estimated for UK in 1996 (DETR, 1998).

The second objective is the investigation of the interfacial transition zone (ITZ) between synthetic aggregate and cement paste matrix. Many observations from the past have suggested the positive impact of using porous lightweight aggregate on the ITZ microstructure. However, most of the available information is based on the qualitative analysis of the secondary electron mode of the scanning electron microscopy (SEM) on the fracture surfaces. The quantitative information about the ITZ microstructure of the lightweight aggregate concrete is still lacking. The SEM-image analysis technique was, therefore, used in order to examine and quantify the ITZ microstructure of the synthetic aggregate concrete. The effect of aggregate type and its moisture condition on the ITZ microstructure were also investigated in this study.

Investigation of the effect of using three different coarse aggregates (synthetic, natural quartz and Lytag) on the mechanical and the permeability properties of concrete is the final objective of this research. These works are aimed to access the potential use of the synthetic aggregate in structural concrete as the coarse aggregate replacement.

1.3 Layout of the thesis

This thesis consists of seven chapters. In chapter two, the relevant knowledge about recycling of waste materials into the lightweight aggregate, bloating process occurred during the aggregate firing and the SEM analysis of the ITZ between aggregate and cement paste matrix are reviewed. In chapter three, the synthetic aggregate production process is described. In chapter four, the detailed information of the materials used in this study, relevant experimental procedure and specimen preparation process are presented. Chapter five gives a basic background of the electron microscopy together with the image analysis techniques used in this research. Chapter six presents the experimental results of all tests performed in this study and their discussions. Chapter seven gives the conclusions and the recommendations for further study.

Chapter 2

Literature reviews

2.1 Introduction

Most of the studies into the use of synthetic aggregate produced from the various waste streams as a substitute for primary materials used in concrete are in the elementary study stage which aims to investigate the possibility of using synthetic aggregate as a primary aggregate replacement. This chapter reviews the relevant knowledge regarding the use of waste materials as the lightweight aggregate and their effect on the microstructure of the interfacial transition zone between cement paste and aggregate.

2.2 The use of waste as coarse aggregate replacement in concrete

At present the most common synthetic lightweight aggregates are made from a variety of materials which include the natural occurring materials, e.g. clay, shale and slate, and the by-product materials, e.g. pulverized fuel ash, blastfurnace slag and incinerator bottom ash. Most of the lightweight aggregate manufacturing processes, with the exception of the processes used for blastfurnace slag, are usually carried out by using 'traditional' style rotary kiln or the sinter strands (Owen, 1993). The raw materials are subject to a process either agglomeration (hardening) or expansion (bloating). Sintering is the widely used agglomeration or hardening technique which is used to fuse the various particles together at the point of mutual contact. This process occurs at high temperature depending on the physical and chemical properties of the raw material. Alternatively, expansion due to bloating occurs when the raw material is heated to the fusion temperature, at which the liquid phase with appropriate viscosity occurs simultaneously with the formation of released gases (Owen, 1993).

Over recent years much research has been carried out into the investigation of the potential use of waste materials as a replacement for natural raw materials for the construction industry. For example Yasuda (1991) presented five technologies for the utilization of the sewage sludge in Tokyo and one of these technologies involves the recycling of this waste into the artificial lightweight aggregate called 'sludgelight'. In this process the incinerated sewage sludge ash (ISSA) was mixed with the alcohol

fermentation wastewater (binder), pelletized and fired in a vertical shaft furnace at temperature 1,000° to 1,100°C. Wainwright (1981), Wainwright and Boni (1983) and Wainwright and Robery (1991) reported on the use of municipal solid waste incinerator (MSWI) bottom ash to produce the synthetic aggregate. The residual ashes from the incinerator were treated to remove the ferrous and non-ferrous metals. The remaining materials were then crushed, blended with clay, pelletized on the inclined disc pelletizer and fired in a rotary kiln. The synthetic aggregate produced was incorporated into concrete as the coarse aggregate. This concrete was tested over a 4½ year period and the results indicated that the synthetic aggregate performs satisfactorily as a coarse aggregate replacement in concrete. Osada (1997) presented the direct melting process used for recycling of the municipal solid waste (MSW) materials. This process permits recycling of this waste by converting them into slag and metal. These slags can be used effectively as construction materials, e.g. concrete aggregate and aggregate for asphalt paving. Wainwright and Cresswell (2001) used a number of different combustion ash, i.e. incinerated sewage sludge ash (ISSA), municipal solid waste incinerator bottom ash (MSWI-BA) and pulverized fuel ash (Pfa), as a raw material for the production of synthetic aggregates by using an innovative rotary 'Trefoil' kiln. The fine fraction of ashes was blended with a binder to enable the mixture to be extruded and pelletized. The obtained pellets were then fired in the Trefoil kiln. The synthetic aggregates were used as the natural aggregate replacement in concrete. Concretes containing this synthetic aggregate achieved 28 day compressive strengths of between 33 to 51 Mpa compared with 45 and 42 MPa for the natural and Lytag aggregate control mixes, respectively.

A large amount of background work on the production of synthetic aggregate from various waste streams by utilising an innovative kiln technology was given by the work done by Wainwright et al. (2001). The project involved the systematic study of a process to take waste materials and convert them to a useful synthetic aggregate by using an innovative design of rotary kiln named 'Trefoil kiln'. This rotary kiln represents the innovation in kiln technology that provides the potential for being able to process a variety of different wastes and the details for this kiln are given in section 3.4.2.1. A wide range of waste materials were considered in this study and the full

engineering process requirements from pre-treatment through to incorporation product in concrete were studied. Six waste types were selected in their study which are:

- River, canal and harbour dredgings
- Quarrying and mining residues
- Municipal solid waste incinerator and other combustion residues
- Automotive shredder residues and other industrial wastes
- Sewage sludge
- Paper making sludges

These chosen materials were characterized in term of their chemical and physical properties. A number of steps for aggregate production were used beginning with the dewatering of the feedstock materials and dried if necessary. The materials were then mixed and extruded, followed by pelletizing to produce the suitable green pellets for firing. A number of different mix proportions between a principal material and the binder were assessed in term of their 'ballability' and the green pellet properties. The ballability used was based on the ability of the mixes to form uniform, spherical green balls that were easy to handle. The green pellets produced were fired and tested for relative density, water absorption and loose bulk density. The properties of concrete made with these aggregates were compared with the concrete made with Lytag and a naturally occurring aggregate. It was found that an increase in the amount of binder in the mixture gave a reduction in relative density and increase in water absorption property. All synthetic aggregates, with the exception of the one made with 40% dredgings, have water absorption figures below that of the Lytag aggregate. The compressive and tensile strength development up to the age of 80 days of the synthetic aggregate concretes were found to be similar and in some cases higher than those of the Lytag and natural aggregate concretes. The same results were obtained for the development of elastic modulus (as measured by dynamic modulus). The leaching characteristics of the raw materials, synthetic aggregate and the aggregate in concrete were also examined in their study in order to assess the environmental compatibility of the aggregate in the various stages of their use. The results from the pH dependent leaching test which provides information on the pH sensitivity of leaching behaviour of the material illustrates that the process used to produce the synthetic aggregates gives a

product with a relative similar leaching behaviour and shows the same generic leaching character in spite of varying raw materials. However, there are some typical deviations noted in their report:

- Comparing to all other mix designs, their results show an increase in the leachability of B, Cr, Mo, As, V, Se and Sr when the amount of coal fly ash in green pellets was increased.
- Significantly increased levels of B, Ca, Mg, Li, Na, Cr (probably as chromate), Mo, V, Se, SO_4, Ba, Sr, K, Cd, Pb and Zn were observed in a mix design with MSWI fly ash.
- An elevated level of P relative to the other mix designs was observed in the case of sewage sludge.
- In the case of car shredder waste, Ca, Mg, B, Li, Mo, Sb, SO_4, Sr, Ni and Pb are the elements that were found deviating from the general pattern.

The results of the synthetic aggregate were compared with the results of raw materials and they found that the metals are reasonably tied up in the mineral matrix provided the levels are not too high. This indicates an improvement in leaching behaviour of the synthetic aggregate by the production process. However, the oxyanions Mo, V, As, Se, Sb and Cr were noted to be more likely to cause increased release levels when they are converted into their oxides during the sintering process. The oxides of the oxyanions become mobile when they are in contact with water.

Van der Sloot et al. (2001) reported the leaching behavior of the synthetic aggregates made from granite washings, paper sludge contaminated river sediment, municipal solid waste incinerator bottom ash and shredder waste by a variety of different leaching tests in order to cover all of the differences in conditions and uses of these aggregates. They found that the synthetic aggregate features a low buffer capacity, which makes it sensitive to externally imposed pH conditions. The leaching curves as a function of pH were found to be very similar, which illustrates that the production process of the synthetic aggregates leads to a product with relatively similar properties in spite of using different raw materials. The results from the column leaching test at the liquid/solid ratio (L/S) equal to 10 on 10-mm aggregates were compared with the same material broken to less than 2-mm at the corresponding pH in the pH dependence test

(L/S = 10). The results were mutually consistent with no significant difference between these two techniques noted for almost all elements. They inferred that the effect of crushing the aggregate has little effect on the leaching of very soluble elements at higher liquid to solids ratios suggesting that the porous nature of the aggregate only leads to a relatively small delay in release. The encapsulation of several metals, i.e. Ca, K, Mn, Ca, Sr, Ba, in the silicate matrix in the sintering process was reported. The synthetic aggregate was found not to adversely affect the concrete in its service life but at the recycling and end of life stage the long term leaching behaviour might be an issue of concern.

Wainwright et al. (2002) reported tests on concrete incorporated with the synthetic aggregate obtained from a variety of waste streams. The main waste used in their study was the granite washings from the Glensanda super quarry located on the West coast of Scotland. The washing was blended with three different types of binder including paper sludge, clay and dredged harbour sediment. The different combinations of waste mixture were extruded, ball (pelletised) and fired in the rotary kiln with final temperatures between 1200 °C and 1230 °C to produce synthetic aggregate. The water absorption, relative densities, and loose bulk density of aggregates were tested in a small scale batch and the results were compared with the results obtained from natural aggregate and a commercially available artificial lightweight aggregate (Lytag). The slightly higher relative densities and significantly lower water absorption of the synthetic aggregate compared to the Lytag aggregate were observed. Two of the synthetic aggregates were chosen for larger scale production with 10% clay and 10% river dredging as a binder and were cast in concrete as a 100% replacement of coarse natural aggregate. The compressive strengths of the 28-day old concrete made with the synthetic aggregate were found ranging from 40 to 48 $N.mm^{-2}$. The potential environmental impact of utilization of the synthetic aggregates in unbound form was assessed by using pH dependence and column leaching test. The information obtained on the leaching of contaminants from the aggregate has given favourable results.

Wainwright and Cresswell (2003) reported the results of the long term tests on concrete containing synthetic aggregates produced from granite quarry waste, harbour dredging, and incinerated sewage sludge ash. The aggregate production process consisted of blending and mixing of the raw materials into the appropriate consistency

to enable the mix to be extruded and then the mixture was pelletised by means of the rotary drum pelletiser that also incorporated a burner drier. The green pellets produced were fired in the rotary "trefoil" kiln. Concrete strength, dynamic modulus of elasticity, drying shrinkage, and permeability up to an age of 18 months were tested and the results obtained were compared with concrete made from a commercially available lightweight aggregate (Lytag). They found that in all tests the performance of concretes made with the synthetic aggregate was similar to that of the Lytag concrete.

Gennaro et al. (2004) used zeolitic rocks for the production of lightweight aggregates. Both expansion at high temperature and the properties of the fired products were investigated. The aspect, volume, bloating index (express the volume change after firing) and the bulk density of aggregates were evaluated to obtain an optimal thermal cycle (maximum temperature and retention time corresponding to the maximum bloating). The results obtained show that both optimal temperature and soaking time are well correlated with the chemical composition of zeolitic tuffs: the higher the silica/fluxing ratio (fluxing = $CaO+MgO+Na_2O+K_2O+Fe_2O_3$), the higher the optimal temperature. The properties of the aggregates prepared at a laboratory scale were found analogous to those of commercial products, such as expanded clays, and comparable to the requirements for high quality lightweight aggregates. Bloating of zeolitic materials was found to depend largely on the chemical and mineral composition of the material. The results indicated that the higher the silica/fluxing ratio, the higher the viscosity of the liquid phase. However, too high silica/fluxing ratios bring about the formation of an insufficient amount of liquid phase, though highly viscous, preventing the material to bloat. On the other hand, a low silica/fluxing ratio involves a lower melting temperature and lower viscosity of the liquid phase, which is unable to entrap a significant amount of gas and thus to bloat during firing. The gas released from the investigated materials was found to be largely represented by water vapour, deriving from the dehydration (and, to a lesser extent, dehydroxylation too) of zeolites and, secondarily, smectite, opal and volcanic glass. They concluded that the bulk density of aggregate can be predicted with reasonable accuracy on the basis of loss on ignition as well as silica/alumina and silica/fluxing ratios of zeolitic materials.

2.3 Bloating behaviour

As mentioned in the previous section, expansion or bloating is one of the important factors that various production techniques for lightweight aggregates rely on. This process develops when either steam is generated, as in the case of molten slag, or an argillaceous material (clay, shale or slate) is heated to fusion temperature, at which point pyroplasticity occurs simultaneously with the formation of gas which bloats the aggregate (Owen, 1993).

Riley (1951) reported that the driving force for the expansion of the aggregate by bloating is essentially the occurrence of thermally unstable gas releasing phases. He stated that two conditions are necessary to get a suitable expanded material:

1. it must contain some mineral or combination of minerals that will dissociate and liberate a gas at high temperature (bloating temperature);
2. it must produce a high temperature glassy phase with a viscosity high enough to trap a gas at the bloating temperature.

By plotting a large number of chemical analyses of bloating and nonbloating clays on a composition diagram with silica, alumina, and total fluxing constituents (CaO, MgO, FeO, Fe_2O_3, $(Na, K)_2O$) as the corner, he was able to define the limits of bloating on a composition diagram. This area showed the desirable composition of clays which satisfy the second necessary condition as mentioned above for bloating. Figure 2.1 is an extract from his paper which shows a composition diagram; a dashed line represents the area of bloating. He tested the validity of the area of bloating by adding silica and alumina to nonbloating clays which have an overabundance of the fluxing agents in order to give their compositions conforming to points within this area. He found that when fired these mixtures bloated. He also developed a method of testing individually the accessory minerals which might be gas producers. The results showed that of all the accessory minerals of the Decorah shale, pyrite, hematite, and dolomite are the only ones which could dissociate and produce a gas at the proper temperature. He also made a discussion about causes of gas evolution when adding these substances into the nonbloating mixtures in his report. Including in his testing program, igneous rocks whose compositions fall within the bloating area were tested and found that they produced good bloats when finely ground and cast into briquettes. From these results he

concluded that the viscosity condition for bloating is dependent only on the chemical composition, regardless of the mineral constituents.

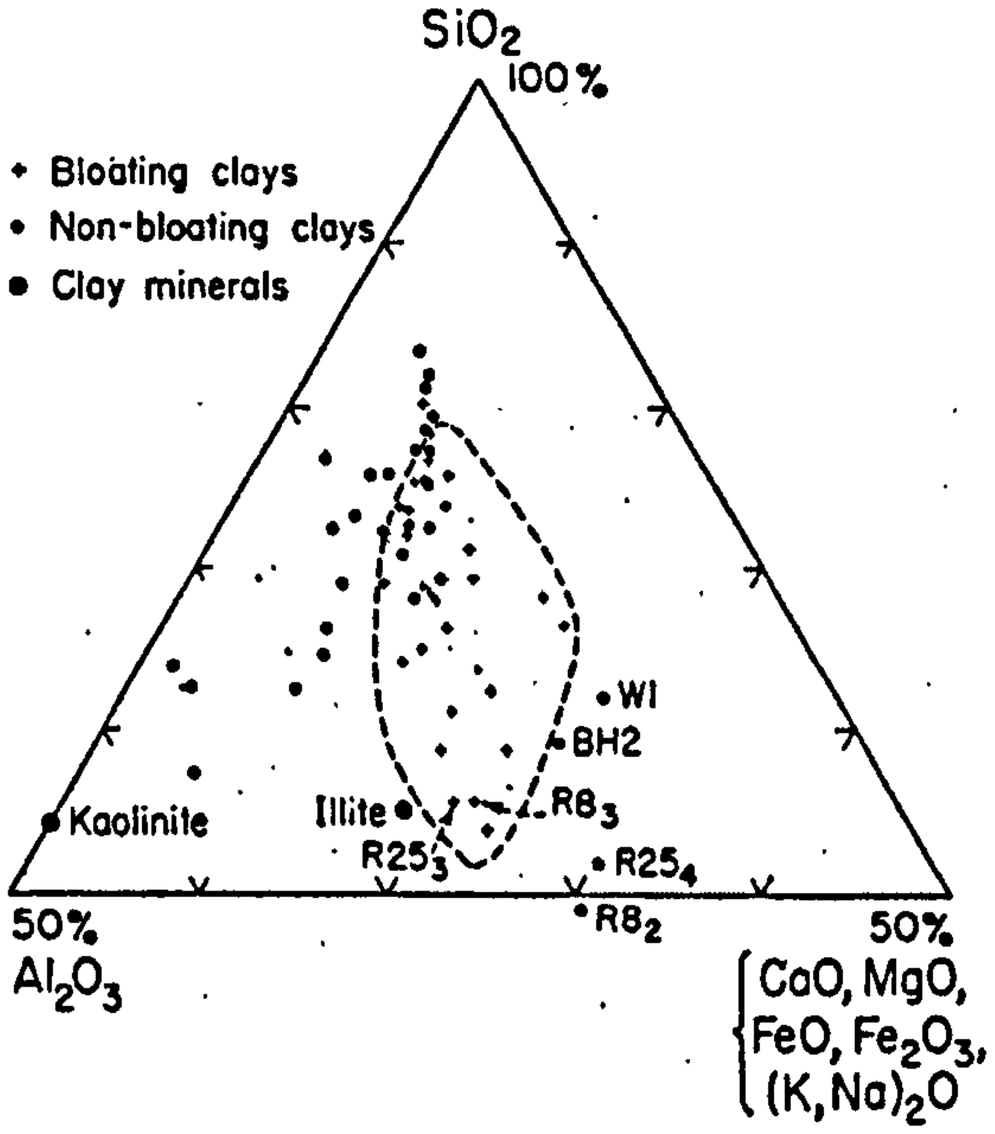

Figure 2.1 Composition diagram of major oxides showing area in which clays fire to a mass viscous enough to insure good bloating. Dashed line represents limits of bloating. (copied from Riley, 1951)

Sandrolini and Palmonari (1976) gave a detailed description of the fundamental role of iron oxides in the bloating of vitrified ceramic materials with iron (III) oxide (Fe_2O_3) content between 1 and 6 %. The results from linear shrinkage, water absorption test combining with the examination of the fracture surfaces in various samples by scanning electron microscopy technique showed that iron oxide contributes significantly to the bloating of the material. It acts both as a flux, promoting the formation of melting phases of proper viscosity and as a direct gas source, by dissociation at elevated temperature with oxygen release. This phenomenon was studied by Hostetter and Roberts (1921) and they found that Fe_2O_3 started liberating oxygen at the temperature as low as 1000°C and 1300°C when it was heated in air and in pure oxygen at a pressure of one atmosphere respectively. They measured the percent of FeO formed when Fe_2O_3 was heated to different temperatures and found that at 1283°C only 0.4% of FeO was present. This increased rapidly until melting of Fe_2O_3 takes place at 1590°C, when the

product consists of magnetite which contains 31.1% FeO. This dissociation proceeds according to the reaction (Riley, 1951):

$$6Fe_2O_3 \Leftrightarrow 4Fe_3O_4 + O_2 \qquad (2.1)$$

They also found that the dissociation of Fe_2O_3 went on equally well when it was dissolved in a glass. It was observed by Sandrolini and Palmonari (1976) that the samples which bloated exhibit a red color at low temperatures, and turn to a more and more greenish-brown color as the temperature increases. This observation confirms the dissociation mechanism of iron oxide. They performed an analysis in order to determine the relative divalent and total iron contents of samples containing iron at the various temperatures. The total iron was determined by usual chemical analysis, while the determination of iron (II) oxide (FeO) was carried out by spectrophotometric analysis with *o* – phenanthroline. The results showed that Fe_2O_3 dissociation between 1000°C and 1100°C for red stoneware, while other samples studied exhibit the same dissociation above 1200°C.

Owen (1993) provides a summary about causes of gas evolution, he described that a gas can be developed by a number of different reactions, either singularly or in combination, from the following:

1. volatilisation of sulphides from about 400°C
2. decomposition of the water of crystallization from clay minerals at approximately 600°C
3. combustion of carbon-based compounds from approximately 700°C
4. decarbonation of carbonates from approximately 850°C
5. reaction of Fe_2O_3, causing the liberation of oxygen from about 1100°C

2.4 Application of the backscattered electron microscopy technique to cementitious materials.

The application of the backscattered electron image (BSE) for the microstructure analysis of the cementitious materials was first introduced by Scrivener and Pratt (1984). It was shown that with flat and well-polished cement sections, distinguishing the different cement phases, e.g. anhydrous, calcium hydroxide, pores, C-S-H gel and

aggregate, is possible. The contrast in the BSE image is produced based on the variations in the average atomic number within the specimen. The regions with high atomic number will appear brighter than those of low atomic number. Based on the calculated mean atomic number of various cement compounds, the brightness of phases could be arranged in the descending order as unhydrated cement grains, calcium hydroxide, other hydration phases and porosity (Scrivener and Pratt, 1984[a]; Zhao and Darwin, 1992). Typical BSE images of concrete microstructure are shown in Figures 7.1 to 7.6 and a more detailed explanation about individual phase identification is given in section 7.2.

The BSE image has been used by many researchers to study the microstructure of cement and concrete materials, including the determination of amount and distribution of the calcium hydroxide, anhydrous and porosity (e.g. Scrivener et. al., 1985; Scrivener et. al., 1987; Scrivener, 1989; Zhao and Darwin, 1992; Lange et. al., 1994; Crumbie, 1994; Diamond and Leeman, 1995; Wang and Diamond, 1995; Darwin et. al., 1995; Diamond, 2001[b]; Gallucci and Scrivener, 2007), analysis of clinkers and anhydrous material (Scrivener, 1987; Stutzman, 2004) and the interfacial transition microstructure between aggregate and cement paste (e.g. Scrivener and Gartner, 1988; Scrivener et. al., 1988; Pope and Jennings, 1992; Brough and Atkinson, 2000; Diamond and Huang, 2001; Head, 2001; Elsharief et. al., 2003; Elsharief et. al., 2005). With no doubt, this technique together with the image analysis system and/or an X-ray analysis system gives very useful information about the microstructure of the hydrated cement systems.

2.4.1 Sample preparation

The quality of the BSE image depends on the preparation of the sample. It is important that the specimen for this technique is really flat in order to eliminate the topographical contrast. Rough surfaces will give a poor image quality and affect the accuracy of the phase discrimination for the quantitative image analysis. The epoxy impregnation of the specimen is an essential process in order to fill pores, support the microstructure and enhance the contrast between the pores and other hydration products (Struble and Stutzman, 1989; Stutzman and Clifton, 1999). There are several artifacts that might occur due to the improper specimen preparation, e.g. cracks introduced

during the cutting or drying process, surface scratches and surface relief (difference in height between individual components), and these artifacts may cause the misinterpretation of the microstructural features. Stutzman and Clifton (1999) Head (2001) and Crumbie (2001) gave an example of artifacts that commonly occur from the specimen preparation process and discussed about how to avoid or minimize them. The procedure and some general guideline about the specimen preparation for the cement paste and concrete materials were given by Kjellsen et. al. (1991), Kjellsen and Monsøy (1996), Scrivener (1997), Stutzman and Clifton (1999), Detwiler et. al. (2001), Kjellsen et. al. (2003).

2.4.2 Selection of field and image magnification

The image analysis technique is normally used together with the stereology in order to quantify any interested parameters from the two dimensional image (see more detail for the image analysis and stereology technique in section 5.3). Generally, the area fraction is measured from the investigated image and for an isotropic material; this parameter is equivalent to the volume fraction (Hilliard, 1968). Because the microstructure of concrete is not homogeneous, a selection of area, image magnification and the number of images are very important steps in the image analysis for obtaining representative and reliable results.

A selection of area must be done as randomly as possible. A uniform random technique of choosing an area from the specimen surface which was subdivided into a set of small areas of equal size was recommended by Diamond (2001[a]). Head (2001) acquired the BSE image by systematic scanning across the specimen surface in a grid fashion. The selected area must have contrast enough for the researcher to differentiate the various interested features on the specimen surface. In addition, the area that contains any features which are not representative for the general microstructure of the investigated specimen should be avoided. Examples of the unwanted features are (Head, 2001; Diamond, 2001[a]):

- areas in which extensive microcracking has occurred (might occur due to the shrinkage cracking during specimen preparation process),

- areas influenced by any forms of attack that affect the concrete microstructure, e.g. sulfate attack and alkali silica reaction,
- areas that are likely to be carbonated.

Magnification of the BSE image is another important parameter that needs to be carefully considered because the sizes of features of interest that can be detected at a set magnification are a direct function of the pixel size. The resolution of individual features (e.g. pore, calcium hydroxide and unreacted cement grain) increases with magnification, but image size decreases. For example, a field at 500x magnification covers the equivalent of 16 fields at 2000x magnification. Therefore, for the higher magnification image, more fields need to be analyzed in order to get representative results. There are many researchers that have studied the effect of the image magnification on the accuracy of results in order to identify the optimum magnification at which all interested components could be adequately distinguished with a minimum number of fields needed for satisfying the required degree of accuracy (Scrivener et. al., 1987; Scrivener, 1989[a]; Mouret et. al., 2001). Scrivener et. al. (1987) found that the difference in the percentage area of porosity determined at 400x and 2000x magnification is small. The porosity at 400x magnification is generally slightly higher than the one at 2000x magnification. The effect of three different magnifications, i.e. 110x, 320x and 1000x, on the porosity measurement were studied by Scrivener (1989[a]). There was a large increase in the amount of porosity measured between 110x and 320x magnification. However, a slight increase of porosity was observed by increasing the magnification further to 1000x. The magnification of 400x was consequently regarded as satisfactory for the measurement of porosity in her study. The magnification of 400x and 1200x were used by Diamond and Leeman (1995) for studying the size distribution of the capillary pores in hardened cement paste samples and these magnifications appeared to provide reasonably accurate results. In general, the magnification of 400x or 500x was normally used for the study of the microstructure of cement paste and concrete (Scrivener et. al. 1987; Scrivener, 1989[a]; Diamond, 2001[a]; Head, 2001; Elsharief et. al., 2003).

A sufficient number of images or fields must be determined in order to obtain a reasonable estimated area fraction of each interested component within the sample. A statistical technique used to estimate the number of images required to achieve a given

level of accuracy was described by Zhao and Darwin (1992). This technique was used in this research (see section 4.10.2 for more detail explanation).

2.4.3 Study of the interfacial transition zone between cement paste and aggregate

In a composite material the behavior of the composite is determined by the physical and chemical properties of the constituents and the interaction between them. Concrete is one type of composite material which consists of aggregate and cement paste matrix. The mechanical bahaviour and durability of the concrete structure is therefore mainly affected by both cement paste and aggregate as well as the properties of the interfacial zone between them.

The electron microscopy technique has been used extensively to investigate the morphology and microstructure of the interfacial transition zone (ITZ) between cement paste and aggregate. Early work on this subject area using the SEM was done using the secondary electron (SE) mode (see section 5.2.3 for more details) which provides the qualitative information of the ITZ microstructure and used the composite model specimen which was initially developed by Farran in 1956 (cited by Scrivener and Pratt, 1996). This model consists of cement paste cast against a flat and usually well-polished block of aggregate and it was used extensively by many researchers in the past (e.g. Barnes et. al., 1978; Langton and Roy, 1980; Zimbelman, 1985). There is a general agreement that the microstructure of cement paste at the aggregate interface region differs from that at the region further away from the aggregate. However, the microstructure of the ITZ based on the qualitative information from the SE mode was still a subject of debate. A number of models of the ITZ were proposed by many researchers (e.g. Barnes et. al., 1978; Langton and Roy, 1980; Zimbelman, 1985; Monteiro, 1986).

Barnes et. al. (1978) described the characteristic of the cement paste at the interface between glass slide aggregate and cement paste as follow:

- A twin layer which they called 'duplex film' of thickness about 1.0 micron. This continuous film was deposited on the aggregate surface composed of layer of calcium hydroxide covered by a parallel layer of rod-shape C-S-H,
- A highly porous region compared to the bulk paste,

- Deposition of the calcium hydroxide crystals,
- This region contains a lot of Hadley grains.

The schematic representation of the ITZ microstructure according to the observation of Barnes et. al. is shown in Figure 2.2.

Langton and Roy (1980) proposed the schematic diagram which represents the characteristic of the multi-layered ITZ for both non-reactive and reactive aggregates. As shown in Figure 2.3, they found that the interfacial morphology depended on the reactivity of the aggregate and the degree of hydration of the cement paste.

Zimbelman (1985) provided a schematic representation of the contact zone between cement and aggregate. His diagram as shown in Figure 2.4 presents a multi-layer ITZ structure. The contact layer with thickness of approximately 2 to 3 microns is composed of calcium hydroxide and ettringite and this layer is followed by a very porous intermediate layer (about 20 microns thick) consisting mainly of larger crystal of calcium hydroxide and ettringite.

Monteiro (1986) believed that the weakness of the aggregate-cement paste transition zone is primary caused by the presence of very large crystals of calcium hydroxide with c-axis preferentially oriented in a direction normal to the aggregate surface. This is due to a higher porosity and water/cement ratio caused by internal bleeding around the interface region which enables a larger crystal with a better morphology of calcium hydroxide to be developed. Figure 2.5 shows the schematic representation of the Monteiro ITZ microstructural model.

These examples of the ITZ model differ mainly in respect of the presence of the C-S-H film and ettringite at the aggregate surface.

Monteiro and Mehta (1985) used the method developed by Grandet and Ollivier (1980) to analyze the interfacial zone. In this technique, successive abrasion of the interface was done in order to remove layers of the ITZ for the X-ray diffraction (XRD) analysis. They found that the concentration profiles for ettringite are very similar to the portlandite (calcium hydroxide) ones in which much larger quantities of ettringite are present immediately next to the aggregate surface than farther away from it. They explained this phenomenon by using the through-solution mechanism according to

which the calcium, sulfate, and aluminate ions quickly migrate to the water film at the aggregate surface and, therefore, more ettringite gets precipitated there.

There are several disadvantages of using the composite model specimen (Scrivener and Gartner, 1988; Scrivener and Pratt, 1996). Firstly, when casting cement paste with one piece of flat aggregate, the microstructure of cement paste can adjust over an infinite distance without any constraint from another aggregate particle. Secondly, the localized bleeding which leads to an increase in water/cement ratio at the interface region are more likely to occur with the flat surface aggregate. Moreover, the local rates of shear of cement paste and the movement of aggregate through the cement paste will significantly alter when the aggregate particles are not present during the mixing procedure.

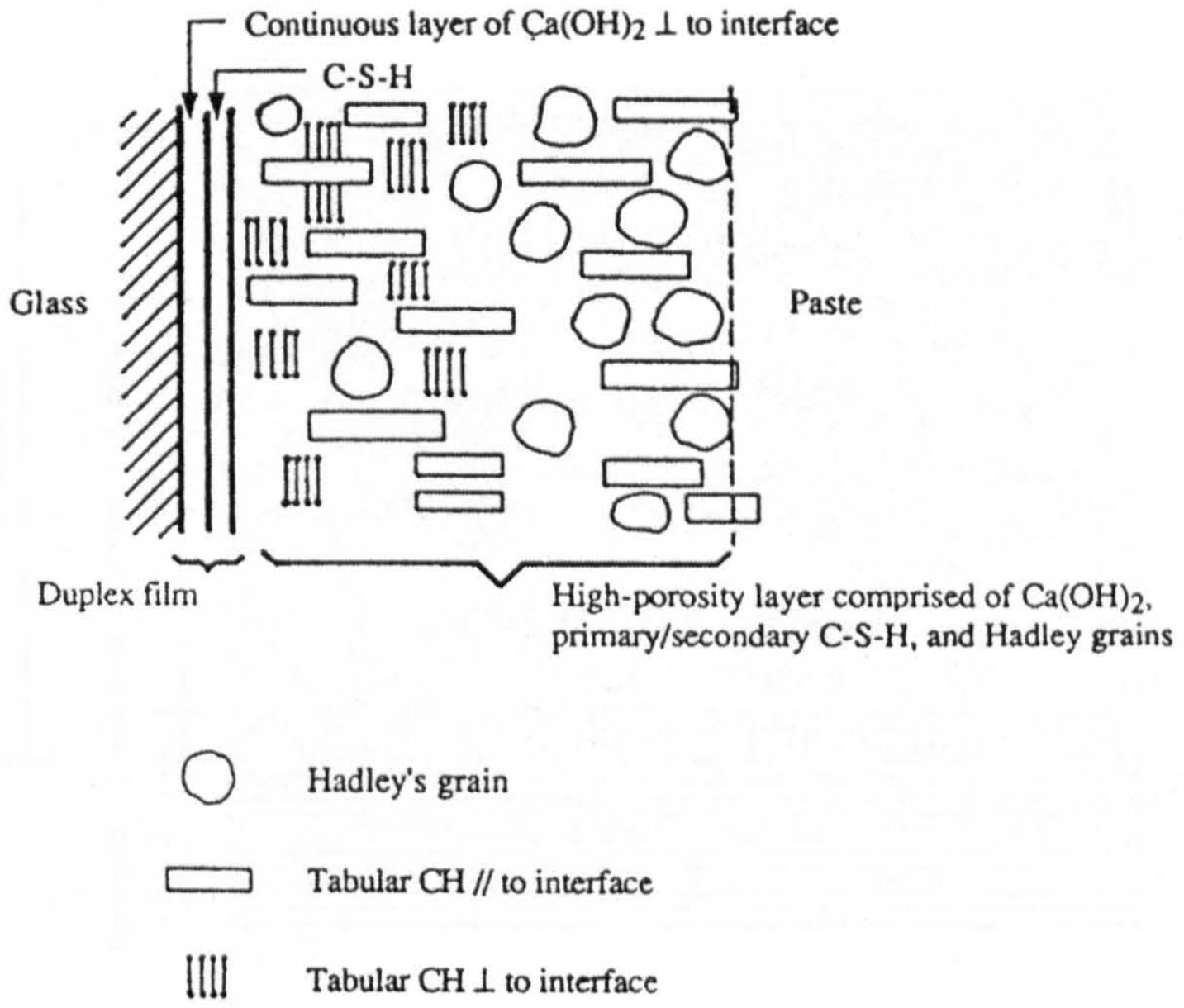

Figure 2.2 Barnes et. al. model presented by Maso (1980)

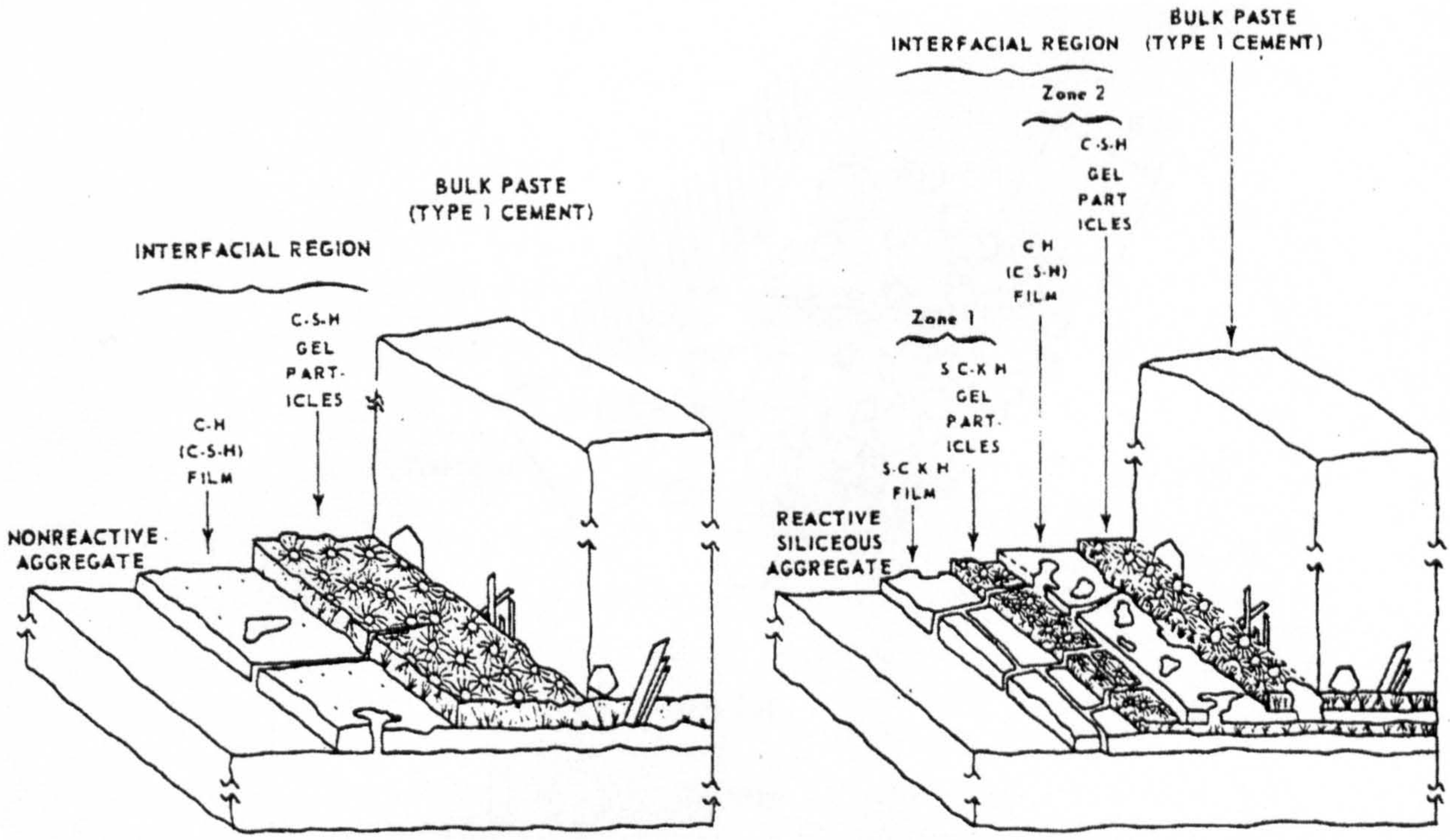

a) ITZ of non-reactive aggregate b) ITZ of reactive aggregate

Figure 2.3 Schematic diagram of the ITZ region (copied from Langton and Roy, 1980).

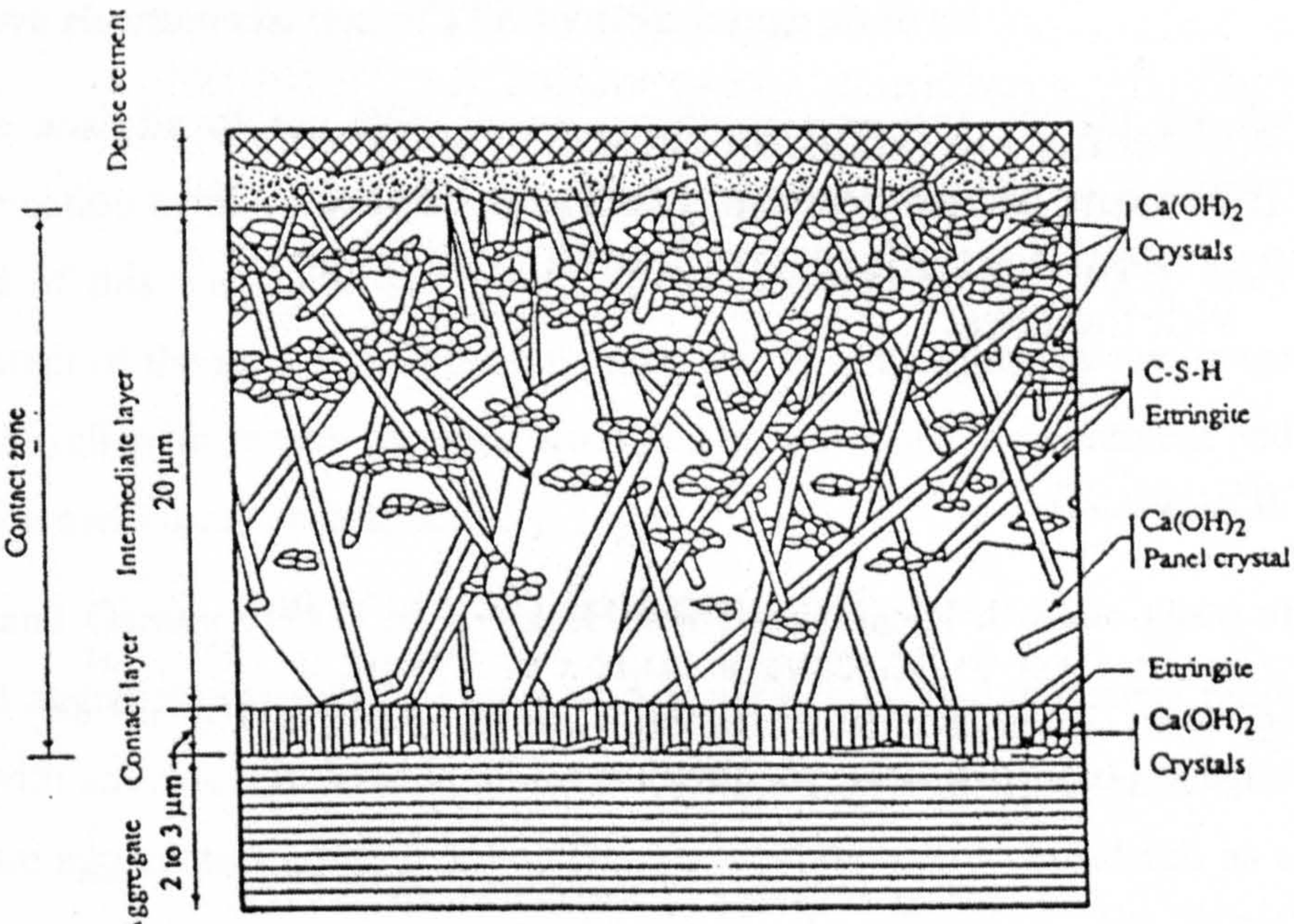

Figure 2.4 Zimbelman ITZ model (copied from Zimbelman, 1985).

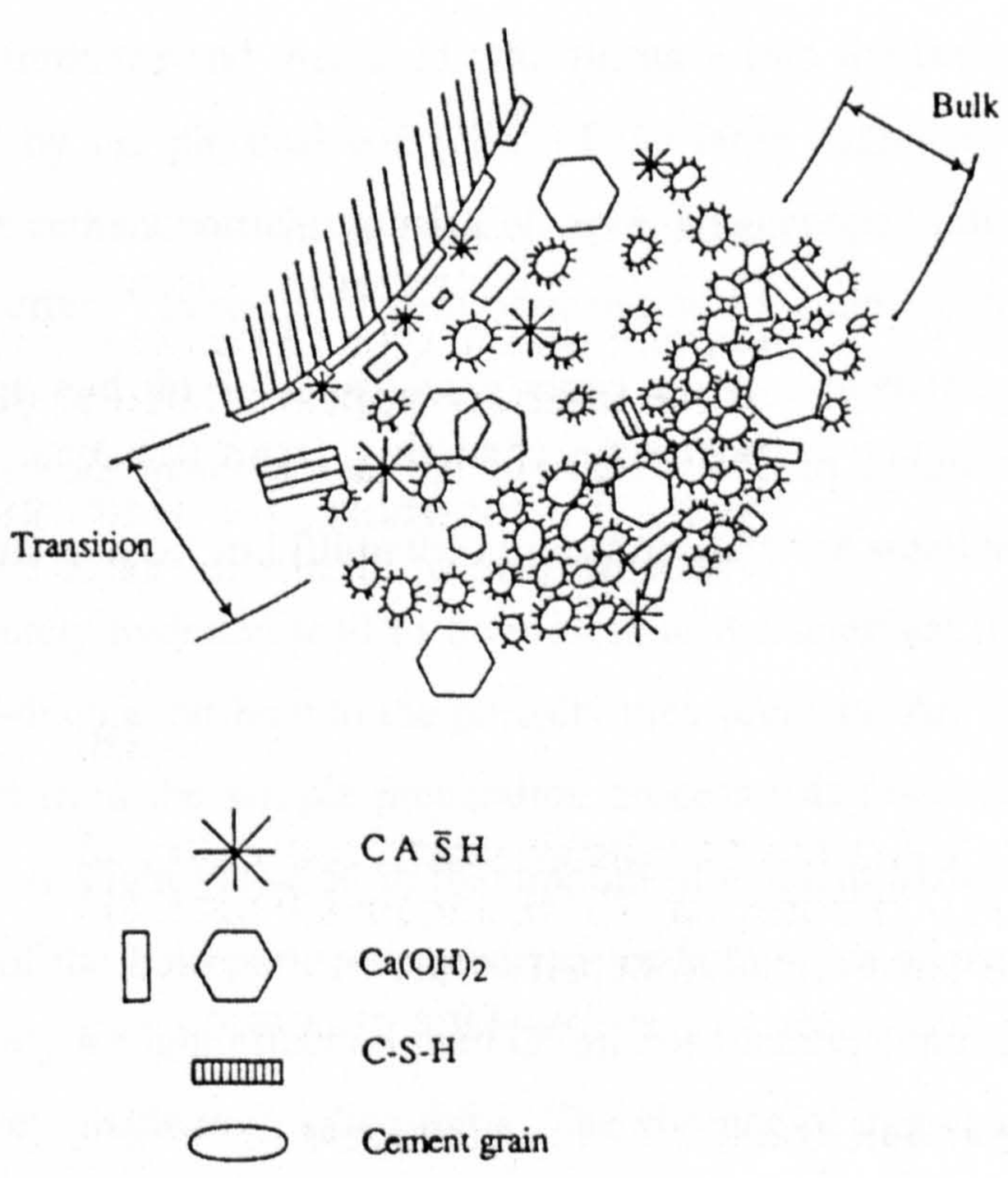

Figure 2.5 Monteiro ITZ model (copied from Monteiro, 1986)

2.4.3.1 Quantitative characterization of ITZ by BSE image analysis

The image analysis of the BSE image technique was first applied for the quantitative investigation of the cement microstructures by Scrivener and Pratt (1987). A general method of this technique was described by Scrivener et. al. (1987). They found that the content of the anhydrous material and porosity determined by the image analysis correlated well with results obtained from the bound water measurement and methanol absorption measurements respectively.

Scrivener and Gartner (1988) used a specimen consisting of a single piece of unpolished natural aggregate (granite, limestone and garnet) embedded in cement paste (w/c = 0.5) both with and without silica fume for studying the microstructural gradients at the cement paste-aggregate transition zone. These specimens were considered as a compromise between the earlier composite models and real concrete specimens. For each sample, 10 randomly selected areas (about 200 microns square) along the interface were taken for an image analysis. The area fraction of the anhydrous, calcium hydroxide and porosity were measured from a series of 3 microns deep bands equidistant from the aggregate surface. They found that the amount of the anhydrous material was very low at the region close to the interface and increased with distance into the cement paste. This result was explained by the physical constraint of the large aggregate particles making it difficult for large cement particles to pack close to the aggregate interface and this is known as the "wall effect". Porosity of both paste showed a dramatic increase as the interface is approached and three factors were given as an explanation for this. Firstly the lack of the anhydrous material near the interface results in a higher porosity and less anhydrous materials to react and fill in the space. Secondly the small anhydrous particles which are completely hydrated tend to be present at the interface region and create hollow pore shells which contribute to the porosity measurement. An increase in porosity due to the artifact from the sample preparation process was given as the last factor in their publication. A slight variation in the amount of calcium hydroxide with the values similar to that of the bulk paste was reported for both types of paste. Silica fume was found to have only a slight effect on the ITZ microstructure, contrasting with the observations for concrete made with silica fume. The absence of aggregate during the mixing process was considered as a primary reason.

The normally prepared concrete sample was used by Scrivener et. al. (1988[b]) for the ITZ characterization. They found that the amount of anhydrous material is very low at the interface and increases almost linearly up to a distance of about 30 μm from the interface. In addition, the porosity increased as the aggregate surface was approached (see Figure 2.6).

The results presented by Scrivener and Gartner (1988) and Scrivener et. al. (1988[b]) show that the BSE-image analysis technique is a very good technique to study the ITZ microstructure. However, with the random sectioning of the concrete specimen, the distance measured on the 2D sections can only be the estimated value. Crumbie (1994) estimated the correction factor by averaging the angles of intersection of random lines with the aggregate surface and the correcting factor of about 1.2 was found.

Scrivener et. al. (1988[a]) studied the microstructure of the transition zone in high strength concrete, with and without silica fume, by using the same technique as mentioned above. The normally prepared concrete and paste samples with the water/cement ratio of 0.33 were used in their study. The microstructure of both paste and concrete specimens were characterized quantitatively at the magnification of 400x and the area fraction of porosity, calcium hydroxide and anhydrous were obtained by the averaging of 8 fields. The distribution of the anhydrous material and porosity were found generally consistent with those reported previously (Scrivener and Gartner, 1988; Scrivener et. al., 1988[b]). However, for 1-day old concrete, silica fume was found to have little effect on the anhydrous distribution which suggested that the particle size distribution of the anhydrous alone determined the packing characteristic of the anhydrous particles at the interfacial zone region during the concrete mixing. On the contrary, significant reduction of porosity at the ITZ by adding the silica fume in the concrete was observed. This result was different from that obtained from the study on the composite model specimen reported by Scrivener and Gartner (1988). The ability of silica fume particles with size about 0.1 microns to pack closer to the aggregate interface during the casting process was given as an explanation. The quantitative analysis result for the calcium hydroxide distribution did not indicate the calcium hydroxide rich zone at the interface region as frequently reported on the basis of the conventional SEM observations on the fracture surfaces. In addition, in concrete sample, calcium hydroxide was found smaller and less distinct than that in the corresponding paste. The effect of the additional shearing of the paste created by the

presence of the aggregate particles during concrete mixing was suggested as a possible reason for this in their publication.

Pope and Jennings (1992) investigated the influence of mixing on the cement paste/aggregate interfacial zone microstructure by using the same technique as Scrivener et. al. mentioned earlier. The mixing process was designed in order to reduce the amount of mixing water and increasing the amount of the anhydrous material at the aggregate surface. This was done by pre-coating aggregate particles with a lower water/cement ratio slurry before the casting process. The distribution of porosity and anhydrous in the interfacial zone for all mixes were found generally similar to that observed previously (Scrivener and Gartner, 1988; Scrivener et. al.,1988[a,b]). However, the results indicated that the distribution of these two phases depends on the relative abundance of water at the aggregate surface during mixing. The paste/aggregate bond was found to be improved by reducing the amount of water that comes into contact with the aggregate during mixing.

The distribution of ettringite is very difficult to analyze by using the BSE-image analysis technique due to the very small crystals of this phase. However, it could be expected to have a higher concentration of this phase in a more porous ITZ region because the small anhydrous particles tend to have more interstitial phases (aluminate and ferrite phases) exposed on their surfaces (Scrivener and Gartner, 1988) and this is supported by many observations based on the model specimen (Monteiro and Mehta,1985; Monteiro, Maso and Ollivier, 1985).

The quantitative investigation of the cement paste and aggregate interfacial transition zone with the BSE-image analysis technique are extensively used by many researchers (e.g. Crumbie, 1994; Brough and Atkinson, 2000; Head, 2001; Elsharief et. al., 2003; Wong and Buenfeld, 2006) and the results obtained confirm the early quantitative observation of lower anhydrous material and higher porosity in the region close to the aggregate interface. The so-called "wall effect" has been used extensively to explain the origin of the ITZ. Scrivener et. al. (2004) gave a detail explanation about this effect and presented the schematic diagram representation of grading of the anhydrous material in concrete. The proposed diagram shows that the small anhydrous material appears predominantly at the region closest to the aggregate interface (about 15 microns) which leads to a significantly higher porosity in this region, while larger particles are found further out.

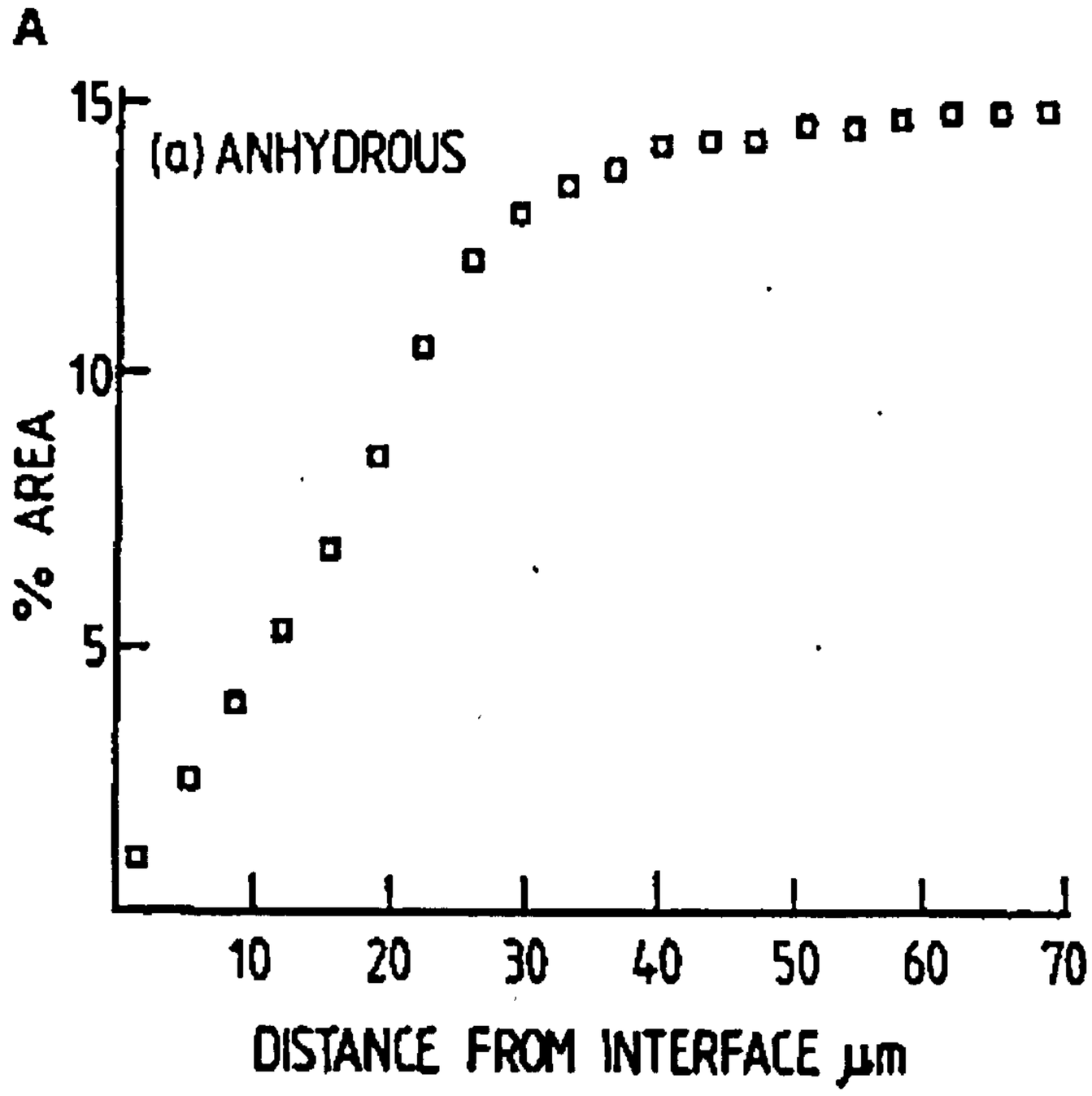

Figure 2.6 Microstructural gradients in the interfacial region of concrete: (a) unreacted clinker phases; (b) porosity (From Scrivener et. al., 1988[b])

2.4.3.2 ITZ microstructure for the lightweight aggregate concrete

In concrete containing lightweight aggregate, many researchers from the literature have suggested that the interfacial zone between cement paste and the lightweight aggregate particles is more dense and homogeneous than that found in normal weight concrete. The reason for this is due to the porous nature, rough surface and higher water absorption characteristics of the lightweight aggregate compared with normal weight aggregate. It is apparent that the characteristic of the transition zone is largely affected by the nature of the aggregate and the nature of the aggregate produced is mainly dependent on the firing condition during the production process.

Fagerlund (1978) analyzed the ITZ in mortar and concrete, and the mathematical equations were proposed to describe the influence of the interfacial zone on strength parameters. A virtually indistinguishable boundary between pumice and cement paste matrix was observed by using the electron microscope. The filtration effect, i.e. only water of the cement paste matrix can enter the porous aggregate particles, was given as a reason for the improvement of the quality of the cement paste matrix at the region close to the aggregate particle.

Zhang and Gjørv (1990) used a scanning electron microscope together with an energy dispersive X-ray analysis system to characterize the microstructure of the interfacial zone between different types of lightweight aggregates (Liapor, Leca and Lytag) and cement paste. The aggregate was first dried in oven at 105°C and then pre-mixed with water for 10 minutes prior to mixing. The rest of the materials were then added and mixed for another 10 minutes. The plastic bottles (35 mm diameter x 55 mm height) were used as a mould and the bottles were rotated for 24 hours in order to avoid separation. The specimens were cured under water at approximately 20°C for 3 months. The section that was cut from the center part of the cured sample was dried in acetone and then impregnated by epoxy resin. The polished section was coated with carbon and then analyzed by the scanning electron microscope. By using the elemental X-ray dot maps of calcium (Ca), sulfur (S) and silicon (Si) in conjunction with the backscattered electron (BSE) images of the same area, they could obtain qualitative information on the nature of the interfacial zone between lightweight aggregate and cement paste. They observed a non-continuous region between the aggregate having a dense outer layer and the cement paste with a thickness of approximately 20 to 60 microns. In addition, the paste appears to be more porous in this region and a band of massive calcium hydroxide

was observed near the aggregate interface. Ettringite that was indicated by using the sulfur (S) dot map was also observed in some areas close to the aggregate particle. For the aggregates without a dense shell or those that had a porous surface texture, rather well bonded between cement paste and lightweight aggregate particle and almost no calcium hydroxide rich zone near the aggregate particle were observed. They also observed the penetration of calcium and ettringite in some areas where the aggregate was very porous. They concluded that for high strength lightweight aggregate having a very dense outer layer the nature of the interfacial zone is similar to the one observed around the normal weight aggregates. On the contrary, the interfacial zone for concrete containing lightweight aggregate with porous outer layer or the one with no dense outer shell was found more dense and homogeneous than that found in normal weight concrete. Moreover, the penetration of the calcium (Ca) and sulfur (S) into the porous lightweight aggregate was observed. The bonding between cement paste and aggregate without dense outer shell was expected to be better partly due to a better ITZ microstructure and partly due to an improvement of the mechanical interlocking between aggregate and the cement paste matrix.

Bentz et al. (1992) applied a digital-image-based microstructural model to simulate the microstructural development of the interfacial zone between cement paste and aggregate in a variety of concretes including concrete containing lightweight aggregate. The results from their simulation showed an improvement of the ITZ microstructure of the lightweight as compared to the normal weight aggregate concrete. They explained that the cement particles were rearranged due to water absorption by the aggregate and this lead to a more dense packing of the cement grains near the lightweight aggregate particle.

Sarkar et. al. (1992) examined the effect of using the expanded clay lightweight aggregate on the concrete strength properties. Four lightweight aggregates used in their studied including a Swedish Leca, and Liapor 5, 6 and 8 from Germany. The results from X-ray diffraction (XRD) showed that the mineralogical compositions of aggregates are composed of quartz, anorthite, ringwoodite, hematite and mullite. Quartz was found to be the principal mineral component but the results from ionic solubility test showed that the ionic dissolution of silicon was recorded as negligible. They explained this phenomenon by the fact that most of the silicon was bound in the crystalline silica and silicate minerals. The optical microscope was used to investigate the outer surface of the lightweight aggregate. The optical micrographs showed a distinct thick external shell in

the Swedish Leca and it also appears to be impermeable. Liapor, on the other hand, has an indistinct outer shell with a number of jagged features. They used the energy dispersive X-ray (EDX) dot maps technique to identify the elemental distribution in the aggregate and cement paste regions. The presence of the calcium-enriched paste-aggregate interfacial zone in some lightweight aggregate concretes as claimed by Zhang and Gjørv (1990) was found indistinguishable in this study. The paste-aggregate bond characteristic was investigated by SEM analysis of the fracture surface. The intimate bond between the paste and aggregate with rough aggregate surface which can act as an anchor for the paste was observed and this is consistent with the observation of Zhang and Gjørv (1990). The microstructural observation also indicates the dependence of the paste-aggregate bonding on the nature of the external shell of the aggregate.

Wasserman and Bentur (1996, 1997) studied the ITZ around the Lytag (sintered fly ash) lightweight aggregate. They modified the structure and properties of aggregate by heating at various temperatures or by polymer treatments to obtain aggregates with different strengths, absorption and pozzolanic activity. The results from XRD showed that the quantity of quartz which is the principal mineral composition of the original aggregate reduced with increase in temperature and part of the reduction in quartz was accompanied by the formation of additional glassy phase. They used the Energy dispersive X-ray analysis in order to determine the calcium (Ca) and silicon (Si) contents and profiles of calcium/silicon ratio across the aggregate-paste interface were drawn. Figures 2.7 to 2.9 were extracted from their publication which show the calcium/silicon ratio profiles across the aggregate-matrix interface for untreated Lytag aggregate, aggregate treated by heating to 1250° C with rapid cooling and 1300° C with slow cooling respectively. It was found that the calcium/silicon ratio of the aggregate shell itself is about 0.15 and that of the bulk paste is about 3. They used the calcium/silicon ratio profiles to estimate the width of the interfacial zone as the zone in which the calcium/silicon ratio is high, and it was about 4, 25 and 40 microns for the original Lytag aggregate and the ones treated at 1200 and 1300° C, respectively. They gave the reason why the untreated aggregate had the lower value was due to the higher water absorption of this aggregate which prevents the accumulation of water at the interface. The width of ITZ was found to decrease linearly with the water absorption of the aggregate. However, for 90 days old concrete, a high calcium/silica ratio curve penetrated deep into the aggregate in the untreated Lytag aggregate (Figure 2.7), whereas in the treated aggregate, in contrast, this ratio declined gradually within the aggregate boundaries. They explained

that in the original Lytag aggregate the pore solution can penetrate effectively into the porous aggregate and the calcium hydroxide was formed in the aggregate pores. A reduction of the calcium/silicon ratio at the ITZ of the high temperature heat treated aggregate after 90 days of curing was attributed to the pozzolanic reaction between aggregate and calcium hydroxide. The results from the compressive strength test showed different trends in strength development at the early and later age of concretes. From these results combining with the SEM observation, they concluded that the additional strength besides from the strength of aggregates were associated with the physical and chemical characteristics of the aggregates. The physical process was found to occur at early age and it was governed by the absorption of water into the aggregate, i.e. the accumulation of water in the fresh matrix in the vicinity of the aggregate was eliminated by higher water absorption which makes the interfacial transition zone denser. The chemical processes were associated with pozzolanic activity of the aggregate and calcium hydroxide and these processes became effective only at the later age, beyond 28 days. The enhancement in strength due to these influences was found to range between 20 and 40%.

Elsharief et. al. (2005) investigated the effect of dry and pre-wetted expand shale lightweight aggregates on the ITZ microstructure by using the BSE-image analysis technique. To the author's knowledge, this is the only publication that reported the quantitative information about the porosity and anhydrous distribution at the ITZ around the lightweight aggregate. The microstructural gradient around the lightweight aggregate in both conditions was found generally similar to that of the normal weight aggregate (see Figure 2.6), i.e. higher porosity and lower amount of anhydrous at the interface region as compared to the bulk paste and these properties change as a function of the distance measured from the aggregate interface until they gradually reach the levels observed in the bulk paste. Only small differences in the ITZ microstructure between dry and pre-wetted lightweight aggregate mortar was observed. The ITZ thickness was estimated based on the porosity distribution and the values of about 10 and 15 microns were discovered for the dry and pre-wetted lightweight aggregate respectively. The thickness of about 35 microns was reported for the normal weight aggregate mortar prepared with the same water/cement ratio. Their results also indicated that the paste located between 10 to 50 microns from the lightweight aggregate interface appears to be denser than the bulk paste matrix and the absorption of water by the lightweight aggregate was given as an explanation.

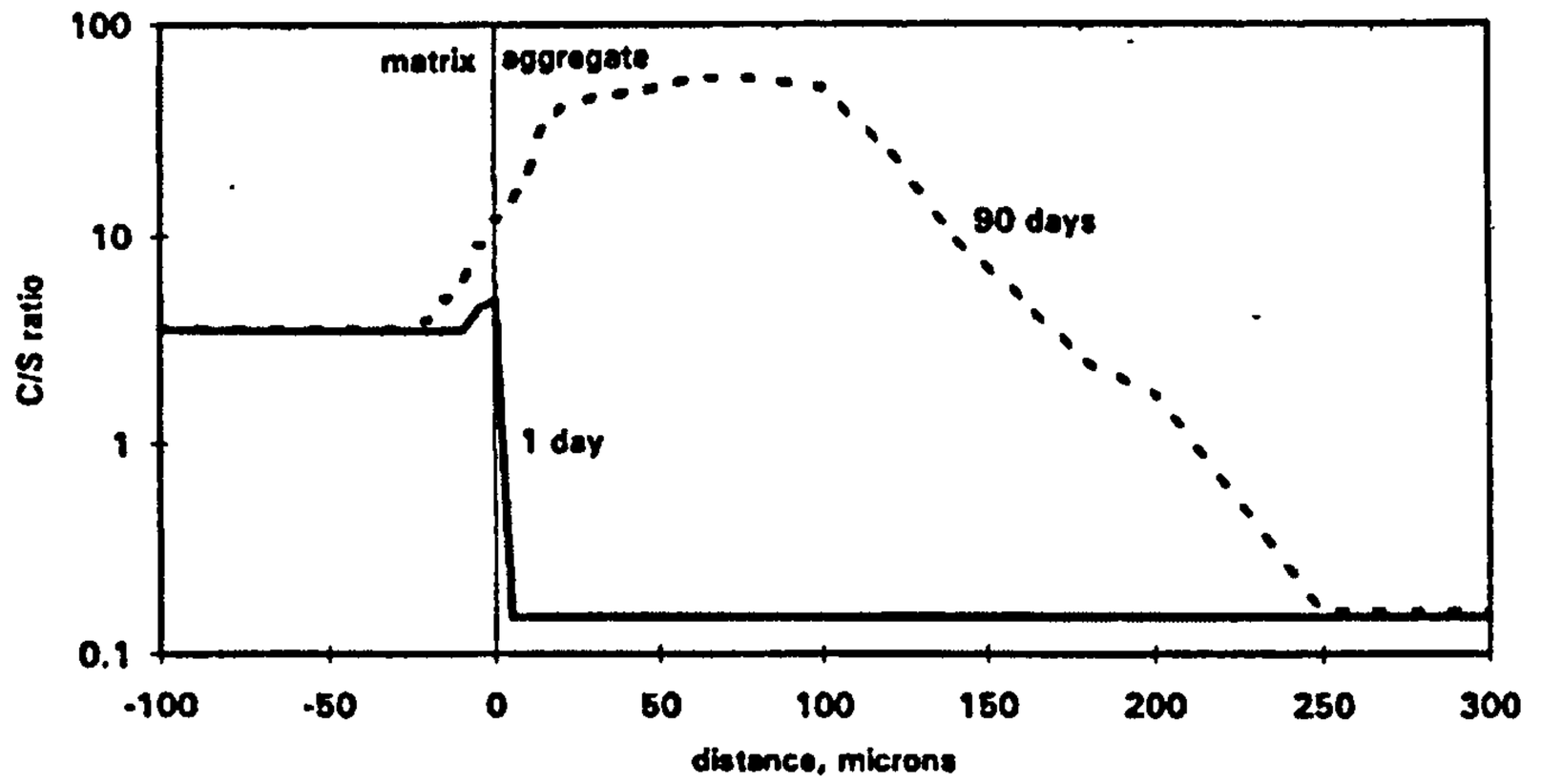

Figure 2.7 C/S ratio profiles across the aggregate-matrix interface in 1 and 90 day-old concretes with untreated Lytag aggregate (from Wasserman and Bentur, 1996).

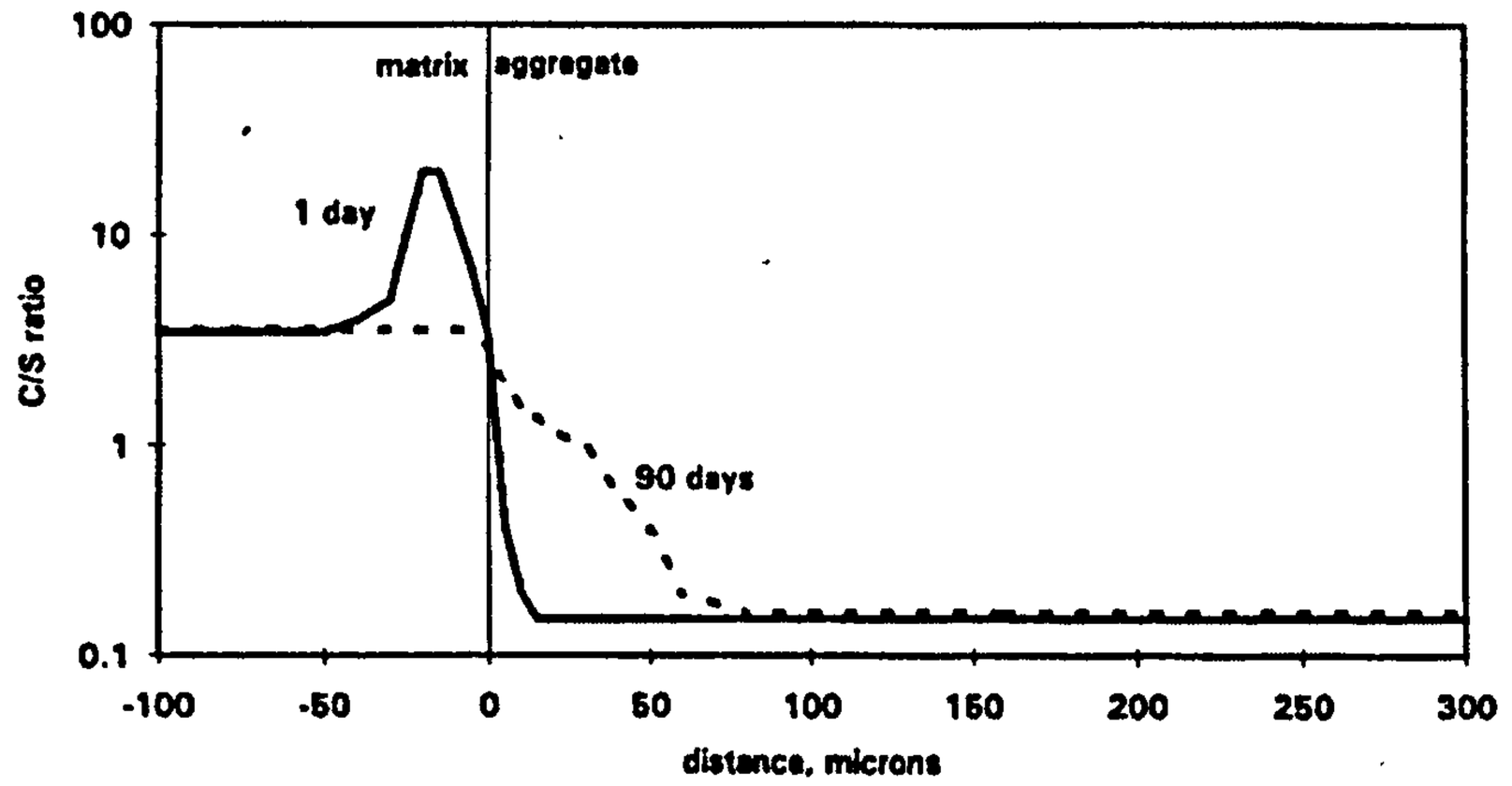

Figure 2.8 C/S ratio profiles across the aggregate-matrix interface in 1 and 90 day-old concretes with L1250 aggregate (from Wasserman and Bentur, 1996).

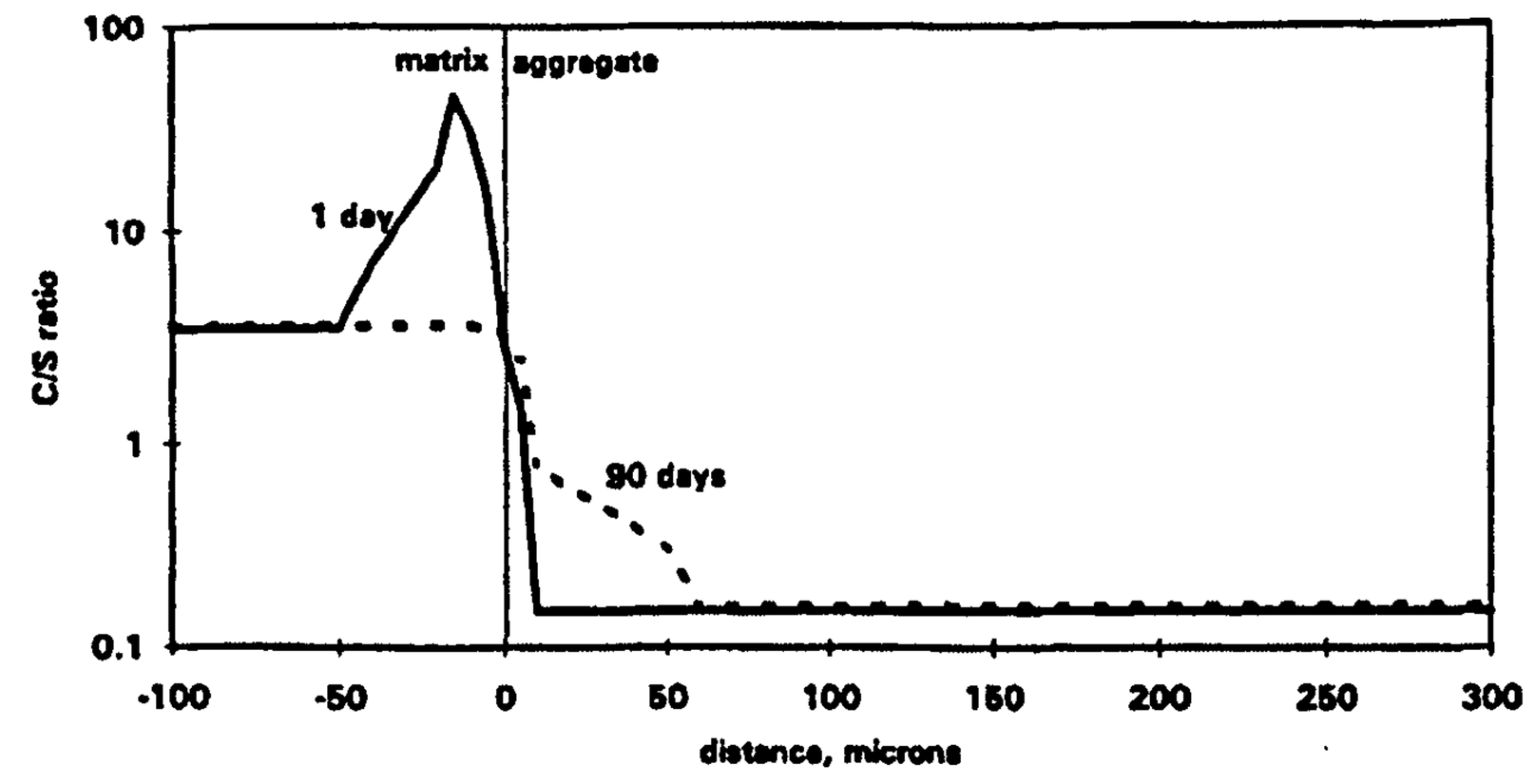

Figure 2.9 C/S ratio profiles across the aggregate-matrix interface in 1 and 90 day-old concretes with L1300SC aggregate (from Wasserman and Bentur, 1996).

2.5 Summary

Most of the studies published in the literature involve only the investigation of the influence of lightweight aggregate produced from waste materials on the properties of concrete. However, there is a lack of data on the effect of the production process on the properties of synthetic aggregate and more information is required in this area to help improve and control the product properties. Therefore, for this research, it was decided to investigate the effect of firing conditions on the properties, i.e. water absorption and relative density, mineralogical and microstructural evolution upon firing of the synthetic aggregate.

The specimen preparation technique for the microstructural analysis of both synthetic aggregate and concrete specimens are highlighted and reviewed within this chapter. There is a generally accepted procedure for the specimen preparation which needs slight modification according to the different types of material tested.

The literature review has revealed that the microstructure of the interfacial transition zone (ITZ) between the aggregate and the cement paste is different from the bulk paste. In addition, results obtained from many studies showed the influence of the ITZ on the performance of concrete. Therefore, it is important to understand the nature of the ITZ. Most of the previous study has been done using natural aggregate and a lot of useful quantitative information about the ITZ microstructure is reported by many researchers. However, the quantitative information of the ITZ for the lightweight aggregate concrete (or synthetic aggregate in this study) is still lacking. Therefore, in order to improve the understanding of the ITZ of concrete containing lightweight aggregate and develop an understanding of the synthetic aggregate-cement paste interface, quantitative analysis of the microstructure was decided to be the second objective of this research.

Chapter 3

Synthetic aggregate production

3.1 Introduction

In this chapter the general information of the raw materials used for the production of the synthetic aggregate are given and then the synthetic aggregate production process including pelletisation and firing are described.

3.2 Glensanda granite quarry waste

This material arises from the washing of crushed stone coarse aggregate and sand from the Glensanda super quarry on the West Coast of Scotland. About 1 million tons (dry weight) of the granite washings cake are created per year from this quarry (Wainwright et. al., 2002). These materials are fine in nature with 99.5 % of the material passing 300 micron sieve and 80.3 % passing 40 micron sieve. The particle size distribution characteristic of this material is given in Figure 3.1.

Microns	Cumulative % passing
300	99.5
150	95.6
75	86.9
40	80.3
20	68.9
10	52.7
5	36.5
2	21.1
1	14.6
0	0

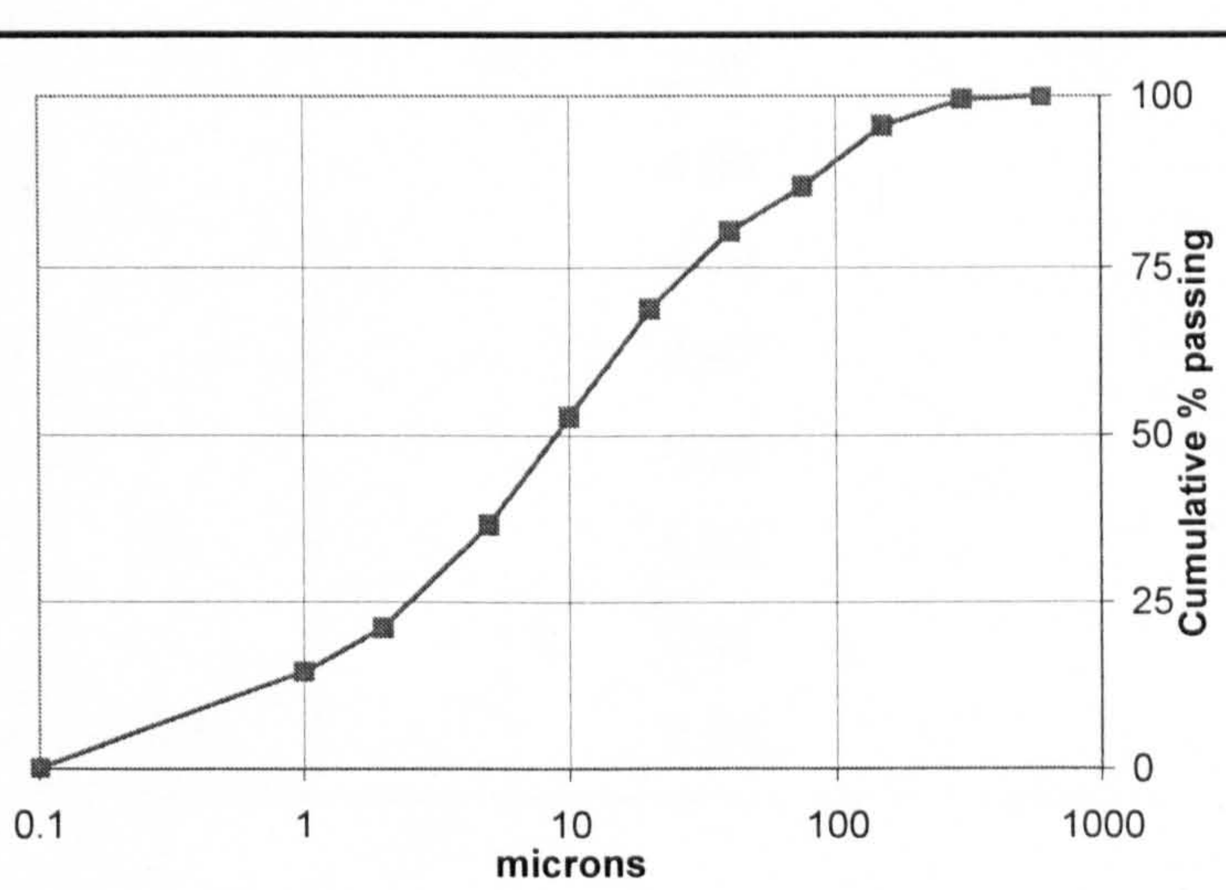

Figure 3.1 Particle size distributions of the Glensanda granite quarry waste (Wainwright et. al., 2001).

The chemical composition of the washings is given in Table 3.1. The main mineral components, according to the results from the XRD and the electron

microprobe analysis, are quartz, feldspars (plagioclase and K-feldspars) and quartz with some mica (biotite and muscovite mica), chlorite and calcite (see section 6.3 and 6.4 for more details). The washings are received in a range of consistencies from thick slurry to a 'cake' corresponding to a dry solids range of between 50 to 70 %. It is very homogenous in nature and forms large agglomerated pieces that have good cohesion, but do not behave in a plastic manner, i.e. when the material is worked with the hands it crumbles and does not form shapes readily. When the washings are oven dried the material is very difficult to break down into a powder except by mechanical means.

Table 3.1 Physical properties and chemical composition data for Glensanda granite washing.

Oxide composition	%
SiO_2	60.04
Al_2O_3	14.08
Fe_2O_3	2.85
MgO	1.29
CaO	2.99
Na_2O	4.04
K_2O	4.14
TiO_2	0.47
P_2O_5	0.16
Mn_3O_4	0.07
Cr_2O_3	0.01
Loss on ignition at 1,025˚C	2.64

3.3 Ball clay

The clay once formed from the parent rock may be deposited at its place of origin, or may be transported by water and redeposited at some distance from its place of origin. Ball clay is sedimentary clay deposited under fresh water or brackish conditions and composes predominantly of kaolinite, mica and fine quartz with a minor amount of mixed layer mineral, smectite and carbonaceous material. It has a fine grain

size in nature and its particle size distribution is shown in Figure 3.2. The kaolinite in ball clay is generally much finer than that found in china clay and this gives ball clay a greater plasticity and dry-strength than the china clay (Ryan, 1978). However, it is often contaminated with high contents of impurities which are not easy to remove. The ball clay used in this research project was supplied by WBB Devon Clays and its chemical and mineral composition is given in Table 3.2.

Table 3.2 Chemical and mineral composition data of the Devon ball clay.

Major oxide	%	Mineral composition	% w/w
SiO_2	60.9	Kaolinite	36 - 42
Al_2O_3	26.0	Micaceous mineral	25 - 29
Fe_2O_3	0.90	Quartz	23 - 27
MgO	0.30	Carbonaceous material	< 1
CaO	0.10		
Na_2O	0.40		
K_2O	2.60		
TiO_2	1.50		
Loss on ignition	7.20		

Note: data from manufacturer's data sheet

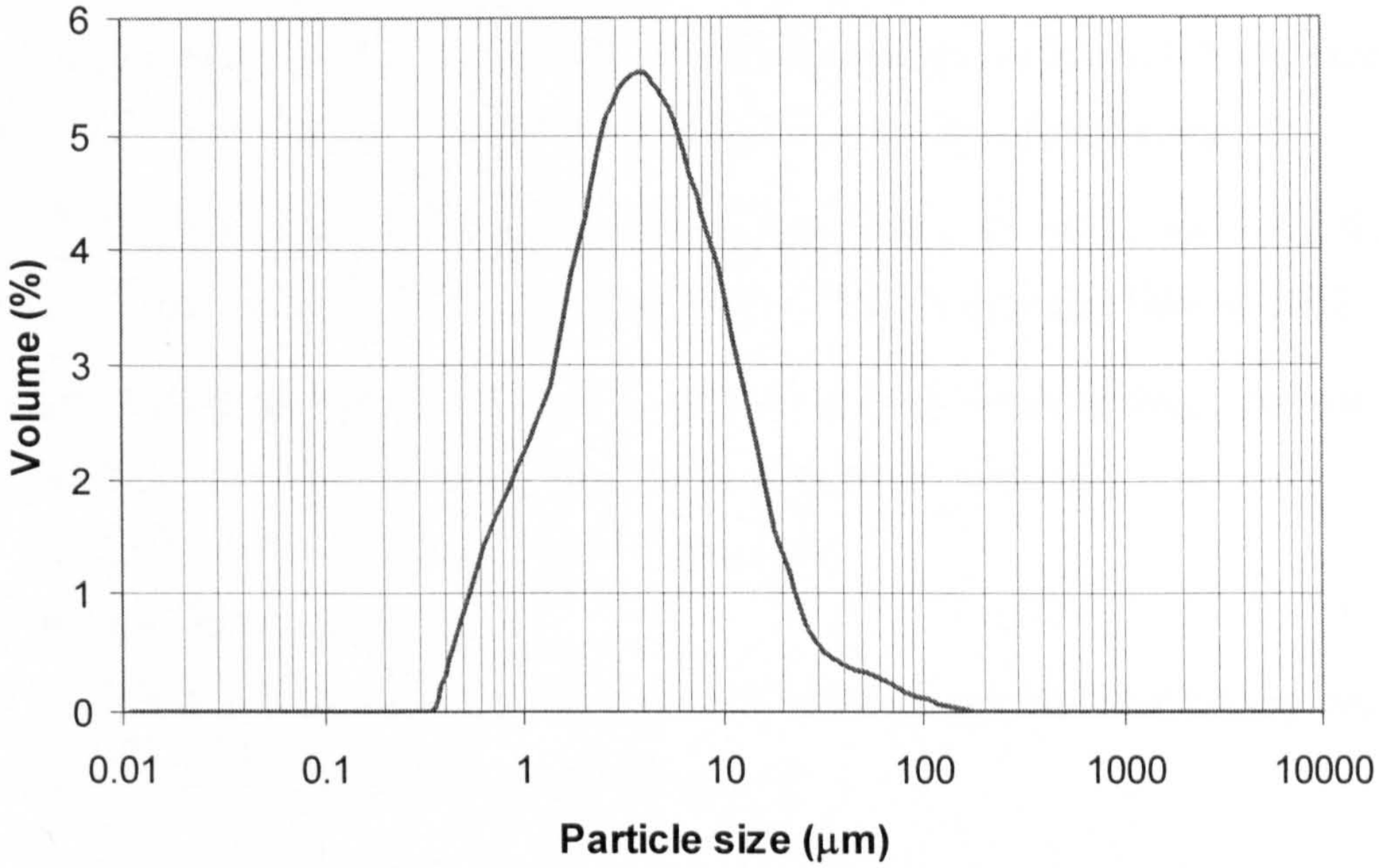

Figure 3.2 Particle size distribution of Devon ball clay used in this research.

3.4 Synthetic aggregate production process

In general, the synthetic aggregate production process consists of the following steps:

- Mixing of raw materials
- Green pellet production by pelletisation process
- Green pellets drying
- Firing of dry pellet by using the Trefoil rotary kiln.

Due to the restricted time allowed on this project, only one mix proportion was considered in this study, this was 95 % of Glensanda granite washing and 5 % of ball clay by weight.

3.4.1 Pelletisation process

The agglomeration of the moisturized fine-grained materials that have cementitious properties either by themselves and/or by blending them with a binder material into larger particles is named as the pelletisation process (Baykal and Döven, 2000). The agglomeration process is conducted by means of a rotating drum or disc and the end products of this process are called 'pellets'. More precise terms such as wet, dry

or green (unfired) pellets may be used to identify this product depending on the stage they are at within the production process. The strength of the pellet must be sufficient to prevent it from breaking up on handling before, during or after firing in the kiln.

The performance of the pelletisation process was shown to be a function of (Sastry and Fuerstenau, 1973; Srb and Ruzickova, 1988; Baykal and Döven, 2000):

- the engineering properties of the material such as surface charge, particle size, particle size distribution, particle shape and surface texture;
- the amount of, and type of binder if required;
- the moisture content;
- parameters from the mechanical process such as the angle of balling drum or disc to the normal and the revolution speed.

There are two different types of force that contribute to the formation of the green pellet, i.e. natural (or physical) and applied (or mechanical) forces (Srb and Ruzickova, 1988). The natural forces responsible to the formation of agglomerates can result from (Sastry and Fuerstenau, 1973; Pietsch, 1991):

- the attraction forces between solid particles due to molecular forces, i.e.Van der Waals' forces and chemical binding forces (valence forces), electrostatic forces and magnetic forces;
- the interlocking effects between particles;
- the adhesion and cohesion forces in not freely movable binders;
- the interfacial and capillary forces due to the presence of liquid phase.

In order that the natural forces can bring about the coalescence of fine particles, mechanical forces are applied in order to bring the individual wetted particles, cluster or agglomerate species within the palletizing charge into contact with one another by means of rolling, tumbling, agitating, kneading, compressing or extruding (Sastry and Fuerstenau, 1973).

There are many types of pelletisation techniques and the choice of each method depends on the binder properties of the powder and the strength, shape and size distribution of the product required. The agglomeration technique can generally be classified as pressure agglomeration, balling pelletisation and pressure extrusion (Boni, 1980). With pressure agglomeration, powders are compressed by static and vibratory

forces into the correct shape. The use of a binder or water is not generally required for this technique. In balling pelletisation, powders are tumbled in a rotating drum or inclined disc and seeded with water droplets. This process relies on the capillary forces developed between the moist fine particles. The initial 'nuclei' is formed when the moisturized particles contact each other. The agitation of the pan or drum provides the mechanical forces necessary to form the ball shape structure and force the air voids out. The size distribution and the strength of the pellets depend on the diameter of the drum, rotational speed and the tilt angle of the pelletiser and the feed rate of the dry powder and the amount of liquid binder. In the pressure extrusion, the powders are mixed with a binder and/or liquid to form a plastic mass and then forced through holes or dies into cylindrical shape pellets.

The extrusion and balling in the rotating drum are the techniques that were found appropriate for the materials used in this research (Wainwright et. al., 2001). The detail explanation of these techniques will be given in the following section.

3.4.1.1 Mixing of raw materials

The first stage of the synthetic aggregate production process was to blend the Grensanda granite washing with the ball clay binder in order to enable the mixture to be extruded and pelletised. The mixes were prepared in a large capacity floor mounted planetary mixer as utilised in the food industry as shown in Figure 3.3(a). This equipment consists of a stainless steel bowl and 'K' hook stirrer with four possible speeds of between 30 and 120 revolutions per minute. The maximum capacity of this mixture is approximately 15 kg when used for mixing the plastic mass that was needed for extrusion, which was the next step of the production process. The materials had to be loaded and unloaded manually. The controlled amounts of the quarry waste and a clay binder were combined in the mixer bowl. The appropriate amount of water was carefully added during the mixing process if necessary. All weights were recorded and representative samples were taken after mixing for moisture content determination.

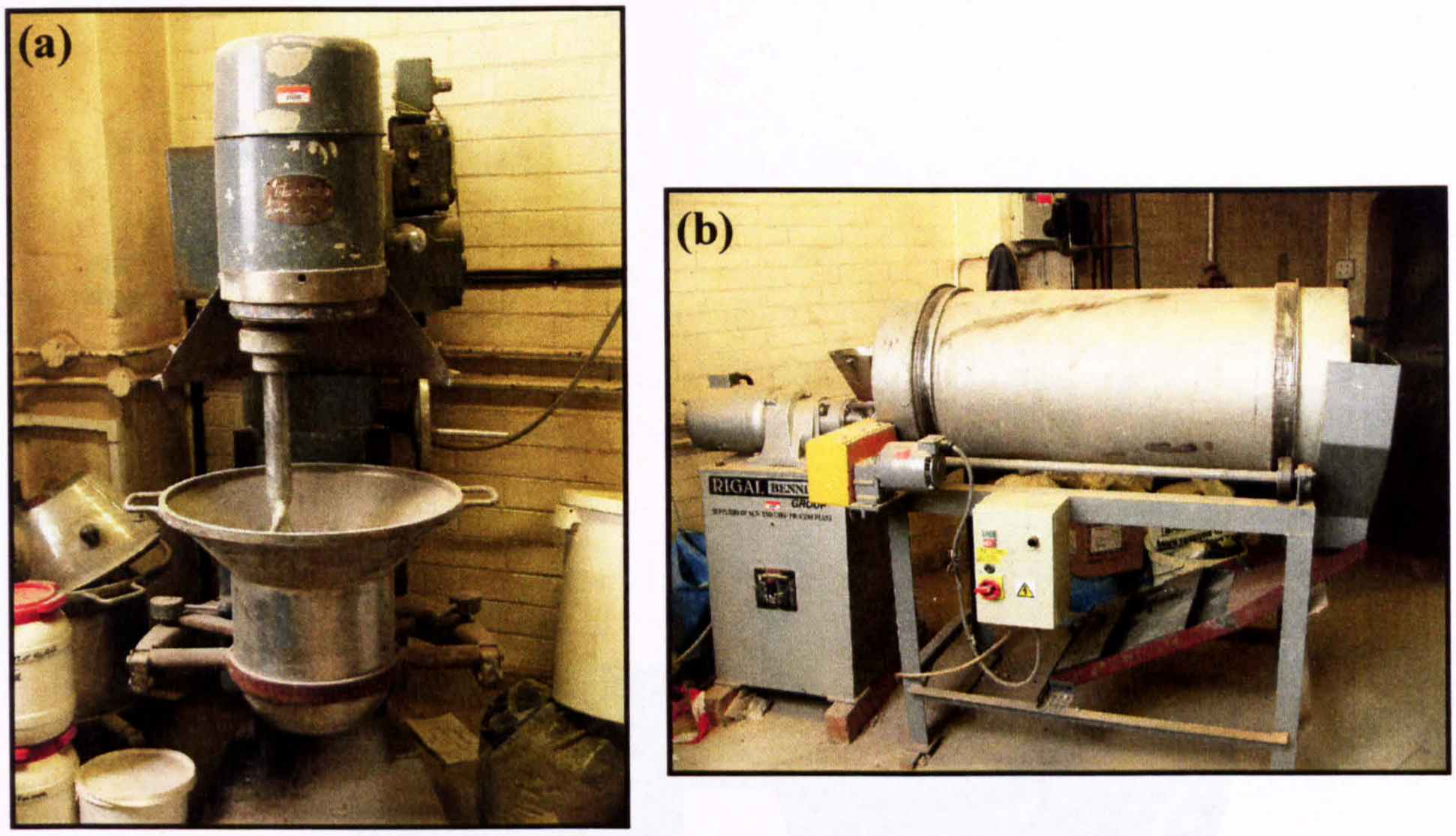

Figure 3.3 The Leeds mixing equipment and the extruder. a) Floor mounted planetary mixer. b) Single screw fed extruder and rotary drum pelletiser.

3.4.1.2 Extrusion and balling

The blended mixture was manually fed through a single screw fed extruder and pelletised by means of a rotary drum pelletiser as shown in Figure 3.3(b). The extruder was fitted with a 5mm thick die plate (end plate) with four holes. A number of plates were made with 8, 10, and 12 mm diameter holes. An end plate incorporating four 12mm diameter holes aligned horizontally across the centre of rotation of the screw was used in this study. The rotation of the screw was approximately 15 rpm and was not variable. The materials were fed by the extruder through the end plate and the slugs of plastic mass material were then produced which broke off and fell directly into a rotating drum. This drum broke down the slugs further and rolled them into a spherical shape pellets. The rotational speed of the drum was approximately 30 rpm and its size was 1200mm (length) x 500mm (diameter). The area of the discharge openings of the drum could be varied from 10 to 40 percent of the circumference of the drum in order to control pellet residence time. The angle of inclination of the drum was set at approximately 1°. The green pellets obtained were then oven dried at 105°C for 24 hours. The dry pellets were kept in a plastic sample bags and kept in the dry place before the firing process. A schematic representation of this pelletisation process is shown in Figure 3.4 and the example of the green pellets is shown in Figure 3.5.

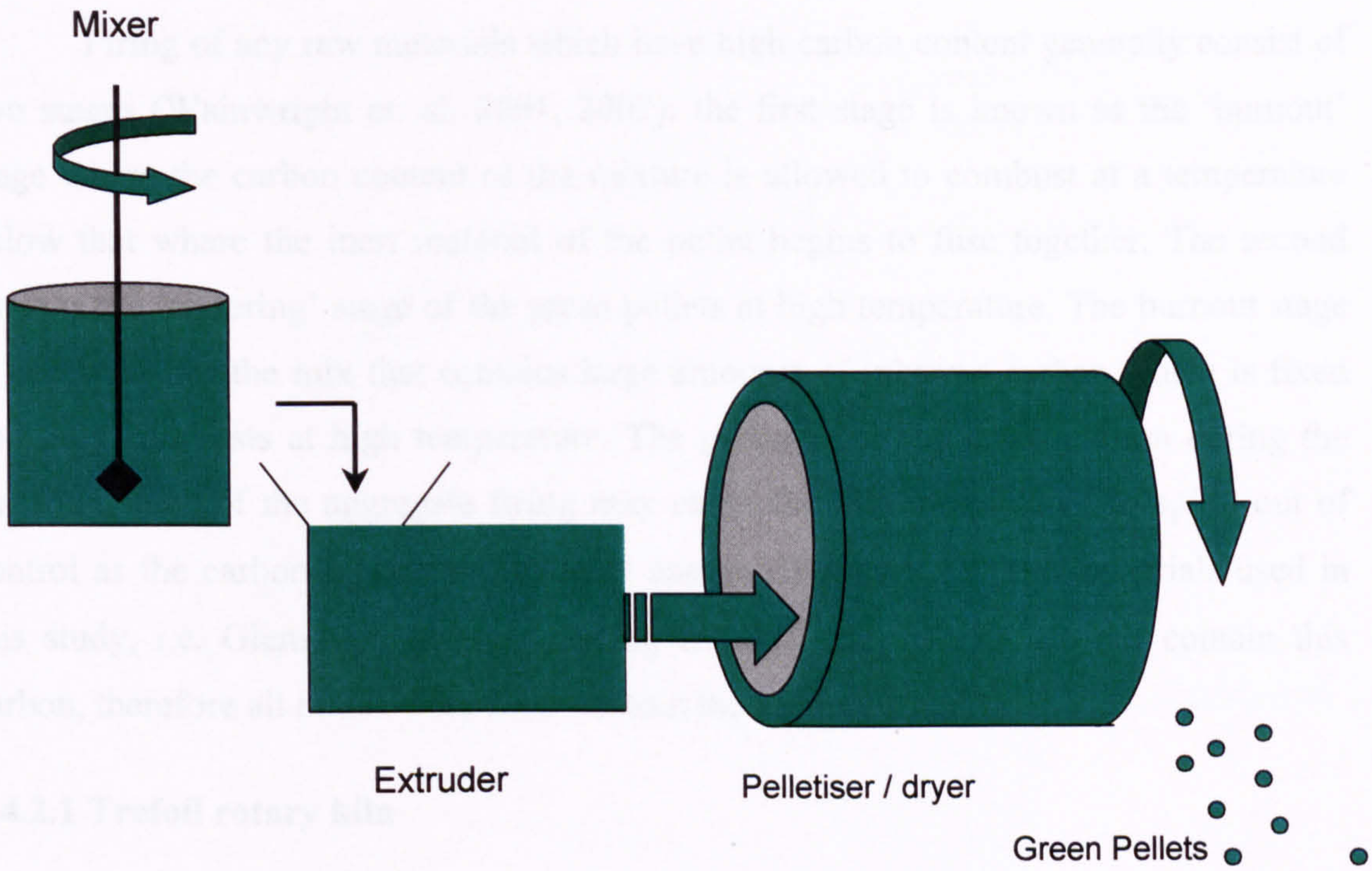

Figure 3.4 Schematic representation of green pellet production process (Wainwright et. al., 2001).

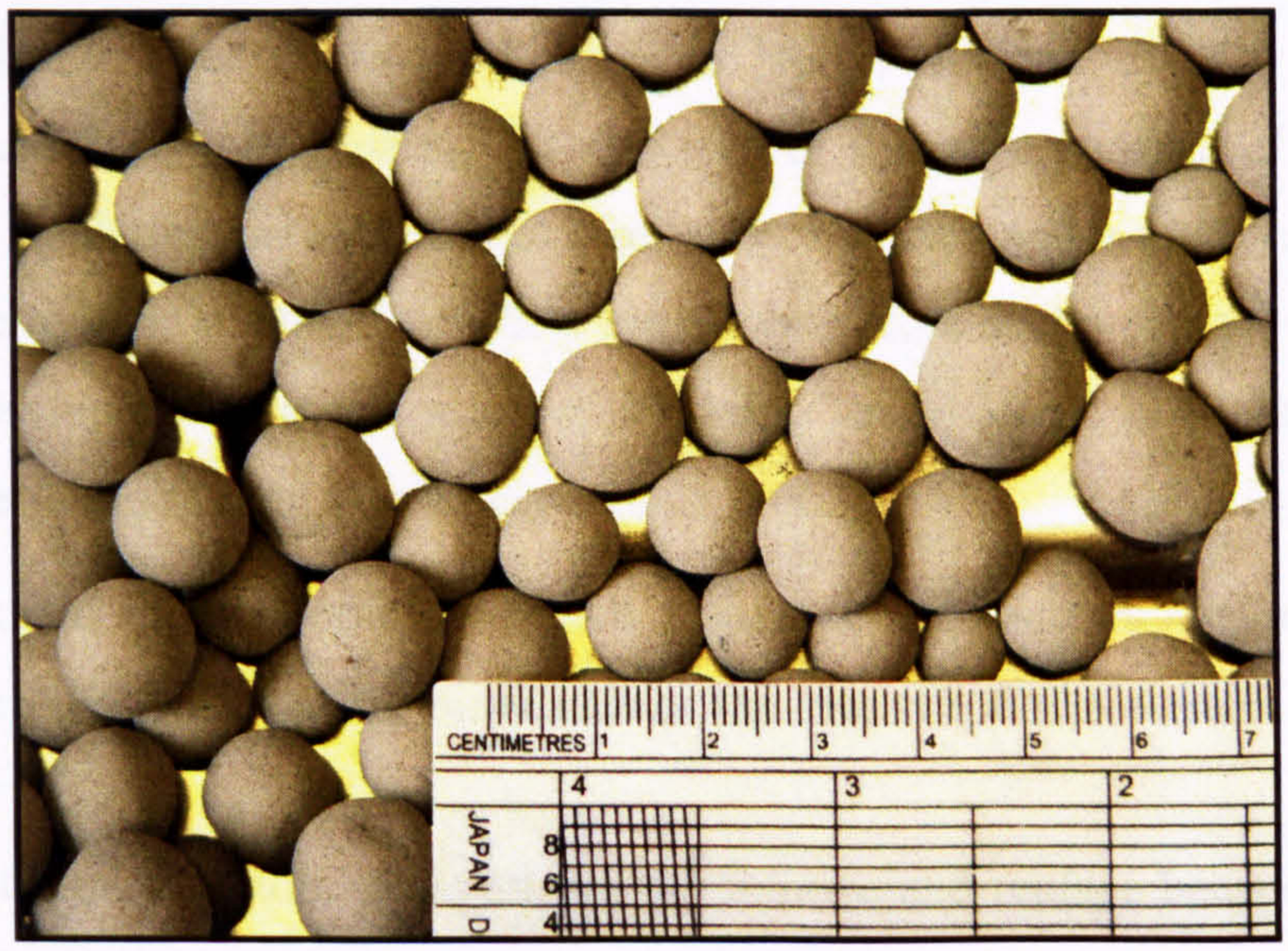

Figure 3.5 Example of the green pellet particles (95 % of granite quarry waste and 5 % ball clay) after oven dried at 105˚C for 24 hours.

3.4.2 Aggregates firing

Firing of any raw materials which have high carbon content generally consist of two stages (Wainwright et. al. 2001, 2002): the first stage is known as the 'burnout' stage where the carbon content of the mixture is allowed to combust at a temperature below that where the inert material of the pellet begins to fuse together. The second stage is the 'sintering' stage of the green pellets at high temperature. The burnout stage is necessary for the mix that contains large amounts of inherent carbon which is fixed and only combusts at high temperature. The presence of too much carbon during the sintering stage of the aggregate firing may cause the kiln temperature to spiral out of control as the carbon ignites and releases energy. However, the raw materials used in this study, i.e. Glensanda granite washing and ball clay binder, do not contain this carbon, therefore all mixes were fired without the burnout stage.

3.4.2.1 Trefoil rotary kiln

The kiln that was used in this study was the rotary type kiln called the Trefoil kiln. This kiln was designed by Sherwen Engineering Company Ltd. (Dartford, Kent, UK) over 30 years ago. It was upgraded and used in the EU research project (Wainwright et. al., 2001). There are two trefoil kilns at the University of Leeds, a larger laboratory model and a small bench top model as shown in Figure 3.7 and 3.8 respectively. The detailed information about the Trefoil kiln was given by Wainwright et al. (2001 and 2002). In general, the structure of this kiln consists of compressed ceramic fiber insulation between a thin steel alloy hot face and a tensioned thin mild steel cold face to form a cartridge with a triple-lobed cross section as shown in Figure 3.6 which represents the cross section of the kiln. The efficiency of this kiln can be summarized as the following (Wainwright et. al., 2002):

- remarkable thermal efficient which results in a large temperature difference between the inner and the outer face of the kiln (1200°C for inner and 60°C for outer);
- easier to manufacture, transport, install, remove and replace because of a much smaller and lighter structure when compare to the traditional kilns;
- a heat-up and cool-down period which is 50 times faster than conventional kilns;
- Higher load factors; and greater bed-load mixing allowing reduced thermal gradient in the bed and improved firing consistency.

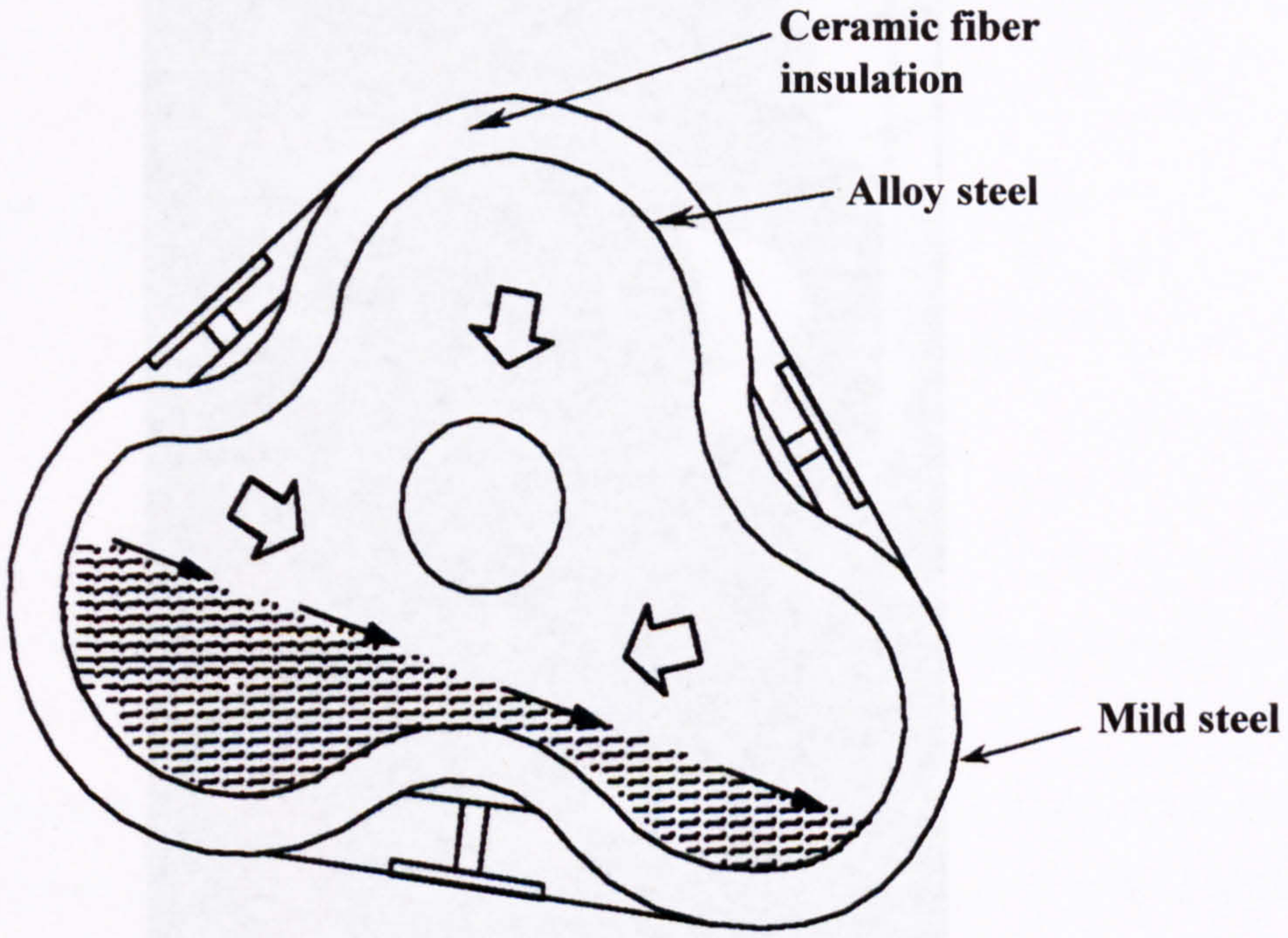

Figure 3.6 The cross-section of the Trefoil rotary kiln (Wainwright et. al., 2002).

Figure 3.7 The University of Leeds Laboratory Trefoil kiln system.

Figure 3.8 The small bench top model Trefoil kiln.

The small bench top model Trefoil kiln, as shown in Figure 3.8, was designed and built in order to gain valuable information about the process conditions required for the synthetic aggregate production. This kiln was used in this research as a small scale test work in order to study the product quality and its microstructure when fired under different regimes. The size of this kiln is approximately 400mm (diameter) x 650mm (length). The kiln control system which was designed by Mckeever from Dublin Institute of Technology is the Programmable Logic Controller (PLC) industrial computer system which is able to monitor and control: the temperature inside the kiln, rate of heat up and the retention time. The PCL system includes a Personal Computer based Supervisory Controller and Data Acquisition (SCADA) system interface for data logging measurements (Wainwright et. al., 2001). In general, all of the physical measurements, e.g. kiln temperature, are converted into the electrical signals by the instrumentation used in the kiln control system and these signals are then used by the PCL for control and data logging.

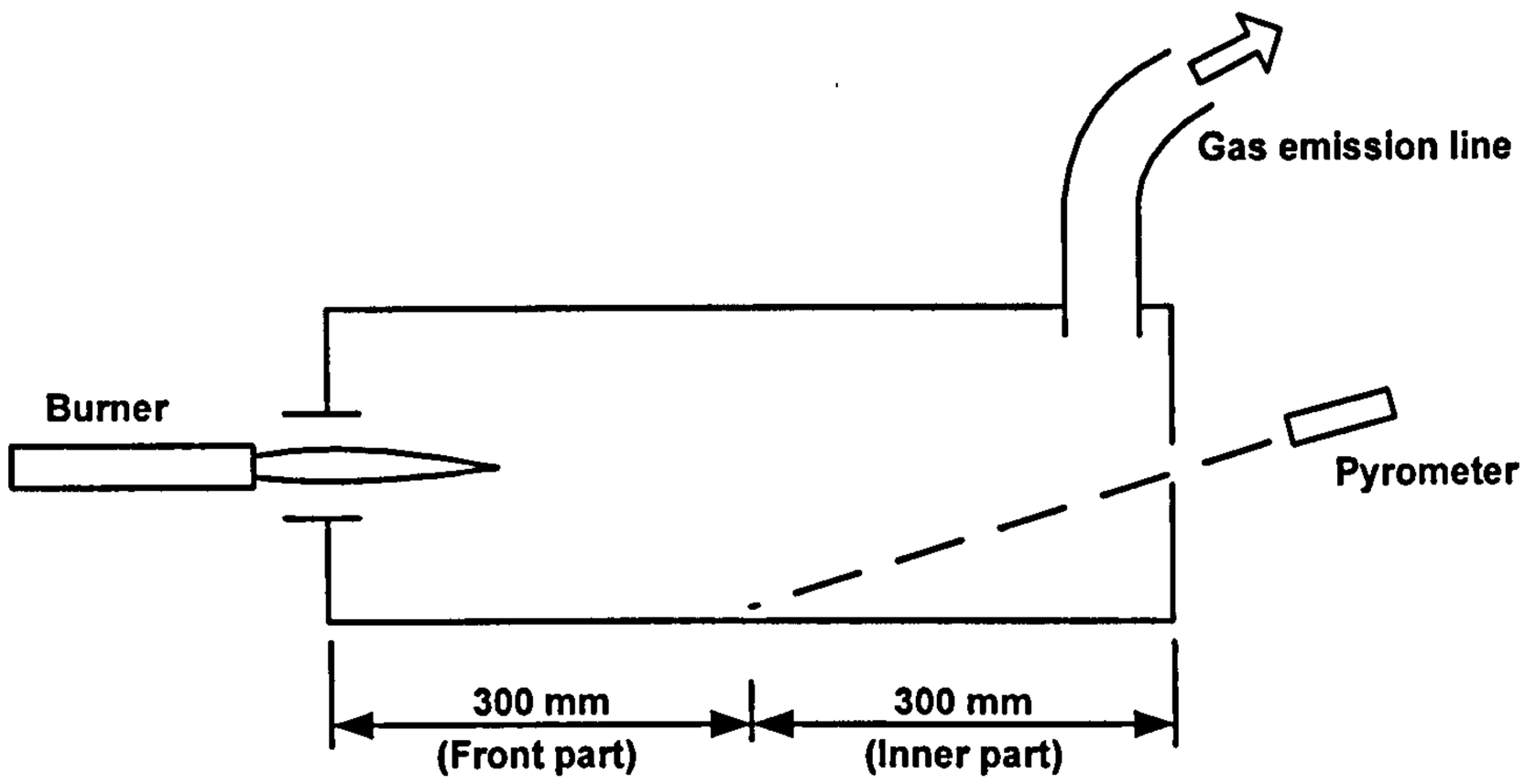

Figure 3.9 Schematic representation of the small bench top model Trefoil kiln.

A pyrometer was used to monitor the temperature inside the kiln by detecting the emitted infrared radiation which radiated from the kiln surface. It should be noted here that the temperature that was read by the pyrometer is not the temperature of each pellet but it represents the temperature at the inside kiln surface. The pyrometer was placed at the back of the kiln, with the lens pointed to the middle region of the kiln (Figure 3.9) and its position was fixed throughout the duration of the project. A continuous measurement of the temperature read by the pyrometer was sent to the controller to decide what corrective action, if any, to take to return the kiln temperature to the desired setting. The upper operating temperature of the kiln is approximately 1350°C.

The following terminology will be used throughout the thesis.

- Pre-set temperature = temperature figure that was inputted by the operator for the kiln control system.
- Ramp rate = rate of increasing temperature to the maximum pre-set temperature.
- Sintering temperature = maximum *pre-set* temperature.
- Sintering time = duration or time period at the sintering temperature.
- Orange and dark grey pellets = see Figure 3.10.

3.4.2.2 Aggregate firing procedure

After waiting until the kiln temperature reached a steady state condition at 800˚C which is a lower limit of the pyrometer, approximately 500 grams of the green pellets were manually loaded into the rotating kiln by using a suitably sized scoop. When the kiln was fully loaded the control system was activated and the firing process allowed to proceed fully automated and controlled by the PLC. When the cycle was complete the hot pellets were then manually taken out of the kiln by the scoop and placed in a metal container/ tray on a heat proof mat in the area set aside for hot sample storage. After cool down to the room temperature, these samples were kept in the plastic sample bags and stored before any further testing. Figure 3.10 shows the example of fired pellets and the colour variation of the fired pellets within the same batch was clearly observed. The colour of each pellet depends on the form of iron within the fired pellet, i.e. the yellowish tint or intense red and the greenish-brown colour are generally given by the ferric and ferrous iron respectively (Hostetter and Roberts, 1921; Sandrolini and Palmonari, 1976).

Figure 3.10 Example of the synthetic aggregate produced by the Trefoil kiln.

Figure 3.11 shows a typical output from the PCL showing the pre-set temperature profile (shown in Table 3.3) versus the actual recorded temperature. It can be seen that it is not possible to follow exactly the pre-set profile. Due to the nature of the process there will always be a degree of over-shoot and under-shoot around the pre-set profile.

Table 3.3 Example of the pre-set temperature for the kiln control system. (1,120ºC Sintering temperature, 3.5 minutes sintering time and 20˚C/min. ramp rate)

Pre-set temperature (ºC)	Time (sec)
800	0
850	150
900	300
950	450
1000	600
1050	750
1100	900
1120	960
1120	1170
800	1500

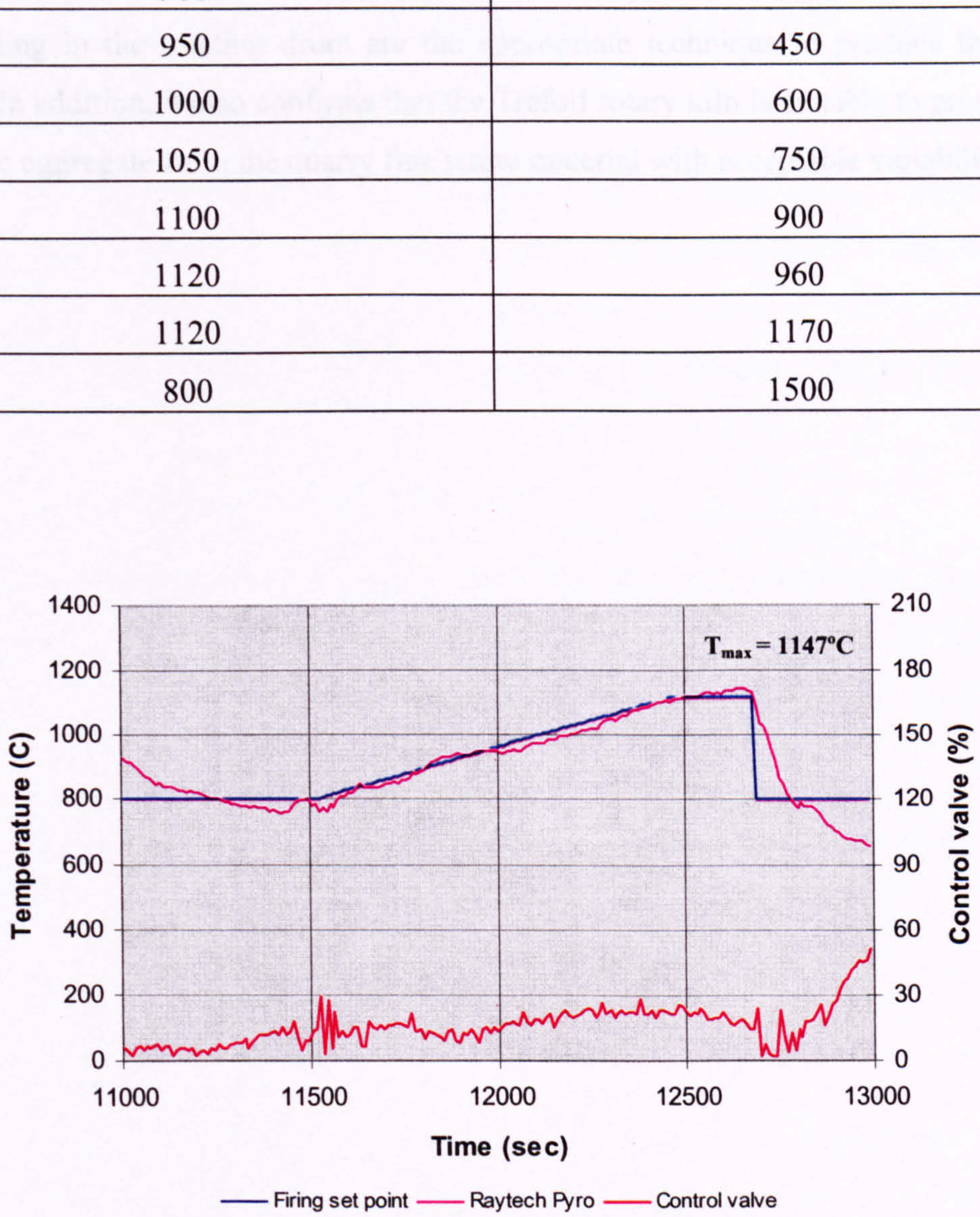

Figure 3.11 Typical temperature profile output from the kiln control system. (1,120ºC sintering temperature, 3.5 minutes sintering time and 20˚C/min. ramp rate).

3.5 Summary

This chapter gives the information about the raw materials used in the synthetic aggregate production process and it describes the technique that was used to form the green pellets and the structure and control system of the Trefoil rotary kiln used during the synthetic aggregate firing.

There are many types of pelletisation techniques available and the choice of each technique depends on the materials used. In this study, it was found that the extrusion and balling in the rotating drum are the appropriate technique to produce the green pellets. In addition, it also confirms that the Trefoil rotary kiln is suitable to produce the synthetic aggregate from the quarry fine waste material with acceptable variability.

Chapter 4

Experiment: materials, sample preparation and testing

4.1 Introduction

This chapter consists of three main parts. General detailed information about the concrete raw materials and its casting procedure were given first. The second part involves a brief summary of all tests that were done in this research. The final part provides a detailed explanation of the sample preparation for the SEM analysis.

4.2 Materials for concrete casting

The raw materials for concrete casting consist of the Portland cement binder, coarse and fine aggregate. The investigation was based on using three different types of coarse aggregate including the synthetic, Lytag and quartz aggregate. Note that the detailed information about the synthetic aggregate was already given in the previous chapter.

4.2.1 Ordinary Portland Cement (OPC)

The Ordinary Portland Cement type I supplied by Castle Cement was used in this study and it follows the requirement of BS12 (1996). The specific surface area is 430 m^2/kg and the initial setting time of 100 minutes. The oxide compositions of this cement are given in Table 4.1.

Table 4.1 Chemical analysis of the Portland cement supplied by Castle Cement

Oxides	Weight Percent	Compounds	Weight Percent
SiO_2	20.69	C_3S	53.9
Al_2O_3	4.72	C_2S	18.2
Fe_2O_3	3.06	C_3A	7.2
CaO	63.76	C_4AF	9.2
MgO	2.08		
SO_3	2.92		
K_2O	0.61		
Na_2O	0.26		
Cl	0.04		
Loss on ignition	0.87		
Non detected	0.99		

Note: data from manufacturer's data sheet

4.2.2 Characteristic of the coarse aggregates

As was mentioned earlier, there were three types of coarse aggregate that were used in this study (synthetic, Lytag and quartz aggregate). These aggregates were used to produce concrete samples for the coarse aggregate-cement paste interface analysis, compressive strength and permeability test. Lytag and quartz aggregate were used as a comparison case for the concrete with synthetic aggregate produced in this research.

4.2.2.1 Quartz coarse aggregate

This aggregate is normally used in the School of Civil Engineering at the University at Leeds and it was supplied by the Tarmac Central Ltd. It was quarried from the Nottinghamshire region. As shown in Figure 4.1, most of this river gravel has smooth particles and it is largely composed of quartz which is a very common natural mineral formed from the crystallization of silica (SiO_2).

Figure 4.1 Quartz coarse aggregate particles.

4.2.2.2 Lytag coarse aggregate

Lytag is a commercially available lightweight aggregate produced from Pulverized fuel ash (PFA) which is processed by pelletising PFA and sintering on a sinter strand. Figure 4.2 presents a simple diagram for the production process of Lytag. In general, an appropriate amount of water (usually around 12-15%) and fine coal are added to the PFA in a mixer and this mixture is then fed at a control rate to the specially designed dish pelletising pans (Owens, 1993). A controlled amount of water is

additionally added as a fine spray during the pelletisation process in order to form the rounded green pellets. The size and the degree of compaction of the green pellet depend on the feeding rate, additional water, inclination and rotational speed of pan. The green pellets are then fed onto a sinter strand and heated to a temperature between 1000°C and 1250°C (www.lytag.co.uk). The final product is a brick like material rounded in shape as shown in Figure 4.3 (for more details see Swamy and Lambert, 1981).

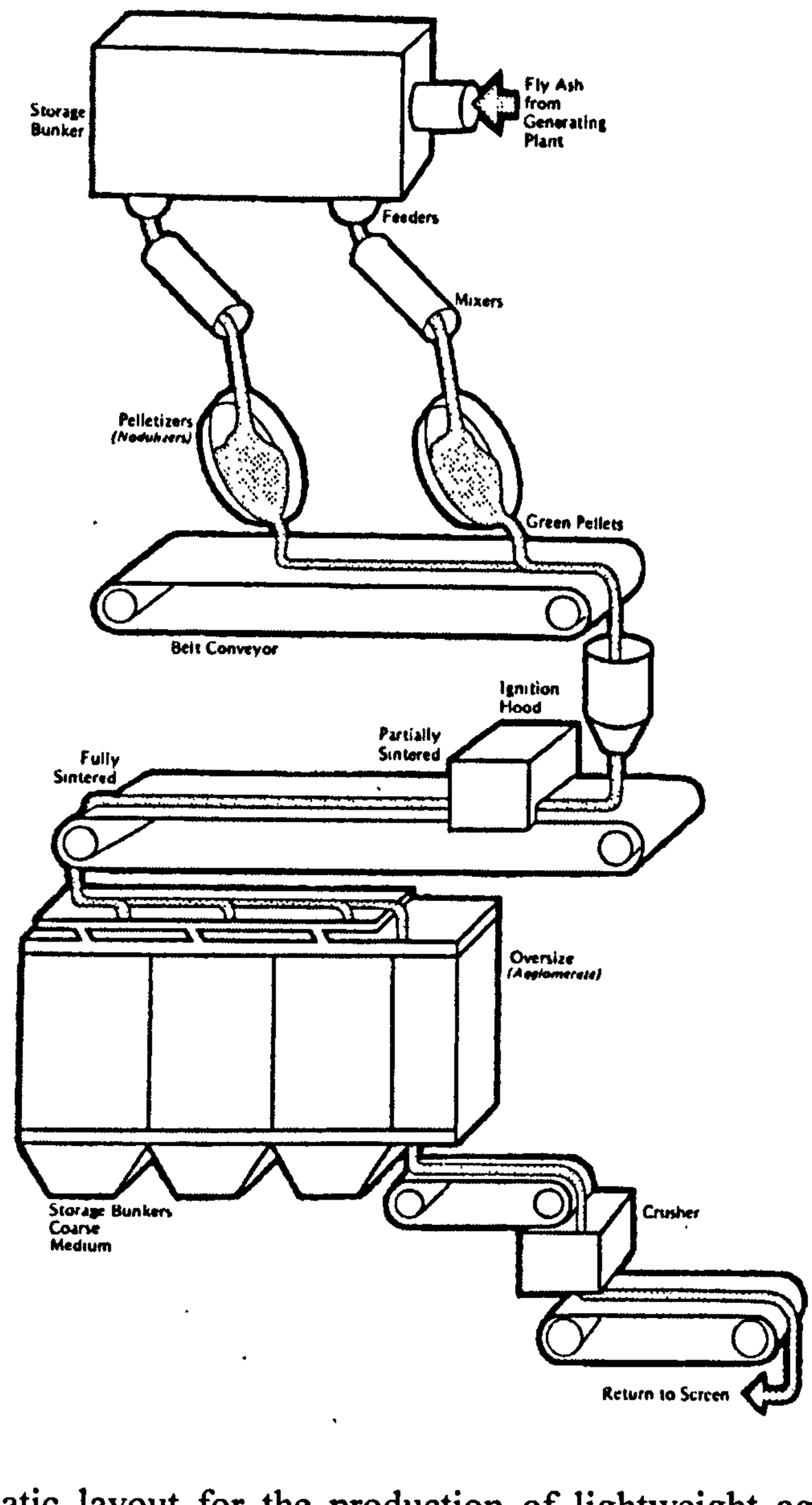

Figure 4.2 Schematic layout for the production of lightweight aggregates produced from sintered pulverized-fuel ash. Courtesy Lytag Ltd. (FIP, 1983).

Figure 4.3 Typical Lytag aggregate particles with maximum size of 12 mm.

4.2.3 Fine aggregate

The fine aggregate that was used for all concrete mixes was the quartz sand particle with a maximum size of 5 mm and it was supplied from commercial deposits in the Nottinghamshire region.

4.2.4 Aggregate gradation

The gradation of coarse aggregate and sand was tested according to the BS 882 (1992). This was done by passing the aggregate through a series or stack of sieves. Sieves size of 20 mm, 14 mm, 10 mm, 5 mm, 2.36 mm and 1.18 mm were used for coarse aggregate. A similar sieves size of 10 mm, 5 mm, 2.36 mm, 1.18 mm, 600 μm, 300 μm and 150 μm were used for sand. The tested sieve size conforms to BS 410 (2000). The sieves were mechanically vibrated for 2 minutes and the weight of aggregate retained on each sieve was then measured. The gradation curve for coarse aggregate and sand are shown in Figure 4.4.

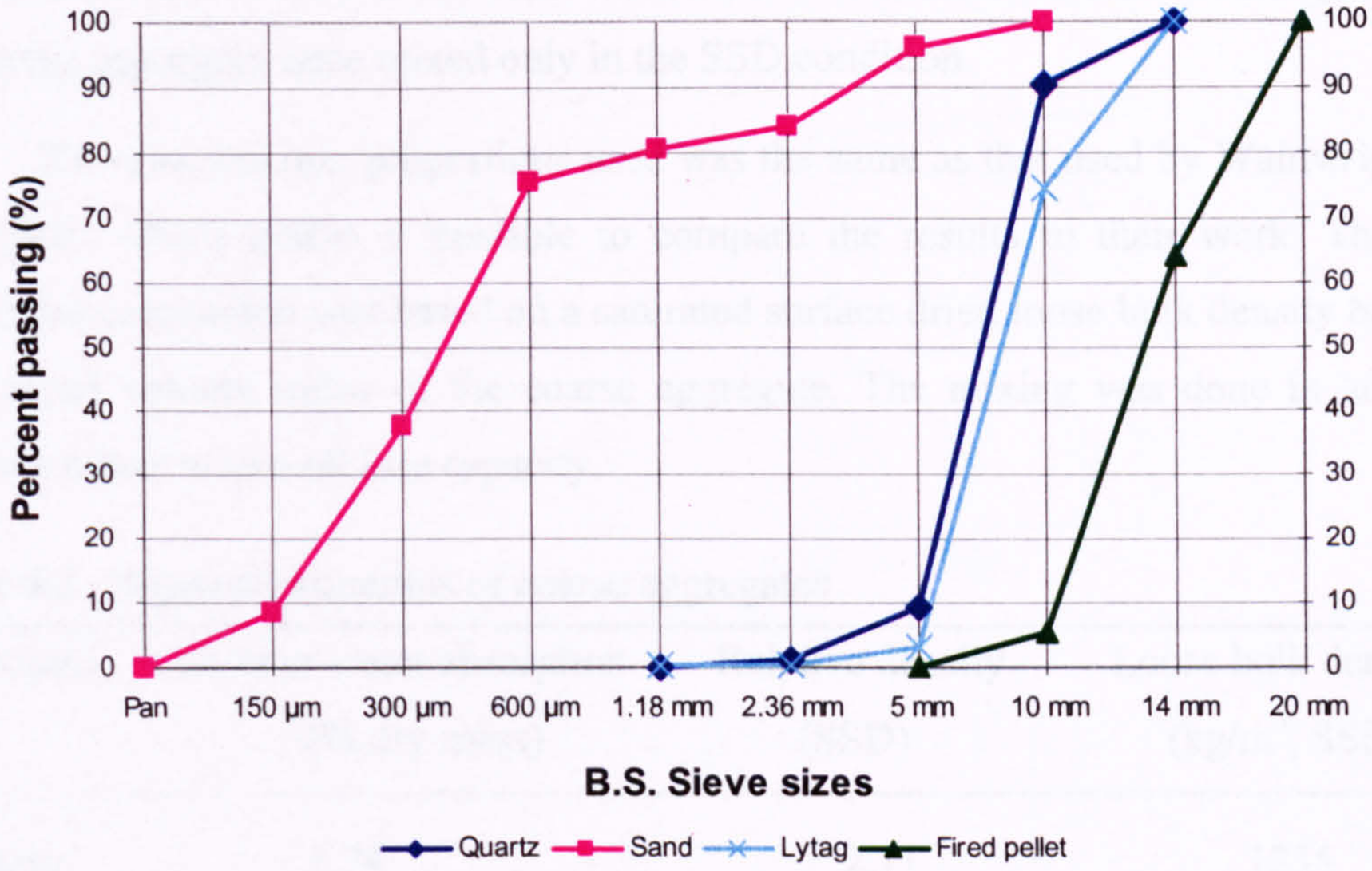

Figure 4.4 Gradation curve of the coarse and fine aggregate.

4.3 Concrete mix proportion and specimen preparation

The following section gives the detailed information about the mix proportion and the casting procedure of concrete used in this study. The synthetic aggregate fired at 1,110˚C with 10 minutes sintering period was chosen for concrete production and was mixed in concrete as a 100% replacement of the coarse natural aggregate. The effect of the dry and pre-wetted synthetic aggregate on the interfacial transition zone (ITZ) between coarse aggregate and cement paste was investigated. The obtained results were then compared with the case of concrete with Lytag and naturally occurring gravel coarse aggregate. As mentioned in section 4.2.2.2, Lytag is a commercially available lightweight aggregate, manufactured in the UK produced from the pulverised-fuel ash (pfa). The natural aggregate used is quartz gravel with the particle size distribution shown in Figure 4.4, part crushed part, rounded (Figure 4.1).

Two sets of synthetic aggregate concrete were prepared. The first set was prepared with dry aggregate. Prior to mixing, these aggregates were dried in an oven at 105°C for 1 day and allowed to cool down to room temperature at the end of the drying period. The second set was prepared with the pre-wetted aggregate. The aggregate was soaked in the water for 24 hours. The water was drained and the aggregate was dried

using a towel until it was in the saturated surface dried condition before mixing. Quartz and Lytag aggregate were mixed only in the SSD condition.

The concrete mix proportions used was the same as that used by Wainwright et. al. (2002), which makes it possible to compare the results to their work. The mix proportion calculation was based on a saturated surface dried loose bulk density basis to keep equal volume ratios of the coarse aggregate. The mixing was done in an ELE concrete mixer with a 60 litre capacity.

Table 4.2 Physical properties of coarse aggregates

Aggregate	24 hour water absorption (% dry mass)	Relative density (SSD)	Loose bulk density (kg/m^3, SSD)
Synthetic	5.74	2.11	1235
Synthetic	4.37[a]	-	1170[b]
Lytag	12.3	1.8	922
Natural coarse	0.8	2.6	1553

[a] 30 minutes water absorption; [b] dry loose bulk density

The amount of compensated water that was assumed to be absorbed by the dry synthetic aggregate was calculated based on the half hour water absorption figure as given in Table 4.2. Figure 4.5 shows the water absorption behavior of synthetic aggregate fired at 1,110°C with 10 minutes sintering time. It shows that more than 70 percent of the 24 hours water absorption has been absorbed within the first 30 minutes. This result is consistent with the other observations reported in the literature (Swamy and Lambert, 1981; Zhang and Gjørv, 1991[a]). It is likely that the absorption characteristics of aggregate when immersed in water may be different from those in fresh cement paste or mortar but experiments indicate that the aggregate within the cement paste matrix which has a water-cement ratio greater than about 0.6 absorbs a proportion of water which is nearly equivalent to the value of the water absorption within the first 30 minutes when immersed in water (cited in Zhang and Gjørv, 1991[a]).

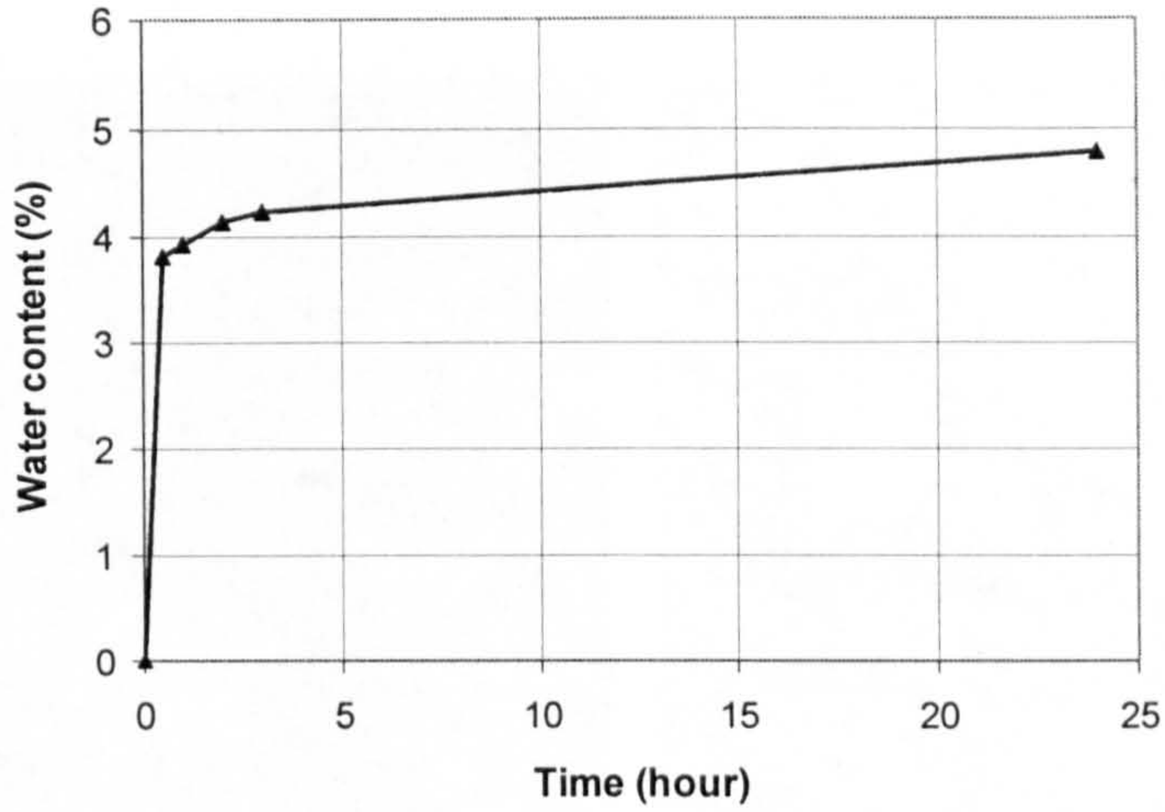

Figure 4.5 Water absorption of synthetic aggregate fired to 1110° C with 10 minutes sintering time.

As mentioned earlier, all mixes were designed to have nominally the same volume proportions of coarse aggregate and the mix proportions by weight are shown in Table 4.3. The mixing of concrete was performed following the same procedure for all mixes. Dry mixing of the coarse aggregate, binder and fine aggregate was performed for one minute, and then the water was slowly added. The wet mixture was mixed together for a further two minutes. Once mixed, the concrete was cast in the 220x220x40 mm slab and two cubes (100 mm), left for one day before de-moulding and then kept in a controlled environment, i.e. 20 ± 2°C and 99% relative humidity. The specimens were left to cure in this condition until the date of testing. The mixing equipment, moulds and an example of the concrete specimens are shown in Figure 4.6.

Table 4.3 Concrete mix ratio by weight (kg) for synthetic and natural aggregates

Aggregate	w/c	Cement	Sand	Coarse aggregate
Synthetic	0.53	1	2.23	2.96
Lytag	0.53	1	2.23	2.21
Natural	0.53	1	2.23	3.72

Figure 4.6 (a) Concrete mixer. (b) Concrete coring equipment. (c) Moulds and example of concrete specimens.

4.4 Water absorption and relative density test

The water absorption and relative density of the coarse aggregate used in this study was established by using the BS812 (1990) as a standard for testing. The general formulas for calculating each value are given below. The different mass values used in each formula are given as follows:

Mass A = mass of aggregate after being soaked in distilled water for 24 hours ± 0.5 hours, and then surface dried by a dry cloth to remove any remaining films of water but still with a damp appearance.

Mass B = mass of the soaked aggregate in a pycnometer filled with water, with no air trapped inside, and the lid on.

Mass C = mass of the pycnometer and lid filled with water only.

Mass D = mass of the aggregate after being dried in an oven at a temperature of 105°C ± 5°C for 24 hours ± 0.5 hours.

(All mass values given are in unit of grams)

4.4.1 Relative density on an oven-dried basis

The relative density of a sintered pellet after being dried in an oven at 105°C for 24 hours in order to remove all trace of moisture is given as follow;

$$\frac{D}{A-(B-C)} \tag{4.1}$$

4.4.2 Relative density on a saturated and surface dried basis

The relative density of a sintered pellet in saturated and surface dried condition is given as follow;

$$\frac{A}{A-(B-C)} \tag{4.2}$$

4.4.3 Apparent relative density

This gives the relative density of a sintered pellet as a ratio of the oven-dry weight of the aggregate to the weight of an equal volume of water and is calculated from the following equation;

$$\frac{D}{D-(B-C)} \tag{4.3}$$

4.4.4 Water absorption

The degree to which the sintered product will absorb water over a period of 24 hours can be calculated from the following equation;

$$\frac{100(A-D)}{D} \tag{4.4}$$

4.5 Mechanical behaviour of concrete

The objective of this test was only to undertake a preliminary investigation into the effect of the use of different coarse aggregates on the load-deformation response of concrete. Due to the limitations on the synthetic aggregate quantity, only two cubes of 100 mm were used for each investigating condition and the test was done on 3-day and 28-day old concrete. The coarse aggregate included the synthetic aggregate (dry and pre-wetted condition), quartz and Lytag. The test sample was left in a controlled room (21 ± 0.5˚C and 42 ± 2 % relative humidity) for 1 day and the electrical resistance strain gauge (ERSG) was then installed for measuring the deformation during the test.

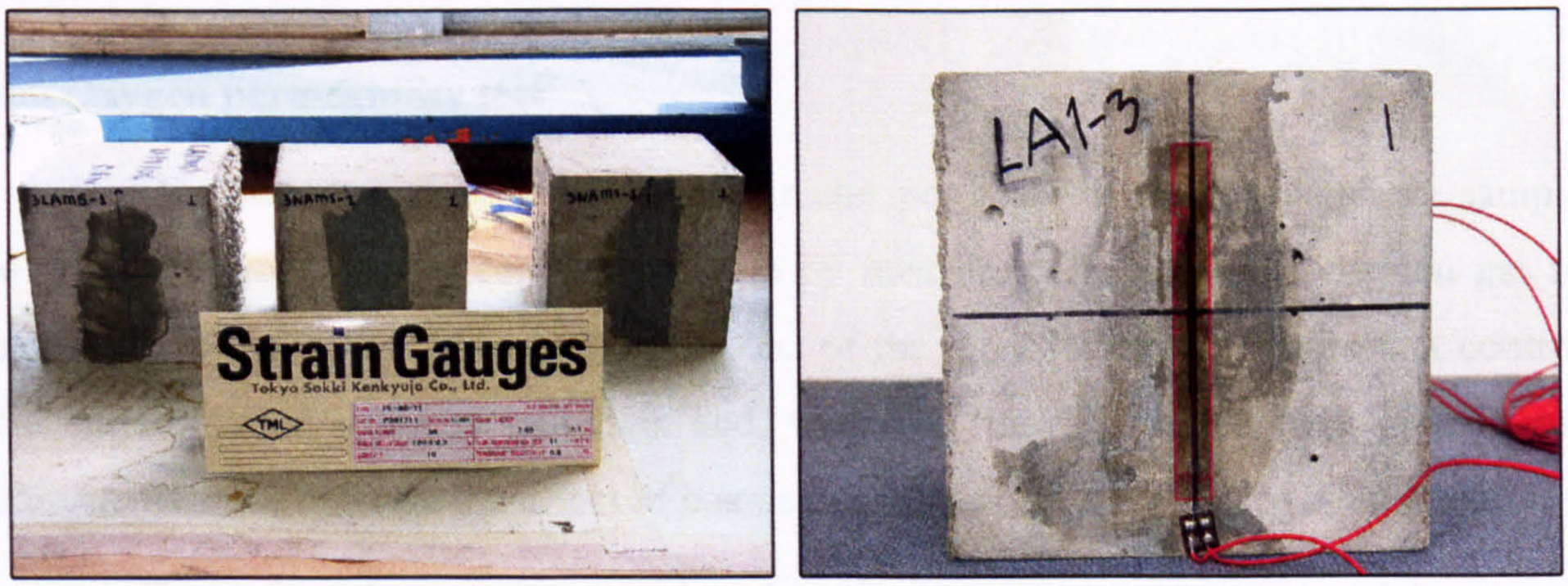

Figure 4.7 Installation of strain gauge on concrete sample.

Any voids on the surface of the concrete sample must first be filled and this surface must be well-polished. After this, two electrical resistance strain gauges were installed on two opposite cleaned surfaces and lead wires were connected.

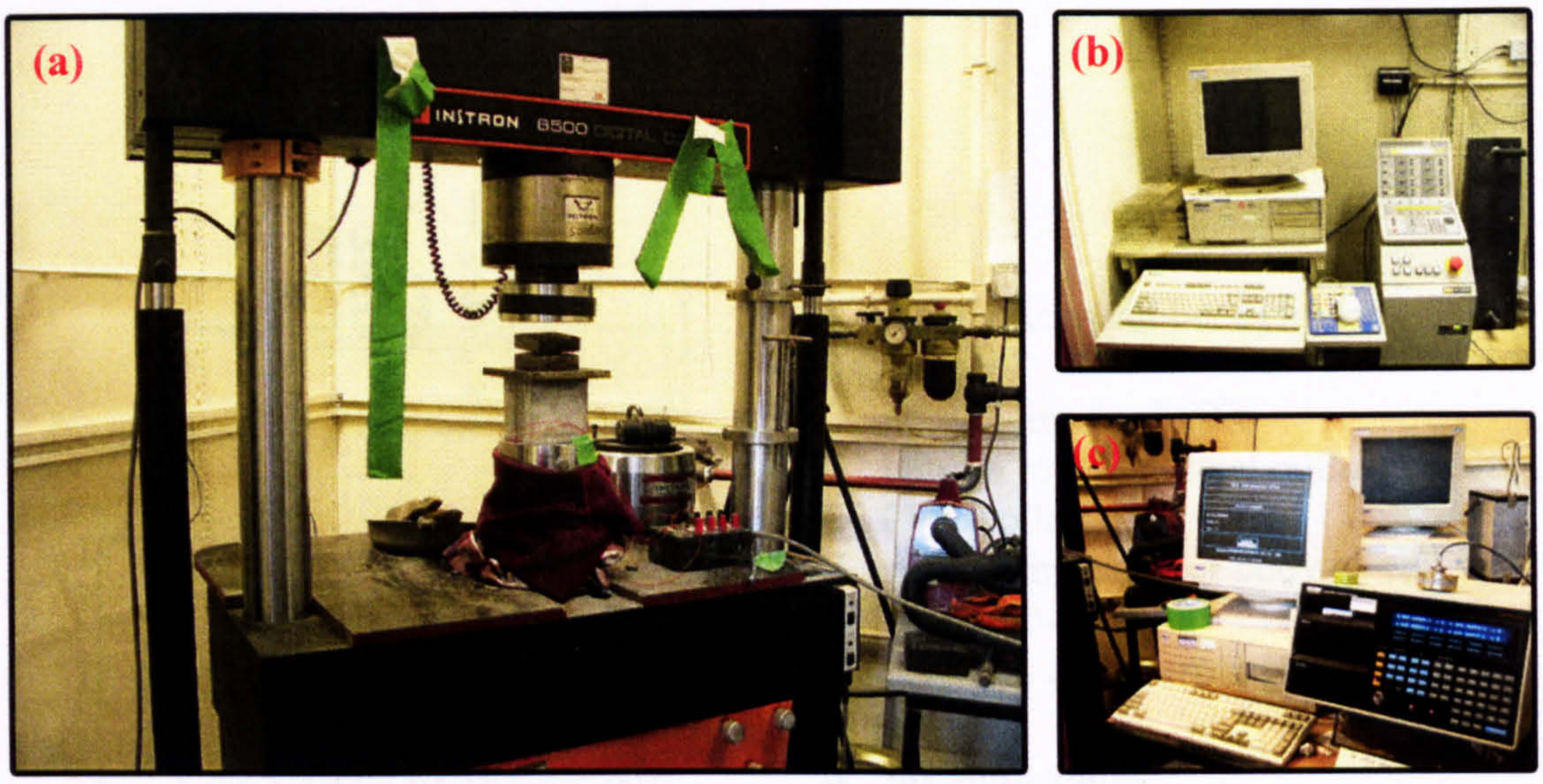

Figure 4.8 The *INSTRON 8500* servohydraulic test system used in this study. (a) Loading frame, (b) Machine controlled unit. (c) Data logging system unit.

After installing the concrete specimen into the testing machine, the pressure was then gradually applied to the test sample until failure occurred, the rate of applying loading was 3 kN/s. At this stage, the force applied on the sample is recorded by the *INSTRON* control unit and, at the same time, the deformation of the sample is recorded by the data logging unit. The test results are given in section 7.4.

4.6 Oxygen permeability test

This test was designed to evaluate the permeability of the concrete sample having different types of coarse aggregate by measuring the ability of oxygen gas to permeate the sample. This parameter is one of the most important factors that control the durability of concrete materials and, therefore, the test results will give useful information that concern the effect of coarse aggregate on the durability of concrete.

The test equipment was developed at the University of Leeds by Cabrera and Lynsdale (1988) and its schematic diagram is given in Figure 4.9. In general, the permeability test cell consists of the sample holder unit, pressure gauge, gas supply and the flow meter (see Cabrera and Lynsdale, 1988 for more detail information).

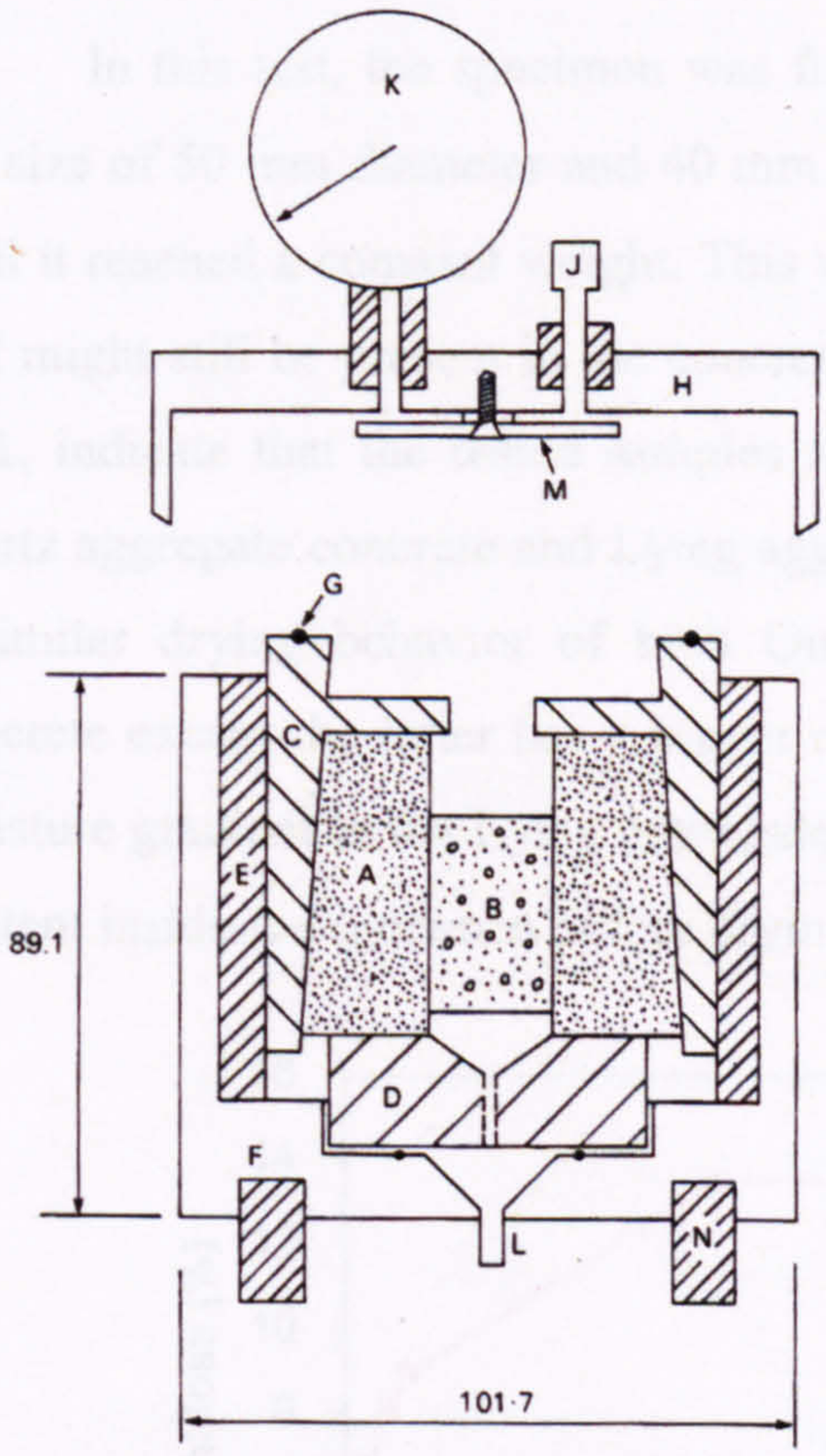

A inner silicon rubber cylinder
B sample
C plastic circular baffle
D bottom stainless steel hollow seating
E PVA collar
F outer stainless steel body of cell
G rubber O-ring
H stainless steel cap of cell
J gas inlet
K pressure gauge
L gas outlet
M water inlet
N sitting guides

Figure 4.9 Schematic diagram of the Leeds permeability cell (copied from Cabrera and Lynsdale, 1988).

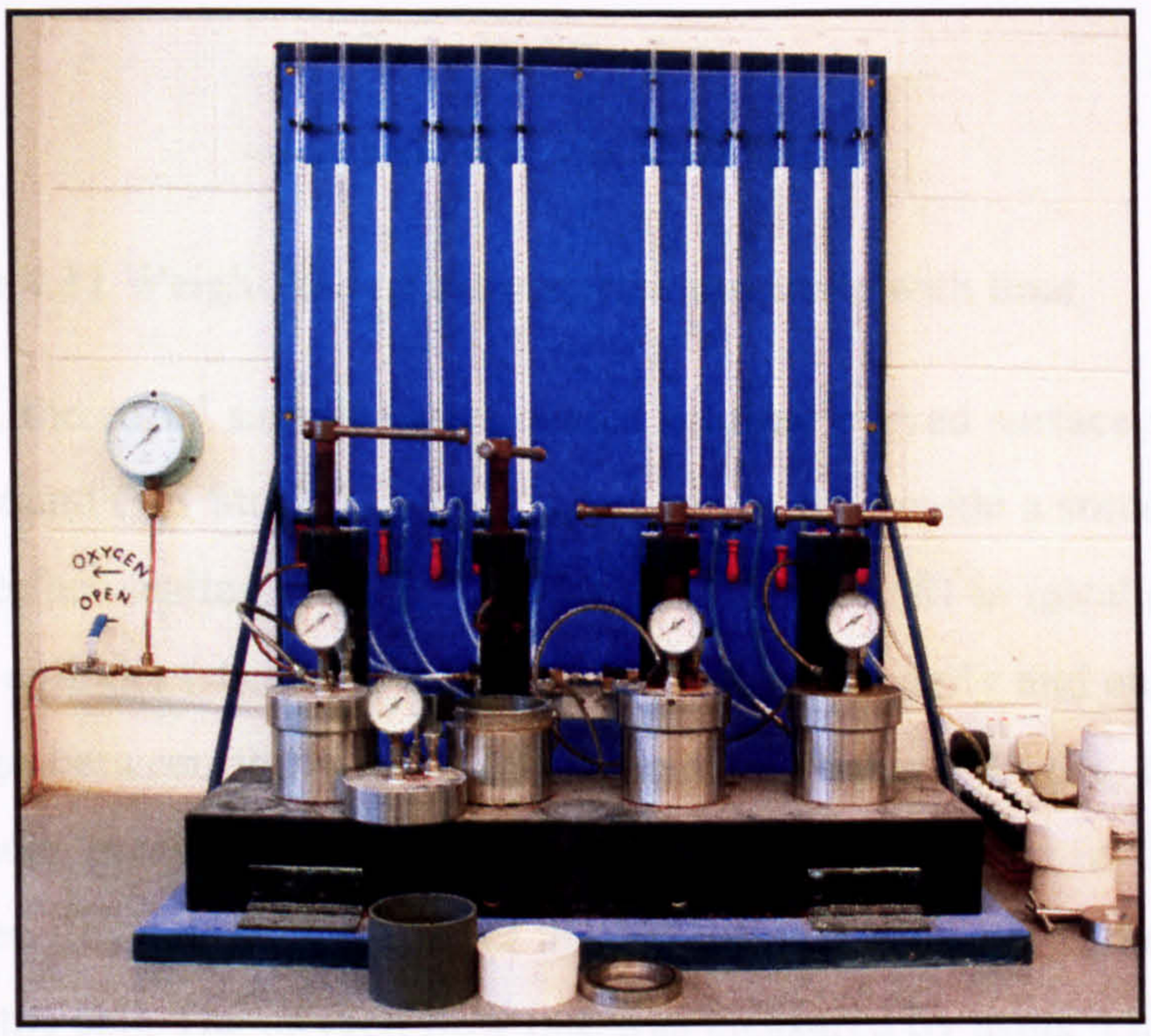

Figure 4.10 The Leeds oxygen permeability test equipment.

In this test, the specimen was first cored from the prepared concrete slab with the size of 50 mm diameter and 40 mm height. Then it was dried in the oven at 105˚C until it reached a constant weight. This was done in order to remove any residual water that might still be present in the concrete pore system. The results, as shown in Figure 4.11, indicate that the tested samples reached their steady state at 24 hours for both quartz aggregate concrete and Lytag aggregate concrete. In addition, these results show a similar drying behavior of both Quartz aggregate concrete and Lytag aggregate concrete except the latter has a bigger reduction during the first 24 hours. The greater moisture gradient in the Lytag aggregate concrete could be because of the greater water content inside the specimen before drying.

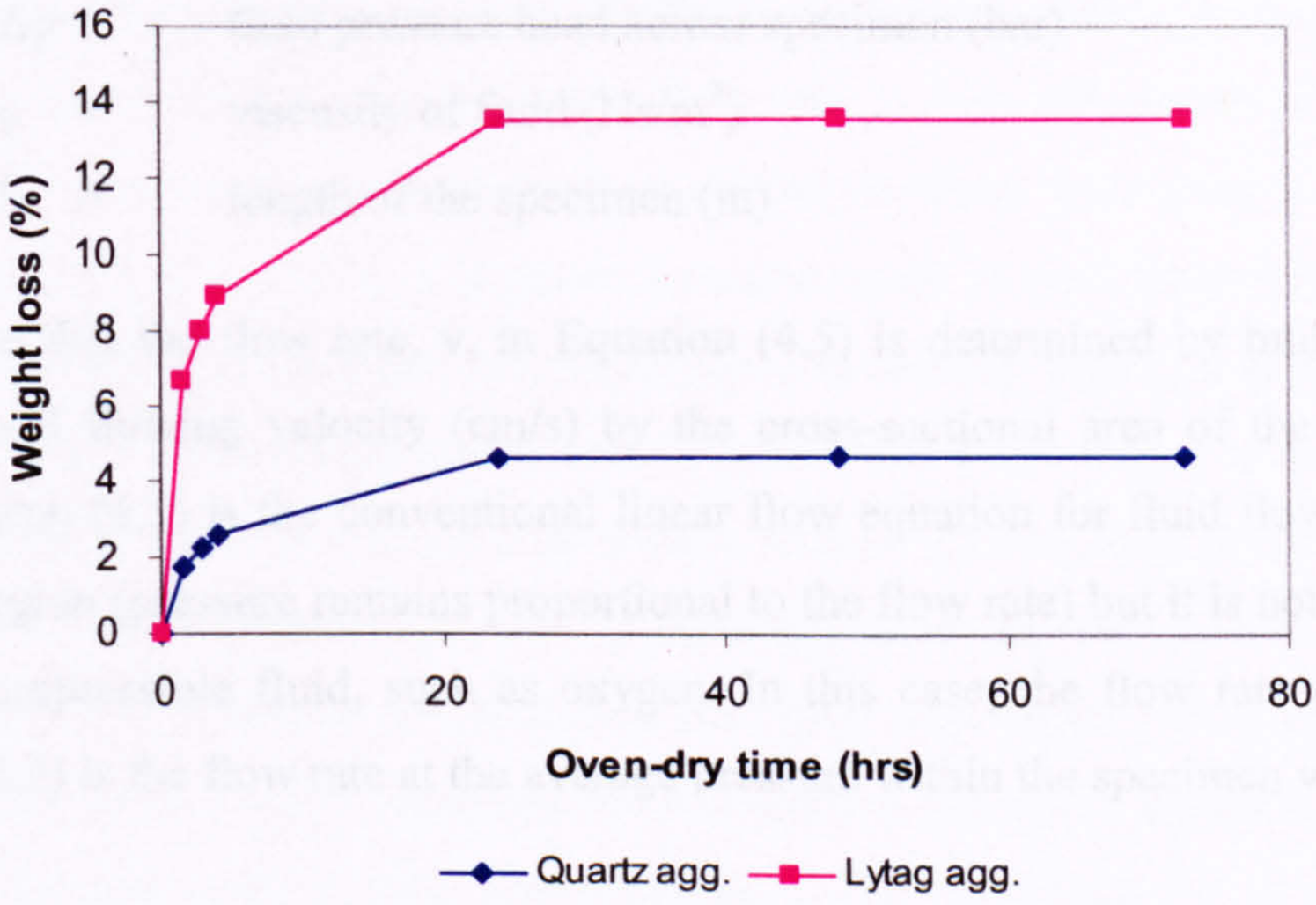

Figure 4.11 Weight loss of the concrete specimen with time.

After drying, the cored samples were coated on their curved surface with a soft silicon rubber compound (RS Stock No. 555-558) in order to provide a smooth surface and ensuring that perfect sealing is achieved when the sample (*B*) is installed into the inner silicon rubber cylinder (*A*). After clamping the cell lid properly and ensuring that there was no leakage between the sample and the silicon rubber cylinder, the oxygen was then forced under pressure of 1 bar to flow through the sample in the vertical direction. The oxygen flows through the lid of the test cell (*H*) and exits at the gas outlet (*L*) at the bottom of the cell. The oxygen flow rate was measured by using a bubble flow

meter (Figure 4.10) and it was recorded when a steady state of flow was reached (about 15 to 20 minutes from the start of the test).

The permeability of an incompressible fluid, e.g. water, flowing through a porous sample can be determined by using the equation that was developed by Darcy.

$$v = \frac{kA\Delta p}{\mu l} \tag{4.5}$$

where v = flow rate (cm^3/s)

k = intrinsic permeability (m^2)

A = cross-sectional area of specimen (m^2)

Δp = fluid pressure head across specimen (bar)

μ = viscosity of fluid (Ns/m^2)

l = length of the specimen (m)

Note that the flow rate, v, in Equation (4.5) is determined by multiplying the apparent fluid flowing velocity (cm/s) by the cross-sectional area of the flow meter tube. Equation (4.5) is the conventional linear flow equation for fluid flow in the low flow rate region (pressure remains proportional to the flow rate) but it is not suitable for a highly compressible fluid, such as oxygen. In this case, the flow rate presented in Equation (4.5) is the flow rate at the average pressure within the specimen which can be written as:

$$p_m = \frac{(p_1 + p_2)}{2} \tag{4.6}$$

where p_1, p_2, p_m = inlet, outlet and average pressure respectively.

The gas flow rate is measured at the pressure of 1 bar (p_2 = 1 bar) in this study. Therefore, the gas flow rate at the average pressure can be written as:

$$v_m = \frac{v_{1bar}}{p_m} \tag{4.7}$$

Substituting Equation (4.6) and (4.7) into (4.5) gives

$$k = \frac{2 v_{1bar} \mu l}{A\left(p_1^2 - 1\right)} \tag{4.8}$$

Substituting the viscosity of the oxygen (2.02 x 10^{-16} N.s/m^2, at 20°C) into Equation (4.9) give:

$$k = \frac{v_{1bar}\, l \times 4.04 \times 10^{-16}}{A\left(p_1^2 - 1\right)} \tag{4.10}$$

Where p_1 = absolute applied pressure (bar).

4.7 Mercury Intrusion Porosimetry (MIP) Test

Mercury Intrusion Porosimetry (MIP) is a technique used to measure pore size distribution, and has an advantage in that it is able to span the measurement of pore sizes ranging from a few nanometers, to several hundred micrometers. Few other techniques exist that are able to measure the same range of pore sizes. This technique consists of the gradual intrusion of mercury (a non-wetting liquid) into an evacuated porous medium at increasingly higher pressures followed by extrusion as the pressure is lowered. Since the mercury has a high surface tension (non-wetting properties) which has a contact angle greater than 90°, it does not enter the pores without applying pressure. Intrusion pressures are relative to pore size, with higher pressures required to force mercury into a smaller pores and the well-known Washburn equation can be used to estimate to pore size at each pressuring step. The expression for the pore radius according to Washburn's equation is as follows:

$$r = -\frac{2\gamma \cos\theta}{p} \tag{4.11}$$

where r = pore radius at pressure of "p"

p = applied pressure

γ = surface tension of the mercury

For this research, the contact angle and the surface tension of mercury were set at 130° and 0.485 N/m respectively, for all specimens. Therefore, Equation (4.11) can be rewritten as:

$$r = -\frac{0.624}{p} \quad \text{microns} \tag{4.12}$$

Note that the Washburn equation was formulated on the basis of cylindrical pore shape. Therefore, this system does not measure the true size distribution of material which has complicated pore geometry. However, there is a lot of useful information that can be obtained by using this technique, including pore size distribution, total porosity, material density (bulk density and skeleton or solid density), pore diameter, specific gravity and pore surface area. This test can be used to investigate the changing of pore structure of the synthetic aggregate at different firing conditions as will be presented in section 6.5.

The test equipment used in this research was a Micromeritics Autopore Model 9200 as shown in Figure 4.13. This machine can generate pressures up to 60,000 psi which covers the pore size range from about 330 to 0.003 microns. As shown in Figure 4.12 and 4.13, this test equipment mainly consist of the specimen container called *penetrometer*, low and high pressure ports, vacuum apparatus, pressure generator, hydraulic fluid and equipment used to control the applied pressure and monitoring the progress of the penetration of mercury into specimen.

This technique is very sensitive to the condition of the test sample. The residual water and the volatile materials have to be removed before performing the test. Therefore, all of the synthetic aggregates were dried in an oven for 24 hours at temperature of 105°C for 24 hours and thereafter stored in a desiccator for the extended period over which the testing was performed. After drying, the specimens were weighed and loaded into the calibrated and sealed penetrometers which were weighed both before and after being loaded with the specimen. Then the penetrometers were loaded into the low-pressure ports of the machine and the low-pressure intrusion run was started. After this, pairs of penetrometers were loaded into high-pressure ports for the high-pressure intrusion run. When the runs were completed the system generates report files, which contain the data recorded during the runs. Recorded data include specimen and calibrated penetrometer details, pre-set system parameters, and a summary of intrusion details. This information was then transferred into a spreadsheet for further detailed analysis.

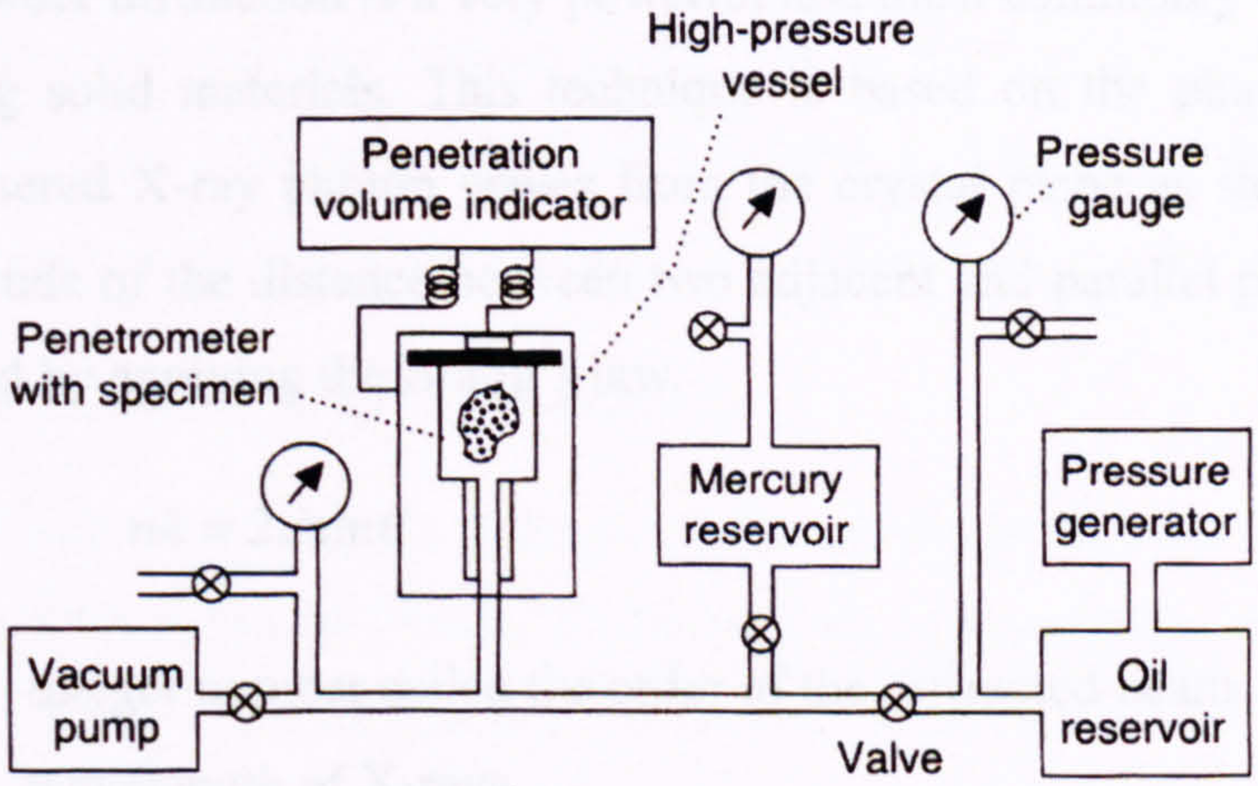

Figure 4.12 Schematic out-of-scale layout of the MIP system (from Aligizaki, 2006).

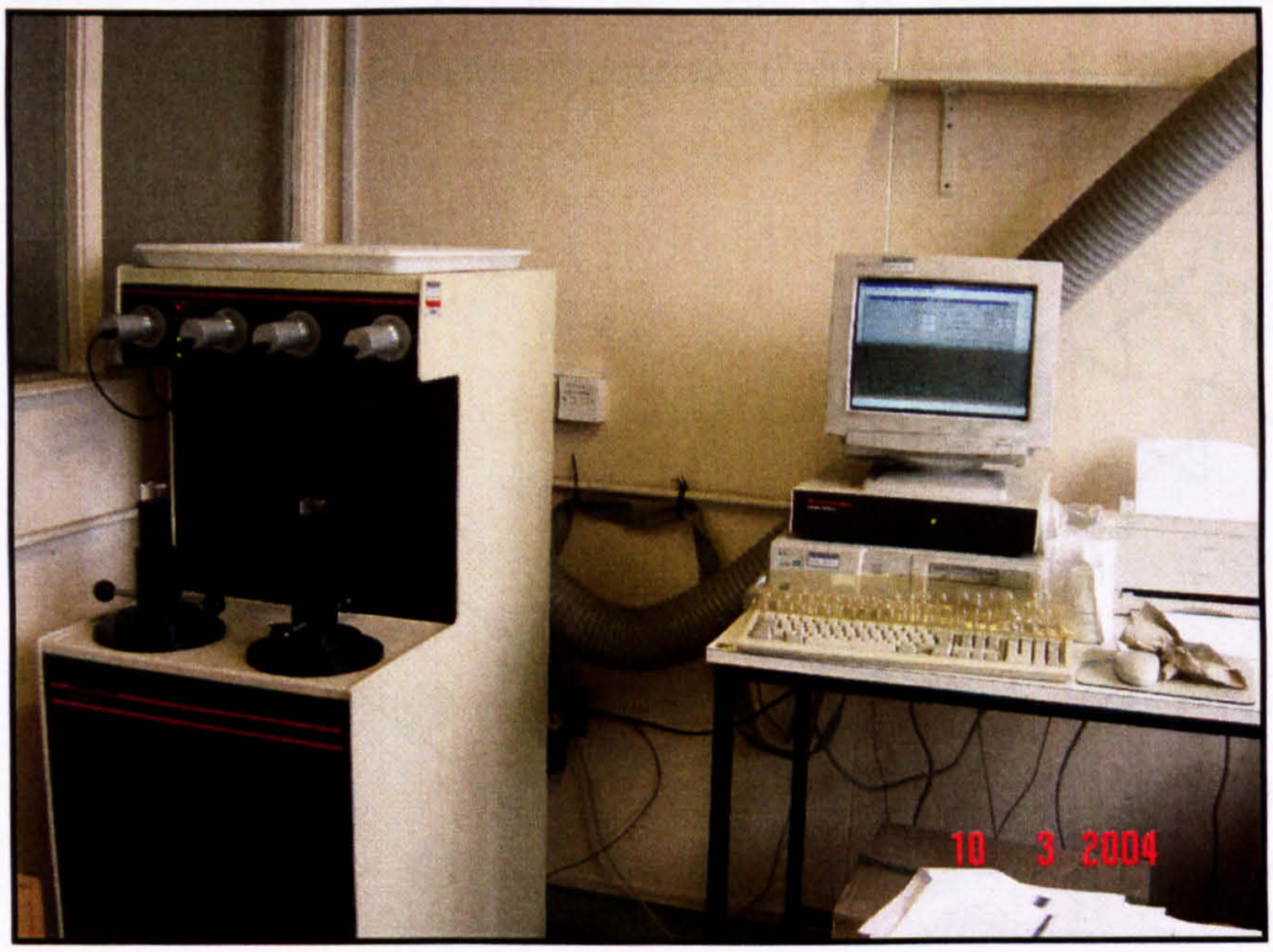

Figure 4.13 The Leeds Micromeritics Autopore Model 9200.

4.8 X-ray powder diffraction (XRD) analysis

X-ray powder diffraction is a very powerful and most commonly used technique for characterizing solid materials. This technique is based on the phase relationship between the scattered X-ray photon waves from the crystal plane as shown in Figure 4.14. The magnitude of the distance between two adjacent and parallel planes of atoms can be determined by applying the Bragg's law.

$$n\lambda = 2d\sin\theta \tag{4.13}$$

Where n = integer number called the order of the diffracted beam

λ = wavelength of X-rays

d = distance between adjacent planes of atoms called d-spacing.

The characteristic d-spacings and the peak intensities can be used as a unique fingerprint of minerals present in the specimen. By proper comparison with the standard reference patterns available for various compounds, the unknown minerals can be identified (for more details about this technique see Cullity and Stock, 2001).

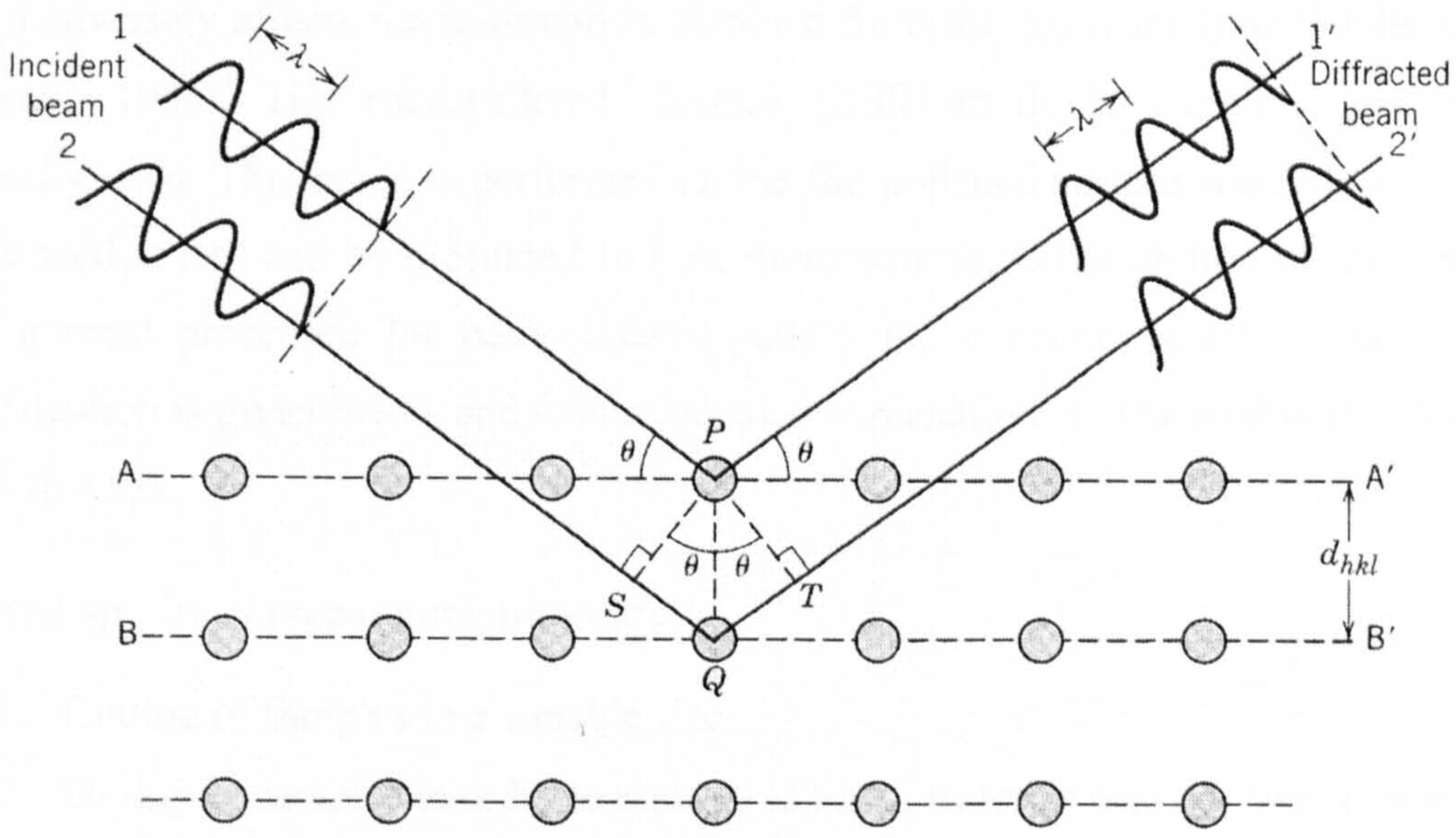

Figure 4.14 Diffraction of X-rays by planes of atoms (A-Á and B-B́) (copied from Callister, 2005).

This technique was used for determining the mineral components of the Glensanda granite quarry waste, ball clay, synthetic aggregates fired at 900°, 1,110°, 1,110° with 10 minutes sintering period, 1,120°C with 1.5 and 3.5 minutes sintering time. A very fine powder of these samples was prepared, and kept in sealed sample bags until tested. The interpreted results are presented in section 6.3.

4.9 Specimen preparation for the SEM analysis

This section provides details concerning the sample preparation of the sintered pellets produced from different firing conditions and concrete that contains natural, Lytag and synthetic aggregate for microscopic investigation. In the SEM analysis, there are two principal modes that are normally used, which are the secondary electron (SE) and the backscattered electron (BSE) mode. A brief detailed explanation about electron microscopy will be given in section 5.2. Most of the SEM studies in the past were normally performed in the SE mode due to it is ease of sample preparation and high degree of image resolution. Analysis in this mode gives the topographical information of the fractured surfaces. The main drawback of using SE mode is the fracture surface is not a representative section of the sample because it represents only a weakest surface and it adversely effects the information obtained from the X-ray analysis (Kjellsen and Monsøy, 1996). The backscattered electron (BSE) mode is therefore now more normally used. This mode is performed on the flat polished surface which is a random cross section and can be presumed to be a more representative section of the sample. The general procedure for both sintered pellets and concrete samples used in this investigation is given below and a more detailed explanation is presented in the sections 4.9.1 to 4.9.5.

General specimen preparation procedure:

1. Cutting of samples to a suitable size
2. Drying of samples in order to remove as much water as possible with minimal damage to microstructure
3. Vacuum resin impregnation of sample – fill pores and stabilize the structure during the grinding and polishing stages
4. Grinding of sample performed with SiC paper using successively finer grades of paper

5. Polishing of sample
6. Coating the sample's surface with a thin layer of electrically conductive material

4.9.1 Cutting of sample

Cutting of sample is the first step of the specimen preparation for microstructural analysis and this is one of the most important stages because improper cutting will lead to misinterpretation of data. Cracks and rough surfaces produced by improper cutting affect the image quality by reducing the image contrast and loss of feature definition (Stutzman and Clifton, 1999). Therefore, damage generated by the cutting process must be minimized.

. In this study, the low speed saw as shown on Figure 4.15 was used to cut the synthetic aggregates. The saw speed and the pressure of the blade that presses on the sample can be adjusted and they are dependent on the hardness of each sample. The lower speed and lighter pressure was used for the lower degree of sintering pellets. The sintered pellets from different firing conditions having the size of about 14 mm were randomly selected. There are seven firing conditions considered for the SEM-image analysis which are 900°C, 1000°C, 1110°C with 0 minute sintering time and 1110°C with 1.5, 5, 10 and 20 minutes sintering time. After cutting, one of the cut pellets was oven dried at 105°C for 24 hours in order to remove water from the pore structure of the pellet allowing resin to be impregnated.

For the case of concrete samples, cylindrical cores with the size of 25 mm diameter were drilled out from the 420x270x40 mm slab with water as a coolant. The core was then cut by using the Discoplan TS cut-off saw manufactured by STRUERS Ltd. as shown in Figure 4.16. In this research, a slice of about 8 mm thickness was cut horizontally from the middle part of the sample (Figure 4.17).

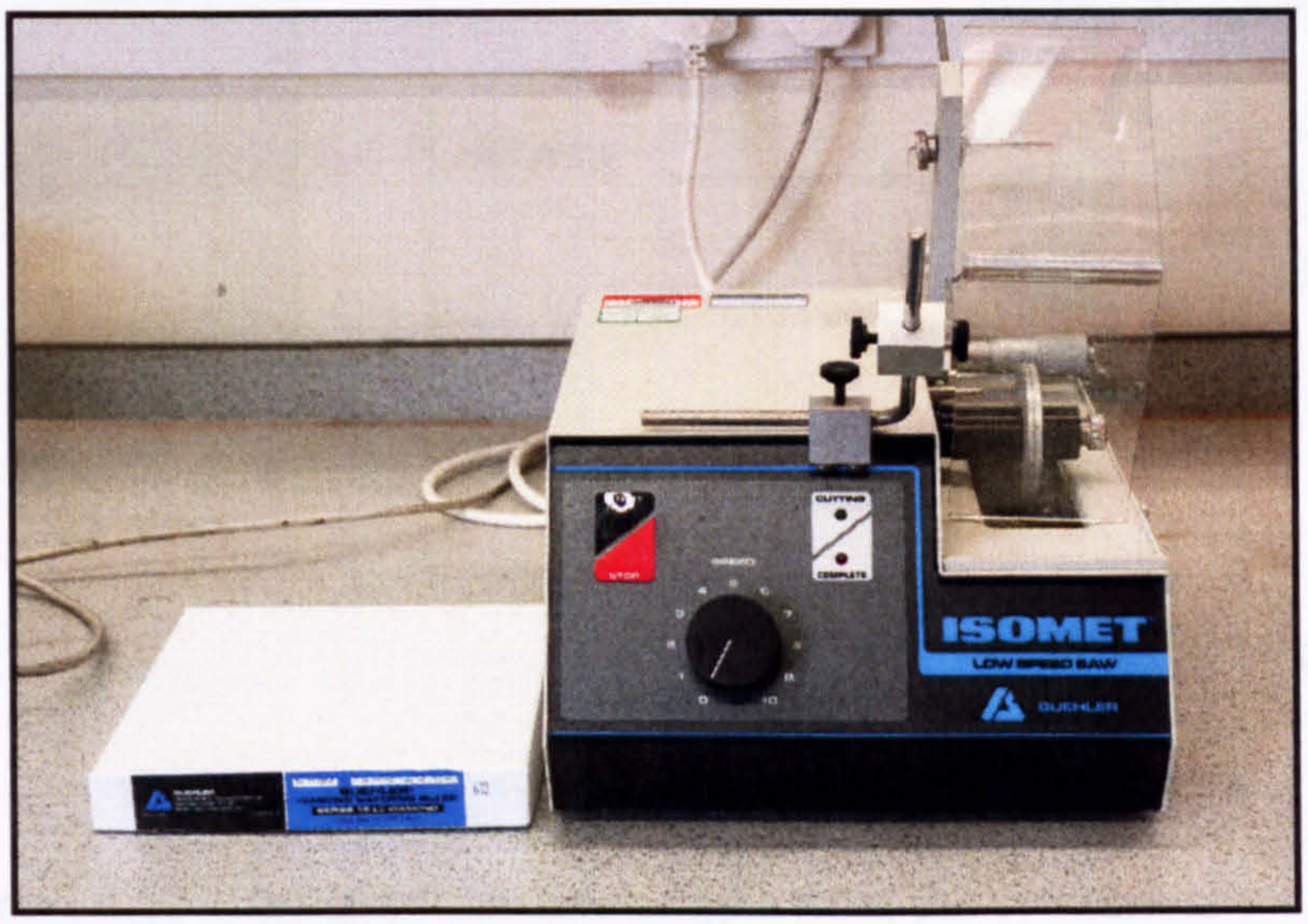

Figure 4.15 Low speed saw used for synthetic aggregate.

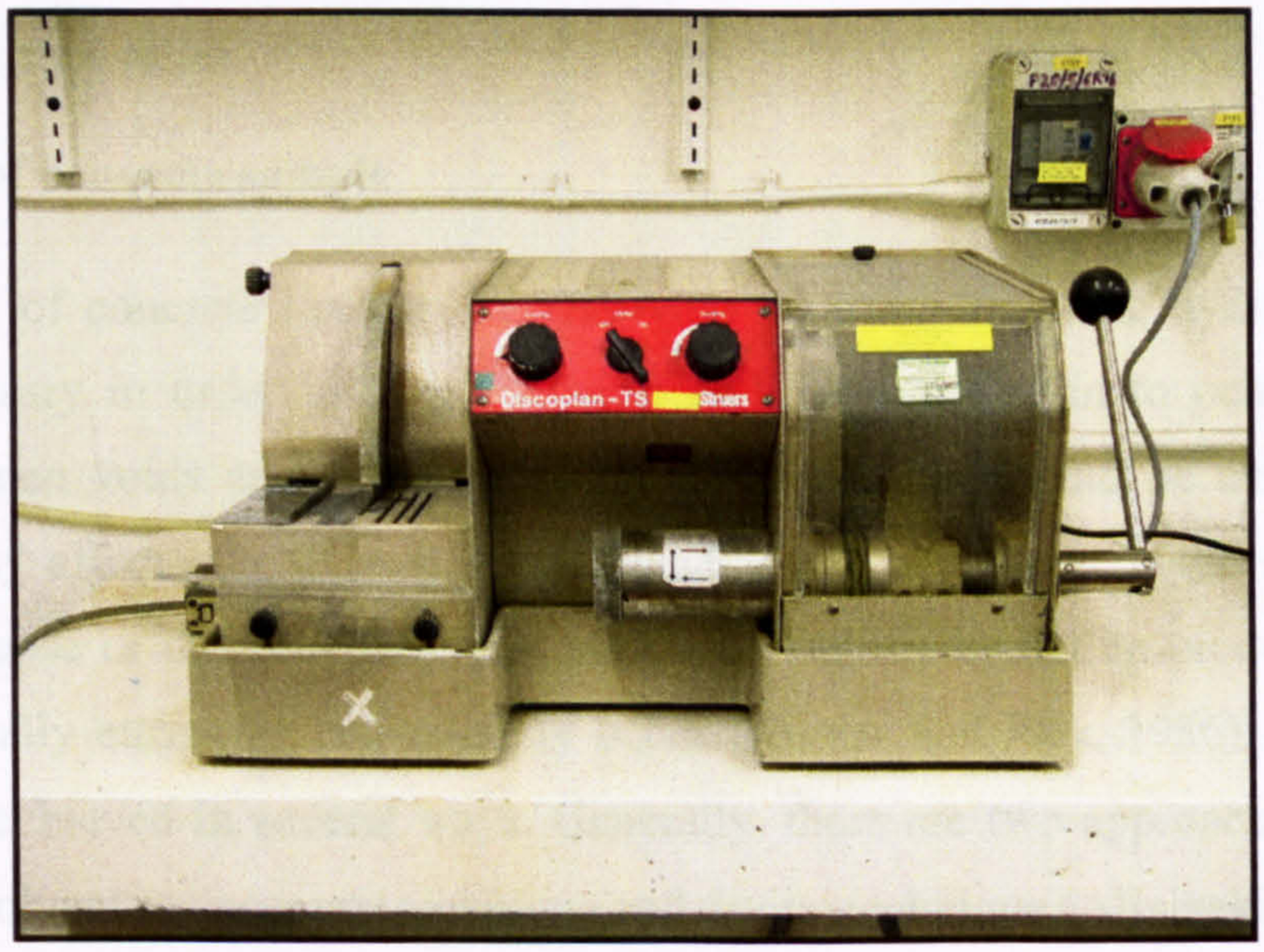

Figure 4.16 Discoplan TS: Cutting and grinding machine.

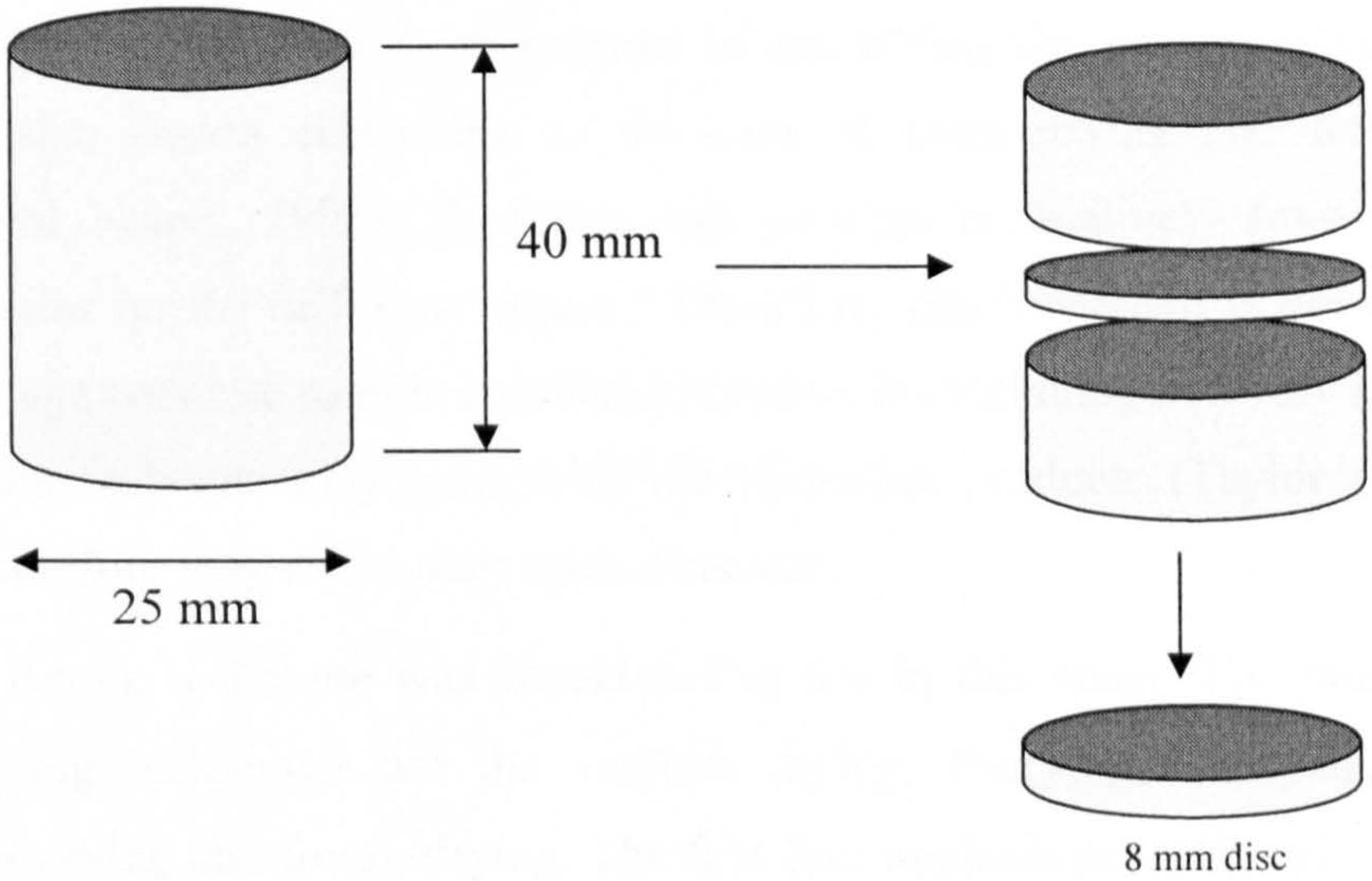

Figure 4.17 Cutting of concrete sample from the cylindrical core.

Grinding with 1200 grit SiC paper after cutting the sample may be necessary in order to make the cut surface as flat as possible. The sample was then carefully cleaned by using the hydrocarbon solution (non-hydrating solution) to remove debris at the end of grinding operation. However, this should be carefully done without causing any damage and surface relief.

4.9.2 Drying of concrete sample

Drying of concrete samples by removing all water from the hydrated cement paste is necessary in order to stop hydration and allow the resin to penetrate freely through the open voids and spaces. However, this process should be carefully done because it may affects the pore structure and the microstructure of the sample. The structural collapse or the dehydration of poorly crystalline hydration products through drying, especially ettringite, can possibly occur (Kumar and Roy, 1986). Removal of water can be achieved in several ways. Generally, there are two approaches for water removal, i.e. solvent replacement technique and drying technique (Aligizaki, 2006).

The solvent replacement technique is the technique that is considered to be less harmful to the structure of the cement paste and it is believed to reduce the extent of microcracking in the sample (Aligizaki, 2006). This technique is done by a replacement of the pore solution in hydrated cement paste with the appropriate organic liquids, e.g. alcohols methanol, ethanol or isopropanol, through a simple counter-diffusion process

(Aligizaki, 2006). It was shown by using the MIP technique that the solvent replacement technique is the best in terms of preserving the pores especially in the finest pore size region comparing to the case of oven drying and freeze drying (Konecny and Naqvi, 1993). However, this process is relatively time consuming because it relies on the diffusion process. Therefore, this technique is not appropriate for the early age concrete sample in which hydration is continuing at a very high rate. In addition, some solvents may react with the hydration products (Taylor and Turner, 1987) and therefore may affect their microstructure.

The drying technique was considered to use in this study. The most common standard drying techniques are the vacuum drying, P-drying, D-drying, desiccant drying, oven-drying and freeze-drying. The first four methods are relatively slow which makes them suitable for samples older than 28 days having fairly low evaporable water contents (Aligizaki, 2006; Detwiler et. al., 2001). The oven-drying technique by placing samples into an oven for a certain period of time with relatively high temperature is normally used because it is easy and a very effective way to remove water from the sample. However, the main drawbacks of this method are the generation of microcracking in the sample and the dehydration of the hydration product. A drying temperature below 35 °C was suggested by Detwiler et al. (2001) in order to reduce these effects.

An alternative technique that was selected for using in this research is the freeze-drying. In this technique, the samples were immersed in the liquid nitrogen at temperature about -195°C. For the small concrete slices of about 8 mm thick used in this study, freezing of water within the sample is almost instant and therefore the hydration process is stopped almost immediately at this point. Very small ice crystals or amorphous ice are developed due to a very fast cooling rate (Goldstein et. al., 2003). Such small ice crystals do not generate any expansive pressures within the pore structure therefore avoiding microstructural damage of the sample. The frozen samples are then transferred to the freeze drying chamber and the vacuum is applied at approximately 3.0×10^{-1} mbar. The ambient temperature was maintained inside the freeze-drying chamber and the temperature in the freezer chamber was maintained at approximately -45 °C ±5 °C (Head, 2001). A period of 24 hours was suggested by Kumar et al. (1986) for effectively removing the water from a water-saturated hardened cement paste sample. However, a period of 2 days was used here for reaching a constant

weight. During this period, as the temperature of the frozen samples are allowed to rise back to the ambient temperature, the water molecules are removed in the vacuum through the process of *sublimation*, that is, the water molecules change state from a solid to gaseous state without passing through a liquid stage. This eliminates the internal hydrostatic stresses that are developed during the drying of water, thus reducing the risk of microcracking (Moukwa and Aïtcin, 1988; Detwiler et. al., 2001). Any damage that could be induced in the fine gel pores in the C-S-H (approximately 2 nm) will not be visible under the SEM because this pore size is well below the resolution of the SEM (Detwiler et. al., 2001). In addition, any solutes presented in the pore solution are deposited on the pore walls without crystallizing, therefore remaining invisible under the microscope.

Figure 4.18 The freeze-drying equipment.

4.9.3 Resin Impregnation

The resin impregnation of samples with low viscosity epoxy resin is a common method for microstructural investigation. This process is necessary for reinforcing the microstructure serving to restrain it against the stress induced during subsequent grinding and polishing. It also helps to minimize the plucking of particles from some of the softer phases and prevents the accumulating deposits of the grinding/polishing media into the pores (Detwiler et. al., 2001). In addition, it increases the contrast

between pores, hydration products and cementitious materials in a visible light when containing a dye (Stutzman and Clifton, 1999; Head, 2001).

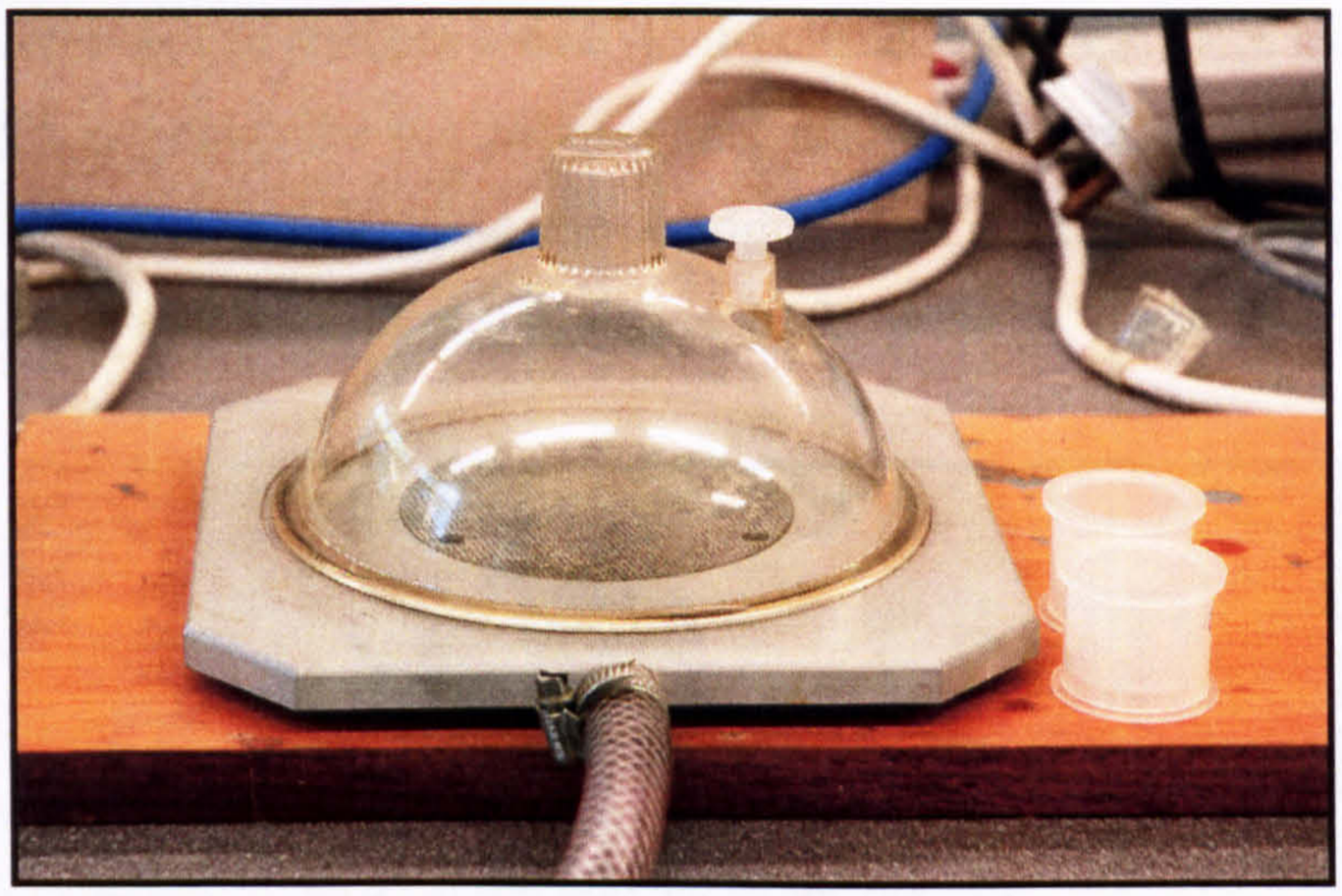

Figure 4.19 Vacuum resin impregnation apparatus.

The impregnation of low viscosity epoxy resin was performed in the vacuum chamber as shown in Figure 4.19. The first step involved the mixing of fifteen volumetric parts of epoxy resin with two parts of hardener in a paper cup while the sample was placed with its plane surface down on the plane surface of the mounting cup at the bottom of the mould which is made from polypropylene and has 30 mm diameter. A very low-viscosity epoxy resin (EPOFIX) used in this study was out-gassed first in a vacuum freeze drying chamber within an appropriate period of time otherwise the hardener will be pulled out from the resin. A warm airflow was then applied to it in order to reduce the viscosity of the resin and enhance the penetration depth in each sample. The resin was poured into the mold until the face of the specimen was completely covered by the out-gassed resin. The samples were then left in the vacuum chamber for a period of 10 minutes after which the vacuum was gradually released and brought back to normal atmospheric pressure in order to push the resin further into the samples. The average penetration depth of resin into concrete samples was around 2 mm as observed by Head (2001). The epoxy was cured at room temperature for at least 48 hours.

4.9.4 Grinding and polishing

The next stage was a very careful grinding and polishing. This process was done in order to remove any damage created during the cutting process and produce a flat surface. It is necessary to produce a really flat-polished sample surface (i.e. minimizing the topographic contrast) for the composional analysis in the backscattered electron mode of the SEM analysis. Grinding and polishing of all resin impregnated samples was done using the Rotopol-35 as shown in Figure 4.20.

Figure 4.20 *STRUERS* 'Rotopol-35' grinding and polishing machine.

The sample was first dry ground with the 240 grade silicon carbide (SiC) abrasive paper until the excess resin from the surface of the sample was removed. The finer grades of the SiC paper, i.e. 500, 1,200 and 2,400, were then successively used in order to remove the damage created by the earlier grit, gradually reducing any scratches and producing a suitable surface for polishing. At each grinding stage, the sample was cleaned by using the hydrocarbon solution which does not promote hydration of the cement particles and the surface condition was carefully checked by using the optical microscope. The applied pressure and the grinding duration at each particular SiC paper depend on the surface condition of each sample.

The final polishing was performed by using the diamond particle sizes of 3, 1, and 0.25 microns. These diamond particles are not fixed to the paper as in the case of

the SiC paper which has SiC particles glued to one side of the paper. A particular size of the diamond paste was applied on a special woven synthetic cloth. This process must be done very carefully. Polishing at high pressure and/or for a long period of time may result in a severe surface relief. At each stage, the hydrocarbon solution was used to clean the sample and the surface relief was carefully checked by using the reflected light microscope.

Note that both of the synthetic aggregate and the concrete samples used a similar grinding and polishing procedure. The only differences are the applied force on each sample, length of time for grinding/polishing and the rotational speed applied at each stage. The quality of the finishing product relies mainly on the experience of the operator.

4.9.5 Coating of sample

The polished samples which are a nonconductive material were then coated with a thin film of the conductive material before being investigated by the SEM. This was done in order to avoid the distortion of the SE and BSE images due to the electric charge which can build-up rapidly on the investigated surface under a high energy incident electron beam. The conducting path formed by a very thin coating layer reduces the build-up of negative charge on the sample surface and, therefore, a distortion of images can be avoided. Coating with carbon on the flat-polished sample was used in this study for the analysis in the BSE mode and gold was used for the SE mode. The coated samples were then stored in the desiccators with silica gel before and after the examination on the microscope.

4.10 Variation of product and sampling sized required

The testing of the synthetic aggregate when using a test such as mercury intrusion porosimetry (MIP) was carried out on a small number of samples obtained by sampling from a much larger number of populations in each batch. The variability of the results from one sample or batch to another is the significant important factor needed to be concerned. A substantial variation can occur during the production stage of the synthetic aggregate which might come from the efficiency of the kiln and can also occur during the testing of the sample. In addition, the variation of the raw materials themselves such as the particle size distribution or the mineral composition also influences the variation of the test result. A similar situation takes place when analyzing the microstructure of material, i.e. pore structure of the synthetic aggregate or the analysis of the aggregate-cement paste interface microstructure, by using the SEM image analysis technique. Because the material is not homogeneous, the results from the image analysis will vary from field to field. It is, therefore, important to know how large these variations are, how representative the samples are and how much reliance can be placed on the outcome of the test results.

Ideally, the expected properties of the sintered product are that it should be largely spherical in shape, a uniform pore size distribution with relatively impermeable outer surface, but it should also provide good adherence to the cement paste. These properties can be ascertained by using the mercury intrusion porosimetry test, water absorption test and SEM image analysis. The parameters of MIP that will be considered here in order to check for the variation of the test results are the total porosity and the mean distribution radius (r_m). The mean distribution radius was suggested by Laskar et al. (1997) which is aimed at establishing a correlation between the pore system characteristics and the durability performance of concrete.

The total porosity is defined as the ratio of the total volume of pores to the bulk volume of sample and can be estimated from the cumulative intrusion volume and relative weight measurements. The mean distribution pore radius is defined as the mean pore size and is the weighted average, weighted with respect to the volume of pores at corresponding pore radius. The estimation of this value can be done by using the following equation:

$$\ln r_m = \frac{\sum_{i=1}^{n} V_i \ln r_i}{\sum_{i=1}^{n} V_i} \tag{4.14}$$

Where, for the continuous intrusion curve divided into '*n*' discrete radii ranges, V_i is the incremental intrusion of mercury corresponding to the '*i*' th radius range represented by the mean radius r_i.

These parameters of water absorption and MIP test therefore must be estimated with sufficient accuracy in order to represent the characteristics of the sintered product. The number of samples or batches required to be tested in order to ensure the required accuracy can be ascertained statistically and this analysis is the subject of the next section.

A similar analysis needs to be done for the case of SEM image analysis of the synthetic aggregate and concrete sample, i.e. a sufficient number of fields or images must be calculated so that the average result of each component of interest is a representative of the investigated sample.

4.10.1 Standard error of mean

Considering the situation where many samples were randomly taken from the whole population which has a normal distribution, the mean and standard deviation of each sample were determined. The obtained sample mean values were then plotted and will have a normal distribution. The mean value of the sample means can prove to be an unbiased estimator of the population mean, while its standard deviation (population standard deviation divided by the sample size) will describe the variability or spread of sample means about the true population mean (Till, 1974).

However, in the practical situation, only one sample mean is normally had. In this case, the deviation of sample mean from the true value can be estimated by using the parameter called the *standard error of mean* (*SE*).

$$SE = \frac{\sigma}{\sqrt{n}} \tag{4.15}$$

Where σ = standard deviation of the population

n = random sample size

This formula obviously can not be used when the population standard deviation is unknown. In this case, the sample standard deviation is used instead in order to estimate the standard error of mean.

4.10.2 Estimation of the sample size

It is desirable to have the sampling units large enough so that they can be representative of the whole batch within acceptable and known limits, but small enough for convenience in handling. The procedure of ascertaining the minimum number of samples to ensure a reasonable accuracy of the test result is based on the following statistical principles. By assuming normal distribution for the sample, the following equation can be used

$$Z = \frac{\overline{X} - \mu}{SE} \tag{4.16}$$

Where Z = standard normal variable for a given confidence interval

$\overline{X}$ = sample mean

μ = expected value or the population mean

SE = standard error of $\overline{X}$, represents the deviation of $\overline{X}$ from its target μ.

The desirable sample size can be estimated by substituting Equation (4.15) into (4.16) and rearranging to obtain the following formula.

$$n = \left(\frac{Z\sigma}{E}\right)^2 \tag{4.17}$$

For 95% confidence interval Z is equal 1.96 as given by the standard normal distribution tables. The number of particles in the samples n, can be given by substituting the value of Z corresponding to 95% confidence in Equation (4.17) as shown below

$$n = \left(\frac{1.96\sigma}{E}\right)^2 \tag{4.18}$$

Where E = specified amount of tolerable error ($\overline{X} - \mu$ or $e.\mu$)

e = permissible error ($\pm$%)

Note that the student's t-distribution can be applied in order to obtained a more accurate and conservative estimation of n by replacing 1.96 in Equation (4.18) by t_{n-1}. However, t_{n-1} approaches 1.96 for a large sample sizes.

4.11 Summary

This chapter deals with the information about the raw materials used for producing the concrete samples, together with the concrete mix proportions and details of the concrete casting procedure. In addition, the details of the experiments that were used in this research and the specimen preparation procedure for the microstructural analysis are presented in this chapter. In the last section of this chapter, a description of the technique used to establish the minimum sampling size needed to obtain a representative result for the synthetic aggregate properties and the SEM image analysis is given.

Preparation of the synthetic aggregate sample by the oven-dried technique in order to remove the residual water and the volatile materials was successfully used in this research and it provided comparatively logical results for the synthetic aggregate pore structure which was produced from different firing condition.

In general, the specimen preparations for the SEM analysis for both synthetic aggregate and concrete sample are similar. However, a slight modification was required. For example, the oven-dried technique was successfully used for the synthetic aggregate samples, while the freeze-drying technique was selected for the concrete sample. Moreover, the duration or the length of time for grinding/polishing, the rotational speed applied at each stage and the force that was applied on each sample also had to be different.

Chapter 5

Electron microscopy and image analysis

5.1 Introduction

Understanding of the basic principle of electron microscopy, e.g. electron beam-specimen interaction, signal/image processing, principle of image formation, etc, is very important for the interpretation of images and analytical results obtained from this technique. Therefore, a brief overview of the basic principle of the electron microscopy is given in the first part of this chapter. The remaining part provides a detailed explanation and discussion about the image analysis techniques that were adopted and developed during the study.

5.2 Scanning Electron Microscopy

There are two principle microscopy techniques which are widely used for study of the cementitious materials; optical microscopy and electron microscopy. Optical microscope uses normal light to form an image. This technique is very popular and has been used extensively for the studying of cement clinker and the concrete aggregate because of it is easy to use and less time consuming. However, the resolution and the depth of focus are the main limitation of this technique.

The electron microscopy can be generally divided into two principal techniques; transmission electron microscopy (TEM) and scanning electron microscopy (SEM). These two techniques are very similar in that they use electrons instead of visible light to generate the object image. However, the ways in which the images are produced and magnified are entirely different. In TEM, this technique uses a high-energy electron beam to penetrate a very thin sample which is usually prepared by ion milling and the image is formed by the projection of the transmitted electrons. It provides the information about the internal structure of the thin samples. The resolution of this microscope is much greater than SEM, around 10 nm comparing to 1 μm in SEM (Scrivener, 1997). However, this technique is not widely used for cementitious materials because of the difficulty of the sample preparation. In SEM, however, a medium-energy electron beam is used to scan the sample surface and the scattered electrons that generate from the interaction between the electron beam and the atom of the specimen are used to generate the sample images (Goodhew and Humphreys, 1997). The main

reason that makes this technique widely used at present to study the microstructure of materials are the large depth of field compared to the optical microscope, its flexibility and a wide range of magnifications (from around 10x to 10,000x) (Goldstein et. al., 2003).

Figure 5.1 The Cambridge Stereoscan 360 used in this study.

The scanning electron microscope used in this study is the 'Stereoscan 360' developed by Cambridge Instrument Ltd., as shown in Figure 5.1. It is a fully computer controlled scanning electron microscope which generally consists of the display units, operating console, computerized control system, column and electron gun unit, specimen chamber and stage and three different types of detector which are the secondary electron, backscattered electron and X-ray detector.

5.2.1 Working principle of the SEM

The SEM generally consists of an electron gun, condenser lenses which are used to de-magnify the electron beam, objective lenses that focus the probe onto the specimen surface, a system that controls the movement of the beam, specimen stage, signal collecting (electron detector), signal amplification and the display unit. All of these features and their arrangement in the microscope of the typical SEM are shown in Figure 5.2. The image formation in SEM is quite different from the optical microscope and a brief explanation is given as follow.

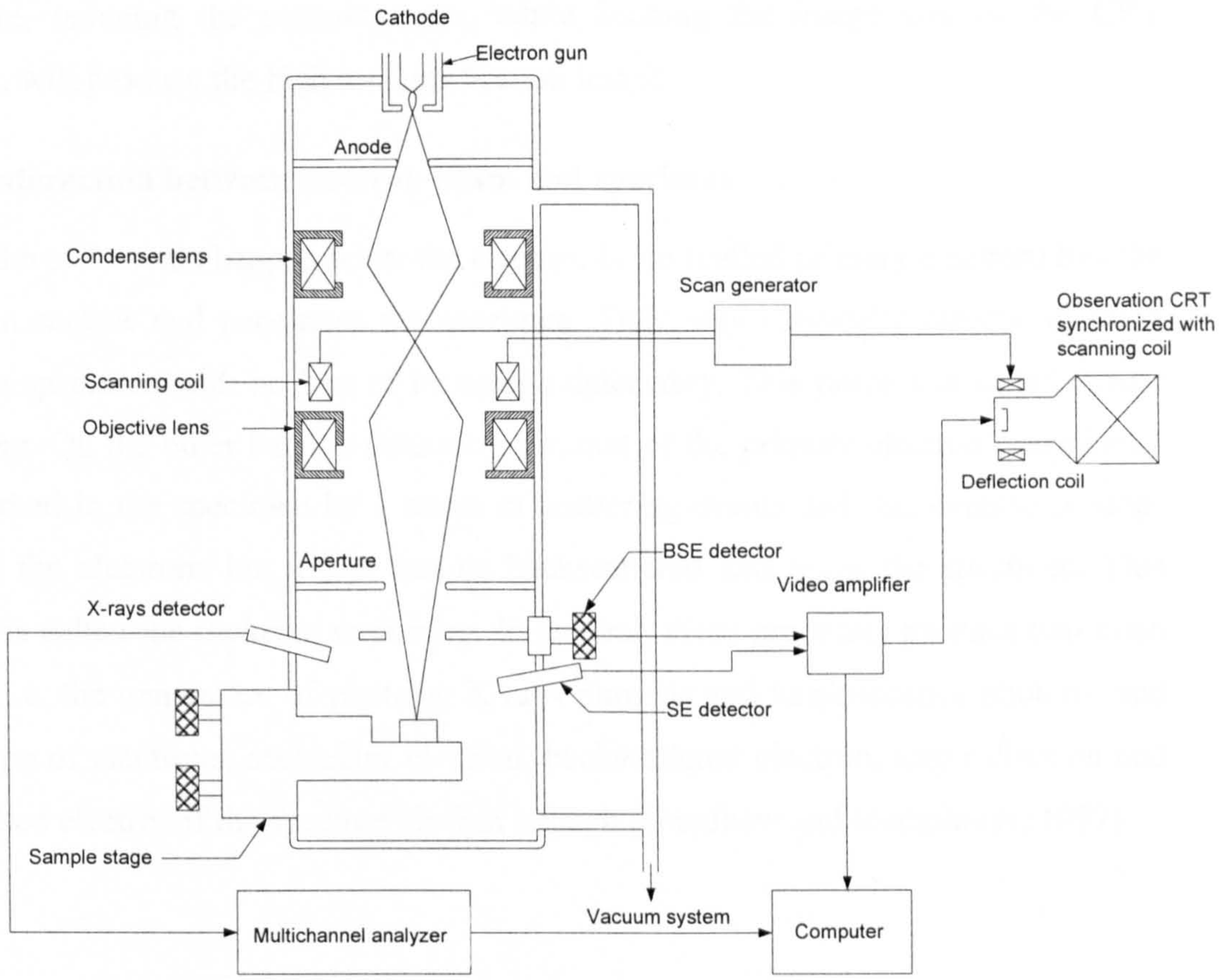

Figure 5.2 Schematic drawing of a typical scanning electron microscope. (Goodhew and Humphreys, 1997)

Firstly, the electron beam is generated by the electron gun and it is focused into a very fine probe on the specimen surface. The probe size depends on the type of the electron gun used; i.e. 5 to 10 nm for a thermionic electron gun and 0.5 to 2 nm for the field emission gun (Aligizaki, 2006). This beam can be accelerated by the voltage difference between the cathode and anode and its movement is controlled by the scanning coils in order to scan over the interesting area as a series of straight lines which form a rectangular frame. This kind of movement is normally known as a *raster*. At the same time, the observation cathode ray tube (CRT) or the display screen is scanned across and its movement synchronizes with the raster movement of the electron beam inside the microscope. Every point that the electron hits on the specimen surface is mapped directly onto the corresponding point of the CRT screen. In this way, the image is formed point by point and line by line during the raster movement of the beam. Moreover, the magnification of the image clearly depends on the scanning area.

Therefore, reducing the scanning area, while keeping the image size on the CRT constant, will produce the higher magnification image.

5.2.2 Interaction between electron beam and specimen

Several events happen when the electron beam (called primary electron) hits the specimen surface and penetrates the specimen. They may elastically change direction from the specimen with no loss of its energy detectably. This process is called *elastic scattering*. On the other hand, a detectable amount of the primary electron energy may be absorbed in the specimen by a series of scattering events and this eventually stops most of the electrons but a few can be backscattered and leave the specimen. This process is called the *inelastic scattering*. In general, these processes produce two main effects, i.e. the generation of photons; X-rays photons and luminescence photons, and other type of electrons; secondary electron, backscattered electron, auger electron and transmitted electron if the specimen is thin enough (Goodhew and Humphreys, 1997).

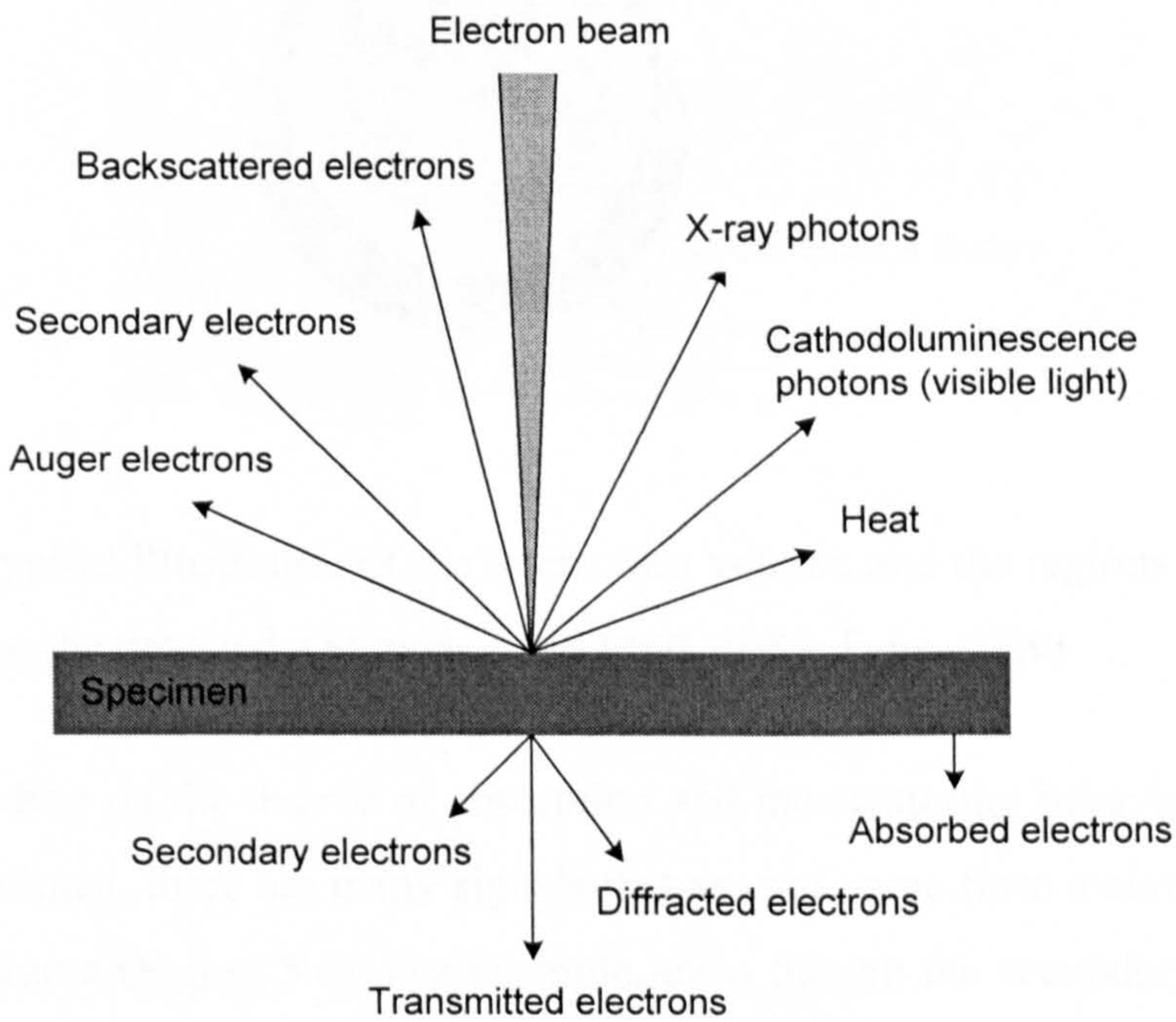

Figure 5.3 A summary of various effects resulting from the interaction between electron beam and specimen, adapted from Krinsley et al. (1998).

Most of these signals are very useful for the analysis of materials but only secondary electron (SE), backscattered electron (BSE) and X-rays will be used in this study and a brief explanation of them is given in the following section.

As mentioned before, most of the electrons will eventually stop in the specimen and this phenomenon occurs within a volume of a tear drop shape as represented in Figure 5.4. This region is known as the *interaction volume* and it is a volume below the specimen surface. Understanding of the interaction volume is very important because its size affects the lateral resolution of the image generated from each signal.

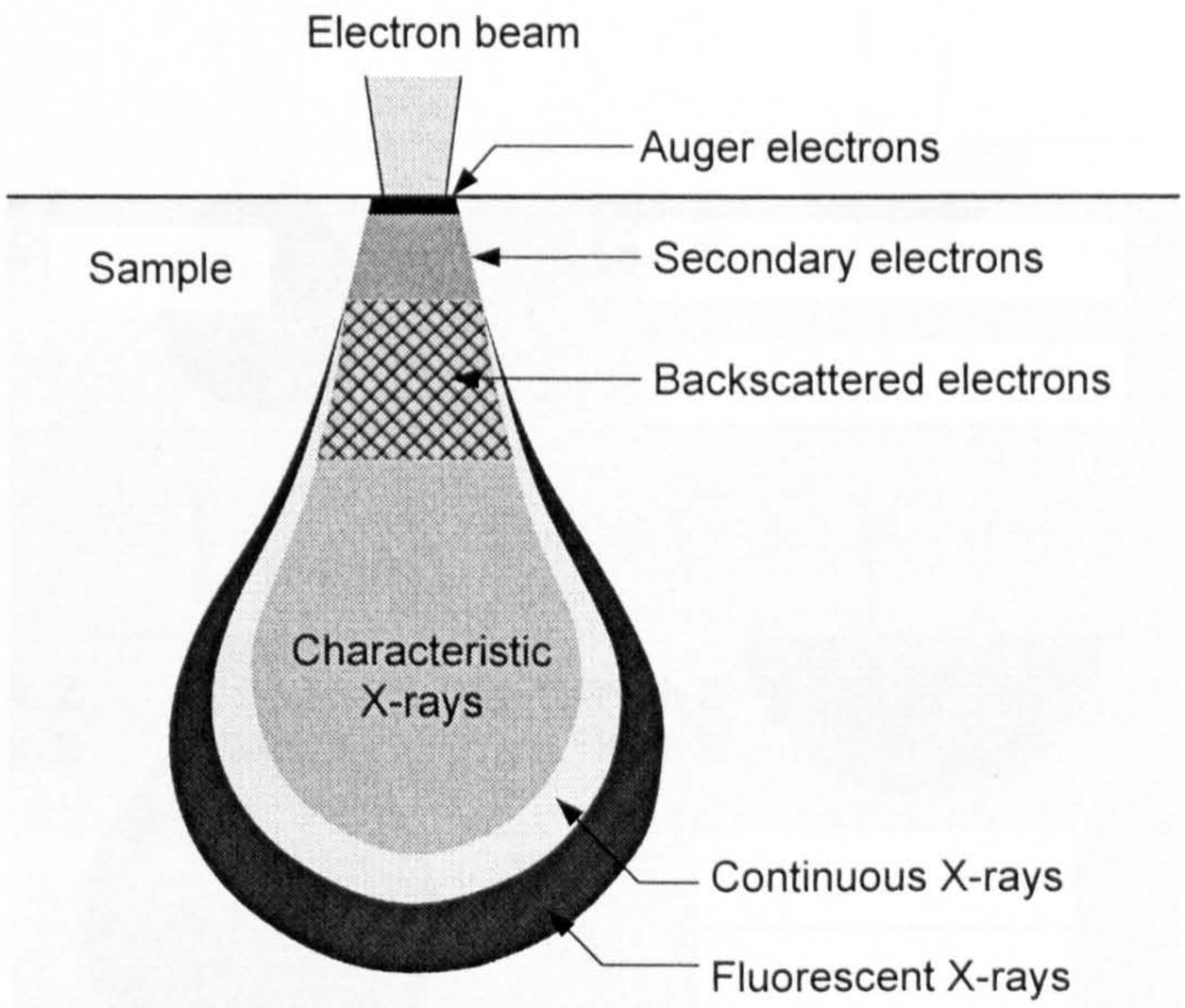

Figure 5.4 Typical illustration of the interaction volume and the regions of the various signals that may be detected. (Scrivener and Pratt, 1984; Fens, 2000)

Depending on the degree of absorption and the scattering behavior of electrons inside the specimen, there are many signals that are not come from a certain part of the interaction volume (Figure 5.4). For example, even though the secondary electron and auger electron are produced throughout the interaction volume, there are only electrons coming from a thin layer of the specimen surface that can be detected. This is because both of them have very low energies that make them very easy to be reabsorbed in the sample.

The penetration depth and shape of the interaction volume mainly depends on the average atomic number of the specimen and the applied accelerating voltage (Figure 5.5). With the higher accelerating voltage, the incident electrons penetrate deeply into the specimen and produce a larger interaction volume. For the higher average atomic number specimen, there is much greater scattering event occurs near the specimen surface; consequently, more electrons are scattered and emerge as backscattered electrons compared to the lower average atomic number sample with the same energy.

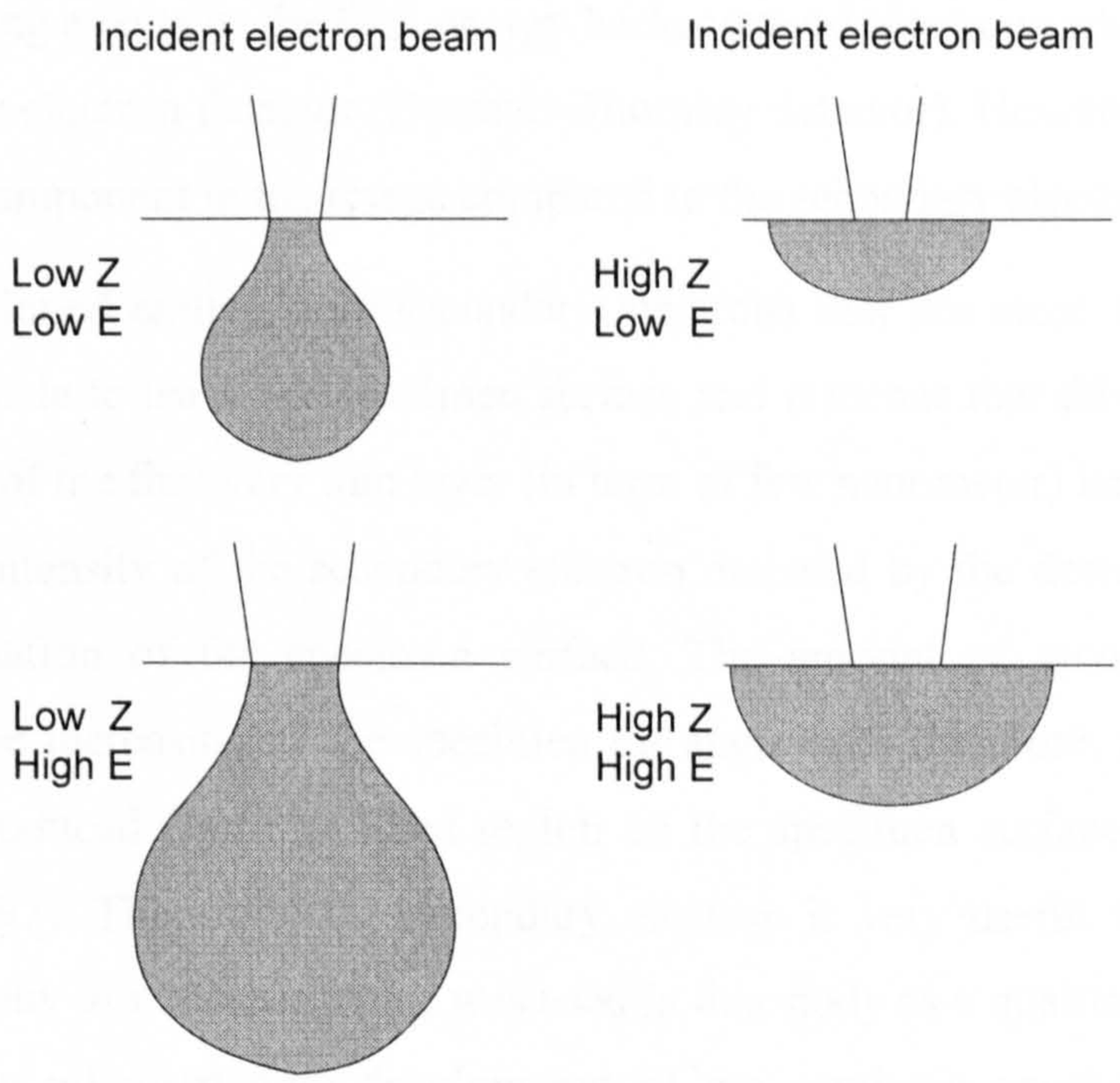

Figure 5.5 Schematic illustrating the variation of the interaction volume shape with the incident electron beam accelerating voltage (E) and the average specimen atomic number (Z).

With the electron beam incident perpendicular to the specimen, the diameter of the interaction volume for cementitious materials is typically about 1 to 2 μm (Scrivener, 2004) and its depth can be estimated by using the expression proposed by Kanaya and Okayama which is known as the K-O range (cited by Zhao and Darwin, 1992) or by using the Monte Carlo simulation technique to simulate the electron-solid interaction (Goldstein et. al., 2003; Wong and Buenfeld, 2006).

5.2.3 Secondary electron imaging

The secondary electron is a term used to describe those electrons, which escape from the sample surface, that have energy less than about 50 eV (normally less than 10 eV) (Goodhew and Humphreys, 1997; Krinsley et. al., 1998; Goldstein et. al. 2003). Most of these electrons result from the collision of the incident electron with the loosely bound outer shell electron in the specimen atoms causing the latter which have sufficient kinetic energy to be rejected and leave the atom. It should be noted here that a few of them could be the primary electrons which have very low energy left after multiple scattering events or the high energy backscattered electrons which travel direct to the secondary electron detector (Everhart-Thornley detector). However, these signals are a minority component in the image compared to the secondary electron.

As mentioned earlier, only secondary electrons that are close to the specimen surface will be able to leave the specimen surface and it means that this signal gives us the information of the first very thin layer (in term of few nanometer) below the surface. Moreover, the intensity of the secondary electron detected by the detector depends on the local inclination of the specimen surface. The amount of secondary electrons increase with the increasing of the specimen tilt angle and, therefore, more secondary electrons are produced from the tilted region on the specimen surface (Goodhew and Humphreys, 1997). Therefore, the secondary electron is very useful for studying the surface topography of materials and it was used in this study as a qualitative analysis for investigating the microstructure development of the synthetic aggregate at different firing condition.

5.2.4 Backscattered electron imaging

The *backscattered electron* (BSE) is the primary electron that undergoes a large deflection due to the multiple elastic scattering events within the specimen which eventually direct back and leave the specimen surface with the remainder of their energy greater than 50 eV. The remaining energy of the backscattered electron could range from 50 eV to that of the primary electrons and it has very high energy comparing to the secondary electrons.

There are two types of backscattered electron detector; the scintillator detector and the solid-state detector. The solid-state detector (annular type semiconductor detector) was used in this study. It consists of four separate elements which are placed above the specimen on either side of the electron optical axis. Each of them is connected to an amplifier and can individually provide a separate BSE signal. These allow the production of either a compositional image or a topographical image by addition or subtraction of the signals from the detectors.

Each quadrant of the detector can be in one of three states including *off*, *normal* or *invert*. When *normal*, the signal from that quadrant is added to the total signal, while subtraction is performed when *invert*. Various combinations of quadrant settings, as given in the detector manual instruction, will give various mixes of the topographical image. This image represents the topography of the specimen surface and it was used together with the secondary electron mode as the final check for the specimen preparation. The compositional image, on the other hand, is obtained by adding those four signals in order to minimize the influence of the topographic contrast. The number of backscattered electrons generated or emitted from the specimen for each incident electron can be quantified by its *backscattered electron coefficient* (η).

$$\eta = \frac{number\ of\ backscattered\ electrons}{number\ of\ incident\ electrons} \tag{5.1}$$

This coefficient was found to be strongly dependent on the atomic numbers (Z) of the specimen constituent elements and η for the pure element can be calculated from the empirical equation proposed by Reuter (cited by Goldstein et. al., 2003).

$$\eta = -0.0254 + 0.016\,Z - 1.86\times10^{-4}\,Z^2 + 8.3\times10^{-7}\,Z^3 \tag{5.2}$$

A simple rule of mixtures which based on the weight (mass) fractions of each elemental component can apply for a homogeneous mixture specimen.

$$\eta_{mix} = \sum_i C_i\,\eta_i \tag{5.3}$$

Where C_i = the weight fraction

η_i = the backscattered coefficient for the element i

It should be noted that in order to observe purely compositional contrast, the topographic effects need to be removed, i.e. a very flat and well polished specimen is required for backscattered electron imaging. The detailed explanation of the specimen preparation used in this study is already given in section 4.9.

As mentioned before, the SEM image is formed point by point and line by line during the raster movement of the electron beam across the specimen surface. When the electron beam is positioned at a particular location on the specimen surface for a fixed time interval, the backscattered electrons are generated beneath the specimen surface and some of them depending on the backscattered electron coefficient (η) leave the specimen and are detected by the solid-state detector where they create the electrical signal which is proportional to the backscattered electron intensity. This signal is then amplified by the signal amplifier and digitized to a numerical value (gray value) typically ranging from 0 (black) to 255 (white) discrete levels for the 8-bit binary number. This grey value is assigned to the associated beam position (pixel) and stored within the computer memory. The electron beam is then moved to the next position and this process is repeated until the whole backscattered image is obtained. Therefore, the backscattered electron image is the grey scale image which the brightness of each pixel clearly depends on the backscattered electron coefficient (η). Any region on the BSE image that covers a high mean atomic number element will appear brighter.

Table 5.1 represents the mean atomic number of various cement compounds and some minerals of ideal formula that might be contained in the synthetic aggregate. The grey level intensity of phases as given in this table are listed in ascending order and, therefore, in cement the unhydrated cement particles will appear as the brightest phase compared to the other hydration phases. In the case of minerals that belong to the solid solution series, such as feldspars and mica, the range of possible value of the mean atomic number and the backscattered electron coefficient is large (Hall and Lloyd, 1981; Pye and Krinsley, 1984) and more details about the variations in chemical composition of these mineral are given in section 6.4.

Table 5.1 Mean atomic numbers and backscattering coefficients of major constituents in Portland cement, their hydration products and some minerals. (Wong and Buenfeld, 2006; Krinsley et. al., 1998)

Phases/Mineral	Mean atomic number $\overline{Z}$	Backscattering coefficient η
Ettringite, $3CaO.Al_2O_3.3CaSO_4.32H_2O$	10.77	0.122
Monosulphate, $3CaO.Al_2O_3.CaSO_4.12H_2O$	11.67	0.132
Calcium silicate hydrate, $C_{1.7}$-S-H	12.09	0.137
Portlandite, $Ca(OH)_2$	14.30	0.162
Tricalcium aluminate, $3CaO.Al_2O_3$	14.34	0.164
Dicalcium silicate, $2CaO.SiO_2$	14.56	0.166
Tricalcium silicate, $3CaO.SiO_2$	15.06	0.172
Ferrite, $4CaO.Al_2O_3.Fe_2O_3$	16.65	0.186
Kaolinite, $Al_4Si_4O_{10}(OH)_8$	10.24	0.125
Albite, $NaAlSi_3O_8$	10.71	0.132
Quartz, SiO_2	10.80	0.132
Muscovite, $K_2Al_6Si_6O_{20}(OH)_4$	11.33	0.138
Calcite, $CaCO_3$	12.57	0.150
Hematite, Fe_2O_3	20.59	0.238

The amplified signal can be adjusted by using the brightness and contrast control until it fills the full dynamic range (grayscale range) of the CRT, i.e. from black to white. This signal adjustment is necessary because clipping of the signal will occur if it reaches one of the limits of the input intensity range of the CRT. In this research, this adjustment was aided by using the line-scan mode. An area that probably contained both brightest and darkest phases at the required magnification was selected first and then the beam was assigned to scan along a particular line which runs across both brightest and darkest phases. The brightness and contrast were adjusted together until the output signal from the detector matched the input intensity range of the CRT. Approximately 15 to 20 grayscales at either end were left free in this research and this is made because of the possibility of encountering phases that may be brighter or darker than phases in the selected area for line scan.

The BSE mode was used in this study in combination with the image analysis software (KS300) which will be mentioned in section 5.3.1 in order to perform the quantitative image analysis of the pore structure of the sintered pellet and the interfacial zone (ITZ) between cement paste and coarse aggregate. In order to obtain the representative result from the image analysis, a sufficient number of fields (or area) must be used at the appropriate magnification. For the ITZ analysis, about 20 areas were captured around randomly selected coarse aggregate particles from a single flat-polished specimen and this was done by scanning across the specimen surface in a grid line pattern. The quantities of the individual microstructural constituents (anhydrous cement, calcium hydroxide and porosity) near the interface were obtained by averaging from two samples (40 fields in combination) for each condition. This should be enough when compared to the number of fields that have usually been used in the literature (Zhao and Darwin, 1992; Scrivener et. al., 1987). However, the adequacy of the number of fields was still checked in this study by calculating the relative standard error (see section 7.2.1).

The selection of the magnification is very important in the SEM analysis. It is the compromise between the image resolution or the details required of the phases of interest and the number of fields that are required to obtain a representative result. It has been shown that the magnification of 400x gives a satisfactory results for the measurement of porosity (Scrivener et. al., 1987) and 200x for the anhydrous cement grain evaluation (Mouret et. al. 2001). The magnification of 500x was selected for this study for the ITZ analysis with the resolution of about 0.48 micron per pixel.

5.2.5 X-ray analysis

The gray levels of aggregate often overlap with the gray levels of the hydration product (see Figure 7.10 to 7.12) and this causes a big problem in the segmentation of each phase during the quantitative analysis. Therefore we need to remove all of the aggregate pixels from the image before any image analysis is performed. The X-ray dot maps of a selected element of aggregate which was captured simultaneously with the BSE image was used here in order to get rid of the aggregate part from the image (the detailed explanation of this process will be given in section 5.3.3.1). In this section, we will describe only the basic background of the X-ray generation, the system used for X-ray analysis and the basic operational setting that was utilized in this research.

The X-ray radiations, i.e. white radiation (or Bremsstrahlung) and characteristic X-rays, are the secondary effect caused by the primary electron beam (Goodhew and Humphreys, 1997). The white radiation is the X-rays photon which have continuum spectrum. This radiation is generated when some of the incident electrons lose their energy by deceleration during undergo interactions without knocking out any inner shell electron. The characteristic X-ray, on the other hand, is generated when the atoms are excited by the electron beam or photons that have enough energy and knock an inner shell electron out of their position leaving an atom in an excited or high energy state. One of the outer shell electrons then jump in to fill that inner shell vacancy, emitting the excess energy in the form of X-ray radiation whose wavelength depend on the nature of atoms in specimen and these resulting in a series of characteristic X-ray which we can use for the analytical purpose. It should be noted here that there also have a possibility for the X-ray photon to be absorbed by the outer shell electrons. In this case, the outer shell electron is then ejecting as the low energy *Auger electron* and the excess energy is carry away with this electron as a kinetic energy.

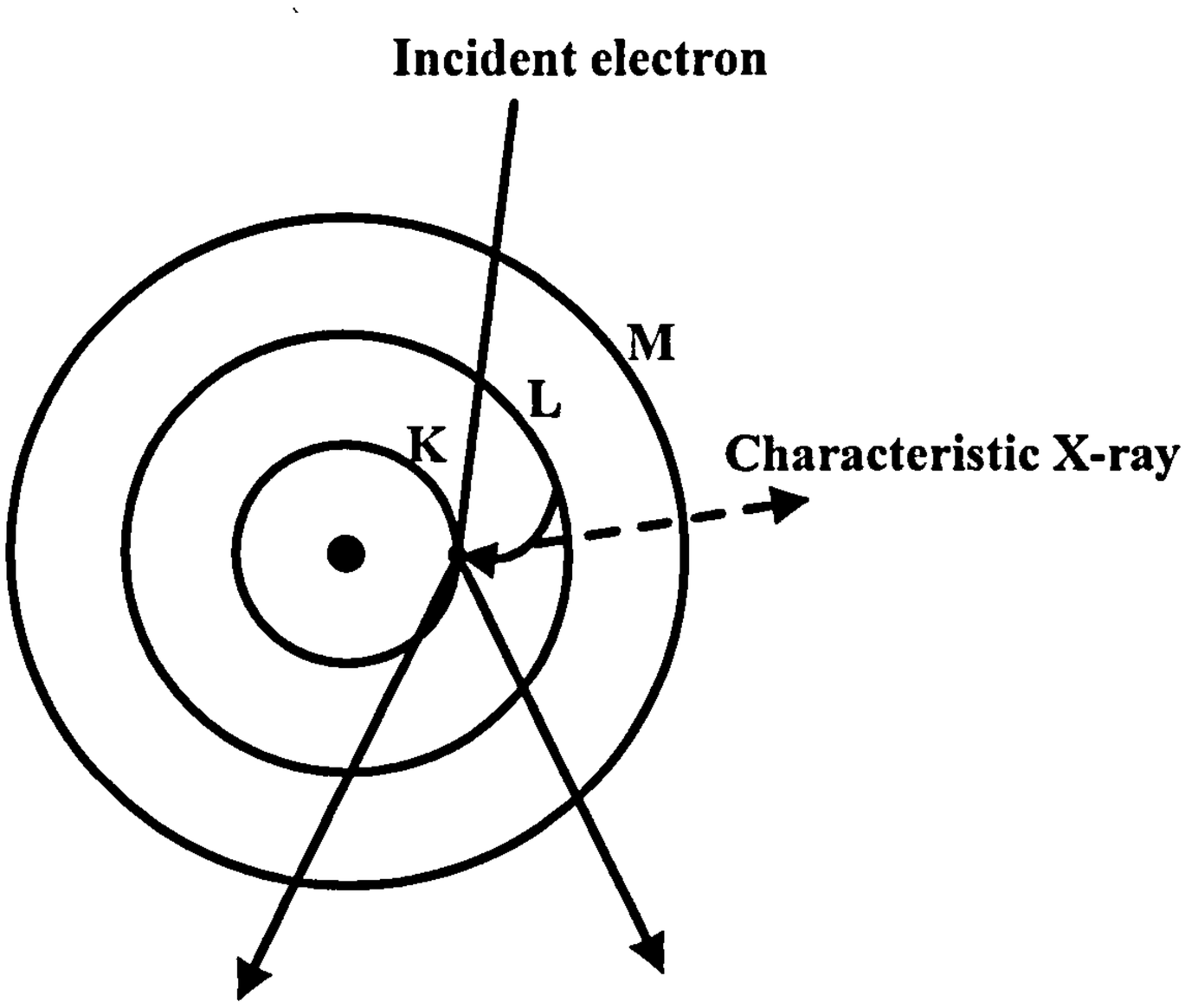

Figure 5.6 A simple schematic diagram representing the production of the characteristic X-ray and Auger electrons.

As shown in Figure 5.6, after the excitation of the K shell, in this example case, this sample atom is relax by the electron from the L shell jump in and fill its vacancy. The X-rays photon is then generated and it is known as K_α X-ray. It also has a

possibility that the K shell vacancy is filled in by the electron from M shell electron and its X-ray is known as K_β X-ray. The electron vacancy in L shell is then fill in by the electron from the outer shell (valence band or M shell if it is exist) and can lead to the generation of another X-ray photon with different wavelength or a low energy photon (light).

The scanning electron microscope used in this study is equipped with an Energy Dispersive Spectrometer (EDS) provided by Princeton Gamma-Tech company (PGT IMIX-PTS microanalysis system). This detector, as shown in Figure 5.7, is capable to detect the characteristic X-rays from the specimen and these X-rays or imaging data can then be analysed qualitatively and quantitatively by the IMIX control center.

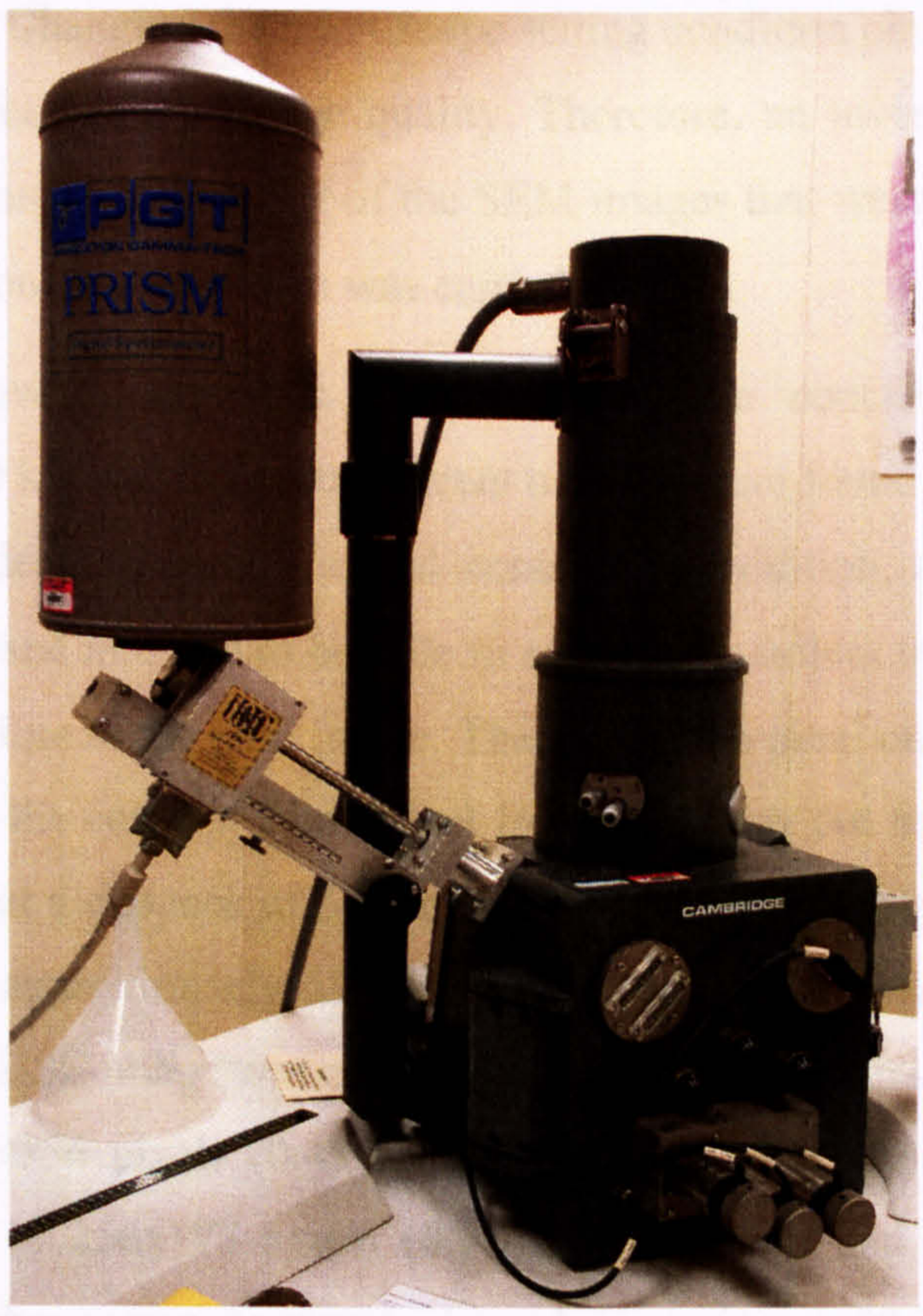

Figure 5.7 The PGT Energy Dispersive Spectrometer system used in this study.

The PGT IMIX X-ray analysis system is controlled via the computer interface running on a UNIX platform. The major components of the IMIX systems include a Sun computer (operating with SunOS™ 4.1.3), color monitor and the electronics cabinet which used to control the detector system and control the electron beam by the IMIX. It

is noted that the images obtained from this system are in the Sun raster file format and they were stored directly into a floppy zip-disc medium. These images were then transfer and converted into a standard *bitmap* format by any software that can support the Sun raster file format in order to be readable by the image analysis software (KS-300).

5.2.6 Operational setting for the SEM

There are some important variables that affect the image quality; i.e. the accelerating voltage, working distance, stigmatism, probe current and probe diameter. These operating variables are, therefore, need to set appropriately in order to obtain a good quality image and the effects of these parameters on the SEM image are summarized in Table 5.2. Changing the microscope setting condition obviously has both positive and negative effect on the image quality. Therefore, an investigation on the effect of a setting condition on the quality of the SEM images that were taken from the synthetic aggregate and concrete specimen was carried out first.

Based on the investigation that was done for the concrete sample, the accelerating voltage of 20 kV and the probe current of 7 nA were found to give the best image resolution with adequate compositional contrast. In addition, a long working distance of 28 mm was used in order to be able to effectively collect the characteristic X-ray signal at the same time as the BSE image. Therefore each pixel on the BSE image can be directly related to the corresponding pixel from the X-ray dot map images. The EDS crystal was located at a distance of 50 mm with a take-off angle of 35° and these giving the count rate of approximately 5000 to 6000 cps with the percent dead time about 6 to 7 percent. The BSE image was captured at the magnification of 500x with the image resolution of 512x356 pixels (0.48 μm per pixel). The X-ray dot maps were acquired at a resolution of 256x178 pixels (0.97 μm per pixel) and this was found enough for identifying the coarse aggregate boundary regions within a reasonable acquisition time (550 second per image was used in this study). For the porosity analysis of synthetic aggregate, the BSE images were acquired at 10 kV with the probe current of 1.3 nA and 14 mm working distance. A magnification of 150x was used for quantifying the macropore, while a higher magnification of 500x and 800x were used for the micropore (for more details see section 5.3.2.4).

It is noted that all images that were taken from a given specimen were captured using the same brightness and contrast settings. This was done in order to minimize the quantitative variations of the result.

Table 5.2 Effect of the operational setting of SEM on image quality (Scrivener et. al., 1987; JOEL Ltd.)

Parameters	Effects	
	Higher	Lower
Accelerating voltage	- Higher edge effect - Higher possibility of charge-up and specimen damage - Decreasing spherical aberration - Bigger interaction volume (especially for low atomic number specimen)	- Less edge effect - Less charge-up and specimen damage - Smaller interaction volume (increase spatial resolution, reduce atomic number contrast)
Working distance	- Greater depth of field - Increasing spherical aberration	- Smaller depth of field - Less spherical aberration effect (improving image resolution)
Probe current	- Higher S/N ratio - Increasing probe diameter	- Lower S/N ratio - Decreasing probe diameter

5.3 Digital Image analysis

The computer-based image analysis technique which is generally defined as an extraction of the interesting numerical information from the investigated image was used together with the stereological techniques in order to perform the quantitative microstructural investigation of the fired pellet and the concrete containing different types of coarse aggregate. A broad definition of stereology can be given as a science of obtaining three-dimensional information from known two-dimensional information. The technique deals with the geometry of features of interest and the quantitative characteristics of points, lines and areas; the technique has been used frequently in concrete science to investigate the porosity, specific surface area and the pore size distribution of the cement-based material (Aligizaki, 2006).

The geometrical properties of the three-dimensional microstructures of a material of interest can be easily estimated from simple counting measurements performed upon the plane section. There are three stereology counting techniques that are most commonly used to measure the fraction of the microstructural features of interest from the plane section; i.e. point counting, linear analysis and section analysis. In this study the stereological relationship which is obtained by applying the mathematical probability was used in combination with the section analysis in order to obtain the volume fraction of the phases of interest in the studied materials and the macropore size distribution of the fired pellet (to be mentioned in section 5.3.2.6).

An image processing process used in this study generally consists of the image enhancement, features segmentation and measurement. The objective of the image processing is to separate the feature of interest from the background and obtain the quantitative information. These can be done by using special image analysis software which deals with the intensity or gray value of each pixel in the BSE image. It should be noted here that an alteration of image by the image analysis software should not change any data present in the original image.

A general overview about the image analysis software used in this study will be given first in the following section and the image processing procedure and the stereological technique for the ITZ analysis of the concrete materials and the pore structure of the synthetic aggregate will then be given in the subsequent section.

5.3.1 Image analysis software

The image analysis software that was used in this research is the KS-300 written by the Carl Zeiss Vision GmbH. The general environments of the display interface of this software consist of a series of useful windows. As shown in Figure 5.8, the image processing and analysis functional menus are on the left hand column of the screen and the menu bar on the top section of the screen. This software allows the operator to work interactively with the system and it also provides the image editor window which allows the user to do the manual editing on the original image if necessary.

A series of image analysis commands are allowed to save in a text file format to create the macro program. This program guides the software to automatically do a series of command functions designed by the operator for their specific project. This is

obviously the most attractive of using this software because it saves time and can be used or edited at any time.

There are two groups of the macro program created in this project for analysis of the synthetic aggregate pore structure and the interfacial transition zone (ITZ) of concrete containing different types of coarse aggregate. The detailed information about the image processing process and the example of the macro program are given in the following sections.

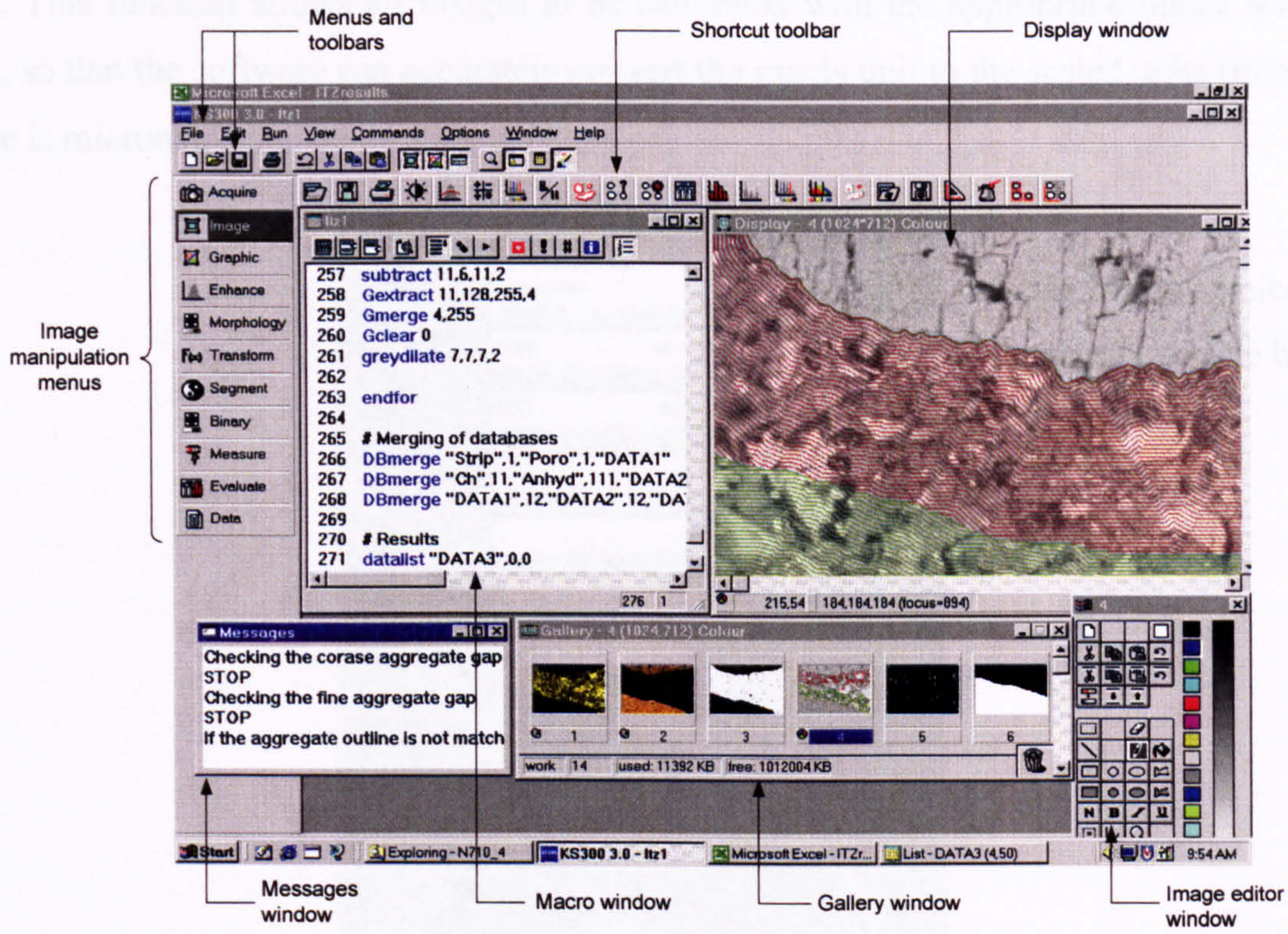

Figure 5.8 The KS 300 image analysis software display interface.

5.3.2 Image analysis for the pore structure of the synthetic aggregate

This section provides detailed information relating to the image analysis procedure that was used for the pore structure analysis of the synthetic aggregate. In general, the basic steps for this analysis consist of:

1. Setting up the measurement parameters
2. Image enhancement
3. Segmentation of the interesting feature

4. Measurement and quantification of interesting features.

5.3.2.1 Setting up the measurement parameters

In order to obtain the information about the section area or the perimeter of each interesting feature, which come from the sum of the area or length of each individual pixel, in a real unit (instead of pixel), we need to perform the calibration setting before we perform any measurement. The software needs to know the actual size of each pixel and this can be done by using the geometrical calibration function as shown in Figure 5.9. This function allows all images to be calibrated with the appropriate image scale bar, so that the software can accurately convert the pixels unit to the scaled units (in our case is microns).

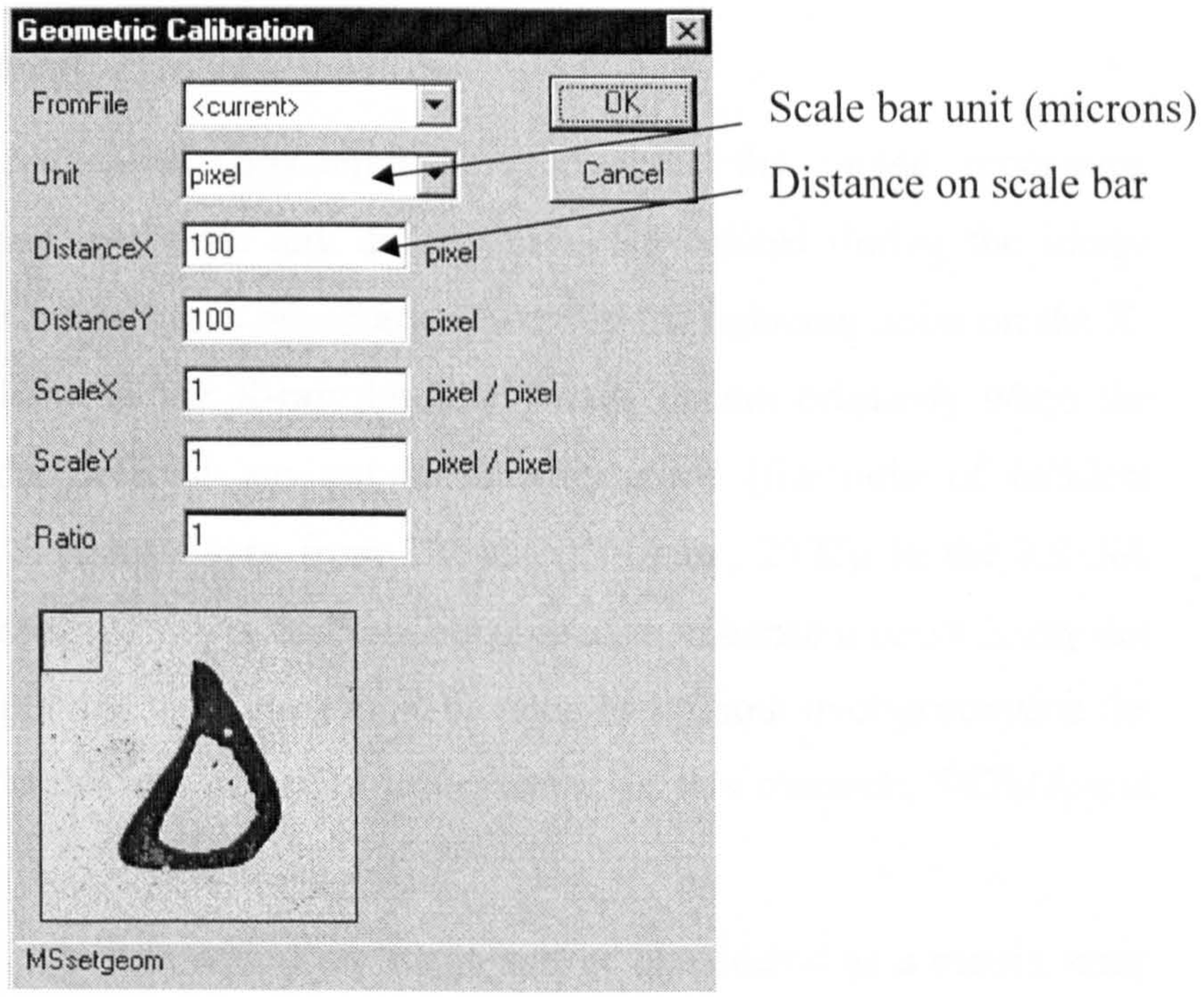

Figure 5.9 Geometric calibration window.

The calibration can be accomplished by moving the mouse to draw a graphic marker over the image scale bar and after that the size of each pixel in the selected unit will be calculated automatically.

In addition to the image calibration, the measurement properties including frame setting, measurement conditions and set features may need to be defined and set for serving the special needs of individual operator. In general, the set features command is

used to define any measurement parameters of interest, e.g. area, perimeter or f_{circle}, and it needs to be defined first before performing any measurement. The frame setting or set frame command is used to make a measurement in a defined area within the BSE image. This command was used for the pore morphology analysis of the synthetic aggregate in order to exclude any pores touching the image boundary. The measurement condition command was used to measure the porosity and the pore morphology of the synthetic aggregate that has pore area within a specific pore size class as defined in section 6.8 and 6.9.

These settings and calibrations can be stored in a file which can be retrieved later by the macro command function. It will help us to process many images by without resetting them again for each image.

5.3.2.2 Image enhancement

The image enhancement considered here involves the image processing operations that were used to reduce any defects or noise created during the image acquisition process. This operation is necessary especially for reducing noise on the X-ray dot map images. Noise in the X-ray dot map image occurs primarily when the counting statistics of the detector are not sufficiently good (the ratio of incident electrons to detected X-rays may vary from 10^5 to 10^6) (Russ, 2002). In the KS-300 software, there are a number of filters that can be applied to enhance a noisy X-ray dot map image. However, applying any filters must be done by without over-processing the image, which can lead to the loss of useful information. In this research, SIGMA and Median filter were used.

An arrangement of pixels within an image can be considered as a matrix array and each pixel contains a different brightness or grey value. A selective noise averaging or SIGMA filter locally averages only those grey values in the specified size matrix that have magnitude within a specific range of deviation (possibly due to noise), with respect to the grey value of the central pixel. The grey values that differ by a larger amount (normally occur at the boundary between two different phases) will not be considered for averaging. The median filter, on the other hand, calculates a new central pixel value based on the median value of its surrounding neighbors which are defined by a square matrix and the median value is found by sorting all grey values within the matrix in ascending order. The effect of these two filters on a part of the BSE image of concrete can be seen in Figure 5.10 (c) and (d).

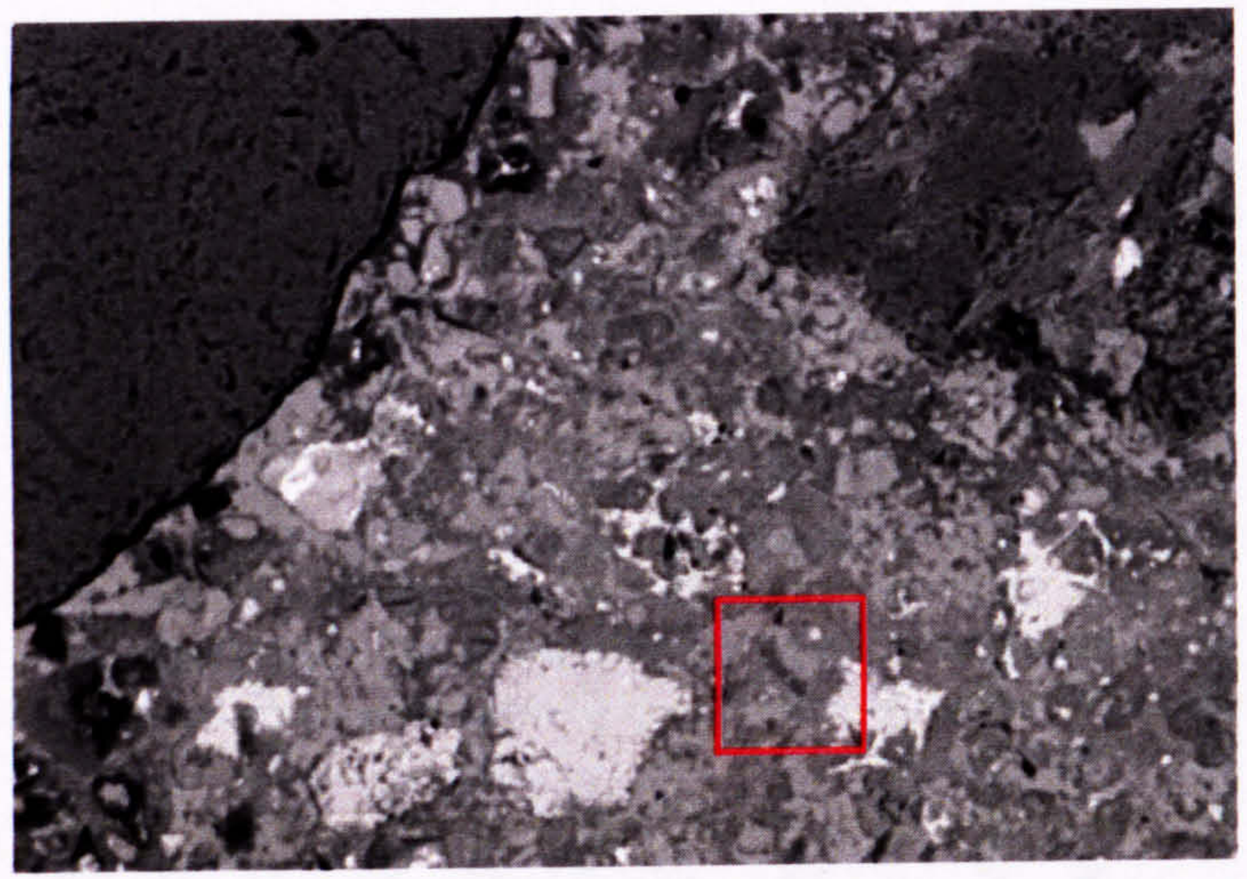

a) Original un-smoothed BSE image of 28-day old concrete containing quartz aggregate with the selected area of 60x60 pixel area.

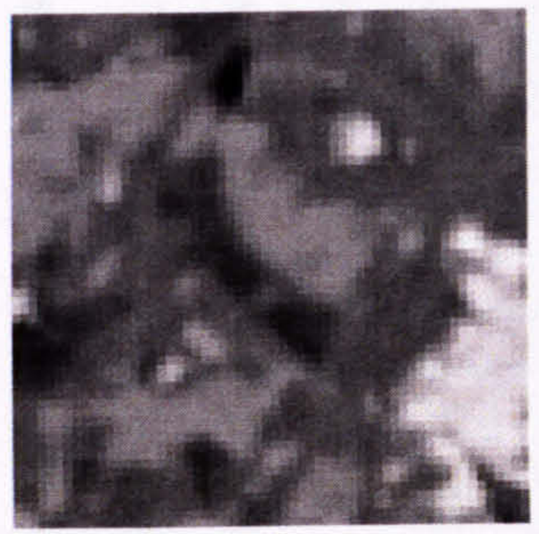

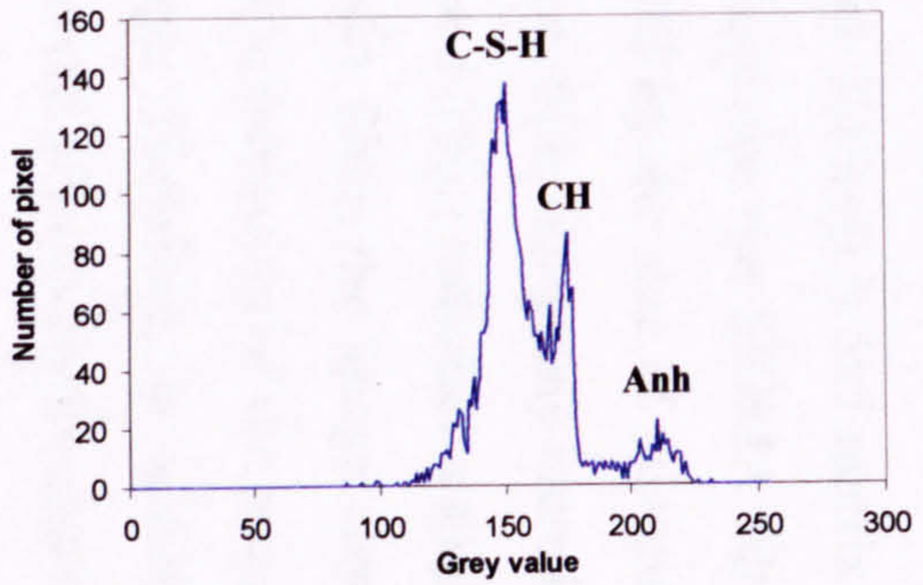

b) Magnification of un-smoothed image selected area and its grey level histogram.

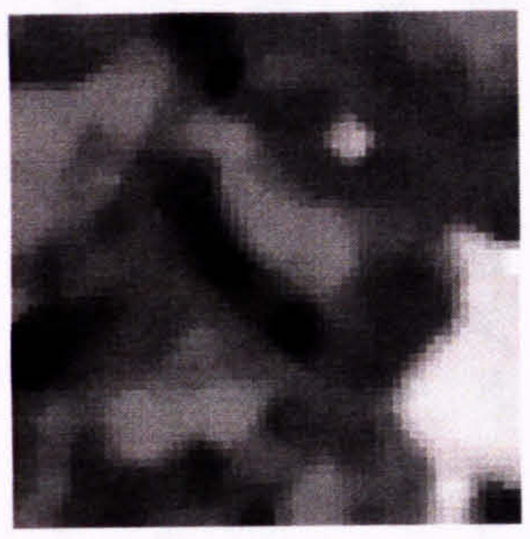

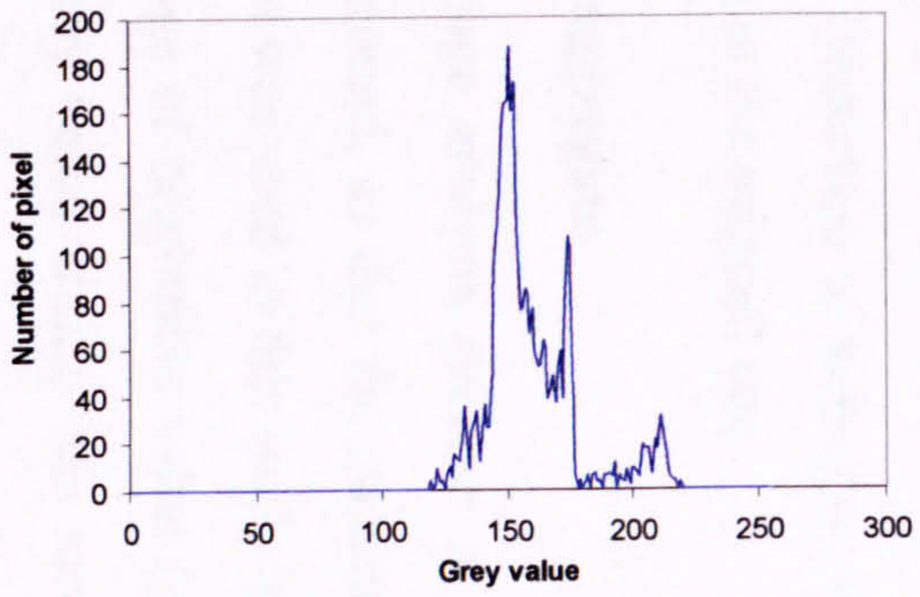

c) Magnification of the box section after application of median filter. (matrix size of 5x5)

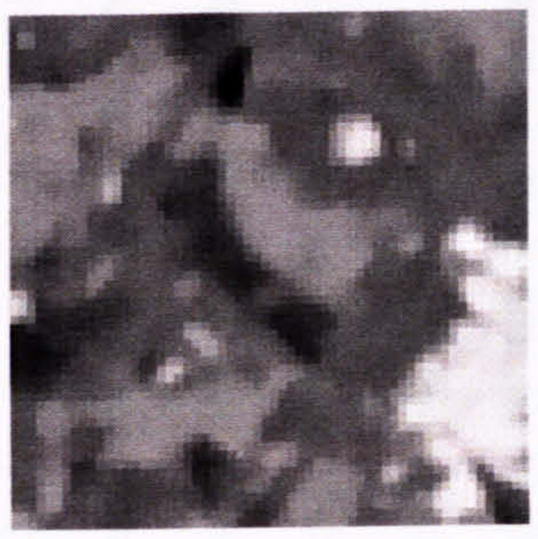

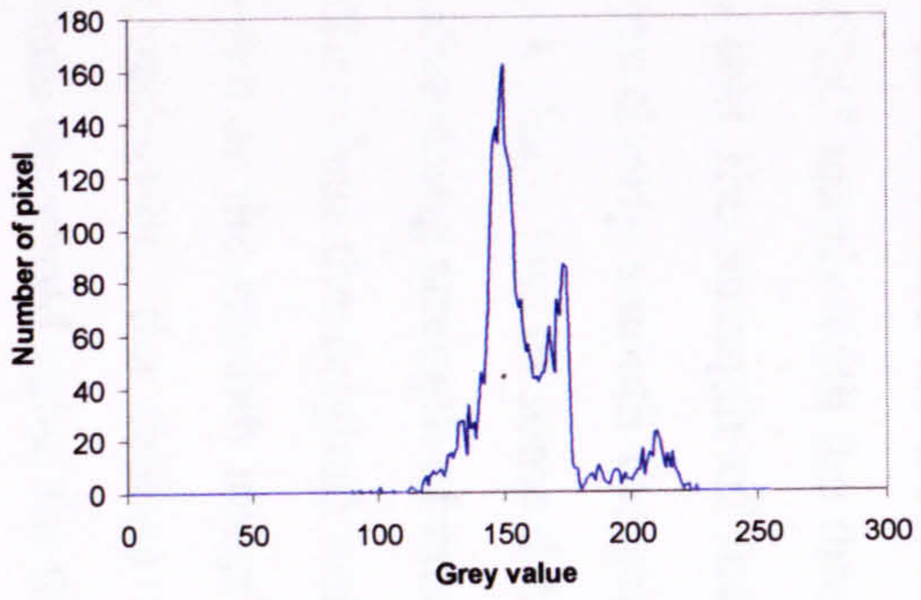

d) Magnification of the same area after application of SIGMA filter. (matrix size of 3x3, threshold value (sigma) = 10)

Figure 5.10 Effect of the smooth filter on the BSE image and its grey level histogram of 28-day old concrete sample.

The size of the median filter square that was used for the example BSE image (Figure 5.10(a)) is 5x5 matrix and the size of 3x3 matrix with the threshold value of 10 are used for the SIGMA filter. It is noted that the strength of image smoothing is defined by the size of this matrix. Both filters clearly smooth the selected image. The median filter obviously blurs image features. A slight loss of some detail information on Figure 5.10(c) indicates a slightly too much smoothing strength of median filter. For the SIGMA filter, the image clearly look smoother than the original one and most of the detail information of the image is sill preserved or the smooth image look virtually no change. Therefore, in addition to a noise reduction, the feature boundary can be preserved effectively by choosing an appropriate threshold value for the SIGMA filter.

These two filters have an effect on the image histogram. Note that the brightness value of each pixel on the BSE image can be graphically represented as a grey level histogram. This histogram is a plot of a number of pixels in the image against the brightness value and each peak on this histogram represents any pixel having similar grey value which is very useful for the feature segmentation. The peaks on the grey level histogram of the smooth images, as shown in Figure 5.10(c) and (d), are sharpened which results in better defined peaks and it facilitates the segmentation of any microstructural features of interest. A better peak definition is due to the pixel grey value on each feature move closer together (reduction of noise) by the effect of these filters resulting in a sharper peaks comparing to the original one.

5.3.2.3 Porosity segmentation of synthetic aggregate

The most important step in the image analysis process is to distinguish or separate the features of interest from background, so that the quantitative information can be obtained. The selection technique that was used in this study is the thresholding. This technique was done by defining a range of brightness value (grey value) in the original BSE image. Any pixels having grey value within this range are set to the foreground (grey value = 255) and all of the rest are rejected to the background (grey value = 0). Therefore, this segmentation procedure obviously produces a two-level or binary image using black and white to identify any interested feature.

In order to allocate each pixel in the BSE image to either solid or pore, it is necessary to define an appropriate range of grey value for segmentation. The methods that are commonly used to locate an appropriate grey value to use as a "cut-off" for the

porosity segmentation are the manual thresholding and the tangent-slope method. In the manual segmentation method, an iterative selection of threshold value is done by the operator until a satisfactorily segmented image is obtained. This technique, however, is very subjective and it is definitely not practical to be used when more than 1,000 BSE images had to be processed in this project. Scrivener et al. (1987) defined the porosity threshold value for the hardened cement paste material by locating an inflection point on the grey level histogram. They found that the grey value at which the intersection between the tangent line drawn against the upper portion of the C-S-H peak and the initial tangent on the histogram peak gave a consistent and satisfactory results (closest to the result obtaining from the manual thresholding method).

The schematic illustration of a hypothetical boundary between two different phases and the grey scale histogram of the pixels across the boundary were represented by Head (2001). It was shown that the logical way to allocate the pixel at the boundary to one phase or the other is to segment by using the pixel which corresponding to 50 percent light phase and 50 percent dark phase. By assuming the normal distribution of each peak, he used the point of mid-way between any two adjacent peaks as the threshold value.

Using the mid-way between any two adjacent peaks or the tangent-slope method were not an appropriate technique in this study. The reason lies on the nature of the BSE generation. The BSE signals which have high energy are generated from a deeper part of the interaction volume and this can be a serious problem on the attainable resolution. For any small features like ball clay (see Figure 3.2) and pores that present on the image may have a size that are not large enough to appear sharp and they will appear somewhat fuzzy. A fuzzy particle appears as a big hump on the grey level histogram and its magnitude reduces or disappears when increasing the firing temperature and sintering time (see Figures 6.25 to 6.28). These create a big problem for the porosity segmentation. Note that a more detailed explanation about the synthetic aggregate grey level histogram is given in section 6.7.

A segmentation procedure was developed in this study in order to overcome these problems. This procedure is based on fitting the porosity peak by using the Gaussian function. The benefit of using this function is that they can fully describe the porosity peak by the three statistical parameters: mean value, standard deviation and

amplitude. This technique will help us to get a reproducible grey level threshold value and makes it possible to reasonably compare the results between samples. To get a best fitting curve, the least square technique was used as the minimization criteria, i.e. the square difference between the sum of the Gaussian function which represent the pore space and the grey scale histogram was minimized. The minimization criterion is mathematically defined as:

$$\min \sum_{g=1}^{255} \left(f(g) - \alpha_p G\left(f(g), \mu_p, \sigma_p\right)\right)^2 \qquad (5.4)$$

In which:

$$G\left(f(g), \mu_p, \sigma_p\right) = \frac{1}{\sigma_p \sqrt{2\pi}} e^{-1/2\left(\frac{f(g)-\mu_p}{\sigma_p}\right)^2} \qquad (5.5)$$

Where $G(f(g),\mu_p,\sigma_p)$ = the porosity Gaussian function,

μ_p = the mean value of porosity peak,

σ_p = the standard deviation of porosity peak,

α_p = the amplitude or the volume fraction of pore,

$f(g)$ = the grey value distribution of the BSE image.

The Newton-Raphson method which is one option in the Generalized Reduced Gradient (GRG2) algorithm of the solver tool in EXCEL was used for the minimization process. Figure 5.11 shows the result of the fit to the porosity histogram of the synthetic aggregate fired at 1,110°C sintering temperature and zero minute sintering time.

The threshold value was then selected based on the mean and standard deviation value of the porosity peak which can be mathematically defined as follows:

$$T_p = \mu_p + Factor.\sigma_p \qquad (5.6)$$

Where Factor = arbitrary constant selected by operator.

The appropriate constant was selected by the operator and a slight adjustment to the threshold value was made, if necessary, to achieve a visually satisfactory cut-off value.

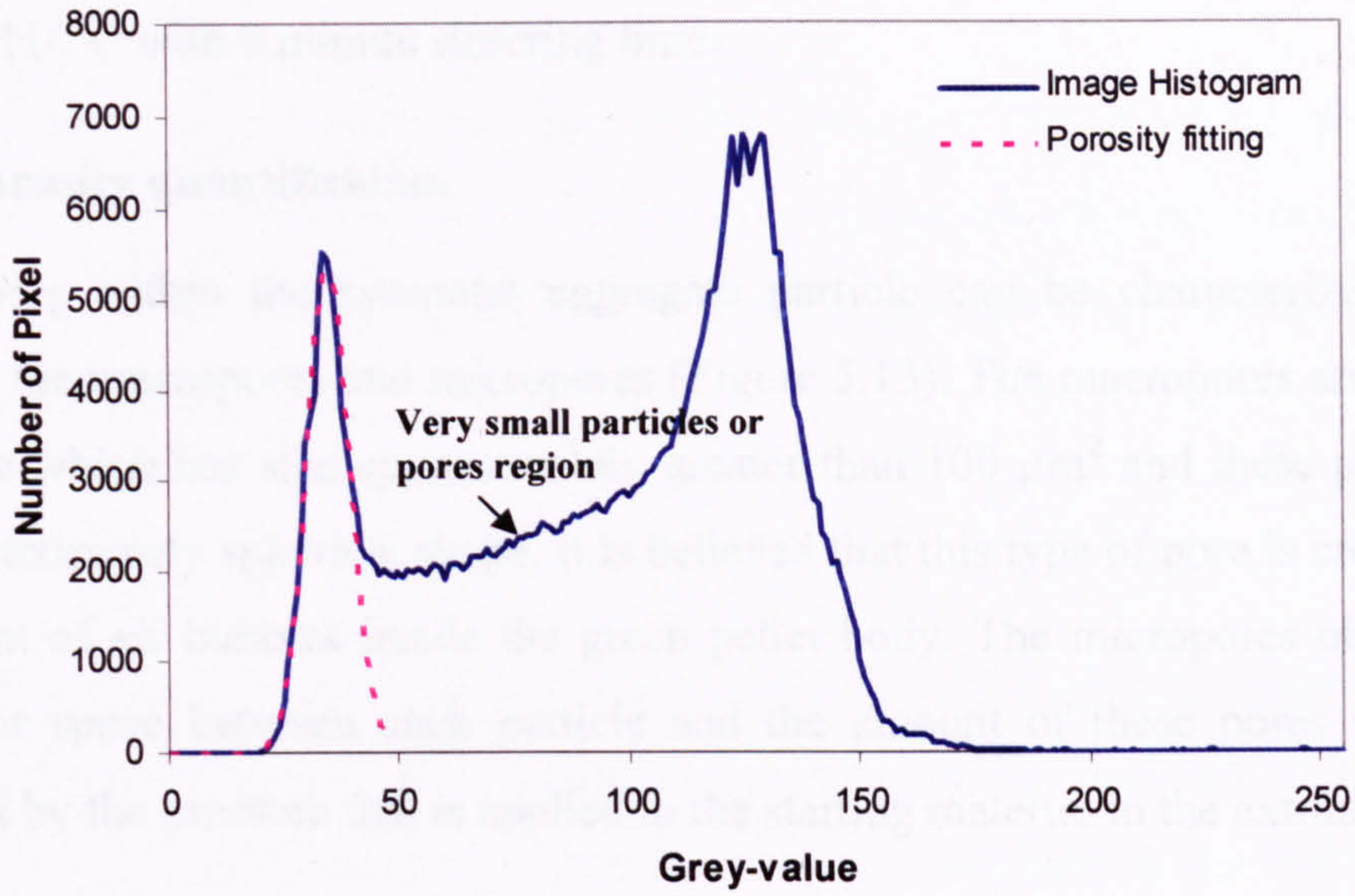

Figure 5.11 Fitting of porosity peak by using the Gaussian function.

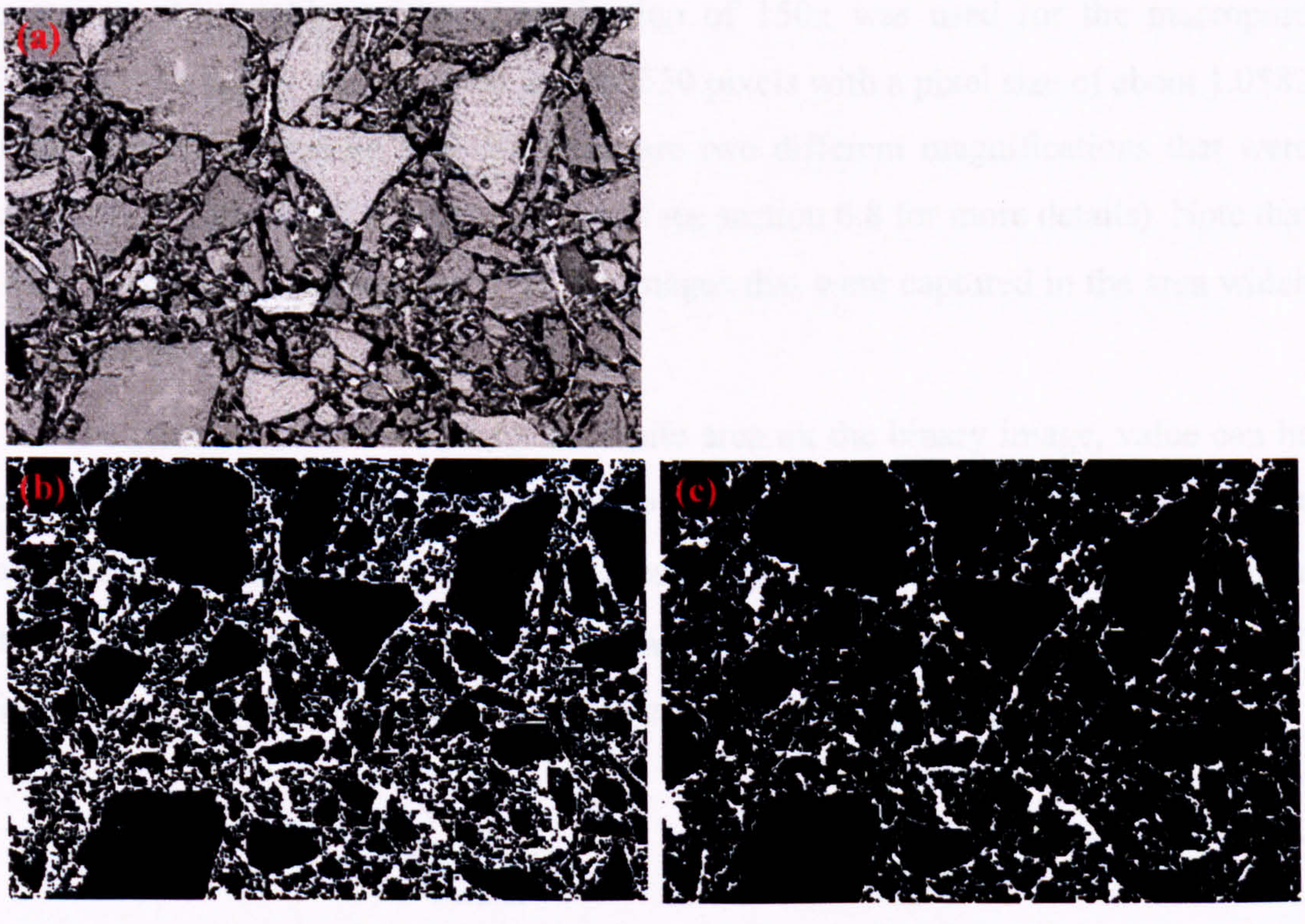

Figure 5.12 Porosity segmentation of synthetic aggregate. (a) BSE image, (b) binary image created by using the mid-way between two adjacent peaks as the criteria, (c) binary image by using the curve fitting technique.

Figure 5.12(b) and (c) show the porosity binary image of the synthetic aggregate fired at 1,110°C with 0 minute sintering time.

5.3.2.4 Porosity quantification

Pores within the synthetic aggregate particle can be characterized into two groups as the macropores and micropores (Figure 5.13). The macropores are defined as a big pore which has size approximately greater than 100 μm^2 and these pores clearly have approximately spherical shape. It is believed that this type of pore is created by the entrapment of air bubbles inside the green pellet body. The micropores obviously are the gap or space between each particle and the amount of these pores is primarily controlled by the pressure that is applied to the starting material in the extruder.

Due to a very big size different between the macropore and the micropore, it was not possible to analyse the total porosity of the synthetic aggregate by using only one magnification. Two different images with two different magnifications were used here to overcome this problem. The magnification of 150x was used for the macropore analysis and the image was digitized as 740x550 pixels with a pixel size of about 1.0582 microns. For the micropore analysis, there are two different magnifications that were used including 500x and 800x magnification (see section 6.8 for more details). Note that the BSE images for the micropores are the images that were captured in the area which has no macropores.

The pore area, represented by the white area on the binary image, value can be measured by the image analysis program (KS-300). The sum of the pore areas from the binary image divided by the entire image area (A_{total}) gives the total porosity (ϕ) of the synthetic aggregate and this calculation is based on the average value from 40 and 60 different image fields for the macropore and micropore analysis respectively.

$$\phi_{mac} = \frac{\sum A_{mac}}{A_{total,150x}} \tag{5.7}$$

$$\phi_{mic} = \frac{\sum A_{mic}}{A_{total,800x}} \tag{5.8}$$

Where ϕ_{mac} , ϕ_{mic} = macroporosity and microporosity,

A_{mac} , A_{mic} = micro and micropore area.

In order to calculate the total porosity ($\varnothing_{total}$) of the synthetic aggregate from these two different magnifications, we have to correct the microporosity by a factor of ($1-\varnothing_{mac}$) taking into account for the lack of microporosity within the macropores and, therefore, the total porosity can be written as:

$$\phi_{tot} = \phi_{mac} + \phi_{mic} \times (1 - \phi_{mac}) \quad (5.9)$$

Note that an artifact due to the grain damage on the mineral particles needs to be removed from the binary image first before performing any calculation. This artifact is created due to inadequate sample preparation and it appears on the BSE images as a small hole in the grains. Small pores that appear within a big quartz or feldspar particles as shown in Figure 5.12(b) is clearly caused by this artifact. Therefore, it can lead to an over-estimation of the porosity of this sample. This artifact might be able to reduce by grinding the resin impregnated sample with the coarser grade of SiC paper (in this study, the 240 grade SiC was normally used at the beginning) in order to remove the damage surface created during the cutting process. However, this process has to be done very carefully because over grinding or polishing can lead to a severe surface relief problem especially for any sample containing phases that have different hardness.

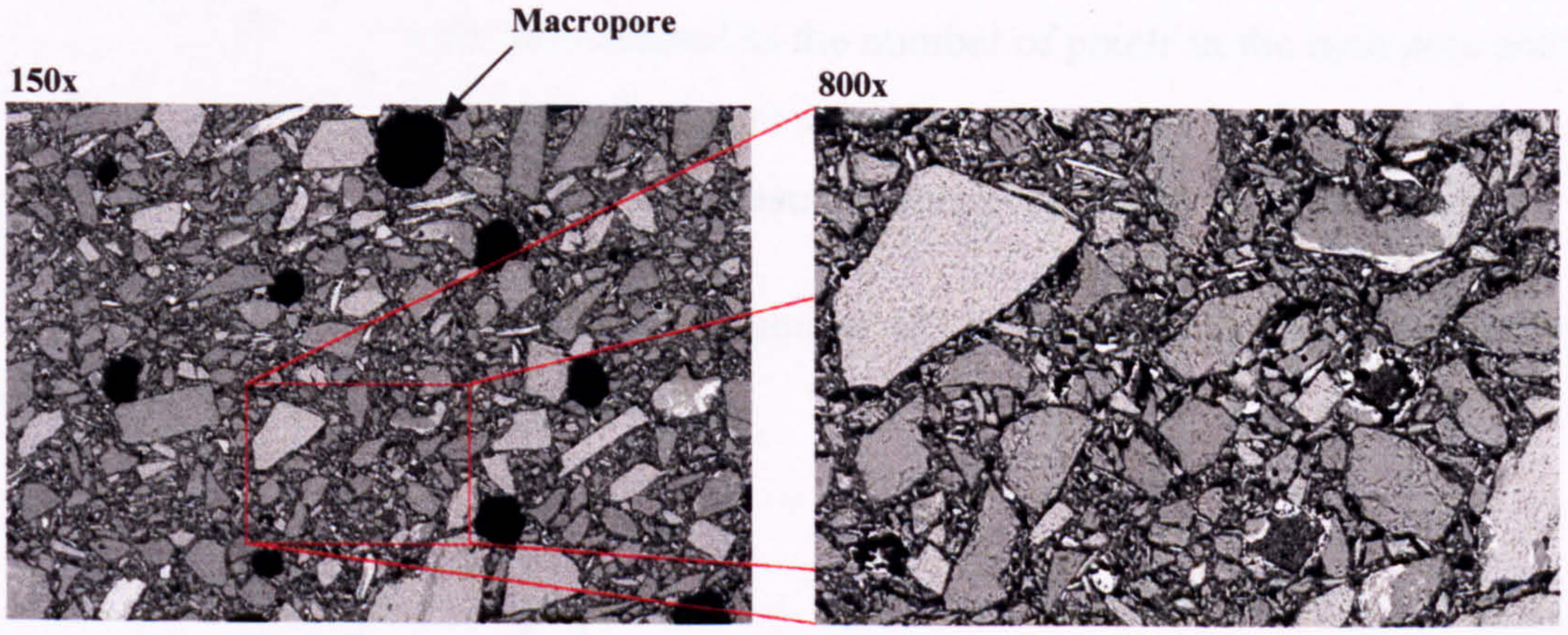

Figure 5.13 Schematic diagrams representing the concept of porosity quantification. Sample: 900°C *pre-set* temperature and 0 minutes sintering time.

5.3.2.5 Pore shape analysis

In this section, an image analysis was used to study the effect of the firing conditions on the pore morphology of synthetic aggregate. There are two parameters, i.e. f_{shape} and f_{circle}, that were used to describe the pore morphology of the synthetic aggregate produced using different firing conditions. These parameters have different geometrical meaning and they were used to describe the morphological characteristics of each pore that can be detected by the SEM. The definitions of these two parameters are given in Equations 5.10 and 5.11. In general, f_{shape} is the parameter that indicates the elongation of a pore, while the f_{circle} represents the pore irregularity. Both parameters have magnitude ranging from 0 to 1. Both parameters equal unity for a circle and approaching 0 for the highly elongated and highly irregular pore shape (see Figure 6.37 and 6.38 for the possible pore morphology at different f_{shape} and f_{circle} values). Note that any pores that were touched or cut by the image boundary were not considered in the analysis.

$$f_{shape} = \frac{D_{min}}{D_{max}} \tag{5.10}$$

$$f_{circle} = \frac{4\pi A}{P^2} \tag{5.11}$$

Where D_{min}, D_{max} = minimum and maximum Feret's diameter (see Figure 5.14),

A = pore area defined as the number of pixels in the each pore and converting to square micron,

P = pore perimeter measured from pixel center to pixel center.

The average value of the shape parameter (F) of one sample was calculated by weighing the individual F by the pore size.

$$\overline{F} = \frac{\sum_i (A_i \times F_i)}{\sum_i A_i} \tag{5.12}$$

Note that for a very small pore, for example, one pixel, the shape parameters are nonsensical. In addition, a very small pore might occur due to noise introduced during the image acquisition. Therefore, removed of these pores from the data set is needed in

order to improve the analysis results. In this study, any pores that had an area smaller than 25 μm^2 were not considered in the analysis. However, a very small pore that was removed from the analysis might also be a tip of a larger pore size sectioned through during the specimen preparation stage. This is obviously the main drawback of the image analysis based on the two dimensional section. In order to overcome this limitation, a serial sectioning technique can be used. This technique reconstructs a three dimensional image from a set of images captured from the different sections. However, the biggest problems for this technique are that the distance between two successive sections needs to be known accurately, the alignment of the images must be done appropriately and this technique is very time consuming. However, only the trend of changing pore morphology of the synthetic aggregate at different firing condition is the objective here. Generally, green pellet is expected to have a highly interconnected and irregular pore structure, while an isolated and spherical pore structure is expected for the fired product. These two parameters, therefore, were found to be adequate to serve the objective here.

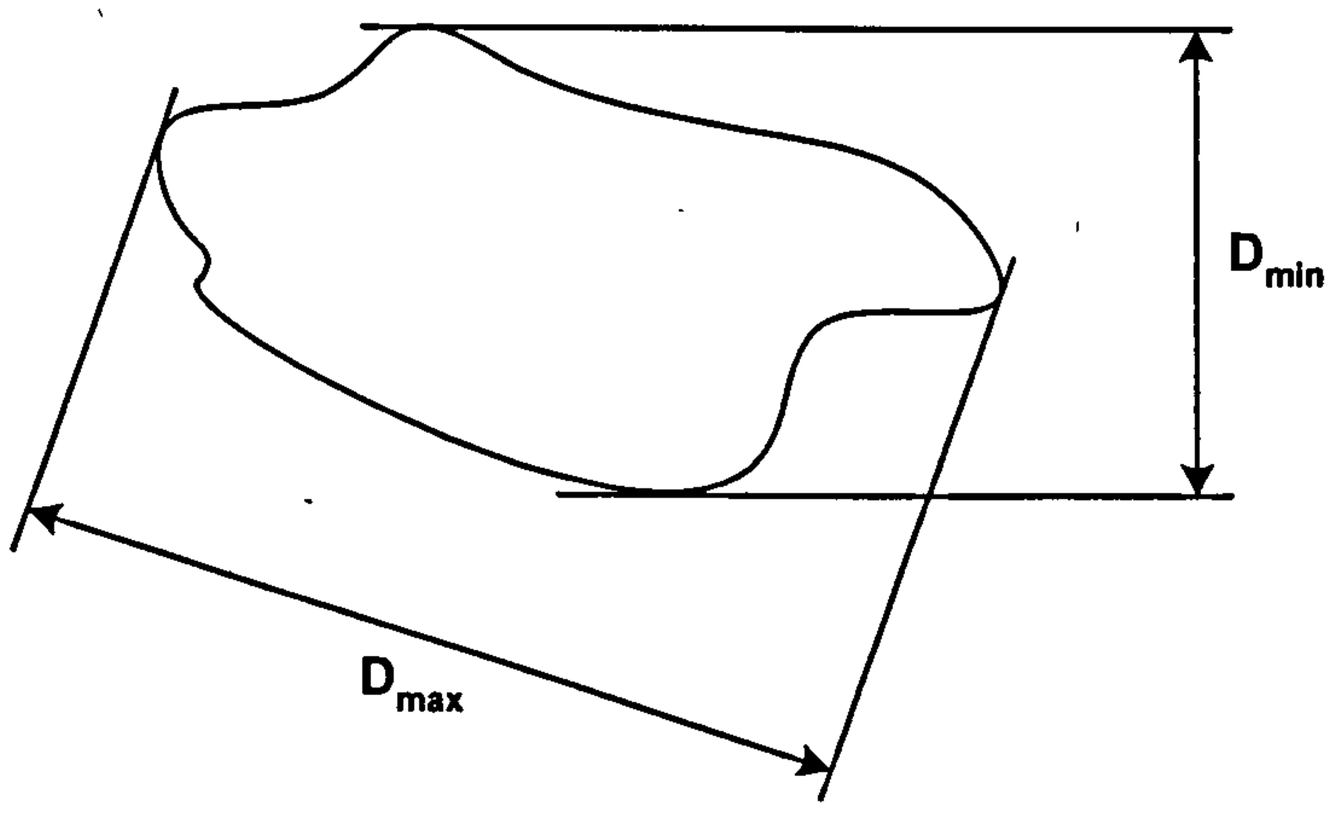

Figure 5.14 Minimum and maximum Feret's diameter definition.

5.3.2.6 Pore size distribution of macropores

As mention previously, the macropores mainly came from the entrapment of the air bubbles inside the green pellet body. An image analysis procedure was utilized to investigate the size distribution of these pores. The diameter of the air bubbles can be measured directly from each sample but these information based on the two dimensional section may not be a correct solution. The diameter of a circular section of a given size

may or may not equal to the actual diameter of sphere depending on where the cut had been made. As demonstrated in Figure 5.15, it is clear that a very small diameter may in fact be due to a section cut at the tip of the larger voids. To solve this problem, the Johnson and Saltykov method (Underwood, 1968) was used in this study.

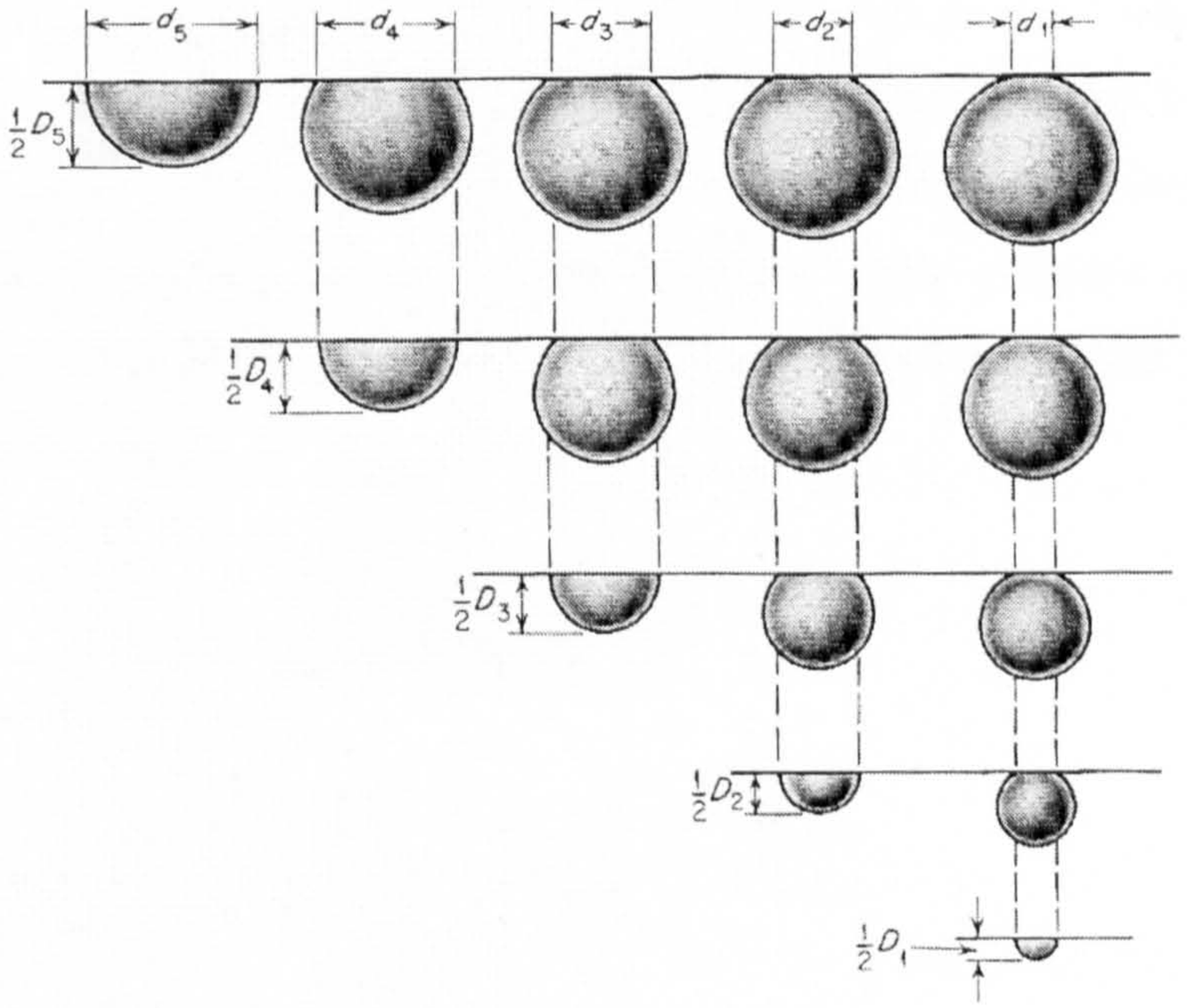

Figure 5.15 Schematic illustration of the contributions of the spheres with diameters D_1 to D_5 to total number of sections with diameters d_1 to d_5 (Underwood 1968).

The Johnson-Saltykov method is the classical technique used for determining a three dimensional particle size distribution based upon the measurements of two dimensional size distribution. In this method, the particle diameters (or grain sizes) are classified in a linear logarithmic scale ranging from log 1000 to log 1.26 microns, that is, from 3 to 0.1 and the scale decreases in steps of 0.1 of the logarithm. It means that the particle diameters are divided into 30 groups, decreasing from 3.0 to 0.1. Note that this scale can be extended easily in both larger and/or smaller direction if necessary. The technique is based on a simple relationship between the section radius determined by the image analysis and the actual radius of a sphere. By applying a simple geometrical probability, the actual void size in the various groups that formed by a plane randomly cutting on the sphere can be predicted.

The first step of this technique is in constructing a table for classification of the circular cross section and calculating the relative area of a given group occupied by the plane polish cross sections. A portion of Saltykov's scale (from log 1000 to log 19.95) was reproduced in column 1, 2, and 3 as shown in Table 5.3. The size of a sphere in each group corresponds to upper and lower diameter limits. The probabilities of a random plane intersecting a sphere to give various sizes of sections falling within each size group can be calculated and these values are given in column 4 of Table 5.3. For a sphere of diameter D intersected by a random plane between a distances h_i and $h_{(i-1)}$ from the center (see Figure 5.16), the probability (p) of the intersection of a random plane between h_i and $h_{(i-1)}$ is equal to the thickness of the circular slice divided by the spherical radius.

$$p = \frac{h}{D_j/2} = \frac{h_{(i-1)} - h_i}{D_j/2} \tag{5.13}$$

and

$$h = \frac{1}{2}\left[\sqrt{D_j^2 - d_{(i-1)}^2} - \sqrt{D_j^2 - d_i^2}\right] \tag{5.14}$$

where h = height of a circular slice, micron,

D_j = diameter of a sphere,

d_i and $d_{(i-1)}$ = upper and lower limits of the section diameters for any group.

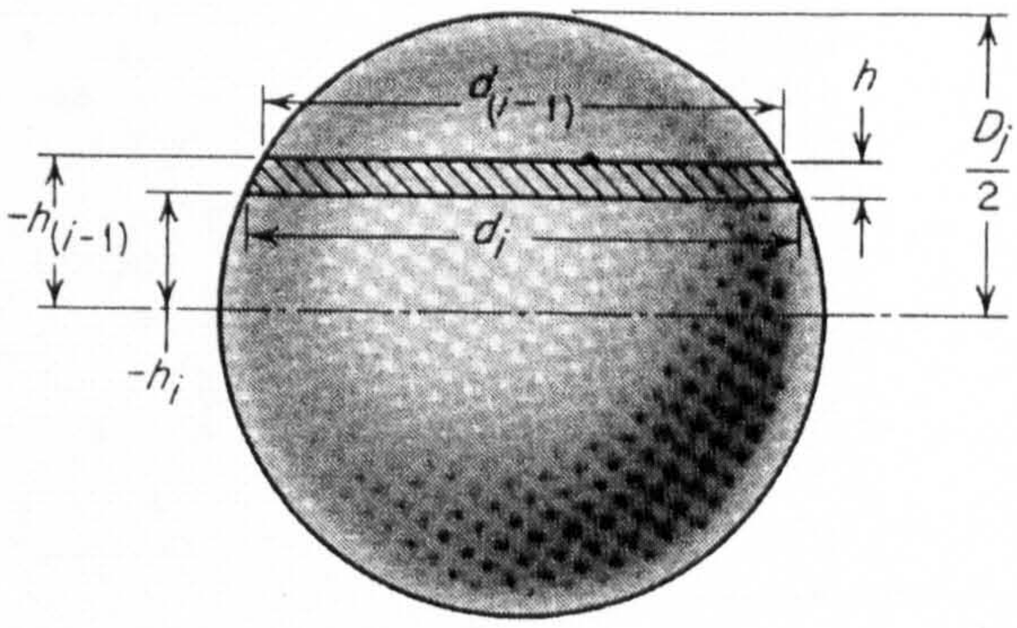

Figure 5.16 Intersection of a sphere by a random plane (Underwood 1968).

The probability obtained is equal to the ratio of the total number of the cross sections which have diameter between d_i and $d_{(i-1)}$ to the total number of all possible

sections of this sphere. The mean area of cross section in each group as given in column 5 is calculated by dividing the volume of the circular slice of each group by its height (*h*). Based on the number distribution of sections and the mean cross sectional area (column 4 and 5), the relative areas distribution in each size group can be obtained and they are given in column 7. These values imply that for the *mono-dispersed* void system or in this case the sphere of diameter 1000 microns randomly cut into sections, the section of maximum size, i.e. group number 30, will occupy an area equal to 79.9 percent of the total area. The cross section of successively smaller groups (29, 28, 27, etc.) will occupy areas equal to 13.1 percent, 4.4 percent, 1.6 percent, etc., respectively.

Table 5.3 Classification of circular cross sections from a single sphere into size groups, relative numbers, and relative areas (Underwood 1968)

(1)	(2)	(3)	(4)*	(5)	(6)	(7)*
No. of group	Limits of log d of cross sections in group	Limits of d, μm	Fraction of the total number of cross sections, by groups, N(i)	Mean area of the cross section in the group A(i), μm^2	Product, A(i)N(i)	Relative area occupied by cross sections of given group, %
30	3.0-2.9	1000-794.3	0.6075	688,794	418,442	79.916
29	2.9-2.8	794.3-631.0	0.1683	407,832	68,638	13.109
28	2.8-2.7	631.0-501.2	0.0895	256,040	22,916	4.377
27	2.7-2.6	501.2-398.1	0.0520	161,258	8,385	1.601
26	2.6-2.5	398.1-316.2	0.0314	101,646	3,192	0.610
25	2.5-2.4	316.2-251.2	0.0192	64,010	1,231	0.235
24	2.4-2.3	251.2-199.5	0.0120	40,439	485	0.093
23	2.3-2.2	199.5-158.5	0.0075	25,494	191	0.036
22	2.2-2.1	158.5-125.9	0.0046	16,091	74	0.014
21	2.1-2.0	125.9-100.0	0.0030	10,160	30	0.006
20	2.0-1.9	100.0-79.43	0.0018	6,412	12	0.002
19	1.9-1.8	79.43-63.10	0.0012	4,053	5	0.001
18	1.8-1.7	63.10-50.12	0.0007			
17	1.7-1.6	50.12-39.81	0.0005			
16	1.6-1.5	39.81-31.62	0.0003			
15	1.5-1.4	31.62-25.12	0.0002			
14	1.4-1.3	25.12-19.95	0.0001			
			0.9998		523,604	100.000

* Columns 4 and 7are independent of the absolute size of the sphere; they apply to one sphere of any size or to a monodispersed system.

The benefit of using the logarithmic scale for subdivision of the cross sectional diameter is that the area distribution of sections, given in Table 5.3 column 7, in the maximum size group will be 79.916 percent regardless of the diameter of the sphere.

The Johnson-Saltykov method can also be applied for calculating the size distribution of the air void in the *poly-dispersed* systems. An actual case of determining the macropore size distribution of the synthetic aggregate will be used to illustrate the application of this technique. The experimental data for 397 sections (total number of macropores) of the synthetic aggregate fired at 900°C with 0 minute sintering time were obtained through the image analysis of the 150x magnification BSE images and they are given in Table 5.4. Note that these data were collected from 44 images of two different samples. The sections of maximum size correspond to group number 21 of the scale and the smaller sections extend down to group number 11. The mean section areas in column 4 were taken from the first working table provided by Saltykov and it is not presented here.

Table 5.4 Example of evaluation of pore size distribution for synthetic aggregate firing at 900 °C with 0 min. sintering time.

(1)	(2) Raw data, no. sections per 20.06	(3)	(4)	(5)	(6)	(7)	(8)	(9)
Group	mm^2	No. sections per mm^2 $N_A(i)$	Mean section area μm^2, A(i)	Section area per group, % $N_A(i)A(i)$	Volume of air voids per group, %	No. of voids per mm^3	Relative Air void distribution, %	Mean group diameter, µm
21	2	0.10	10062	0.1004	0.1256	1	0.27	113.2
20	8	0.40	6349	0.2533	0.2963	6	1.29	89.9
19	39	1.94	4006	0.7791	0.9194	35	8.00	71.4
18	62	3.09	2528	0.7816	0.8085	61	14.03	56.7
17	76	3.79	1595	0.6045	0.5665	86	19.62	45.1
16	78	3.89	1006	0.3913	0.3314	100	22.89	35.8
15	64	3.19	635	0.2027	0.1440	87	19.84	28.4
14	37	1.85	401	0.0740	0.0302	36	8.30	22.6
13	24	1.20	253	0.0303	0.0105	25	5.75	17.9
12	6	0.30	159	0.0048	-	-	-	14.2
11	1	0.05	101	0.0005	-	-	-	11.3
Total	397	19.80		3.2223	3.2324	438	100.00	

The calculation of the section area percent of each group in column 5 is self evident. The volumes of air voids per group presented in column 6 are obtained by

using the Johnson-Saltykov method and a detailed calculation is presented in Table 5.5. The calculations begin by considering that the maximum section areas are formed by the particles of maximum size. In this example, assuming that the specimen was composed completely (100 percent) of particles of group number 21, then the section of group 21 would occupy 79.916 percent of the total section area. However, based on the investigation, the sections of this group occupy only 0.1004 percent of the total area (see column 5 of Table 5.4). Hence the volume percent of air voids in group number 21 is

$$100V_v(21) = \frac{0.1004}{79.916}100 = 0.1256 \text{ percent}$$

The air voids of maximum size also contribute sections to a smaller size group. This means that 13.109 percent of the total section area of group number 21 will occupy to group number 20 (see column 7 of Table 5.3); 4.377 percent will occupy to group number 19; and so on. Thus the area sections of the 20th and 19th group that belong to the air void of group 21 are

$$\frac{0.1256(13.109)}{100} = 0.0165 \text{ percent}$$

and $$\frac{0.1256(4.377)}{100} = 0.0055 \text{ percent}$$

and so on.

The next calculating step is to exclude the section area that belong to group number 21 from the smaller groups and the cross sections of successively smaller groups (group 20 in this example case) becomes the next maximum size group. Therefore, the area of sections which entirely belong to the air void of group number 20 is

$$0.2533 - 0.0165 = 0.2368 \text{ percent}$$

The volume percentage of air void of this group is

$$100V_v(13) = \frac{0.2368}{79.916}100 = 0.2963 \text{ percent}$$

Based on the procedure described above, the general equation for the Johnson and Saltykov method can be written as

$$V_v(i) = \frac{A_A(i) - \left[0.13109A_A(i+1) + 0.04377A_A(i+2) + ... + C_K A_A(K)\right] / 0.79916}{0.79916} \quad (5.15)$$

Instead of performing a series of calculations as illustrated previously, the operation can be systematically performed in table format as shown in Table 5.5. Row number 1 presents the percentage of section area obtained from the plane polished sample (column 5 in Table 5.4). The number that falls on the left of the staggered line in Table 5.5 is the volume percentage of air void occupied by each group, e.g. 0.1256 and 0.2963 for the 21st and 20th group respectively. The other number within the same row are the contributive sectional area from the bigger pore size group to a successively smaller size group, for example, 0.0388 is the area section of the 19th group that belong to the air void of group number 20. The number in blue color is the area of section formed entirely by the air void of the smaller group. The results from this calculation were put in column 6 of Table 5.4 and the macropore size distribution is now easily obtained as given in column 8.

Table 5.5 Converting section areas into equivalent volume of void per group

21	20	19	18	17	16	15	14	13	12	11
0.1004	0.2533	0.7791	0.7816	0.6045	0.3913	0.2027	0.0740	0.0303	0.0048	0.0005
0.1256	0.0165	0.0055	0.0020	0.0008	0.0003	0.0001	0.0000	0.0000	0.0000	0.0000
	0.2368	0.7736	0.7796	0.6037	0.3910	0.2025	0.0739	0.0303	0.0047	0.0005
	0.2963	0.0388	0.0130	0.0047	0.0018	0.0007	0.0003	0.0001	0.0000	0.0000
		0.7348	0.7666	0.5990	0.3892	0.2018	0.0737	0.0302	0.0047	0.0005
		0.9194	0.1205	0.0402	0.0147	0.0056	0.0022	0.0009	0.0003	0.0001
			0.6461	0.5587	0.3745	0.1962	0.0715	0.0293	0.0044	0.0004
			0.8085	0.1060	0.0354	0.0129	0.0049	0.0019	0.0008	0.0003
				0.4528	0.3391	0.1833	0.0666	0.0274	0.0036	0.0001
				0.5665	0.0743	0.0248	0.0091	0.0035	0.0013	0.0005
					0.2648	0.1585	0.0575	0.0239	0.0023	-0.0005
					0.3314	0.0434	0.0145	0.0053	0.0020	0.0008
						0.1151	0.0430	0.0186	0.0003	-0.0012
						0.1440	0.0189	0.0063	0.0023	0.0009
							0.0241	0.0123	-0.0020	-0.0021
							0.0302	0.0040	0.0013	0.0005
								0.0084	-0.0034	-0.0026
								0.0105	-	-

5.3.3 Study of the interfacial transition zone between coarse aggregate and cement paste by image analysis technique

The basic procedure for the ITZ analysis of concrete is generally the same as for the pore structure analysis of the synthetic aggregate, including the setting of the measurement parameter, image enhancement, feature segmentation and measurement of the interested feature. However, the feature segmentation in this case is slightly more complicated than the case of the synthetic aggregate. This is due to the overlap between the cement paste and aggregate grey level histogram (see section 7.2.2 for more detail) and, therefore, the grey-level thresholding technique could not be used directly to differentiate these two phases. The feature segmentation for the aggregate and cement paste interface analysis used in this study were divided into two different stages. The aggregate particles within the BSE image of concrete need to be separated first and the remaining features of interest or phases which are the porosity, calcium hydroxide and the anhydrous are subsequently segmented.

5.3.3.1 Aggregate segmentation

Due to the overlapping of the aggregate grey level histogram and the histogram of cement paste, it is impossible to do any quantitative analysis of the concrete sample without first removing the aggregate pixels from the BSE image. Therefore, the segmentation of the aggregate and production of the coarse aggregate binary image are the first important steps of the ITZ analysis of concrete samples.

Werner and Lange (1999) developed an approach that segments the aggregate particles from the paste matrix that surrounds them. Their method involves the use of a conventional grey-level thresholding technique in combination with a texture filtering operation (including smoothing, edge detection) and the imagemath to differentiate the textures and segment the phases. However, their technique relies on the textural difference between the aggregate and the cement paste matrix which is not suitable for any aggregates which have textures similar to the cement paste matrix.

Yang and Buenfeld (2001) proposed an algorithm for separating aggregate particles from the cement paste matrix in the BSE image. Their algorithm combines the conventional grey-level thresholding with the edge detection filter and a series of morphological operations, e.g. opening, erosion, hole filling, and closing. The proposed

technique seems to work very well with different types of aggregate. However, as was cited by Head (2001), an erosion process that was used to erase the residual paste fragments will also remove very small aggregate particles from the image. These small aggregate particles are probably the sections that were cut at the tip of the larger aggregate particle. In addition, the aggregate boundary profile might have a distortion (especially for the aggregate with the irregular boundary profile) due to the effect of the shape factor used during the erosion and the reconstruction (dilation) process.

An alternative procedure that might be used is the manual segmentation of the aggregate boundary which was used by Crumbie (1994). However, manually defining the aggregate boundary pixels is very laborious and prone to systematic and random errors.

In this study, the procedure proposed by Brough and Atkinson (2000) was adopted for the aggregate segmentation. This technique 'automatically identifies the aggregate boundary based on the chemical compositional difference of each feature on the image. Therefore, in order to apply this technique, it is necessary to know the chemical composition of each phase appearing on the image. This can be done easily by using the X-ray analysis from the EDS detector (see section 5.2.5). In general, the calcium (Ca) dot map can be used to identify the cement paste region as clearly shown in Figure 5.17(d). The elemental dot map used for identifying the aggregate region depends on the mineralogical composition of each aggregate particle. The silicon (Si) dot map is normally used for quartz aggregate. Based on the mineralogy analysis (section 6.3), it was found that the synthetic aggregate used for the ITZ analysis consisted of quartz, feldspar, feldspar glass and relict of mica. Therefore, the silicon (Si), aluminium (Al) and, in some cases, potassium (K) or iron (Fe) dot map were used for the synthetic aggregate. The same elements that were used for the synthetic aggregate were found suitable for the identification of Lytag aggregate region.

The concrete containing synthetic coarse aggregate presented in Figure 5.17(a) is used to demonstrate the procedure of the aggregate segmentation used in this study. For this image, it was found that only Ca, Si and Al dot maps were needed for the aggregate segmentation. After acquiring the necessary images, a smooth filter was first applied to the X-ray dot maps in order to remove noise in the image. Although, all of the aggregates have high levels of Si, the counting statistic is still not good enough to

accurately distinguish the aggregate area. Figure 5.18(a) and (b) show the histograms for the Si and Ca dot map images and it is very difficult to accurately locate the threshold value for the aggregate segmentation from these two histograms. Therefore, the composite images were constructed by using the Si, Ca and Al dot map images in the form of Ca/(Si+Al). As shown in 5.19(a), the contrast of this image is clearly good enough to give a better-defined image histogram as presented in Figure 5.18(c). This allows the accurate segmentation of the aggregate boundary.

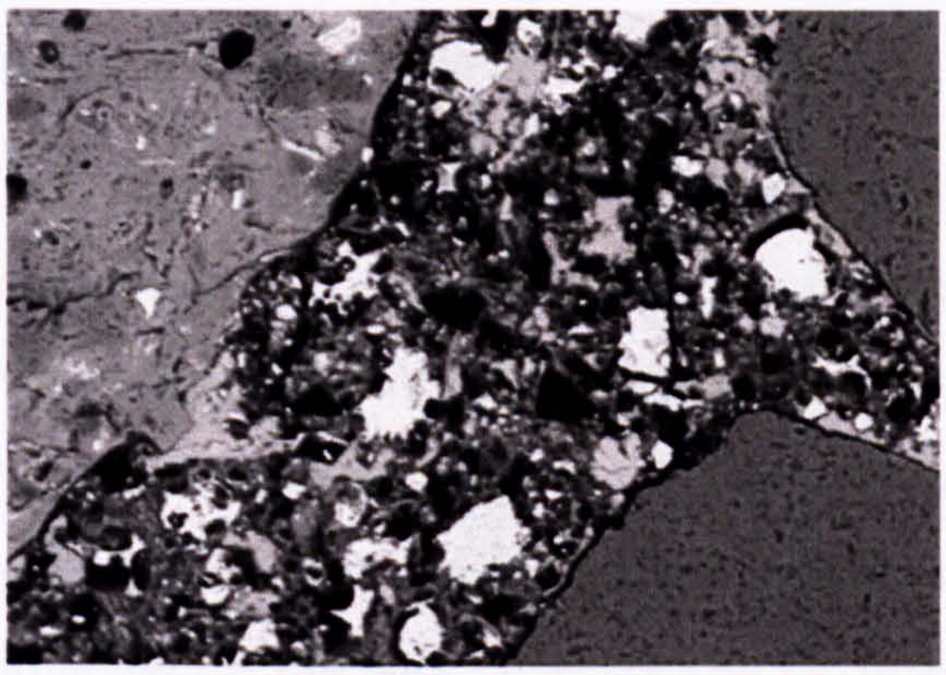

a) Backscattered electron image

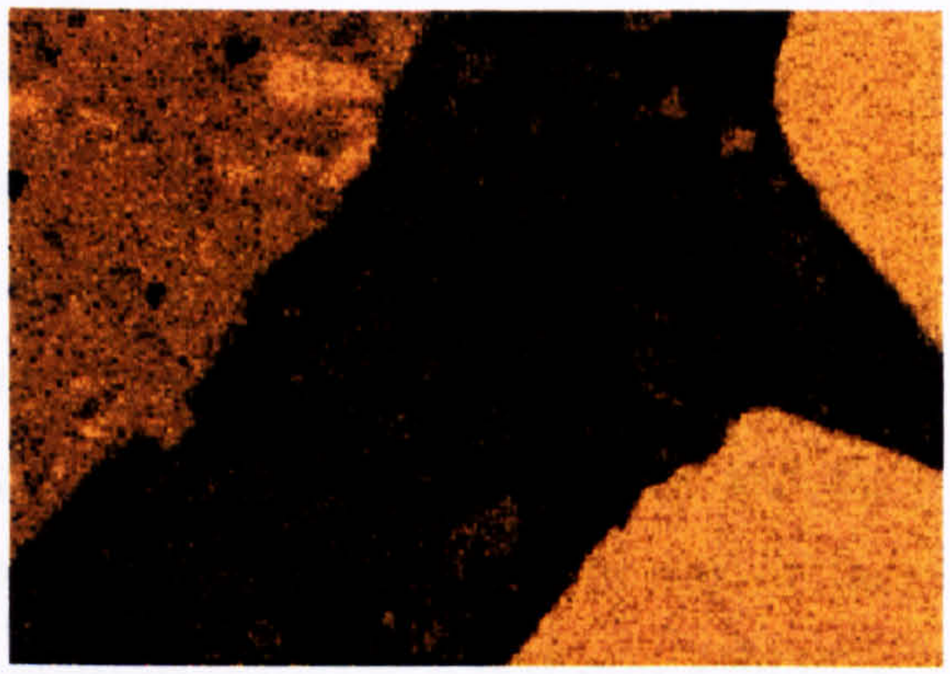

b) Silicon (Si) dot map image

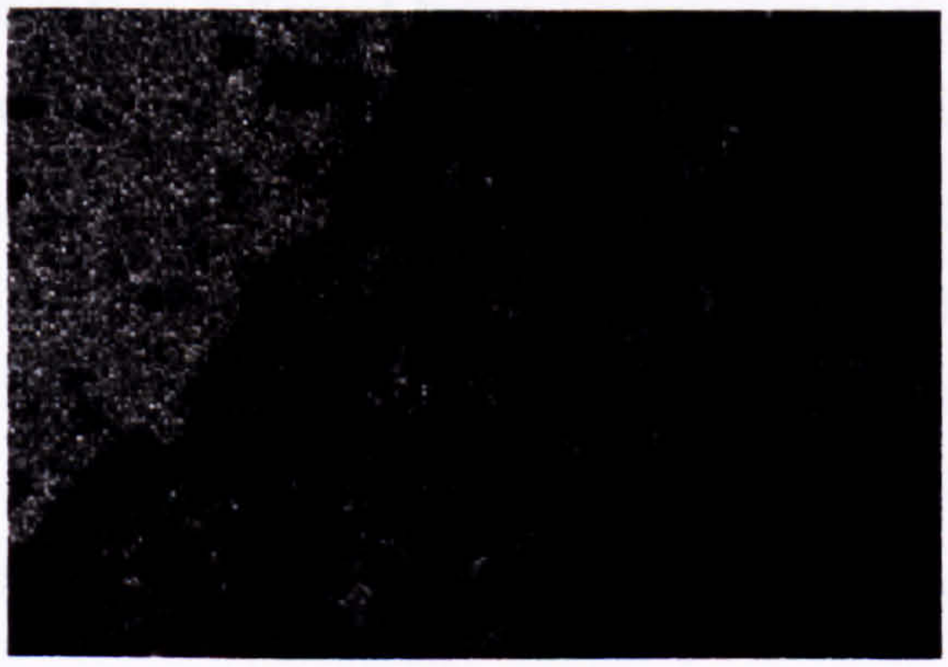

c) Aluminium (Al) dot map image

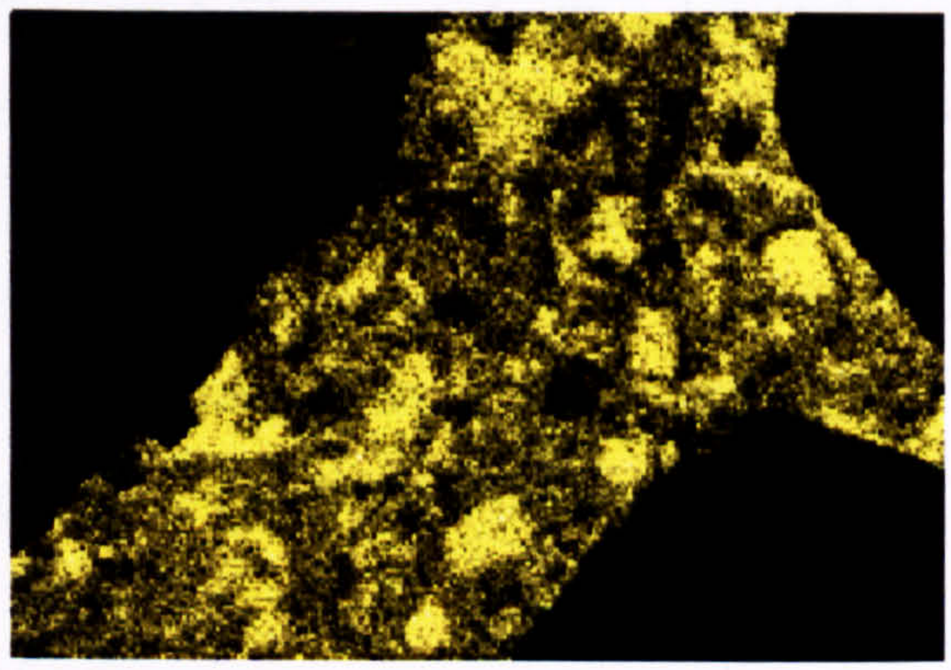

d) Calcium (Ca) dot map image

Figure 5.17 Backscattered electron image and X-ray dot map images of synthetic aggregate concrete. Images were acquired at 500x magnification.

A standard thresholding technique can now be applied on the composite image which results in a binary image as shown in Figure 5.19(b). The segmented image was then subtracted by the porosity mask segmented by its grey value range from the BSE image. This was done in order to get a more accurate aggregate boundary. However, there is still be some noise and unwanted particles left on both outside and inside the aggregate boundary as can be seen in Figure 5.19(d). In order to remove these unwanted

particles or noise, the *binscrap* and the *binnot* functions that are provided by the KS-300 software were applied to this image. Binscrap function, like its name, scraps or deletes the foreground (grey value = 255) region in a specified size range. The region size of this function was adjusted until all of the unwanted particles were completely removed. The binnot function is one of the Boolean operators that convert the grey value of each pixel to the invert value on the grey scale, i.e. pixel with a value of 255 is changed to 0 and pixel with a value of 0 is inverted to 255. The unwanted particles in the black regions of the binary image shown Figure 5.19(d) were removed first by the binscrap function, then the image was inverted and the binscrap function was applied again.

At this stage, the aggregate boundary still looks noisy and, in many cases, it is connected by the residual fragments of cement paste which cannot be removed by the binscrap function. This binary image is, therefore, required to remove noise and/or erase any paste fragments attached to the aggregate interface. The *close* operator and the smooth filter were applied to serve this purpose. The close function is one of the morphological operators provided by the image analysis software. It performs a *dilation* and is then followed by an *erosion* operation. The initial dilation gradually enlarges the boundary of regions of foreground pixel (pixel with grey value of 255) and closes a small hole and crack within those regions. The enlargement of the aggregate region can be subsequently reversed by erosion. The end product from these operations was shown in Figure 5.19(k). Note that the manual editing by the operator was made, if necessary, in order to get a more accurate boundary. Figure 5.19(l) shows the resulting image which is ready for the next measurement stage.

The same procedure was applied for the concrete containing quartz and Lytag coarse aggregate. The only difference is that the Ca/Si and Ca/(Si+Al+K+Fe) were used as the composite images for the case of quartz and Lytag aggregate, respectively.

The results clearly demonstrate that this technique can be effectively used to produce the accurate and reliable aggregate binary mask. However, it is noted that the accuracy of this technique relies on the quality of the X-ray dot map image which is mainly corresponds to the image acquisition time. As mentioned in section 5.2.6, an acquisition time of 550 seconds was needed in order to obtain image with enough quality for the segmentation process and, therefore, this is a fairly time consuming process, e.g. it took about four and a half hours to acquire 30 images.

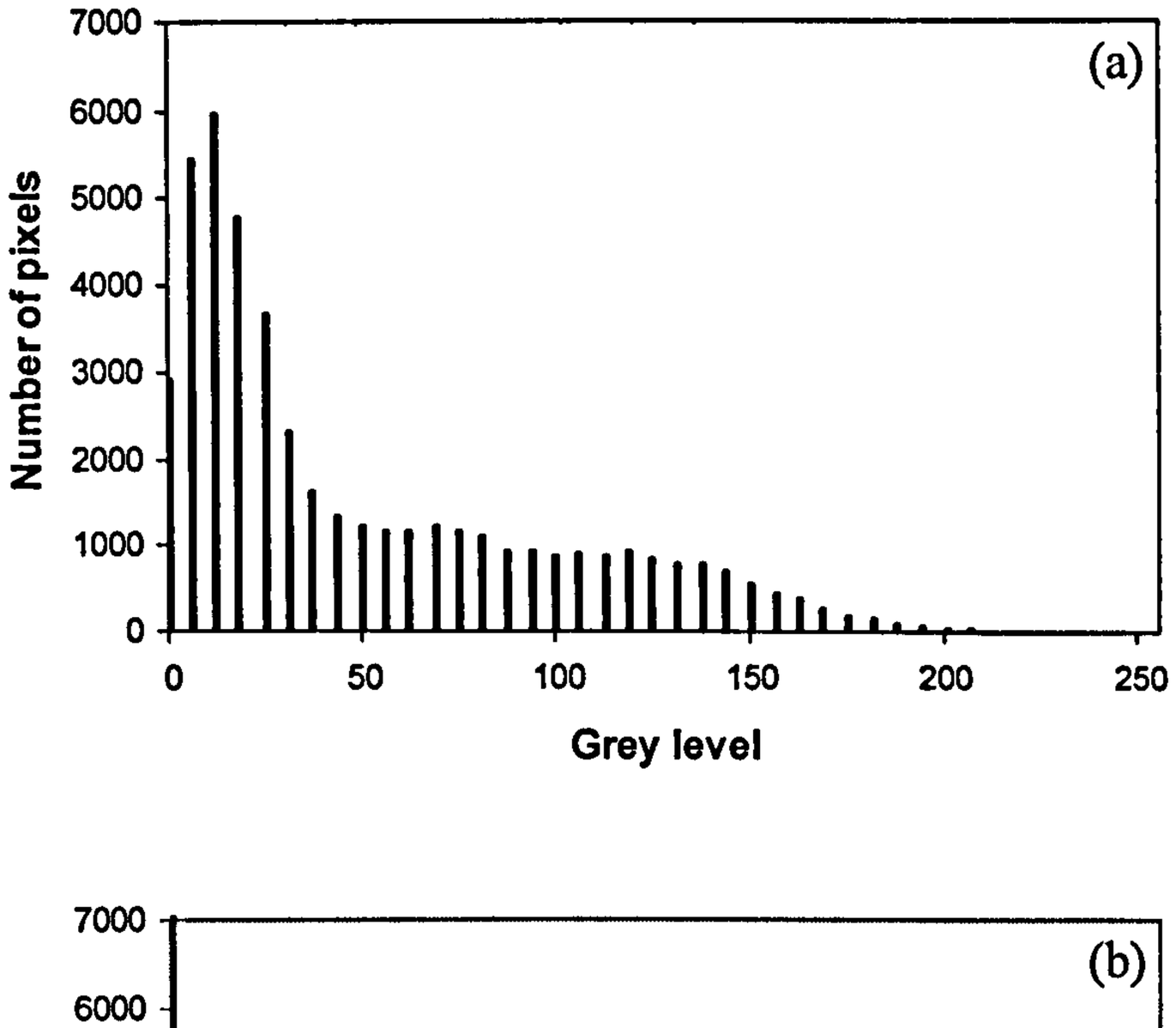

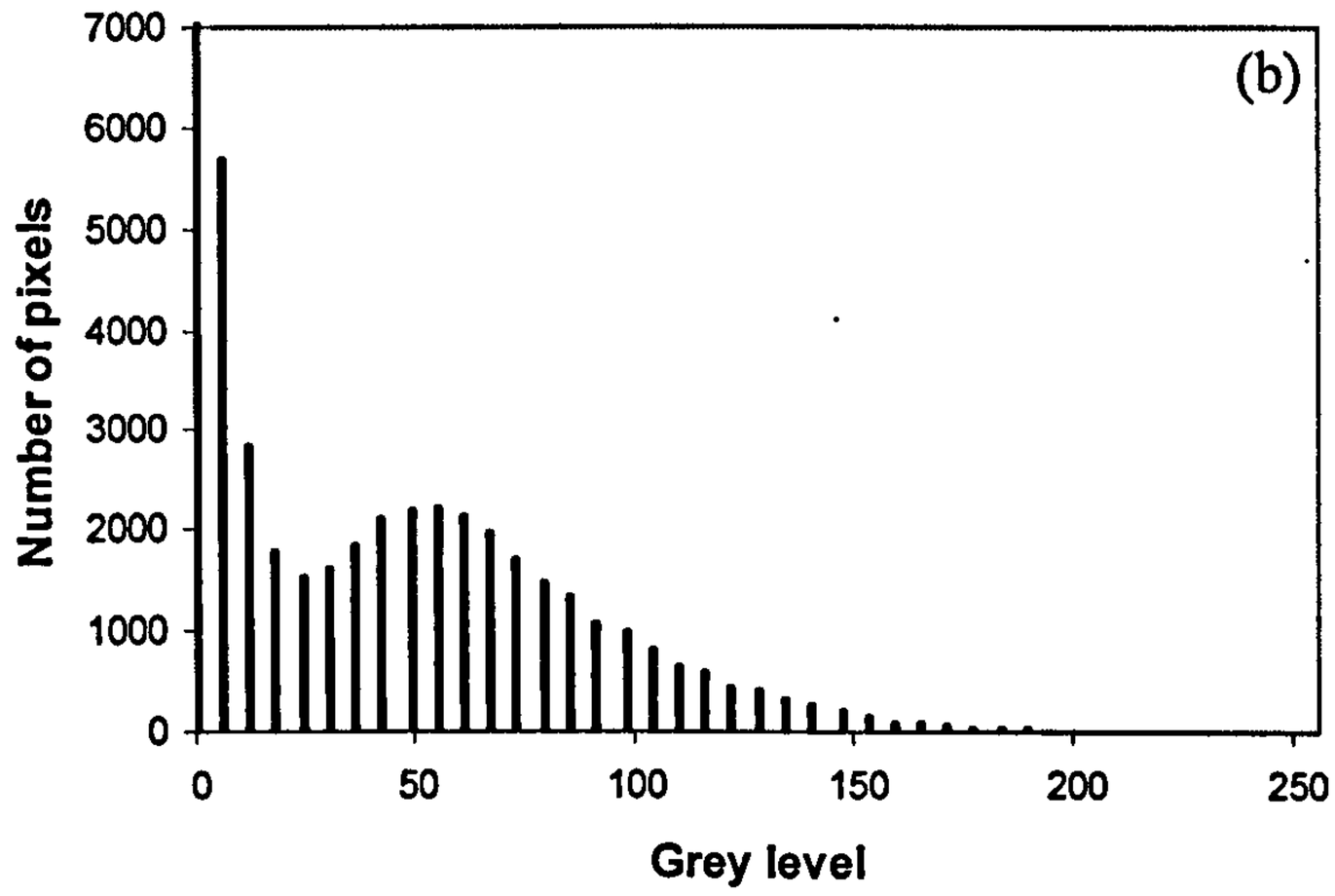

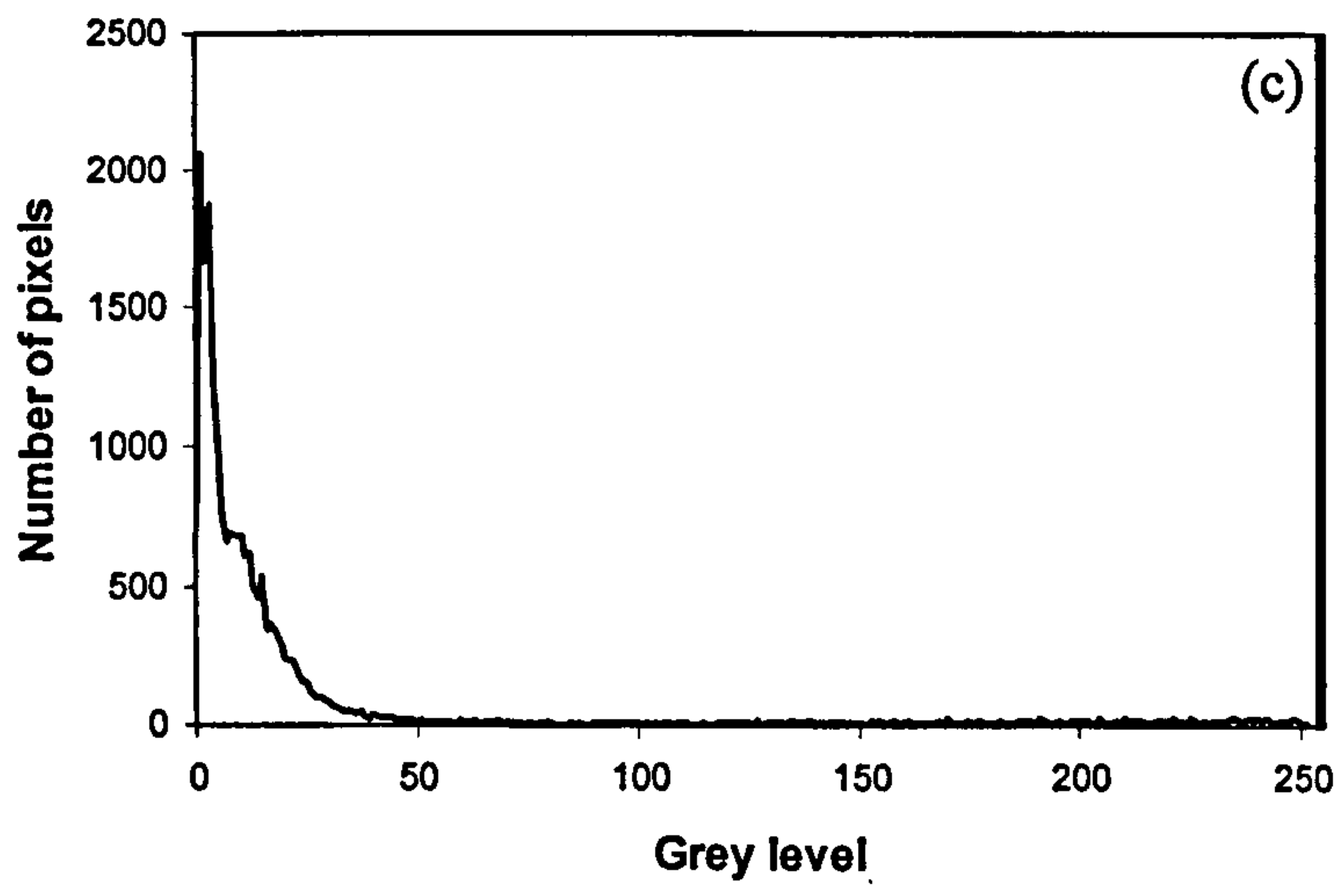

Figure 5.18 Grey level histogram of the images presented in Figure 5.17. a) Silicon (Si) dot map image, b) calcium (Ca) dot map image, c) the composite image Ca/(Si+Al).

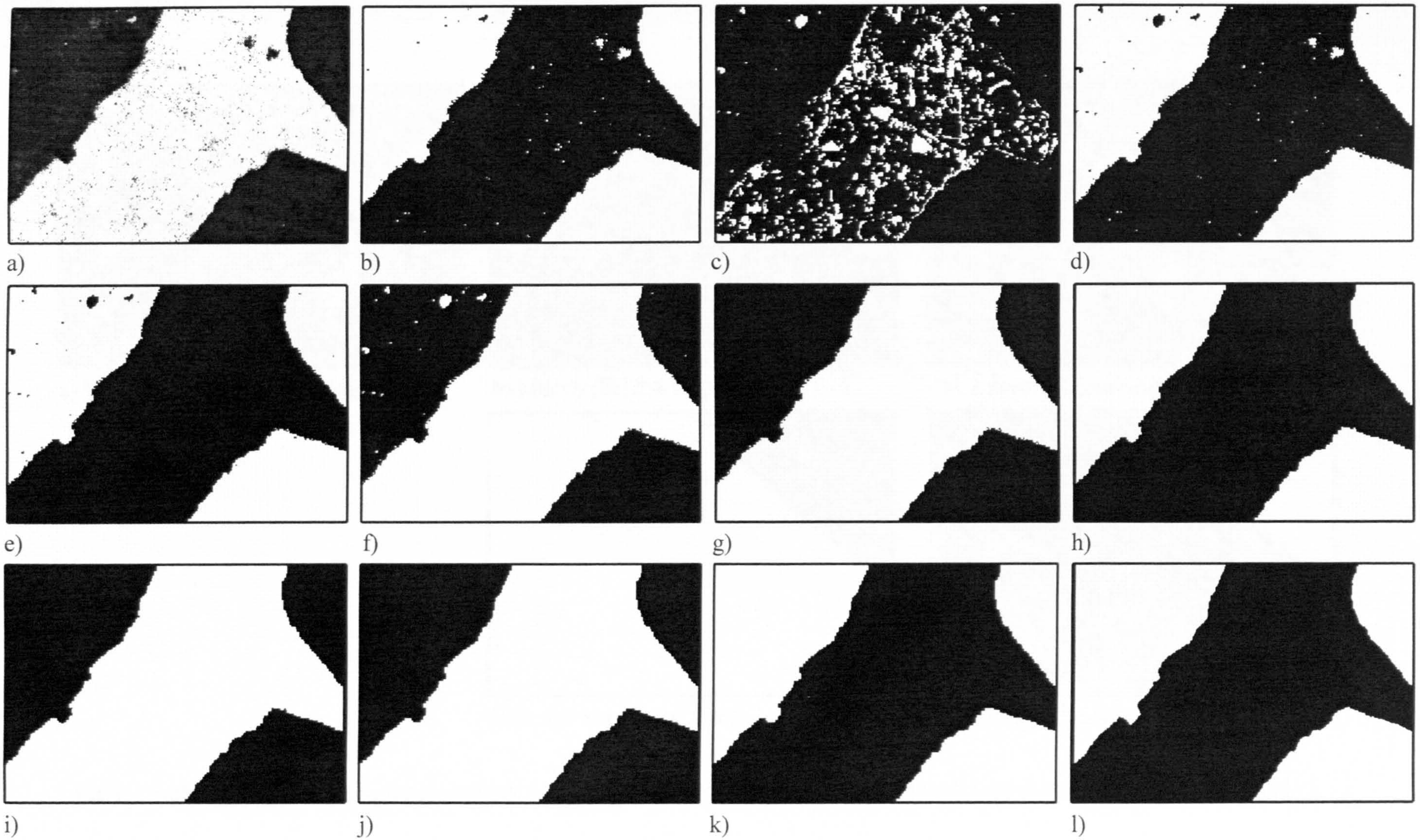

Figure 5.19 a) Composite image, b) binary image produced from a), c) porosity mask, d) binary image of b) – c), e) binscrap on d), f) inverted image of e), g) scrap on f), h) inverted image of g) and then performed *close* operation, i) inverted image of h), j) *close* operation performed on i), k) inverted image of j), l) final aggregate mask after performed median filter on k).

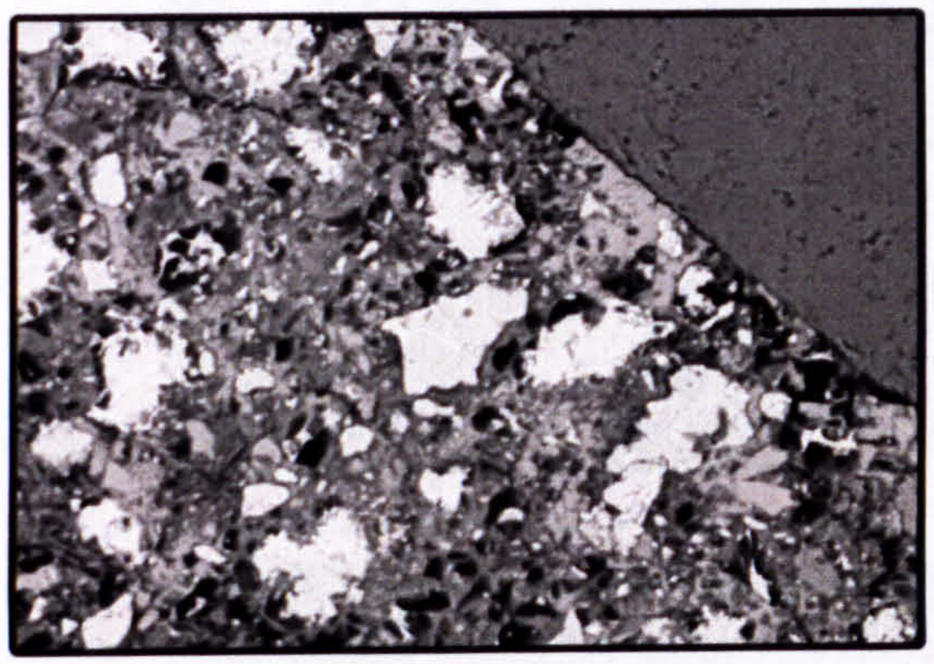

a) Backscattered electron image

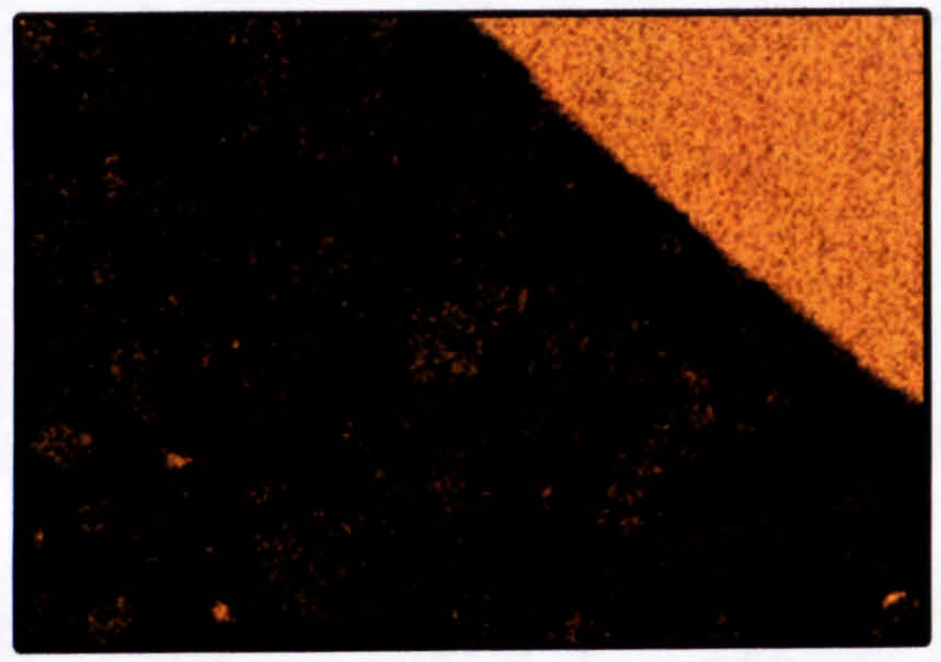

b) Silicon (Si) dot map image

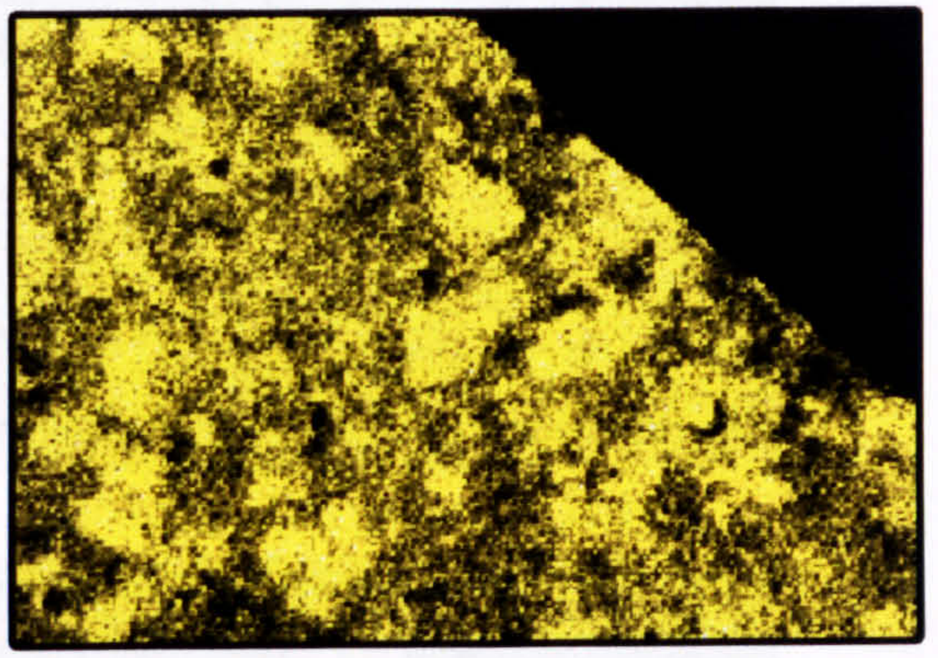

c) Calcium (Ca) dot map image

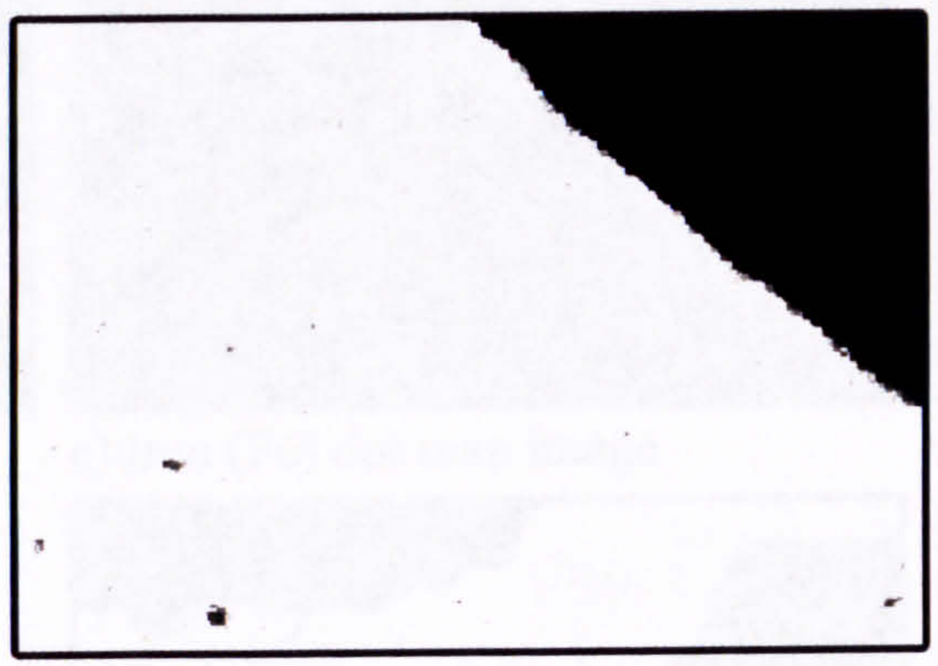

d) Composite image, Ca/Si

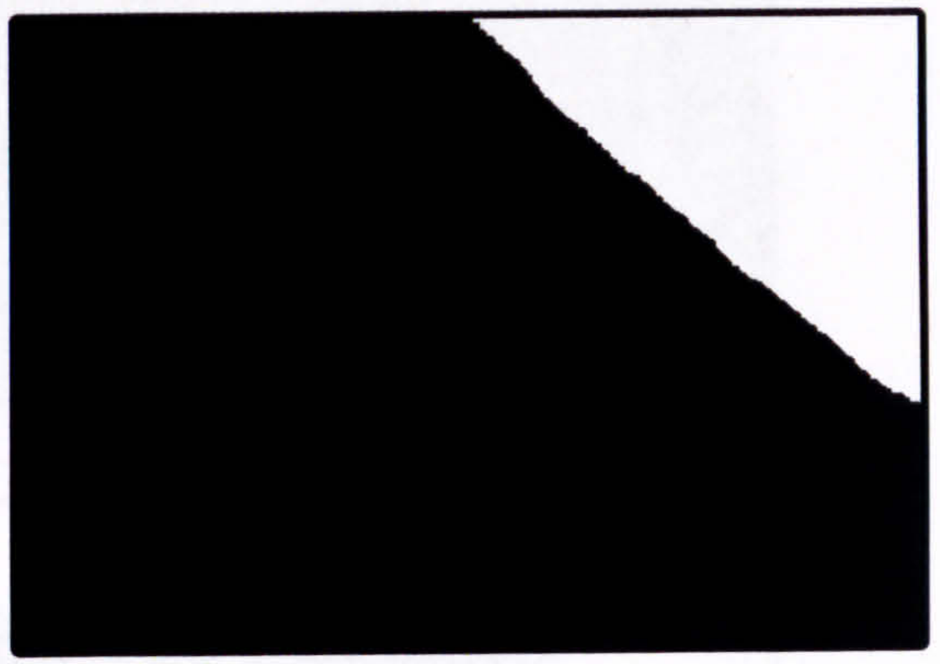

e) Final aggregate binary mask

Figure 5.20 Aggregate segmentation example case for quartz aggregate concrete sample. Image acquired at 500x magnification.

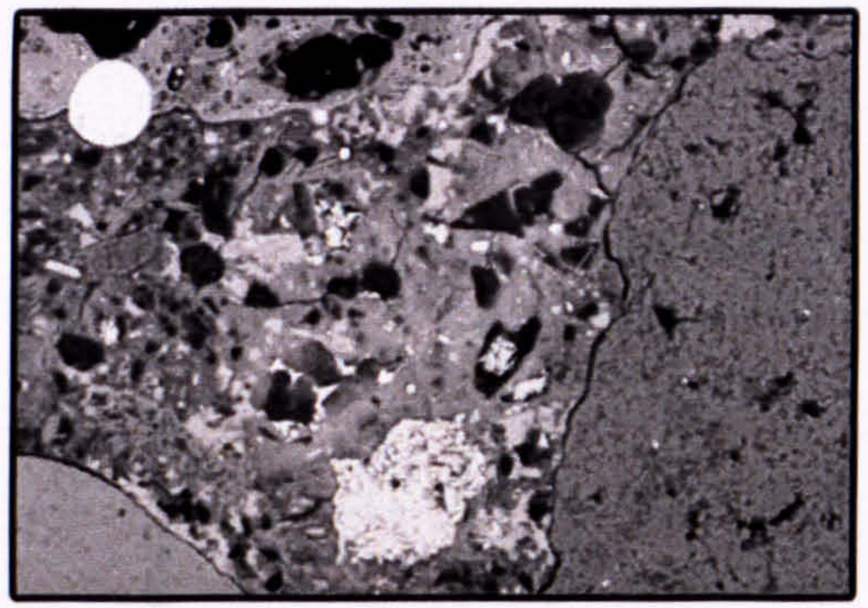

a) Backscattered electron image

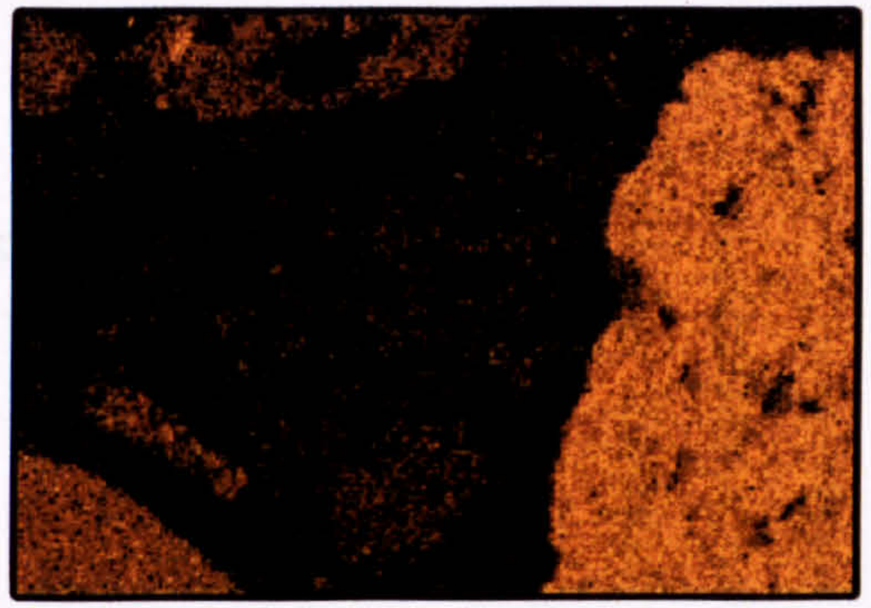

b) Silicon (Si) dot map image

c) Aluminium (Al) dot map image

d) Potassium (K) dot map image

e) Iron (Fe) dot map image

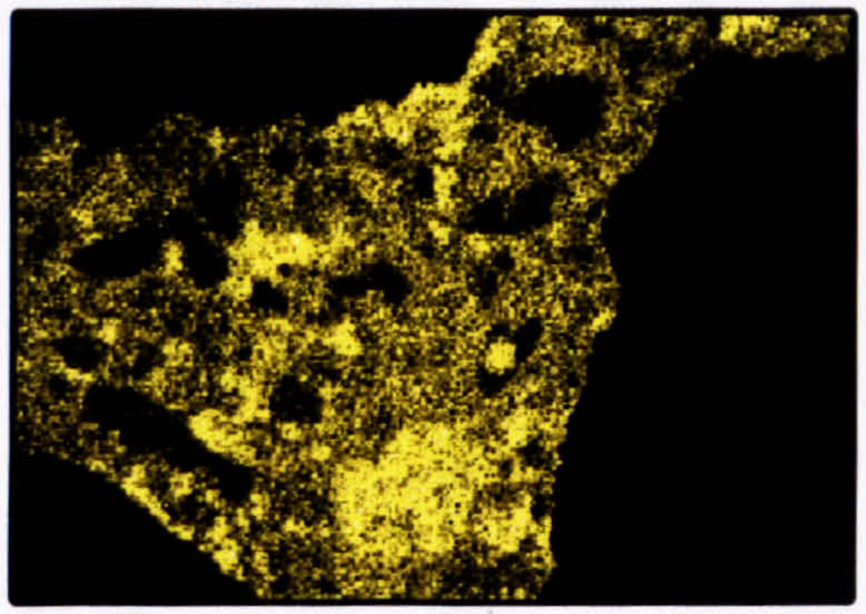

f) Calcium (Ca) dot map image

g) Composite image, Ca/(Si+Al+K+Fe)

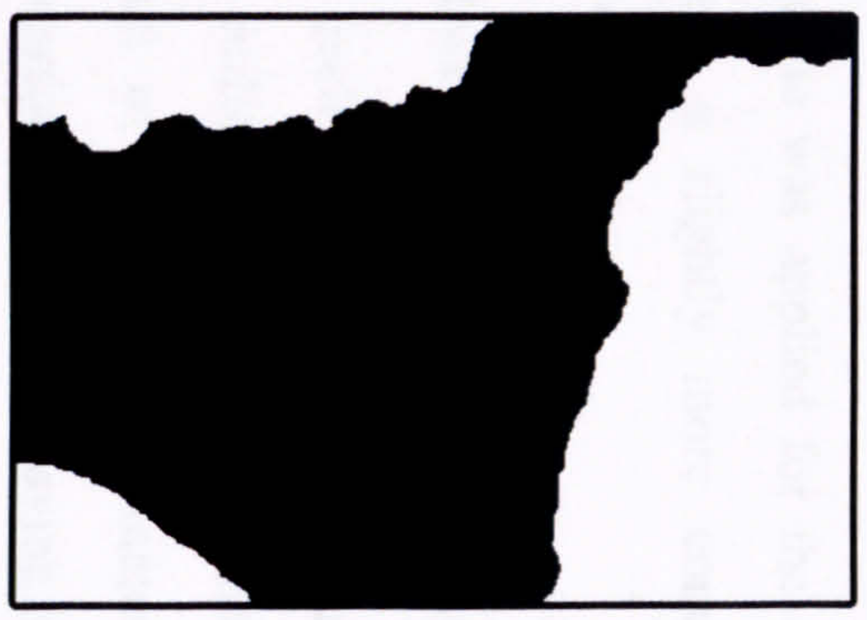

h) Final aggregate binary mask

Figure 5.21 Aggregate segmentation example case for Lytag coarse aggregate concrete sample. Image acquired at 500x magnification.

5.3.3.2 Feature segmentation

After obtaining the coarse and fine aggregate mask images, the next step involves the production of the porosity, calcium hydroxide (CH) and the anhydrous (Anh) mask image. A standard thresholding technique was applied for the calcium hydroxide and the anhydrous segmentation, while a slightly more complicated processing was used for the porosity binary mask production.

5.3.3.2.1 Segmentation procedure for calcium hydroxide and anhydrous materials

A thresholding technique is used to assign each pixel to either the interested feature or the background and this can be done by utilizing the grey level histogram. Figure 5.22 shows a typical grey level histogram of cement paste material. As mentioned previously, each peak on this histogram represents any pixel having a similar grey value. Based on the mean atomic number or the backscattered coefficient of the constituents in the Portland cement paste given in Table 5.1, each peak on the histogram can be identified by their differences in grey or brightness value, i.e. in order of descending brightness, Anh, CH, DIP, C-S-H and pore (read section 7.2.2 for more details).

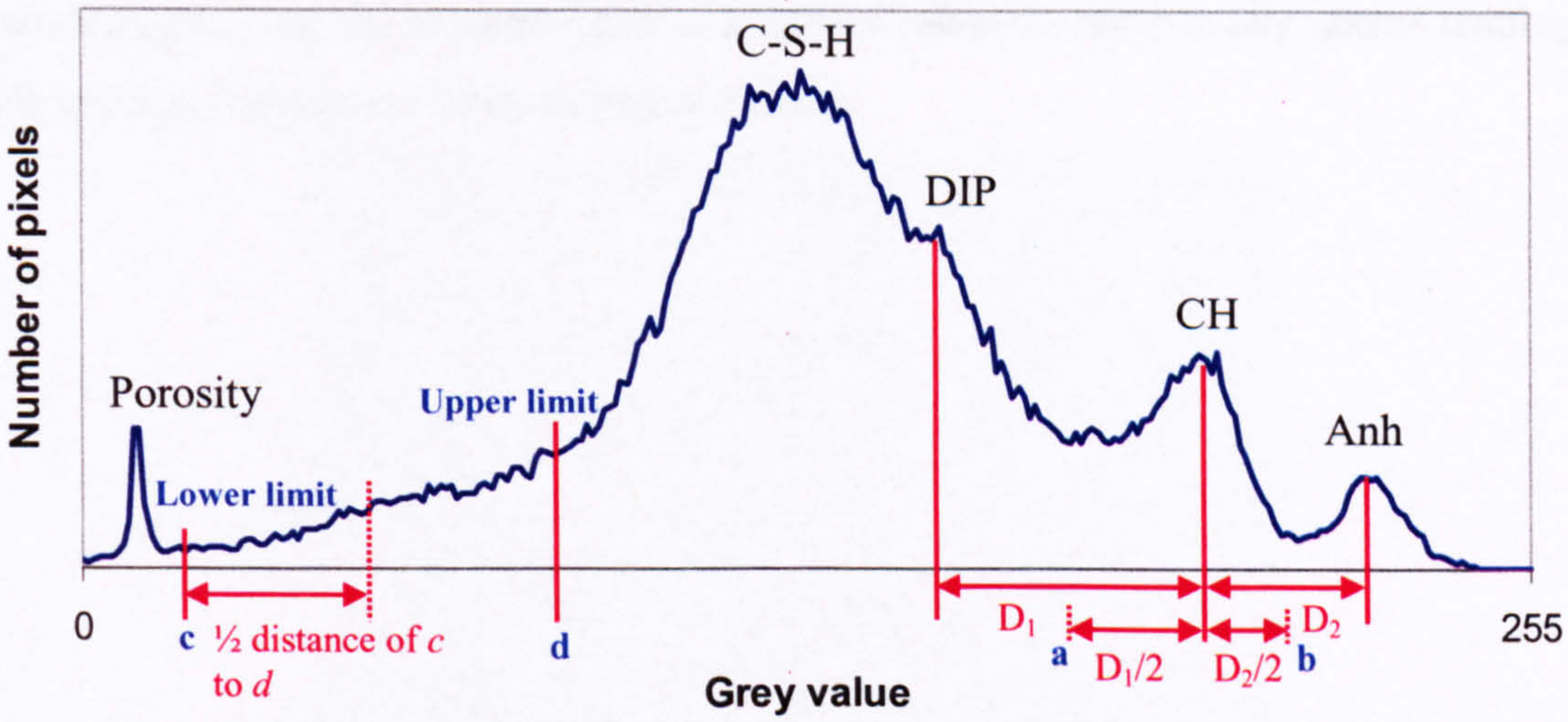

Figure 5.22 Thresholding criteria used for the segmentation of CH and anhydrous in concrete sample.

Ideally, peaks corresponding to each of the phases on the grey level histogram should be well-defined which make it easy to do the segmentation of each phase.

Unfortunately, those pixels that straddle the boundary will display an intermediate grey value averaging from the two different phases. The brightness value of these pixels is, therefore, proportional to the area of each phase subtended within the pixel. As proposed by Head (2001), it is the logical choice to segment by using the pixels consisting of 50 percent signal from one of the phases and 50 percent from the other phase. Therefore, by assuming a normal distribution of each peak in the grey level histogram, the grey values at the mid-way between two adjacent peaks, as illustrated in Figure 5.22, were used as the threshold criteria in this study, i.e. the grey value range from point *a* to *b* is used for the calcium hydroxide segmentation and from *b* to 255 is used for the anhydrous materials.

Figure 5.23(a) and (b) shows the backscattered electron image of concrete containing quartz aggregate and the initial binary images of the calcium hydroxide. Note that the separation of each phase was done purely based on the criteria mentioned previously. The edge effect due to misidentification of pixels located at the boundary between the anhydrous and the C-S-H clearly appeared on Figure 5.23(b). These pixels were clearly mistaken as the calcium hydroxide and they need to be removed from the calcium hydroxide image. The correction of the calcium hydroxide binary image was done by applying the dilation operation on the anhydrous binary image and then subtracting it from the calcium hydroxide binary image to remove any untrue readings. The corrected image is shown in Figure 5.23(c).

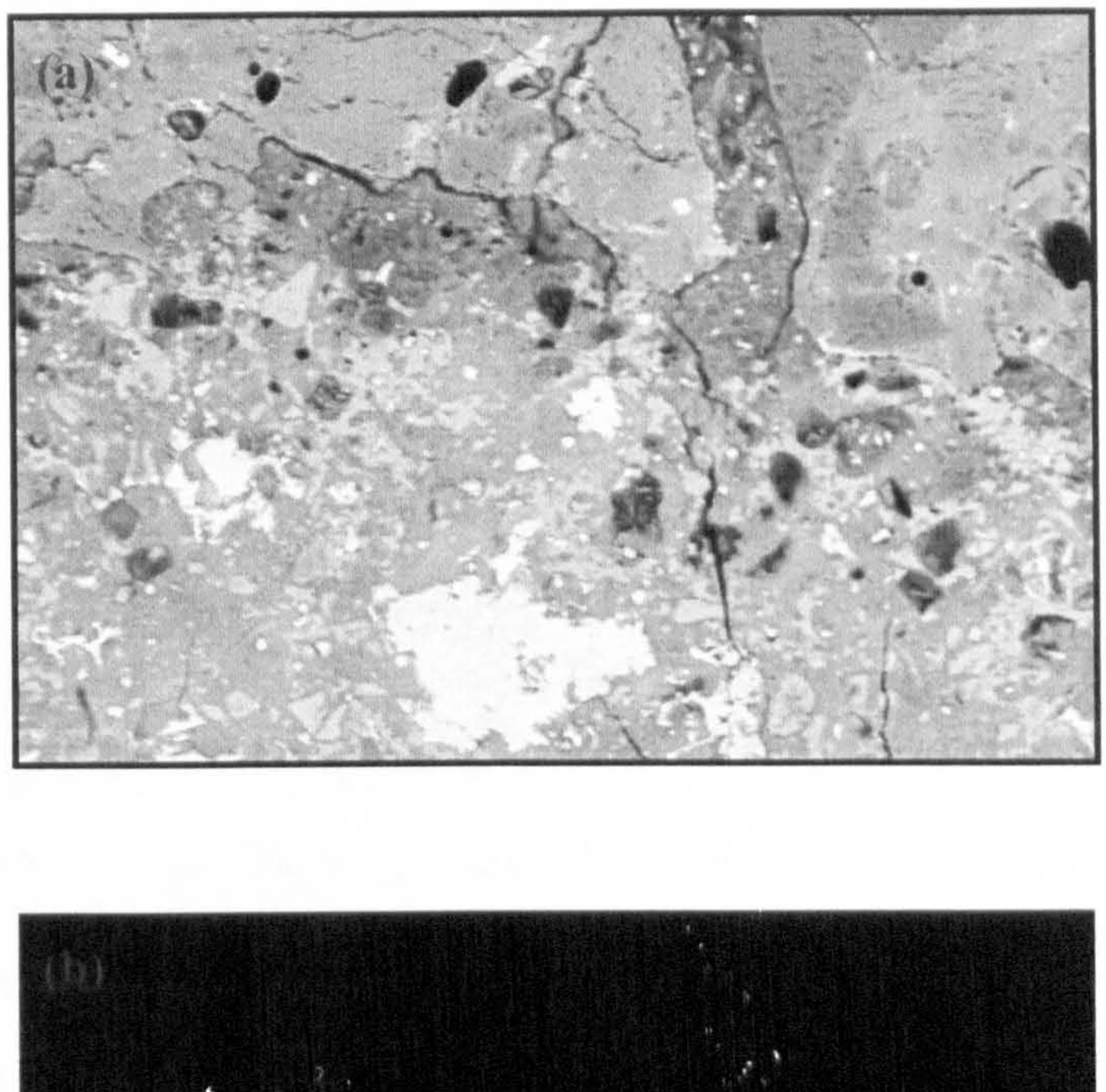

Figure 5.23 (a) a BSE image of 28-day old quartz aggregate concrete. (b) Calcium hydroxide binary image from the initial discrimination process. (c) A further improved image of calcium hydroxide binary image.

5.3.3.2.2 Porosity segmentation of concrete sample

Several techniques were proposed in the past to locate the threshold value for the porosity segmentation, for example, the tangent technique used by Scrivener et al. (1987) and the mid-way between peaks proposed by Head (2001). More recently, Wong et al. (2006) proposed the technique to segment pores from the BSE image called the *overflow* method. Their technique involves a construction of the cumulative brightness histogram and a point corresponding to the inflection of this histogram was used as the upper threshold level for the porosity. This technique seems to work very well for the porosity segmentation. However, none of the proposed techniques concern the existence of the low density C-S-H which occasionally appears in the originally small cement grain. Since this hydration product appears dark on the BSE image, as shown in Figure 5.24(a), it will, therefore, be identified as pores if using the existing segmentation techniques. In addition, use of a single threshold cut-off value for porosity segmentation does not really give an accurate result. The gradual transition of the grey level always occurs from pore to solid due to the influence of beam interaction volume on the BSE signal and/or the inclination of the pore at the boundary. The pore edge or boundary is, therefore, very difficult to define. Therefore, in order to obtain a more accurate result, a new thresholding criteria is needed for this study.

The proposed technique combines the overflow technique with the technique proposed in section 5.3.2.3. The overflow technique is used to define the pixel that has a grey value equal to the upper end of the transition region (upper limit or point *d* on Figure 5.22), while the curve fitting technique is used to detect the large pore or any pixels consisting of 100 percent signal from epoxy resin (lower limit or point *c* on Figure 5.22). The threshold value for the porosity segmentation is, therefore, half-way between the upper and the lower limit.

To get the upper limit for the BSE image as shown in Figure 5.24(a), the total pore area segmented was first plotted against the threshold level. The inflection point of this histogram, referred as the critical overflow point, can be estimated from the intersection of the two linear segments (dotted line shown in the Figure 5.24(c)). The grey value at this point was then multiplied with the factor of 0.8 and it was used as the upper limit. This multiplication factor was found to give a visually satisfactory binary image. The lower limit was obtained by fitting the porosity peak with the Gaussian

distribution function as given in Equation 5.5 and the lower limit was then calculated by applying Equation 5.6 with a factor of four. Figure 5.24(b) and (d) show the pore segmented image obtained by using the proposed and the over-flow technique.

It is noted that for any pixels (pore or solid) located in the transition region the existing pore segmentation techniques (including the technique proposed here) gives an approximate result. This is due to the main drawback of the SEM technique, i.e. it is impossible to separate any features that have sizes less than the pixel resolution by using grey level thresholding. However, as clearly presented in Figure 5.24(b), the resulting image visually produces a reasonable and more accurate segmented pore image compared with the one created by the overflow technique. In addition, reproducible and reliable results from this technique make it possible to do comparative studies for concrete containing different types of coarse aggregate.

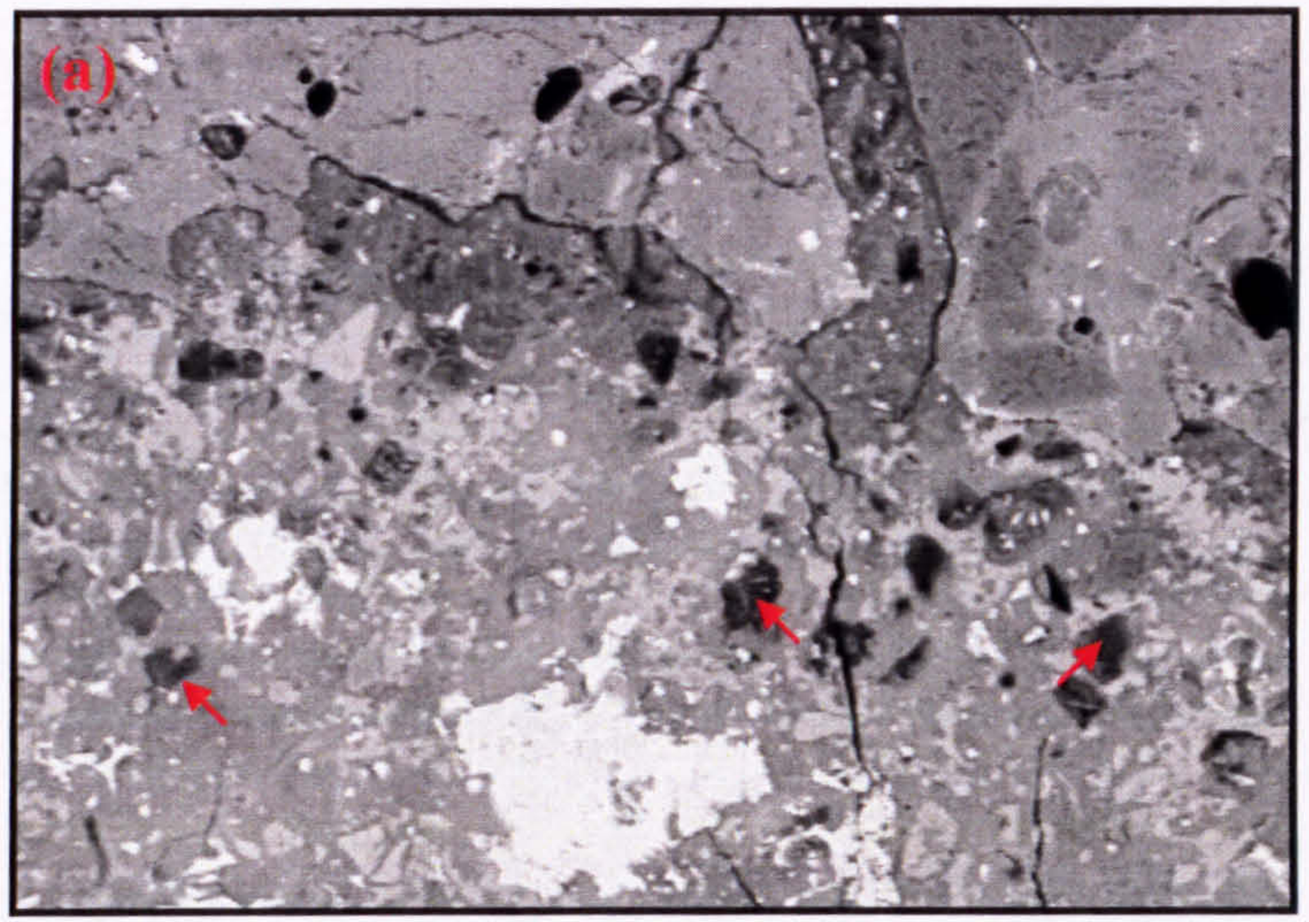

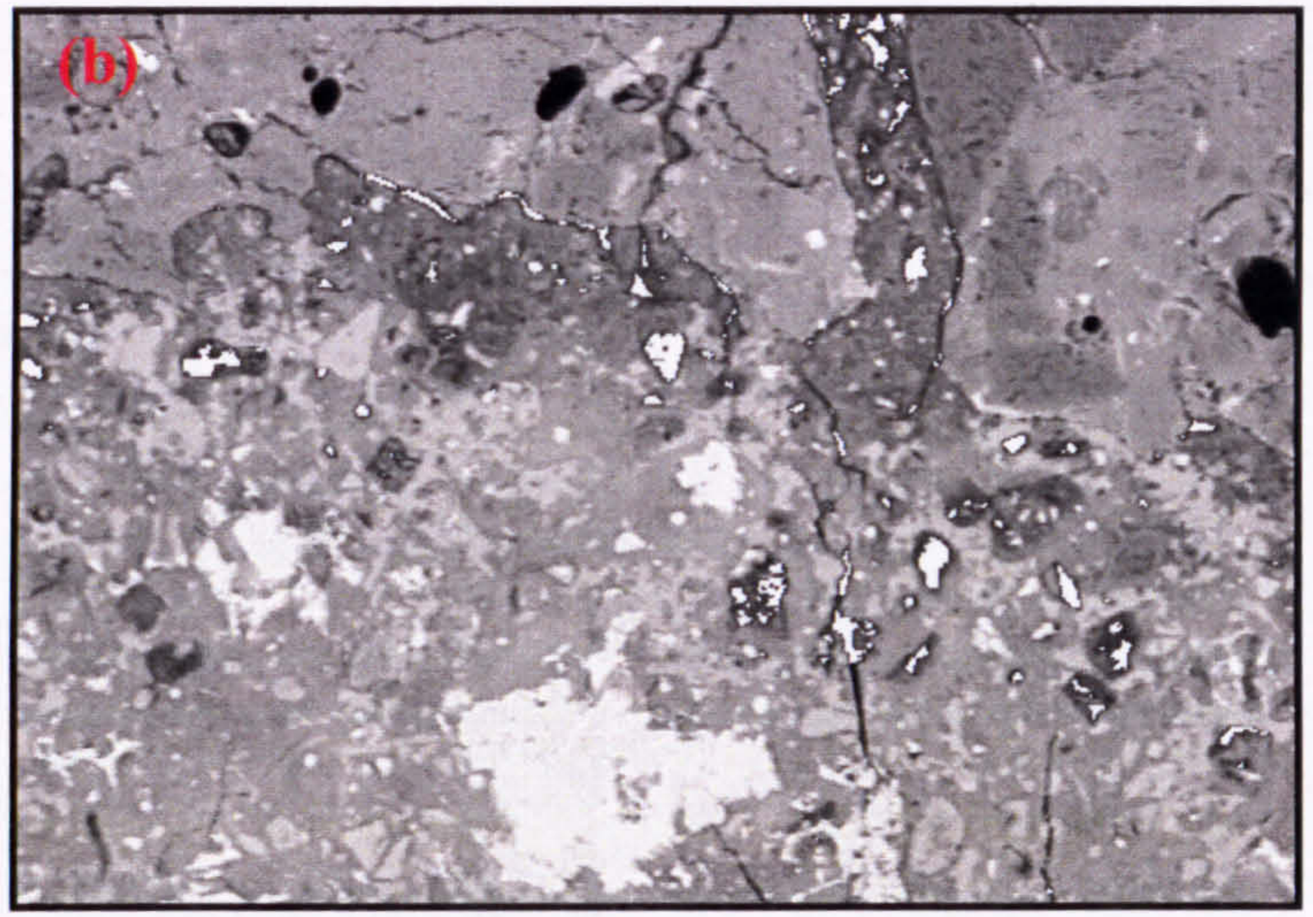

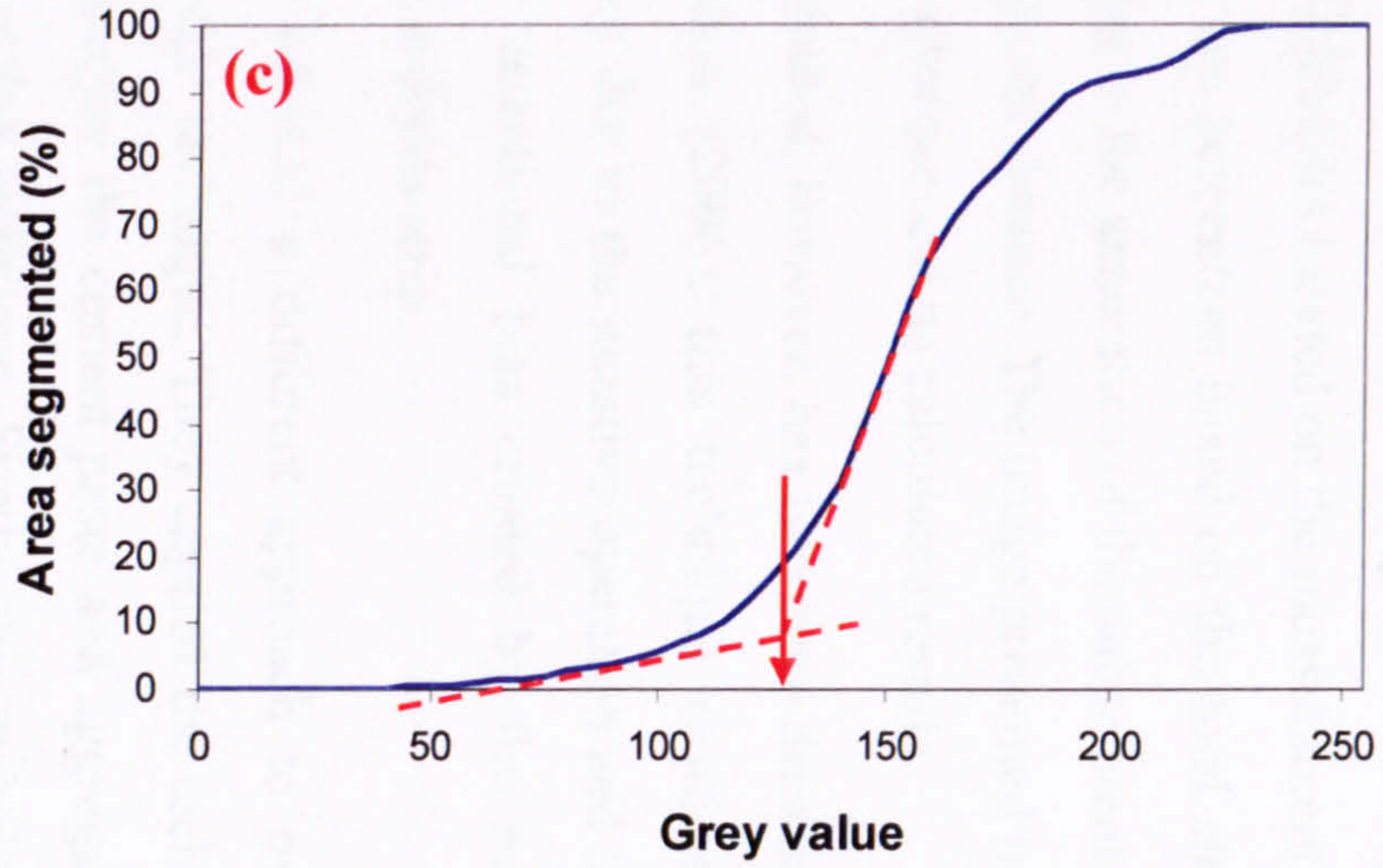

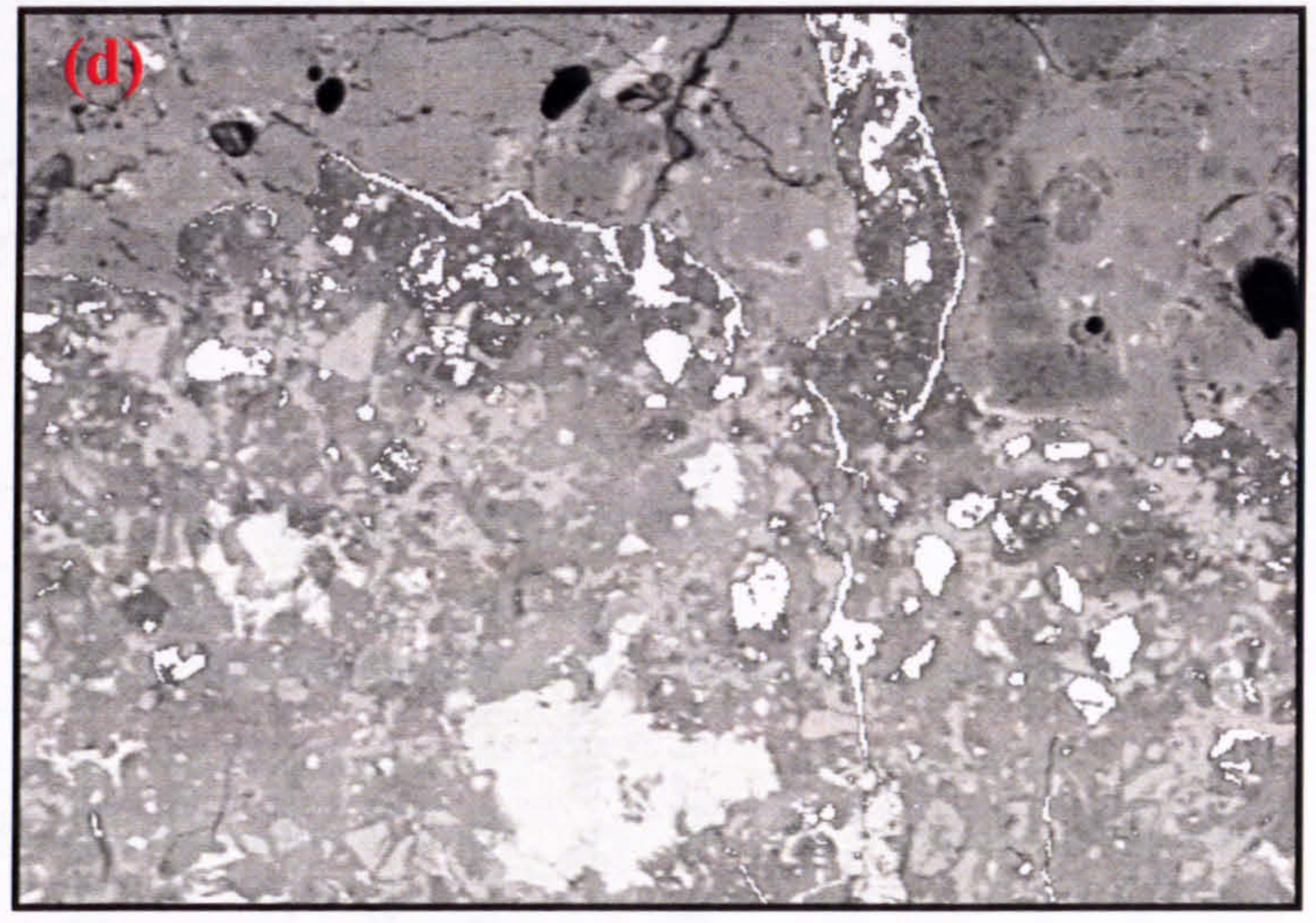

Figure 5.24 (a) A BSE image of the 28-day old Portland cement concrete containing synthetic aggregate (W/C = 0.53). An arrow points at the low density hydration product. (b) Pores segmented (white pixels) from (a) by the proposed technique. (c) Cumulative grey level histogram of (a). (d) Pores segmented (white pixels) from (a) by the over-flow technique with factoring of 0.8.

5.3.3.3 Image quantification

The binary masks of image features that will be used in this measurement stage include:

- Coarse aggregate binary mask
- Fine aggregate binary mask
- Porosity binary mask
- Calcium hydroxide (CH) binary mask
- Anhydrous (Anh) binary mask

The measurement technique that was normally used for the ITZ analysis involves the computing of the area fraction of each interested feature in a series of the equidistant strips. The first strip starts at the aggregate interface and then extends outward to the bulk paste. This process is done by applying the dilation operation on the binary aggregate mask and the number of operations depends on the size or width of the strip to be created. The first interfacial strip is obtained by subtracting the original aggregate binary mask from the new dilated image. This strip is then combined with the interested features (porosity, CH and Anh) by using the logical *AND* operator. This process gives the fraction of interested features located on the measurement strips which are then measured and calculated as the percentage based on the total strip area. The whole process is repeated again leading to the generation of the subsequent strip and the procedure stops when it reaches a required distance. The image presented in Figure 5.26 demonstrates the application of this technique and its calculated results.

The dilation and subtraction method, however, has two main drawbacks. Firstly, as was cited by Wong and Buenfeld (2006), this technique requires significant processing time and computer memory due to the iterative operation and large number of images involved. Secondly, the directional bias created by the morphological operation will affect the profile of the analysis strip.

Wong and Buenfeld (2006) adopted a different approach to overcome the limitation of the dilation and subtraction technique. They applied the technique called Euclidean distance map (EDM) to analyse the cement paste and aggregate interface. There are two main benefits of using this technique. Firstly, this technique does not involve iterative strip measurement anymore. Secondly, the directional bias can be avoided especially for the circle image.

The technique proposed by Wong and Buenfeld was used in this study but a slight modification was made which will be demonstrated later. In general, this technique transforms the binary image into the distant or grey scale image. Each pixel in the distant image contains the brightness or grey value equal to its Euclidean or straight line distance to the nearest pixel in the background (Russ, 2002). The calculation of the Euclidean distance is based on Pythagoras's theorem and Figure 5.25 presents the distance from the center pixel to the neighborhood pixels in *Pythagorean* units. This function is also available in the KS-300 software with the macro command as *distmapeuclid.*

√18	√13	√10	3.0	3.2	3.6	4.2
√13	√8	√5	2.0	2.2	2.8	3.6
√10	√5	√2	1.0	1.4	2.2	3.2
√9	√4	√1	0	1.0	2.0	3.0
√10	√5	√2	1.0	1.4	2.2	3.2
√13	√8	√5	2.0	2.2	2.8	3.6
√18	√13	√10	3.0	3.2	3.6	4.2

Figure 5.25 Arrays of the unit square pixels with their Euclidean distance measured from the center pixel.

The BSE image of concrete sample as shown in Figure 5.26 will be used to demonstrate the procedure of this technique and only porosity measurement will be illustrated here because the same procedure was applied for the remaining phases. The first step involves the transformation of the coarse aggregate and fine aggregate binary mask into the grey scale or EDM image. As shown in Figure 5.27(c), for example, it is the grey scale or EDM image of the aggregate binary mask and the grey value on each pixel represents its linear distance to the nearest aggregate pixel. The subtraction operation was then applied on these three images in order to obtain the EDM image of the only region ranging from the coarse aggregate interface to the mid-distance to the next aggregate particles and the resulting image was shown in Figure 5.27(d) with the

white pixel representing the coarse aggregate region. This is because the microstructure of the coarse aggregate interface is the only subject of interest here. This process is a modification of Wong and Buenfeld procedure because, without this process, the information from the fine aggregate region will be included in the result. The next step was the construction of the EDM image of a pore. This process was done by applying the *multiply* operator between the resulting image from the subtraction process (image shown in Figure 5.27(d)) and the porosity binary mask. The resulting image is shown in Figure 5.27(e) and each pixel in this image has a grey value equal to its linear distance to the nearest aggregate pixel.

The analysis was then performed by first plotting the grey level histogram of the aggregate EDM image (Figure 5.27(d)) and the porosity EDM image (Figure 5.27(e), as shown in Figure 5.28(a) and (b), respectively. Next, the grey level histogram of the porosity EDM image was normalized by the aggregate EDM image histogram. Finally, the grey values of the normalized histogram were converted to the actual distance resulting in the required porosity distribution as shown in Figure 5.28(c). Note that the same procedure was applied for the calcium hydroxide and the anhydrous binary mask. The analysis results for these two phases are also presented in Figure 5.28(d) and (e). The results obtained clearly agree very well with the results from the dilation-subtraction technique.

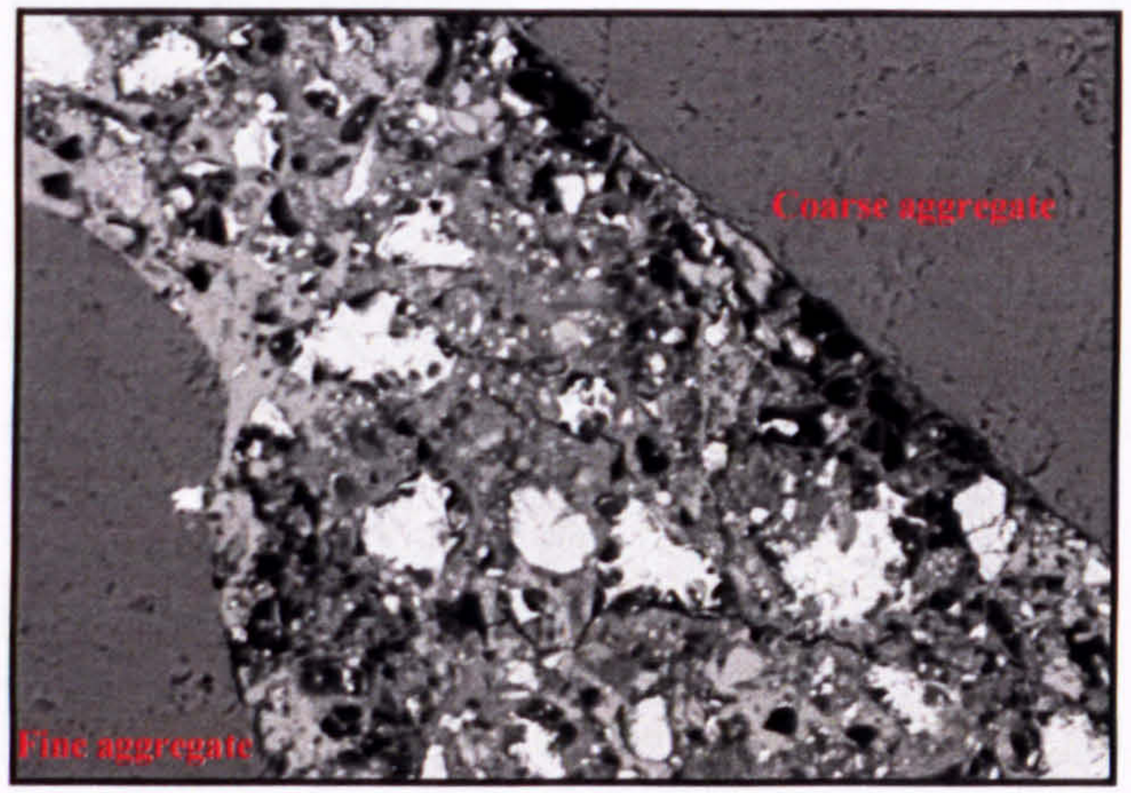

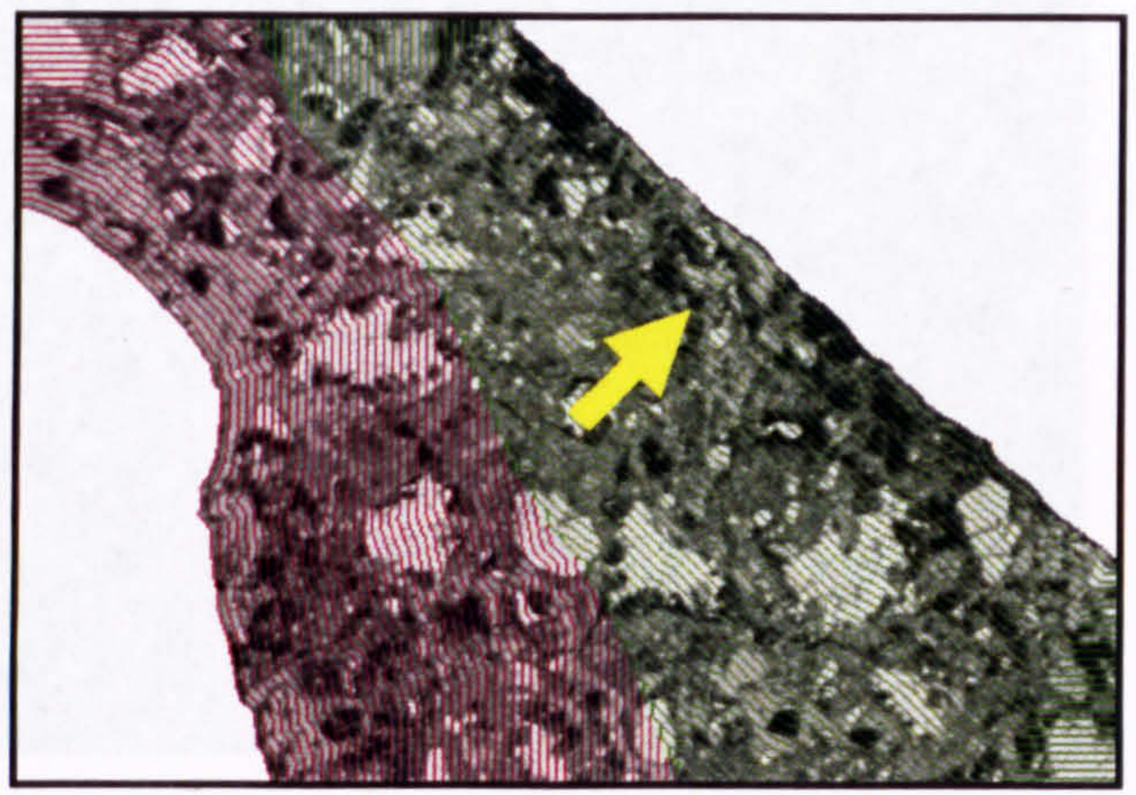

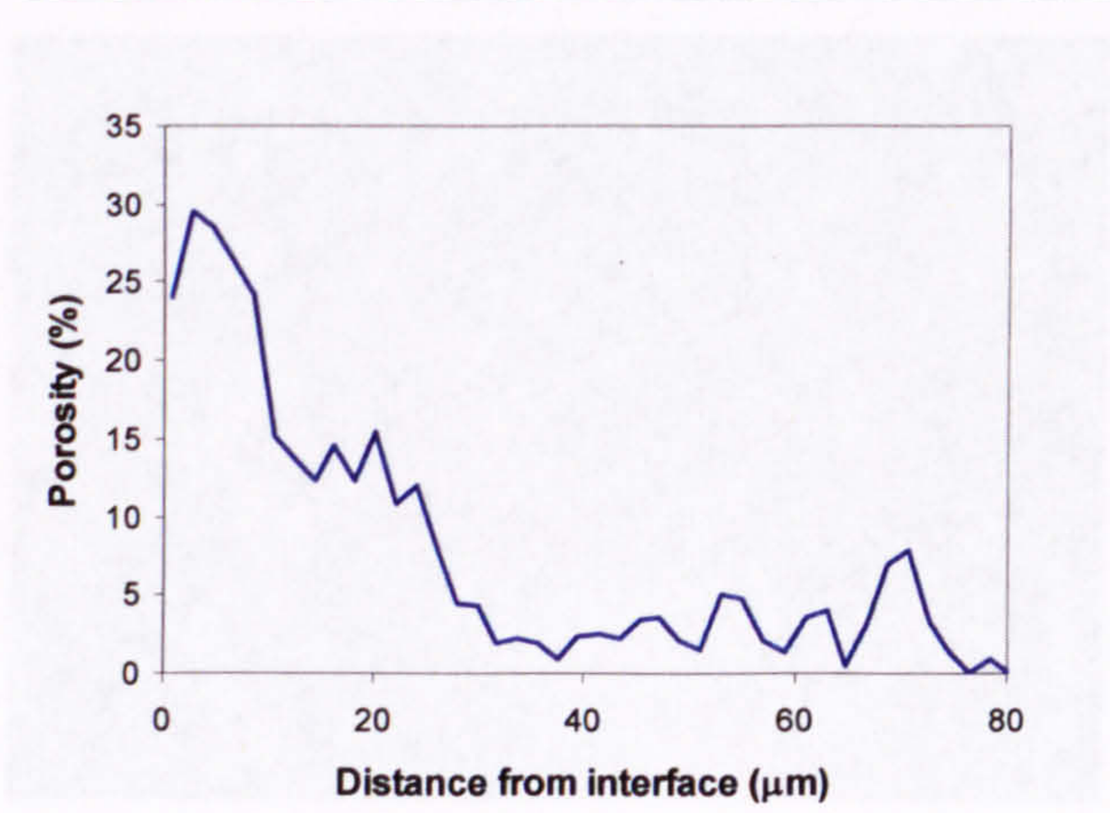

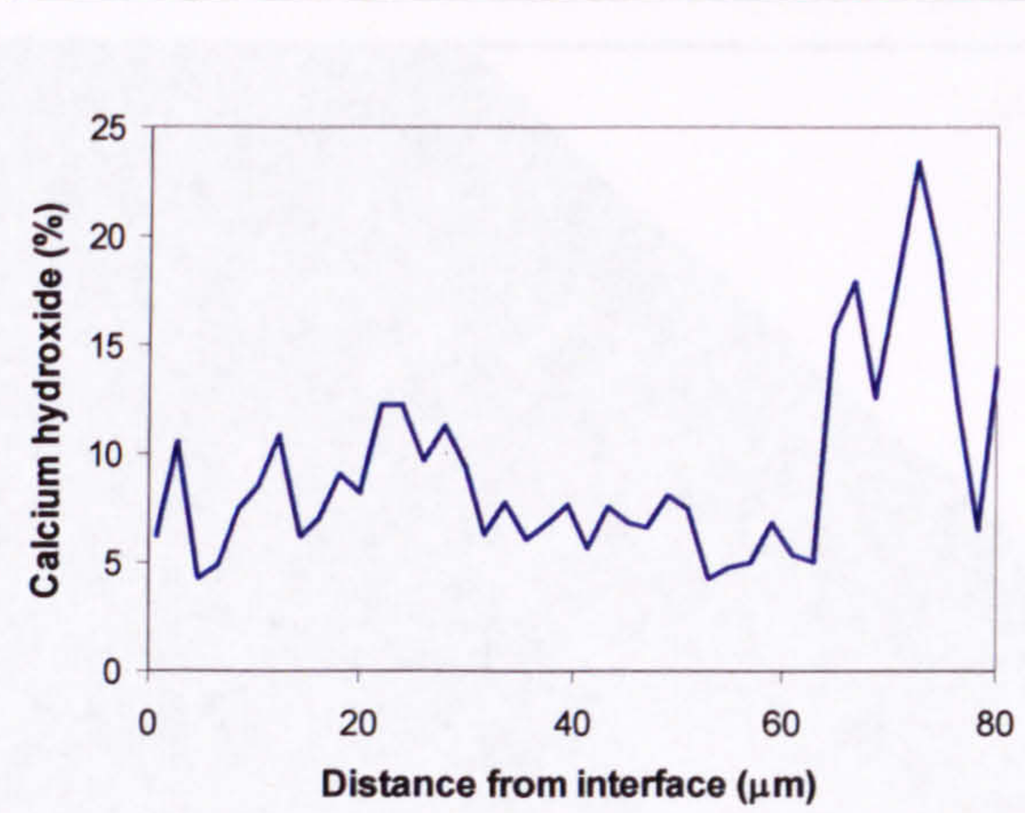

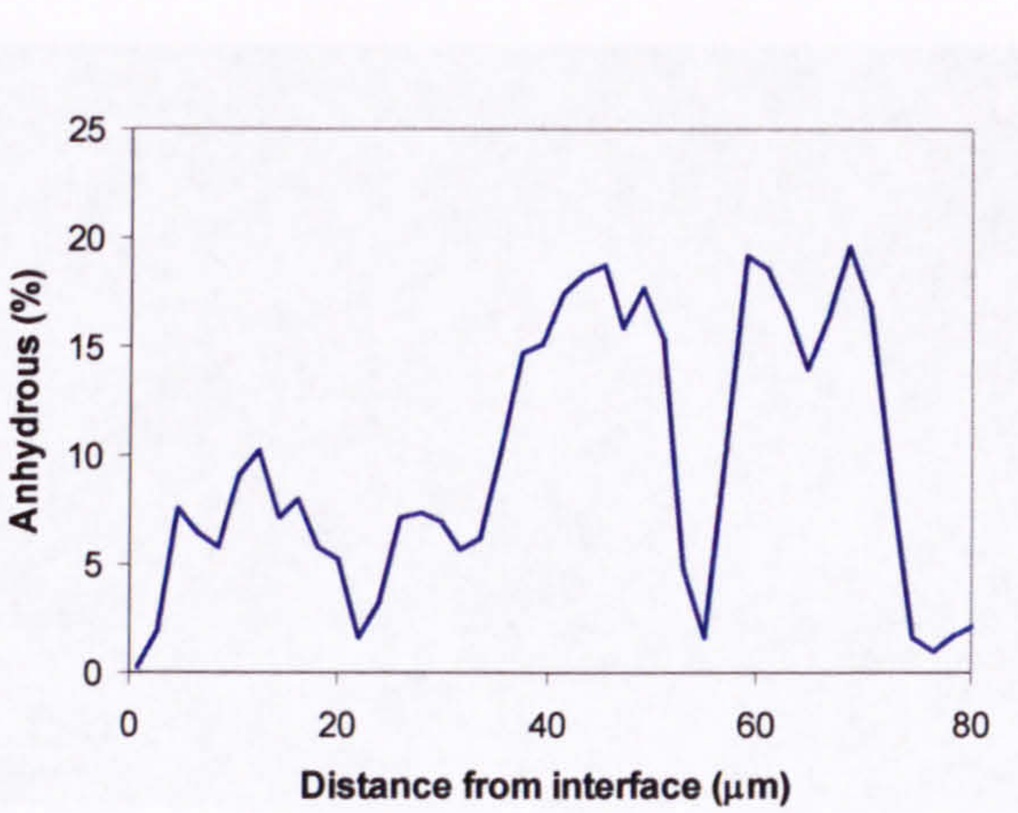

Figure 5.26 Application of the dilation-subtraction method on the 3-day old concrete containing quartz aggregate (W/C = 0.53). The microstructural gradient was measured from the coarse aggregate interface to the mid-distance between coarse and fine aggregate particles. Measurement was done at 4 strip widths (1.94 microns).

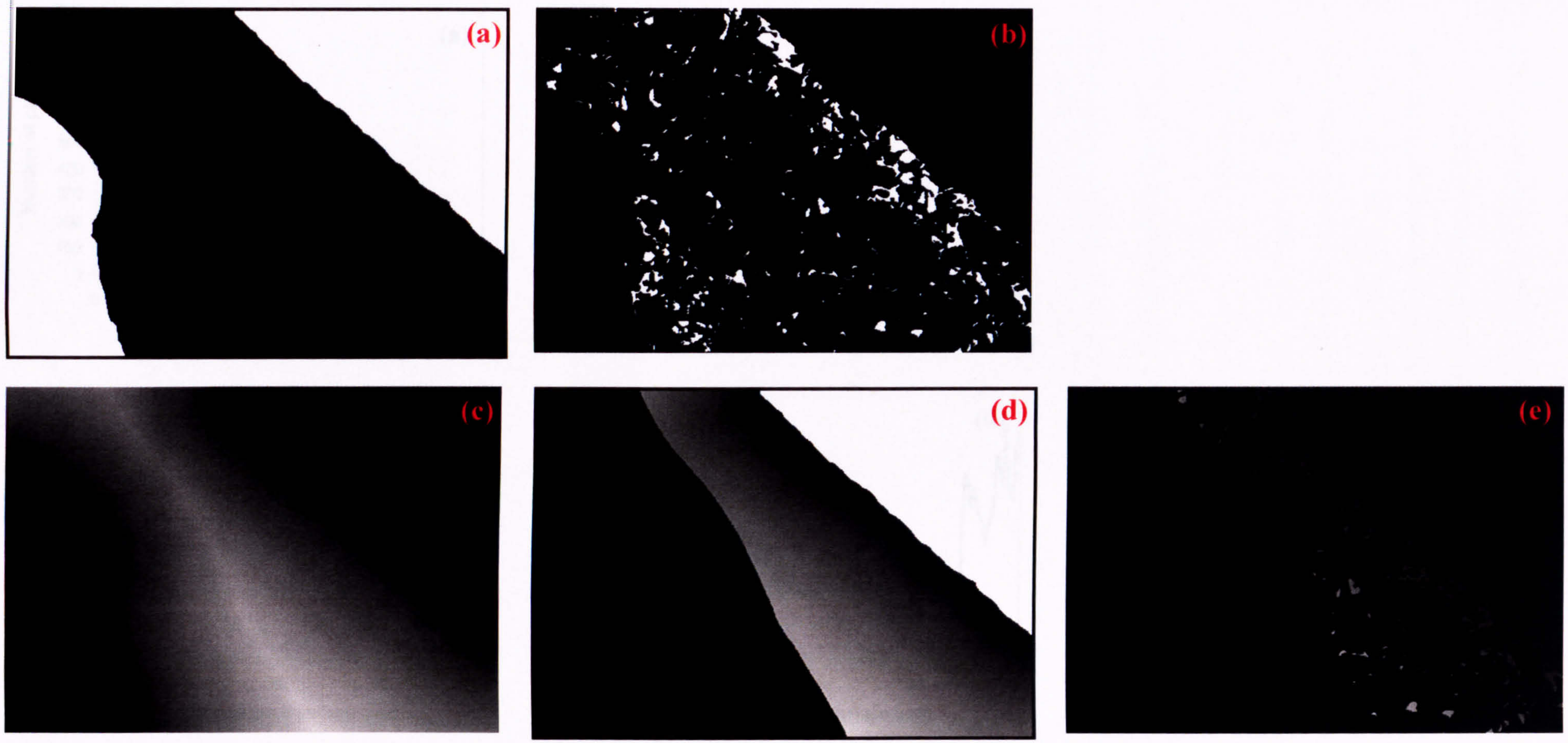

Figure 5.27 Application of the EDM technique on the BSE image presented on Figure 5.26. (a) Aggregate binary image, (b) Pore binary image, (c) Applying EDM on image (a), (d) EDM image of the region measured from coarse aggregate interface to the mid-way between coarse and fine aggregate particles, (e) Porosity EDM image and only the investigated region was take into account.

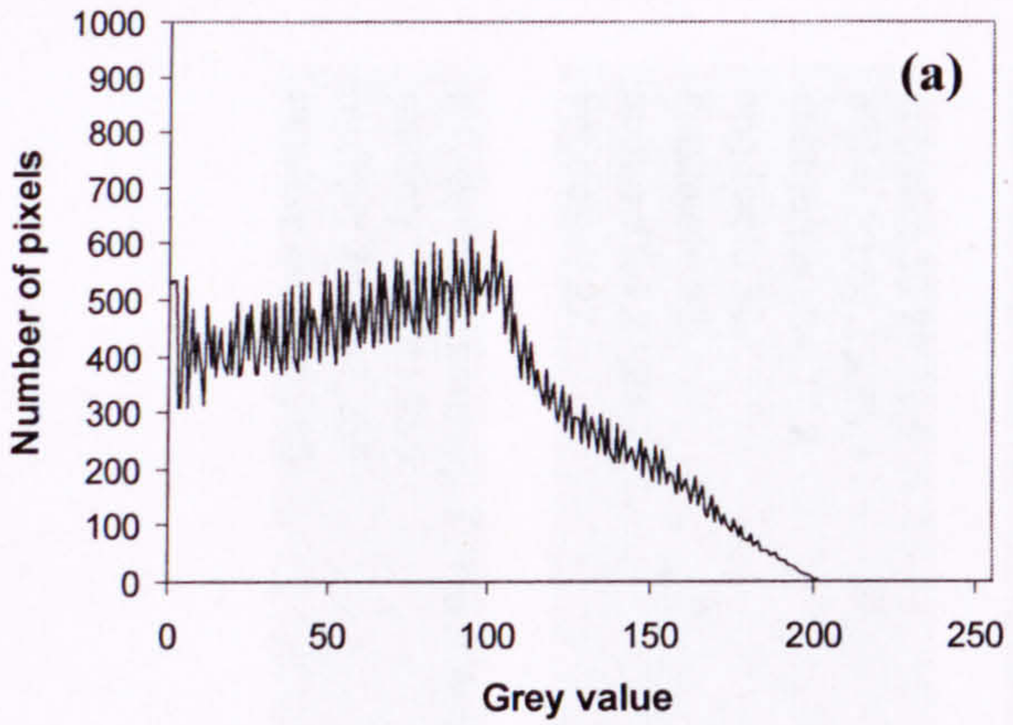

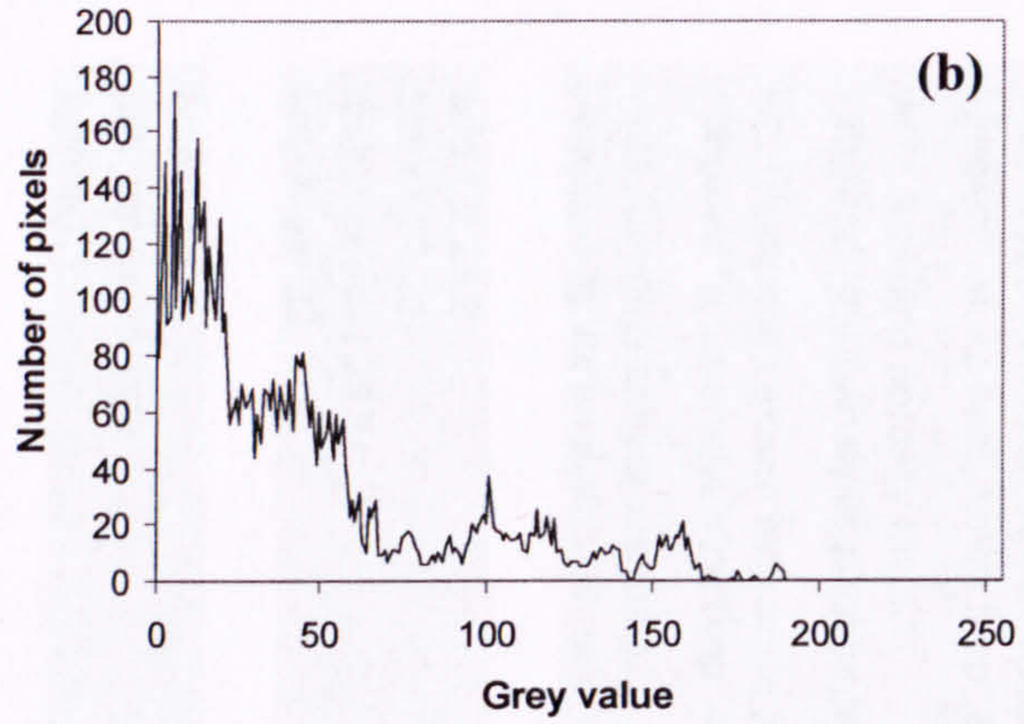

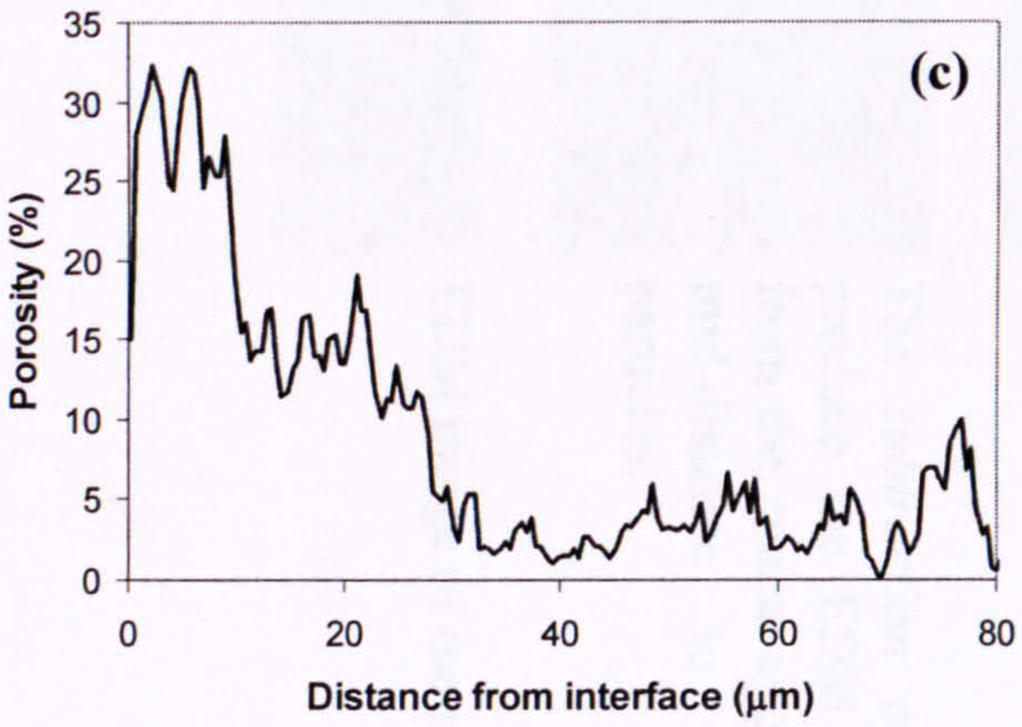

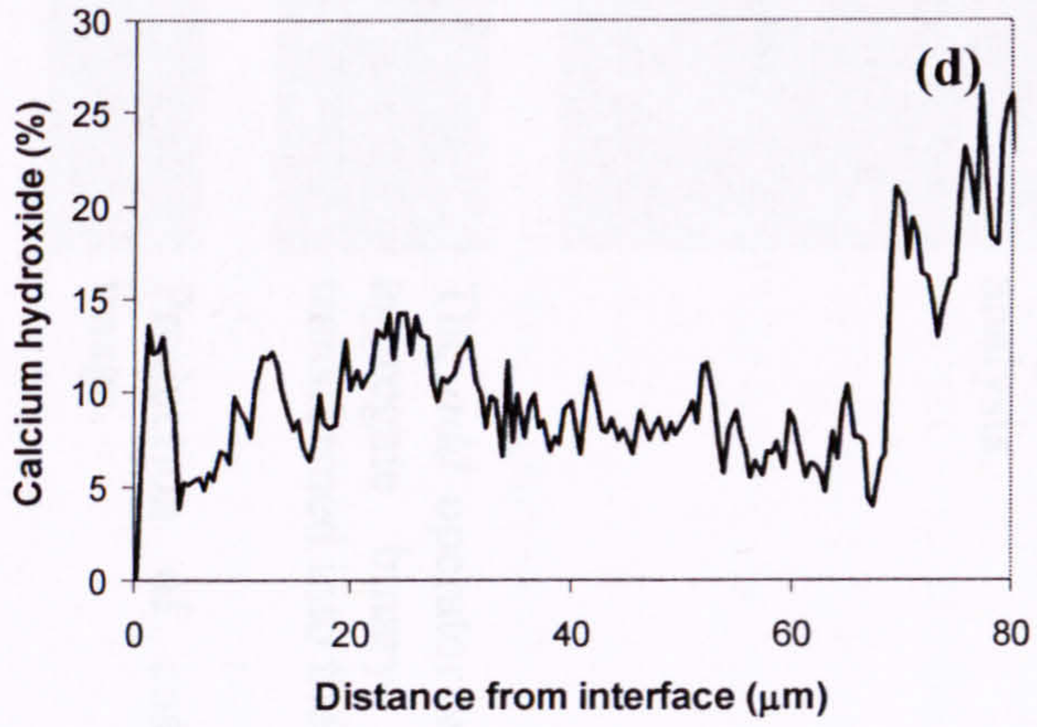

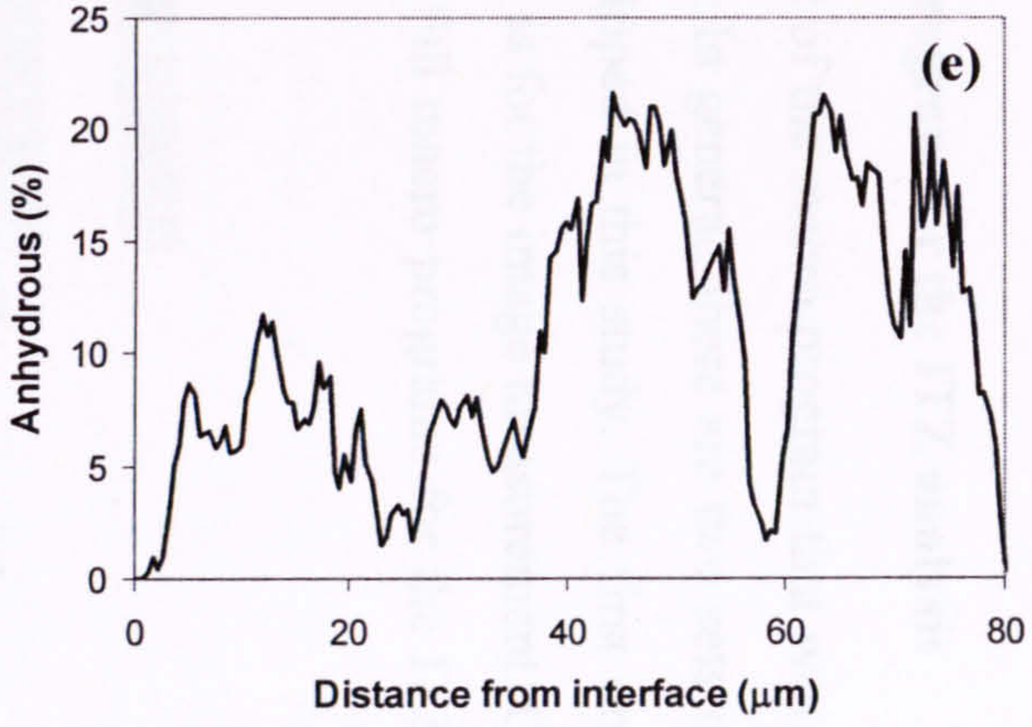

Figure 5.28 Application of EDM technique for quantitative analysis of phases at the interface between coarse aggregate and cement paste. (a) Grey level histogram of Figure 5.27(d). (b) Grey level histogram of Figure 5.27(e). (c) to (d) Porosity, calcium hydroxide and anhydrous distribution from the coarse aggregate interface (1 pixel or 0.48 microns strip width).

5.3.3.4 Example of the macro program for the ITZ analysis

This section presents part of the macro program that was used for cement paste and aggregate interface analysis. In general, there are two sets of macro programs for the ITZ analysis that were developed in this study. The first one is for the aggregate segmentation and the second one is for the image measurement. Only part of the second one will be presented here. The full macro programs for the ITZ analysis are given in Appendix B.

```
# Euclidean mapping analysis
```

```
write "Loading coarse aggregate mask"
! imgload "g:\itz analysis\cm.bmp",1

write "Loading fine aggregate mask"
! imgload "g:\itz analysis\fm.bmp",2

write "Loading porosity mask"
! imgload "g:\itz analysis\pore.bmp",3

write "Loading calcium hydroxide (CH) mask"
! imgload "g:\itz analysis\ch.bmp",4

write "Loading anhydrous mask"
! imgload "g:\itz analysis\anh.bmp",5
```

This part of the macro is to load the binary image needed for the Euclidean mapping analysis.

```
add 1,2,23,2
binnot 23,23
distmapeuclid 23,24
imgdelete 23
```

The *add* operator was used to create the aggregate binary mask; it was then transformed into the grey scale image.

```
binnot 1,1
distmapeuclid 1,29
binnot 1,1
```

Production of coarse aggregate EDM image.

```
binnot 2,2
distmapeuclid 2,30
```

Production of fine aggregate EDM image.

```
subtract 30,29,33,2
dislev 33,34,1,255,1
subtract 30,34,27,2
imgdelete 30
imgdelete 33
subtract 24,27,24,2
imgdelete 27
```

The *subtraction* operator was used to produce the EDM image at the region from the coarse aggregate interface to the mid-distance to the next aggregate particles.

```
# Creating of porosity, CH and Anh EDM image
multiply 24,3,41,255
multiply 24,4,42,255
multiply 24,5,43,255
```

EDM image of the interested features.

5.4 Summary

This chapter gives a brief overview of the basic background of the electron microscopy which is very important for the interpretation of any results obtained from this technique. In addition, the operational settings for the scanning electron microscope (SEM) and the image analysis procedure that were used through out this study were given.

The technique which was based on fitting the porosity peak in the grey level histogram of the synthetic aggregate by the Gaussian function has been presented (section 5.3.2.3). It was used for the porosity segmentation of the image analysis of the backscattered electron (BSE) images of the synthetic aggregate microstructure.

A technique for capturing the backscattered electron images simultaneously with the X-ray dot map images from the same region in order to accurately identify the aggregate boundary has been presented (section 5.3.3.1). This technique was successfully used to produce the accurate binary mask images of the quartz (or natural), Lytag lightweight and synthetic aggregate.

A technique used to segment pores from the backscattered electron image of the cement-based materials is presented in section 5.3.3.2.2. This technique was found to provide a more reasonable and more accurate porosity binary mask compared to the one obtained by the existing method. This technique also gave reproducible and reliable results that make it possible to do a comparative study between concrete made with different types of coarse aggregate.

The Euclidean distance mapping technique (section 5.3.3.3) that was first used by Wong and Buenfeld (2006) for the ITZ analysis was modified and the special macro program that utilizes this technique in order to compute the microstructural gradients at the interfaces between coarse aggregate and cement paste matrix was developed and successfully used in this research.

Chapter 6

Effect of firing conditions on the properties and microstructure of the synthetic aggregate

6.1 Introduction

This chapter is separated into two main parts. The first part presents the experimental results and the discussion in relation to the effect of firing condition on the macro properties of the synthetic aggregate. The microstructure and the phase transformation of the synthetic aggregate which experienced different firing regime were investigated using a number of techniques and the results and discussion are given in the second part of this chapter.

6.2 Engineering properties of the synthetic aggregate

In this section, the effect of firing condition on the water absorption and relative density of the synthetic aggregate is investigated. Due to the variable nature of the material in question it was important to try and establish at the outset the magnitude of this variability. This would enable an estimate to be made of the minimum sample size required to give a representative result.

6.2.1 Variability of the test results

There are two types of variation considered in this section including the in-batch and between batch variations. The in-batch variation is the variation that occurs between each particle of the synthetic aggregate. It might be due to the temperature variation inside the kiln or come from the variation of the material itself. One firing condition was selected in order to study the variability of the sintered product properties, i.e. sintering temperature at 1120°C with ramp rate of 20°C/minute and a sintering time of 180 seconds. The temperature control of the kiln for this firing condition is shown in Figure 6.1. The green pellets were prepared with 95% of Glensanda quarry waste and 5% of ball clay by weight. The synthetic aggregate sample after firing with a chosen condition was taken out of the rotary kiln and cooled down to the room temperature. Then 40 pellets were randomly collected from this batch in which 20 of them were taken from the inner part of the kiln and the remaining were from the front part location (see Figure

3.9) for checking the in-batch variation of the test results. The between batch variation was also checked by using the results from 10 different batches of the same mix and firing condition.

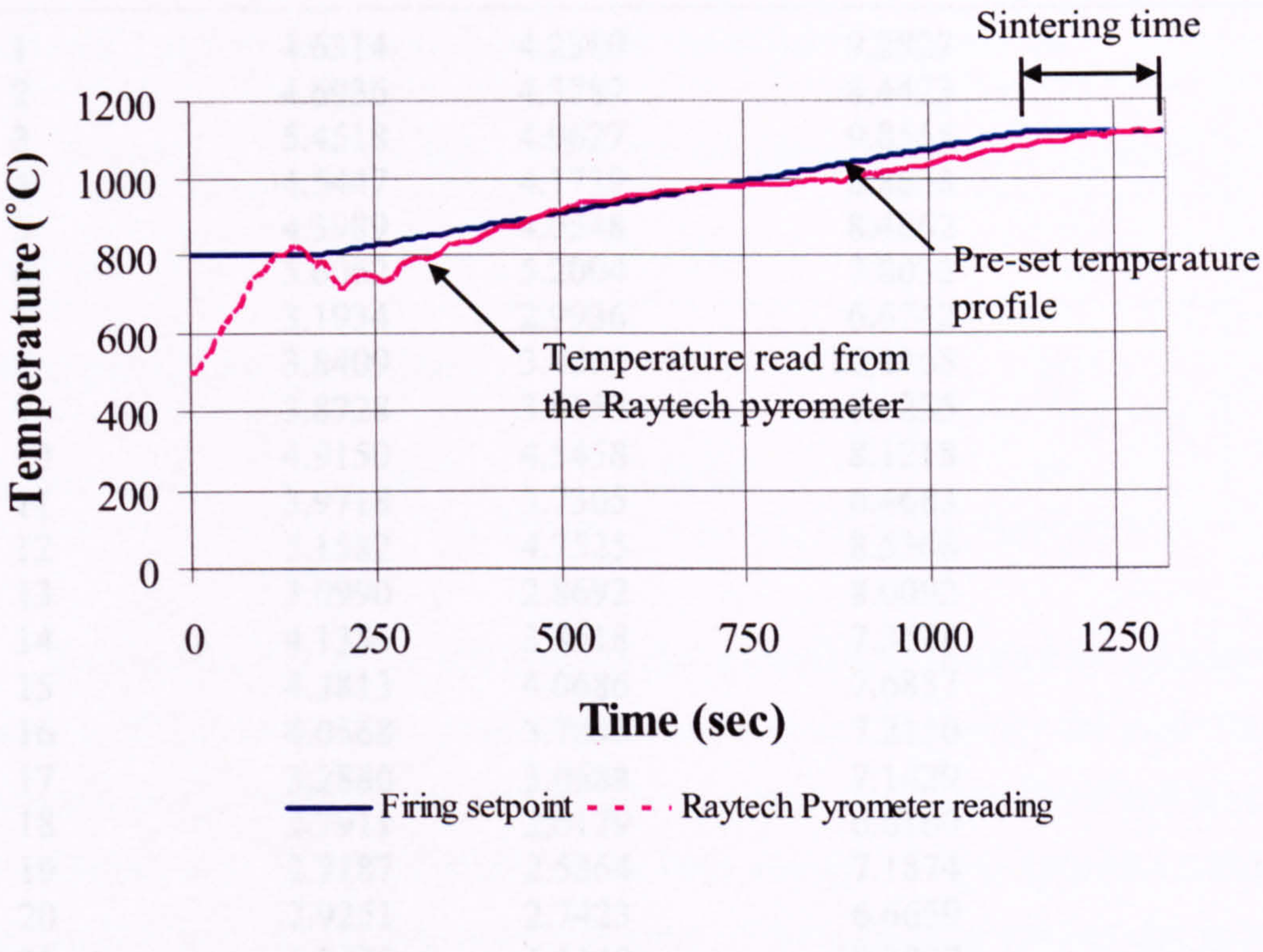

Figure 6.1 Temperature control of kiln with sintering temperature of 1120ºC and ramp rate of 20ºC/minutes with 3 minutes sintering time.

The property that was considered for the in-batch variation test was the water absorption of each synthetic aggregate particle and the experimental results and their statistical analysis are given in Table 6.1 and 6.2 respectively. Based on the statistical analysis of the results and the color variation of the fired pellets as visually observed by the operator it was concluded that the in-batch variation of the fired pellets collected from the front part of the kiln was slightly greater than that of the pellets taken from the inner part.

Table 6.1 Water absorption test results for in-batch variation test

Firing Condition: 20°C/min, 1120°C, 180 sec.			
Aggregate	Mass (g)		Water Absorption
No.	A	D	(% dry mass)
1	4.6314	4.2380	9.2827
2	4.6936	4.3282	8.4423
3	5.4518	4.9627	9.8555
4	4.5447	4.1739	8.8838
5	4.3989	4.0548	8.4862
6	5.6062	5.2004	7.8032
7	3.1934	2.9936	6.6742
8	3.8409	3.4660	10.8165
9	3.8728	3.6152	7.1255
10	4.9150	4.5458	8.1218
11	3.9718	3.7305	6.4683
12	5.1582	4.7525	8.5366
13	3.0990	2.8692	8.0092
14	4.1354	3.8518	7.3628
15	4.3813	4.0686	7.6857
16	4.0568	3.7838	7.2150
17	3.2880	3.0688	7.1429
18	2.7911	2.6179	6.6160
19	2.7187	2.5364	7.1874
20	2.9251	2.7423	6.6659
21	6.7488	6.1140	10.3827
22	4.9499	4.6220	7.0943
23	4.2984	3.9848	7.8699
24	4.1744	3.9073	6.8359
25	4.9959	4.6247	8.0265
26	5.0749	4.7262	7.3780
27	6.3348	5.8556	8.1836
28	5.4301	5.0107	8.3701
29	6.9344	6.4234	7.9553
30	4.9375	4.5666	8.1220
31	5.5719	5.0364	10.6326
32	4.7710	4.4305	7.6854
33	4.1495	3.7289	11.2795
34	4.4585	4.1450	7.5633
35	4.3738	4.0320	8.4772
36	3.6058	3.2310	11.6001
37	4.5237	4.2153	7.3162
38	3.2894	2.9730	10.6424
39	3.8079	3.5234	8.0746
40	5.4356	4.9581	9.6307

Note: No. 1-20 collected from the inner part of kiln and 21-40 collected from the front part of kiln

See section 4.4 for the definition of mass *A* and *D*.

In order to assess the differences in the pore structure, 10 pellets were randomly taken from the same batch and tested using mercury intrusion porosimetry (MIP). The detail for this test is given in section 6.5.

Table 6.2 The statistical analysis results for the in-batch variation test

Samples	Mean (μ)	Standard deviation	Number of pellet
Inner part of kiln	7.9191	1.1590	20
Front part of kiln	8.6560	1.4711	20
Whole batch	8.2875	1.3594	40

The repeatability of the pellet production process was checked by considering the variation of the results from 10 different batches having nominally the same firing condition and mix proportions, i.e. 95% of granite quarry waste and 5% of ball clay. It is acknowledged that 10 batches might not be large enough to do a rigorous statistical analysis but it should be able to give an indication of the number of batches that should be used to obtain a reasonable estimation of the water absorption and the relative density of the synthetic aggregate. The firing condition used for the between batch variation test was sintering temperature of 1120°C with a 3 minutes sintering time and ramp rate of 20°C/minute. Two examples of the temperature control curves of the kiln from these 10 batches are shown in Figure 6.2 and 6.3 and the remaining curves are given in Appendix A.

Table 6.3 presents the relative density and the water absorption test results of the 10 batches and their statistical analysis results are given in Table 6.4. The statistics clearly indicate that the water absorption test results have more variation than the relative density as shown by a larger standard deviation. These results suggest that the number of batches required for averaging the water absorption is much larger than for relative density.

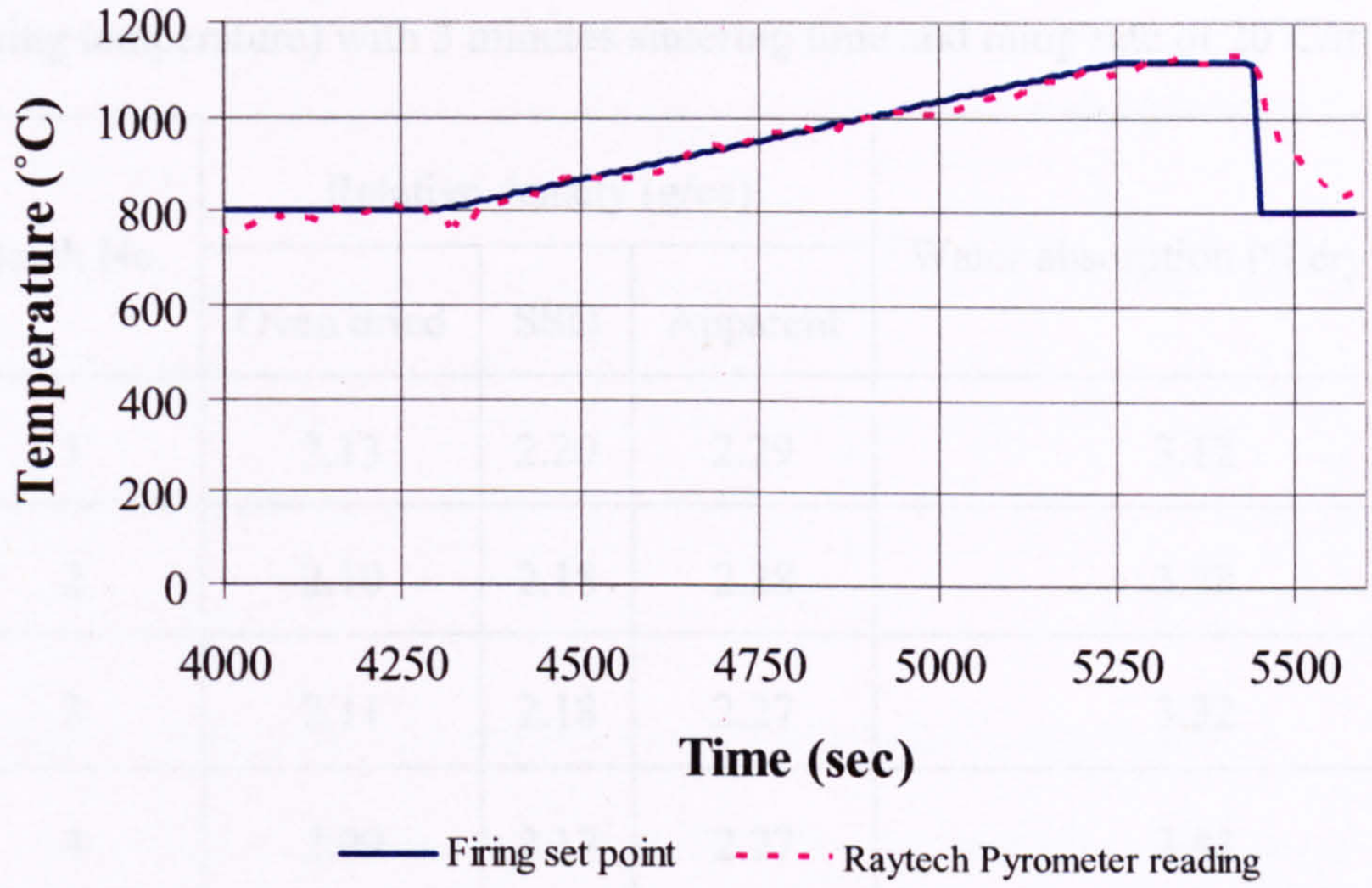

Figure 6.2 Temperature control of kiln for batch number 2.

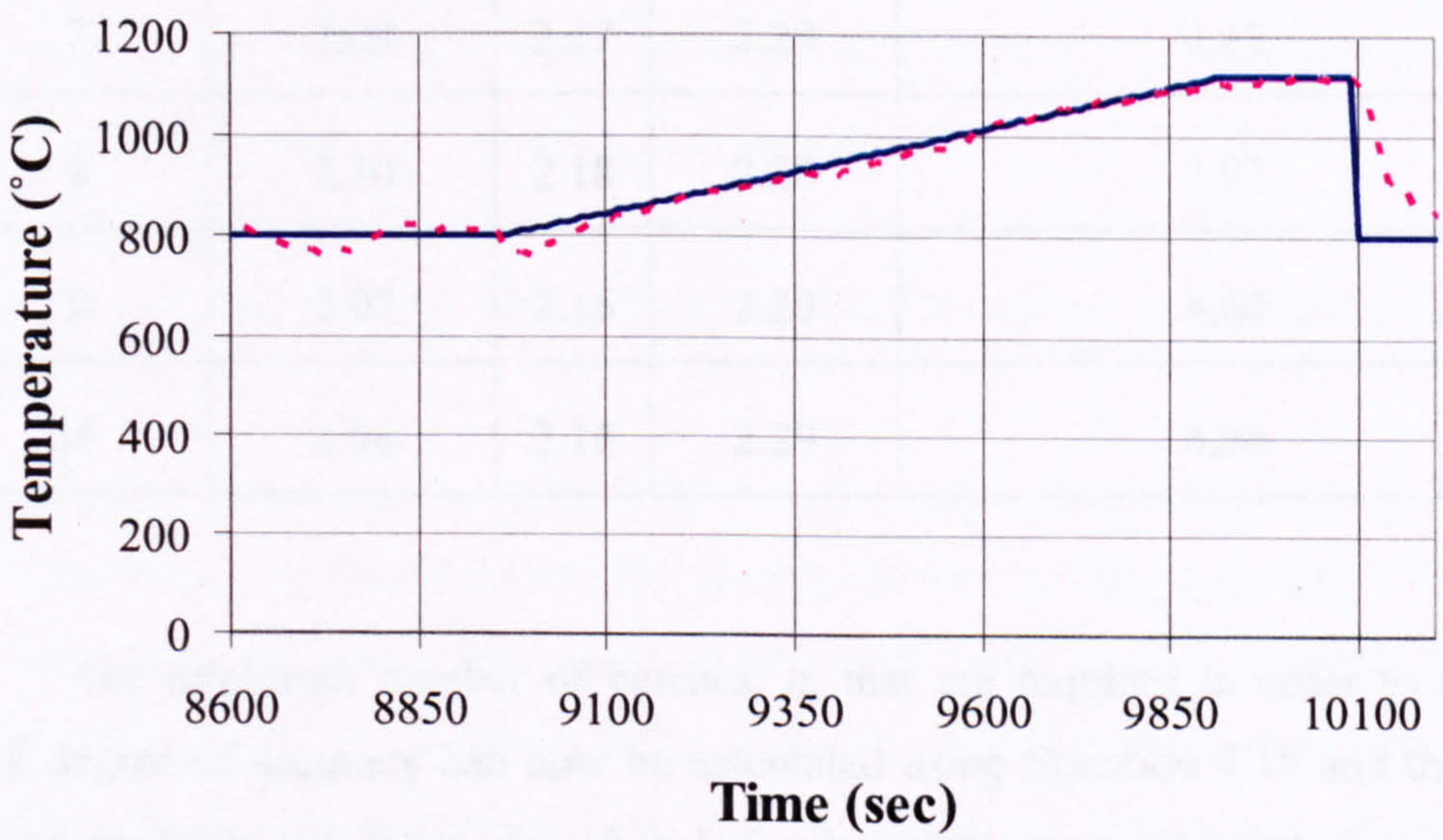

Figure 6.3 Temperature control of kiln for batch number 7.

Table 6.3 Physical properties of different batches of synthetic aggregate fired at 1120°C (sintering temperature) with 3 minutes sintering time and ramp rate of 20°C/minute.

Batch No.	Relative density (g/cc)			Water absorption (% dry mass)
	Oven dried	SSD	Apparent	
1	2.13	2.20	2.29	3.12
2	2.10	2.18	2.28	3.78
3	2.11	2.18	2.27	3.32
4	2.09	2.17	2.27	3.83
5	2.09	2.18	2.30	4.34
6	2.08	2.17	2.30	4.67
7	2.09	2.17	2.29	4.17
8	2.10	2.18	2.28	3.93
9	2.07	2.16	2.29	4.69
10	2.06	2.16	2.29	4.96

The minimum number of batches, *n*, that are required in order to ensure a desired degree of accuracy can now be calculated using Equation 4.18 and the results are given in Table 6.4. It was found that, for the water absorption test, the number of batches required to be tested to achieve a 95% degree of confidence for the results to be within 10, 15 and 20 % of the true value were found to be 9, 4 and 2 batches respectively. Only one batch is required for all permissible errors in the case of the relative density test. The average value from 3 batches was chosen in this study and thus the expected permissible error is slightly greater than 15%.

Table 6.4 The statistical analysis results for the between batch variations test

Parameter	Mean (μ)	Standard deviation	Number of batches required		
			E = 10 %	E = 15 %	E = 20 %
Water absorption	4.08	0.60	9	4	2
Relative density (SSD)	2.18	0.01	1	1	1

6.2.2 Water absorption and relative density of synthetic aggregate

The effect of the two main manufacturing parameters, which are the sintering temperature and the sintering time, on the water absorption and relative density of the synthetic aggregate were investigated in this section. The sintering temperature ranged from 1,110˚ to 1,130˚C, while the sintering time varied from 0 to 20 minutes. It is very important to note that these temperatures are the *pre-set* temperatures which were set by the control system of the kiln, while the actual temperature inside the kiln is normally different as can be seen, for example, in Figures 6.1 to 6.3 (see section 3.4.2.1 for more details about the temperature control system of the Trefoil kiln). The sintering time is defined as the length of time that pellets spend at the highest pre-set temperature (see Figure 6.1).

Figure 6.4 and 6.5 shows the influence of sintering temperature and the sintering time on the water absorption and relative density of the synthetic aggregate. The results show that when increasing the *pre-set* temperature from 1110˚ to 1130°C, the water absorption decreases. An increase in the sintering period causes a reduction of water absorption for all temperatures. For 1,110°C sintering temperature, there was a significant decrease in absorption for sintering periods of 0 to 10 minutes (range from 14.9 to 2.4%), after which there was only a slight reduction up to 20 minutes sintering time. A figure of 2.1% was recorded at 20 minutes sintering period which is about 15% lower than the value at 10 minutes.

The relationship between the sintering time and relative density (Figure 6.5) shows an opposite trend to that of absorption with an increase in sintering period

resulting in an increase in the relative density. The higher the *pre-set* sintering temperature used the higher the rate of increase of the relative density. A reduction of water absorption and increase in density is a basic densification behavior of a common ceramic material. However there was a slight reduction in the relative density for 1,110°C and 1,120°C from 10 to 20 minutes and 3 to 3.5 minutes respectively. This might indicate the occurrence of bloating which will be confirmed later by the SEM and MIP techniques. Moreover, the rapid rate of decrease of the water absorption and, at the same time, increase in relative density when increasing the sintering temperature suggests that the development of the liquid phase for the high temperature firing was faster than the low temperature firing.

The results show that similar values of water absorption and relative density were achieved by reducing the sintering time from 20 to 3.5 minutes and increasing the *pre-set* sintering temperature from 1,110° to 1,120°C. However, bear in mind that the synthetic aggregates produced from these two firing conditions have a different firing experience. For the higher set point of 1,120°C, the actual maximum temperature recorded by the pyrometer was 1,147°C and the time that the pellets experienced a temperature higher than 1,130°C was approximately 2.2 minutes. The average temperature at the sintering period recorded by the pyrometer was 1,134°C. At this high level of sintering temperature with a very short period of time the degree of densification of the outer part of the pellets may be much different to the inner core. A different microstructure may occur at the lower *pre-set* sintering temperature, i.e. 1,110°C, with a much longer period of time. In this case, the maximum temperature was 1,145°C which is similar to the case of 1,120°C *pre-set* temperature. However, the average temperature at the sintering period was 1,113°C. These results suggest that the feldspar mineral melted within a narrow range of temperature (about 1,113° to 1,134°C) and it will discussed in more details in section 6.3.

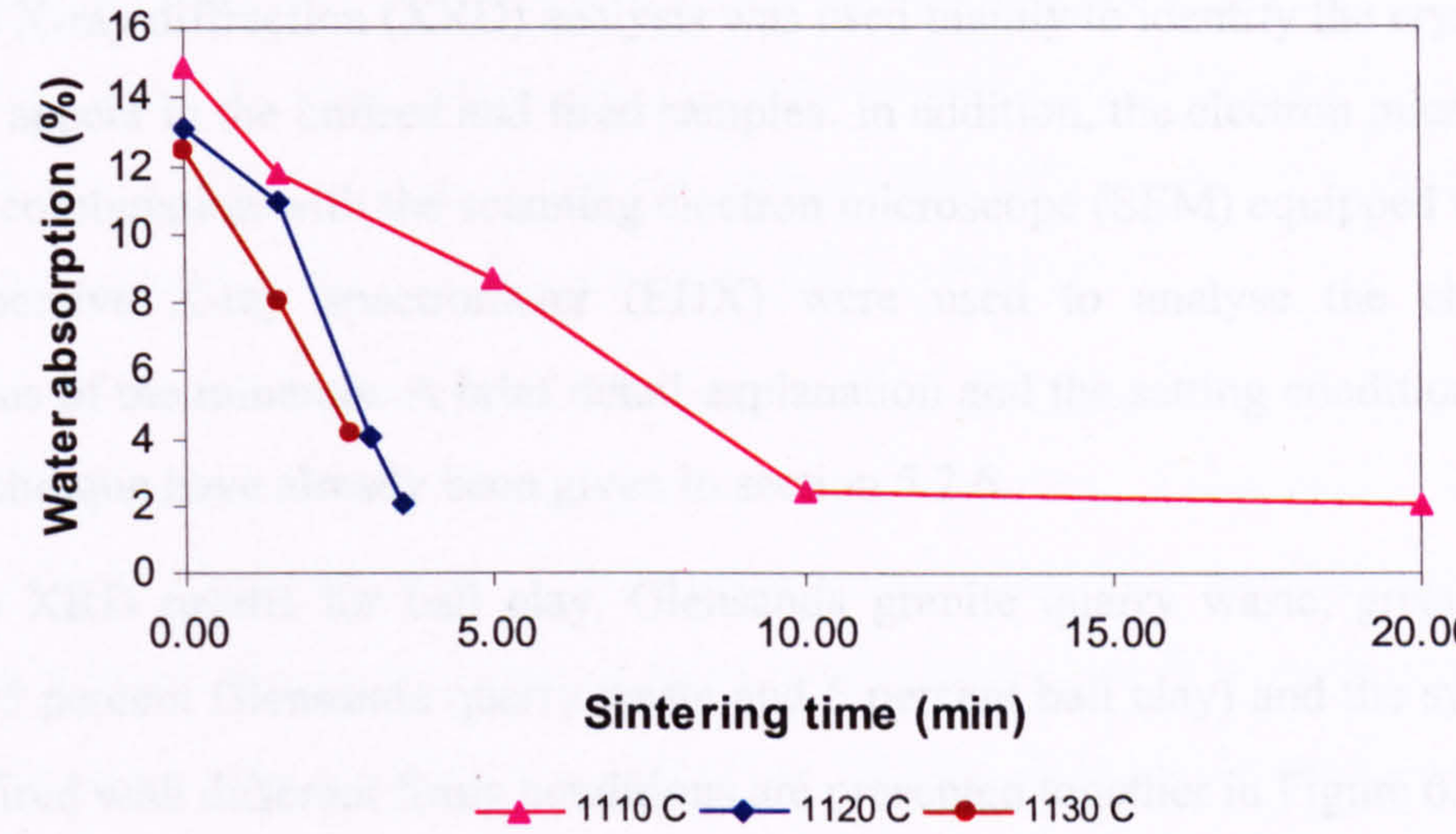

Figure 6.4 Influence of firing condition on the 24-hour water absorption of synthetic aggregate.

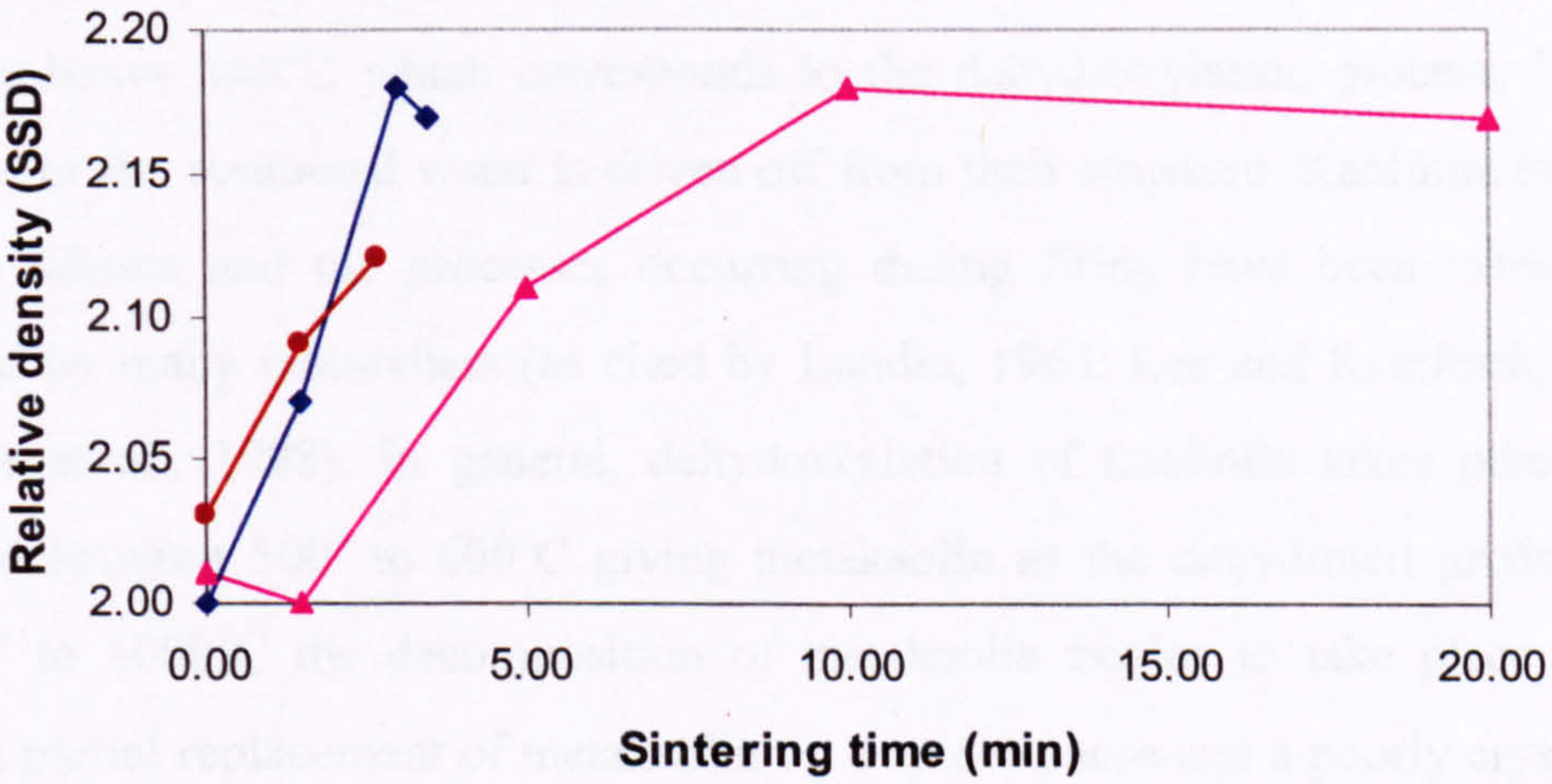

Figure 6.5 Influence of firing condition on the relative density of synthetic aggregate.

6.3 Mineralogy analysis by powder X-ray diffraction

The X-ray diffraction (XRD) analysis was used mainly to identify the crystalline phases that appear in the unfired and fired samples. In addition, the electron microprobe analysis in combination with the scanning electron microscope (SEM) equipped with an energy-dispersive X-ray spectrometer (EDX) were used to analyse the chemical compositions of the minerals. A brief detail explanation and the setting conditions used for each technique have already been given in section 5.2.6.

The XRD results for ball clay, Glensanda granite quarry waste, green pellet (made of 95 percent Glensanda quarry waste and 5 percent ball clay) and the synthetic aggregate fired with different firing conditions are presented together in Figure 6.6.

One of the main differences between the two raw materials (i.e. clay and Glensanda quarry waste) is that the granite quarry waste contains a lot of feldspar while it is absent in ball clay. The raw clay material contains kaolinite, mica and quartz and there is mica, chlorite, calcite, feldspars and quartz in the granite quarry waste. The composition of the green pellet is, therefore, a combination of the minerals from these two raw materials. The kaolinite and chlorite peaks clearly disappear at some temperature below 900°C which corresponds to the dehydroxylation process, i.e. the OH^- groups or the combined water is driven off from their structure. Kaolinite is a two layer (1:1) silicate and the processes occurring during firing have been extensively investigated by many researchers (as cited by Lundin, 1964; Lee and Rainforth, 1994; McConville et al., 1998). In general, dehydroxylation of kaolinite takes place at a temperature between 500° to 600°C giving metakaolin as the dehydrated product. At about 900° to 1000°C the decomposition of metakaolin begins to take place which results in a partial replacement of metakaolin by a spinel phase and a poorly crystalline mullite also begins to form. However, a defect spinel type phase and mullite were not detected in this study. It should be noted that for any phase with a very low concentration (less than 5%), the XRD technique is not a very accurate technique (Rodriguez Navarro et al., 2003). Therefore, any phases with a very low concentration may not be detected by this technique.

As shown in Figure 6.6, the decomposition of the calcite takes place at a temperature lower than 900°C. This is due to the decomposition of calcite ($CaCO_3$) by transformation into calcium oxide (CaO). The decomposition of calcite has been shown by other works to begin at temperatures higher than 700°C and it disappears at temperatures higher than 800°C (Cultrone et al., 2001 and 2004).

There are two different types of mica present in the green pellet, i.e. muscovite [ideally $KAl_3Si_3O_{10}(OH)_2$] and biotite [approximate chemical formula $K(Mg,Fe)_3AlSi_3O_{10}(F,OH)_2$]. Both of these minerals are commonly found in the granite rock. It should be noted here that mica is a collective name given to a group of hydrous alumino-silicates of iron, magnesium, potassium etc and they are characterized by a perfect cleavage enabling them to be split into thin sheets (Crockett, 1975). Their XRD peaks, as shown in Figure 6.6, clearly disappear at 1110°C which indicates that the transformation of mica happens between 900° to 1110°C. The dehydroxylation is believed to be the reason for the disappearance of the mica peak. The dehydroxylation or the changing of mica upon heating has been studied by many authors (Roy, 1949; Sundius and Byström, 1953; Sanz et al., 1983; Vassányi and Szabó, 1993; Mazzucato et al., 1999; Barlow and Manning, 1999; Rodriguez-Navarro et al., 2003). It was reported that the transformation of muscovite due to the dehydroxylation process begins at a temperature greater than 350°C (Vassányi and Szabó, 1993). This process was found to continue and still not be completed at 950°C (Barlow and Manning, 1999; Rodriguez-Navarro et al., 2003). Muscovite was found to decompose into one or a series of the following phases: quartz, mullite, γ- and α-alumina, spinel, leucite, sillimanite, K-feldspar (Roy, 1949; Sundius and Byström, 1953; Barlow and Manning, 1999; Rodriguez-Navarro et al., 2003). Biotite which is generally refered to as *dark mica* is a sheet silicate structure that is primarily a solid-solution series between the iron rich mica (annite) and magnesium rich mica (phlogopite) (Giese and Oss, 2002). In addition to the dehydroxylation process, the oxidation of Fe makes the transformation of biotite due to temperature more complicated than muscovite (Sanz et al., 1983; Chon et al., 2003). As already mentioned, the XRD results indicate the transformation of biotite occurs at some temperature between 900° to 1110°C. According to Roy (1949), the biotite lost its structure at about 1100°C which resulted in a high-Fe magnetic spinel, leucite and

probably mullite. However, phases resulting from the decomposition of muscovite and biotite at high temperatures, as were mentioned by other researchers, were not found by the author in this study. The reason for this might be kinetic constraints due to rapid heating and a short duration at the highest temperature.

Quartz and feldspar are found to be the major mineral component within the green pellet as can clearly be seen in Figures 6.6 to 6.12. Feldspar is a name that applies to a group of minerals which have a general chemical formula of $XAl_{(1-2)}Si_{(3-2)}O_8$, where X in this formula can be sodium and/or potassium and/or calcium. The compositions of the major elements in common feldspar can be represented in terms of the three end members, i.e. orthoclase ($KAlSi_3O_8$), albite ($NaAlSi_3O_8$) and anorthite ($CaAl_2Si_2O_8$) (Giese and Oss, 2002). Based on the electron microprobe analysis that will be mentioned in the next section, there are two types of feldspar present in the synthetic aggregate including the alkali feldspar and the plagioclase feldspar. The alkali feldspar is a solid solution between orthoclase and albite while plagioclase feldspar, on the other hand, is the solid solution of albite and anorthite. The XRD analysis results revealed that the feldspar peaks become difficult to clearly identify at a temperature of 1,110°C, indicating the melting of this phase. The melting of feldspar is also clearly observed on the SEM secondary electron image as shown in Figure 6.21.

Quartz (SiO_2) is one of the three main polymorphic forms of silica (quartz, tridymite and cristobalite) that occur in nature. Their crystal structures are made up of different arrangements of the SiO_4 tetrahedra (Sosman, 1965; Lee and Rainforth, 1994). There are two sub-forms of quartz which are low-temperature form quartz (α) and high-temperature form quartz (β). The transformation of α- to β-form of quartz occurs at 573.3°C. This transformation is a *displacive* type transformation, i.e. no atomic bonds are broken, only stretching of the bonds, and it occurs relatively fast, is reversible and complete. The transformation from quartz to tridymite and then to cristobalite occurs at a higher temperature and that is a reversible process with the rate of change exceedingly slow because the transformation involves a complex rearrangement within the crystal (*reconstructive* transformation) (Grimshaw, 1971). Therefore, with rapid heating and a very short period of time at the highest temperature, only the α to β quartz

transformation is expected to take place. Melting or dissolution of quartz is not observed in this investigation. This is because it has a very high melting point (Sosman, 1965). Quartz was found to be relatively insoluble and has a very low reactivity by the other components at temperature below 1,250°C (Ludin, 1964; Iqbal and Lee, 2000).

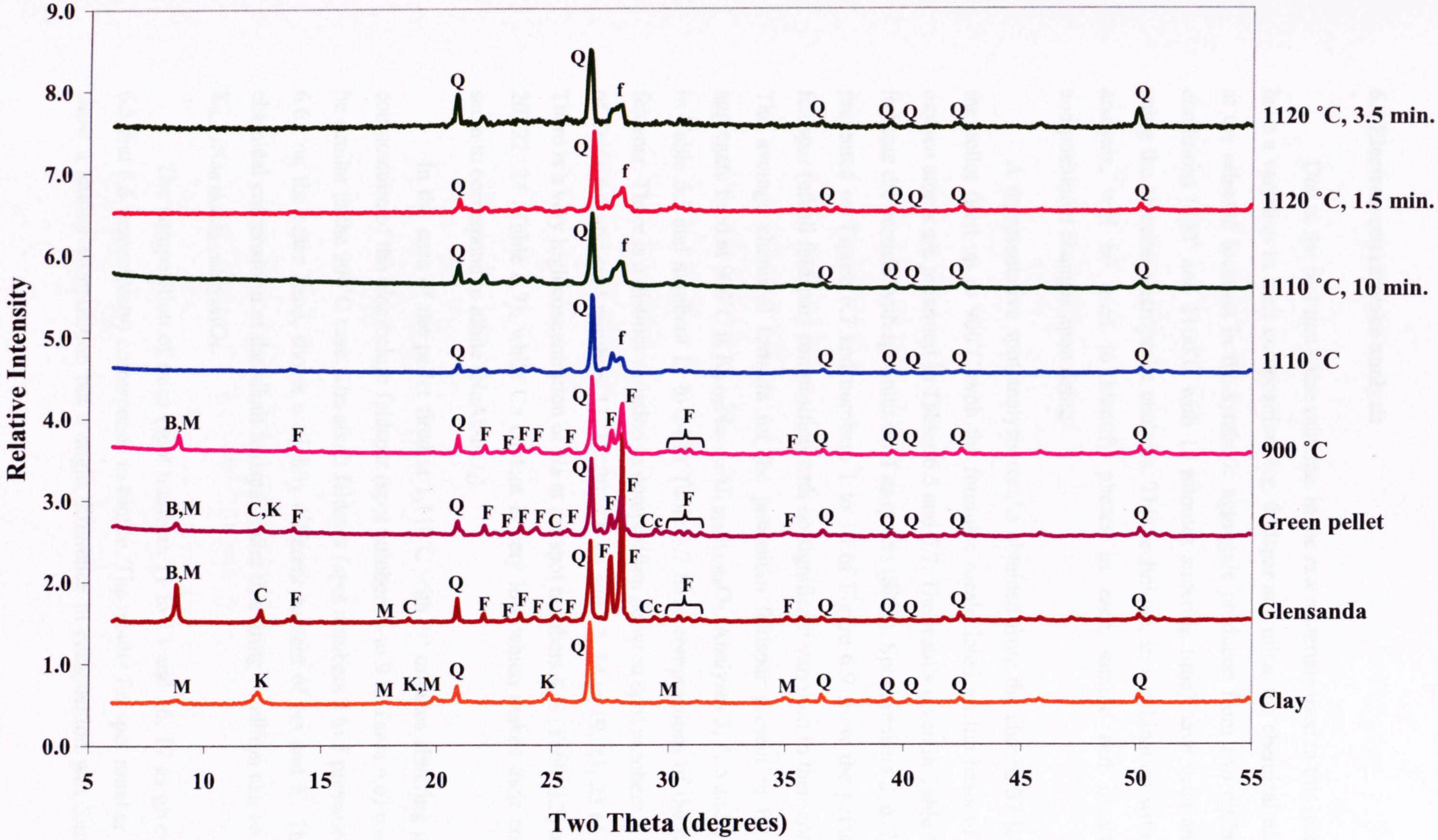

Figure 6.6 XRD patterns of the ball clay, glensanda granite quarry waste, green pellet and synthetic aggregate fired at different temperatures: B = Biotite; C = Chlorite; Cc = Calcite; F = Feldspar; f = broadening of feldspar peak; K = Kaolinite; M = Muscovite; Q = Quartz.

6.4 Electron microprobe analysis

Due to the fact that some minerals in the raw materials used in this research may have a variation in their composition, e.g. feldspar and mica, the chemical composition at the selected location in the synthetic aggregate produced from two different firing conditions (900° and 1100°C with 10 minutes sintering time) have been analysed by using the electron microprobe analysis. This technique, in combination with the XRD analysis, will be used to identify phases in each sample and investigate the compositional changes upon firing.

A representative spot analysis results obtained from the chosen 37 locations of the pellet fired up to 900°C with the formulae recalculated on the basis of 8 and 24 oxygen atoms are presented in Tables 6.5 and 6.7. The results given in Table 6.5 clearly indicate the particle with spot number 1 as quartz (SiO_2). Spot numbers 2, 6, 7, 9 and 10 presented on Figure 6.7 and numbers 1 to 10 of Figure 6.9 show the potassium rich feldspar (alkali feldspar) composition with no significant variation in their composition. The average chemical formula for the potassium feldspar present in the synthetic aggregate fired at 900°C is $K_{0.899}Na_{0.064}Al_{1.016}Si_{2.988}O_8$. Analyses 3, 4, 5 and 8 presented in Table 6.5 and numbers 11 to 24 in Table 6.7 have compositions of the plagioclase feldspar. There is a distinct variation in composition between spot numbers 3, 5 and 4, 8 of Table 6.5 and spot numbers 11, 13, 20, 22, 24 and 12, 14 to 19, 21, 23 of Table 6.7. There is a very high concentration of Na at the spot numbers 4, 8 (Table 6.5) and 11, 13, 20, 22, 24 (Table 6.7), while Ca content is very low which makes their composition seem to correspond to albite ($NaAlSi_3O_8$).

In the case of the pellet fired at 1,110°C with 10 minutes sintering period, the composition of the plagioclase feldspar (spot numbers 6 to 9 in Table 6.6) was found to be similar to the 900°C case. The alkali feldspar (spot numbers 2 to 5 presented in Table 6.6), on the other hand, shows a slightly different content of Na and K. The average chemical composition of the alkali feldspar under this firing condition can be written as $K_{0.608}Na_{0.369}Al_{1.006}Si_{2.991}O_8$.

The composition of mica (spot numbers 11 to 13 and 16, 17 as given in Table 6.5 and 6.6 respectively) corresponds to biotite. The results for spot number 11 and 13 show a similar composition but a slight difference in composition was found at spot

number 12. Some K of biotite at 1,110°C, 10 minutes sintering time is found to be replaced by Na. Moreover, a slight increase in Ca content and decrease in Si was detected when compared to the 900°C case.

The compositional variation of feldspar and mica at different firing conditions might be attributable to the effect of temperature. However, due to the fact that the raw materials used in this study are waste materials, the compositional variation of minerals within each batch due to the natural weathering process is expected to occur. In addition, the loss of alkali during analysis might happen and create, to some degree, the variation too. Therefore, it is very difficult to give a reason or explain the whole variation of the feldspar or mica composition in this study.

The results for the spot numbers 10 to 15 as given in Table 6.6 and spot numbers 4 to 23 of Table 6.8 were collected from the melt area. It is noted that these analytical data for the melt phase just give a general chemical composition of this phase collected from a different location within the sample. It is not possible to analyse phases that have a very fine-grained nature such as melt or phases that may form after the mica breakdown. Therefore, other techniques, e.g. transmission electron microscopy (TEM), need to be used in order to obtain the more accurate chemical composition of the melt. In general, the melts composition at 26 different locations is similar to the composition of feldspar which indicates that the pore spaces inside the synthetic aggregate were filled or densified by the feldspar melt. There is a slight variation in composition of the melts. For example, as shown in Figure 6.8, spot number 15 shows a much lower Ca content than the one at spot numbers 10 to 13. A relatively high content of Al in melts as compared to the feldspar might indicate very little or no mullite crystallization. This is because of the Al which is preferentially included in the newly formed mullite (Rodriguez-Navarro et al., 2003).

Figure 6.11 and 6.12 present BSE and X-ray dot map images of the synthetic aggregate fired at 900°C and 1,110°C with 10 minutes sintering period. As shown in Figure 6.11, the plagioclase feldspar and quartz clearly are the major component on this image. The particles which are rich in potassium are the alkali feldspar. On the BSE image, quartz appears slightly darker than the plagioclase feldspar and, sometimes, it is very difficult to differentiate between these minerals based only on the difference in

their grey level. Most of the feldspar and quartz particles are still not melting. When the synthetic aggregate was heated to 1,110°C with 10 minutes sintering time (Figure 6.12), it is clear that the space between each mineral particle was filled by the melting phase which, based on the mapping image, is obviously rich in silicon and aluminium. It is difficult to identify the feldspar particle by only using the X-ray mapping and this suggests that their composition is very similar to the composition of the glassy phase.

Table 6.5 Representative analytical electron microprobe analyses of the pellet fired to 900°C with 0 minute sintering period. Data were taken from the BSE image shown in Figure 6.7.

	SiO_2	Al_2O_3	Na_2O	K_2O	TiO_2	Fe_2O_3	MnO	MgO	CaO	Total
1	100.15	0.03	0.00	0.03	0.07	0.18	0.05	0.00	0.00	100.51
2	64.13	18.66	0.82	15.15	0.17	0.30	0.10	0.02	0.10	99.44
3	62.89	23.36	9.24	0.36	0.13	0.25	0.10	0.01	4.19	100.54
4	67.67	19.83	11.70	0.17	0.07	0.25	0.13	0.01	0.47	100.29
5	64.54	22.69	9.68	0.23	0.11	0.12	0.01	0.00	3.30	100.68
6	65.19	18.70	0.71	14.89	0.08	0.16	0.05	0.02	0.09	99.89
7	64.11	18.72	0.63	15.21	0.10	0.17	0.04	0.04	0.08	99.12
8	68.05	19.92	11.67	0.05	0.10	0.26	0.03	0.03	0.40	100.50
9	64.07	18.45	0.40	15.81	0.13	0.26	0.07	0.00	0.04	99.23
10	64.81	18.53	0.84	15.01	0.17	0.35	0.10	0.02	0.08	99.91
11	37.38	15.27	0.12	9.02	3.36	19.58	0.41	10.90	0.13	96.16
12	35.36	16.71	0.20	6.22	2.69	18.26	0.46	12.43	0.31	92.62
13	38.14	16.11	0.13	9.19	3.89	18.24	0.31	10.18	0.04	96.24
Formulae based on 8 oxygen atoms and 24 oxygen atoms (marked *)										
	Si	Al	Na	K	Ti	Fe^{3+}	Mn	Mg	Ca	Total
1	3.992	0.001	0.000	0.001	0.002	0.005	0.002	0.000	0.000	4.001
2	2.974	1.020	0.074	0.897	0.006	0.010	0.004	0.001	0.005	4.991
3	2.775	1.215	0.791	0.020	0.004	0.008	0.004	0.000	0.198	5.015
4	2.961	1.022	0.993	0.009	0.002	0.008	0.005	0.000	0.022	5.023
5	2.828	1.172	0.823	0.013	0.004	0.004	0.000	0.000	0.155	4.998
6	2.996	1.013	0.063	0.873	0.003	0.006	0.002	0.001	0.004	4.961
7	2.979	1.025	0.057	0.902	0.003	0.006	0.002	0.003	0.004	4.981
8	2.965	1.023	0.986	0.003	0.003	0.008	0.001	0.002	0.019	5.010
9	2.983	1.012	0.036	0.939	0.005	0.009	0.003	0.000	0.002	4.989
10	2.986	1.006	0.075	0.882	0.006	0.012	0.004	0.001	0.004	4.977
11*	6.154	2.963	0.038	1.893	0.416	2.696	0.057	2.675	0.023	16.915
12*	5.936	3.306	0.065	1.331	0.339	2.563	0.065	3.109	0.055	16.770
13*	6.213	3.093	0.040	1.909	0.477	2.484	0.043	2.471	0.008	16.738

Table 6.6 Representative analytical electron microprobe analyses of the pellet fired to 1,110°C with 10 minutes sintering period. Data were taken from the BSE image shown in Figure 6.8.

	SiO_2	Al_2O_3	Na_2O	K_2O	TiO_2	Fe_2O_3	MnO	MgO	CaO	Total
1	100.17	0.01	0.00	0.03	0.00	0.09	0.00	0.00	0.00	100.31
2	65.97	18.71	4.45	10.14	0.11	0.10	0.00	0.02	0.16	99.65
3	65.55	18.70	4.23	10.47	0.04	0.14	0.07	0.04	0.18	99.42
4	65.24	18.69	3.84	10.92	0.09	0.19	0.00	0.01	0.09	99.06
5	65.59	18.75	4.19	10.27	0.05	0.15	0.00	0.01	0.14	99.14
6	62.57	23.43	8.75	0.77	0.11	0.31	0.00	0.01	4.46	100.41
7	63.69	22.89	9.57	0.25	0.03	0.08	0.00	0.02	3.69	100.23
8	66.32	20.88	10.32	0.66	0.05	0.10	0.05	0.02	1.70	100.09
9	64.38	22.46	9.57	0.17	0.13	0.15	0.00	0.00	3.37	100.23
10	58.70	20.16	3.61	2.37	0.79	1.80	0.21	0.89	10.70	99.23
11	58.61	14.28	3.15	3.20	1.19	3.35	0.37	1.99	12.23	98.36
12	59.34	14.06	2.96	3.11	0.80	3.30	0.34	1.79	12.67	98.36
13	61.29	14.79	3.31	3.75	1.25	2.99	0.24	1.31	10.03	98.97
14	58.88	21.61	4.14	3.25	0.32	3.16	0.15	1.47	6.50	9.46
15	63.35	17.01	4.12	5.47	0.33	3.24	0.12	2.64	2.41	98.68
16	31.27	18.66	1.82	2.60	0.20	30.85	0.43	13.17	1.04	100.03
17	34.05	18.87	2.26	3.19	0.81	26.46	0.66	12.19	1.11	99.60
Formulae based on 8 oxygen atoms and 24 oxygen atoms (marked *)										
	Si	Al	Na	K	Ti	Fe^{3+}	Mn	Mg	Ca	Total
1	3.997	0.001	0.000	0.001	0.000	0.003	0.000	0.000	0.000	4.002
2	2.994	1.001	0.392	0.587	0.004	0.003	0.000	0.001	0.008	4.989
3	2.989	1.005	0.374	0.609	0.001	0.005	0.003	0.002	0.009	4.997
4	2.988	1.009	0.341	0.638	0.003	0.007	0.000	0.000	0.004	4.991
5	2.993	1.008	0.371	0.598	0.002	0.005	0.000	0.000	0.007	4.983
6	2.768	1.221	0.750	0.044	0.004	0.010	0.000	0.001	0.211	5.009
7	2.809	1.190	0.818	0.014	0.001	0.003	0.000	0.002	0.174	5.010
8	2.914	1.081	0.879	0.037	0.002	0.003	0.002	0.001	0.080	5.000
9	2.833	1.164	0.817	0.009	0.004	0.005	0.000	0.000	0.159	4.991
10	2.695	1.091	0.322	0.139	0.027	0.062	0.008	0.061	0.526	4.932
11	2.766	0.794	0.288	0.193	0.042	0.119	0.015	0.140	0.619	4.975
12	2.795	0.780	0.271	0.187	0.028	0.117	0.013	0.126	0.639	4.957
13	2.842	0.809	0.298	0.222	0.044	0.104	0.010	0.091	0.499	4.917
14	2.686	1.162	0.366	0.189	0.011	0.109	0.006	0.100	0.317	4.946
15	2.896	0.916	0.365	0.319	0.011	0.112	0.005	0.180	0.118	4.921
16*	4.836	3.401	0.545	0.513	0.023	3.590	0.057	3.037	0.172	16.174
17*	5.216	3.407	0.671	0.624	0.093	3.049	0.085	2.784	0.182	16.110

Table 6.7 Representative analytical electron microprobe analyses of the pellet fired to 900°C with 0 minute sintering period. Data were taken from the BSE image shown in Figure 6.9.

	SiO_2	Al_2O_3	Na_2O	K_2O	TiO_2	Fe_2O_3	MnO	MgO	CaO	Total
1	64.66	18.56	0.99	14.74	0.00	0.12	0.09	0.00	0.02	99.19
2	65.08	18.18	0.69	15.41	0.00	0.14	0.00	0.00	0.01	99.51
3	65.29	18.51	0.91	15.05	0.00	0.14	0.04	0.02	0.03	99.98
4	64.65	18.73	0.54	15.60	0.04	0.12	0.07	0.00	0.00	99.74
5	65.04	18.61	0.46	15.69	0.01	0.20	0.00	0.00	0.00	100.01
6	64.92	18.60	0.65	15.71	0.00	0.24	0.00	0.00	0.02	100.14
7	64.61	18.67	0.97	14.90	0.00	0.18	0.10	0.01	0.01	99.46
8	64.78	18.80	0.82	14.86	0.00	0.03	0.00	0.02	0.05	99.34
9	64.40	18.80	0.68	15.43	0.00	0.18	0.02	0.00	0.00	99.52
10	62.70	18.89	0.62	15.00	0.05	0.21	0.02	0.01	0.01	97.50
11	68.20	19.97	11.47	0.09	0.04	0.00	0.03	0.00	0.41	100.21
12	65.17	22.27	9.65	0.24	0.04	0.13	0.00	0.00	3.15	100.64
13	69.13	20.27	11.49	0.40	0.00	0.06	0.00	0.02	0.23	101.59
14	63.79	23.23	8.95	0.29	0.00	0.10	0.00	0.01	4.28	100.63
15	63.74	23.04	9.24	0.29	0.00	0.24	0.00	0.00	3.95	100.49
16	64.67	22.60	9.55	0.35	0.00	0.23	0.00	0.00	3.34	100.73
17	65.59	21.96	10.18	0.10	0.00	0.18	0.00	0.00	2.81	100.81
18	63.06	23.81	8.78	0.27	0.00	0.22	0.00	0.00	4.60	100.74
19	64.33	22.44	9.77	0.23	0.00	0.15	0.00	0.00	3.14	100.07
20	66.55	21.33	10.71	0.53	0.00	0.07	0.00	0.01	0.89	100.10
21	65.59	21.83	10.21	0.20	0.00	0.16	0.00	0.00	2.39	100.38
22	66.63	21.70	10.70	0.60	0.00	0.04	0.00	0.04	1.16	100.85
23	65.77	22.10	9.90	0.21	0.00	0.14	0.00	0.00	2.89	101.02
24	68.57	20.16	11.74	0.02	0.00	0.07	0.00	0.00	0.26	100.82
Formulae based on 8 oxygen atoms										
	Si	Al	Na	K	Ti	Fe^{3+}	Mn	Mg	Ca	Total
1	2.995	1.013	0.089	0.871	0.000	0.004	0.004	0.000	0.001	4.977
2	3.010	0.991	0.061	0.909	0.000	0.005	0.000	0.000	0.001	4.977
3	3.001	1.003	0.081	0.883	0.000	0.005	0.002	0.002	0.001	4.977
4	2.987	1.020	0.048	0.920	0.001	0.004	0.003	0.000	0.000	4.983
5	2.996	1.010	0.041	0.922	0.000	0.007	0.000	0.000	0.000	4.977
6	2.991	1.010	0.058	0.923	0.000	0.008	0.000	0.000	0.001	4.991
7	2.988	1.018	0.087	0.879	0.000	0.006	0.004	0.001	0.001	4.984
8	2.993	1.024	0.074	0.876	0.000	0.001	0.000	0.001	0.002	4.970
9	2.982	1.026	0.061	0.911	0.000	0.006	0.001	0.000	0.000	4.988
10	2.963	1.052	0.056	0.904	0.002	0.007	0.001	0.000	0.001	4.986
11	2.975	1.027	0.970	0.005	0.001	0.000	0.001	0.000	0.019	4.998
12	2.852	1.149	0.819	0.013	0.001	0.004	0.000	0.000	0.147	4.986
13	2.976	1.028	0.959	0.022	0.000	0.002	0.000	0.001	0.011	4.999
14	2.801	1.202	0.762	0.016	0.000	0.003	0.000	0.000	0.201	4.985
15	2.804	1.194	0.788	0.016	0.000	0.008	0.000	0.000	0.186	4.997
16	2.833	1.167	0.811	0.019	0.000	0.008	0.000	0.000	0.157	4.995
17	2.865	1.131	0.862	0.005	0.000	0.006	0.000	0.000	0.132	5.000
18	2.771	1.233	0.748	0.015	0.000	0.007	0.000	0.000	0.216	4.991
19	2.836	1.166	0.835	0.013	0.000	0.005	0.000	0.000	0.148	5.003
20	2.916	1.102	0.910	0.030	0.000	0.002	0.000	0.001	0.042	5.002
21	2.875	1.127	0.868	0.011	0.000	0.005	0.000	0.000	0.112	4.998
22	2.902	1.114	0.903	0.033	0.000	0.001	0.000	0.002	0.054	5.009
23	2.866	1.135	0.836	0.012	0.000	0.005	0.000	0.000	0.135	4.988
24	2.973	1.030	0.987	0.001	0.000	0.002	0.000	0.000	0.012	5.005

Table 6.8 Representative analytical electron microprobe analyses of the pellet fired to 1,110°C with 10 minutes sintering period. Data were taken from the BSE image shown in Figure 6.10.

	SiO_2	Al_2O_3	Na_2O	K_2O	TiO_2	Fe_2O_3	MnO	MgO	CaO	Total
1	63.81	23.25	9.49	0.20	0.00	0.20	0.00	0.02	3.98	100.94
2	64.54	23.11	9.45	0.27	0.01	0.17	0.00	0.03	4.00	101.58
3	64.77	22.62	9.47	0.27	0.00	0.17	0.00	0.00	3.66	100.94
4	64.30	22.01	5.40	6.53	0.00	0.32	0.03	0.10	2.01	100.70
5	66.25	18.54	4.23	6.58	0.08	1.69	0.08	1.16	1.79	100.38
6	66.44	18.89	4.32	9.47	0.00	0.35	0.00	0.19	0.54	100.18
7	67.15	19.17	4.40	9.85	0.03	0.14	0.00	0.05	0.38	101.16
8	62.45	20.38	4.19	5.12	0.15	2.04	0.00	1.44	4.13	99.90
9	60.92	17.70	4.00	4.57	0.65	3.69	0.10	1.89	5.25	98.76
10	65.90	19.63	4.49	8.99	0.00	0.18	0.00	0.06	0.82	100.08
11	66.74	18.47	4.61	6.54	0.16	1.35	0.00	0.93	1.91	100.69
12	62.48	21.98	5.08	4.79	0.00	0.96	0.04	0.84	4.27	100.42
13	62.91	19.73	3.68	4.64	0.25	2.84	0.00	1.57	5.31	100.94
14	63.96	21.53	5.39	5.58	0.00	0.74	0.02	0.23	2.53	99.96
15	64.55	22.13	8.12	2.10	0.00	0.14	0.05	0.02	3.30	100.40
16	64.25	16.64	3.94	6.16	1.26	3.11	0.14	2.21	2.02	99.73
17	62.99	17.88	4.58	6.00	0.86	2.85	0.01	2.16	2.43	99.75
18	64.79	19.62	5.02	6.18	0.03	1.00	0.00	0.79	2.34	99.78
19	60.29	18.63	4.41	5.28	1.04	3.64	0.07	2.32	3.19	98.87
20	66.89	18.83	4.28	9.94	0.03	0.27	0.00	0.06	0.40	100.70
21	63.81	18.38	4.21	5.31	0.23	2.24	0.02	0.95	3.47	98.61
22	64.75	18.79	4.60	6.90	0.09	1.51	0.00	1.39	1.54	99.58
23	64.54	20.90	5.38	6.61	0.00	0.53	0.00	0.41	2.00	100.36
24	64.73	18.87	1.67	14.06	0.04	0.13	0.00	0.02	0.08	99.58
25	65.49	18.82	2.39	12.70	0.00	0.23	0.00	0.04	0.14	99.81
26	65.86	21.99	9.94	0.48	0.00	0.25	0.00	0.01	2.80	101.33
27	64.83	22.66	9.66	0.19	0.00	0.20	0.00	0.00	3.68	101.21
28	66.82	21.20	10.43	0.23	0.02	0.24	0.00	0.01	2.16	101.11
Formulae based on 8 oxygen atoms										
	Si	Al	Na	K	Ti	Fe^{3+}	Mn	Mg	Ca	Total
1	2.796	1.201	0.806	0.011	0.000	0.007	0.000	0.001	0.187	5.009
2	2.809	1.185	0.798	0.015	0.000	0.006	0.000	0.002	0.187	5.002
3	2.832	1.165	0.803	0.015	0.000	0.005	0.000	0.000	0.171	4.992
4	2.864	1.156	0.466	0.371	0.000	0.011	0.001	0.007	0.096	4.971
5	2.956	0.975	0.366	0.374	0.003	0.057	0.003	0.077	0.086	4.896
6	2.990	1.002	0.377	0.544	0.000	0.012	0.000	0.012	0.026	4.963
7	2.994	1.007	0.380	0.561	0.001	0.005	0.000	0.003	0.018	4.969
8	2.817	1.083	0.367	0.295	0.005	0.069	0.000	0.097	0.200	4.932
9	2.808	0.961	0.358	0.268	0.022	0.128	0.004	0.130	0.259	4.938
10	2.966	1.041	0.391	0.516	0.000	0.006	0.000	0.004	0.039	4.964
11	2.967	0.968	0.397	0.371	0.005	0.045	0.000	0.062	0.091	4.905
12	2.797	1.159	0.441	0.273	0.000	0.032	0.001	0.056	0.205	4.964
13	2.814	1.040	0.319	0.265	0.008	0.096	0.000	0.105	0.254	4.902
14	2.864	1.136	0.468	0.319	0.000	0.025	0.001	0.015	0.121	4.949
15	2.850	1.151	0.695	0.118	0.000	0.004	0.002	0.002	0.156	4.979
16	2.910	0.888	0.346	0.356	0.043	0.106	0.005	0.149	0.098	4.901
17	2.860	0.957	0.403	0.348	0.029	0.097	0.000	0.146	0.118	4.959
18	2.913	1.040	0.438	0.355	0.001	0.034	0.000	0.053	0.113	4.946
19	2.776	1.011	0.393	0.310	0.036	0.126	0.003	0.159	0.157	4.972
20	2.999	0.995	0.372	0.569	0.001	0.009	0.000	0.004	0.019	4.968
21	2.907	0.987	0.372	0.309	0.008	0.077	0.001	0.065	0.169	4.893
22	2.924	1.000	0.403	0.398	0.003	0.051	0.000	0.094	0.075	4.947
23	2.888	1.102	0.467	0.377	0.000	0.018	0.000	0.027	0.096	4.975
24	2.981	1.024	0.149	0.826	0.001	0.004	0.000	0.001	0.004	4.991
25	2.991	1.013	0.212	0.740	0.000	0.008	0.000	0.003	0.007	4.974
26	2.866	1.128	0.838	0.026	0.000	0.008	0.000	0.001	0.131	4.998
27	2.828	1.165	0.817	0.010	0.000	0.007	0.000	0.000	0.172	4.999
28	2.905	1.086	0.879	0.013	0.001	0.008	0.000	0.001	0.100	4.993

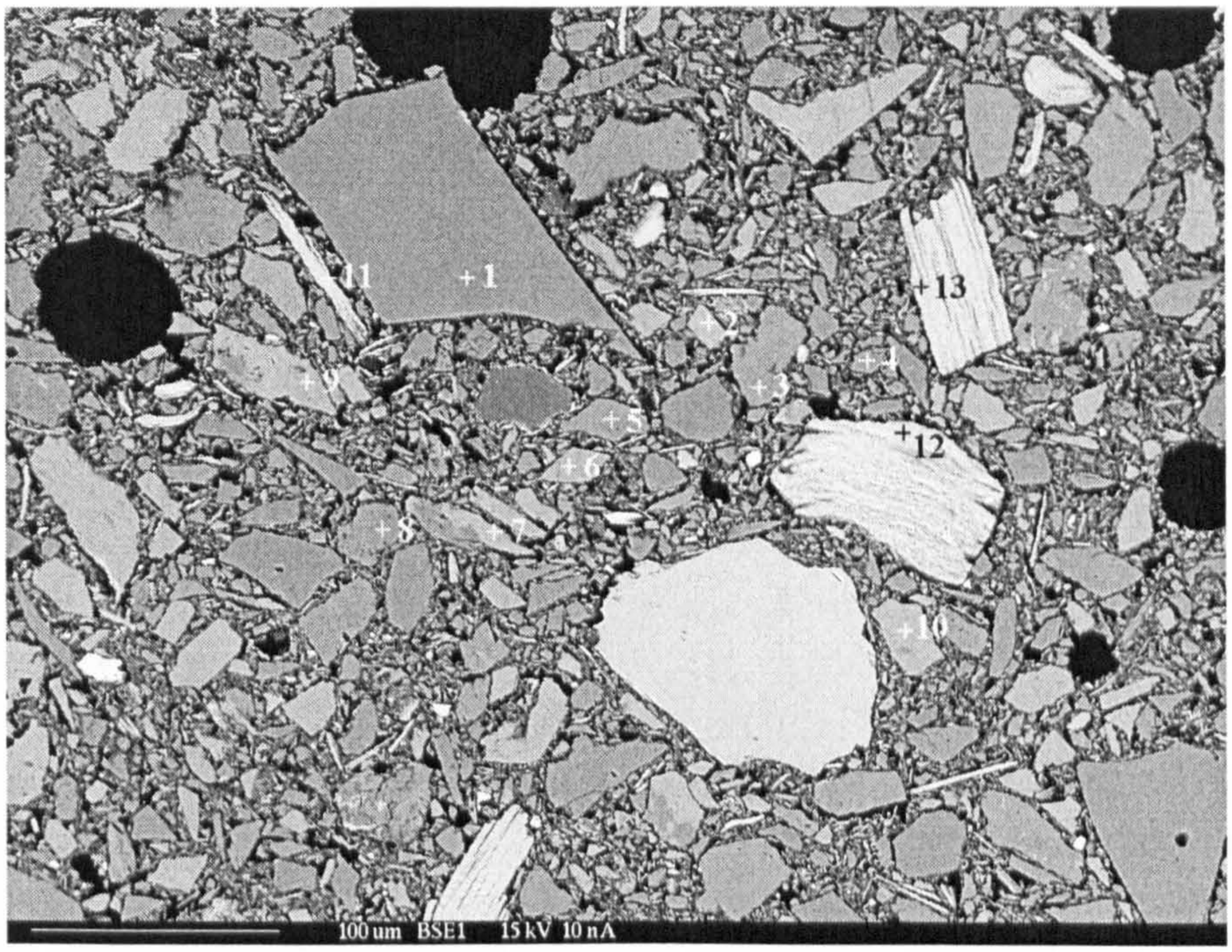

Figure 6.7 BSE image obtained from the electron microprobe analysis of the synthetic aggregate fired to 900˚C. Image shows the number and location of each spot that was used for the X-ray spot analysis.

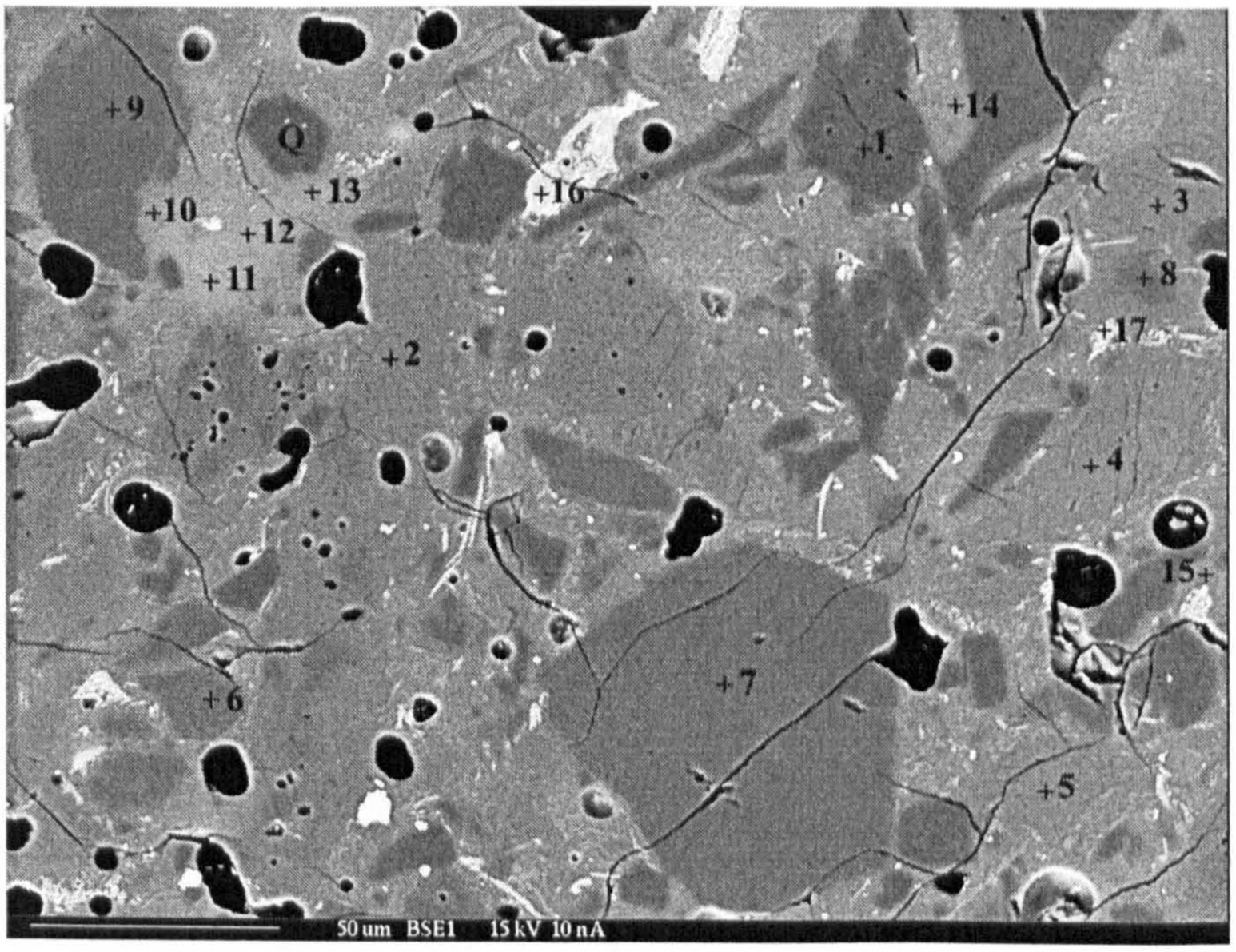

Figure 6.8 BSE image obtained from the electron microprobe analysis of the synthetic aggregate fired to 1,110˚C with 10 minutes sintering period. Image shows the number and location of each spot that was used for the X-ray spot analysis.

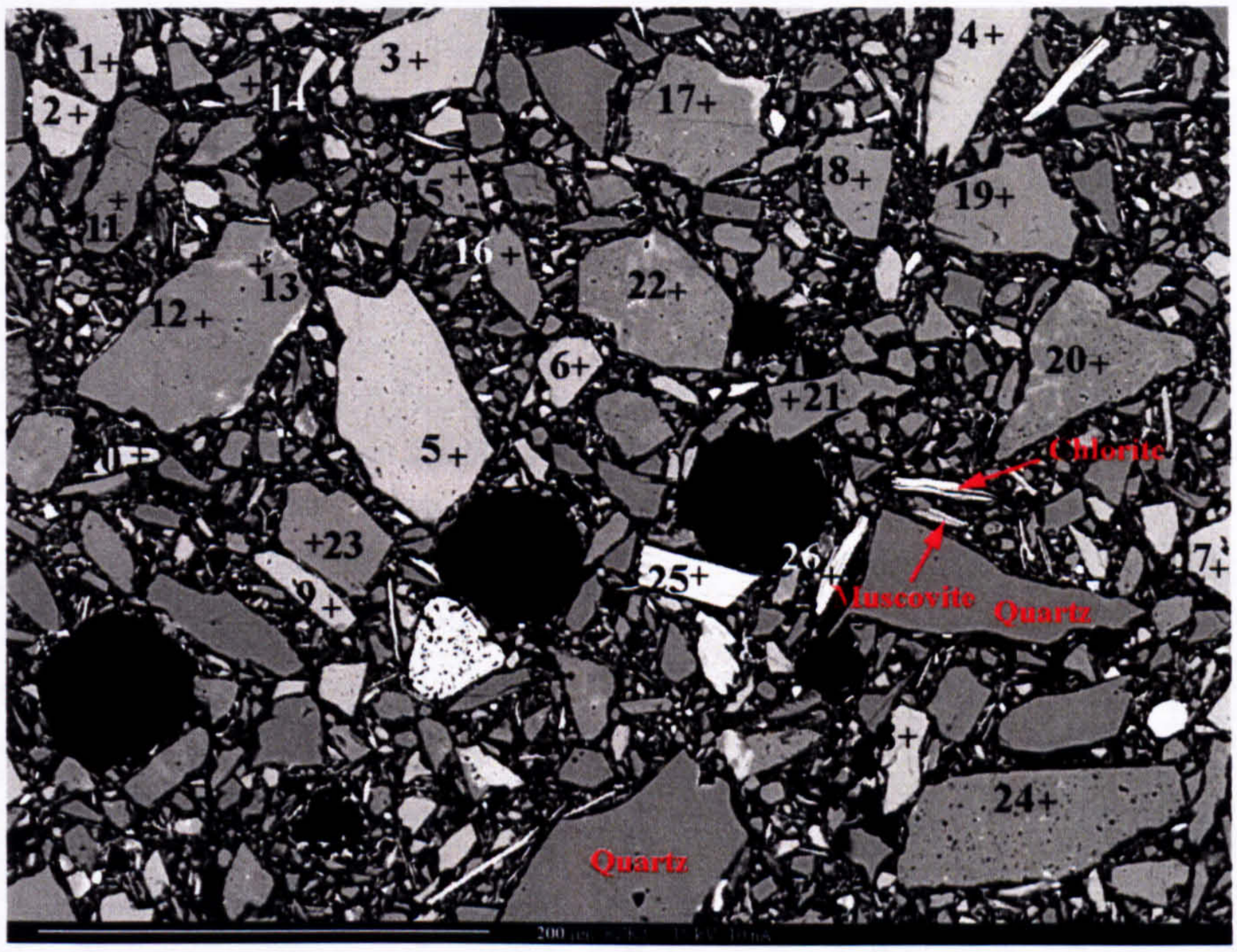

Figure 6.9 BSE image obtained from the electron microprobe analysis of the synthetic aggregate fired to 900˚C. Image shows the number and location of each spot that was used for the X-ray spot analysis.

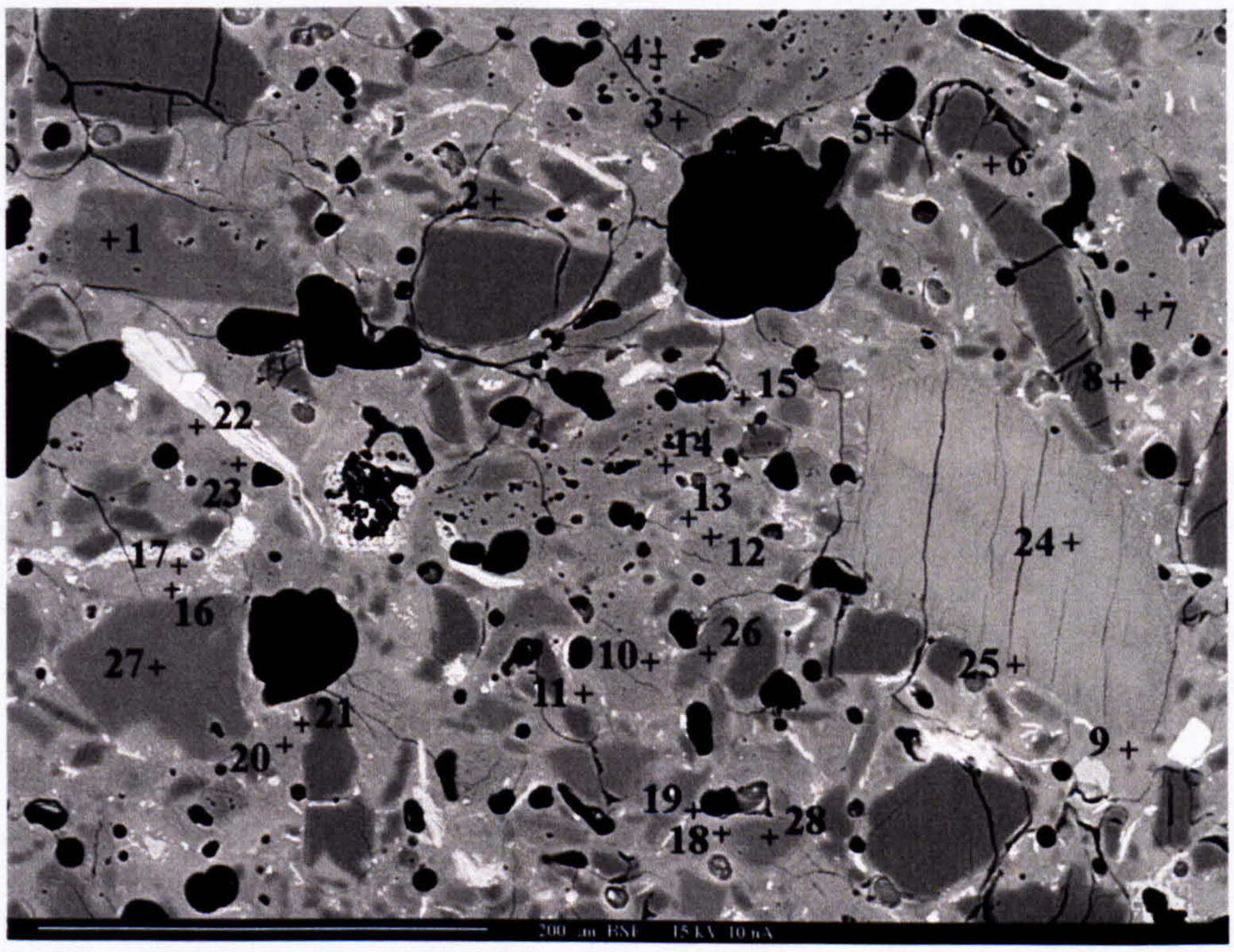

Figure 6.10 BSE image obtained from the electron microprobe analysis of the synthetic aggregate fired to 1,110˚C with 10 minutes sintering period. Image shows the number and location of each spot that was used for the X-ray spot analysis.

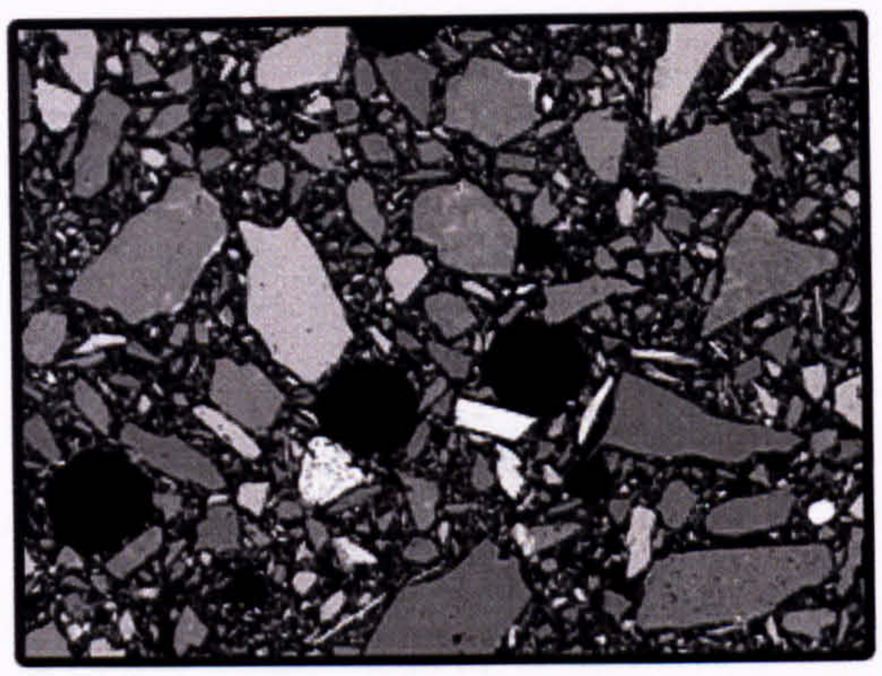

a) Backscattered electron image

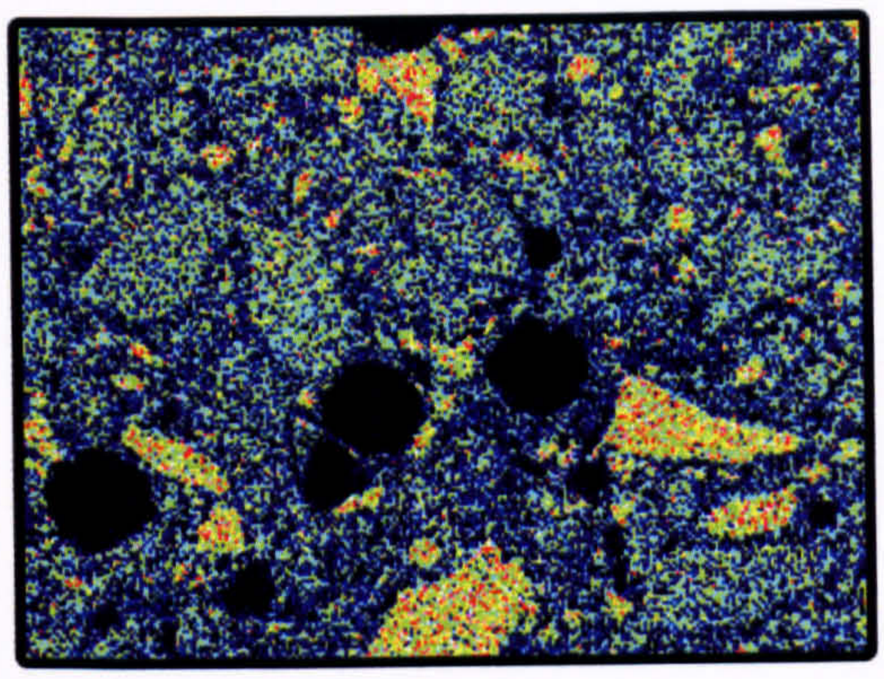

b) Silicon (Si) dot map image

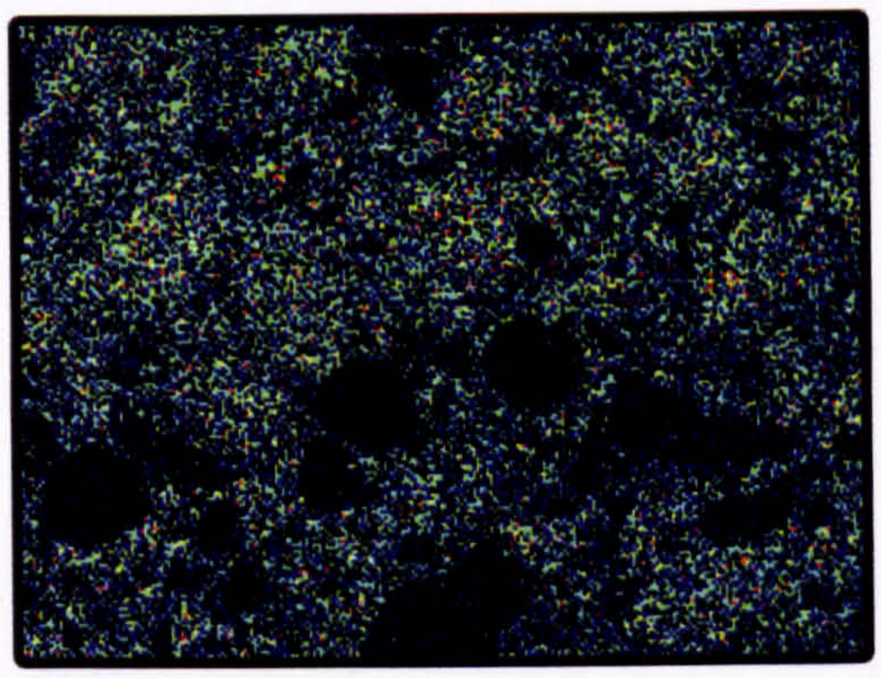

c) Aluminium (Al) dot map image

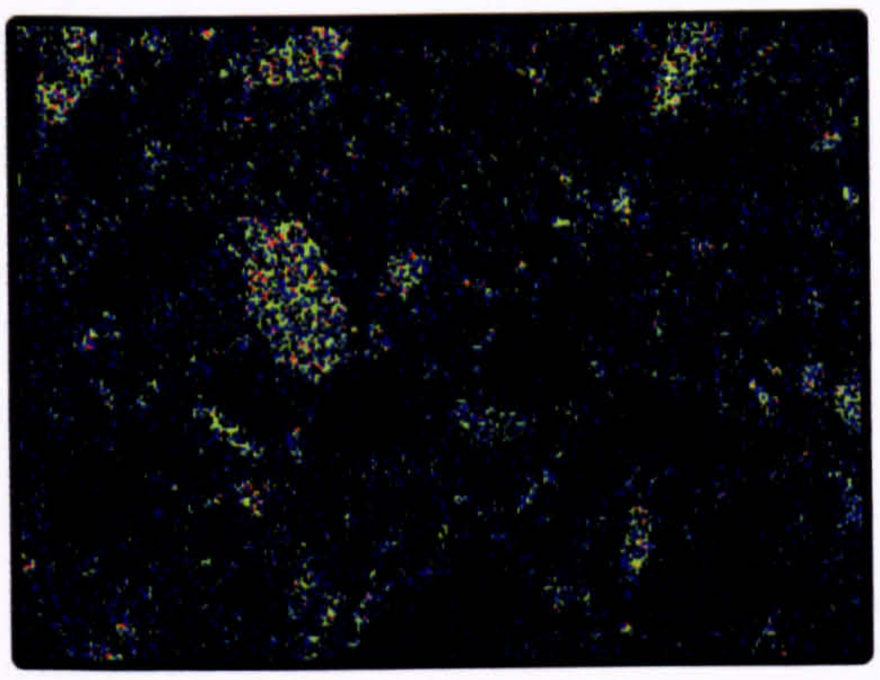

d) Potassium (K) dot map image

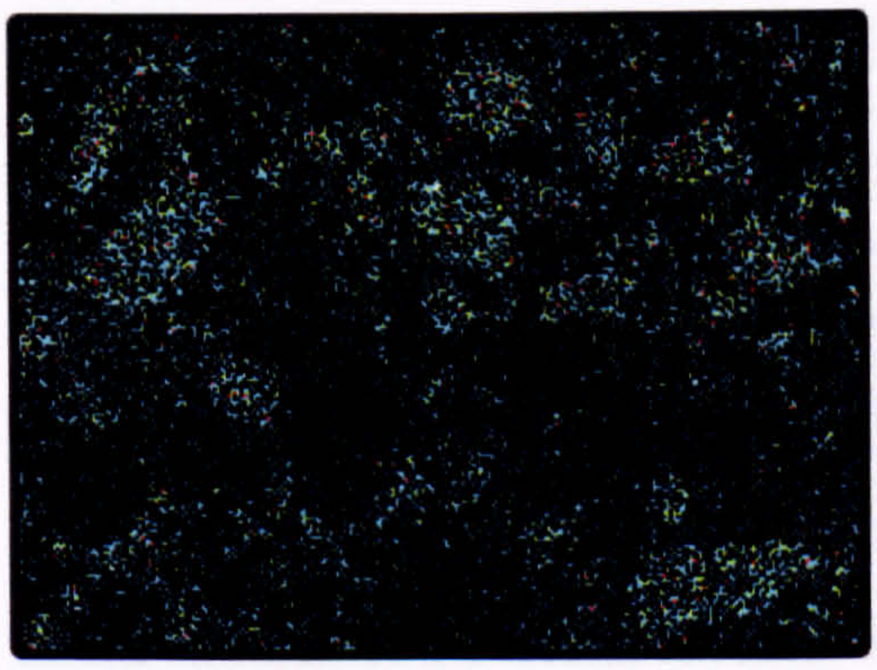

e) Sodium (Na) dot map image

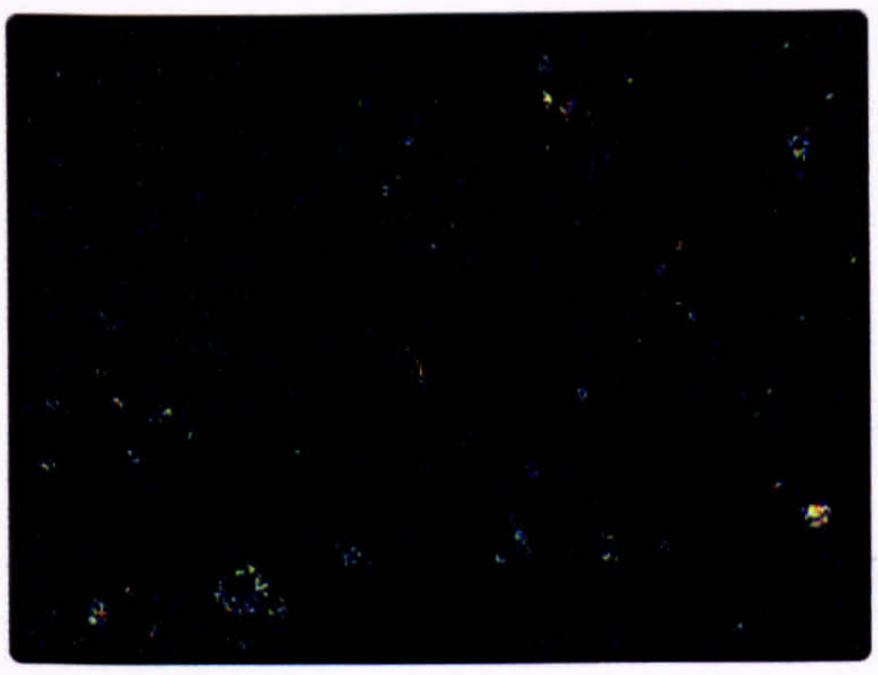

f) Calcium (Ca) dot map image

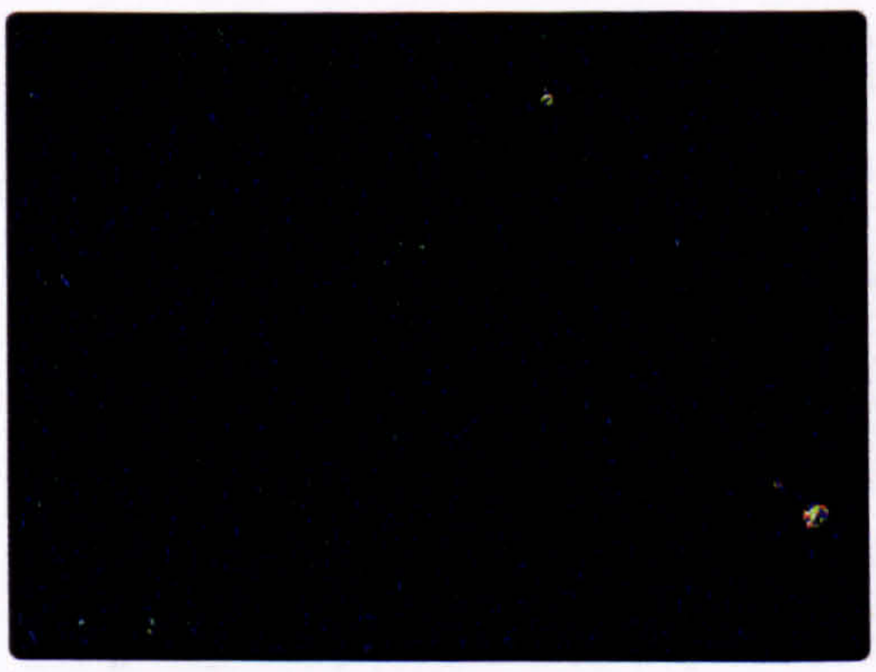

g) Phosporus (P) dot map image

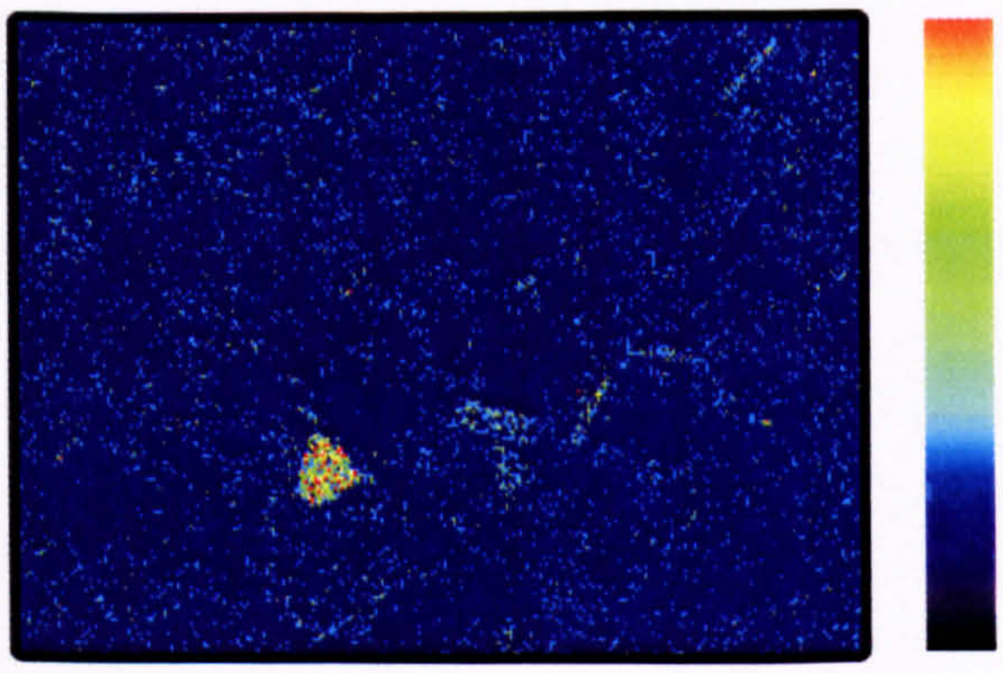

h) Iron (Fe) dot map image

Figure 6.11 BSE image and its X-ray dot map images of the synthetic aggregate fired at 900˚C.

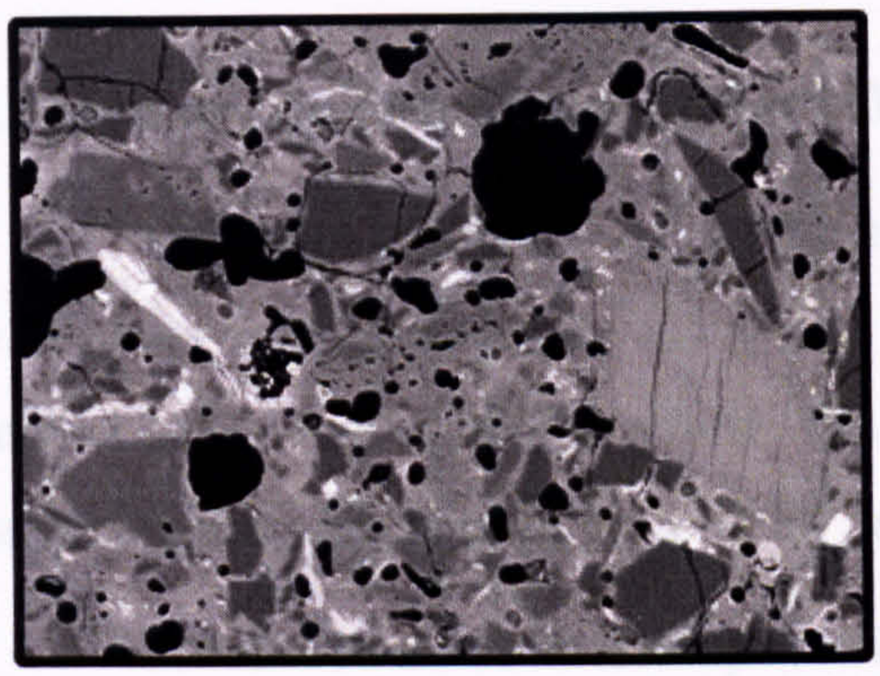

a) Backscattered electron image

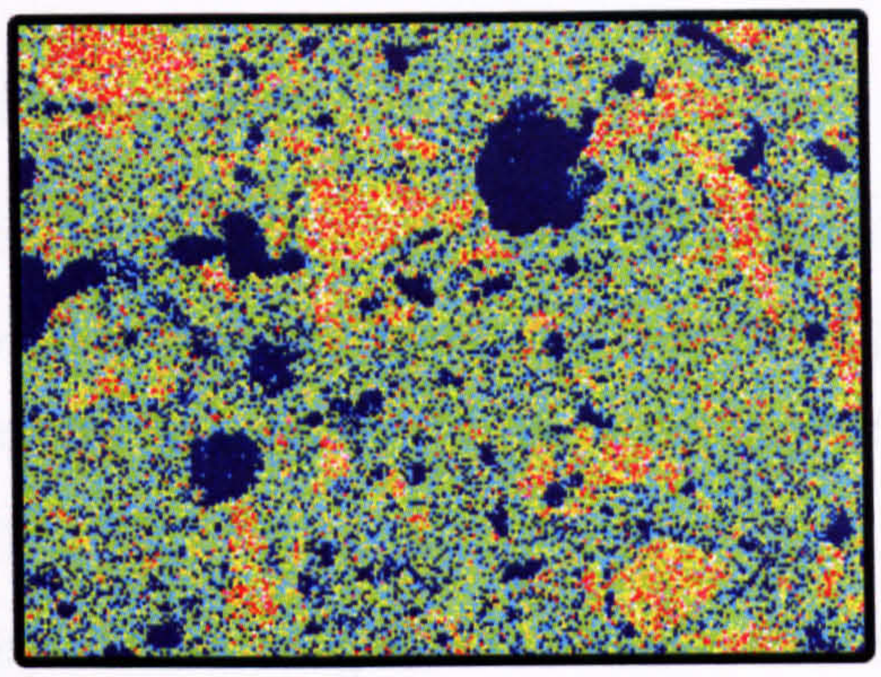

b) Silicon (Si) dot map image

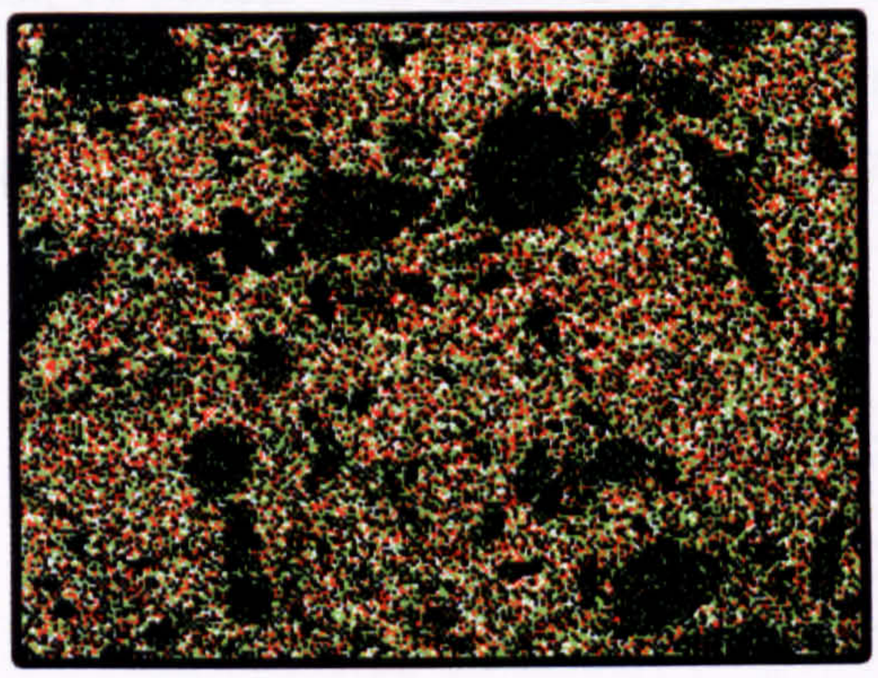

c) Aluminium (Al) dot map image

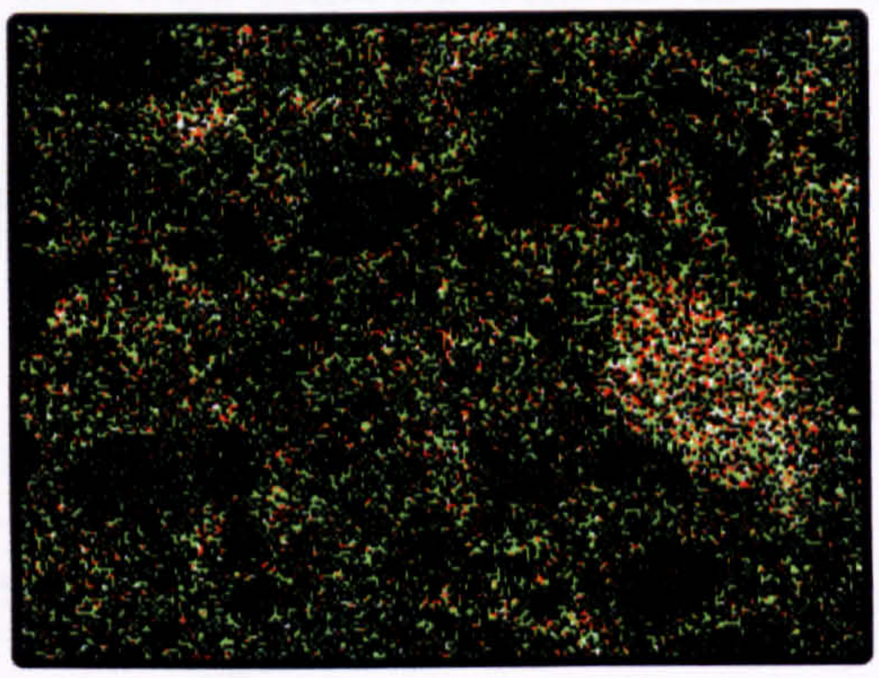

d) Potassium (K) dot map image

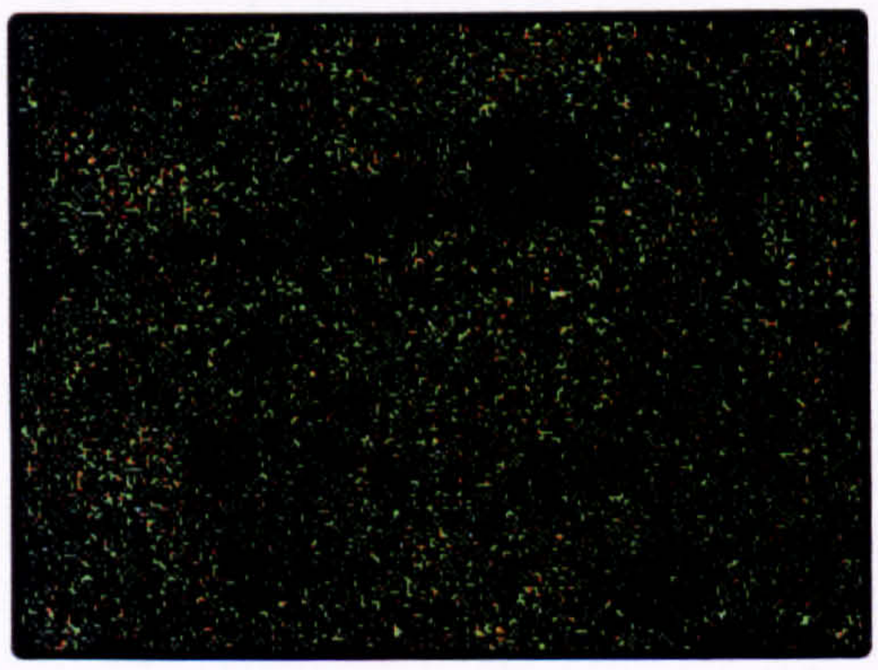

e) Sodium (Na) dot map image

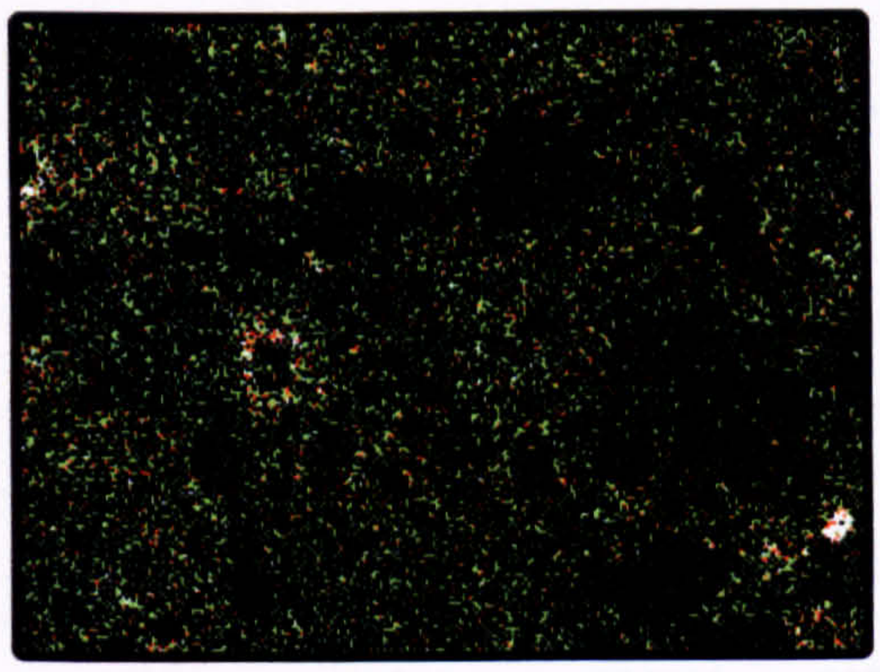

f) Calcium (Ca) dot map image

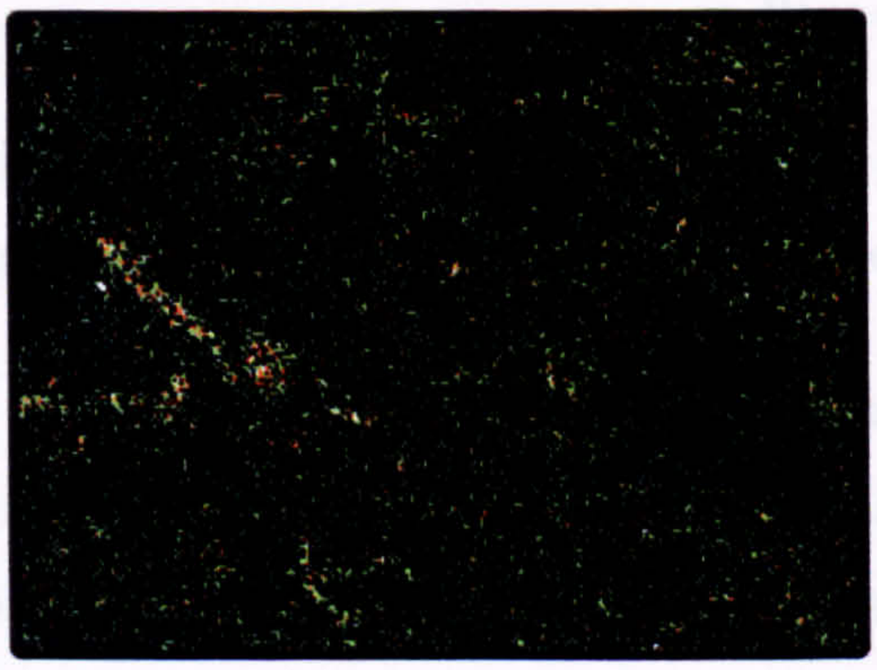

g) Iron (Fe) dot map image

Figure 6.12 BSE image and its X-ray dot map images of the synthetic aggregate fired at 1,110˚C and 10 minute sintering period.

6.5 Mercury intrusion porosimetry (MIP) test results

The pore structure of the synthetic aggregate produced at different firing conditions was investigated using the MIP technique. However, this technique was carried out on one sample at a time. Therefore, the repeatability of the testing results for each condition needs to be considered first.

In order to evaluate the repeatability of the testing results obtained from the MIP test, 10 pellets with diameter of about 14 mm were collected from the same batch that was fired at 1,120˚C with 3 minutes sintering period and ramp rate of 20ºC per minute. The results are shown in Table 6.9 and Figure 6.13.

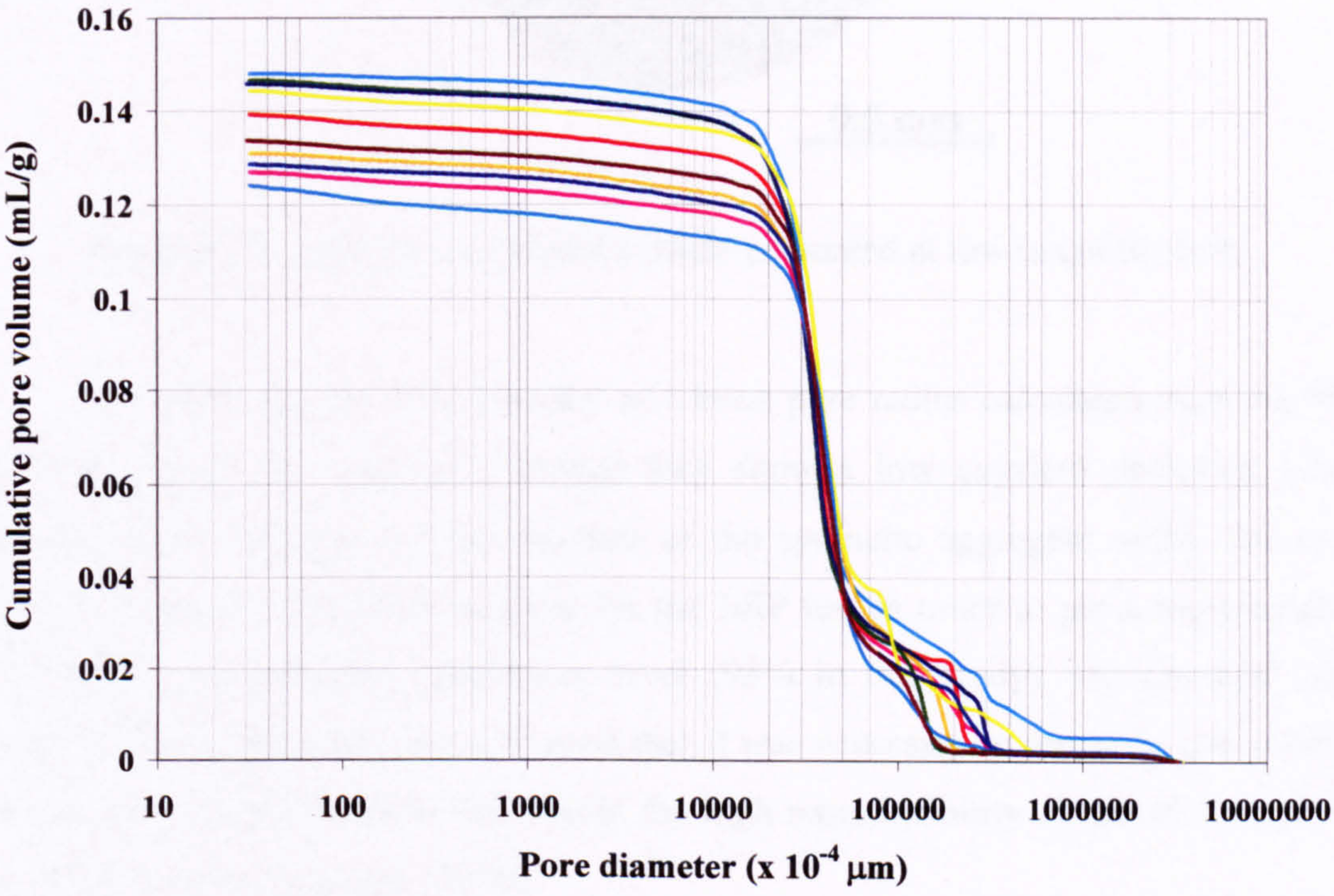

Figure 6.13 Pore size distribution of 10 pellets taken from the same batch (1,120˚C, 3 minutes sintering time and 20ºC / minute).

Figure 6.13 shows the pore size distribution of the 10 pellets taken from the same batches. The results show a qualitatively small variation especially for the pore size ranging from about 3 to 10 microns. There is some variation taking place in the region of the larger pores with a size range from about 10 to 70 microns. These larger pores probably correspond to the flaws in the pellet as indicated in Figure 6.14. These flaws are likely to be a result of the pelletisation process of the green pellet. The flaw

was formed when the slug of a plastic material was rolled into a spherical shape. The volume of the flaw is expected to depend primarily on the length of the slug which is, therefore, varying in nature as revealed by the MIP results.

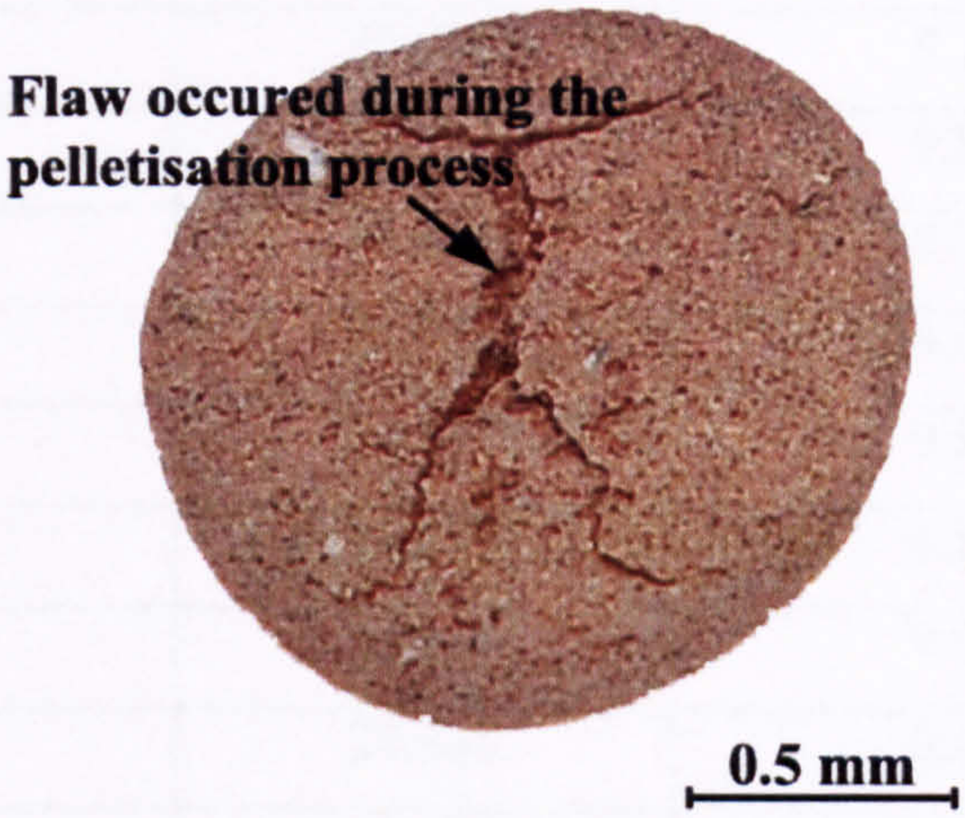

Figure 6.14 Synthetic aggregate particle presented at low magnification.

The results for the total porosity and mean pore radius calculated from the MIP results are given in Table 6.9. Overall they show a low standard deviation which indicates little variation in pore structure of the synthetic aggregate within the same batch. The number of pellets required for the MIP test in order to get a representative result within a reasonable confidence level (95% in this study) was checked using Equation (4.18). The calculation showed that it was necessary to test only one pellet in order to give a representative MIP result; the high reproducibility of this technique was also mentioned by Diamond (2000).

In the following section, MIP was used to investigate the pore structure of the synthetic aggregate fired at different firing conditions and the test results are given in Table 6.10. The average pore sizes of the pellets fired up to 1,120°C (*pre-set* temperature) with sintering periods between 0 and 3 minutes were only slightly different to each other but a big reduction occurred at 3.5 minutes. A similar significant reduction was found at 5 minutes for the case of 1,110°C *pre-set* temperature.

Table 6.9 The total porosity from the MIP test and the mean pore radius, as described in section 4.10, calculated from the 10 intrusion curves of the 10 chosen sintered pellets.

Pellet number	Total porosity (%)	Mean pore radius, ln r_m
1	27.849	9.993
2	25.035	9.794
3	25.263	9.834
4	26.613	9.763
5	27.405	9.693
6	27.614	9.803
7	27.688	9.862
8	24.895	9.846
9	24.385	9.629
10	26.083	9.735
Average	26.283	9.795
Standard deviation	1.322	0.100

The test results given in Table 6.10 show a reduction in the skeleton or particle density (the ratio between sample weight and the solid volume) of the synthetic aggregate with an increase in temperature and the sintering period. A reduction in the particle density might be attributed to the transformation of the crystalline products to more glassy ones (Wasserman and Bentur, 1997). However, this reduction might be attributed to the closed pores within the aggregate that were not filled with mercury. The solid volume that was used to calculate the particle density is the volume that includes the closed pores. For this reason, the solid volume of the pellet containing closed pores is higher than the actual volume and, therefore, it causes a reduction in the particle density of the pellet.

Table 6.10 shows an overall trend of reducing porosity with increasing firing time and temperature except in the case of 1,110°C at 20 minutes sintering time. The increase in porosity at this firing condition indicates the occurrence of bloating, i.e. expansion due to gas formation inside the pellet, which leads to the formation of closed pores inside the pellets as can be seen in Figure 6.24. It should be noted that there is a

possibility for microcracks to occur around the large quartz particles which might create the pathway for the mercury to enter the closed pores inside the pellet. These cracks could occur due to a big difference between the coefficient of thermal expansion of quartz ($\alpha \approx 23 \times 10^{-6}\ K^{-1}$) and the glassy phase ($\alpha \approx 3 \times 10^{-6}\ K^{-1}$) within a temperature range from 20° to 750°C (Mattyasovszky-zsolnay, 1957). The sudden volume contraction of quartz due to the transformation from β- to α-quartz during the cooling stage might be another reason for cracks forming.

There are two necessary conditions for the occurrence of bloating, i.e. minerals or substances that generate gases at high temperature must be present and the highly viscous liquid phase must be produced in order to trap these gases (Riley, 1951). The chemical composition from the XRF analysis (recalculated to 100%) of the Gelnsanda granite washing was checked within the region of the SiO_2, Al_2O_3 and fluxing (Fe_2O_3, FeO, MgO, CaO,Na_2O and K_2O) diagram (see Figure 2.1) which was defined by Riley. This area shows a desirable chemical composition of materials which is required to produce a high temperature glassy phase with a viscosity high enough to trap a gas at the bloating temperature. It was found that the composition of the Glensanda quarry waste falls within this area. Therefore, the remaining condition necessary for bloating of this material is the presence of gas-releasing minerals. Based on the XRD analysis (section 6.3), there are some minerals or substances contained in the synthetic aggregate that can release gas. Kaolinite and chlorite were found to dehydroxylate and release the combined water at temperatures between 500° and 900°C. The dehydroxylation of mica (muscovite and biotite) took place between about 900° and 1,110°C. Decomposition of calcite into calcium oxide with the release of carbon dioxide (CO_2) occurred at temperatures higher than 700°C. The iron oxide contained in the Grensanda granite washing was found to dissociate and release oxygen (O_2) at high temperatures (> 1,000°C) (Hostetter and Roberts, 1921; Riley, 1951; Sandrolini and Palmonari, 1976). The dissociation of the ferric iron (red iron oxide) was evident by the initial red or orange color of the fired pellet which changed into a darker color at higher temperatures. This suggests that the raw materials used in this study can produce a good bloat with an appropriate firing condition. Based on the porosity results given in Table 6.10, it would appear that bloating occurred in the 1110°C firing condition at somewhere between 10 to 20 minutes sintering time.

Figures 6.15 to 6.17 present the pore size distribution of the synthetic aggregate after firing at different temperatures and various periods of time. It is clear that the synthetic aggregate has a bimodal pore size distribution. The majority of pores, as represented by the first peak from the left of the image, correspond to the porosity of the pellet resulting mainly from the extrusion process. The remaining smaller peak is due to a flaw that was formed during the rolling of the plastic mass and it was not considered in this investigation. The results for the synthetic aggregate fired between 900° and 1,140°C with 0 minute sintering time, as shown in Figure 6.15, show an increase in pore size with increase in temperature, as can be seen by the shift in the first peak to the right. A similar pore growth was found with increasing firing time in the case of 1,120°C with 0, 1.5 and 3 minutes sintering times, as shown in Figure 6.16. This observation agrees with the reports in the past (Kellam and Nicholson, 1971; Whittemore, Jr. and Sipe, 1974). There are many mechanisms that were proposed to explain the pore growth process including surface diffusion, particle size distribution effects, particle coalescence and phase transformation (Whittemore, Jr. and Sipe, 1974). Due to the very wide particle size distribution of the green pellet ranging from about 0.4 to 300 microns (see Figures 3.1 and 3.2), the mechanism that is the most likely to be a primary cause in this study is the effect of particle size distribution. The shrinkage that occurred during the densification of the very small particles was inhibited by a rigid framework of large and relatively inert particles. A larger gap was then developed through the interstices of the big particles resulting in an increase in pore size and this behavior is evidently supported by the secondary electron image as shown in Figure 6.21 which clearly shows a coalescence of the very small particles.

It is interesting that the increase in pore size occurs without a corresponding increase in total porosity as shown in Table 6.10. This indicates the concurrent occurrence of the densification, as evidenced by the decrease in total porosity, and pore growth. The densification process is a competing process with pore growth during the sintering of ceramic material. A significant reduction in total porosity and average pore size at 5 and 3.5 minutes sintering time for the *pre-set* sintering temperature of 1,110°C and 1,120°C respectively suggests that densification of the synthetic aggregate body has already started to overcome the pore growth.

Table 6.10 The MIP test results

Firing Condition	Average Pore Diameter (Å)	Bulk Density (g/mL)	Skeleton Density (g/mL)	Total Porosity (%)
900(0)	899	1.74	2.75	36.76
1000(0)	1906	1.75	2.73	35.92
1110(0)	2722	1.70	2.62	35.37
1110(5)	1339	1.94	2.56	24.15
1110(10)	461	2.10	2.44	13.91
1110(20)	157	2.03	2.48	17.85
1120(0)	2186	1.85	2.64	29.98
1120(1.5)	2623	1.89	2.63	28.17
1120(3.0)	3185	1.94	2.62	26.03
1120(3.5)	465	2.12	2.52	15.69

Note: Numbers in the parenthesis are the sintering time in minute.

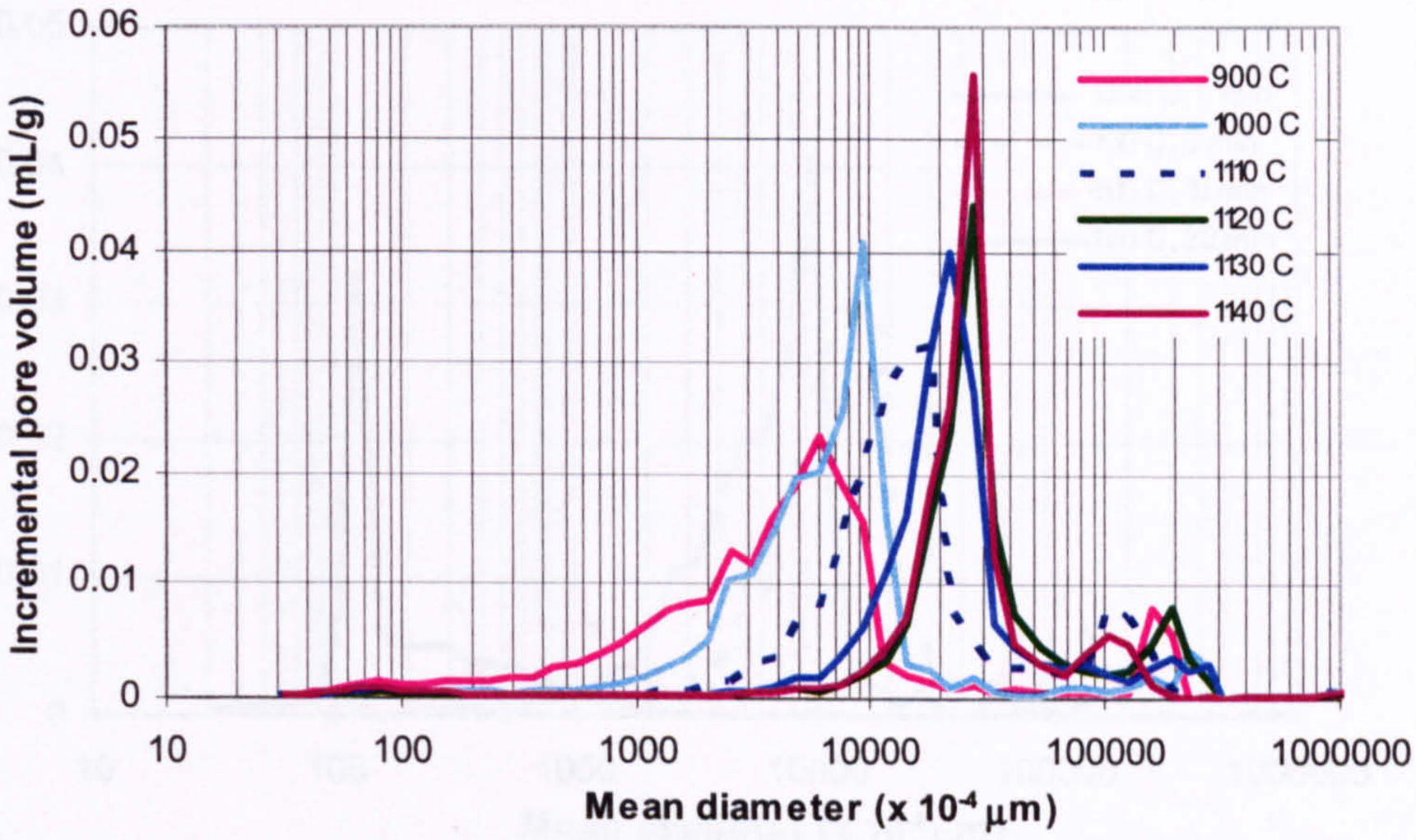

Figure 6.15 Pore size distribution of the synthetic aggregate fired at temperatures range from 900˚ to 1,140˚C.

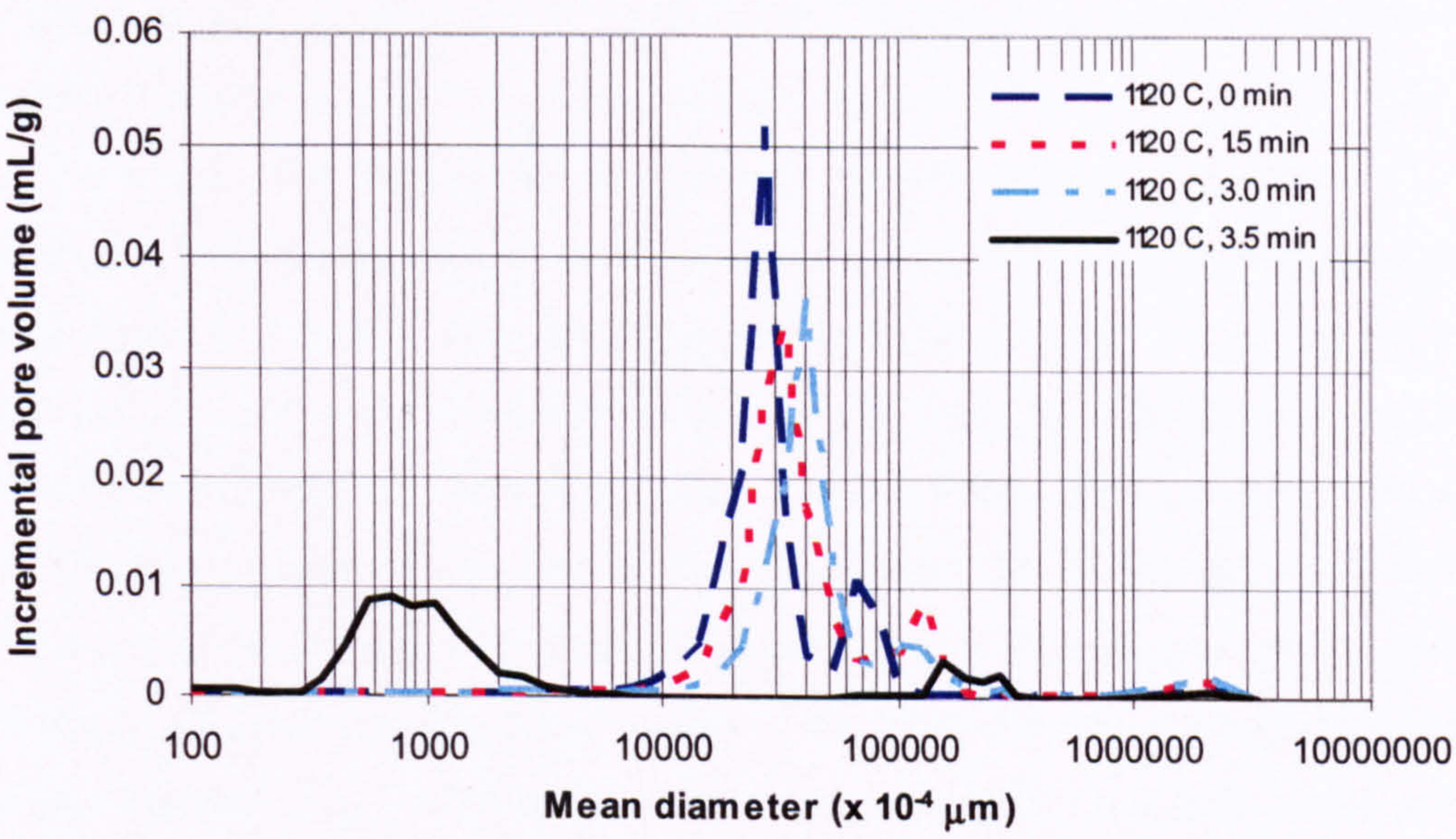

Figure 6.16 Pore size distribution of the synthetic aggregate fired at 1,120˚C with the sintering period ranges from 0 to 3.5 minutes.

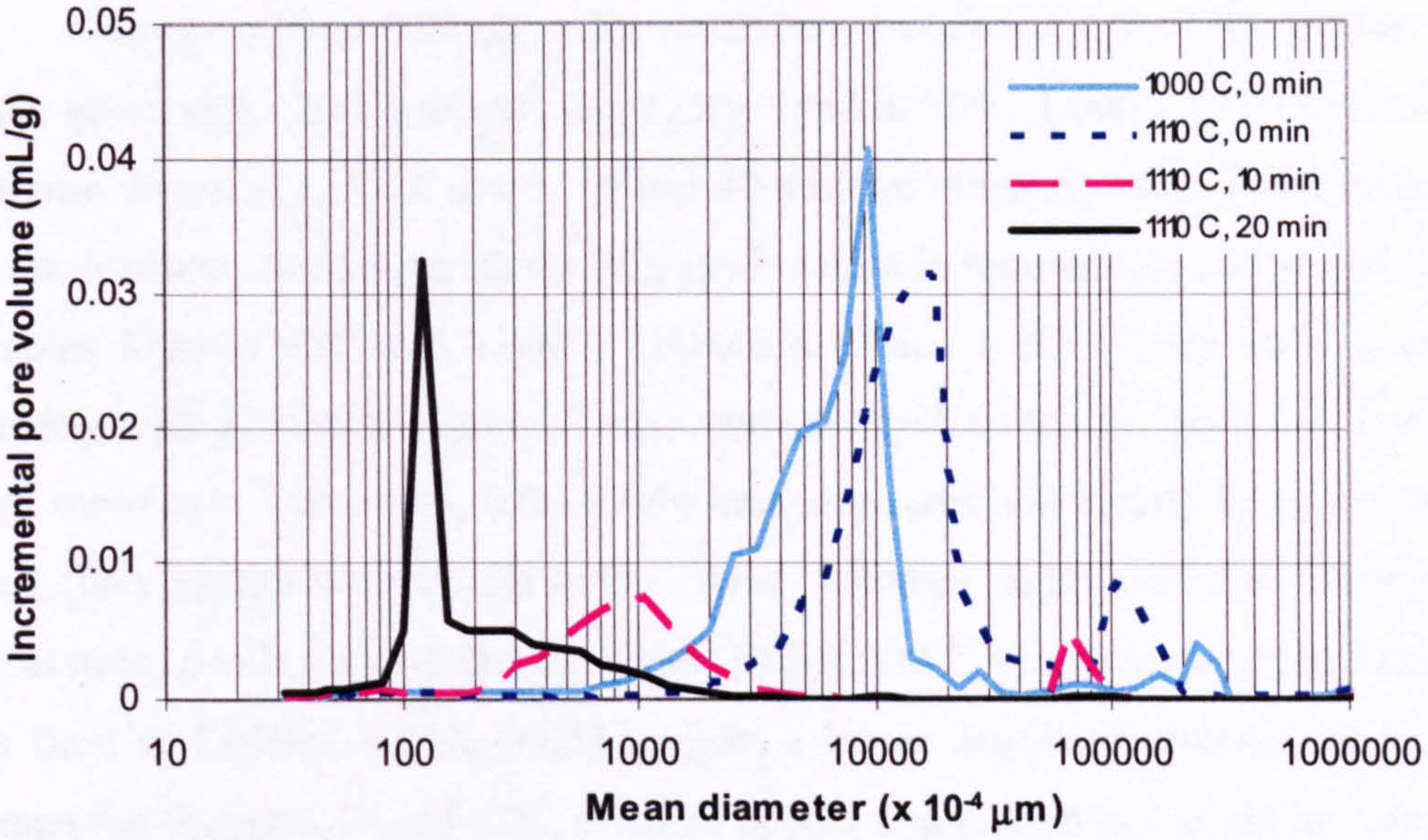

Figure 6.17 Pore size distribution of the synthetic aggregate fired at 1,000˚C and 1,110˚C with the sintering period ranges from 0 to 20 minutes.

6.6 Microstructure evolution in fired synthetic aggregate

Figures 6.18 to 6.24 show the secondary electron image of the fracture surface of the green pellet and synthetic aggregates fired at 900°, 1,000°, 1,110°C for 0 minute sintering time and 1,110°C for 5, 10 and 20 minutes sintering time. These clearly show the microstructural changes induced by the increase in temperature and sintering period. Samples fired at 900° and 1,000°C (Figure 6.19 and 6.20) clearly show a very poor sintering with a limited degree of interconnectivity between the particles. Pore size in these samples is very small, extensively interconnected and clearly being controlled by small flaky particles which fill in the spaces between larger particles. During sample preparation, it was noticed that the pellet fired at 900°C was more prone to damage than that fired at 1,000°C which would suggest a better degree of sintering at a 1,000°C. Comparing Figure 6.19 and 6.20, it would appear that there was a slight increase in pore size at 1,000°C.

At 1,110°C, the coalescence of very small particles which leads to an increase of the mean pore size is clearly detected as shown when comparing Figures 6.19 to 6.20. Pore shape at this temperature is irregular and angular. In addition, the extensive intergranular connected porosity can still clearly be seen and, is consistent with the high water absorption. The melting of the feldspar mineral was clearly observed which supports the XRD results and its amount was seen to increase with temperature and sintering time. At 1,110°C and a sintering time of 5 minutes, the volume of the liquid phases formed was found to be sufficient to fill most of the pores resulting in a decrease in porosity, this liquid phase also acts as a bond between individual particles. Pore shape clearly became rounder and smaller in size. In addition, small isolated, approximately spherical closed pores were also observed in this sample. This image supports the MIP result which suggests that the densification of the synthetic aggregate body started at some time between 0 to 5 minutes sintering time resulting in a reduction of the average pore size. A further vitrification of the body, as expected, was observed for the samples fired at a longer sintering period. The SEM image of 10 and 20 minutes sintering time (Figure 6.23 and 6.24) clearly present a very dense structure with a large number of isolated approximately spherical pores due to bloating. It is very obvious that the melt or glass formation was the dominating microstructural change during sintering. The low water absorption of these samples is most likely due to the closed nature of the pores together with a very dense matrix material.

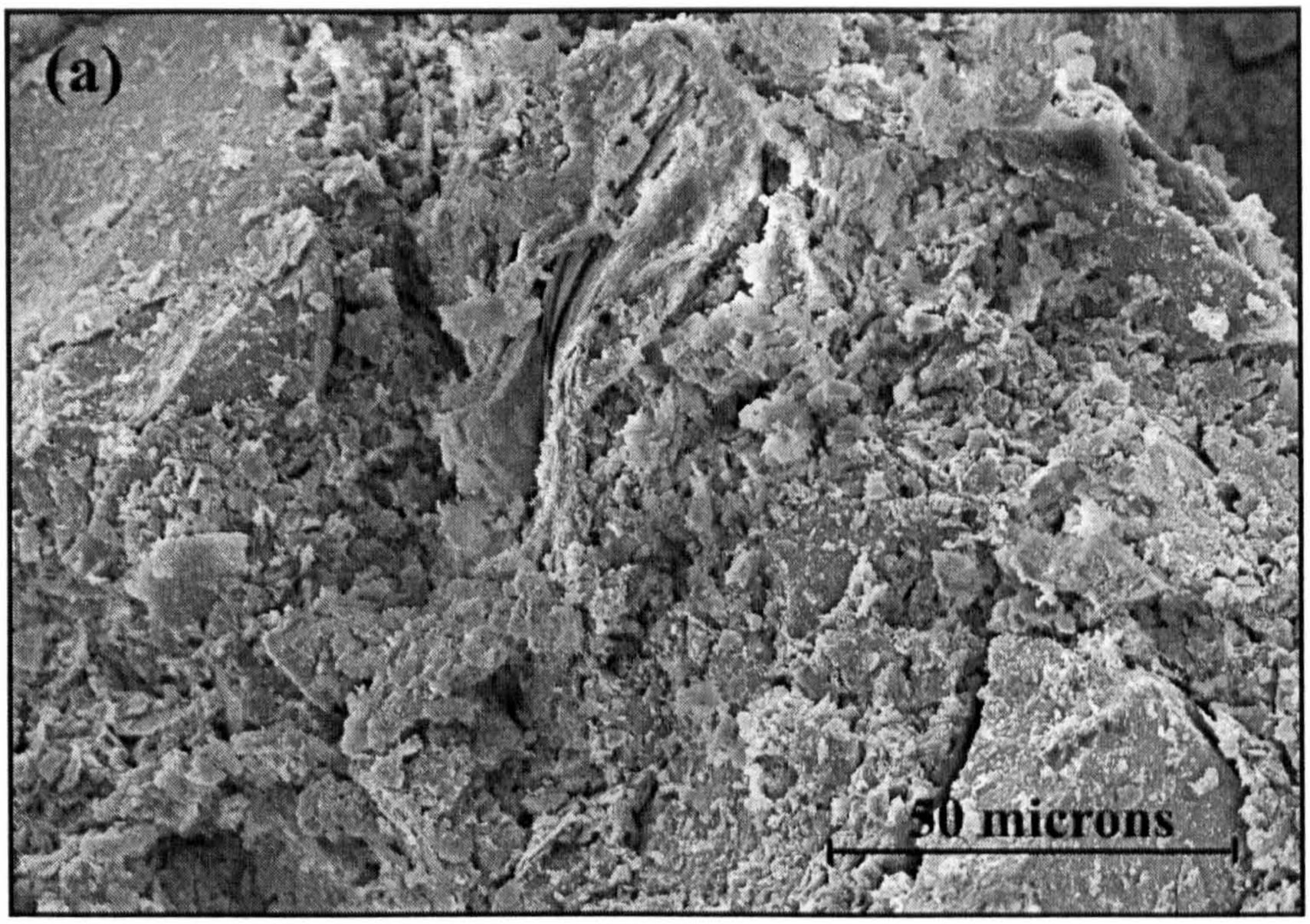

Figure 6.18 Secondary electron images of the green pellet.

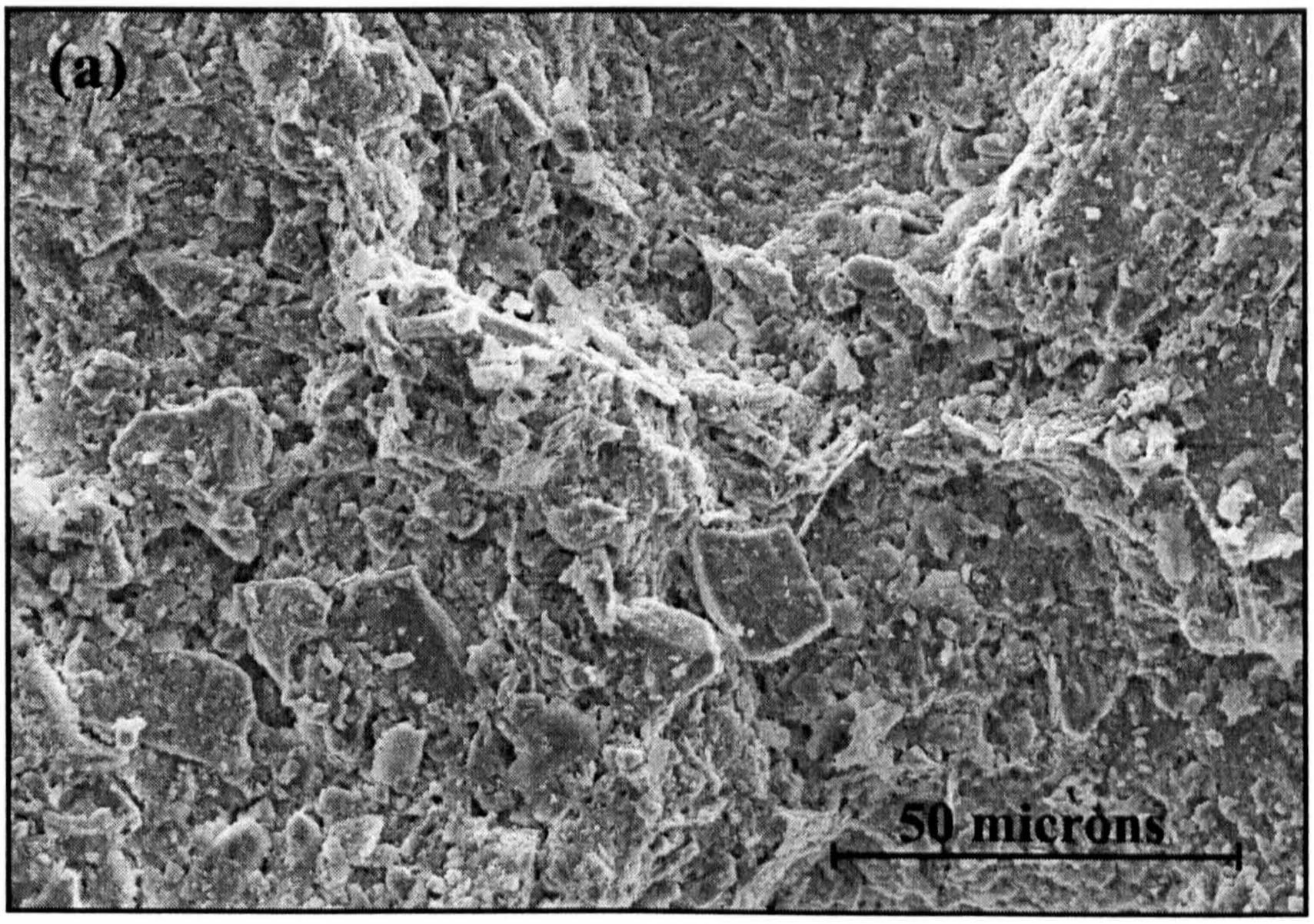

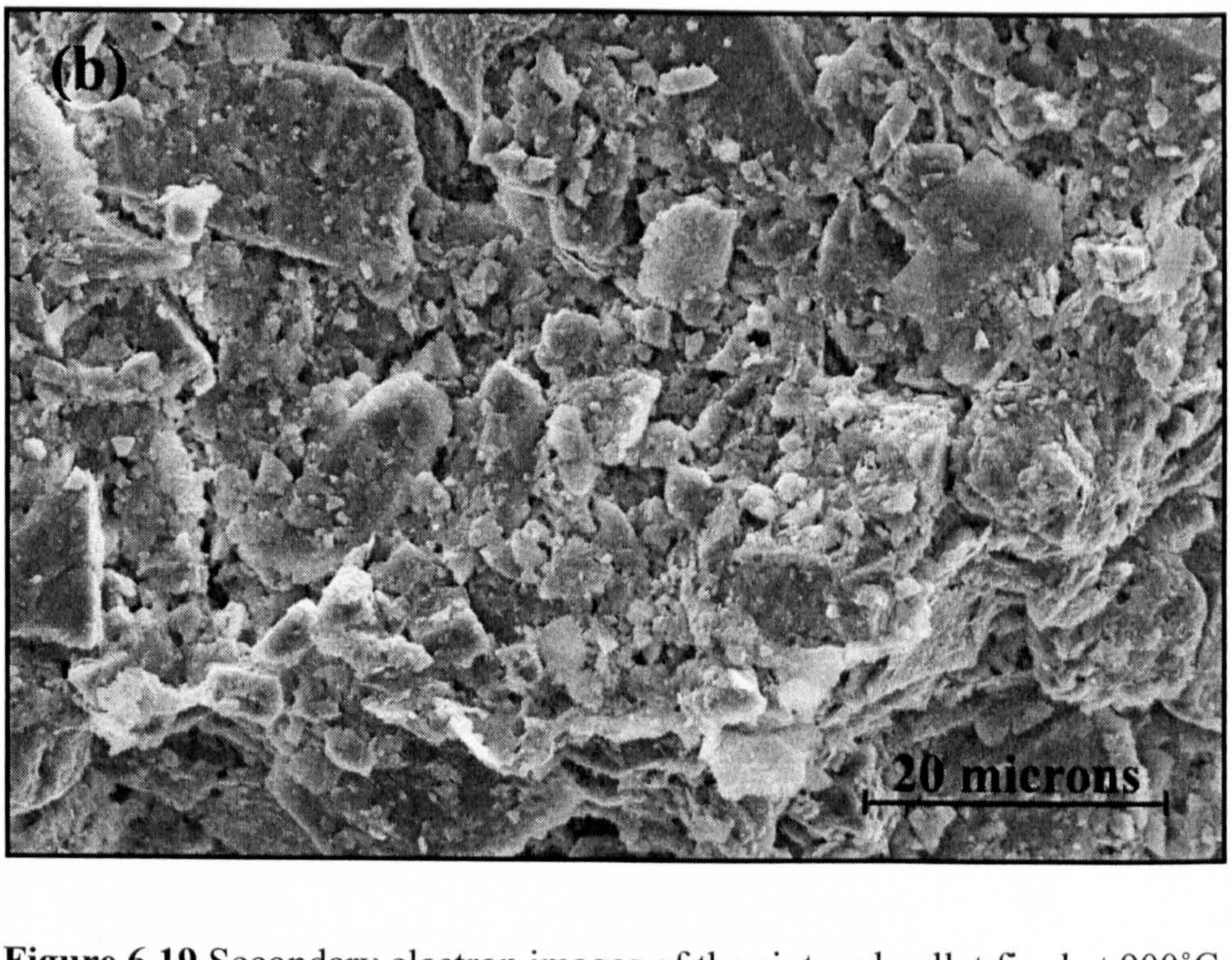

Figure 6.19 Secondary electron images of the sintered pellet fired at 900˚C.

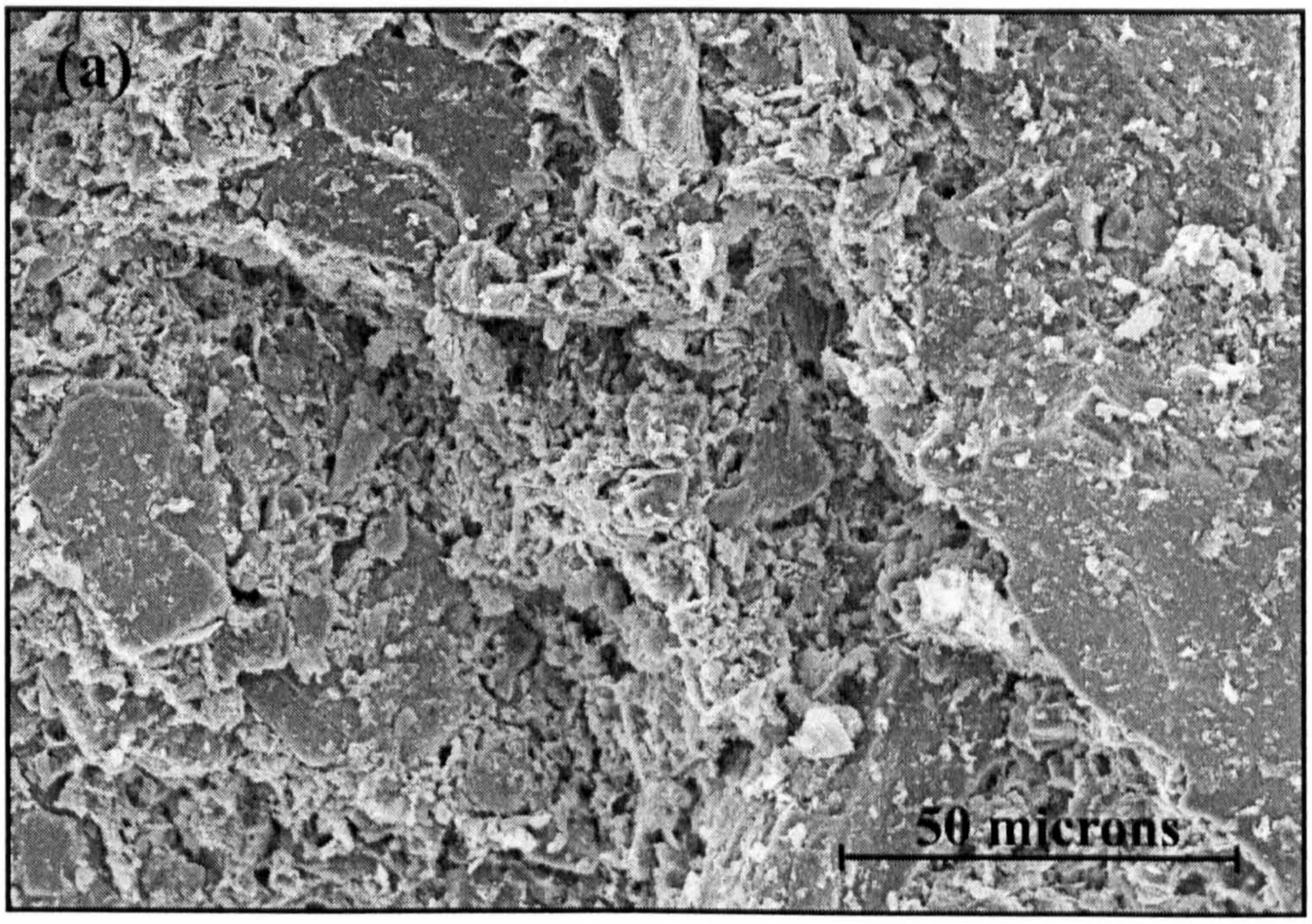

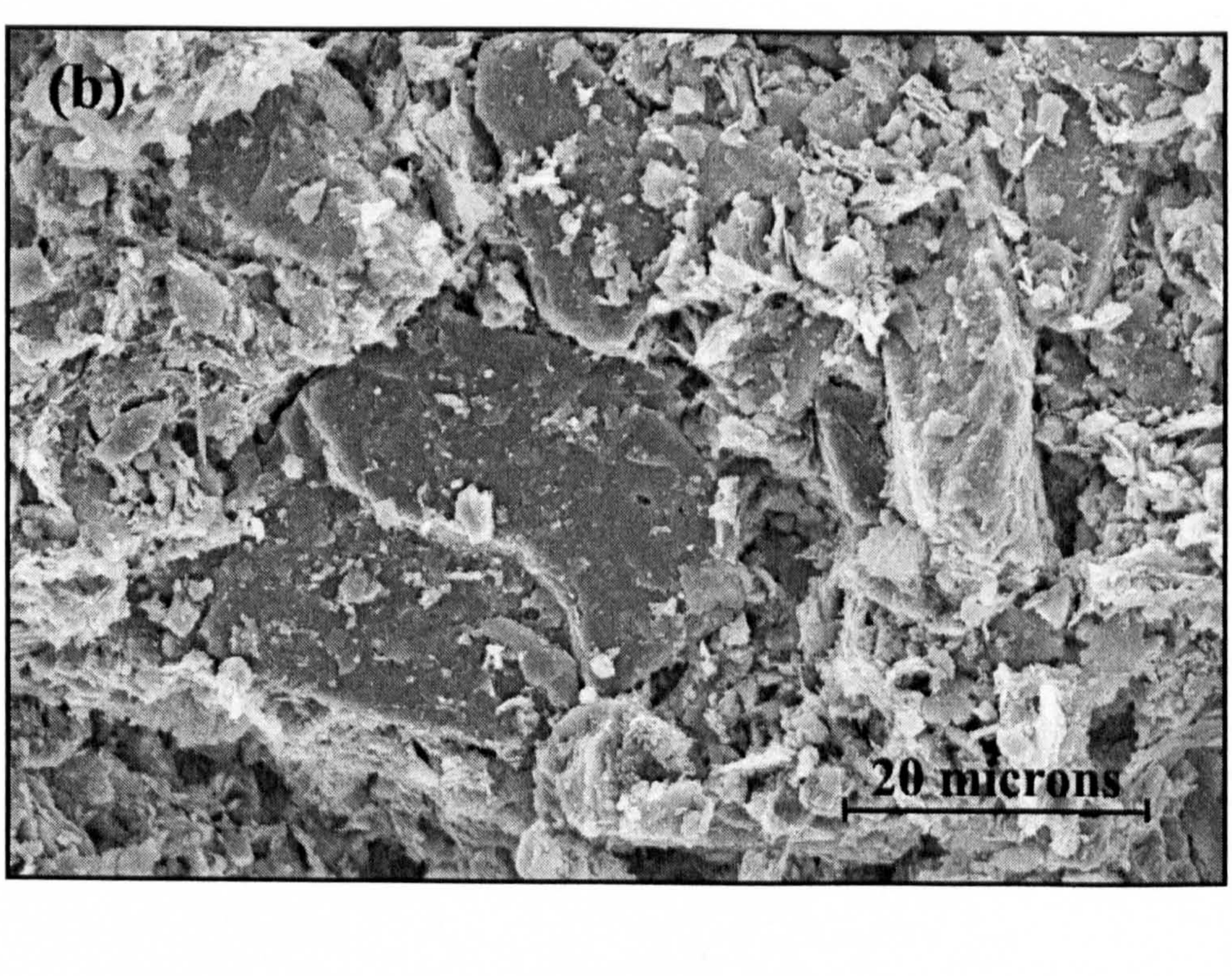

Figure 6.20 Secondary electron images of the sintered pellet fired at 1,000˚C.

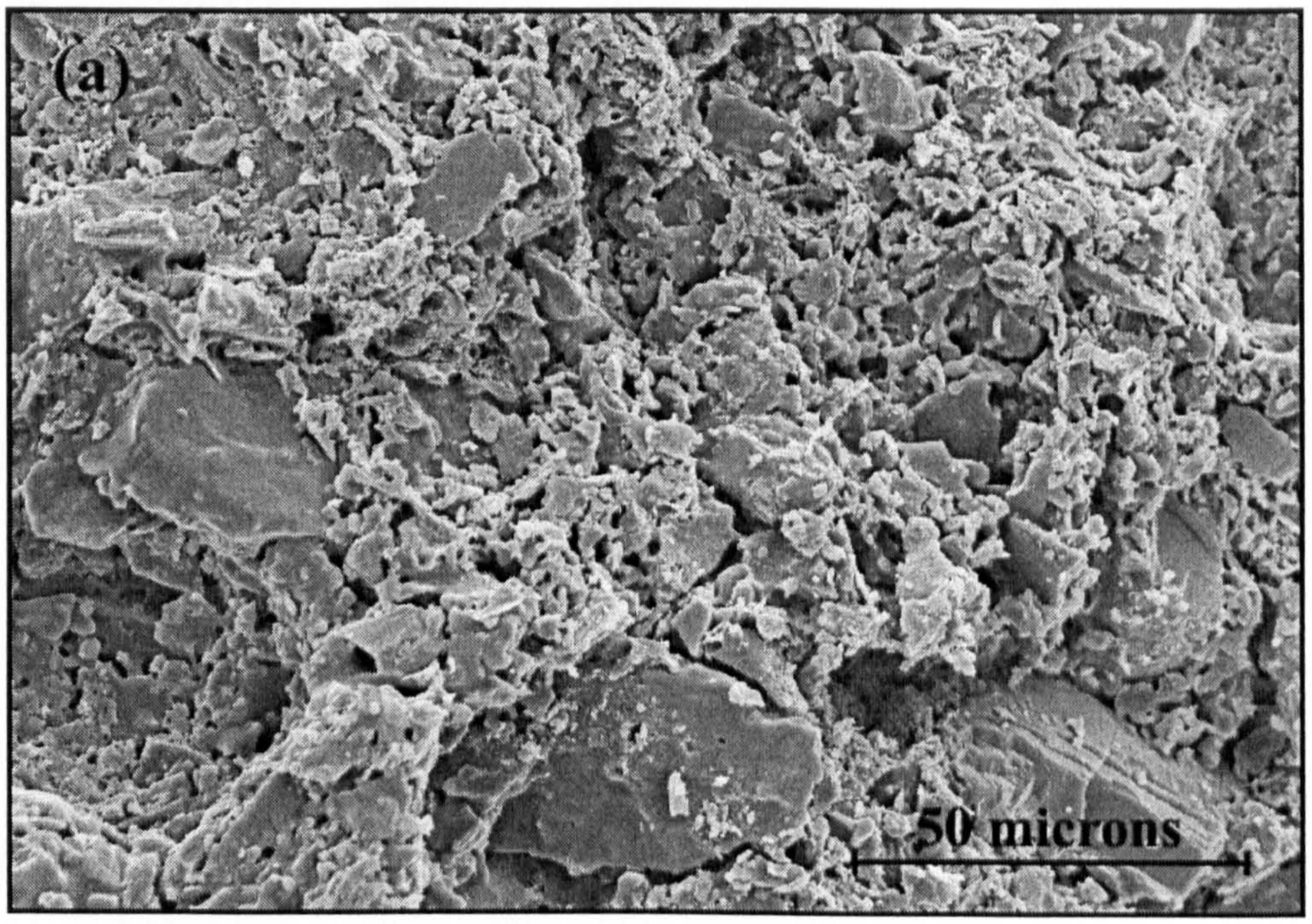

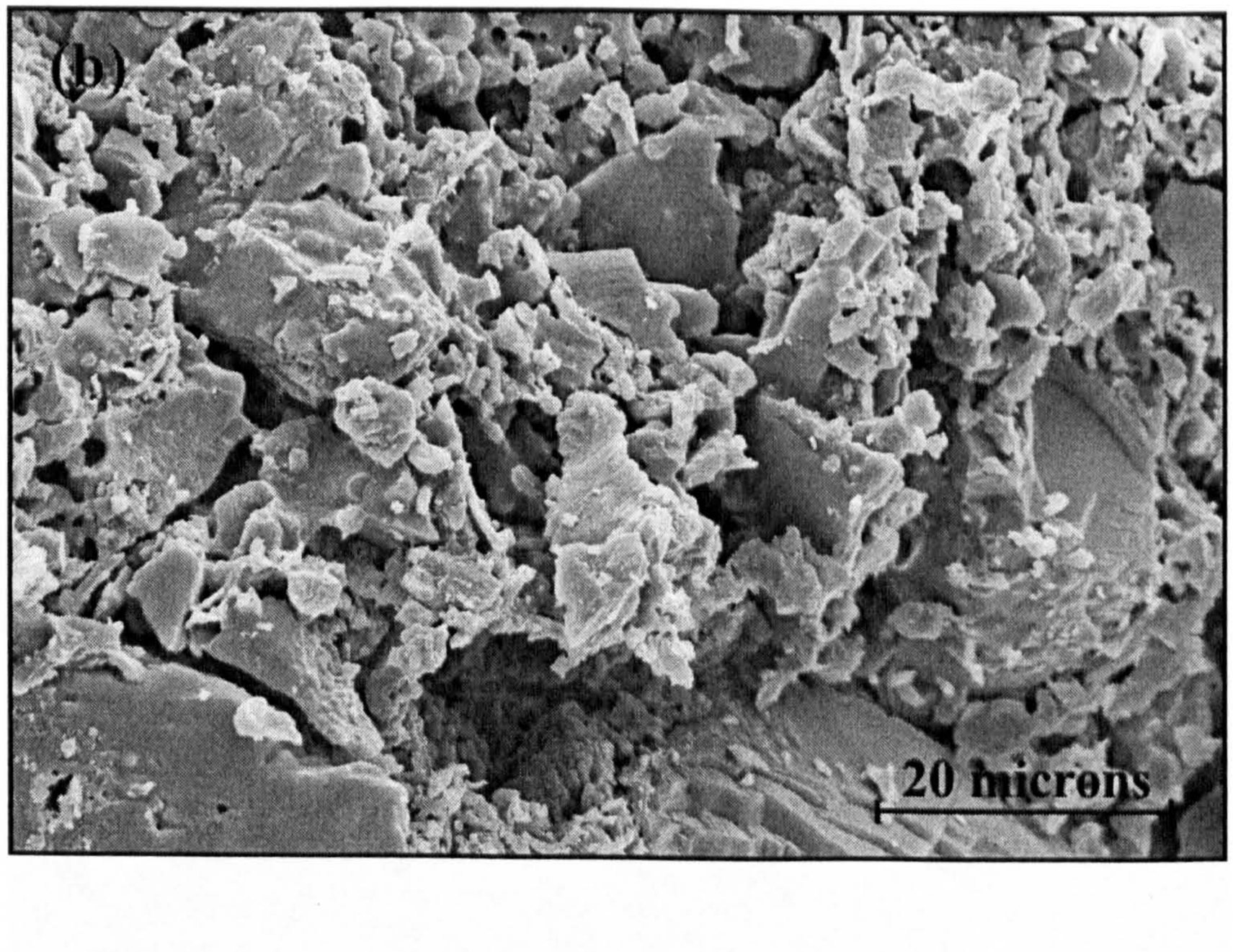

Figure 6.21 Secondary electron images of the sintered pellet fired at 1,110˚C.

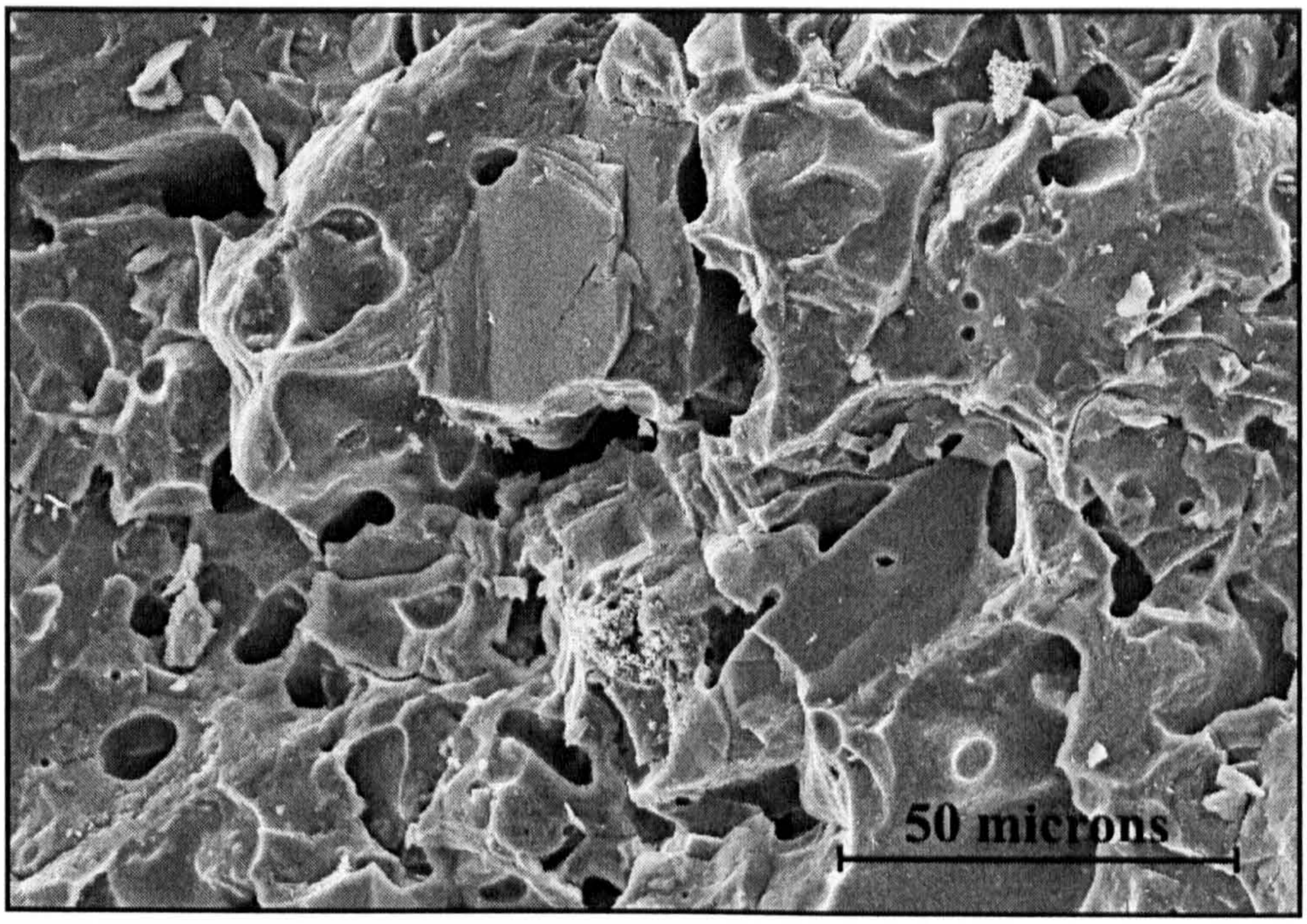

Figure 6.22 Secondary electron image of the synthetic aggregate fired at 1,110˚C with 5 minutes sintering time.

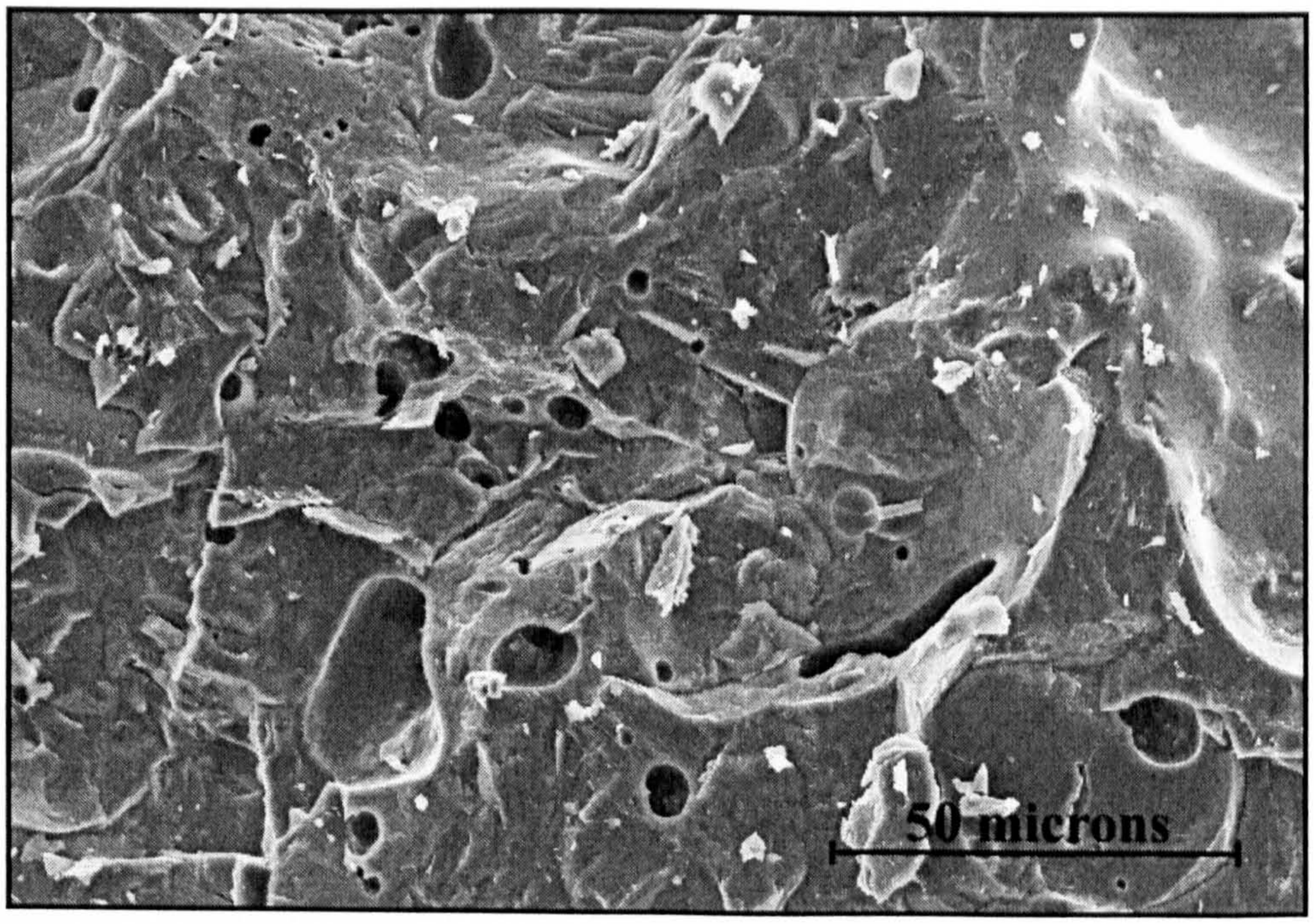

Figure 6.23 Secondary electron image of the synthetic aggregate fired at 1,110˚C with 10 minutes sintering time.

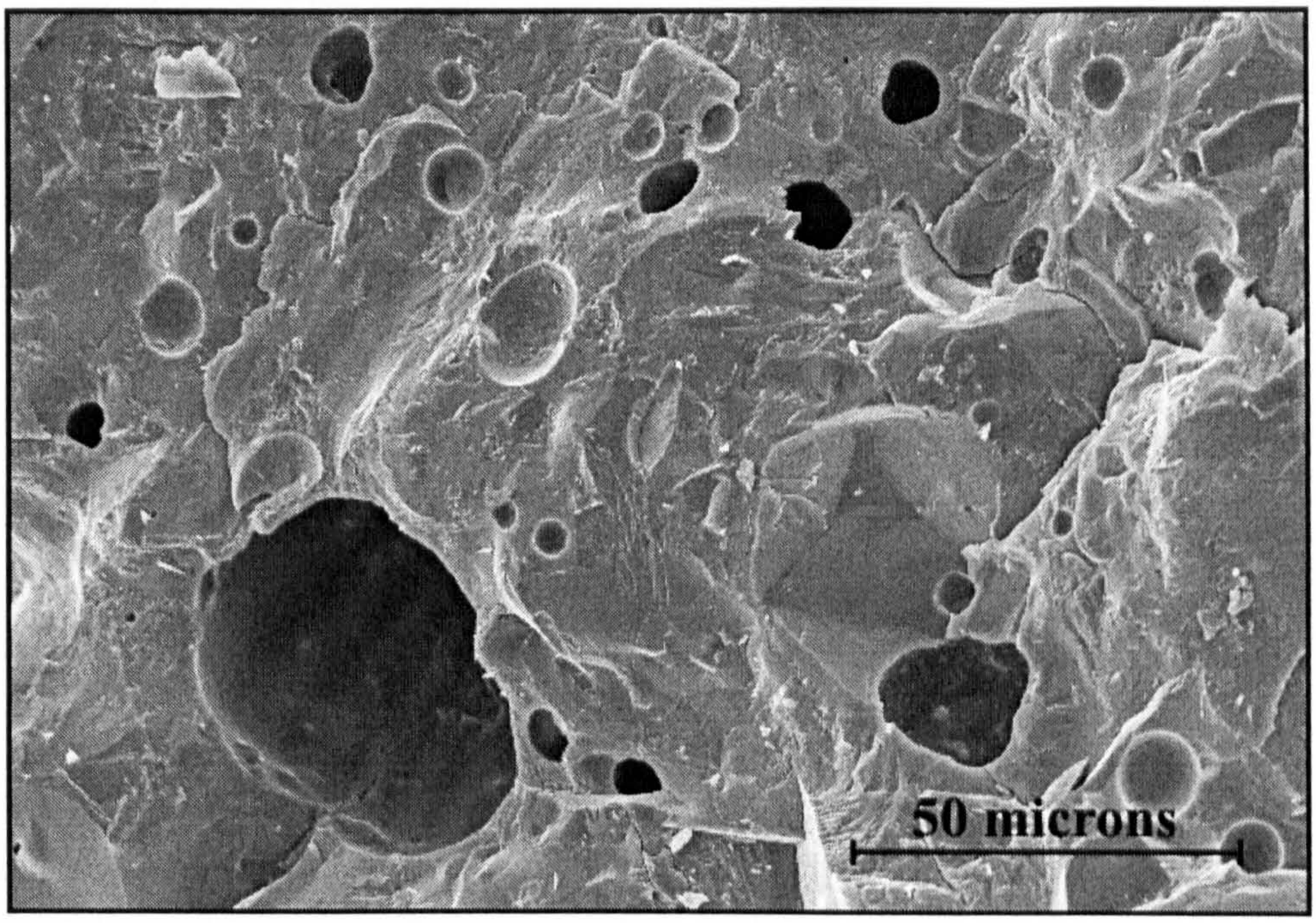

Figure 6.24 Secondary electron image of the synthetic aggregate fired at 1,110°C with 20 minutes sintering time.

6.7 Backscattered electron image and image histogram for synthetic aggregate

Many features presented on the backscattered electron image (BSE image) can be distinguished on the basis of differences in their grey level which depends on their average atomic number. Each pixel on the BSE image contains the brightness value, ranging from 0 (black) to 255 (white), of the feature at that particular location and they can be presented as the diagram which plots the number of pixels as a function of their brightness values. Each peak appearing on this histogram corresponds to a region which has a similar average atomic number. Typical BSE images and their grey-level histogram for the green pellet and synthetic aggregate fired at different temperatures and sintering periods are shown in Figures 6.25 to 6.28. Typically, there are four peaks presented on the histogram which represent the following four different phases: pores, quartz, feldspar and mica. The pore space filled with a low atomic number epoxy resin appears as a dark area in the BSE image (first left peak in the grey level histogram). The medium grey value as indicated on the histogram is quartz and it therefore appears as a dark grey region on the BSE image. The grey value of the feldspar minerals depend on their chemical composition. For example, the plagioclase feldspar will appear slightly brighter than quartz due to a slightly higher grey value, while the potassium rich feldspar (alkali feldspar) will appear as a light grey region on the BSE image which is represented on the histogram by the peak located adjacent to the quartz peak. Without using the X-ray analysis, the differentiation between quartz and plagioclase feldspar using the difference in grey color is very difficult. The second brightest area represents the mica mineral. Due to a very low concentration of this mineral, its peak as presented on the histogram, in some cases becomes difficult to distinguish. The brightest areas represented by the right most peak in the histogram belong to the minerals that have higher mean atomic number like calcite or iron oxide.

For the histogram of a micrograph for a green pellet, there is another small broad peak located adjacent to the porosity peak. This peak represents a very small mineral whose size is less than the resolution of the BSE image. The resolution of the BSE images is defined by the area on the specimen surface from which the backscattered electrons can emerge (Fen 2000). By using the Monte Carlo simulation, the resolution of the BSE image with the acceleration voltage of 10 keV for the quartz or feldspar sample is about 1.5 microns. The minerals that could have size less that this value are

quartz and kaolinite which can be seen as very small flaky particles as shown in Figure 6.18. On the other hand, this peak might also represent any pixels on the BSE image that cover the region having very small pores which have a size less the image resolution. Therefore, any pixels on the BSE image that represent these minerals or pores will contain a combination of brightness values between these minerals and the epoxy filled pores. It was found that the height of this peak reduces with an increase in temperature and sintering time, as shown in Figures 6.26 to 6.27. It is believed that this reduction, when the firing temperature increases to 1,110°C, is due to the coalescence of very small particles which leads to an increase in the particle and pore size. This peak was found to disappear at 1,110°C with 10 minutes sintering time (Figure 6.28), which was probably because most of the very small pores (micropores) became filled by the liquid phase.

These grey level histograms are a very important tool for the segmentation of the image which is the first very important step in the quantitative image analysis. This process can be accomplished by defining a range of brightness or grey values in the original image of any features of interest in order to produce a segmented image. However, only porosity is considered in this study and a more detailed explanation of the porosity segmentation technique is given in section 5.3.2.3.

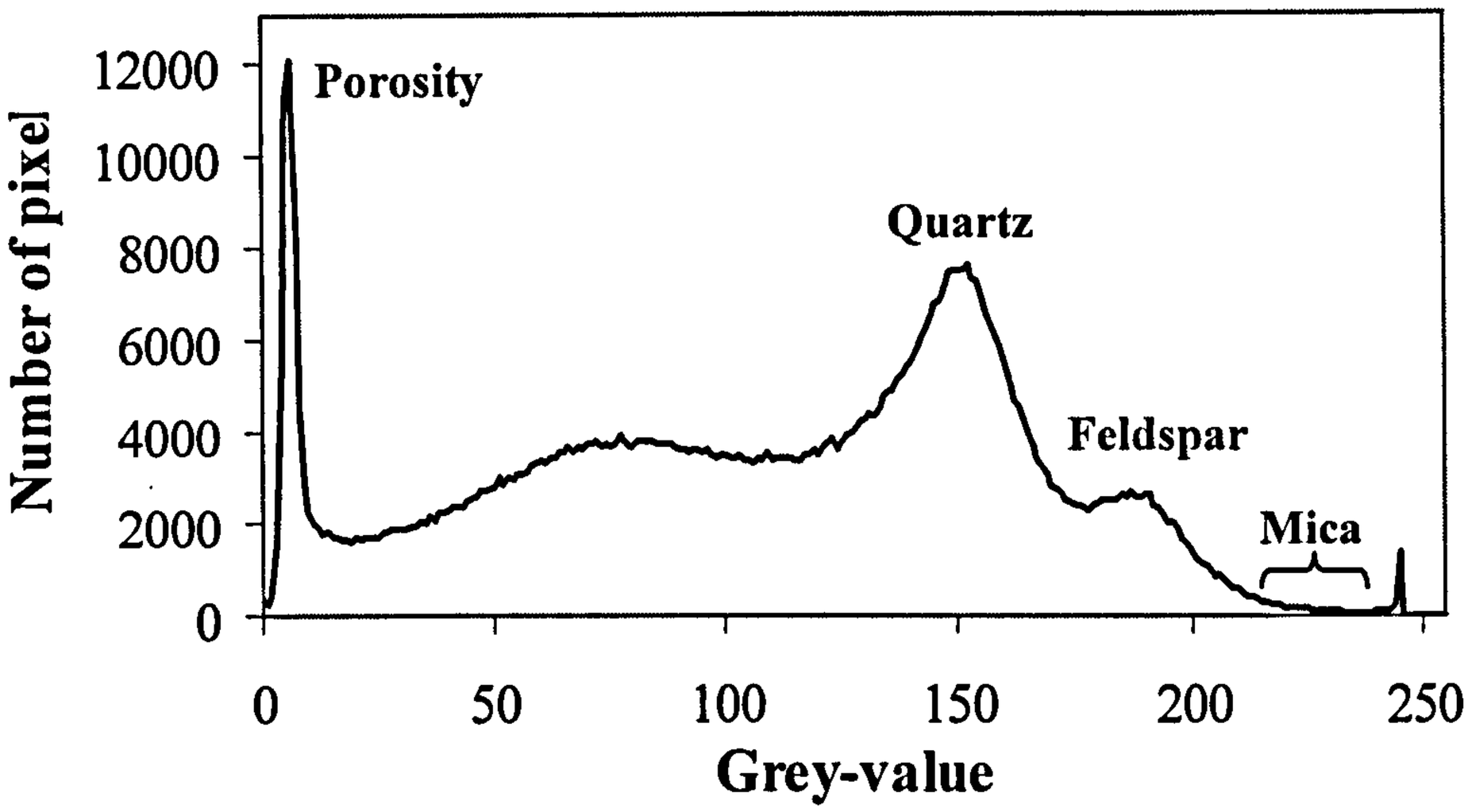

Figure 6.25 Grey-level histogram of the green pellet. The BSE image was captured at the magnification of 150x.

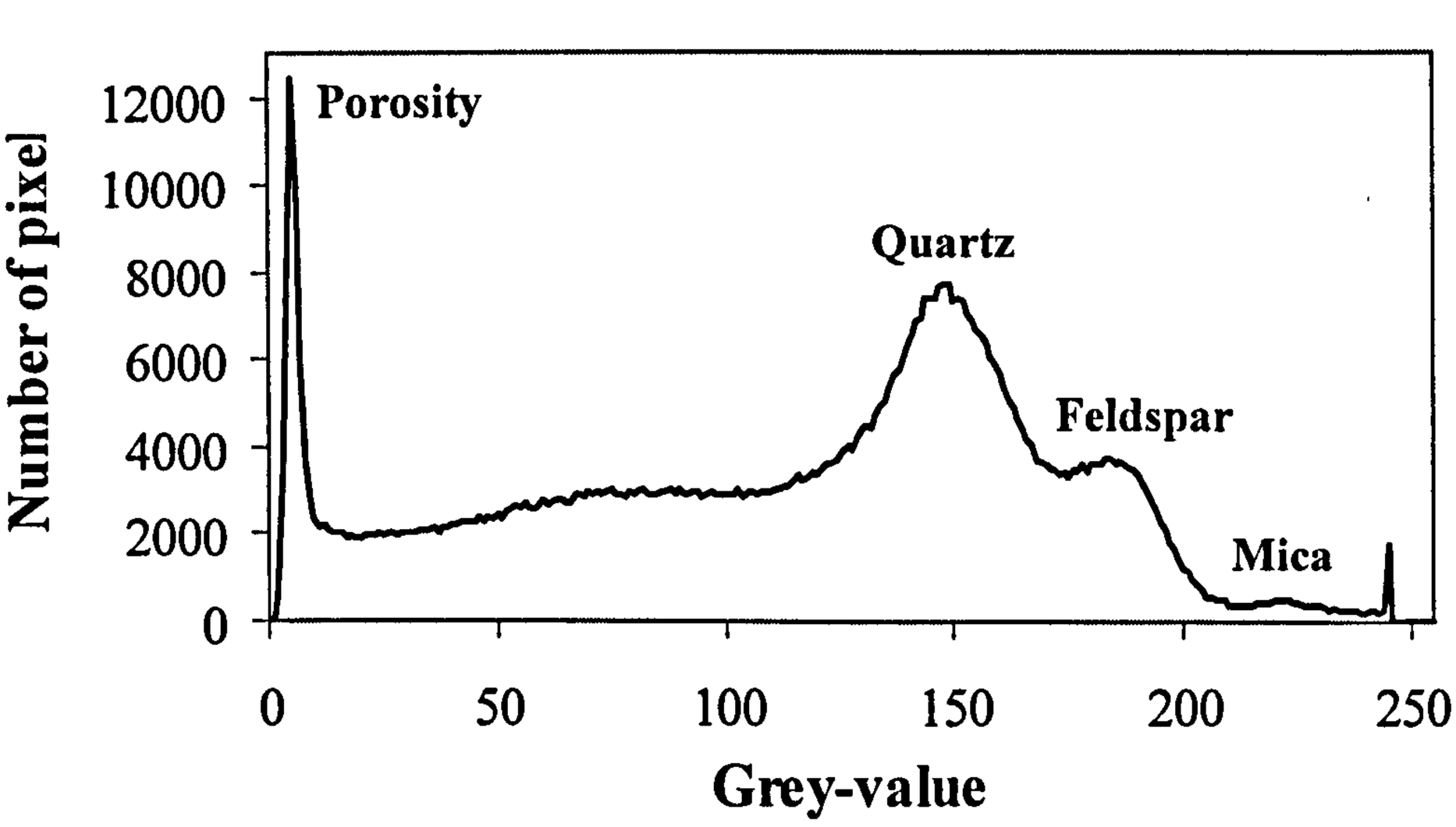

Figure 6.26 Grey-level histogram of the synthetic aggregate fired at 900°C with 0 minute sintering time and the BSE image was captured at the magnification of 150x.

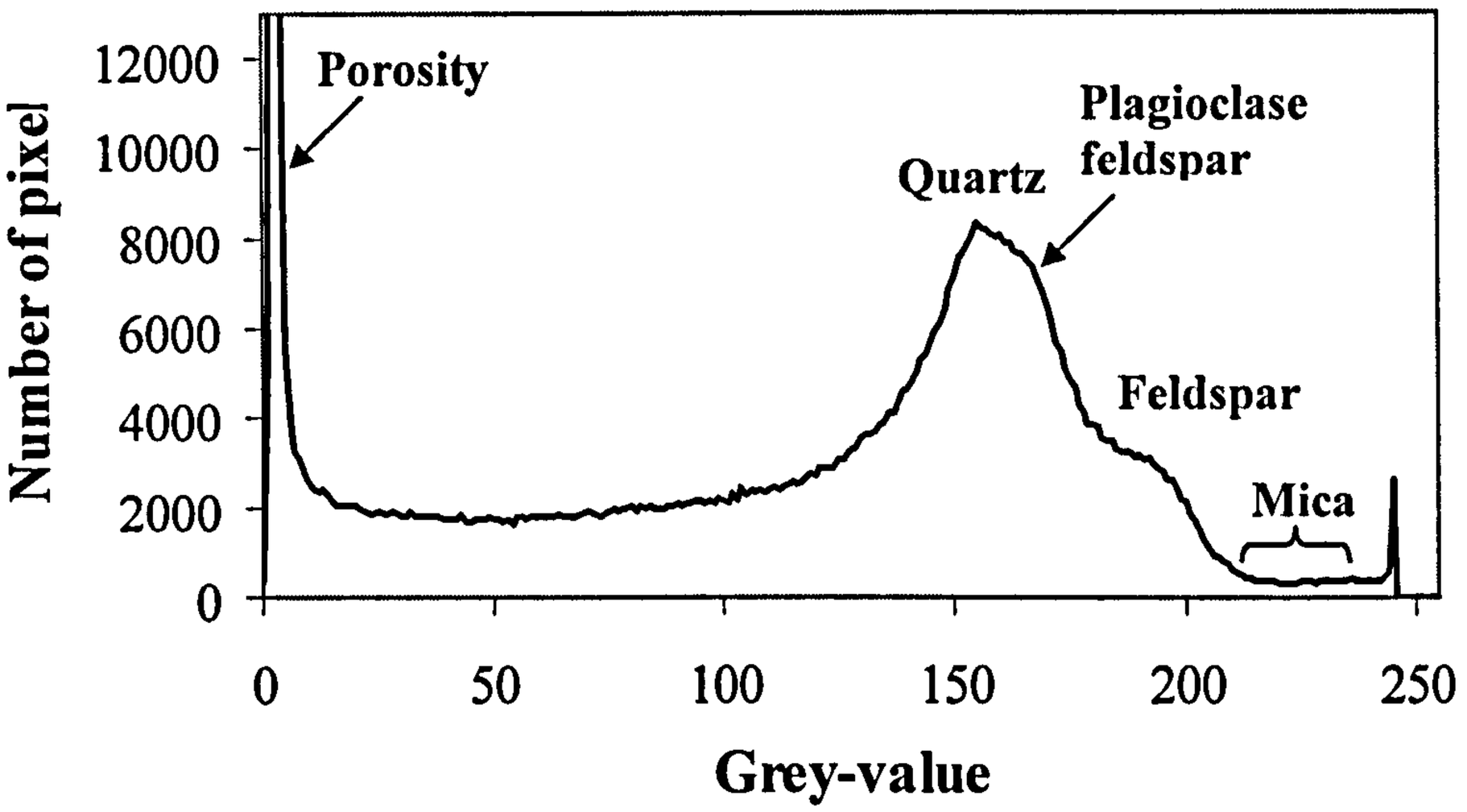

Figure 6.27 Grey-level histogram of the synthetic aggregate fired at 1,110°C with 0 minute sintering time. The BSE image was captured at the magnification of 150x.

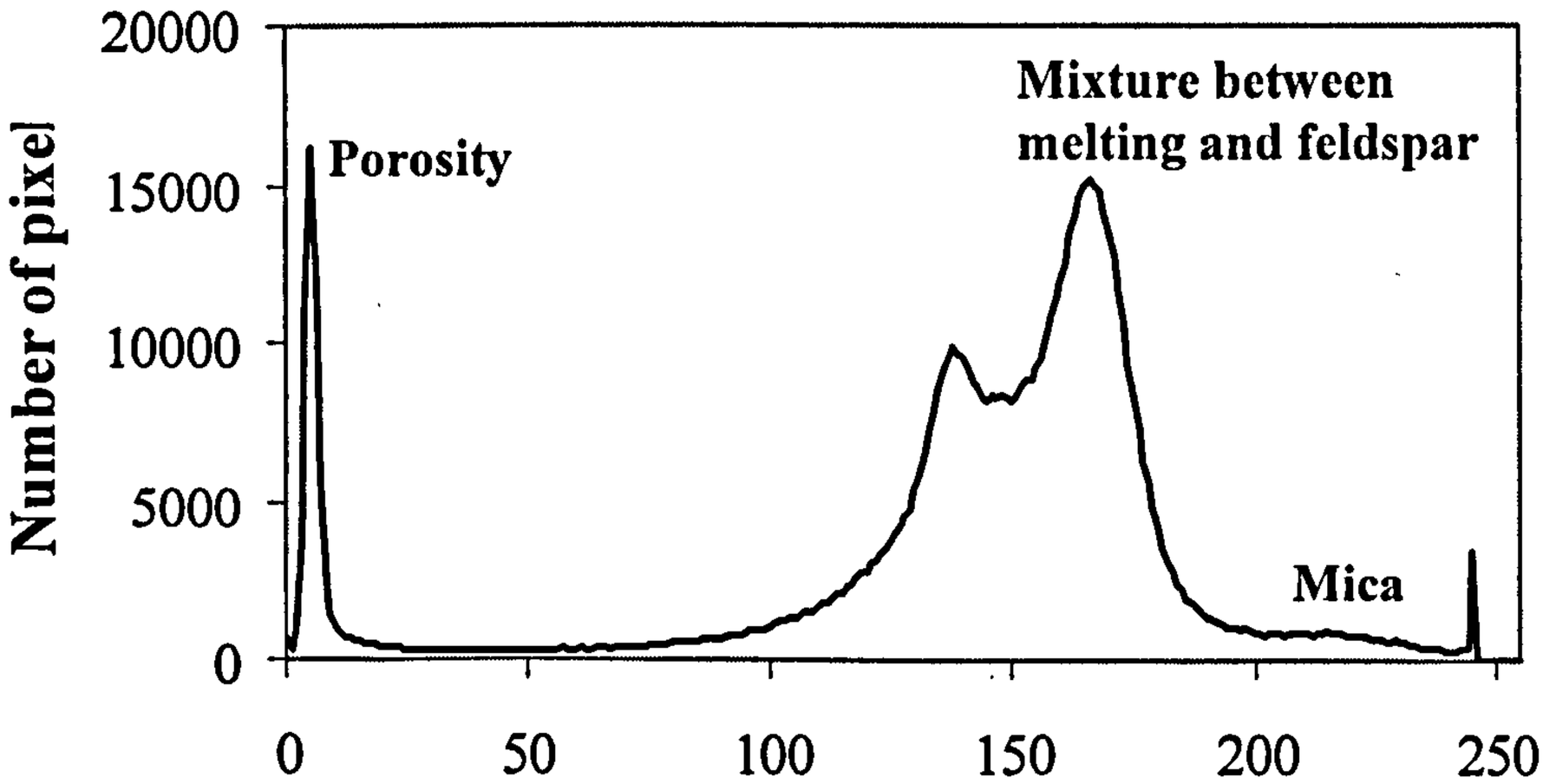

Figure 6.28 Grey-level histogram of the synthetic aggregate fired at 1,110°C with 10 minutes sintering time. The BSE image was captured at the magnification of 150x.

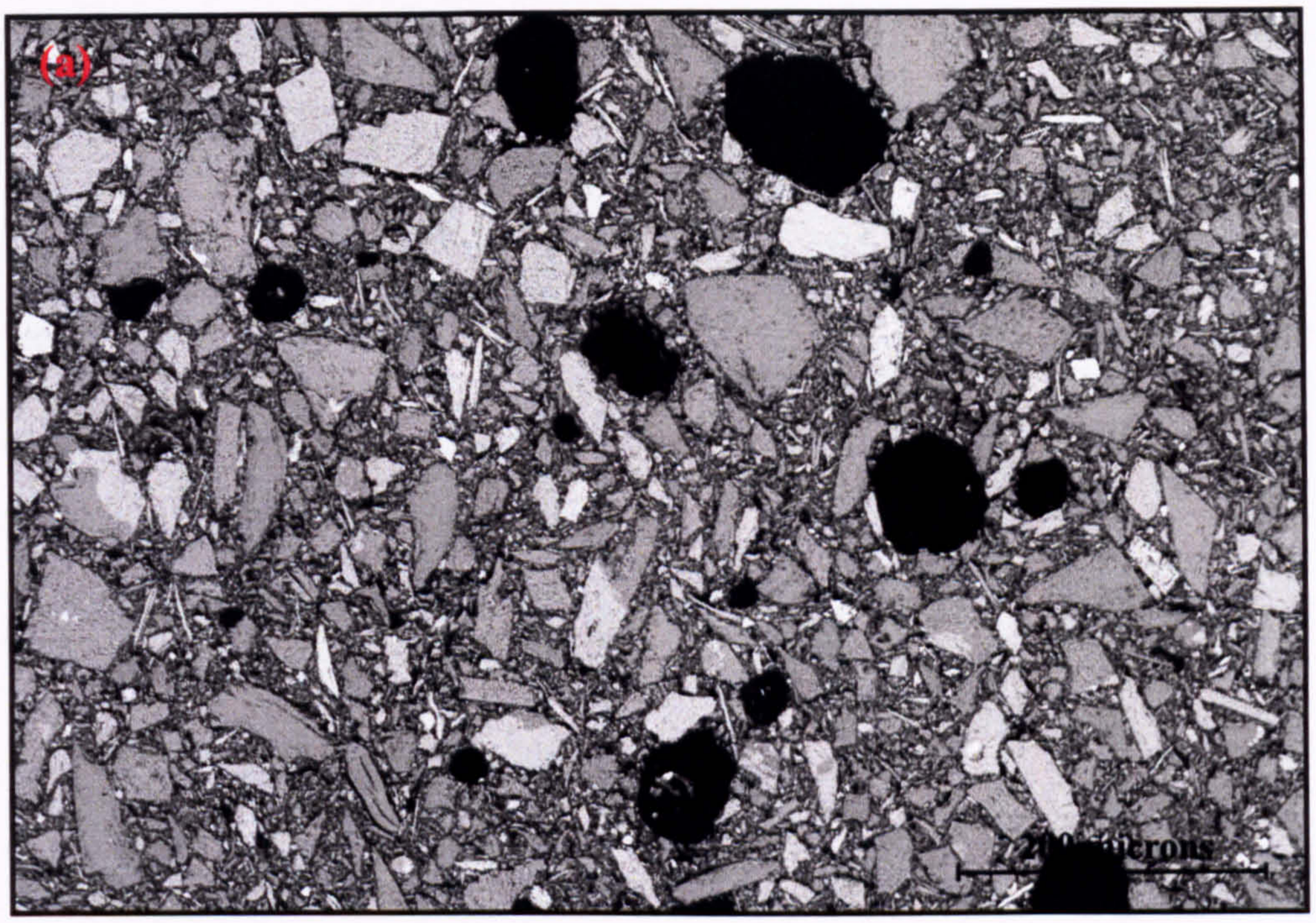

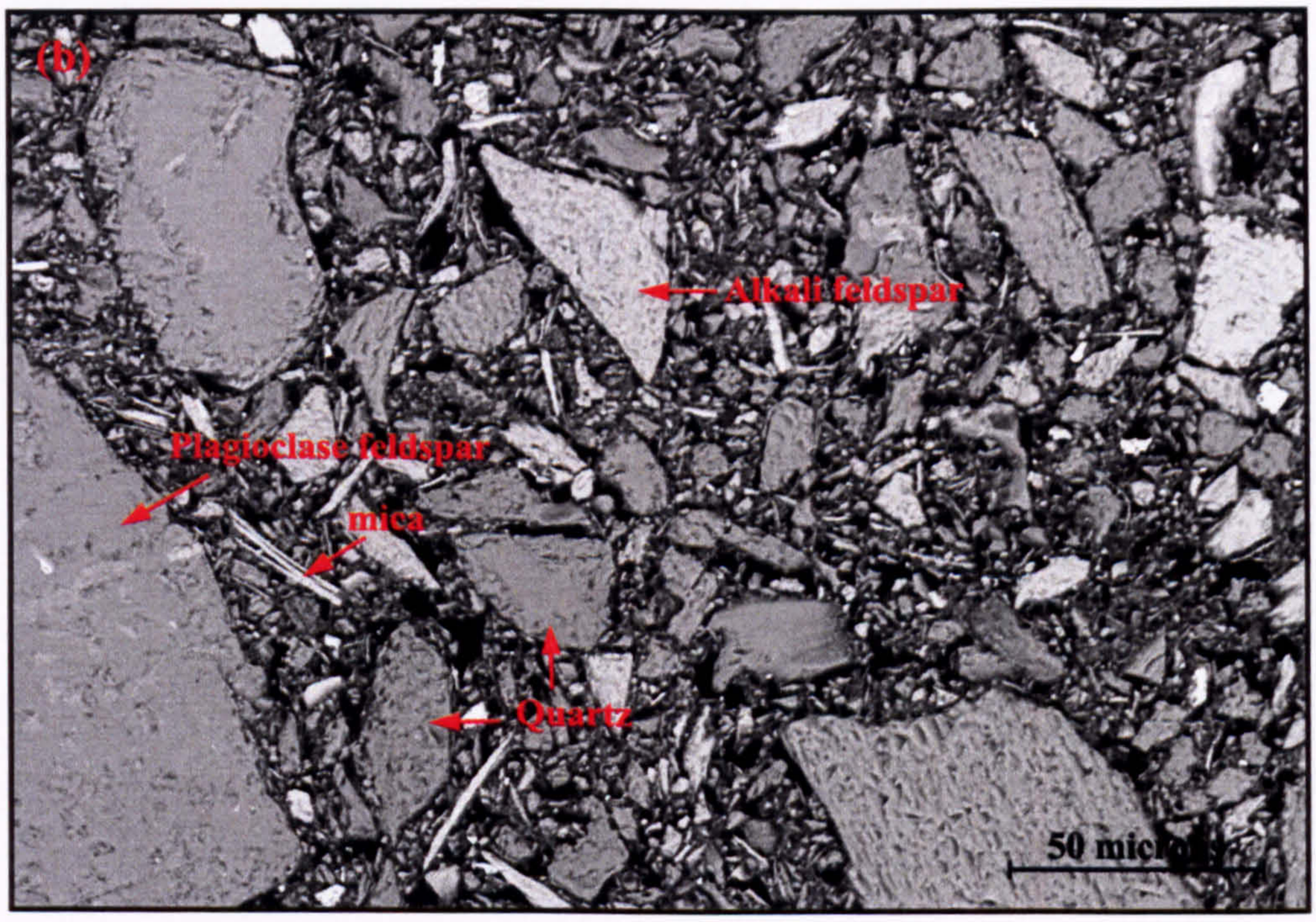

Figure 6.29 BSE images of the green pellet produced from 95 percent of Grensanda quarry waste and 5 percent of Ball clay. (a) Image captured at 150x magnification, (b) Image captured at 500x magnification.

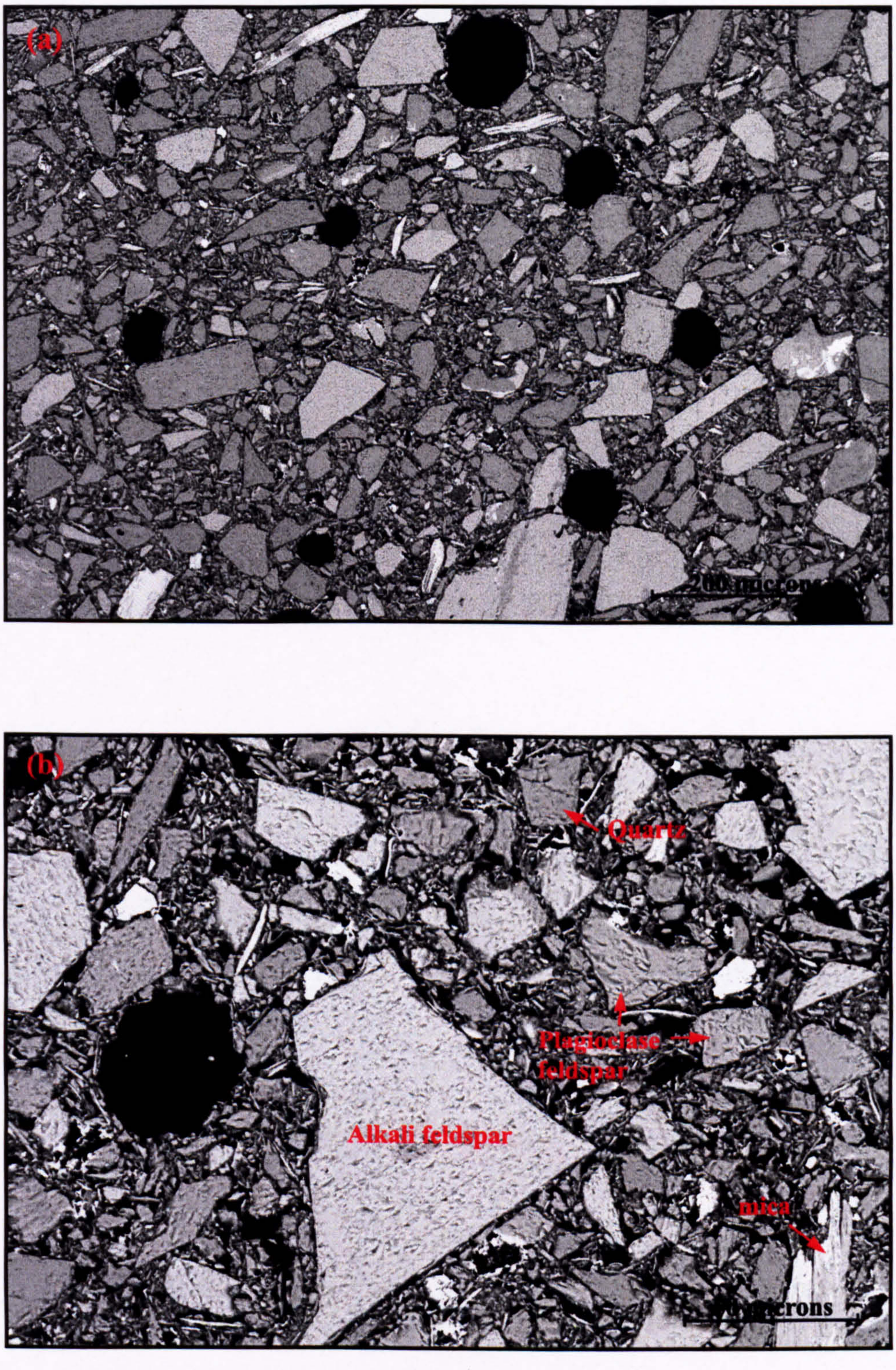

Figure 6.30 BSE images of the synthetic aggregate produced from 95 percent of Grensanda quarry waste and 5 percent of Ball clay and fired to 900 ˚C. (a) Image captured at 150x magnification, (b) Image captured at 500x magnification.

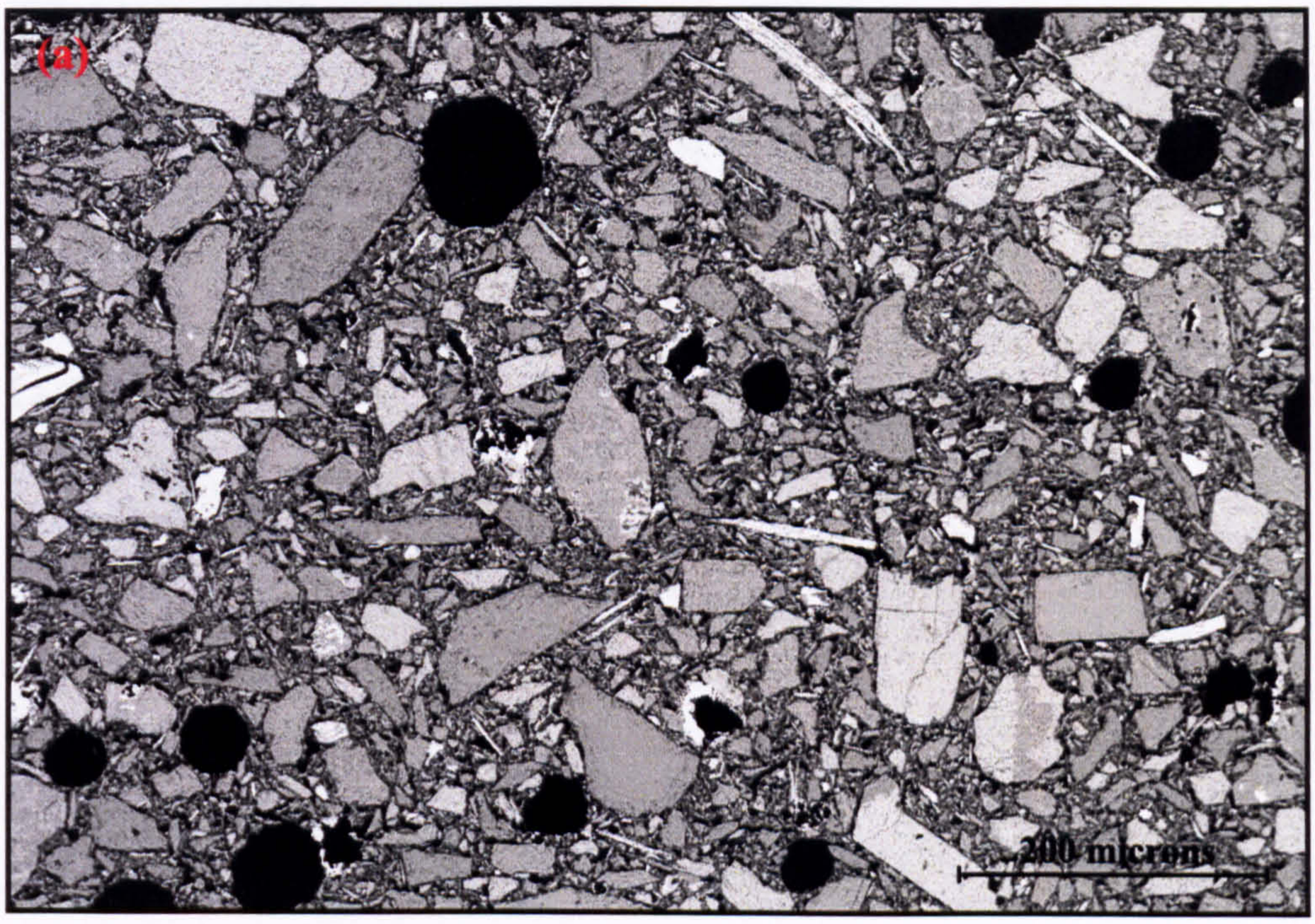

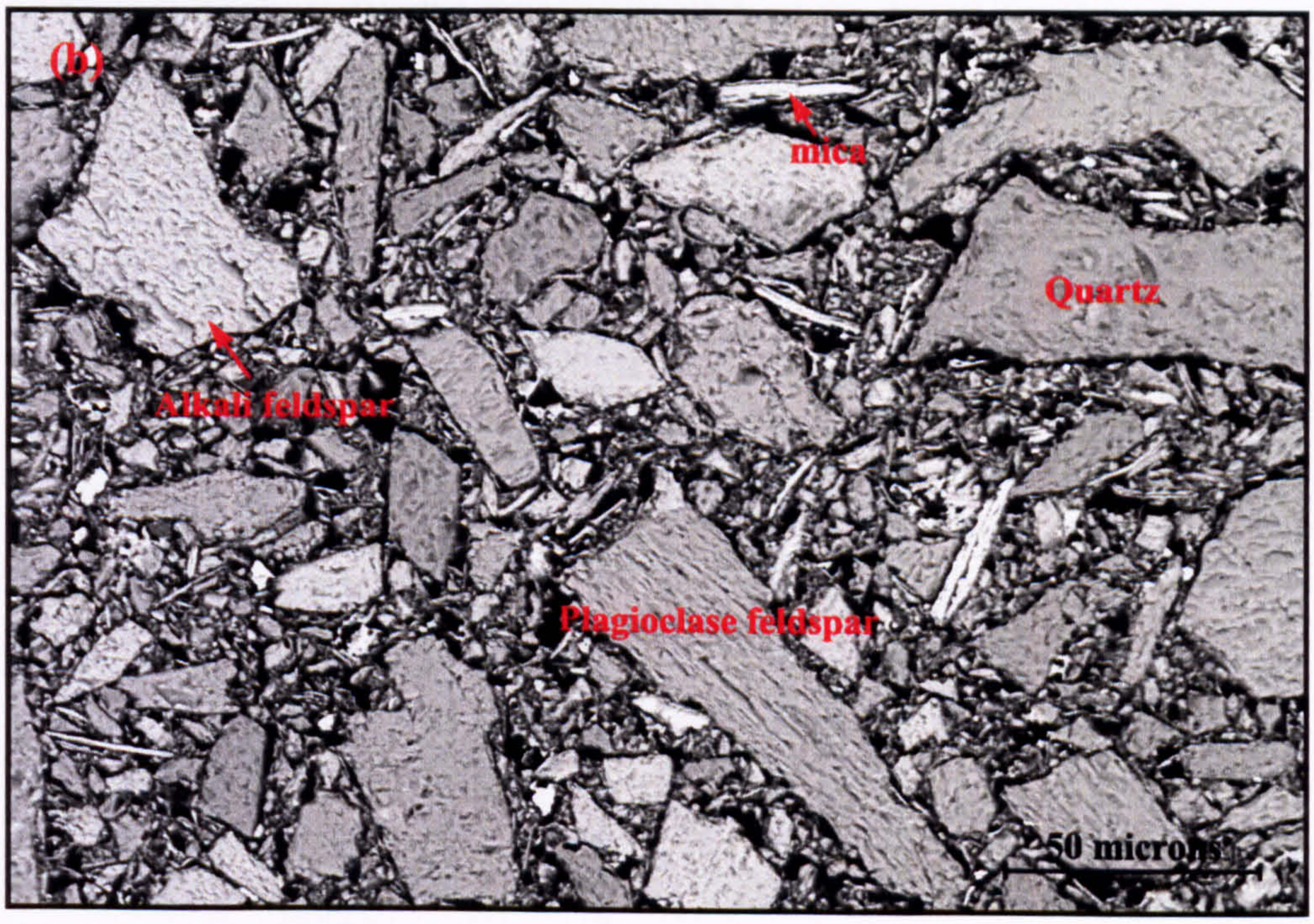

Figure 6.31 BSE images of the synthetic aggregate produced from 95 percent of Grensanda quarry waste and 5 percent of Ball clay and fired to 1000 °C. (a) Image captured at 150x magnification, (b) Image captured at 500x magnification.

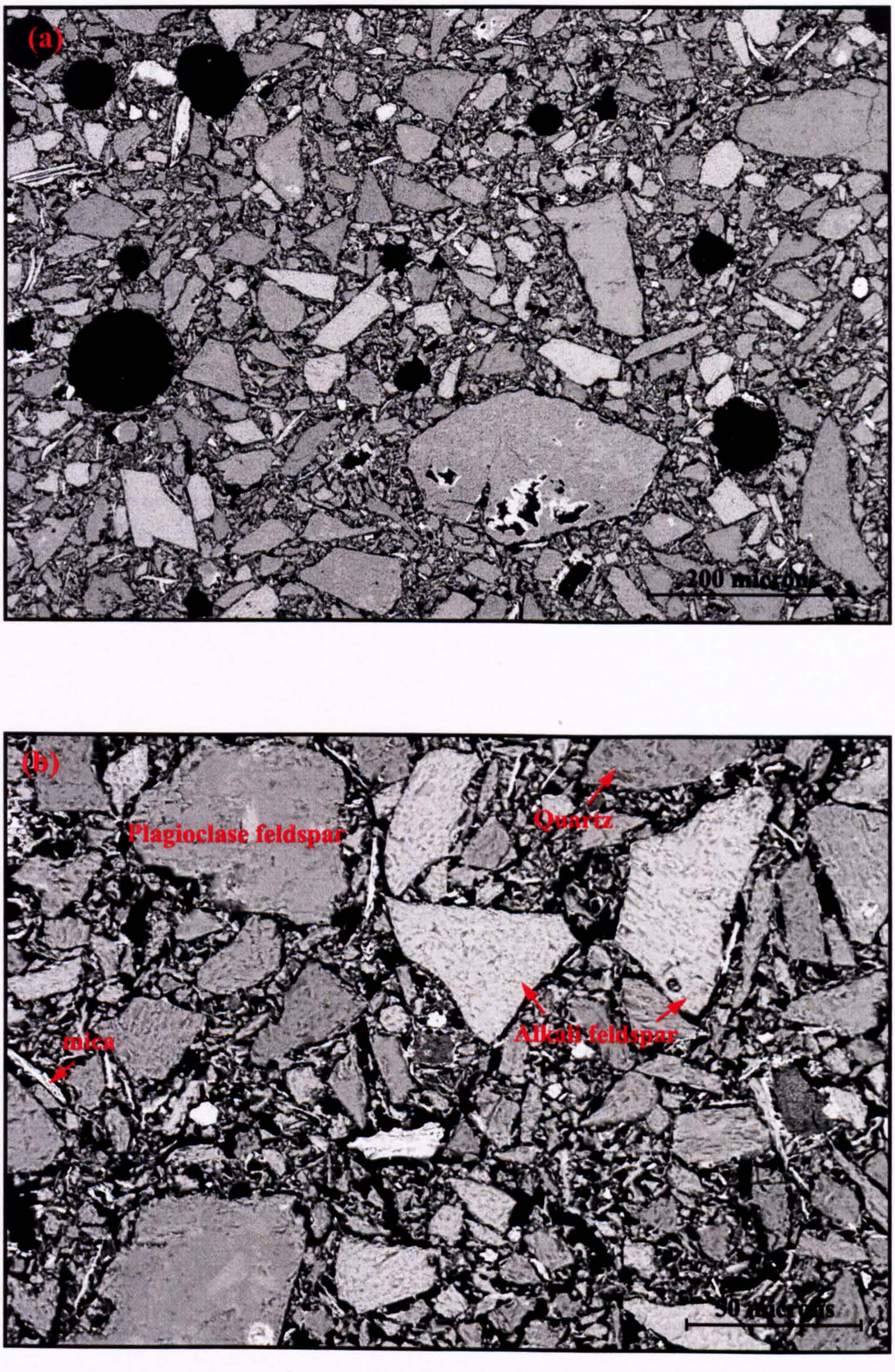

Figure 6.32 BSE images of the synthetic aggregate produced from 95 percent of Grensanda quarry waste and 5 percent of Ball clay and fired to 1110 °C. (a) Image captured at 150x magnification, (b) Image captured at 500x magnification.

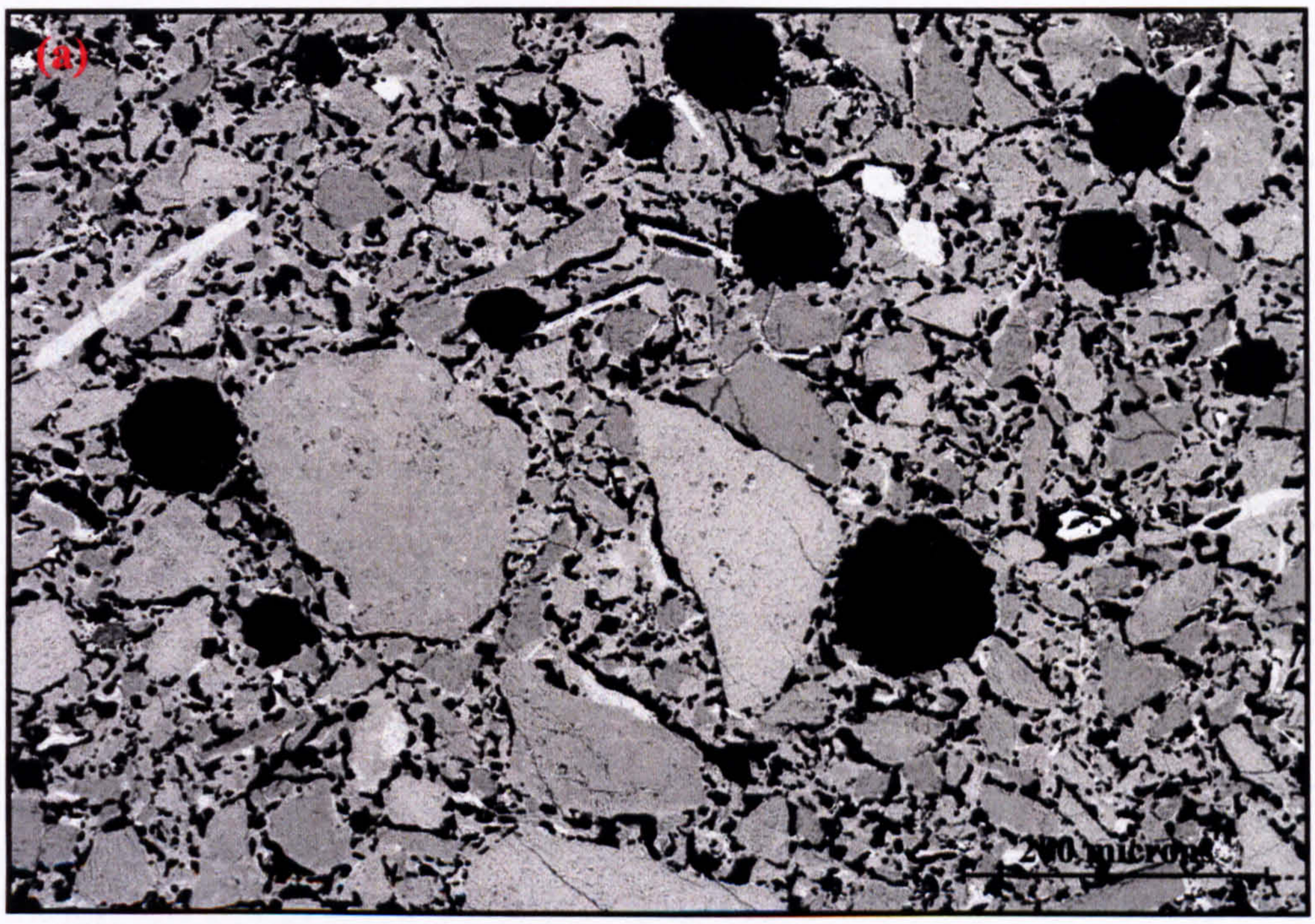

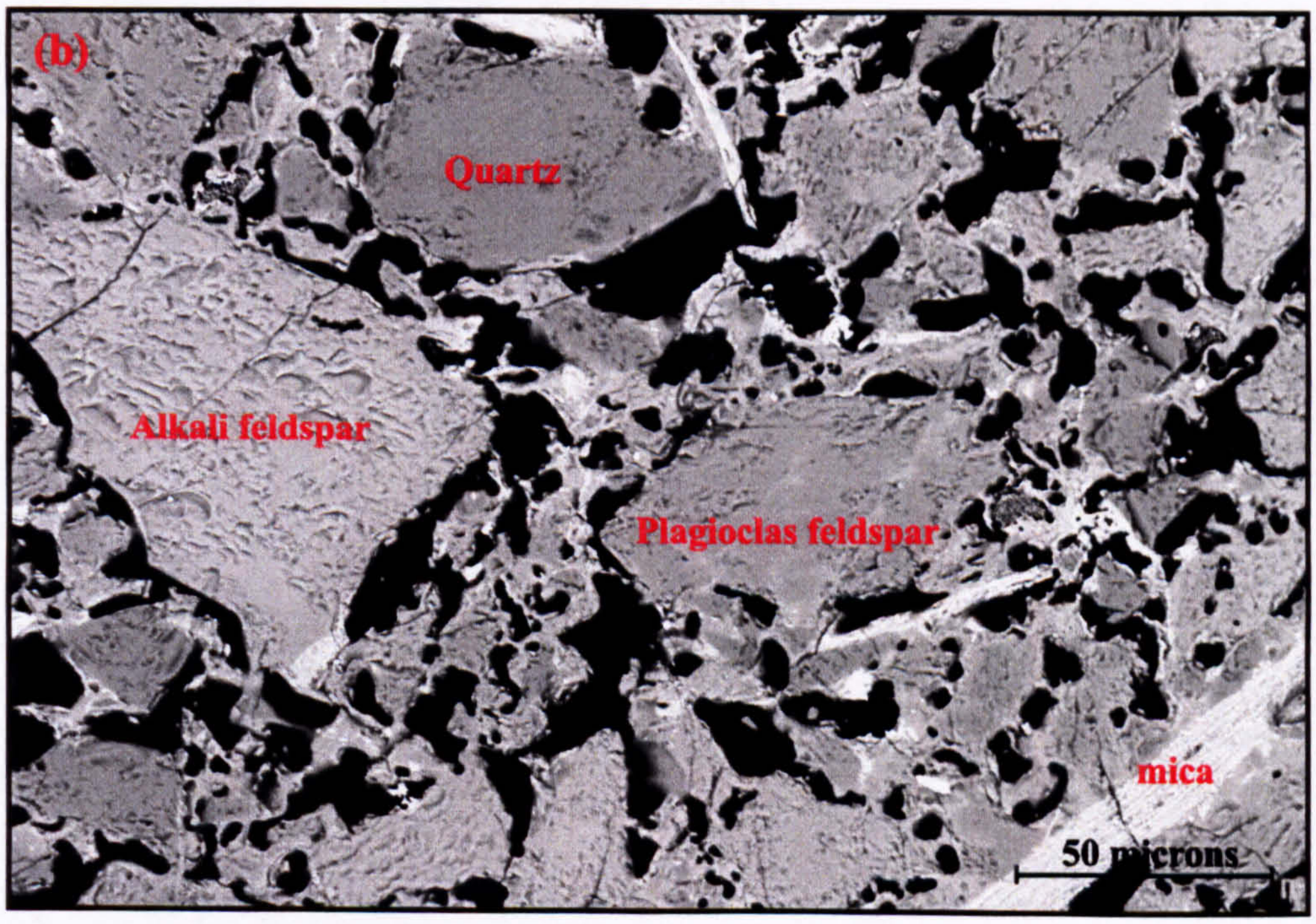

Figure 6.33 BSE images of the synthetic aggregate produced from 95 percent of Grensanda quarry waste and 5 percent of Ball clay and fired to 1110 ˚C with 5 minutes sintering period. (a) Image captured at 150x magnification, (b) Image captured at 500x magnification.

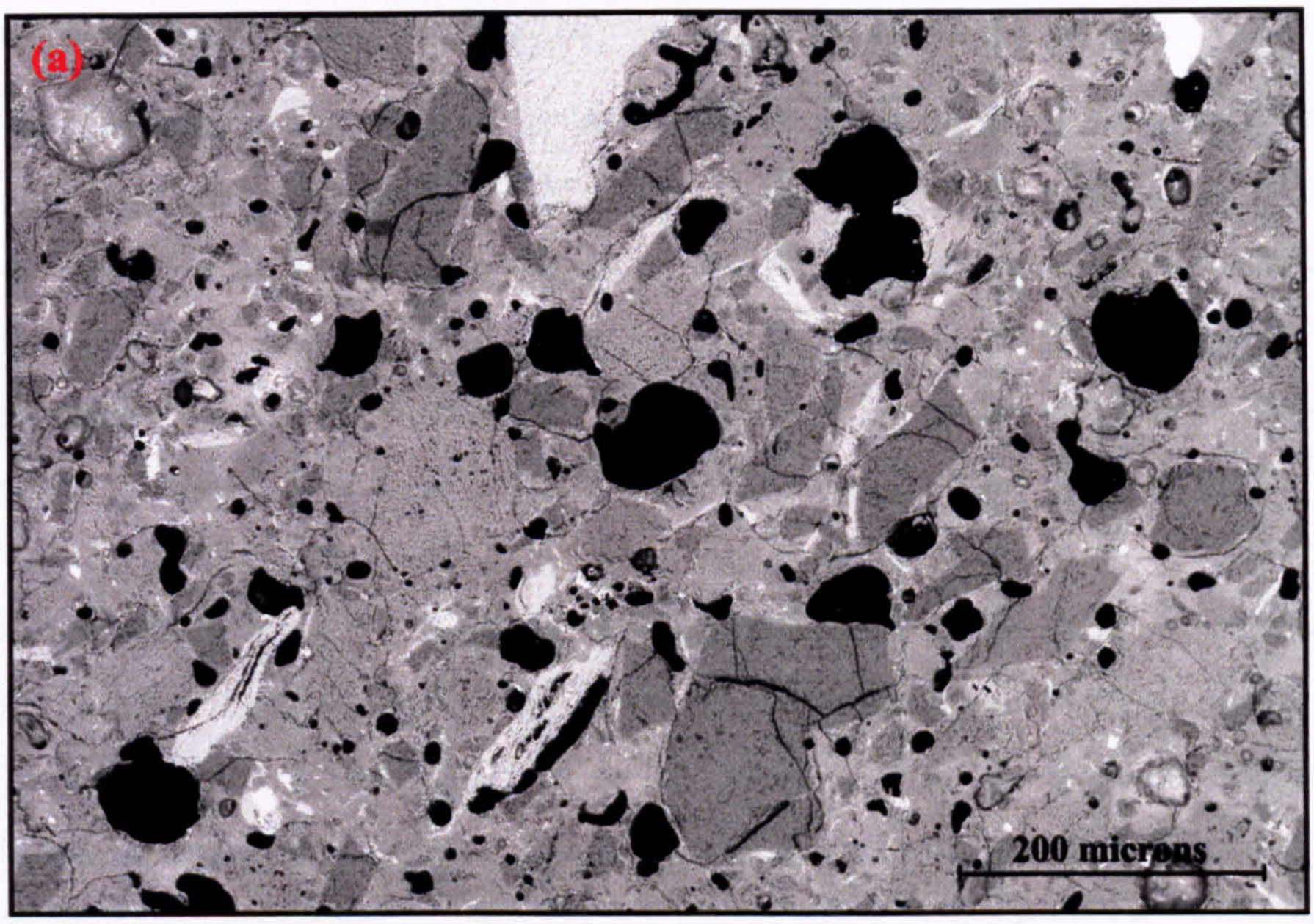

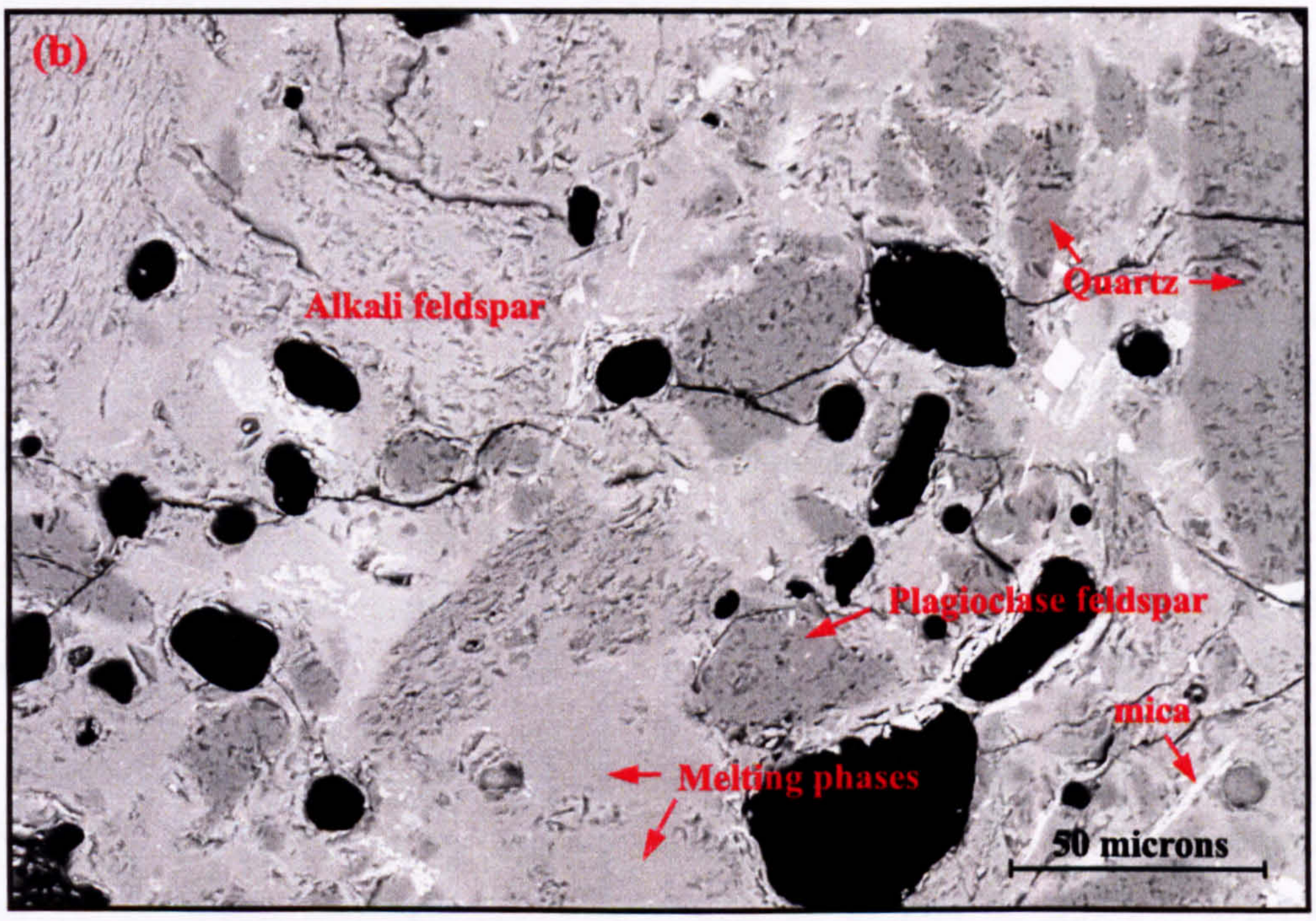

Figure 6.34 BSE images of the synthetic aggregate produced from 95 percent of Grensanda quarry waste and 5 percent of Ball clay and fired to 1110 ˚C with 10 minutes sintering period. (a) Image captured at 150x magnification, (b) Image captured at 500x magnification.

6.8 Pore structure of synthetic aggregate by image analysis technique

In this section, the porosity of the synthetic aggregate fired at different firing conditions was analyzed by the SEM-image analysis technique. The images were acquired from the resin impregnated, flat-polished samples. Two different magnifications were used in this investigation. This made it possible to analyze two different types of pores which had very different sizes, i.e. macro and micro porosity. The macro porosity is defined as the large pore size (pores which have areas approximately greater than 100 μm^2). It was found that these pores already existed in the green pellet (see Figure 6.29(a)). In addition, most of these pores are approximately spherical in shape (see Figures 5.13 or 6.29(a) to 6.34(a)) which suggests that they possibly come from the entrapped air in the matrix of the plastic mass during the pelletisation process. The micropores are very much smaller pores compared to the macropores and these pores are formed due to spaces between particles. It should be noted that a flaw formed during the rolling of the plastic mass at the pelletisation process (Figure 6.14) is not considered in this analysis.

The selection of the magnification is very important in the SEM analysis. It is a compromise between the resolution or the details required of the features of interest and the number of images that are required to obtain a representative result. It was discovered that the magnification of 150x is an appropriate magnification for the macro porosity analysis and the magnification of 500x and 800x for the micro porosity analysis. It was found that the minimum magnification required to identify the micro porosity was 800x in the case of the green pellets and those fired at 900° and 1,000°C. At the higher firing temperatures at which pore coarsening occurred it was possible to use magnifications of 500x.

It is noted that in order to estimate the porosity of the synthetic aggregate, the fraction of the volume of the whole pellet occupied by the pore was assumed equal to the area fraction measured from the two dimensional section. In addition, a sufficient number of images must be checked so that the average area fraction of a pore is representative of the whole pellet. For each sample, the images were randomly captured and this was done by scanning across the specimen surface in the grid line pattern. If any artifacts or flaws on the specimen surface were observed in the image field, the field

was then shifted horizontally until a good area was obtained. The porosity of the synthetic aggregate was then obtained by averaging two samples for both types of pore and 40 and 60 images were found sufficient to give a representative result for the macro and micro porosity respectively.

Table 6.11 Porosity of the synthetic aggregate

Pellet condition	Porosity (%)		
	Macro porosity	Micro porosity	Total porosity
900°C	6.44	16.83	22.18
1000°C	7.67	17.15	23.51
1110°C, 0 min.	10.22	24.39	32.13
1110°C, 1.5 min.	8.80	24.52	31.25
1110°C, 5 min.	9.22	14.94	22.79
1110°C, 10 min.	-	-	14.53

The results of the area fraction measurement of the synthetic aggregate at different firing conditions are given in Table 6.11. Only detectable pores which have a pore size greater than the resolution of the BSE image were investigated. The area percentage of the macropore was found to range from about 6 to 10 percent. A standard statistical approach, i.e. the Johnson and Saltykov method (Underwood 1968), was applied in order to determine the size distribution of these pores and their pore size distribution for the synthetic aggregate fired at 900°, 1,000° and 1,110°C sintering temperature with 0 minute sintering time are shown in Figure 6.36. It was found that these macropores have sizes ranging from about 20 to 120 microns.

The micro porosity results show a slight increase from 900° to 1,000°C. At 1,110°C with 0 minute sintering time, there is a big increase in porosity compared to 1,000°C. These results indicate the occurrence of pore coarsening which support the results from MIP analysis (see Figure 6.15). In addition to the particle size distribution effect mentioned earlier, a more likely explanation for this pore coarsening is that the water vapor from the dehydroxylation process of mica developed a pressure which consequently pushed each particle apart but the gas pore was not observed because the amount of liquid phase was insufficient to entrap the water vapor. Another possibility is the decomposition of the very fine particle which will then free the pore between particles. Sintering especially at the tip or the sharp edge of each particle was visually

observed at this temperature (1,110°C) by using a higher magnification images (Figure 6.21).

There was a big reduction in the micro and total porosity at the 5 minutes sintering time. These results agree with the MIP results and indicate that vitrification started at some time between 1.5 and 5 minutes sintering period in which some pores and/or cavities in the fired pellet were filled with the melting phase and this process progressed further for a longer time period. At 10 minutes sintering time, with an increase in the amount of melting phase, most of the micropores were filled as can be seen in Figure 6.23, while the macropores still exist. It is noted that only total porosity was considered at this firing condition because it was very difficult to discriminate between the macropore and the bloating pore. In addition, most of the micropores were already filled by the melting phase and, therefore, the remaining pores consist primarily of the macropores and the bloating pores. Even though there was no macropore information for the 10 minutes sintering time, the amount of these pores can be approximated by using the average value from the other four cases which is 8.47 %. Due to the fact that most of the micropores were filled by the melting phase, the difference between the total porosity and the macro porosity is, therefore, a reasonable approximation of the porosity that was created by the bloating process. The bloating porosity for synthetic aggregate fired at a sintering temperature of 1,110°C with 10 minutes sintering time is, therefore, about 6 % and this value is believed to increase with the increase in sintering time.

The total porosity results obtained from the image analysis compare well with the MIP results, as given in Table 6.10, except for the case of 900°C and 1000°C. This might be due to the resolution of the BSE images which may not be high enough. The pores with sizes less than about 1.5 microns will not be included in the porosity analysis. Most of the micropores for these two cases were found to be very small and it is very difficult to see them even at 1,000x magnification as shown in Figure 6.19(b) and 6.20(b).

In order to obtain the information about the pore size distribution based on the image analysis technique, all pores were sorted according to area and then each pore was assigned to one of the seven pore size classes ($\geq 1000\ \mu m^2$, $1000 > A \geq 500\ \mu m^2$,

500 > A ≥250 μm^2, 250 > A ≥100 μm^2, 100 > A ≥50 μm^2, 50 > A ≥25 μm^2 and A < 25 μm^2). The two largest pore size ranges mainly correspond with the macropores, whereas the remaining cover the micropores. The fractional amount of porosity from each pore size class contributing to the total porosity was then calculated. It is noted that the pore size measured from the two dimensional section might not be the actual size. Many standard statistical techniques for determining the particle size distribution from two dimensional section areas exist (Underwood, 1968). However, due to the assumption made in each technique, the existing techniques are only applicable for any pores which have very simple geometrical shapes and distribution. Therefore they would not be suitable to use for any materials having a complex pore network like the micropores of the synthetic aggregate.

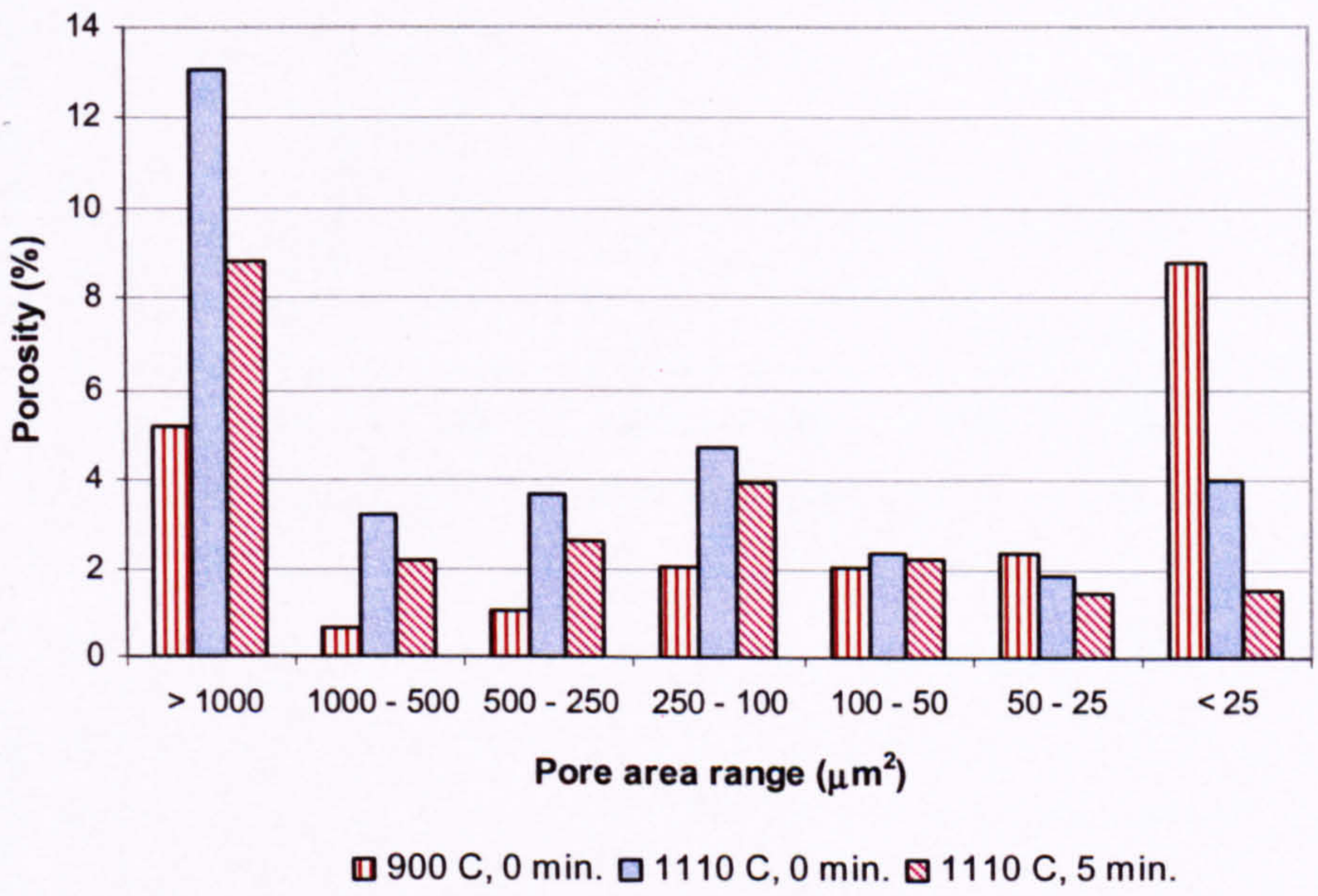

Figure 6.35 Contribution of pore size classes to the total porosity.

As shown in Figure 6.35, all samples display similar pore size distributions. The two left peaks in the histogram mainly represent the macropores, whereas the remaining peaks indicate the micropores. The results clearly show a reduction in the micropores that have a size less than 50 microns when both the temperature and the sintering period increase. The amount of micropores which have sizes ranging from 50 to 500 microns increase at 1,110°C with 0 minute sintering time. At 5 minutes sintering period with the

same temperature, the amount of this size pore reduced. These results elucidate the pore growth and densification process that occurs during the initial stage of sintering. Between 900° and 1,110°C, pore growth is the dominating process. This process reduces the amount of pores which have a size less than 50 microns and leads to an increase in the bigger pore size (50 to 500 microns). The densification process began to overcome the pore growth at some time between 0 to 5 minutes sintering time and lead to a reduction of all micropores.

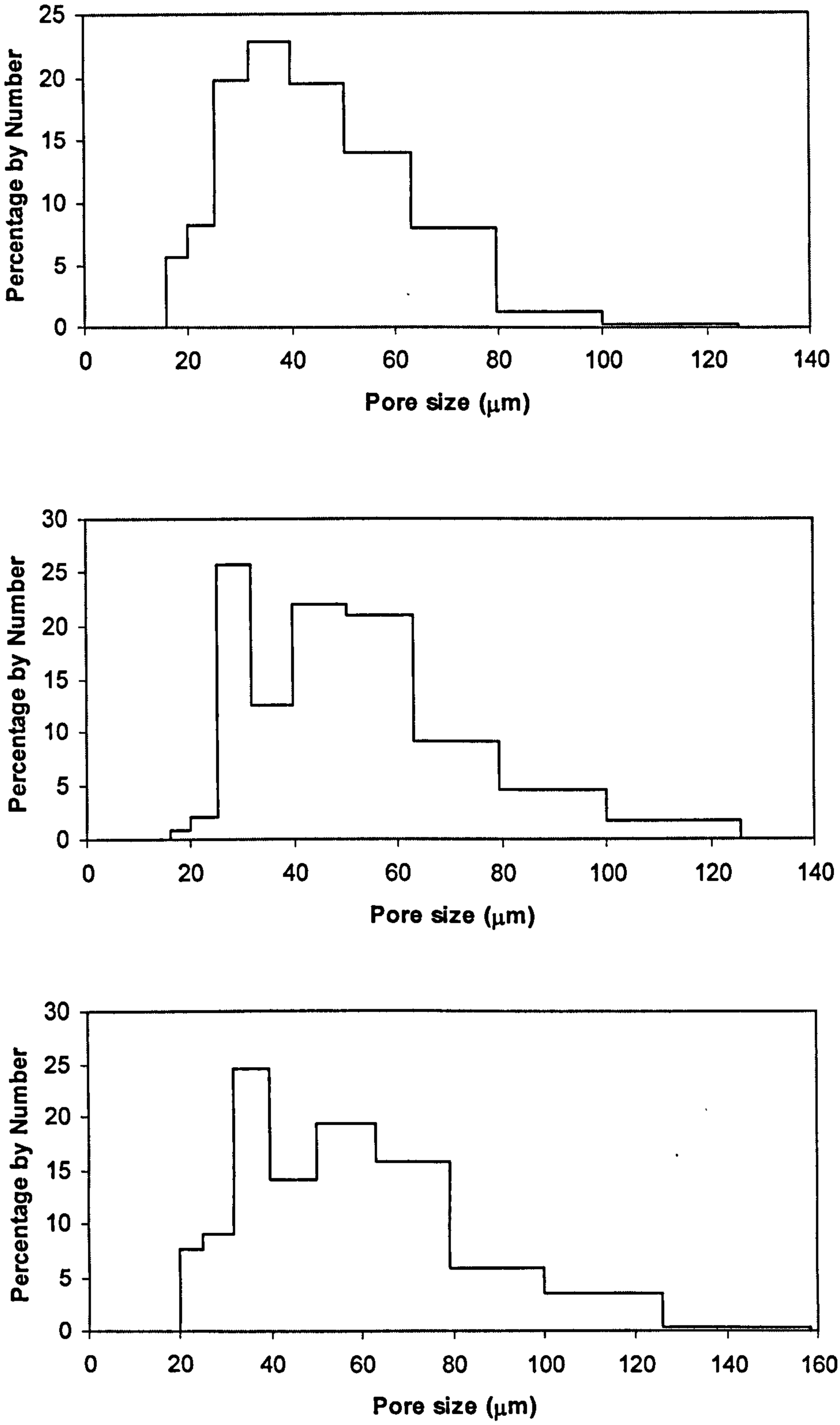

Figure 6.36 Pore size distribution for the synthetic aggregate by Johnson-Saltykov method: (a) 900° C with 0 min, (b) 1000° C with 0 min., and (d) 1110° C with 0 min.

6.9 Pore morphology analysis

In general, porosity has an adverse effect on the mechanical properties of a material, i.e. a porous sintered ceramic material has lower mechanical properties than one that has a dense structure. The influence of porosity on mechanical properties depends on many factors including quantity, interconnectivity, size, distribution and morphology of pores. The main objective of this section was to study the pore shape characteristics of the synthetic aggregate at different firing conditions and perform a qualitative investigation of the degree of pore connectivity, i.e. the higher degree of pore connectivity is likely to occur with complicated or irregular pore shapes. The BSE images of the resin impregnated and well-polished synthetic aggregate samples were analyzed by the image analysis techniques in order to obtain the shape parameter of the individual pores. All pores were sorted according to area and then each pore was assigned to one of the two and six pore size ranges of the macropores and micropores respectively (macropores: $A \geq 1000\ \mu m^2$ and $1000 > A \geq 500\ \mu m^2$; micropores: $A \geq 1000\ \mu m^2$, $1000 > A \geq 500\ \mu m^2$, $500 > A \geq 250\ \mu m^2$, $250 > A \geq 100\ \mu m^2$, $100 > A \geq 50\ \mu m^2$ and $50 > A \geq 25\ \mu m^2$). It is noted that any pores that appeared to be connected or touching the image boundary were not included in this analysis.

The f_{circle} and f_{shape} parameters were measured individually for each pore in order to reveal the pore shape characteristics of the synthetic aggregate upon firing. These two parameters have different meanings. f_{shape} is used to characterize the elongation of the pore, while its irregularity is quantified by the f_{circle} parameter (Puscas et. al. 2003). Both parameters have values ranging between 0 and 1. Pores that are elongated and irregular in shape will have a small value of f_{circle} and f_{shape}. On the other hand, if a pore's shape approaches a circle, both parameters approach unity. Figure 6.37 and 6.38 show some possible pore morphology in order to get a better picture of the effect of these two parameters on the pore shape.

Figures 6.39 to 6.42 represent the results of the macropore and micropore morphology of the synthetic aggregate fired to 1110°C with two different sintering times, i.e. 0 and 5 minutes. Each point represented on these Figures was the area average (Equation 5.12) within the same pore size class of the studied image and 60 images were used from two different samples. From the results presented here, it is

clear that the morphology of the micropores is more influenced by the sintering time than are the macropores. In the case of macroporosity (Figure 6.39 and 6.40), the range of values for f_{shape} is about 0.40 to 0.80 and is little affected by the sintering time. Values for f_{circle} range from about 0.05 to 0.60 and show a slight shift to the right as sintering time increases.

For the micropores on the other hand (Figures 6.41 to 6.42), there is a slight narrowing of the range for f_{shape} from 0.3 to 0.8 for 0 minute sintering time to 0.4 to 0.7 for 5 minutes sintering time. However, there is a significant increase in the range for f_{circle} from 0.0 to 0.2 (0 minute sintering time) to 0.1 to 0.7 (5 minutes sintering time).

From these results, it appears that the sintering time seems to have a greater effect on the irregularity of the micropores than on the elongation. Pores are more elongated and irregular with 0 minute sintering time. The data points move towards to the upper right corner of the diagram with a longer sintering period. This is because with 5 minutes sintering time, vitrification had started, the sample densified and the pores became rounder and less interconnected. In general, the mechanical properties of porous materials depend on the quantity, size, morphology, connectivity and distribution of pores. Regardless of the flaws created during the pelletisation process, synthetic aggregates that have a close and high density of irregular pores can expect to have lower mechanical properties when compared with one with round pores of the same quantity.

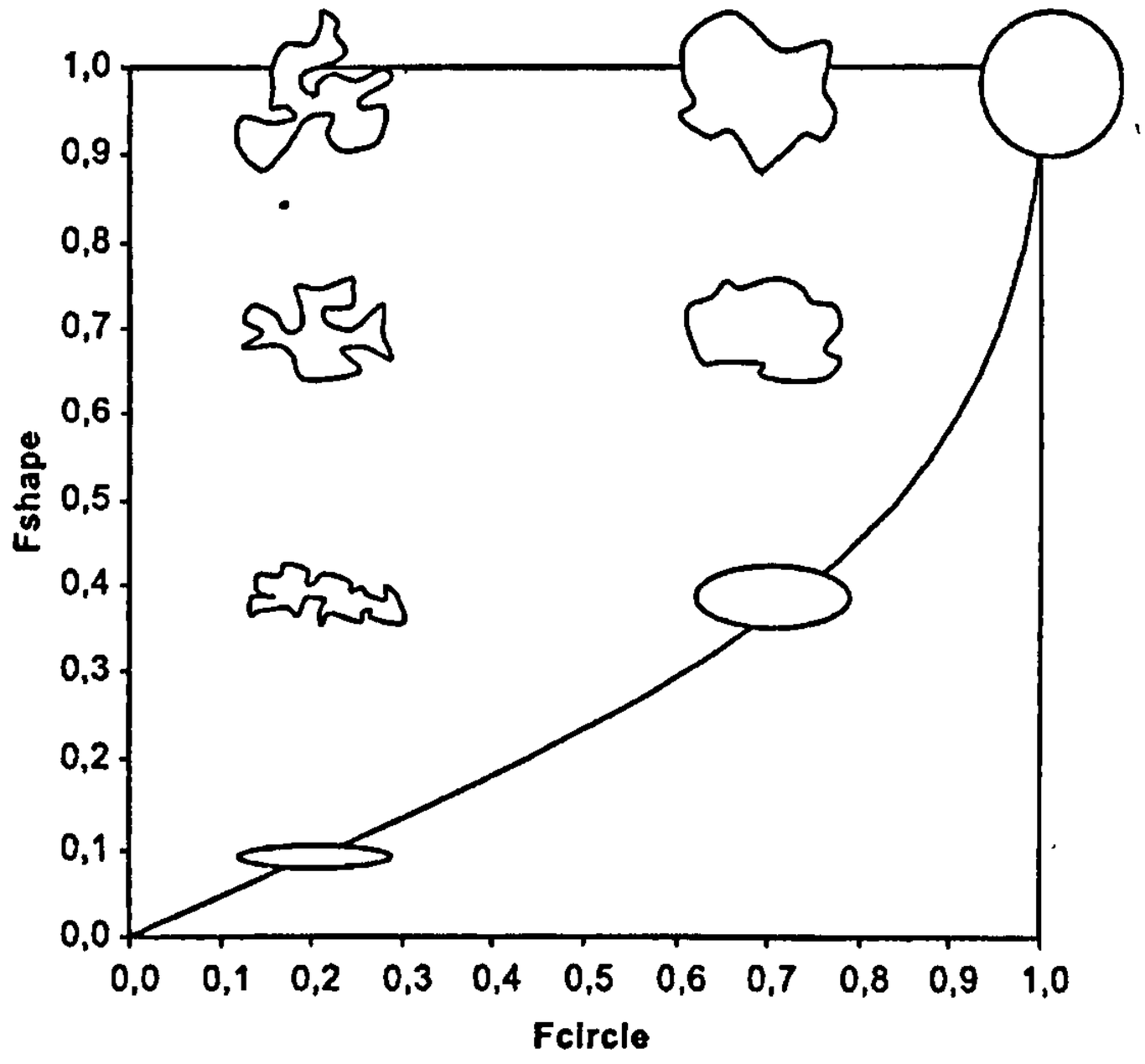

Figure 6.37 Example for some possible pore morphology in the f_{shape}-f_{circle} diagram (extracted from Puscas et. al. 2003).

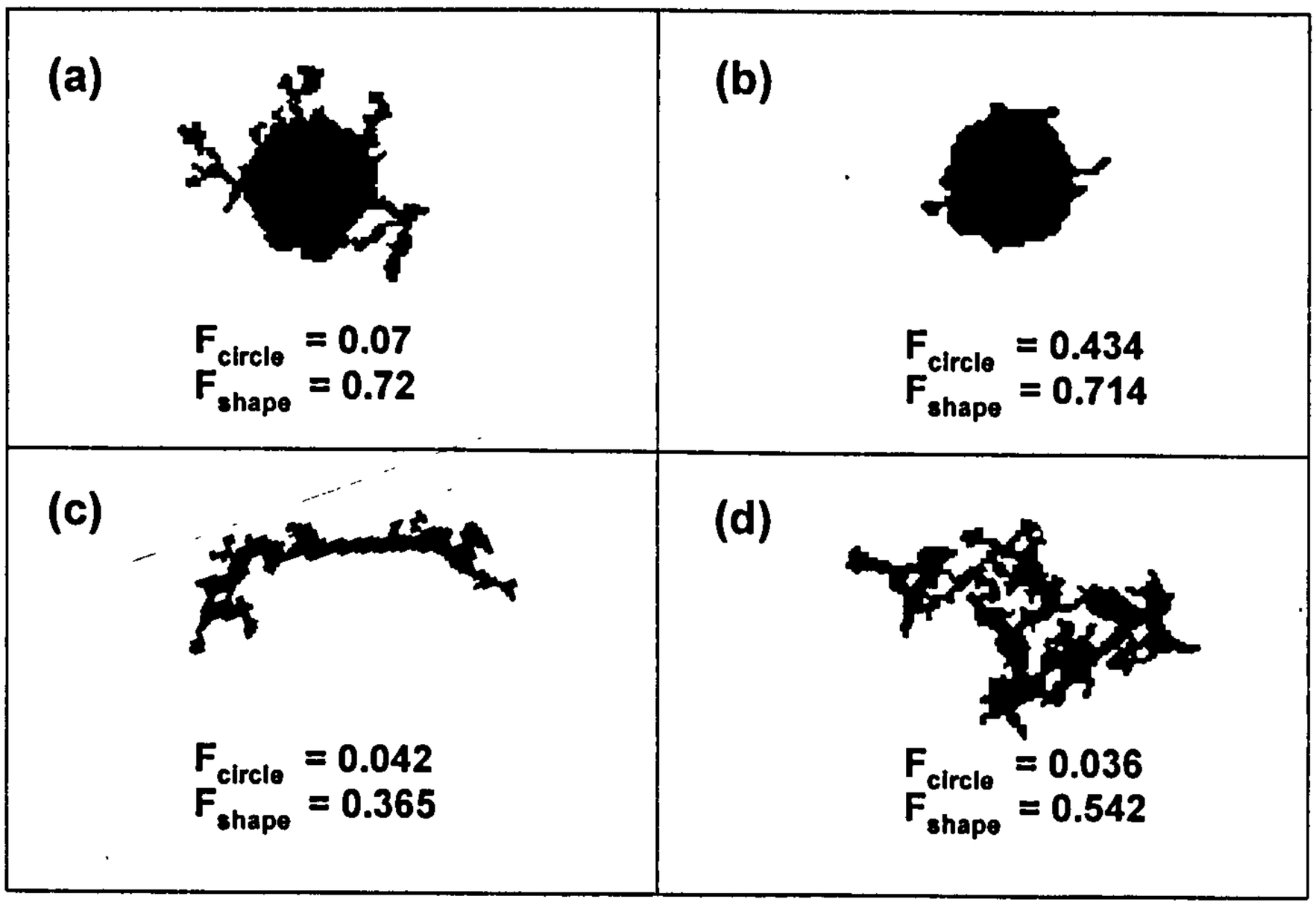

Figure 6.38 Some possible pore shapes with different values of F_{circle} and F_{shape}

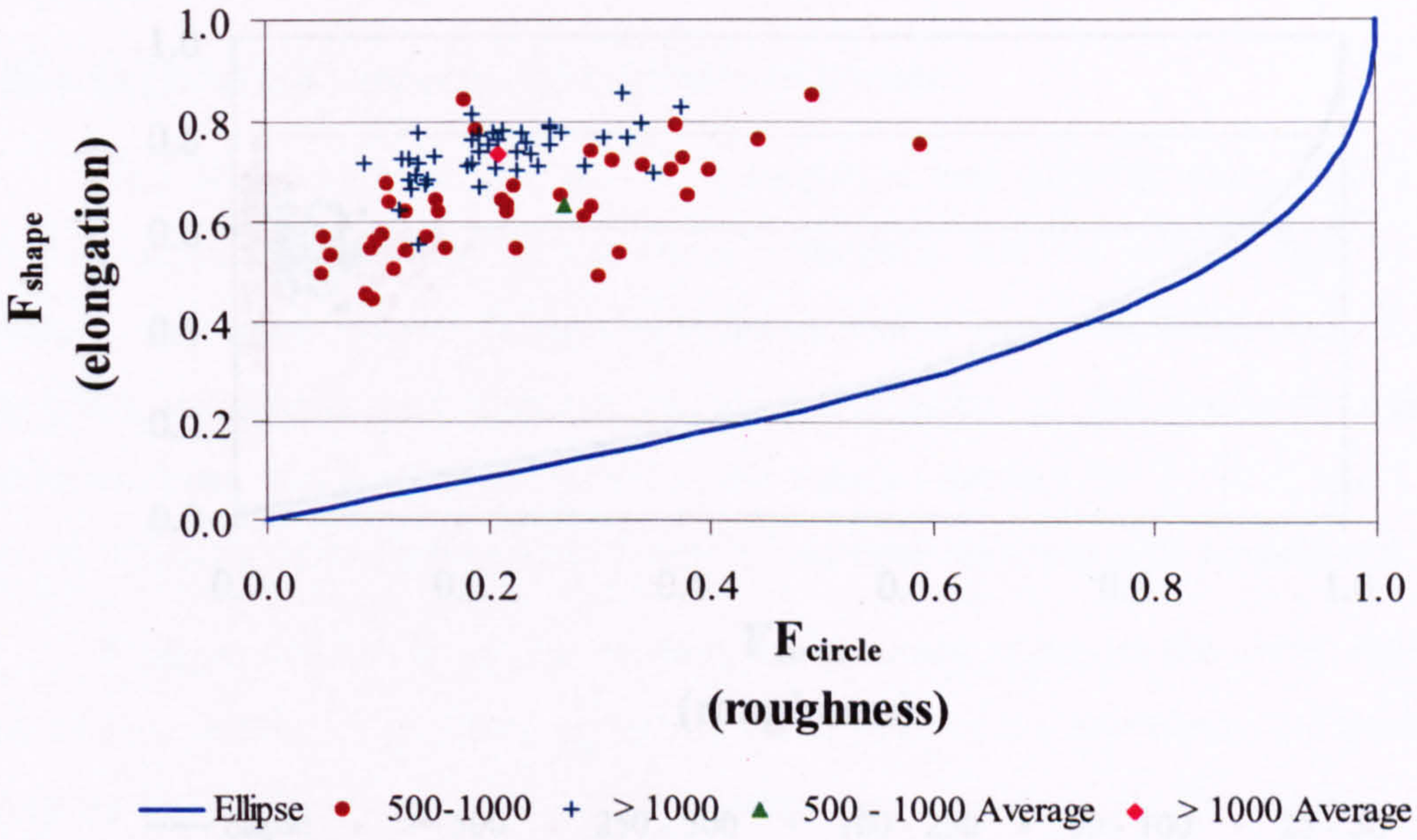

Figure 6.39 Macropore morphology of synthetic aggregate fired to 1110° C with 0 minute sintering time.

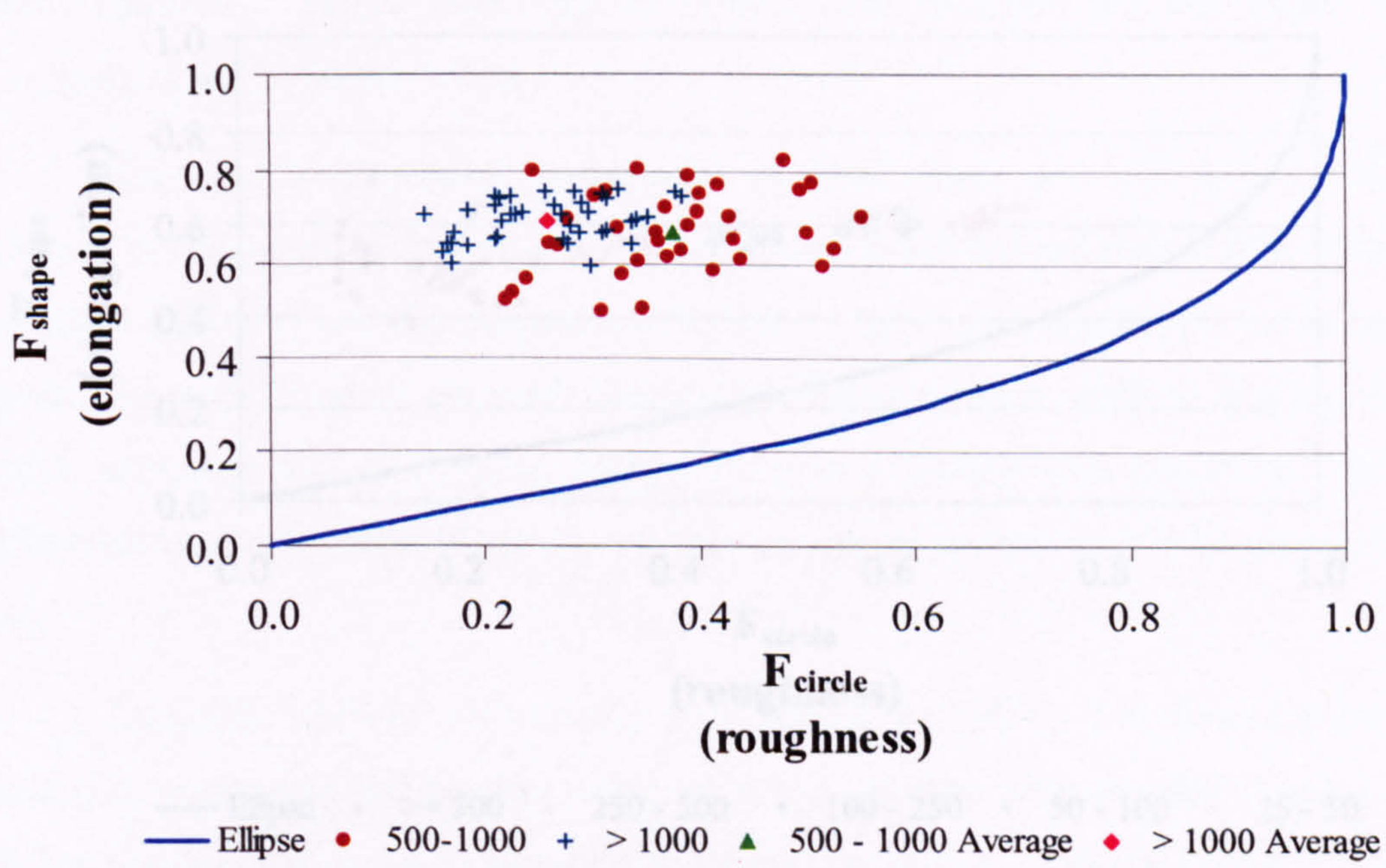

Figure 6.40 Macropore morphology of synthetic aggregate fired to 1110° C with 5 minutes sintering period.

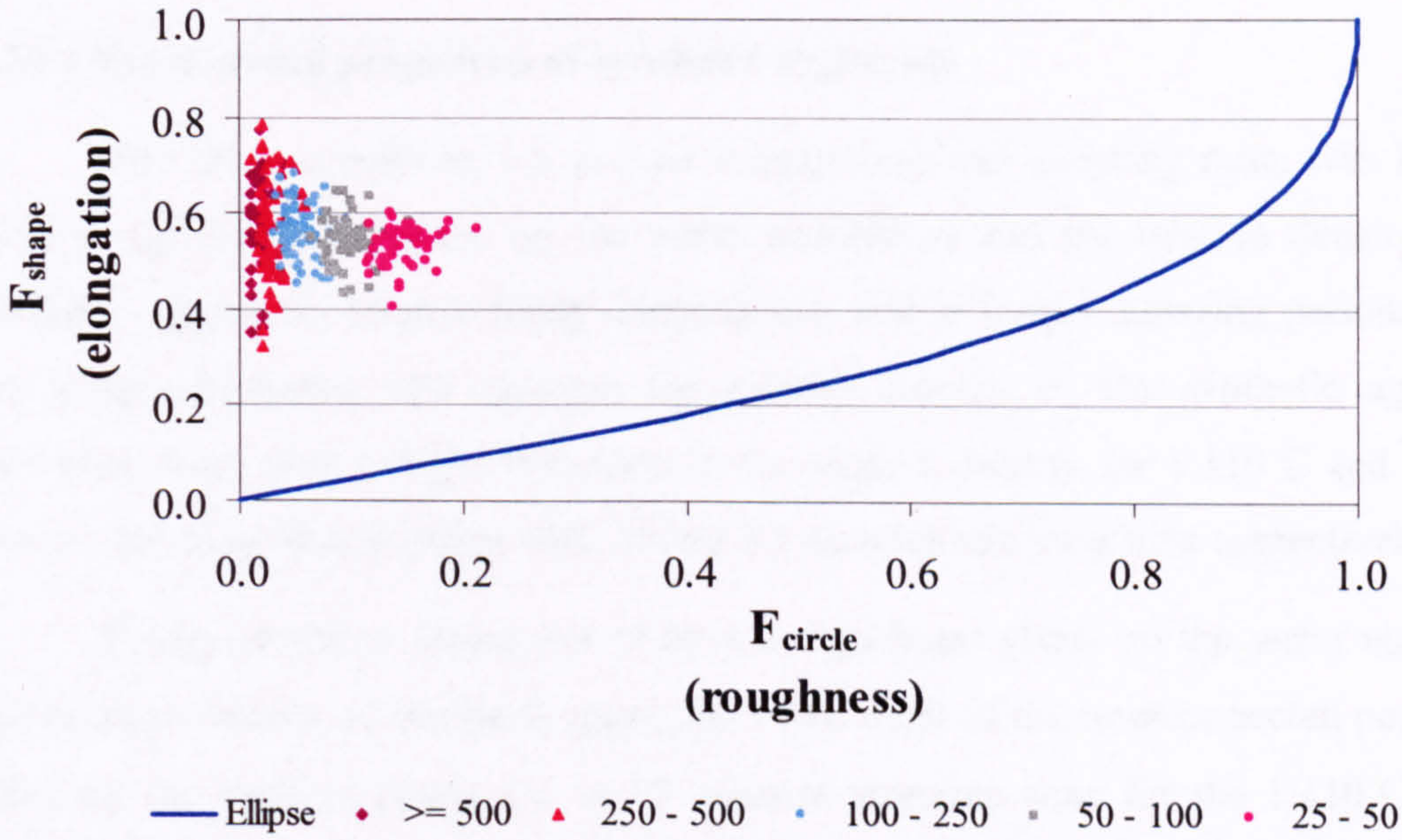

Figure 6.41 Micropore morphology of synthetic aggregate fired to 1110° C with 0 minute sintering period.

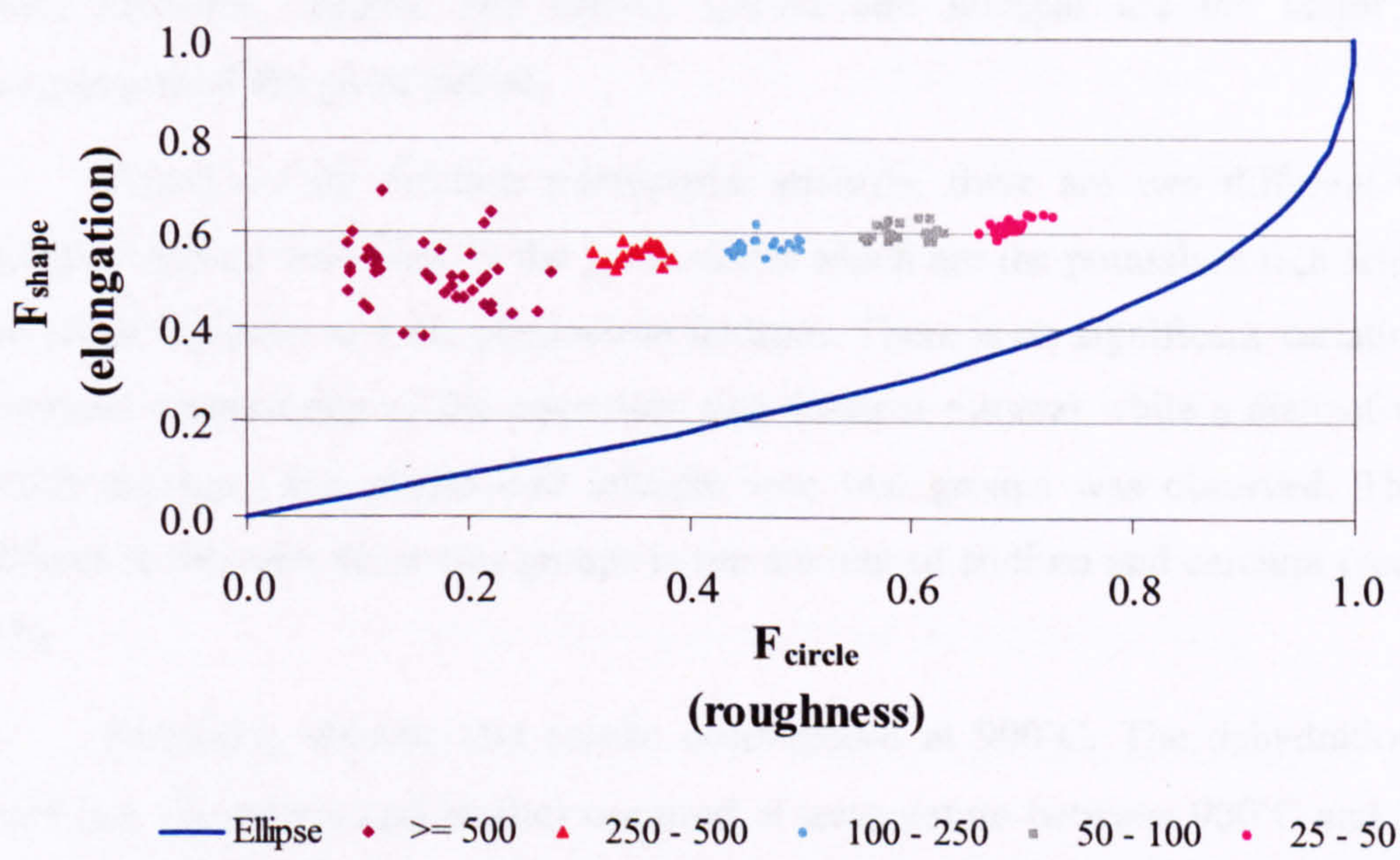

Figure 6.42 Micropore morphology of synthetic aggregate fired to 1110° C with 5 minutes sintering period.

6.10 Summary and conclusions

6.10.1 Engineering properties of synthetic aggregate

1. The firing condition, i.e. *pre-set* temperature and sintering time, was found to have a significant influence on the water absorption and the relative density of the synthetic aggregate. Higher firing temperatures and/or longer sintering periods reduce the water absorption and increase the relative density of the synthetic aggregate. However, there was a slight reduction in the relative density for 1,110°C and 1,120°C *pre-set* sintering temperatures with 20 and 3.5 minutes sintering time respectively.

2. Firing condition began not to have a significant effect on the water absorption and relative density of synthetic aggregate when most of the interconnected pores were filled by the melting phase, i.e. at 10 minutes sintering time for the 1,110°C *pre-set* temperature.

6.10.2 Mineralogy of synthetic aggregate

1. The raw material used to produce the green pellets contains quartz, feldspar, mica, kaolinite, chlorite and calcite. Quartz and feldspar are the major mineral components of the green pellets.

2. Based on the electron microprobe analysis, there are two different types of feldspar mineral contained in the green pellet which are the potassium rich feldspar (or the alkali feldspar) and the plagioclase feldspar. There is no significant variation in the chemical composition of the potassium rich feldspar mineral while a distinct variation which separates the plagioclase feldspar into two groups was observed. The major difference between these two groups is the amount of sodium and calcium (see section 6.4).

3. Kaolinite, chlorite and calcite decomposed at 900°C. The dehydration of the mica (i.e. muscovite and biotite) occurred at temperature between 900°C and 1,110°C. Phases resulting from the decomposition of these minerals were not found in this study and the possible reason may be the kinetic constraints due to a rapid heating and a short duration of sintering time.

4. The melting of feldspar occurred at about 1,110°C, which filled the pores and densified the fired pellet bodies, and the liquid formed increased in amount with

temperature and sintering time. There is a slight variation in the chemical composition of the melting phase throughout the microstructure.

5. Melting or dissolution of quartz was not observed and the transformation between the low-temperature form of quartz (α) and the high-temperature form (β) at temperatures of about 573°C was the only transformation that occurred for this mineral.

6.10.3 Pore structure of synthetic aggregate according to the MIP

1. Synthetic aggregate clearly shows a bimodal pore size distribution. The majority of pores correspond to the space or gap between each particle and the remaining larger pores are due to flaws that were formed during the pelletisation process.

2. Firing condition has two different effects on the pore structure of the synthetic aggregate; pore growth and densification process. Substantial pore growth occurred at the initial stage of sintering as can be seen by the pore size distribution shifts to larger pores. The densification process started to overcome the pore growth at 5 and 3.5 minutes sintering time for the *pre-set* sintering temperature of 1,110°C and 1,120°C respectively.

3. Firing temperature and sintering time affected the density of the synthetic aggregate. The skeleton or particle density reduced with increasing temperature and sintering period. This might indicate an increase of the glassy phase inside the synthetic aggregate body.

4. Total porosity of the synthetic aggregate reduced with an increase in both temperature and firing period except for the case of 1,110°C and 20 minutes sintering period. The increase of total porosity indicates the occurrence of bloating, which might occur during 10 to 20 minutes sintering time, inside the aggregate body.

6.10.4 Pore structure according to the SEM and image analysis technique

1. No major pore structure differences between the green pellet and the synthetic aggregate fired at 900°C was visually observed from the secondary electron images. At 1,000°C there was a slight increase in pore size, it clearly observed in the pellets fired at 1,110°C *pre-set* temperature with 0 minute sintering time.

2. At the initial stage of sintering, pores are very small, highly irregular in shape and extensively interconnected which is consistent with the high water absorptions measured in the water absorption tests. At 1,110°C, melting of the feldspar mineral and the coalescence of very small particles were clearly observed in the SEM images which supports the XRD and MIP results.

3. At 1,110°C with 5 minutes sintering time, the secondary electron images reveal that most of the micropores were filled by the liquid phase and that the pore shape became rounder. This supports the MIP results which showed a significant reduction in the total porosity and indicates that the densification of the synthetic aggregate body started during 0 to 5 minutes sintering time. A further densification of the aggregate body was observed for samples fired at a longer sintering period.

4. A very dense microstructure with plenty of isolated spherical pores was clearly observed for the synthetic aggregate fired at 1,110°C with 10 and 20 minutes sintering time.

5. The porosity of the synthetic aggregate and its evolution upon firing depends mainly on the mineralogical composition and the homogeneity of the starting materials.

6. In addition to the flaws created during the pelletization process, there are two different types of pore within the synthetic aggregate which are defined as macropores and micropores. The macropores are the entrapped air bubbles inside the body of the green pellet and have size range from 20 to 120 microns. The amount of these pores was found to range from 6 to 10 percent. Micropores are the space or gap between each particle of the starting materials and, according to the MIP results and the SEM images, the size of these pores is much smaller than the macropores.

7. There was a slight increase in the micro porosity from 900°C to 1,000°C. At 1,110°C with 0 minute sintering time, there was a large increase in the micro porosity and a significant reduction of this property occurred at 5 minutes sintering time for the same *pre-set* temperature. These results agree very well with the MIP results which indicate the domination of the pore growth process at firing temperature between 900°C and 1,110°C. The densification process started to overcome the pore growth at any period between 1.5 and 5 minutes sintering time for the *pre-set* temperature of 1,110°C.

8. The results of the quantitative image analysis indicated that the amount of pores which have a pore size less than 50 microns were reduced by the pore growth process and this leads to an increase in the bigger pore size.

9. According to the SEM images, most of the micropores of the pellet fired at 1,110°C with 10 minutes sintering time were already filled with the liquid phase, while the macropores still existed. Bloating already occurred and the amount of bloating pores was reasonably estimated to be about 6 %. This figure is believed to increase with an increase in sintering time. This result proves that the Glensanda granite washing can be used in the production of the lightweight aggregates, even without adding any gas-releasing materials.

10. The influence of the two different sintering times on the pore morphology of the synthetic aggregate was studied. The results indicated that an increase in sintering time had a greater effect on the irregularity of pores than the elongation. Pores became rounder with the longer sintering period.

Chapter 7

ITZ microstructure and properties of concrete

7.1 Introduction

In the previous chapter, it was found that firing condition has a significant effect on the properties, mineralogy and microstructure of the synthetic aggregate. In this chapter the synthetic aggregate manufactured from one particular firing regime, i.e. 1,110°C *pre-set* temperature with 10 minutes sintering time, was chosen for the concrete casting. The studies in this chapter involve the investigation of the effect of the synthetic aggregate on the concrete properties. The results presented can be divided into two main sections. The investigation in the first section uses the image analysis technique on the backscattered electron images (BSE) to do a quantitative analysis of the interfacial transition zone between the cement paste and three different types of coarse aggregate, namely: synthetic aggregate, Lytag aggregate and quartz aggregate. The macro properties of concrete, i.e. permeability and compressive strength, are presented in the second section.

7.2 Investigation of the interfacial transition zone (ITZ) of concrete containing different types of coarse aggregate by using the quantitative image analysis

The typical BSE images which show the microstructure of 3 and 28-day old concrete containing the natural, Lytag and synthetic aggregates are shown in Figures 7.1 to 7.6, respectively. The very bright white area of different sizes that can be seen clearly in all images is the grains of unreacted Portland cement. In general, there are four principal components that are found in ordinary Portland cement, i.e. alite (impure C_3S), belite (impure C_2S) and the aluminate and ferrite phases (average compositions of C_3A and C_4AF). The ferrite phase typically appears as the brightest phase in the BSE image and appears not to react at all for both 3 and 28-day old concrete. It is quite difficult to differentiate between alite and belite especially at early ages without using the X-ray microanalysis. This is because the contrast between alite and belite phases is very weak due to a similar mean atomic number (see Table 5.1). The rate of hydration of alite is generally much higher than that of belite. Typically, about 70 percent of alite is reacted

in 28 days while only 30 percent or less is taken place for belite (Ramachandran et al., 2003).

The separation of C-S-H shells from some of the larger cement grains is clearly observed in the 3-day old concrete and the gap between them is filled with the very porous low density hydration products. Most of the very small·cement particles that are hydrated completely have a pore space within a thin-walled hydration shell which is generally called a hollow pore shell. Some of the cement grains are only partially hollow, with some anhydrous material remaining inside. Others are hydrated completely with no visible cement core inside and they contain a low density inner product instead. Hollow shell pores also clearly appear to present in the 28-day old concrete.

It is interesting to note that, for 28-day old concrete, there are three specific types of grain; partially-hydrated, fully-hydrated and anhydrous grains that have no hydration shell. The partially-hydrated cement grains normally have a dense inner product shell with remnant cement cores. However, many of these grains are filled with the low density inner hydration product and plenty of them are clearly observed in the Lytag coarse aggregate concrete. This indicates that, for some reason, the alite grains within Lytag concrete appear to hydrate fairly quickly and leave these type of features that contain low density inner product and/or residual anhydrous material inside. In contrast, very few of these features are observed in the natural quartz and synthetic aggregate (mixed in dry conditions) concrete.

Calcium hydroxide (CH), which can be distinguished on the BSE image of concrete as light grey, generally appears as a cluster of various sizes and shapes in both 3 and 28-day old concrete. For 28-day old concrete, the high concentration of calcium hydroxide was clearly observed near the natural quartz and pre-wetted synthetic coarse aggregate interface. The quantity of calcium hydroxide in both the 3 and 28-day old orange synthetic aggregate (mixed in dry condition) concrete is qualitatively much lower than the other cases.

The straight cleavage-like shrinkage features which seem to be the monosulfate phase, are also commonly observed. For some reason, on many BSE images of the Lytag coarse aggregate concrete, there is qualitatively much more monosulfate than with the other aggregates. The cracks of the monosulfate lie along the basal plane of the

platy hexagonal crystals and they are believed to form because of drying (Scrivener, 2004).

The incorporation of synthetic coarse aggregate with different microstructure in concrete has induced a significant effect on the porosity of the interfacial transition zone. A very porous microstructure was clearly observed for the 28-day old concrete containing porous synthetic aggregate mixed in dry conditions while a very dense microstructure was observed in the case of very dense synthetic aggregate.

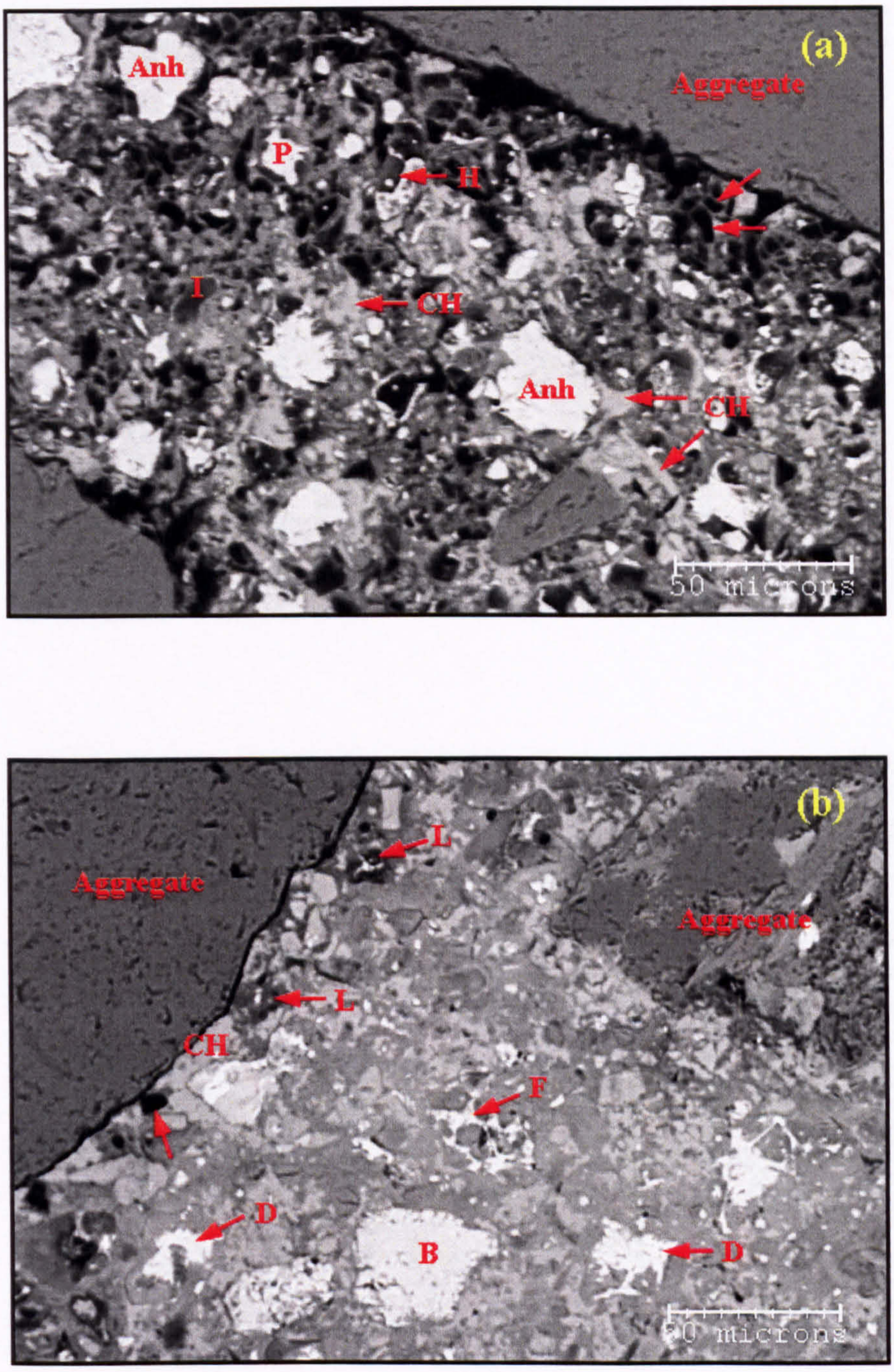

Figure 7.1 BSE images of (a) 3-day old and (b) 28-day old natural aggregate concrete with 0.53 water/cement ratio. I, Fully-hydrated cement grain with low density inner product inside; P, partially-hydrated grain with a very thin rim of C-S-H separated from the cement grain surface; H, partially hollow shell; red arrow, completely hollow shell; B, belite; D, partially-hydrated cement grain with dense inner product shell; F, unreacted ferrite phases; L, relict of cement grain with low density product.

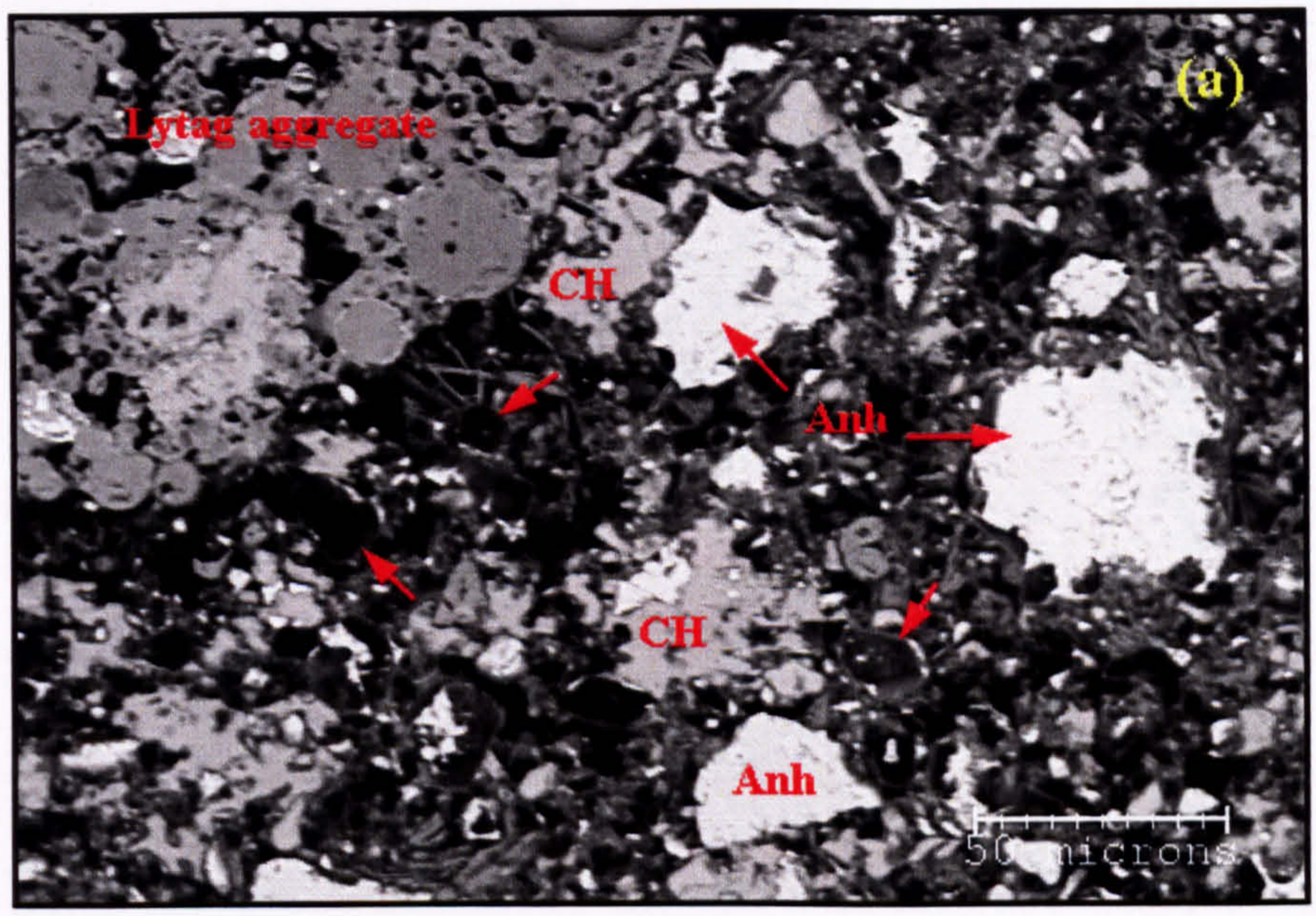

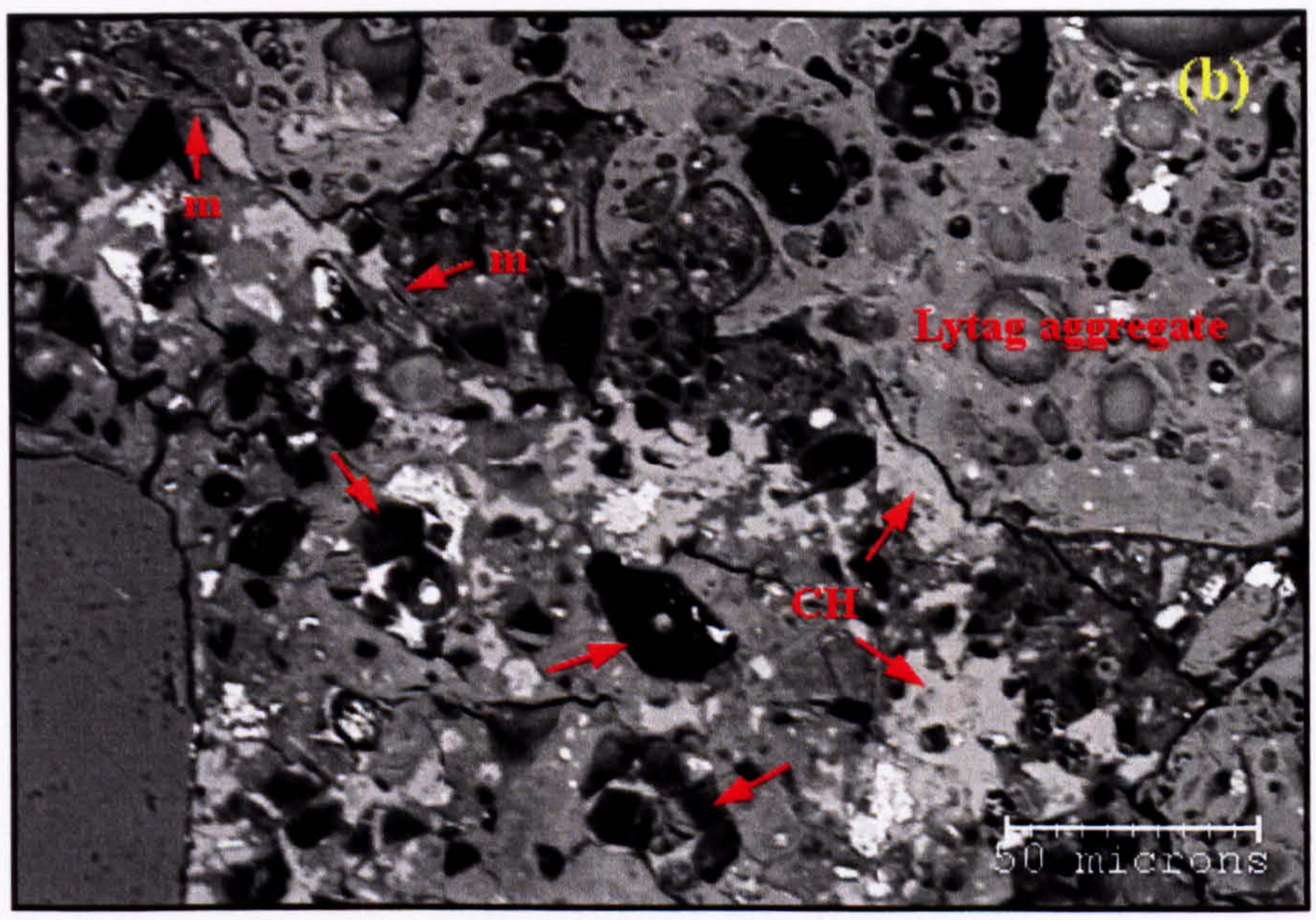

Figure 7.2 BSE images of (a) 3-day old and (b) 28-day old Lytag aggregate concrete with 0.53 water/cement ratio. Aggregate was mixed in SSD condition. CH, calcium hydroxide; m, monosulfate masses (AFm); red arrow, relict of cement grain with low density product inside.

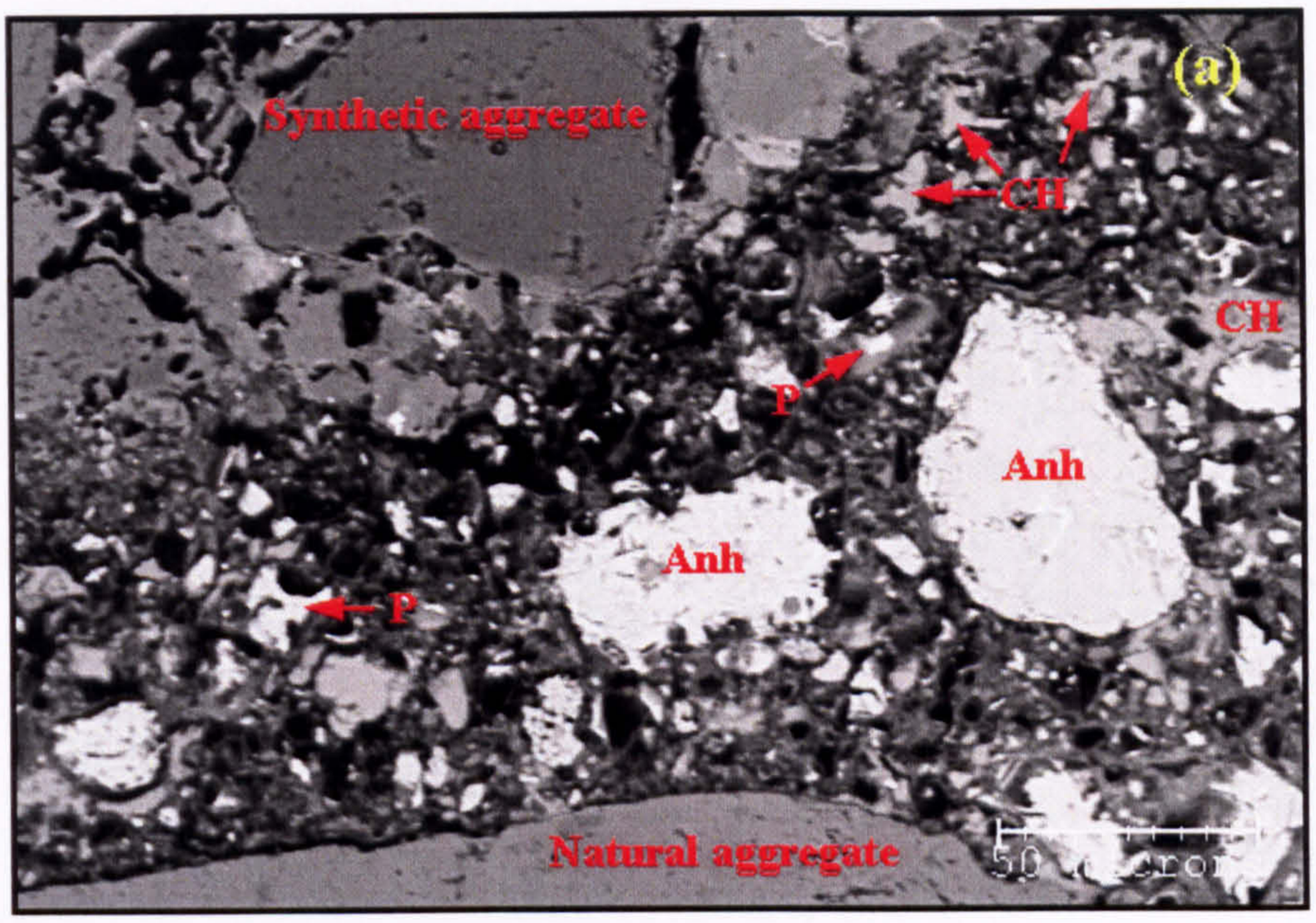

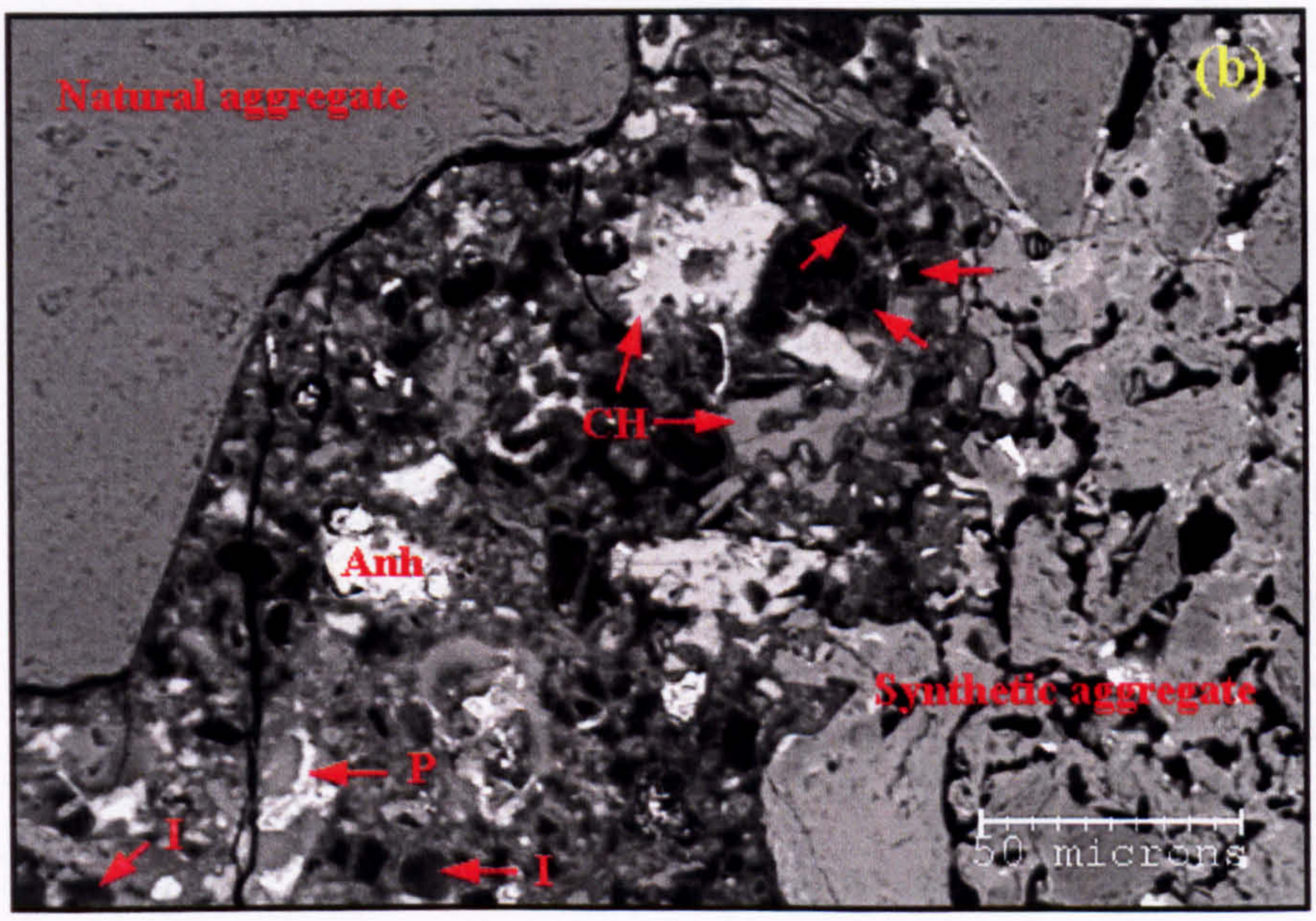

Figure 7.3 BSE images of (a) 3-day old and (b) 28-day old synthetic aggregate concrete with 0.53 water/cement ratio. Aggregate was mixed in dry condition. CH, calcium hydroxide; I, completely hydrated cement grain with low density product inside; P, partially-hydrated cement grain; red arrow, hollow pore shell.

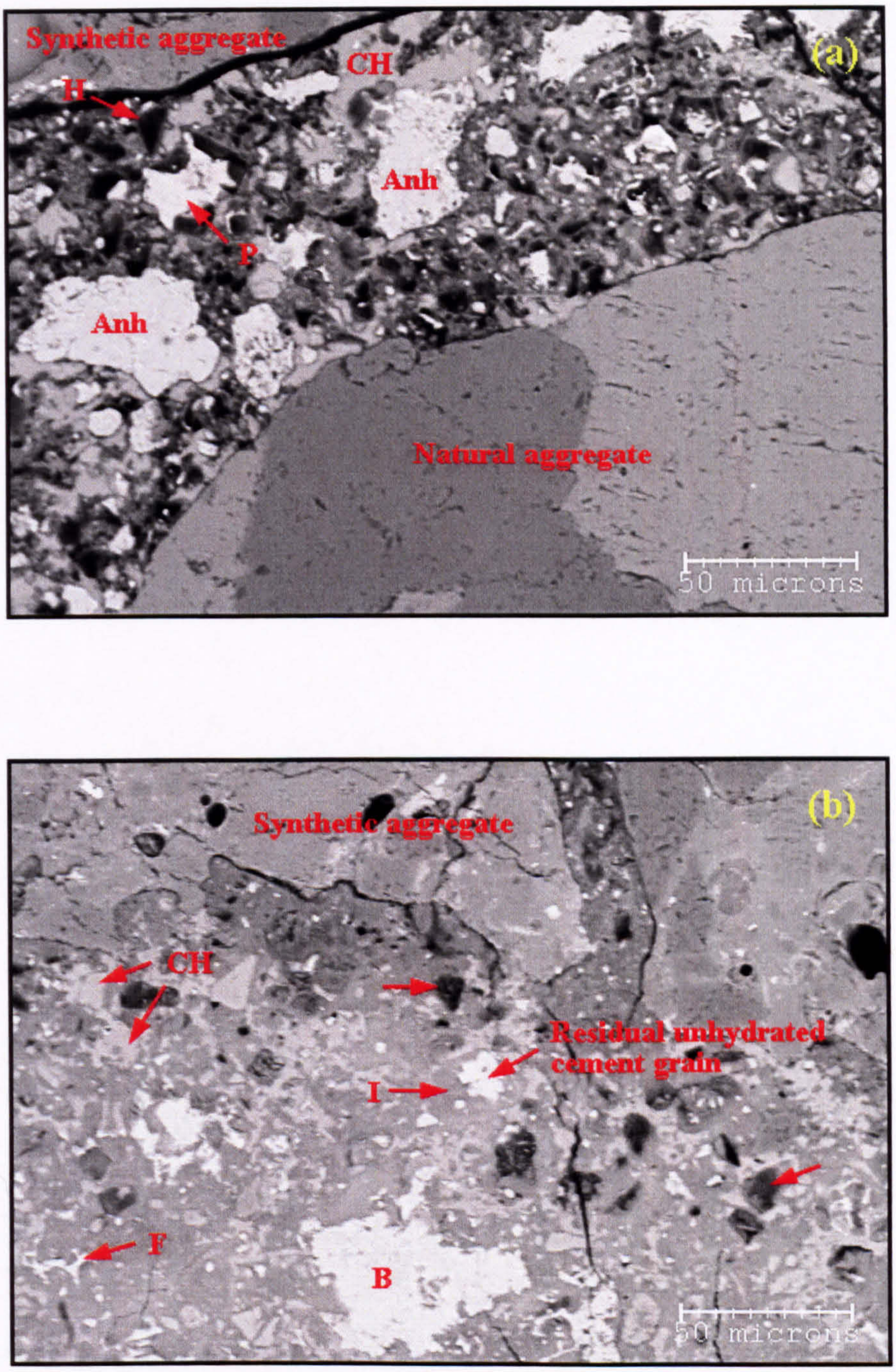

Figure 7.4 BSE images of (a) 3-day old and (b) 28-day old synthetic aggregate concrete with 0.53 water/cement ratio. Aggregate was mixed in dry condition. B, belite ; CH, calcium hydroxide; H, hollow pore shell; I, dense inner product; F, relict of cement grain in which the ferrite phase (white) is unreacted; P, partially-hydrated cement grain; red arrow, relict of cement grain with low density product inside.

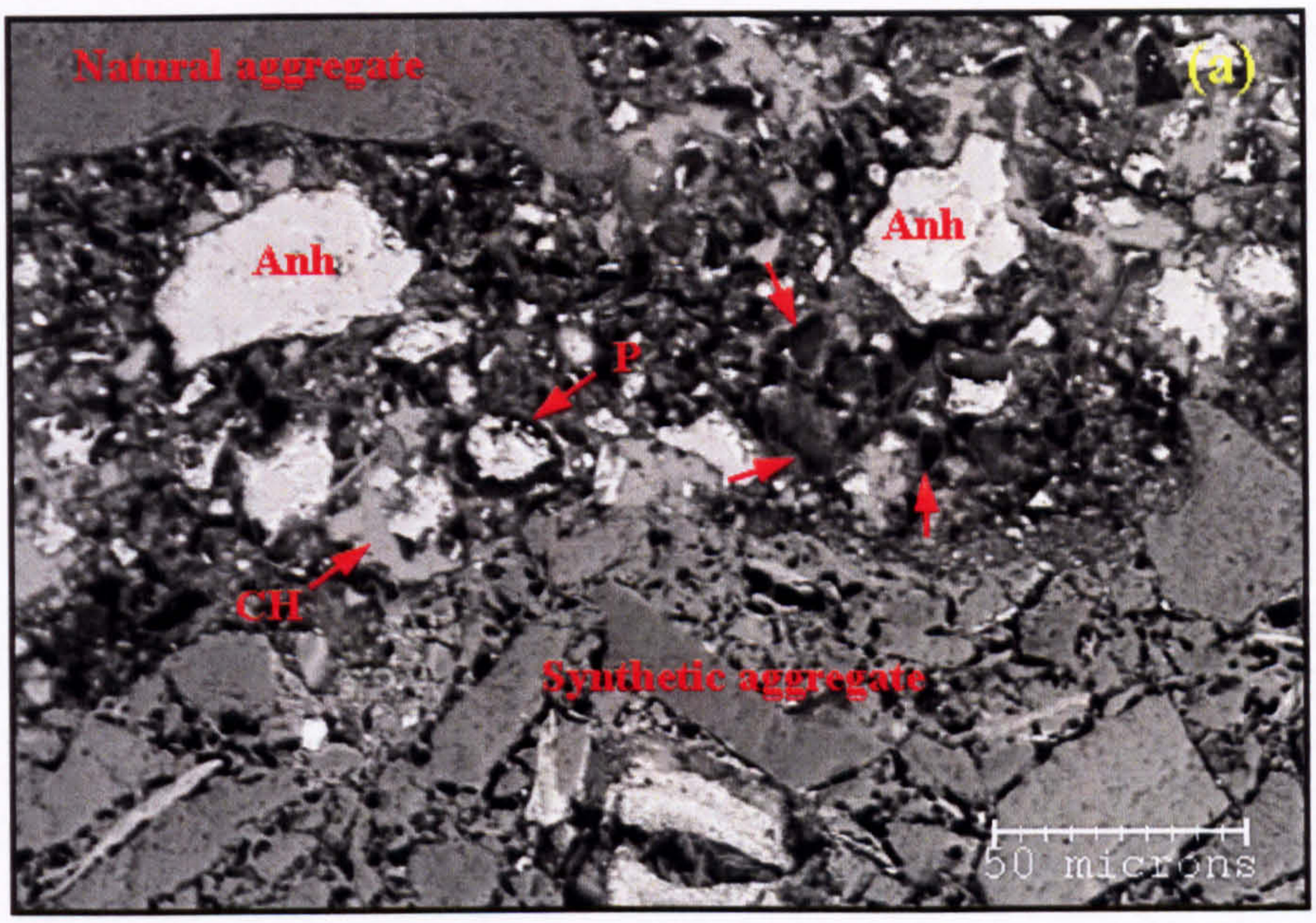

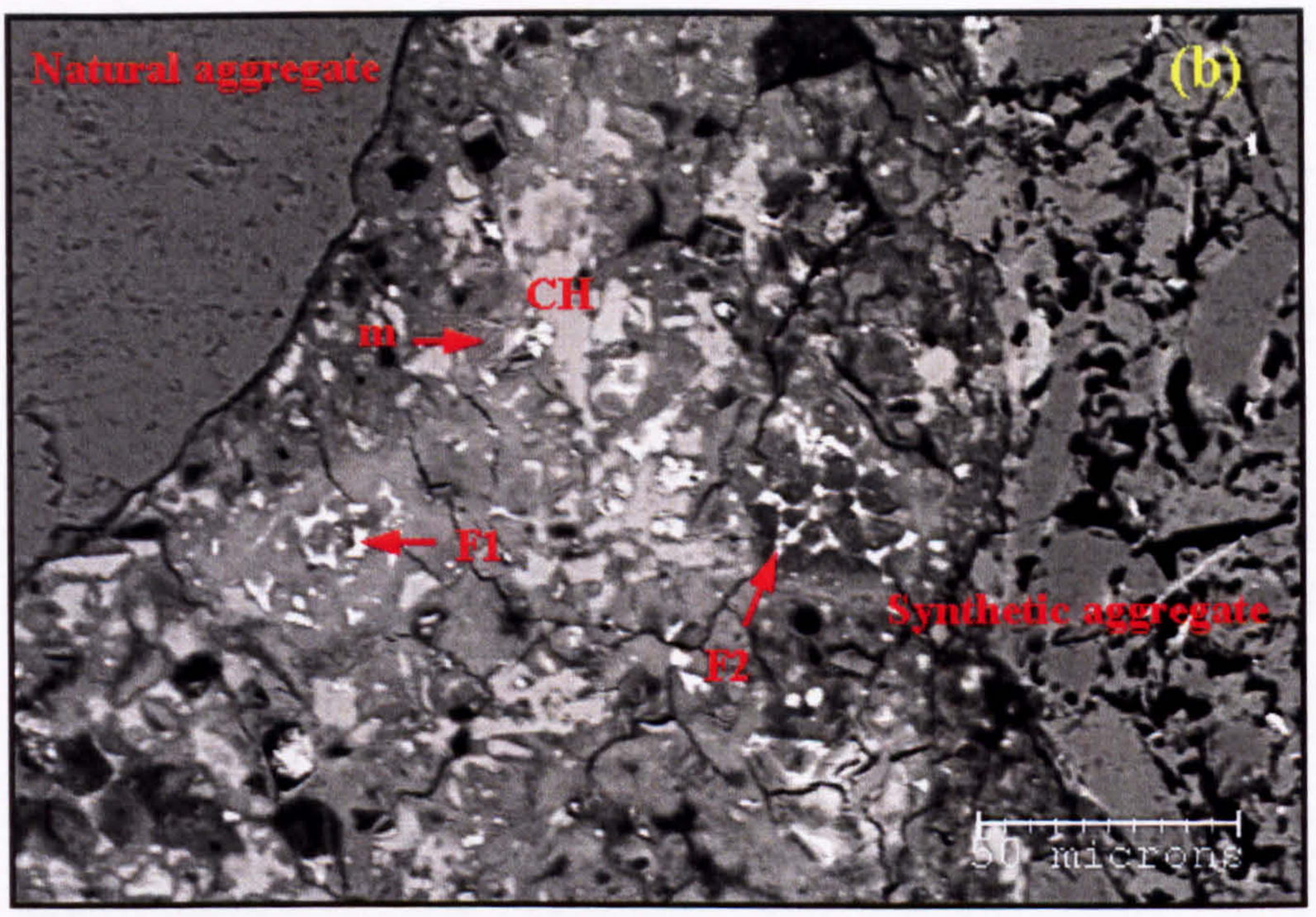

Figure 7.5 BSE images of (a) 3-day old and (b) 28-day old synthetic aggregate concrete with the 0.53 water/cement ratio. Aggregate was mixed in a pre-wetted condition. CH, calcium hydroxide; F1, virtually unreacted ferrite phases (white) with dense inner product shell; F2, ferrite phases with low density inner product; P, partially-hydrated cement grain; m, AFm phases; red arrow, fully hydrated cement grain with low density inner product.

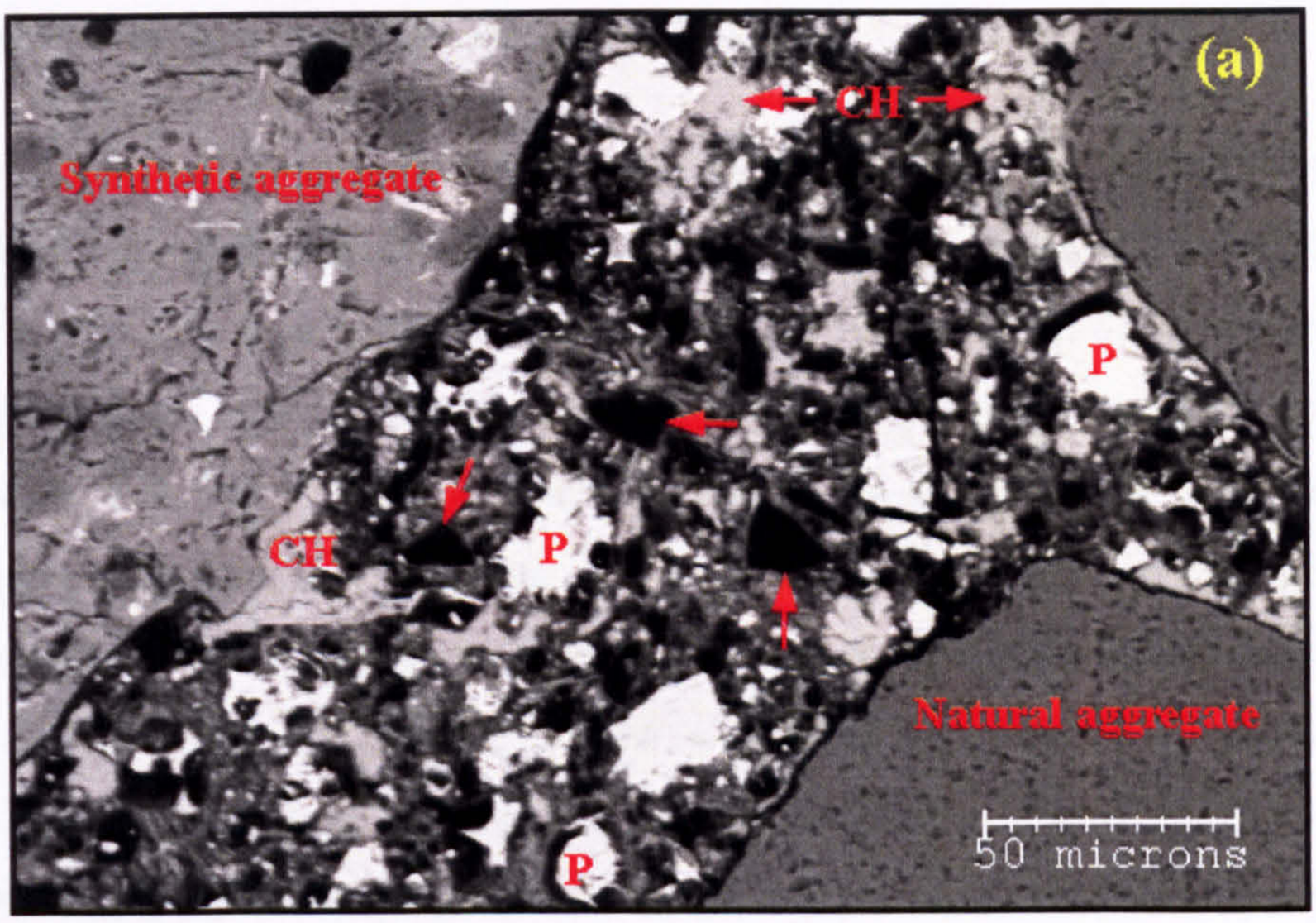

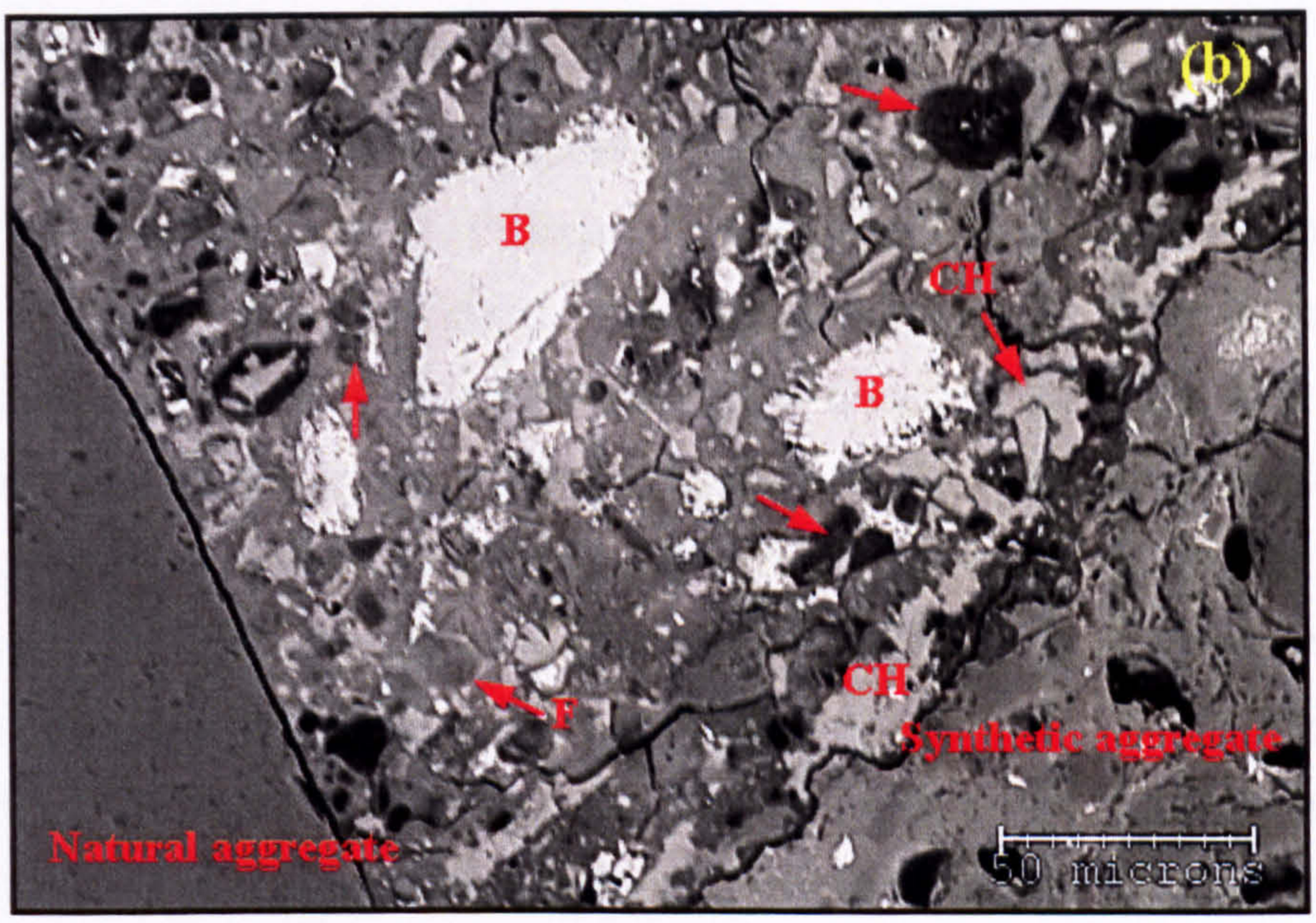

Figure 7.6 BSE images of (a) 3-days and (b) 28-day old synthetic aggregate concrete with 0.53 water/cement ratio. Aggregate was mixed in a pre-wetted condition. CH, calcium hydroxide; B, belite phases; F, relict of cement grain with very dense inner product and ferrite (white) phases; P, partially hydrated dement grains; red arrow, cement grain relicts with low density inner product.

7.2.1 Number of images required for image analysis

The number of images that must be captured so that the average area fraction of each component is representative of the true value within a required level of statistical confidence is the first and very important question that needs to be answered before doing image analysis and this can be done by using the parameter called the *standard error of means* (SE). As mentioned in section 4.10.1, the standard error of means is the parameter that estimates the deviation of the sample mean from the true population mean. This parameter is obtained by dividing the population standard deviation by the square root of the number of the sample size as given in Equation (4.15). However, the population standard deviation is practically not easy to obtain. Therefore, this value was estimated by using the standard deviation of the sample mean instead and it was then expressed in term of a percentage of the estimate which is called the *relative standard error* (RSE). This parameter is a measure of a reliability of an estimate value. The estimates with large RSE are considered unreliable.

In order to determine the number of images that are sufficient to give a representative result, the number of images for averaging were varied between 10 and 38. Figure 7.7 shows the distribution of the average area percentage of the interested features considered in this study in the interfacial transition zone and their relative standard error distribution are also plotted in Figure 7.8. The results clearly indicate that a smoother and more consistent distribution of both average value and relative standard error value can be achieved by increasing the number of images or fields for averaging. The RSE of each concrete microstructural constituent was then averaged through out the distance within the interfacial transition zone region, i.e. 80 microns and it was plotted with the number of images used for averaging as shown in Figure 7.9. The results show a rapid reduction of the average RSE of all constituents between 10 and 30 images and a slight reduction takes place between 30 to 38 images for all interested constituents. These results suggest that the minimum number of images or fields to be analysed in order to get representative results is about 30 images. Therefore, the number of images used for averaging in this research are between 30 and 40 depending on the availability of the images and, especially, the time remaining in this study.

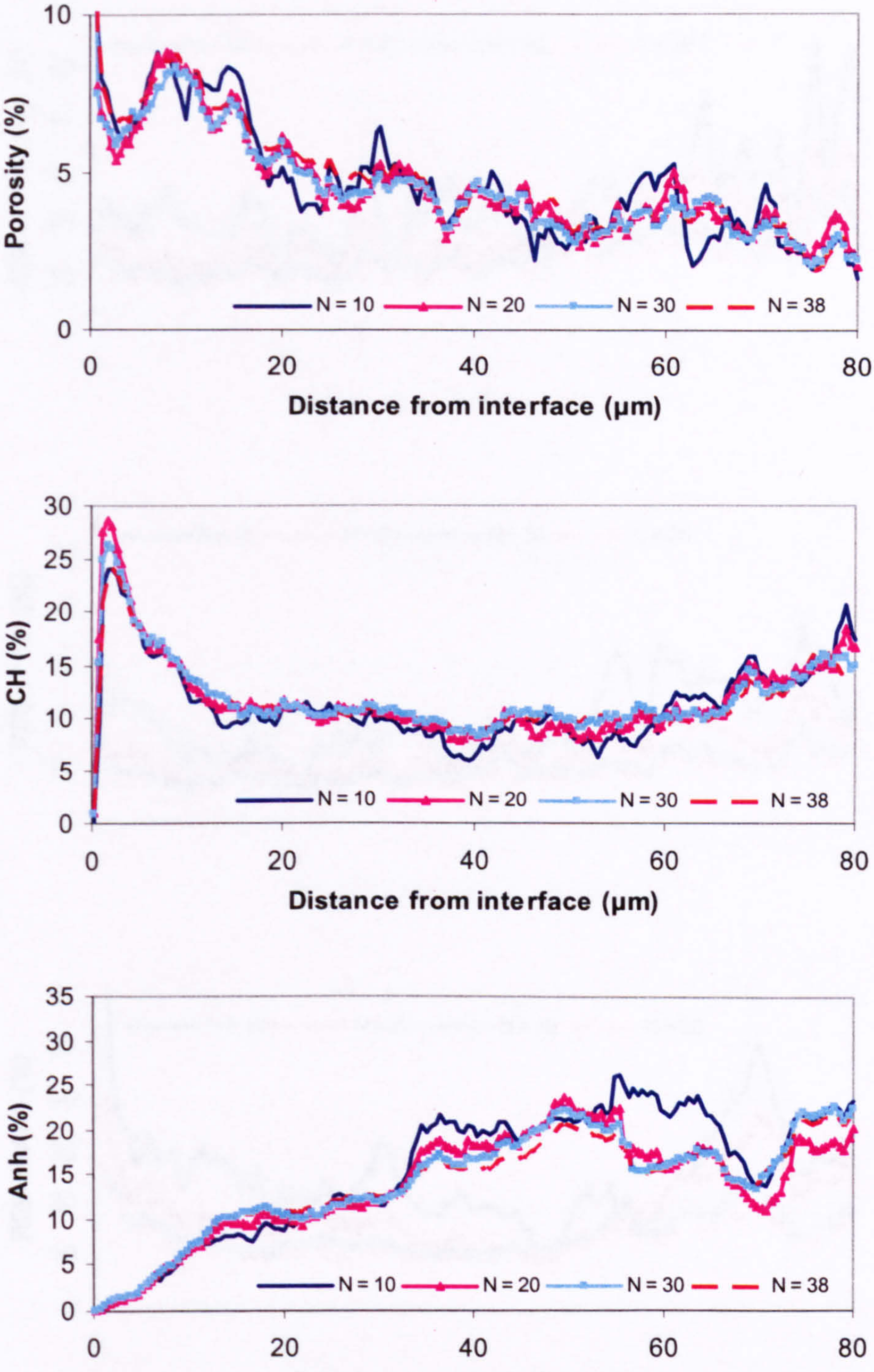

Figure 7.7 Effect of number of image analysed on the concrete microstructural constituents distribution plotting with distance from the coarse aggregate interface (N = number of images used for averaging). (3-days synthetic aggregate concrete and aggregate mixed in dry condition).

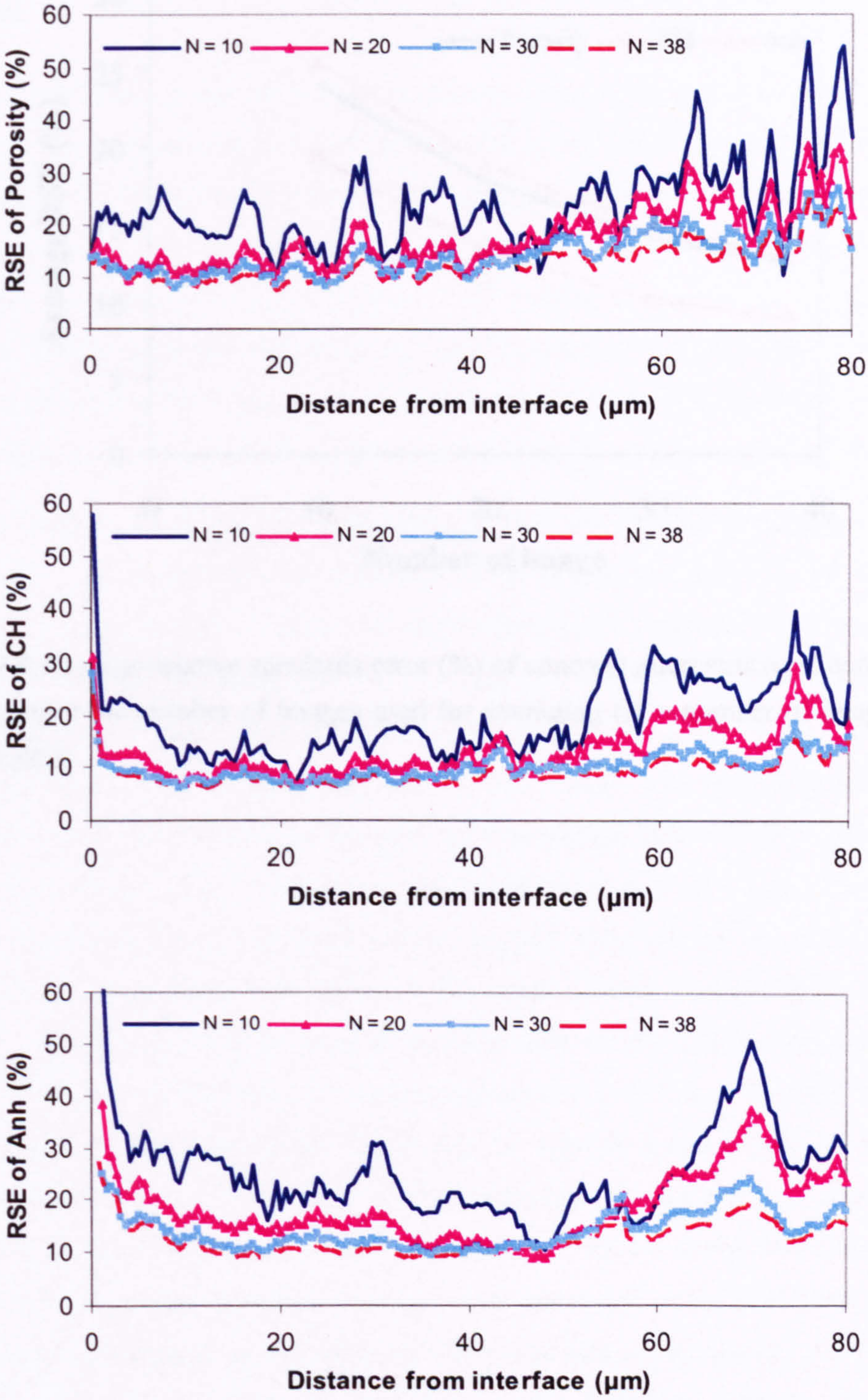

Figure 7.8 Effect of number of image analysed on the relative standard error (%) of concrete microstructural constituents distribution plotting with distance from the coarse aggregate interface (N = number of images used for averaging). (3-days synthetic aggregate concrete and aggregate mixed in dry condition).

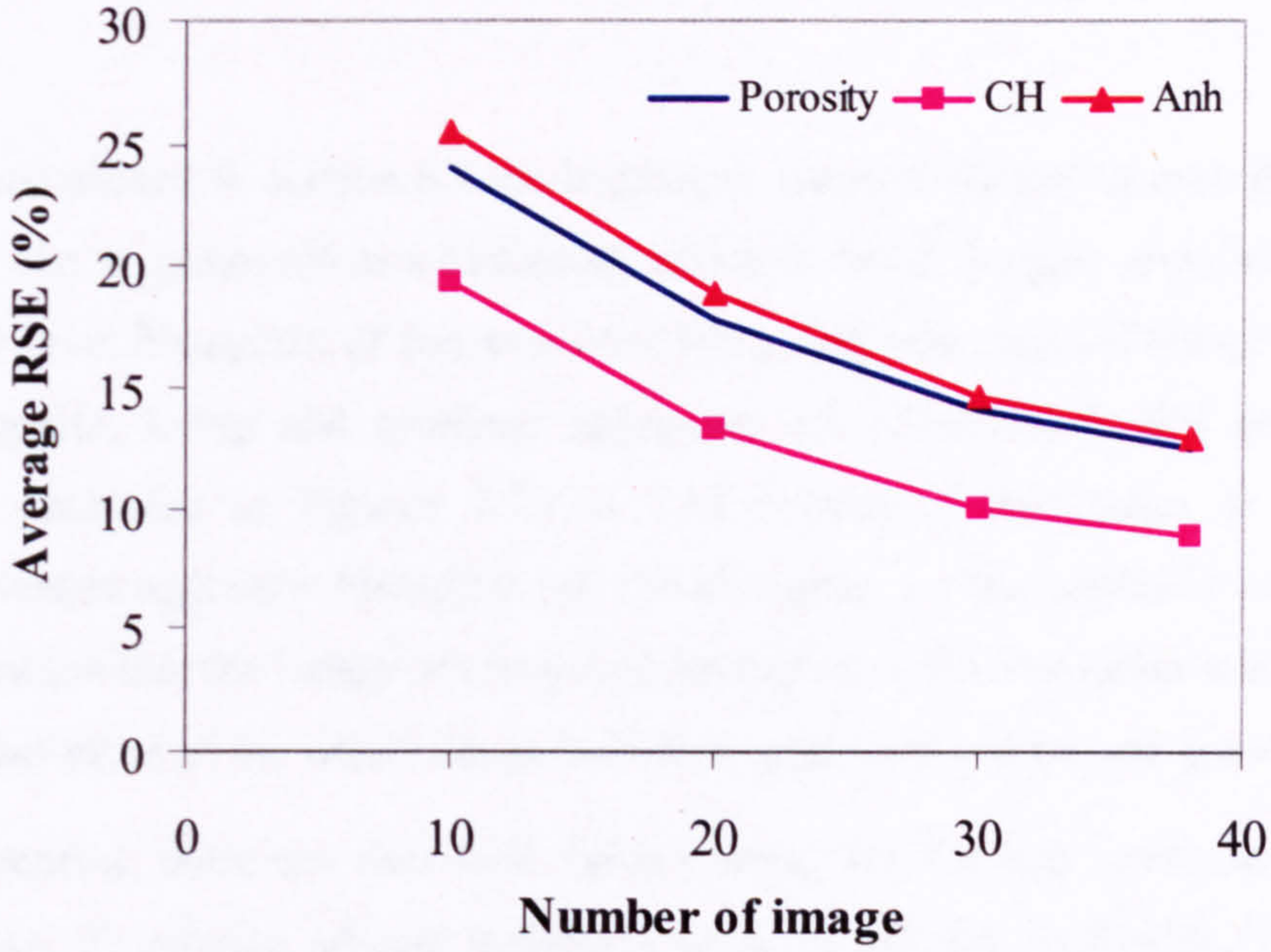

Figure 7.9 Average relative standards error (%) of concrete microstructural constituents plotted against the number of images used for averaging (N = number of images used for averaging).

7.2.2 Grey level histogram of concrete containing different types of coarse aggregate

As mentioned in section 6.7 the brightness value contained in each pixel on the BSE image can be presented as a histogram which is called the grey level histogram. A typical grey level histogram of concrete containing different types of coarse aggregate, including quartz, Lytag and synthetic aggregate, are presented in this section. The histograms presented in Figures 7.10 to 7.12 consist of the image or composite histogram, coarse aggregate histogram and the histogram for the hardened cement paste (hcp). It is noted that the image or composite histogram is the histogram that represents the brightness value of the whole image including aggregate and cement paste region.

In general, there are four well defined peaks for the hcp histogram: 1) pores and/or cracks, 2) calcium silicate hydrate, C-S-H, 3) calcium hydroxide, CH, and 4) unhydrated cement particles. Based on the backscattered coefficient (η) as given in Table 5.1, a well distinguished peak on the right of a given histogram, which has the highest brightness value, corresponds to the anhydrous materials and therefore appears as light grey particles of different sizes on the BSE image. The anhydrous peak some times appears as a double peak on the grey level histogram as shown in Figure 7.10(a) and 7.11(a). The first peak of the anhydrous represents one of the major phases of the ordinary Portland cement grain which is *belite* (impure C_2S) and the second peak that is located on the right hand side of the belite peak is *alite* (impure C_3S). Calcium hydroxide has a mean atomic number between that of the C-S-H and that of the anhydrous phases and, therefore, it appears brighter than C-S-H and the other hydration products. The peak for this phase can clearly be seen as a small peak on the right shoulder of the C-S-H peak on the grey level histogram. Cracks and pore space which were filled by the low atomic number epoxy resin will appear as the darkest region on the BSE image and will appear on the grey level histogram as the first peak from the left. A broad peak located on the left hand side of the calcium hydroxide peak is the C-S-H peak. This is primarily due to C-S-H is the hydration product of variable compositions, particularly in terms of Ca/Si ratio. The terminology of *outer* and *inner* product is generally accepted for the C-S-H. The inner product C-S-H is the hydration product developed within the original boundaries of cement grains, while the outer product C-S-H is formed and deposited in the originally water-filled spaces. In addition,

the inner product C-S-H generally has a brightness value slightly greater than the outer product and, therefore, its peak normally appears as a small hump on the left hand shoulder of the C-S-H peak.

The aggregate histograms, which were included in Figures 7.10 to 7.12, present the brightness value of all pixels covered by the coarse aggregate fraction of the BSE image. It is clear that the grey level of all coarse aggregates used in this study overlaps the grey level of the cement paste components to be analysed. Therefore, the boundaries of aggregate need to be accurately defined and all of the aggregate pixels have to be removed from the BSE image before doing any image analysis. The procedure that was used for the aggregate segmentation is given in section 5.3.3.1.

The quartz aggregate histograms are shown in Figure 7.10. They typically show a relatively large, sharp peak for the quartz mineral and, in some cases, there is a small peak adjacent to the right that might correspond to the feldspar mineral. Lytag coarse aggregate is commercially sintered fly ash lightweight aggregate. The mineralogical composition of this aggregate was found to consist of quartz, mullite, anorthite, hematite and glassy phase (Wesserman and Bentur, 1997). These phases can be identified on the BSE image by the differences in their brightness value and, from bright to dark, phases can be identified as hematite, anorthite, quartz and mullite. The appearance of the glassy phases depends on their chemical composition. Figure 7.12(a) and (b) show the grey level histogram for 3 and 28 day old concrete containing synthetic aggregate. The detailed description for the synthetic aggregate histogram was already given in section 6.7.

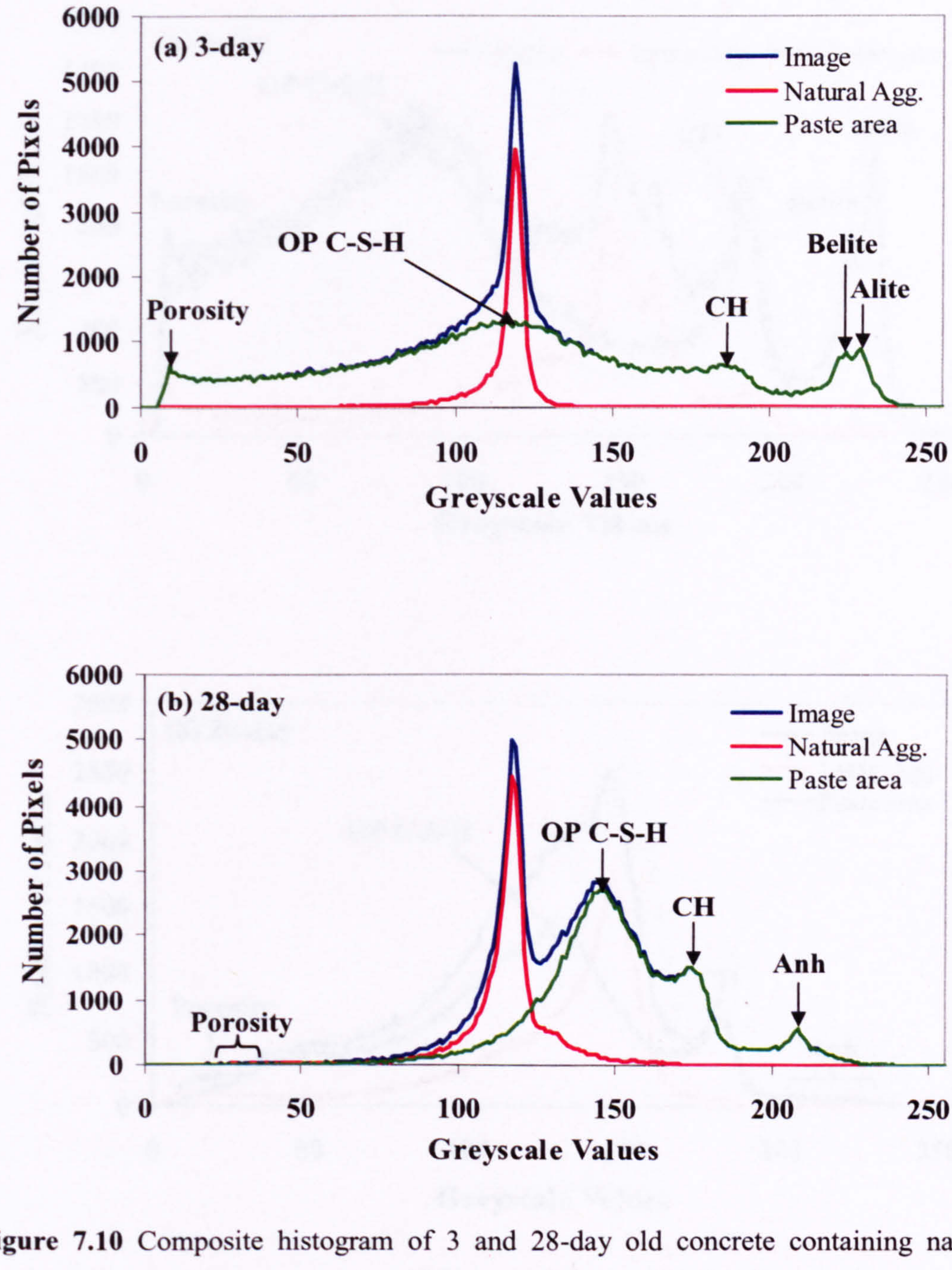

Figure 7.10 Composite histogram of 3 and 28-day old concrete containing natural quartz aggregate. Image captured at 500x magnification. OP C-S-H, outer product C-S-H; CH, calcium hydroxide; Anh, anhydrous cement particles.

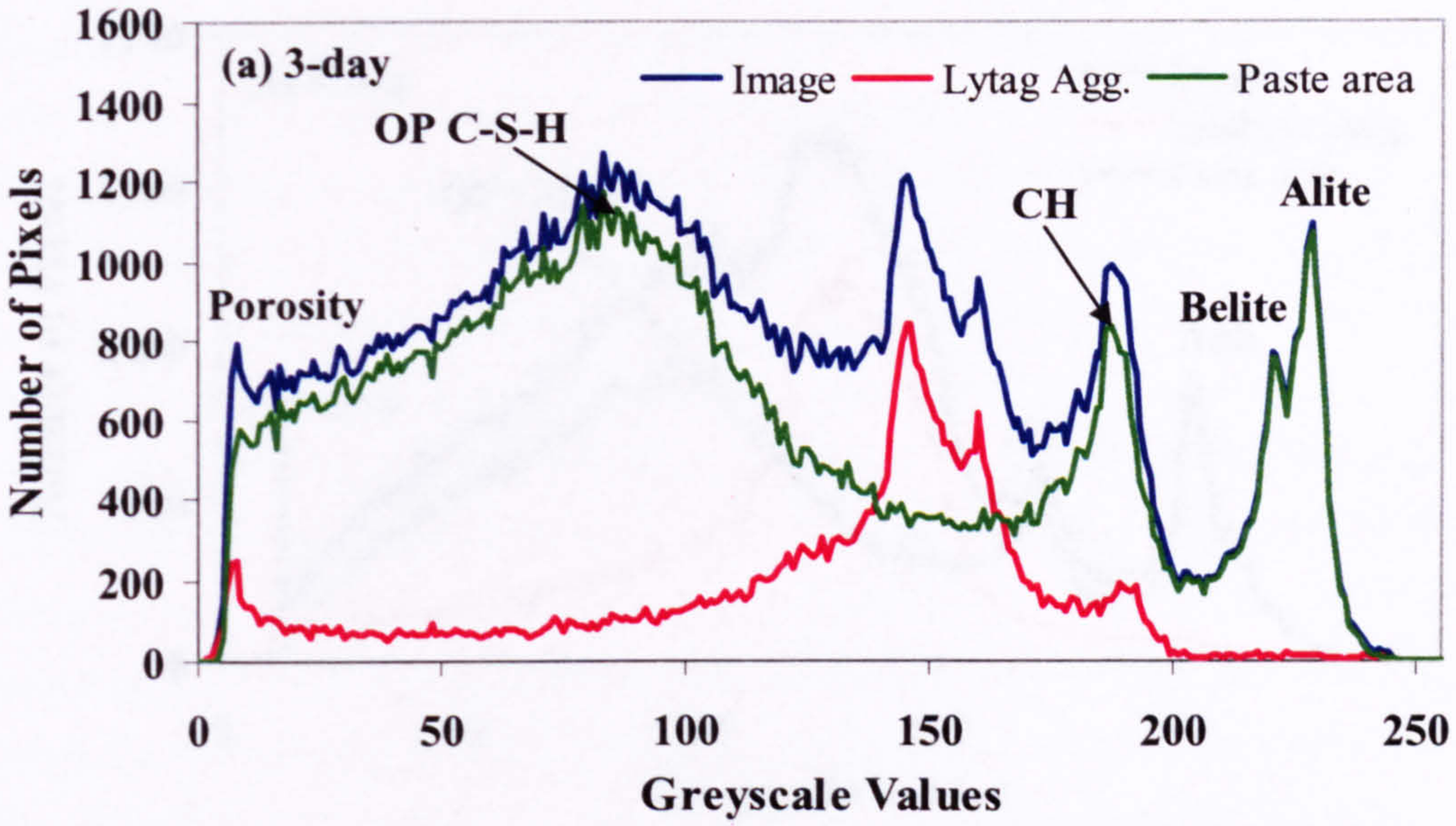

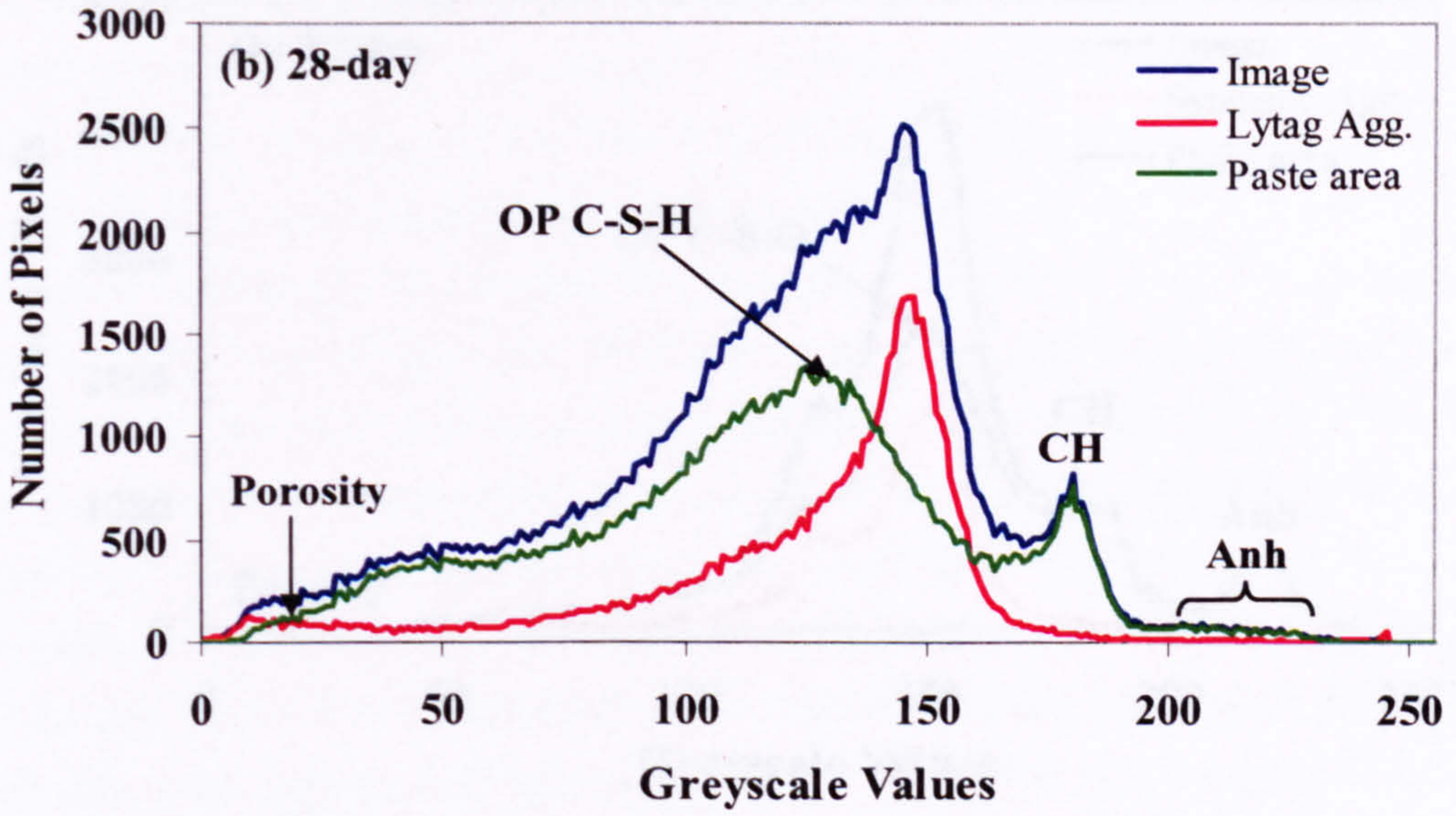

Figure 7.11 Composite histogram of 3 and 28-day old concrete containing Lytag lightweight coarse aggregate. Image captured at 500x magnification. OP C-S-H, outer product C-S-H; CH, calcium hydroxide; Anh, anhydrous cement particles.

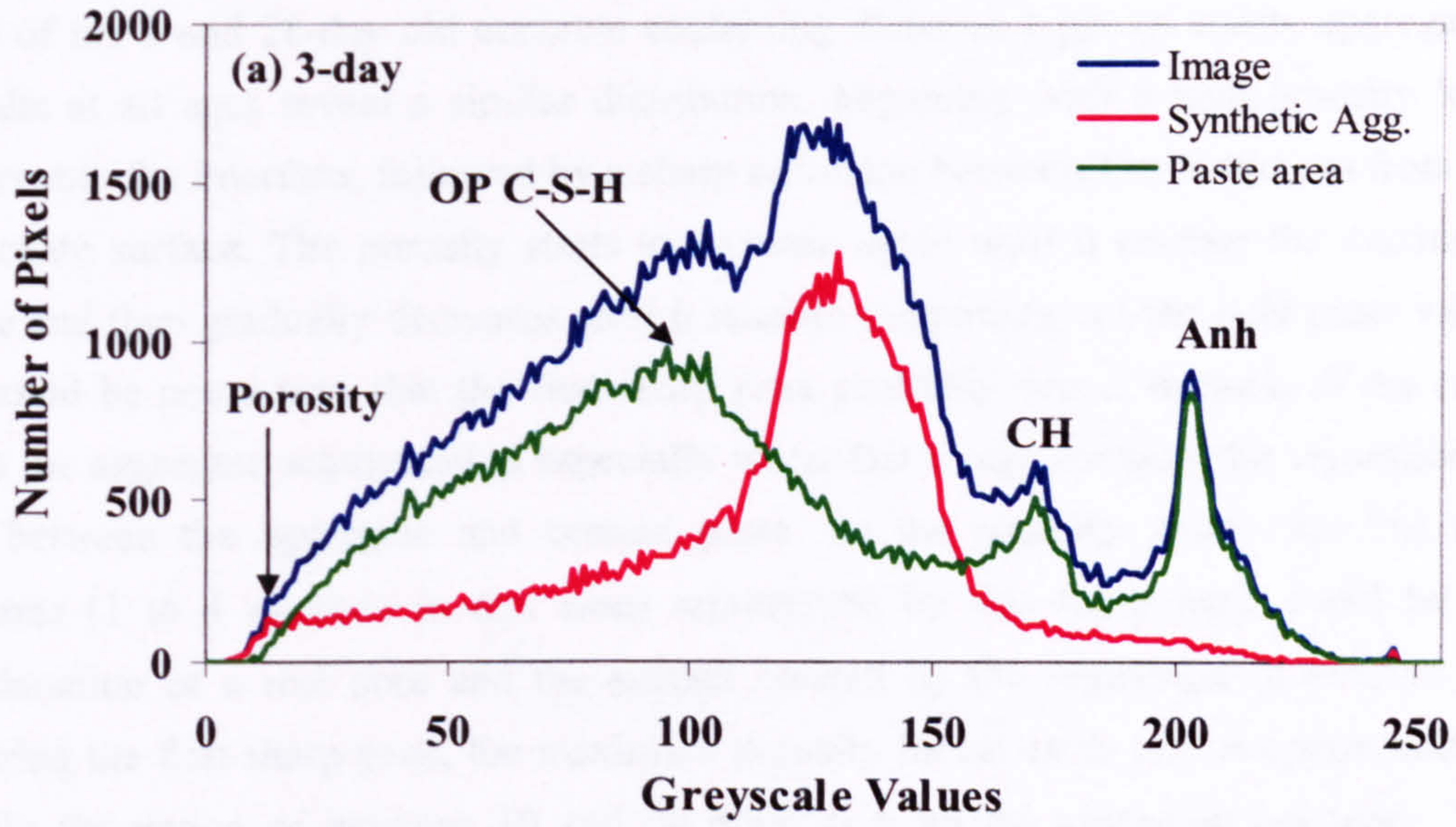

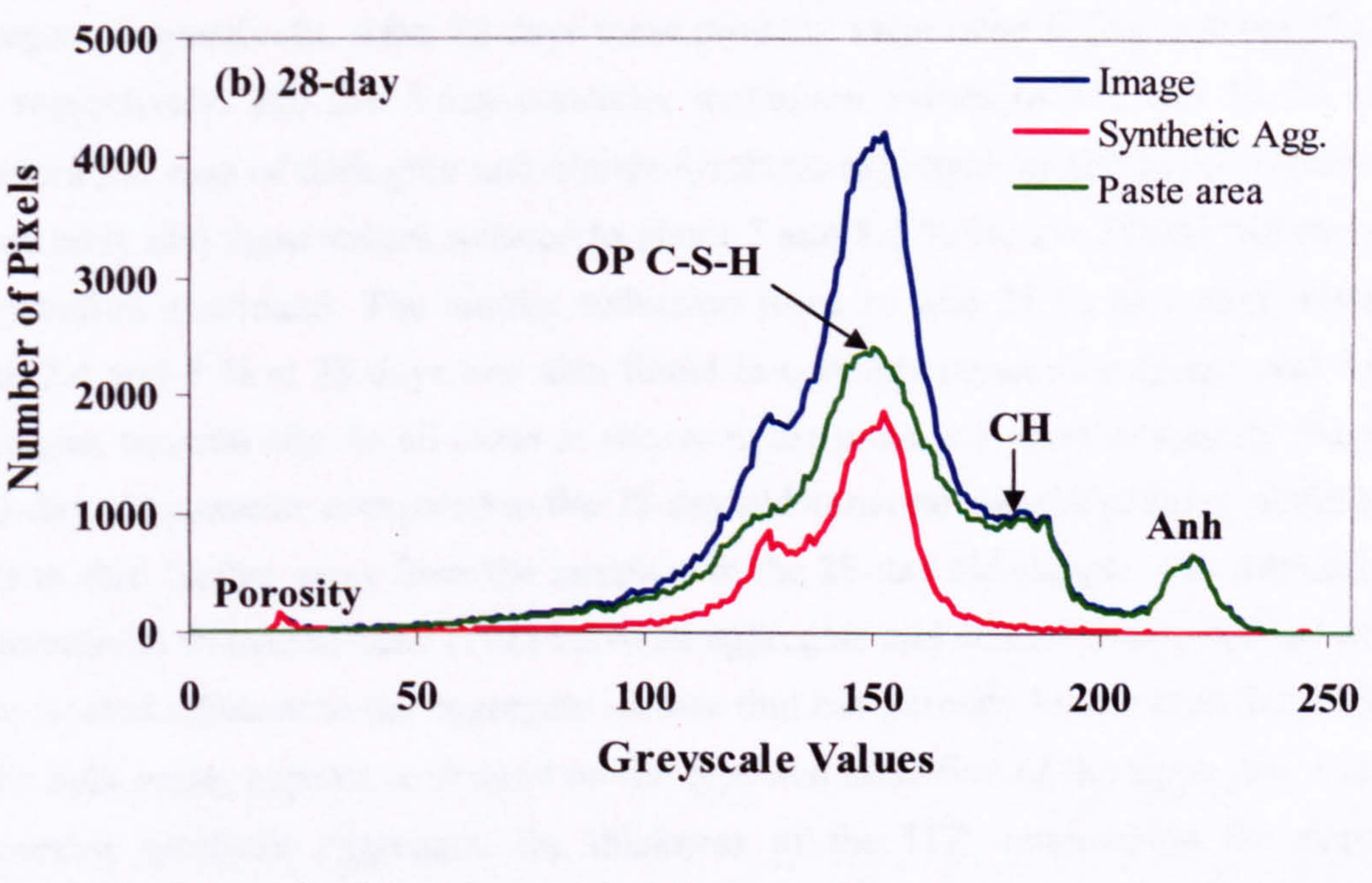

Figure 7.12 Composite histogram of 3 and 28-day old concrete containing synthetic coarse aggregate. Image captured at 500x magnification. OP C-S-H, outer product C-S-H; CH, calcium hydroxide; Anh, anhydrous cement particles.

7.2.3 Effect of hydration time on porosity distribution

Figures 7.13 to 7.15 show the porosity distribution at the interfacial transition zone of the 3 and 28-day old concrete containing different types of coarse aggregates. Results at all ages reveal a similar distribution, beginning with a high porosity level adjacent to the interface, followed by a sharp reduction between 1 to 4 microns from the aggregate surface. The porosity starts to increase again until it reaches the maximum value and then gradually decreases until it reaches the porosity of the bulk paste value. It should be noted here that the first sharp peak probably occurs because of the error from the aggregate segmentation especially when that image contains the separation or gap between the aggregate and cement paste. So the porosity within the first few microns (1 to 4 microns in this case) represented by this sharp peak could be the combination of a real pore and the artifact created by the segmentation process. By ignoring the first sharp peak, the maximum porosity for all cases occurs approximately within the region of between 10 and 20 microns from the aggregate boundary. The maximum porosity of the 3-day old concrete containing the pre-wetted synthetic aggregate is approximately 10.5% and 13% for the orange and dark grey color aggregate, respectively. After 28 days these porosity values had fallen to about 7% and 4%, respectively. For the 3-day concrete, maximum values of 9% and 13.5% were found for the case of dark grey and orange synthetic aggregate mixed in dry conditions, respectively and these values reduced to about 3 and 8.5 % for the 28-day old concrete as hydration continued. The similar reduction from 14 and 11 % at 3 days down to about 2.4 and 7 % at 28 days was also found in concrete containing Quartz and Lytag aggregate, respectively. In all cases as shown in the plots, it is easy to identify the peak for 3-day old concrete compared to the 28-day old concrete and the position of the peak tends to shift further away from the interface of the 28-day old sample. The thickness of the interfacial transition zone (ITZ) between aggregate and cement paste, defined as the paste located adjacent to the aggregate surface that has porosity higher than the porosity of the bulk paste, appears to depend on the type and condition of the aggregate. For the pre-wetted synthetic aggregate, the thickness of the ITZ, considering the porosity distribution of 3-day old concrete, is approximately 50 and 30 microns for dark grey and orange color pellet, respectively. The interfacial zone of concrete mixed with dry synthetic aggregate extends approximately 25 and 40 microns into the bulk cement paste for dark grey and orange color aggregate, respectively. The ITZ thickness for quartz aggregate is difficult to define and it seems to extend about 55 microns into the cement paste. About 40 microns was observed for the Lytag aggregate concrete.

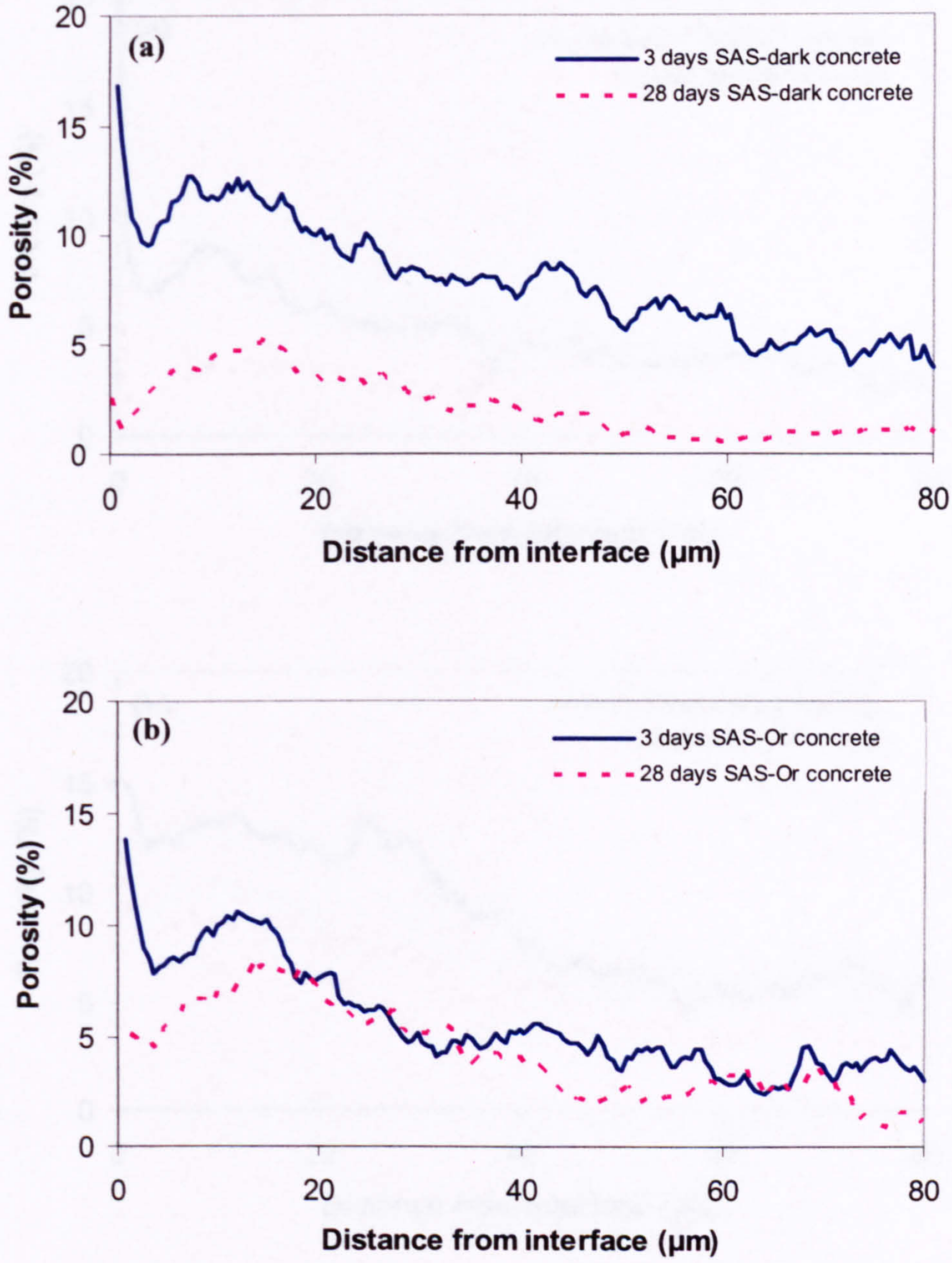

Figure 7.13 Porosity distributions for concrete mixed with the pre-wetted synthetic aggregate. (a) synthetic aggregate with dark grey color, (b) synthetic aggregate with orange color.

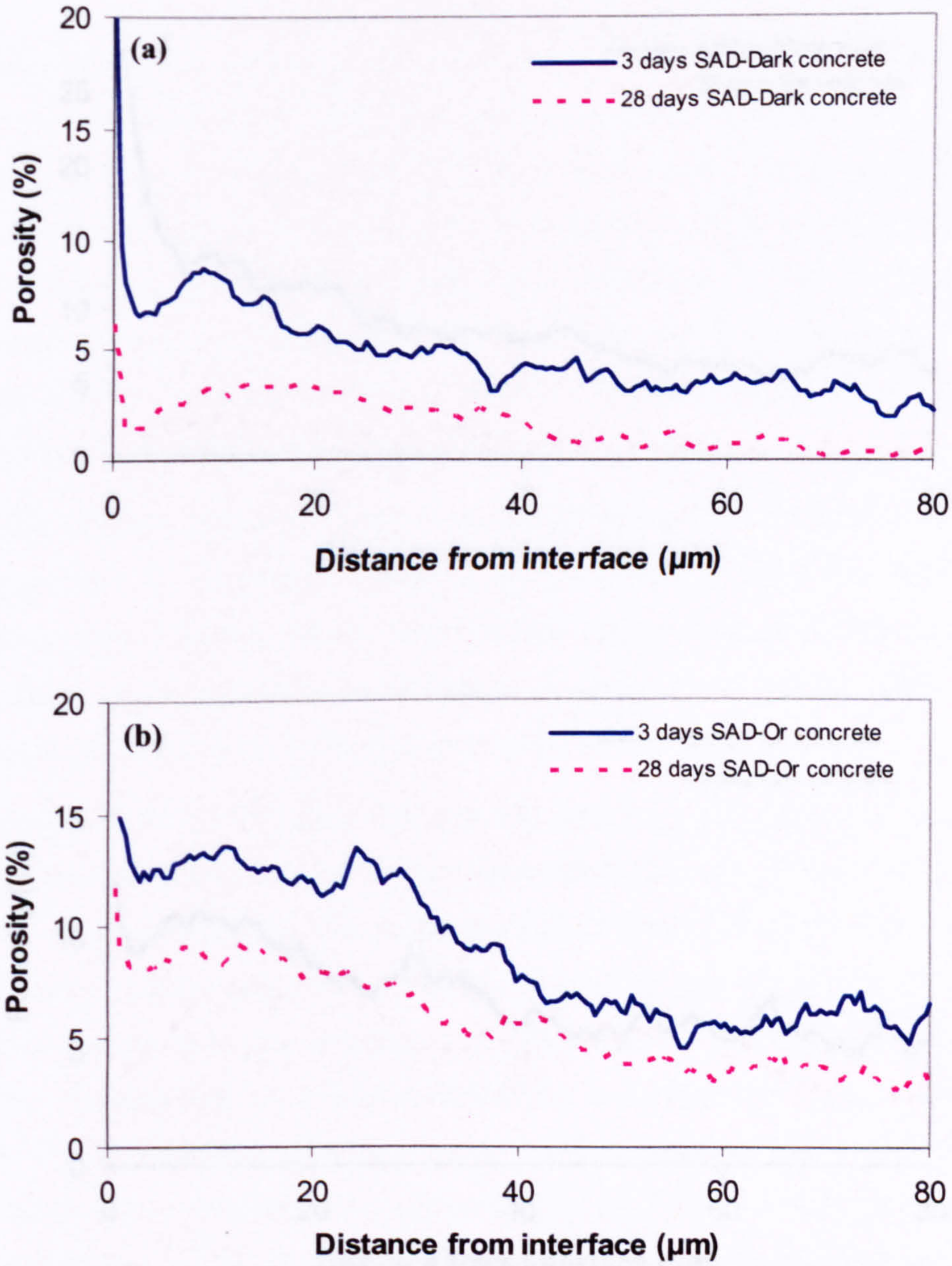

Figure 7.14 Porosity distributions for concrete mixed with the dry synthetic aggregate. (a) synthetic aggregate with dark grey color, (b) synthetic aggregate with orange color.

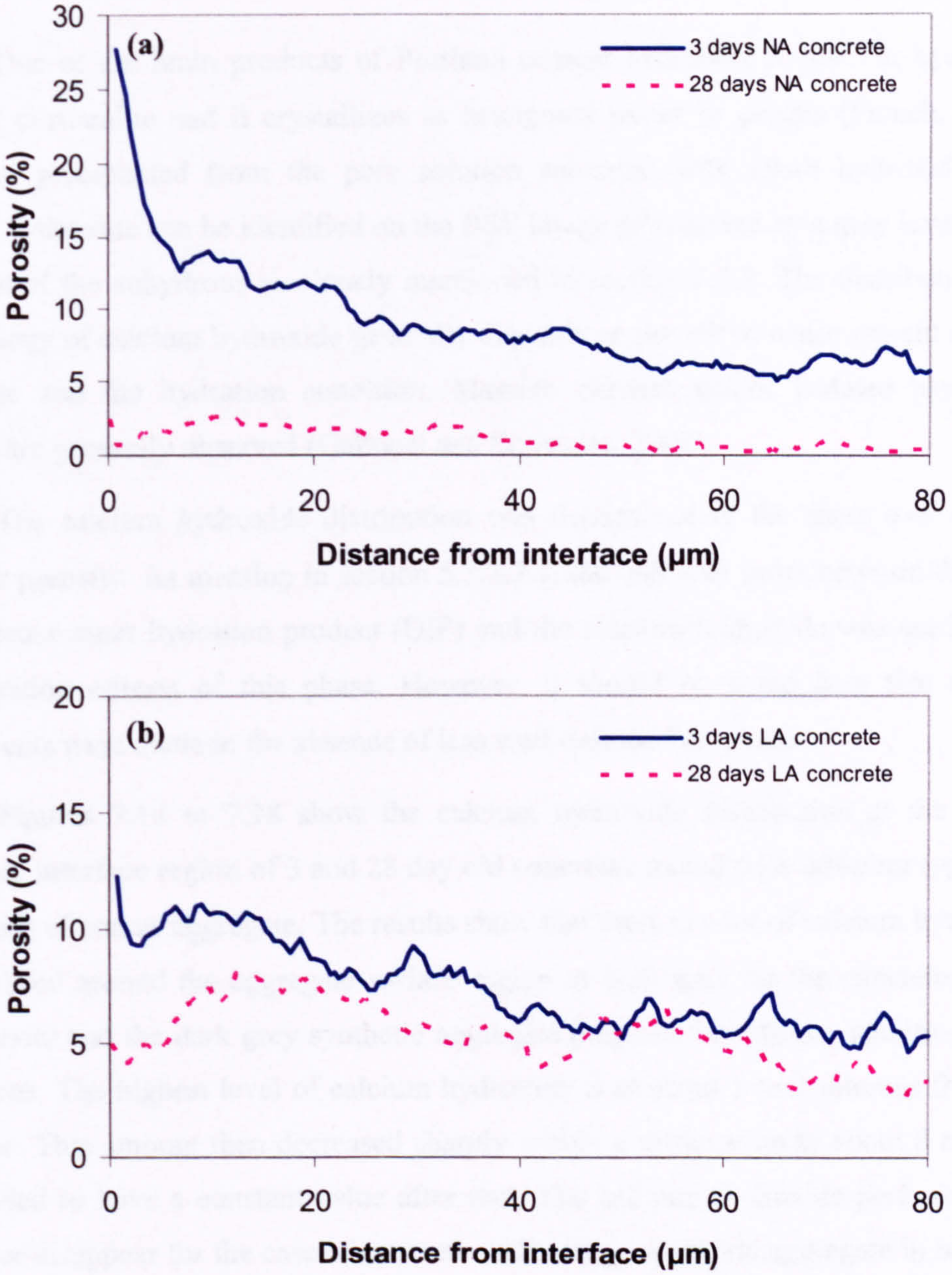

Figure 7.15 Porosity distributions for concrete mixed with the pre-wetted coarse aggregate. (a) natural quartz aggregate, (b) Lytag aggregate.

7.2.4 Effect of hydration time on calcium hydroxide distribution

One of the main products of Portland cement hydration is calcium hydroxide (CH) or portlandite and it crystallizes as hexagonal plates or prisms (French, 1991). They are precipitated from the pore solution saturated with alkali hydroxide. The calcium hydroxide can be identified on the BSE image of concrete by a grey level lower than that of the anhydrous as already mentioned in section 7.2.2. The distribution and morphology of calcium hydroxide generally depends on the initial water cement ratio of the paste and the hydration condition. Massive clusters and/or isolated hexagonal crystals are generally observed (Gallucci and Scrivener, 2007).

The calcium hydroxide distribution was determined in the same way as was done for porosity. As mention in section 5.3.3.2.1, the half way point between the peak of the dense inner hydration product (DIP) and the calcium hydroxide was used as the segmentation criteria of this phase. However, it should be noted here that manual adjustments were made in the absence of less well-defined DIP peaks.

Figures 7.16 to 7.18 show the calcium hydroxide distribution at the coarse aggregate interface region of 3 and 28 day old concretes mixed with different types and conditions of coarse aggregate. The results show that there is a lot of calcium hydroxide accumulated around the aggregate surface region at both ages for the concretes made with Quartz and the dark grey synthetic aggregate prepared in both dry and pre-wetted conditions. The highest level of calcium hydroxide is at about 1 to 2 microns from the interface. This amount then decreased sharply within a distance up to about 8 microns and tended to have a constant value after that. The calcium hydroxide peak seems to reduce or disappear for the case of concrete with orange synthetic aggregate in both dry and pre-wetted condition. The similar trend happens within the 3-day old Lytag concrete.

There was little development of calcium hydroxide with hydration time between 3 and 28 days and these results indicate that most of the calcium hydroxide developed within the first few days. In some regions, the amount of calcium hydroxide of 3-day old concrete is slightly greater than that of the 28-day old sample. This can be attributed to the variability of the measurement of this phase. It was found that the variability of the calcium hydroxide measurement is generally higher than that associated with the

measurement of porosity or the anhydrous particle (Scrivener et al., 1987 and Scrivener and Gartner, 1988). In addition, concrete is not a homogeneous and uniform material and therefore microstructural variation between sample is expected.

The lowest amount of calcium hydroxide which was recorded within the first few microns seems to indicate the separation of calcium hydroxide from the aggregate surface which was also mentioned by Head (2001). This is probably because of the porosity or the space in this region being filled by the low density C-S-H gel produced from the relatively small cement grain which tends to accumulate in this area (Scrivener and Gartner, 1988). However it is also probably due to the mistake from defining the threshold value during the image analysis. The boundary pixels of a phase of interest, i.e. calcium hydroxide in this case, are always mixed with other phases and therefore the grey level is changed. In addition, a cluster of calcium hydroxide that seems to precipitate directly on the aggregate surface is observed in many BSE images. This observation is agreement with the observations from other researchers (Monteiro et al., 1985; French, 1991; Bonen, 1994 and Diamond, 2004). Therefore, it is reasonable to ignore the information of the first strip.

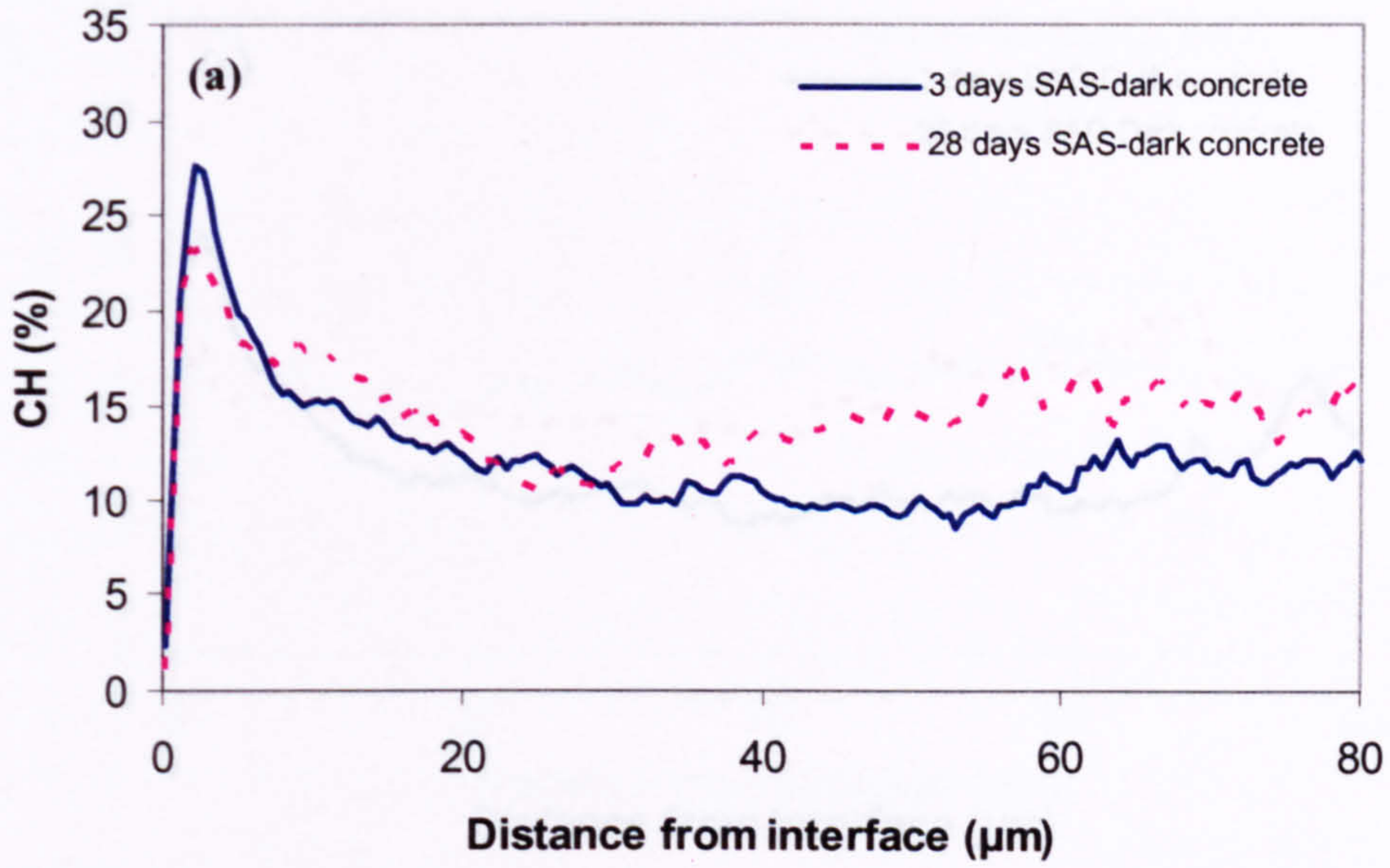

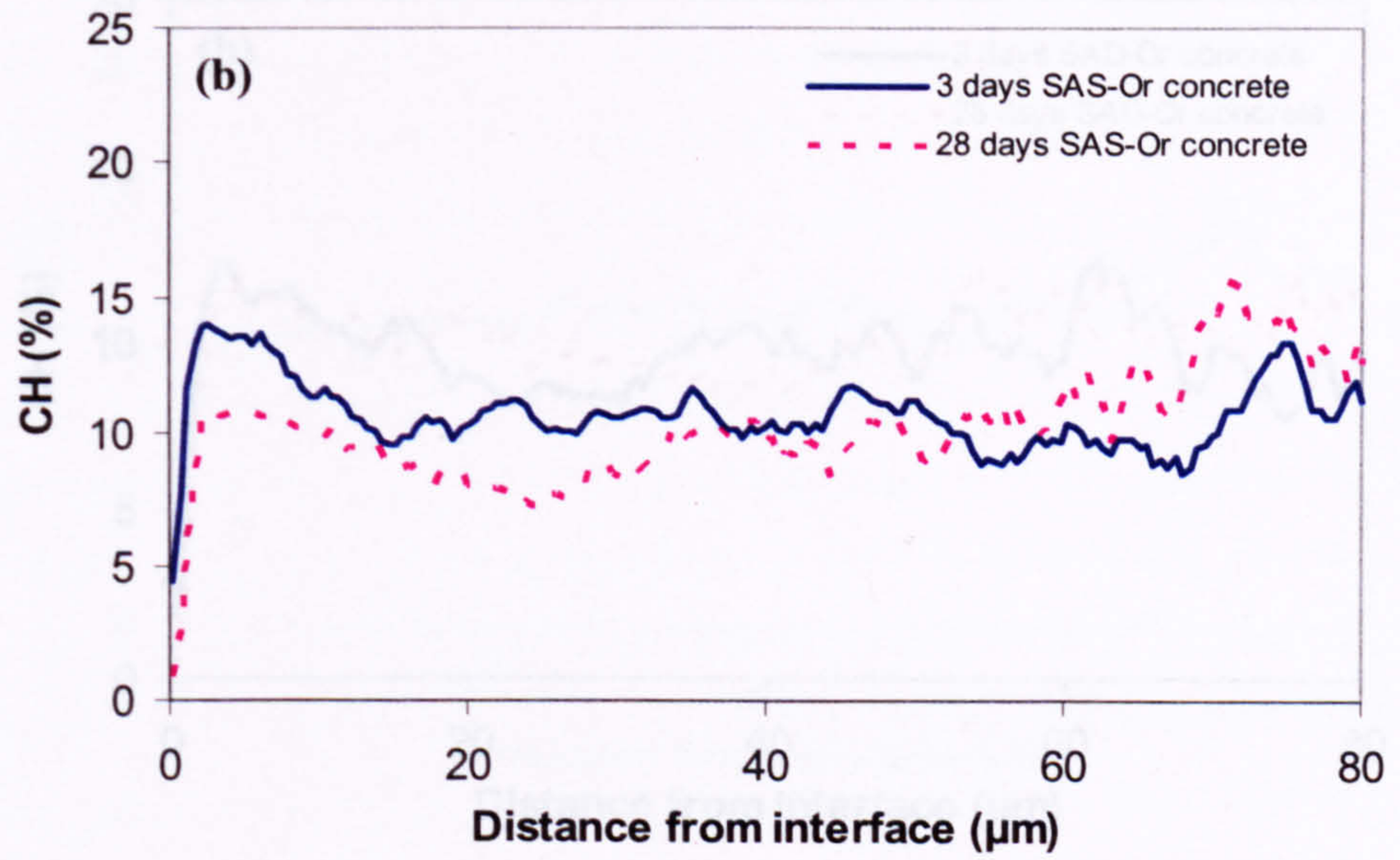

.**Figure 7.16** Calcium hydroxide distribution of concrete mixing with pre-wetted synthetic aggregate. (a) synthetic aggregate with dark grey color, (b) synthetic aggregate with orange color.

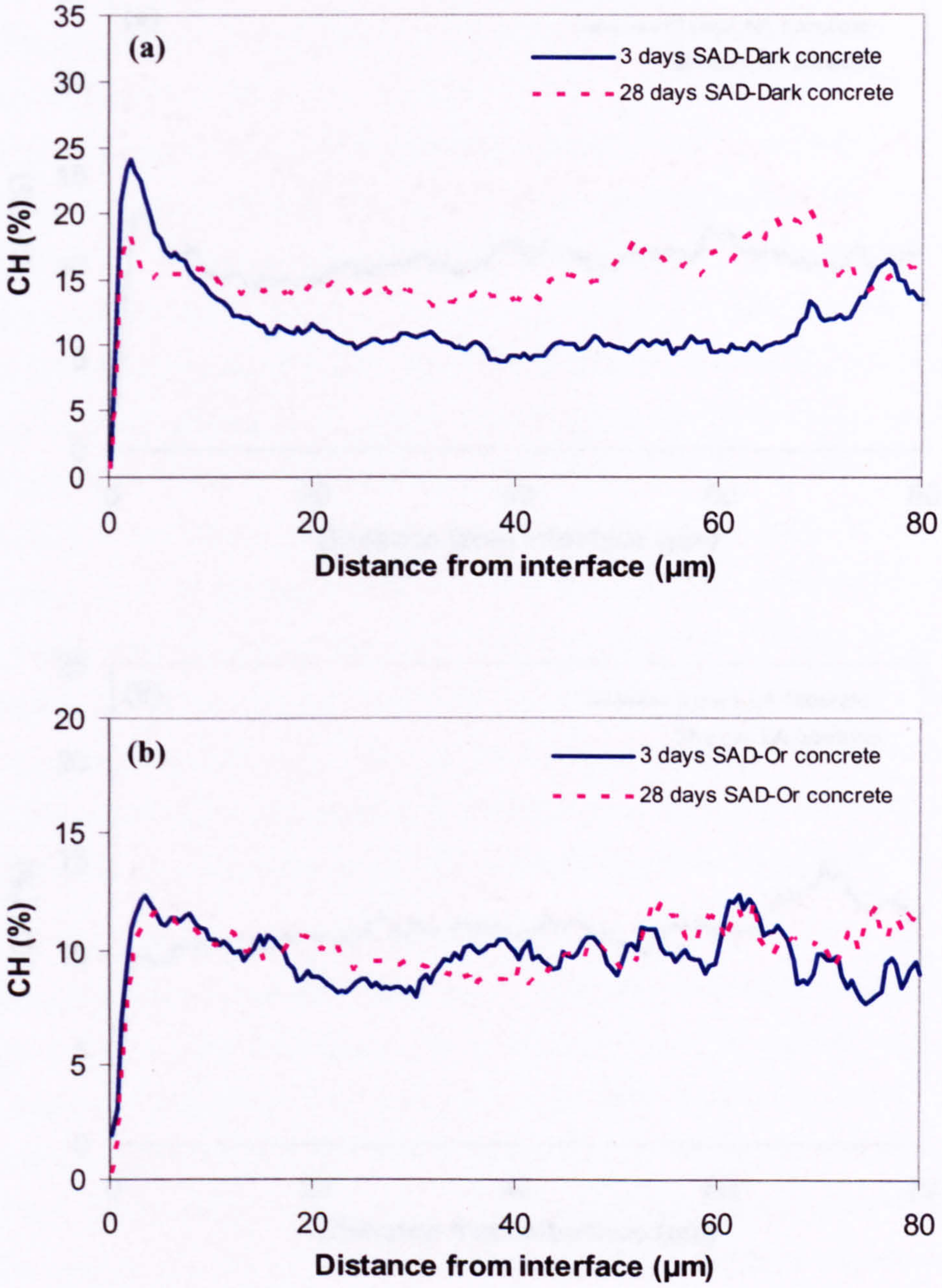

Figure 7.17 Calcium hydroxide distribution of concrete mixing with dry synthetic aggregate. (a) synthetic aggregate with dark grey color, (b) synthetic aggregate with orange color.

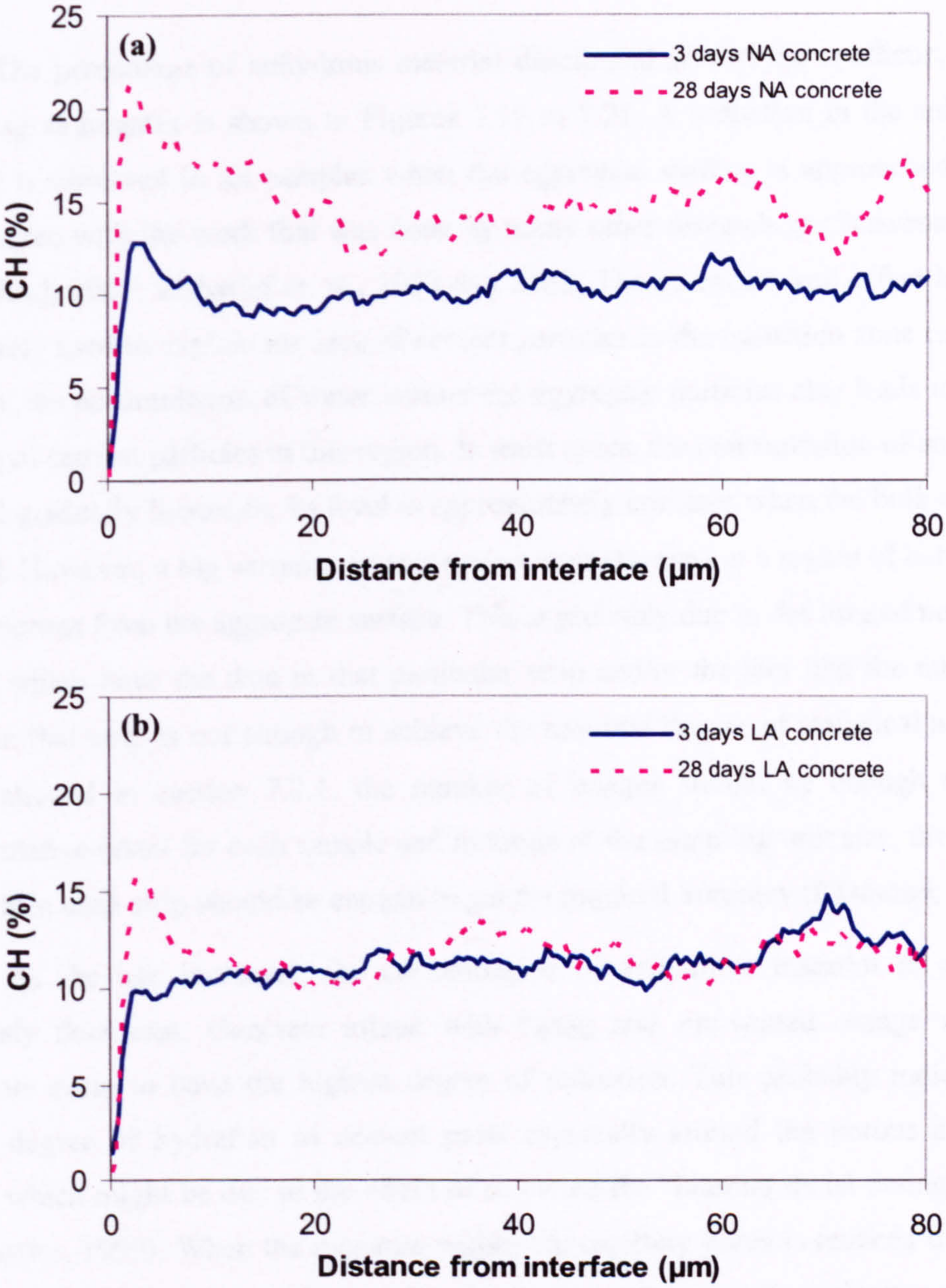

Figure 7.18 Calcium hydroxide distribution of concrete mixing with the pre-wetted coarse aggregate. (a) quartz or natural aggregate, (b) Lytag aggregate.

7.2.5 Effect of hydration time on anhydrous distribution

The percentage of anhydrous material distributed around the synthetic, natural and Lytag aggregates is shown in Figures 7.19 to 7.21. A reduction in the anhydrous material is observed in all samples when the aggregate surface is approached. These results agree with the work that was done by many other researchers (Scrivener et. al., 1988; Head, 2001; Elsharief et. al., 2003 and 2005).The so-called wall effect has been extensively used to explain the lack of cement particles in the transition zone region. In addition, the accumulation of water around the aggregate particles also leads to a poor packing of cement particles in this region. In most cases, the concentration of anhydrous material gradually increases; its level is approximately constant when the bulk region is reached. However, a big variation in some cases was observed at a region of between 60 to 80 microns from the aggregate surface. This is probably due to the limited number of images which have the data in that particular strip and/or the fact that the number of pixels in that strip is not enough to achieve the required degree of statistical accuracy. As mentioned in section 7.2.1, the number of images should be enough to get a representative result for each sample and in terms of the sampling unit size, the number of pixels in each strip should be enough to get the required accuracy (Diamond, 2001[a]).

As the age increases, the concentration of anhydrous material in all cases obviously decreases. Concrete mixed with Lytag and pre-wetted orange synthetic aggregate seem to have the highest degree of reduction. This probably indicates the higher degree of hydration of cement paste especially around the porous aggregate region which might be due to the effect of so called the "internal moist curing" (Bentz and Snyder, 1999). When the moisture within the capillary pores is reduced due to the hydration process, the water kept inside the porous aggregate then migrates outwards into the cement paste and leads to the enhancement of the degree of hydration. The greater and more interconnected pore space which normally occurs in early age concrete makes this process more effective.

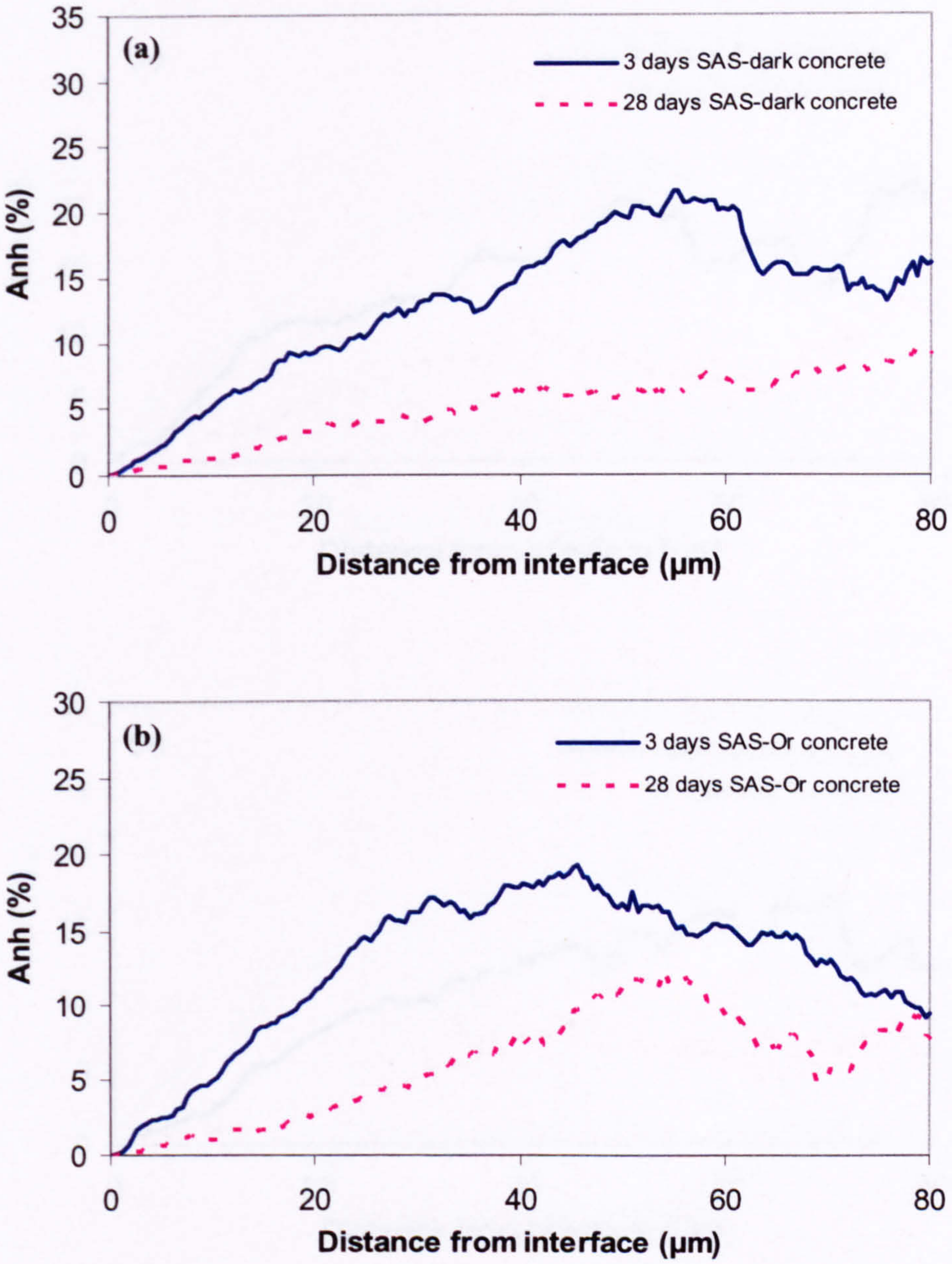

Figure 7.19 Anhydrous distributions for concrete mixing with the pre-wetted synthetic aggregate. (a) synthetic aggregate with dark grey color, (b) synthetic aggregate with orange color.

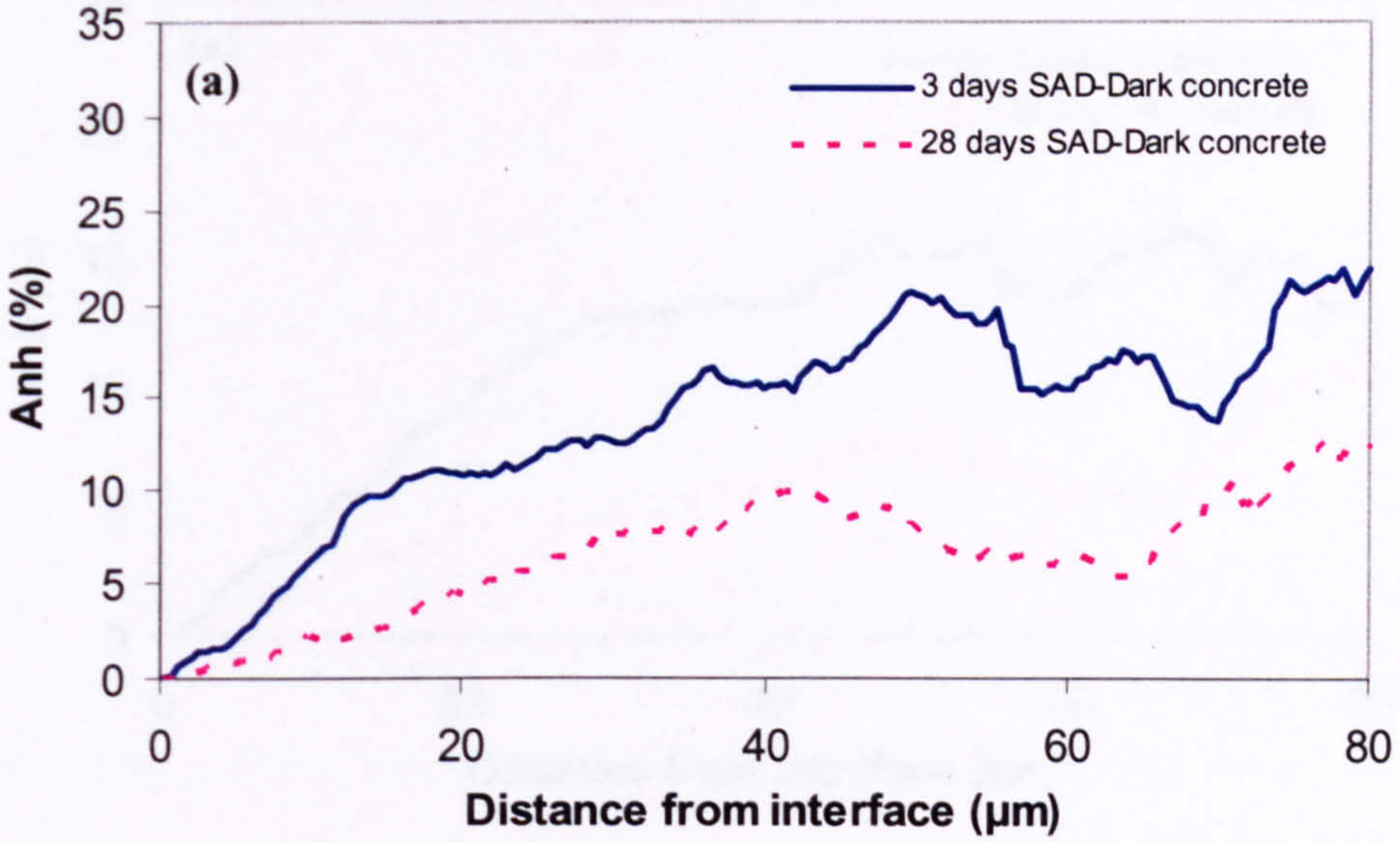

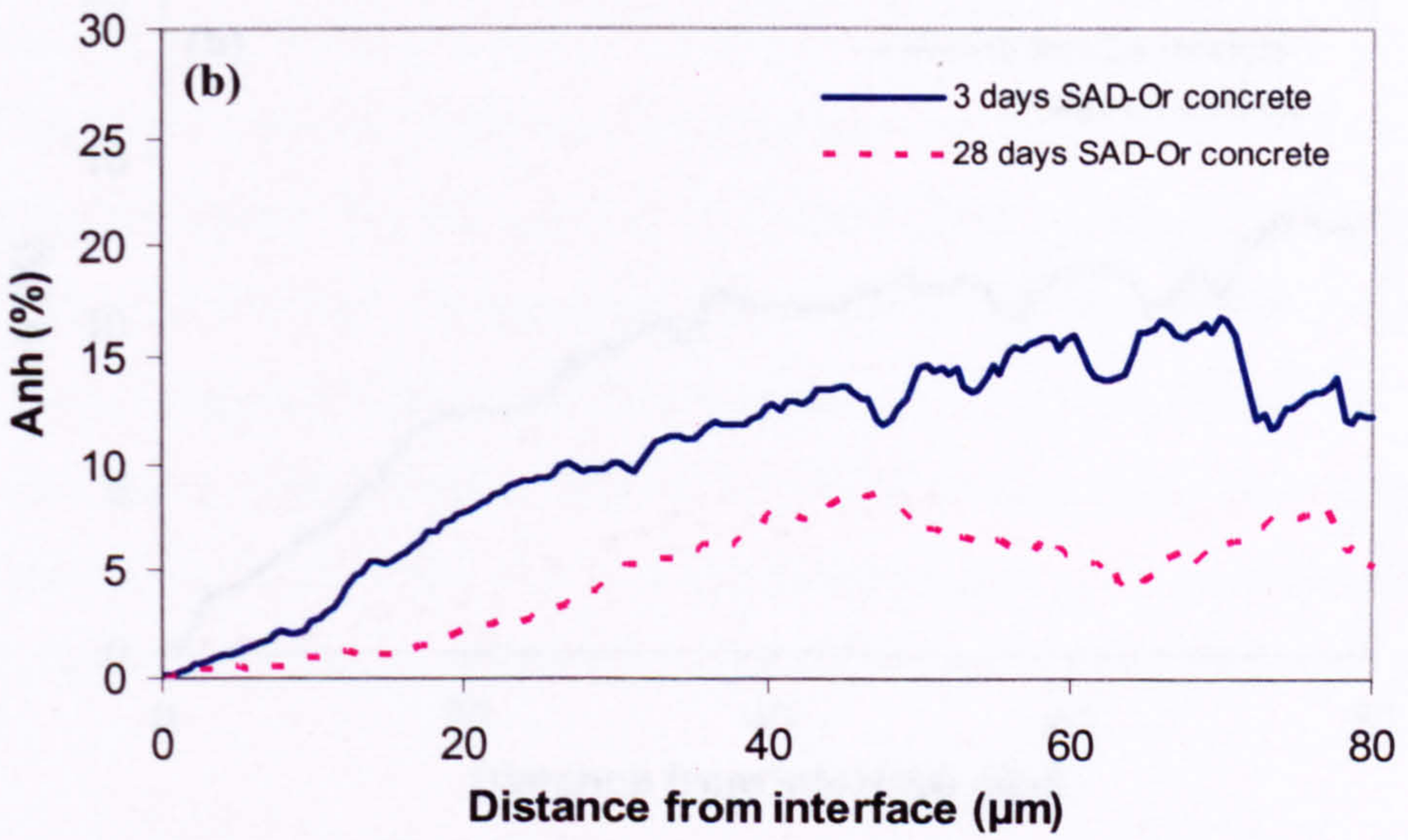

Figure 7.20 Anhydrous distributions for concrete mixing with dry synthetic aggregate. (a) synthetic aggregate with dark grey color, (b) synthetic aggregate with orange color.

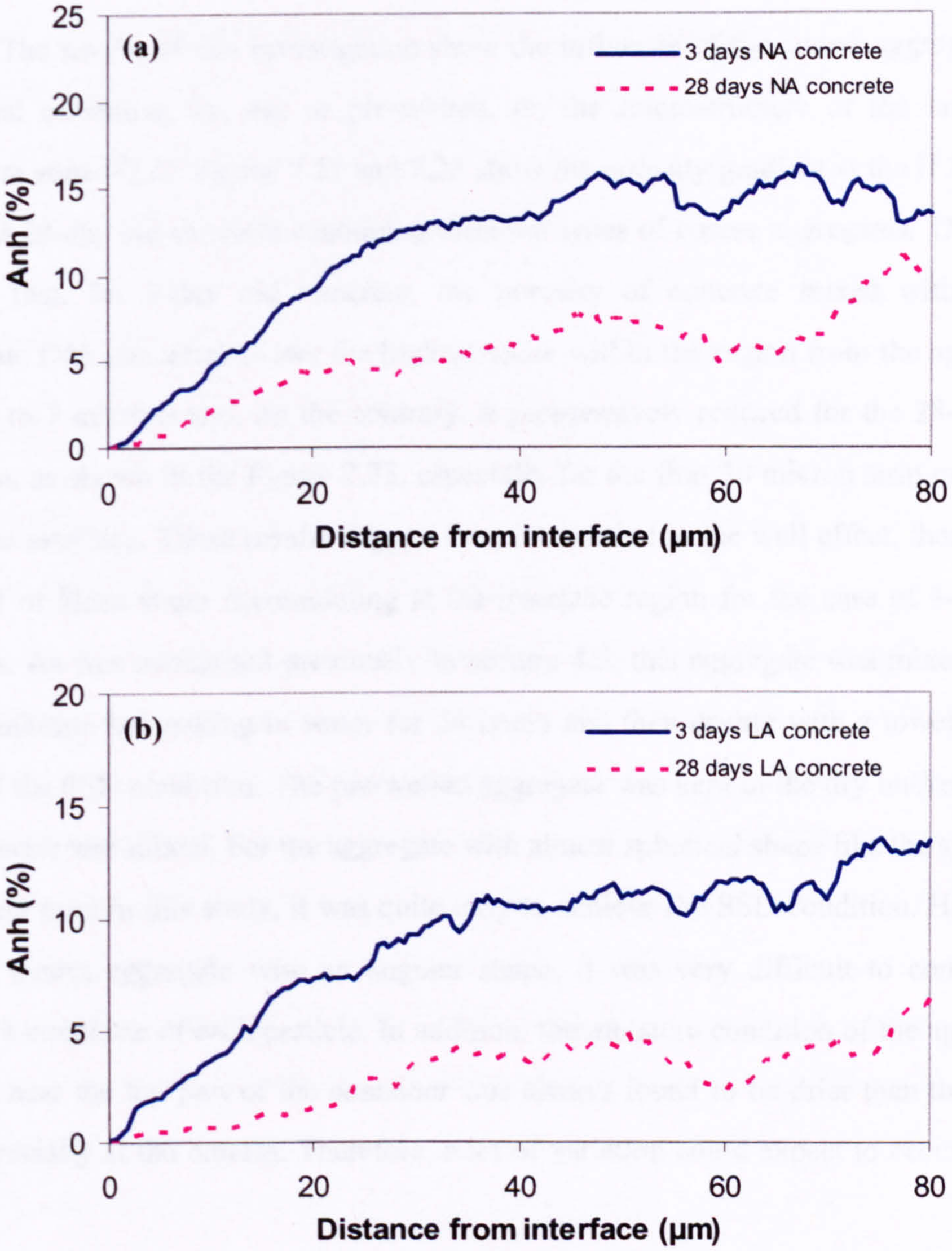

Figure 7.21 Anhydrous distributions for concrete mixing with the pre-wetted coarse aggregate. (a) quartz or natural aggregate, (b) Lytag aggregate.

7.2.6 Effect of the aggregate type and its moisture condition

The results of this investigation show the influence of the coarse aggregate and its initial condition, i.e. dry or pre-wetted, on the microstructure of the interfacial transition zone (ITZ). Figure 7.22 and 7.23 show the porosity gradient at the ITZ region of 3 and 28-day old concrete containing different types of coarse aggregates. The result reveals that, for 3-day old concrete, the porosity of concrete mixed with quartz aggregate (NA concrete) shows the highest value within the region from the aggregate surface to 7 microns and, on the contrary, it progressively reduced for the 28-day old concrete, as shown in the Figure 7.23, especially for the first 30 micron strip measured from the interface. These results suggest that, in addition to the wall effect, there could be a lot of bleed water accumulating at the interface region for the case of 3-day old samples. As was mentioned previously in section 4.3, this aggregate was mixed in the SSD condition by soaking in water for 24 hours and then drying with a towel until it reached the SSD condition. The pre-wetted aggregate was kept in the dry bucket before the concrete was mixed. For the aggregate with almost spherical shape like the synthetic aggregate used in this study, it was quite easy to achieve the SSD condition. However, for the quartz aggregate with an angular shape, it was very difficult to control the moisture condition of each particle. In addition, the moisture condition of the aggregate located near the top part of the container was always found to be drier than the lower part especially at the bottom. Therefore, a lot of variation could expect to occur in this mix.

The orange coloured synthetic aggregate, mixed in a dry condition (SA-Dry Or), has the highest porosity within the regions between about 11 to 40 microns and 0 to 35 microns for 3 and 28-day old concretes, respectively. For 3-days old, the maximum porosity is reached at a distance of about 25 microns from the aggregate interface and there is a slight variation in the porosity from this point to the aggregate surface. The maximum value is reached at around 8 microns for 28-day old sample. It should be emphasized here that the porosity within the first 10 microns for both 3 and 28-day old concrete is different from the other cases which show a big reduction in the porosity

around the aggregate surface region. This is probably due to the excessive or too rapid absorption of water by the dry porous aggregate. A lot of pores and the inter-granular cracks (see Figure 7.3) observed at this region also support this idea. It should be noted that too much and/or so rapid absorption of water can affect the degree of hydration at the interface region because of desiccation. T. C. Powers showed that hydration will almost stop resulting in no additional improvement of the quality of the cement paste when the moisture content remains below a critical level, i.e. internal relative humidity of about 80 percent, (cited by Carrier and Cady, 1970). However, this microstructural characteristic is not observed in the dark grey particles mixed in the same condition. The difference in pore structure which leads to a different effect on the movement of water around the aggregate particle is the possible reason for that.

The porosity distribution in the case of the dark grey synthetic aggregate mixed in dry condition (SA-Dry dark) for both 3 and 28-day old concrete is generally similar to the others; i.e. a large drop of the porosity value around the aggregate surface where the highest porosity is approximately 10 microns away from the aggregate surface followed by a gradual reduction in the porosity until it reaches the point that has not much changing the porosity level. As shown in Figure 7.22, the results clearly show that the porosity of concrete mixed with SA-Dry dark aggregate in the region from the aggregate surface to approximately 30 micron has the lowest porosity value and the remaining cases can be arranged, in ascending order, into the pre-wetted synthetic aggregate with orange color (SA-SSD Or), Lytag coarse aggregate and the dark grey pre-wetted synthetic aggregate (SA-SSD dark). Both of the SA-Dry Or and NA concrete have the highest porosity in the region between 7 and 22 microns. For the 28-day old concrete, considering the strip from the aggregate surface to a distance about 30 microns, the porosity of the SA-Dry Or is the highest. The quartz aggregate concrete appears to have the lowest porosity followed by the SA-Dry dark and SA-SSD dark concrete. Based on the results for these two latter cases, they generally agree with the results that were reported by other researchers who suggested that the absorption of water by the porous lightweight aggregate can lead to the reduction of the interfacial transition zone porosity (Zhang and Giorv, 1990; Lo et. al., 1999; Elsharief et. al.,

2005). During the concrete casting, the water that tends to accumulate around the aggregate particle will be absorbed by the synthetic aggregate particles. The movement of water into the aggregate will continue until the aggregate is fully saturated by water and this process leads to the reduction of the original water cement ratio (w/c) of the cement paste around the interface region. In addition, the reduction of water can lead to a better packing of the cement particles in this zone. However, as mentioned before, this conclusion is valid as long as the water migration from the paste into the aggregate particle is not too high or too rapid.

As shown in Figure 7.23, a similar porosity distribution for the 28-day old concrete containing the Lytag and the SA-SSD orange at the region from the aggregate surface to a distance around 34 microns was observed. These two conditions seem to have a porous interfacial transition zone as observed in the case of the SA-Dry Or. However, as shown in Figure 7.2(b) and 7.5(b), a fairly dense microstructure with a lot of isolated pores filled with a low density hydration product was observed in both cases. These pores are obviously a relict of the cement grain which is generally called the 'hollow shell pore' and was first discovered by Hadley in 1972 (Hadley, 1972). Similar findings were reported by Scrivener et al. (Scrivener et al., 1988 and Scrivener, 1989) in concrete containing silica fume, where they found some increase in the porosity which was almost entirely due to the presence of the hollow-shell pore. Although there are many researchers who have reported the existence of the hollow shell pore (Barnes et al., 1978; Dalgleish et al., 1982; Pratt and Ghose, 1983; Kjellsen et al., 1996; Kjellsen and Helsing Atlassi, 1999 and Hadley et al., 2000), it should be noted that some of these pores might be an artifact created during the specimen preparation and the segmentation for the porosity. A relatively small particle of low density product with substantial porosity surrounded by a zone of relatively dense C-S-H was observed by using the much higher resolution technique of TEM on the ion-thinned section (Groves, 1987; Richardson and Groves, 1993 and Richardson, 2002). As mentioned by Richardson (2002), the porous area inside the dense rim may not be filled by the resin during the resin impregnation. The low density product can then be removed during the grinding and polishing process and make that grain look like an isolated pore on the BSE images.

On the contrary, some of the low density product inside the pore can also possibly occur because the pore depth is less than the depth of the electron beam interaction volume. The backscattered electrons that come from the solid phase at the bottom part of the pore increase the brightness of that area on the BSE image and make it look like a very low density product.

Hollow shell pores occur due to the cement particles, especially with the size smaller than about 5 microns, hydrating very quickly before the hydration shell becomes less permeable (Scrivener and Gartner, 1988 and Scrivener, 1989). The size and the rate of hydration of the anhydrous particle at the early age seems to be a key factor for the occurrence of this kind of pore. Brown et al. (1984) and Groves (1987) found a strong dependence of the rate of early age hydration on the water-binder ratio. They found that the reaction rate increased rapidly with increasing water-cement ratio.

A lot of hollow shell pores that occurred in the Lytag and SA-SSD Or concrete might be due to a coating of these wet and porous aggregates by small anhydrous material during concrete casting. In addition, the migration into the cement paste of the water that was kept inside these aggregates every time the water in the capillary pores reduced due to cement hydration might influence the rate of hydration. It would be of interest to study this phenomenon but time constraints did not allow it to be investigated further.

As shown in Figures 7.1 to 7.6, in general, most of the calcium hydroxide for all cases appear as a massive cluster with irregular shape and various sizes. The shape and size of this phase generally depends on the space available. For example, Diamond (2001[b]) observed the elongated shape of calcium hydroxide and he suggested that it corresponds to the precipitation of this feature in narrow spaces between the partially reacted cement grains. However, it can also be the thin hexagonal platelets that orientate perpendicular to the section (Gallucci and Scrivener, 2007). The results, as shown in Figure 7.24 and 7.25, show that the calcium hydroxide tends to precipitate on the quartz and the dark grey synthetic aggregate surface especially for the case of 28-day old concrete. The enrichment of the calcium hydroxide on the siliceous aggregate surface,

i.e. quartz and dark grey synthetic aggregate (mainly composed of small quartz particles), is consistent with the observation by other researchers (French, 1991; Bonen, 1994 and Head, 2001). On the contrary, there is no peak that represents a build up of calcium hydroxide on the surface of the orange synthetic aggregate. Holm et. al. (1984) and Sarkar et. al. (1992) also observed the absence of this feature at the paste-aggregate interface of the Lightweight aggregate concrete. The local enrichment of the calcium hydroxide in the area adjacent to the aggregate surface may be attributed to several factors, i.e. the availability and composition of the anhydrous material in that region, the aggregate surface characteristic, the absorption capacity of the aggregate and the higher porosity derived from the high water-cement ratio (Sarkar et al. 1992, Bonen 1994 and Crumbie 1994). Based on the difference between the dark grey and orange synthetic aggregate, both the aggregate surface characteristic and the water absorption capacity might be the possible explanation for the lack of calcium hydroxide adjacent the orange synthetic aggregate surface. The diffusion of the Ca^{2+} and OH^- ions into a very porous aggregate like the orange synthetic aggregate is another possible reason for the lack of the calcium hydroxide at the region adjacent to the aggregate surface. The penetration of Ca into porous lightweight aggregate was also observed by Zhang and Gjørv (1990) and by Wasserman and Bentur (1996).

Figure 7.26 and 7.27 show the distribution of the anhydrous material with distance from the coarse aggregate surface for the concrete containing different types of aggregates. In general, the concentration of anhydrous material gradually decreases until it reaches the aggregate surface and the amount of this feature clearly reduces with age for all cases considered. The results reveal that there is no anhydrous material at the aggregate surface and a very low amount of this phase within the first 10 microns. The so-called wall effect combined with the effect of bleed water around the aggregate surface might be a good explanation for this. An increase in the anhydrous slope at the distance of about 10 to 15 microns for the 3-day old samples suggests that bigger cement grains tend to appear in that area. A similar finding was obtained by Crumbie (1994) and Scrivener et. al. (2004). Different types of aggregate which have different shapes and microstructure can affect the distribution of the anhydrous material

especially at the region very close to the aggregate boundary. The porous nature of the coarse aggregate can affect the amount of water that tends to accumulate at the aggregate surface region and therefore influence the porosity and the packing of the anhydrous particles in that area.

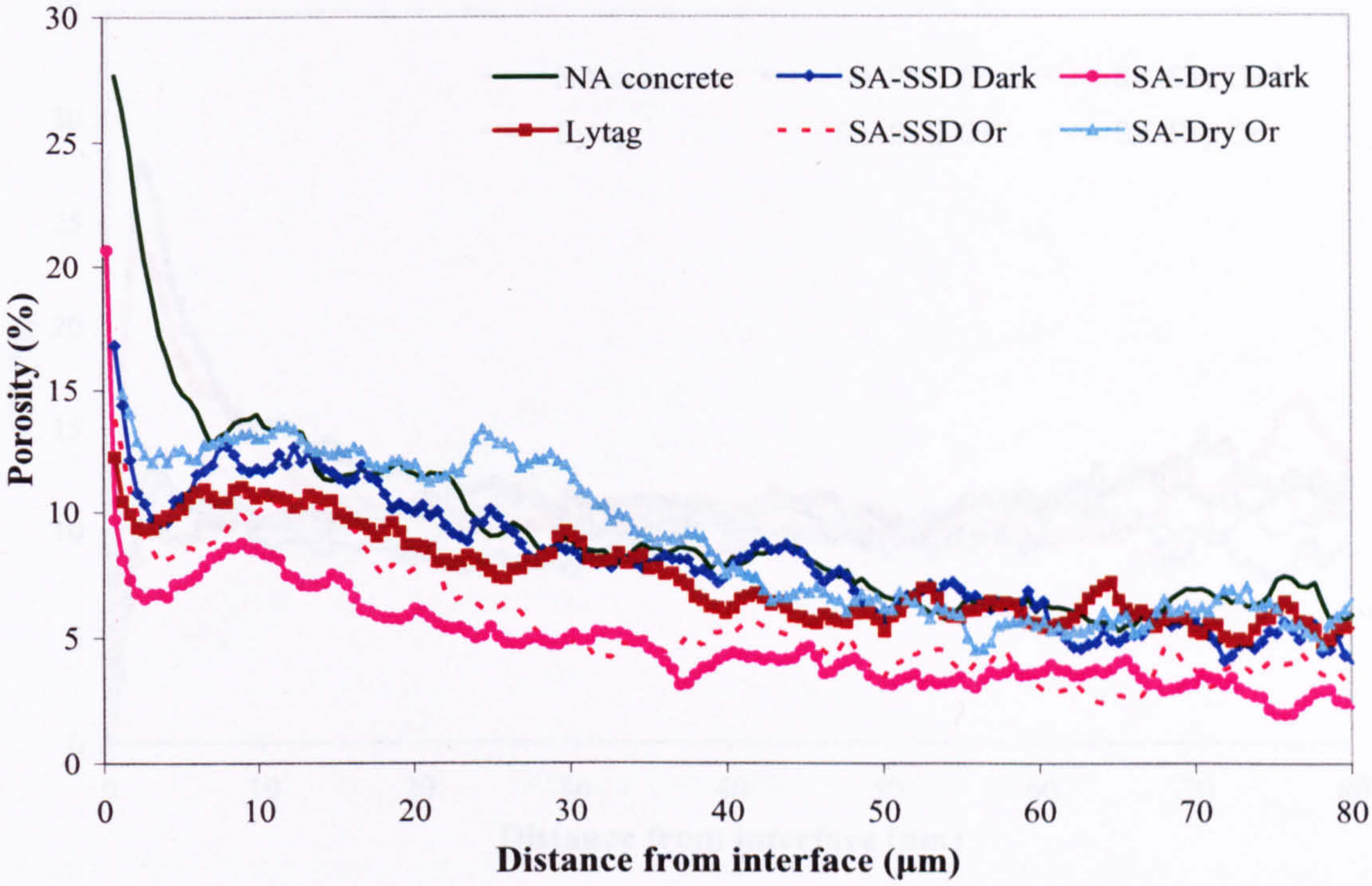

Figure 7.22 Porosity distribution plotting with distance from the interface of 3-day old (w/c = 0.53) concrete containing different types of aggregate.

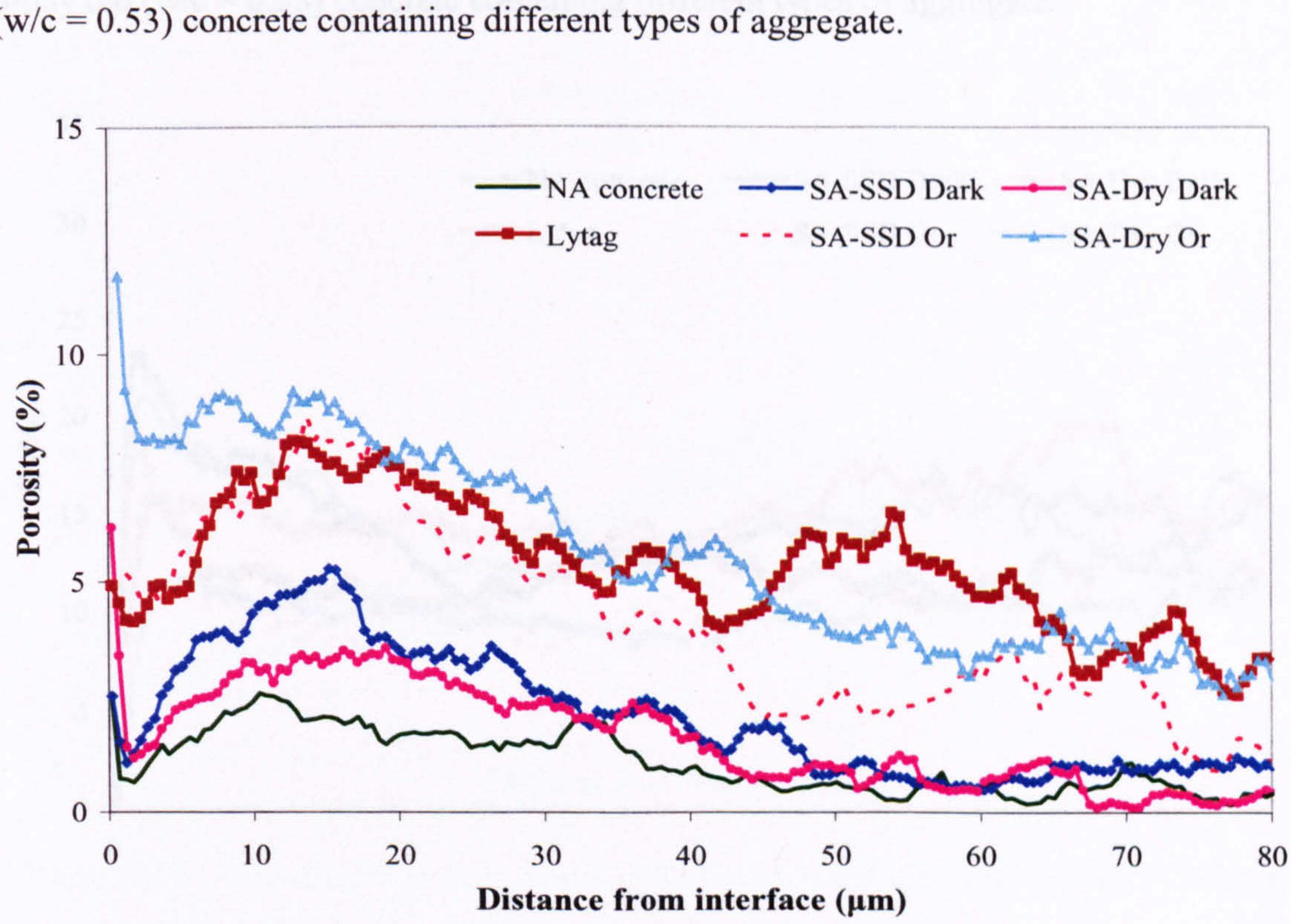

Figure 7.23 Porosity distribution plotting with distance from the interface of 28-day old (w/c = 0.53) concrete containing different types of aggregate.

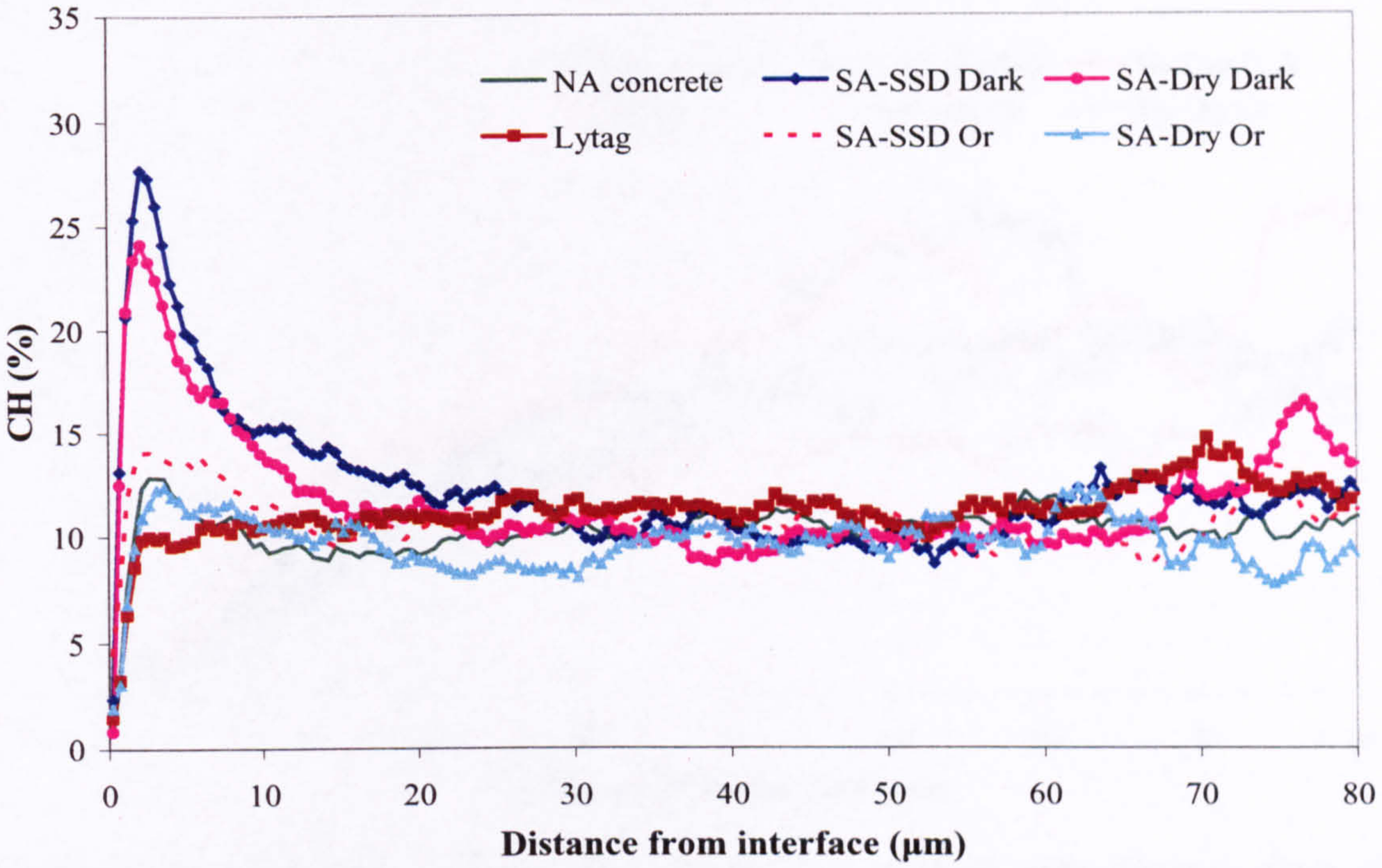

Figure 7.24 Calcium hydroxide distribution plotting with distance from the interface of 3-day old (w/c = 0.53) concrete containing different types of aggregate.

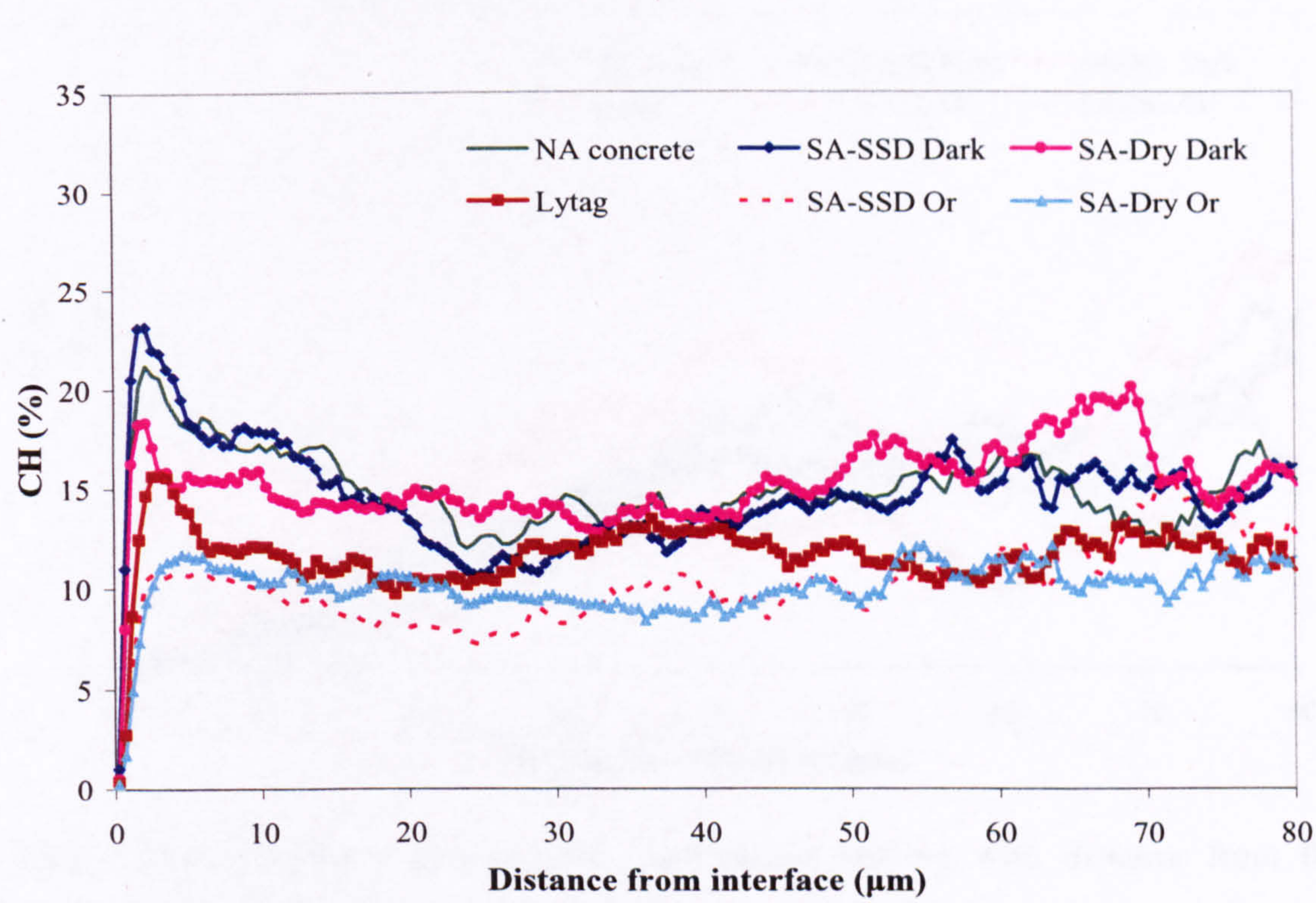

Figure 7.25 Calcium hydroxide distribution plotting with distance from the interface of 28-day old (w/c = 0.53) concrete containing different types of aggregate.

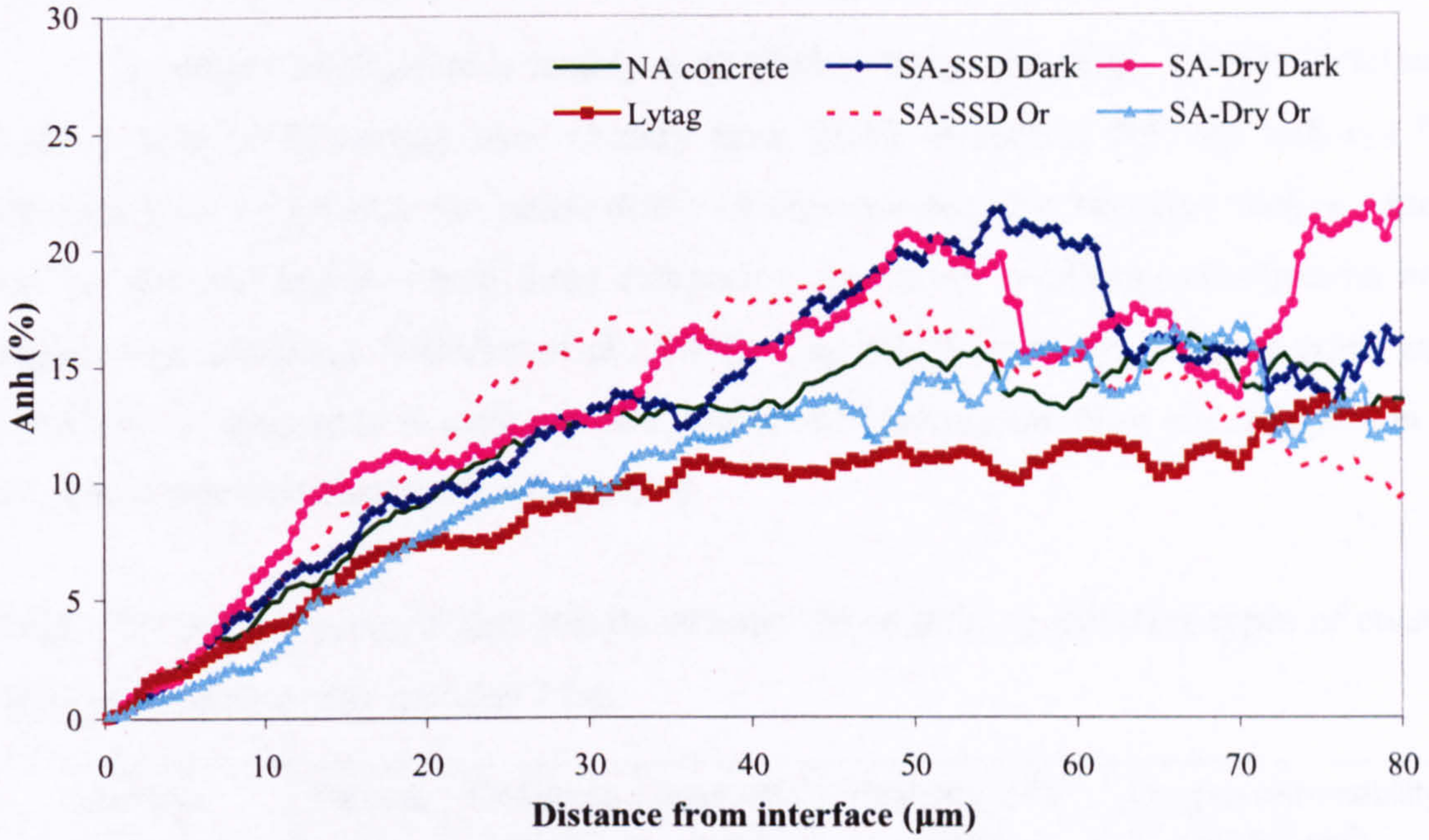

Figure 7.26 Anhydrous cement grain distribution plotting with distance from the interface of 3-day old (w/c = 0.53) concrete containing different types of aggregate.

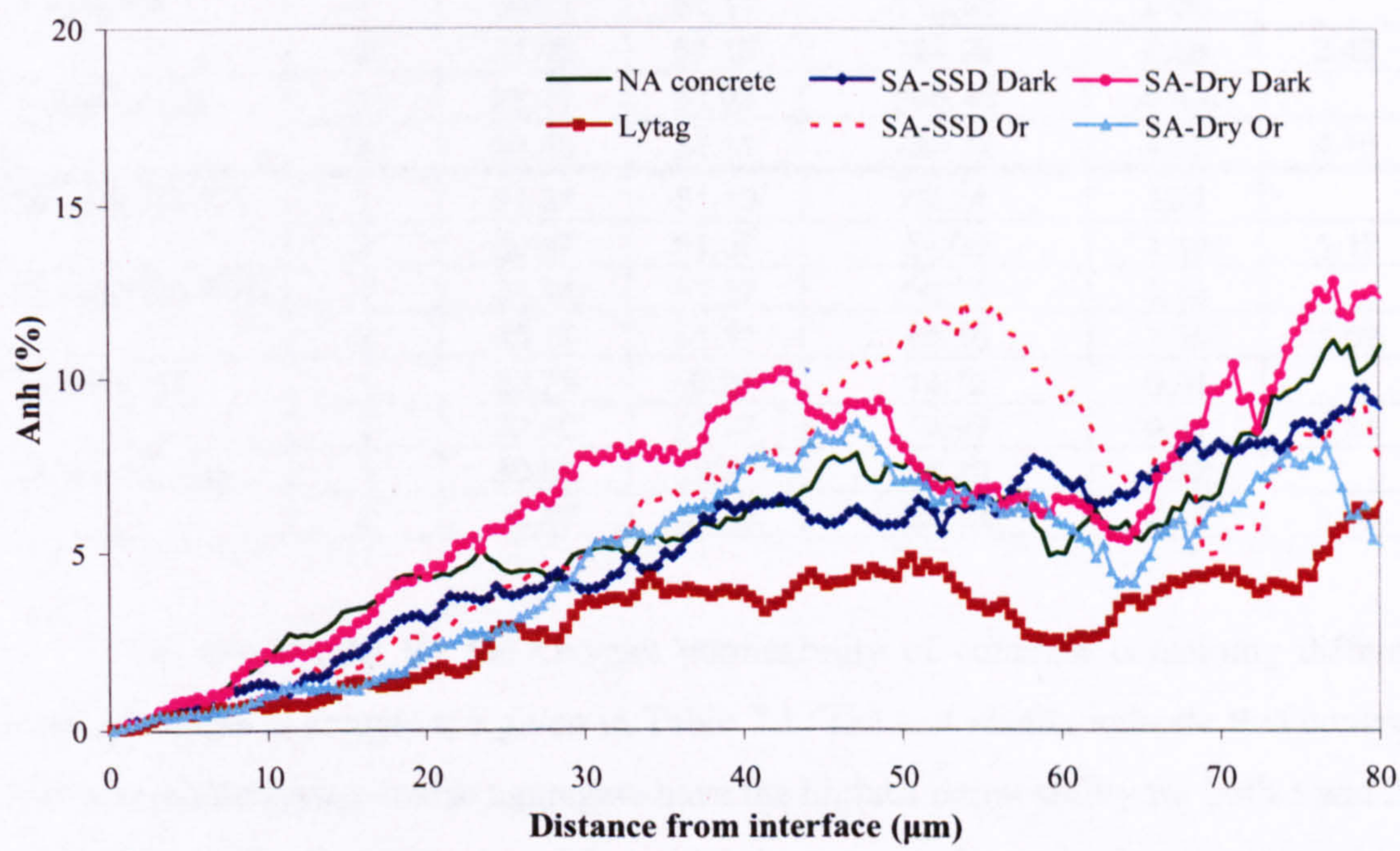

Figure 7.27 Anhydrous cement grain distribution plotting with distance from the interface of 28-day old (w/c = 0.53) concrete containing different types of aggregate.

7.3 Permeability of concrete with different types of coarse aggregate

Durability of concrete is mainly controlled by its permeability. Details of the test method used in this study have already been given in section 4.6 and will not be repeated here. In general, the permeability of concrete depends on many factors which can be grouped together into three categories, i.e. stress condition, constituents and sample characteristics (Ollivier et al., 1995). The effect of using different types and conditions of aggregate in concrete (see section 4.3) having the same mix proportion is the main parameter that is of concern here.

Table 7.1 Oxygen permeability results of concrete containing different types of coarse aggregate. Sample was tested at 1 bar.

Sample	Sample No.	Thickness (mm)	Diameter (mm)	Flow rate x 10^{-3} (cm^3/s)	Oxygen permeability x 10^{-16} (m^2)	
3 days SA-Dry	1	31.67	51.08	65.60	1.37	
	2	29.12	51.03	114.32	2.19	1.78
3 days SA-SSD	1	34.84	50.90	78.14	1.80	
	2	33.71	51.00	114.65	2.55	2.18
3 days NA	1	30.81	51.11	116.90	2.36	
	2	31.46	51.16	124.05	2.56	2.46
3 days Lytag	1	28.21	51.03	265.48	4.93	
	2	31.08	51.11	224.32	4.58	4.76
28 days SA-Dry	1	31.31	51.10	60.24	1.24	
	2	30.97	51.07	54.06	1.10	1.17
28 days SA-SSD	1	34.44	51.17	50.06	1.13	
	2	35.18	51.11	45.36	1.05	1.09
28 days NA	1	33.29	50.97	14.12	0.31	
	2	33.80	51.07	13.95	0.31	0.31
28 days Lytag	1	30.50	50.97	90.20	1.82	
	2	30.57	50.95	103.15	2.08	1.95

The test results for the Oxygen permeability of concrete containing different types of coarse aggregate are given in Table 7.1. The test results indicate that concrete with pre-wetted Lytag coarse aggregate have the highest permeability for both 3 and 28-day old concrete. Concrete containing natural aggregate have the lowest permeability for the 28-day old concrete but, in the case of 3-day old concrete, the permeability is slightly greater than the concrete mixed with synthetic aggregate.

In general, there are three distinct ways in which the aggregates affect the permeability of concrete, i.e. it reduces the effective area of flow, increases the flow

path length and introduces fissures and cracks around the interface (Powers et al., 1954; Nyame, 1985). Increasing of the pore turtiosity by the aggregate inclusion makes the oxygen move around the aggregate and leads to a reduction of permeability while the presence of the porous interfacial transition zone which will create passage ways for the oxygen to get through the concrete resulting in an increase in permeability. Therefore, there are two opposite phenomena occurring within the concrete sample and they will influence the permeability of the whole sample (Delagrave et. al., 1997). The effect of the porous interfacial transition zone on the permeability of mortar or concrete is supported by the works done by Nyame (1985) and Winslow et. al. (1994). Nyame found that the permeability of mortars increases with increasing aggregate volume concentration and this effect was attributed to the porous interfacial zone. Winslow et al. used the mercury intrusion porosimetry (MIP) technique to investigate the pore structure of mortar which has different volume fractions of sand. They found that the 28-day old mortar, which had a sand content more than about 48 percent by volume, showed extra intruded pore space. The hard core/soft shell computer model was used to interpret their experimental results and the percolation of the completely overlapping porous interfacial transition zone was given as an explanation. Based on all this information, the lowest porosity at the interfacial transition zone for the 28-day old quartz aggregate concrete (Figure 7.23) and the increase in the flow path length caused by the dense quartz aggregate inclusion seems to be a reasonable reason for the lowest permeability coefficient (see Table 7.1) in this case.

Several researchers believe that the permeability of the porous lightweight aggregate concrete is similar to or lower than normal weight aggregate concrete (FIP report, 1982 and Zhang and Gjørv, 1991[c]). This is because of the improvement of the transition zone due to the effects of aggregate absorption. However, the opposite results were obtained in this study. The 28-day old synthetic aggregate concrete and both of the 3 and 28-day old Lytag concretes have a permeability coefficient higher than that of the quartz aggregate concrete. This might be due to the combined effects of the porous interfacial transition zone, as can be seen in Figure 7.22 and 7.23, and the porous nature of these coarse aggregates that results in it having no effect on increasing the pore turtiosity in concrete.

Figures 7.28 to 7.31 show the BSE images acquired at low magnification for the 28-day old concrete samples used in this research. Many detectable pores were clearly observed and these pores tend to appear in the closely spaced region between the aggregate particles. The tendency of mixing water to segregate around the tightly packed aggregate and the lack of large anhydrous grains due to the space restriction in this area might be the possible explanation for this phenomenon (Pope and Jennings, 1992). The porous regions tend to connect together and it is possible that they are linked together to form continuous flow channels within the sample. Moreover, there was a possibility for the microcracks to occur especially around these connected porous regions and the aggregate interface due to the very fast drying rate achieved by leaving the sample in the oven at 105°C for about 24 hours. These cracks provide an easy path way for the oxygen to access a porous lightweight aggregate particle, despite the good quality of the cement paste matrix used. The permeability of the investigated sample is therefore affected by the porosity of the aggregate. Similar observations were also found by Nyame (1985) and Lydon (1995). However, the opposite trend was found in the case of the 3-day old synthetic aggregate concrete. The highest porosity at the transition zone region (see Figure 7.22) of the quartz aggregate concrete might be the reason for the higher permeability coefficient when comparing with the case of the synthetic aggregate concrete.

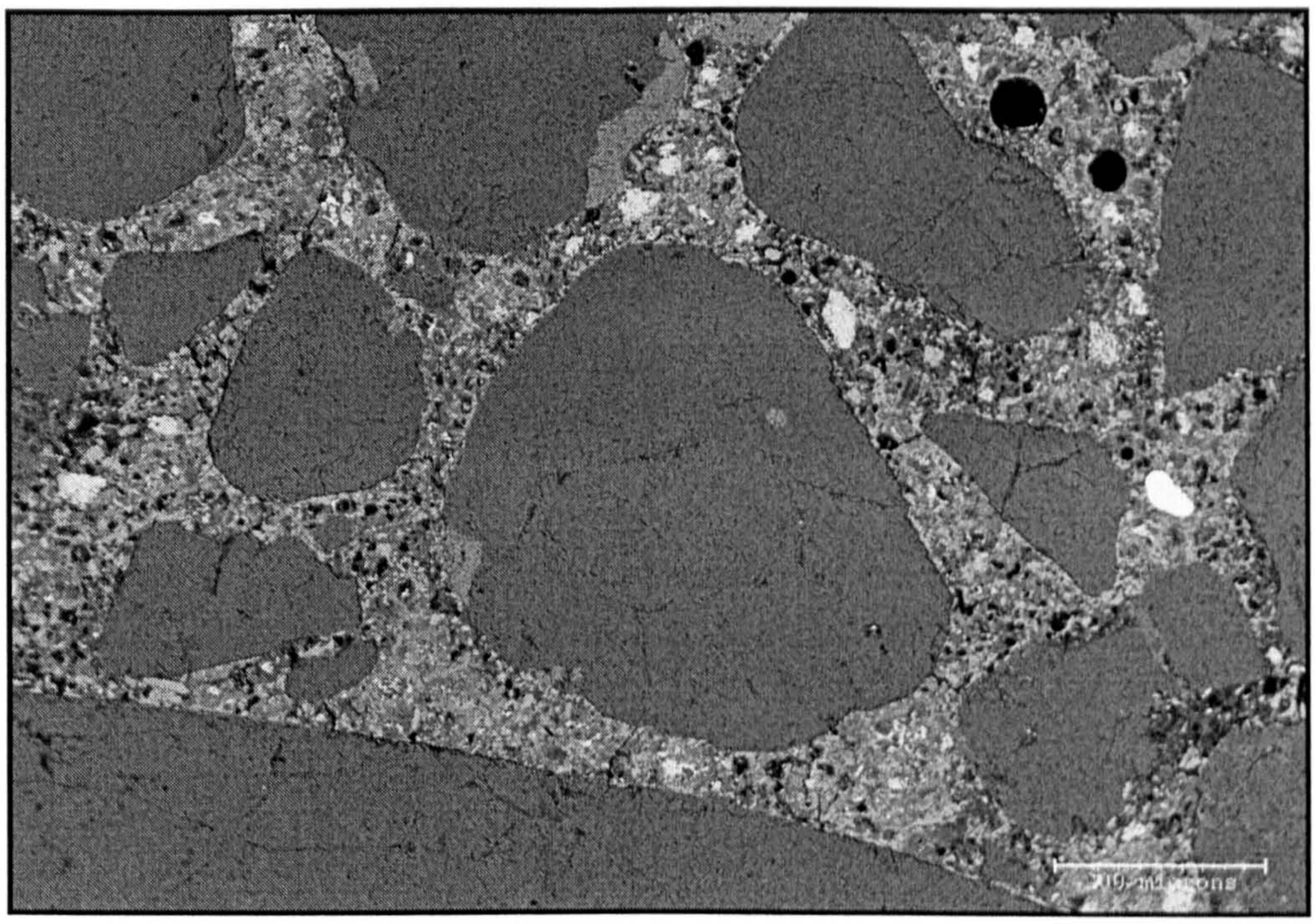

Figure 7.28 Typical BSE image of 28-day old natural aggregate concrete at low magnification.

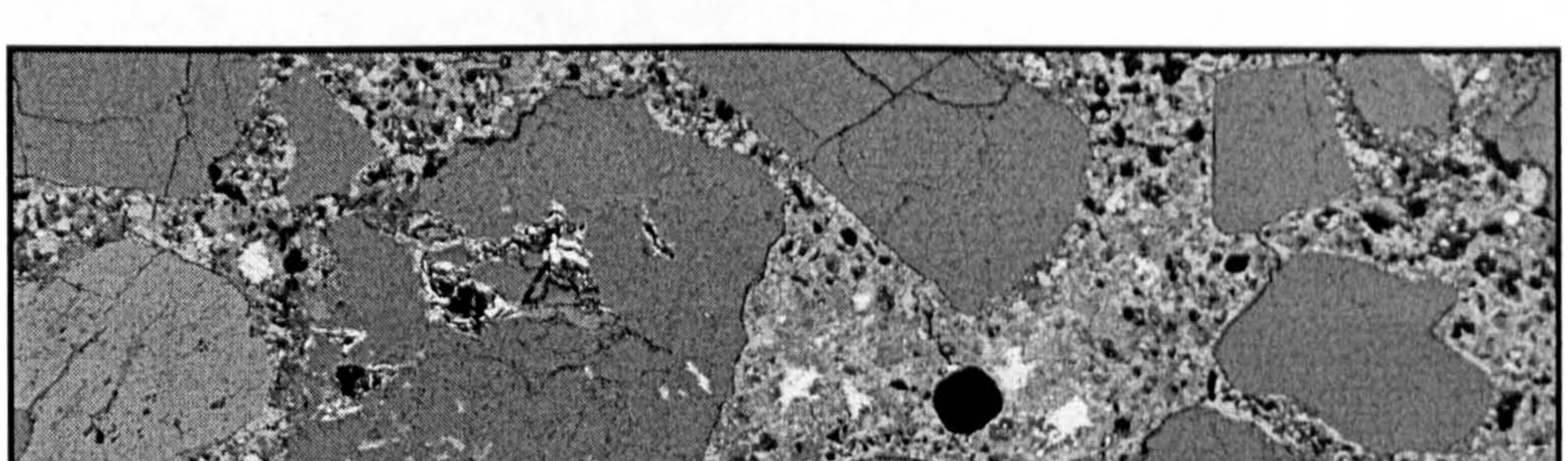

Figure 7.29 Typical BSE image of 28-day old Lytag aggregate concrete at low magnification.

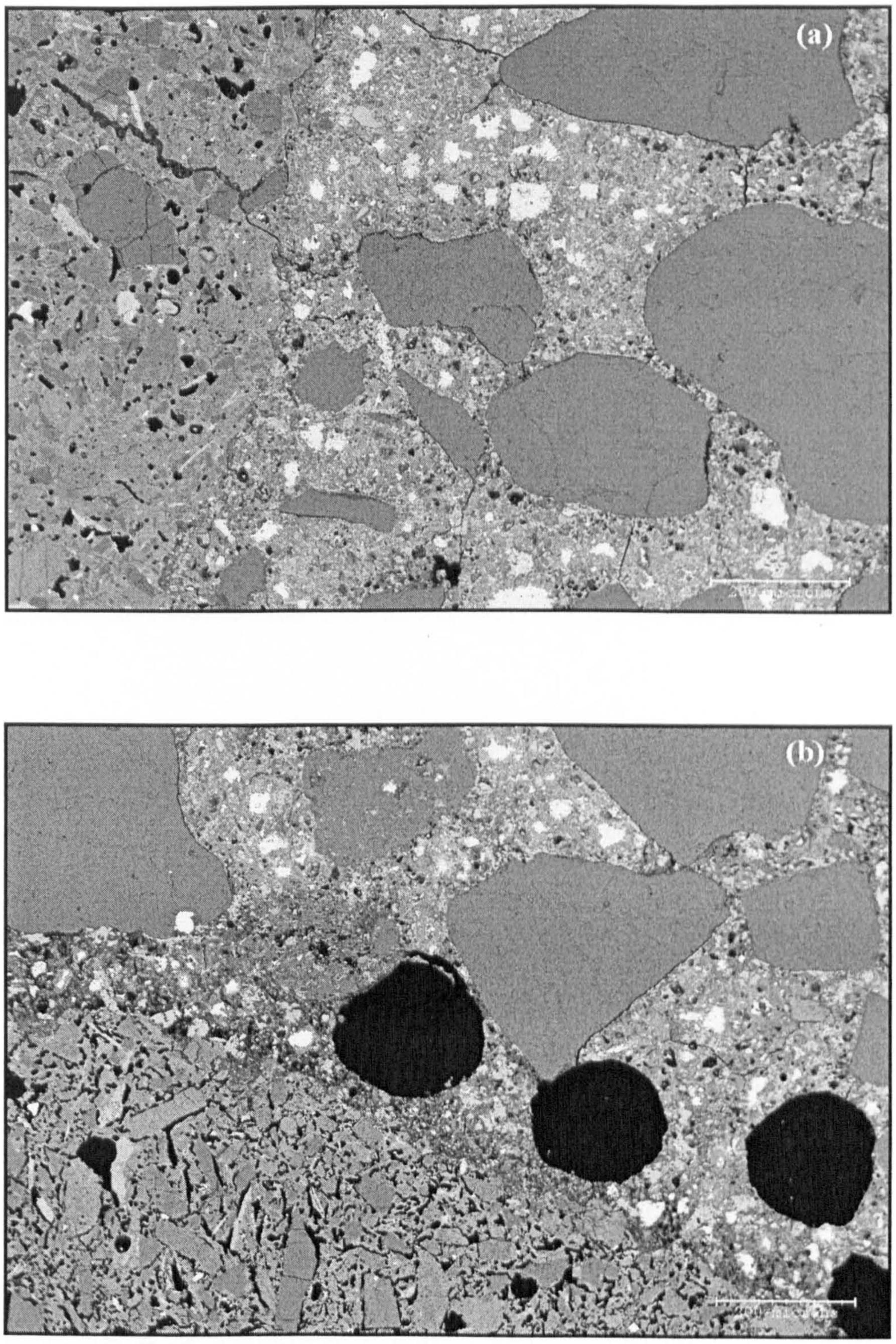

Figure 7.30 Typical BSE image of 28-day old dry synthetic aggregate concrete at low magnification.

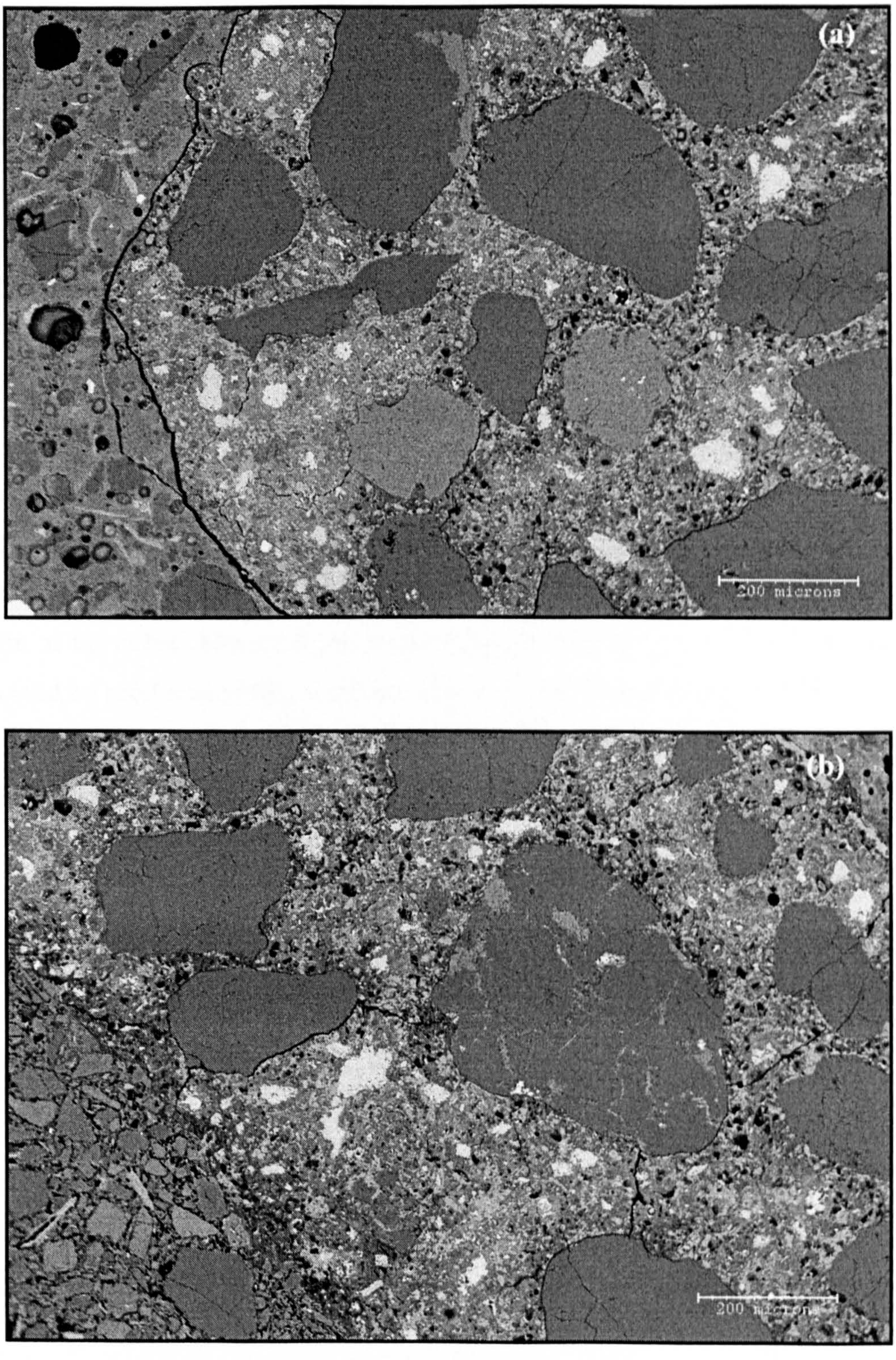

Figure 7.31 Typical BSE image of 28-day old pre-wetted synthetic aggregate concrete at low magnification.

7.4 Compressive strength and modulus of elasticity

The test procedure used for measuring compressive strength and modulus of elasticity was given in section 4.5. In the case of modulus of elasticity the results obtained here may not be comparable with other results from the literature because of the non standard test conditions used by the author (i.e. cube sample was used instead of prism; no load cycling). In general, the testing conditions, i.e. the end condition or the type of loading platens, the sample slenderness ratio and the loading rate, have significant effects on the stress-strain behavior of concrete.

The uniaxial stress-strain curves of 3 and 28-day old concrete containing different types of coarse aggregate are shown in Figure 7.32 and 7.33. It should be noted that only the ascending branch (the pre-peak behavior) and the peak are obtained and presented here. This is mainly because of the difficulty in measuring the descending portion of the curve. Moreover, because of the limiting amount of synthetic aggregate that could be produced within a certain period of time (for example, it will take around 1 to 1.5 months in order to produce about 25 to 30 kg of the synthetic aggregate), only two cube samples for each condition were used for these tests.

Table 7.2 Compressive strength test results

Sample	Compressive strength (N/mm^2)	Modulus of Elasticity (GPa)
3 days NA	25.72	46.59
3 days LA	26.68	27.68
3 SA-SSD	28.26	28.69
3 SA-Dry	30.78	29.56
28 days NA	44.15	114.76
28 days LA	36.55	27.72
28 SA-SSD	44.45	32.23
28 SA-Dry	37.03	44.83

The elastic modulus E_c of concrete was calculated based on the stress corresponding to 33 percent of the ultimate load which is according to the BS1881 and they are given together with the compressive strength results in Table 7.2. Clearly, the extremely high value of 114.76 GPa for the 28-day NA concrete is in error. The only explanation that can be offered for this is experimental error which might come from

the following reasons. Firstly, there were only two strain gauges applied on the two opposite sides of the sample which might not be enough to give an accurate result. Secondly, the gauge length of the strain gauge, which is 80 mm long, might be too long and, therefore, the test result may possibly be affected by the end condition of the sample. Based on previous knowledge and on the other results presented in the table, one would expect a value about 45 GPa to be more realistic. The moduli of elasticity of synthetic and Lytag coarse aggregate concrete are approximately 30 to 40 percent less than that of the natural aggregate concrete, respectively. These results can be explained based on the rules of mixtures which state that the stiffness and volume fractions of the constituting phases (aggregate, cement paste matrix and interfacial transition zone) are the primary factors that influence the Young's modulus or the *E-value* of the composite (Van Mier, 1997). Since the Lytag and the synthetic aggregate have porous microstructures this results in a lower modulus of elasticity than the dense natural aggregate. The overall modulus of elasticity of the Lytag and synthetic aggregate concrete is, therefore, much lower than the quartz aggregate concrete.

There are about 20 and 34 % differences in the compressive strength and the *E-value*, respectively, for the 28-day old synthetic aggregate mixed in dry and pre-wetted condition and yet there is very little difference (about 9% for compressive strength and 4% for *E-value*) between them at 3 days. Due to the fact that the concrete *E-value* mainly depends on the aggregate property (both mixes used the same type of aggregate) and to a lesser extent the w/c ratio (which for this investigation was 0.53 for all mixes), therefore, the inherent variability of the material might be the possible reason for this difference.

It is interesting to note that in this small scale test the strength of the synthetic aggregate concrete was similar to the control concrete made with natural quartz and Lytag lightweight aggregate. As can be seen, there is little difference in compressive strength between them. The compressive strength of the 3 and 28-day old concrete ranges from 26 to 31 N/mm^2 and 36.5 to 44.5 N/mm^2, respectively. Base on the fact that all mixes used the same free water/cement ratio, a similar strength in all mixes suggests that the strength of concrete is mainly being controlled by the strength of the cement paste. The strength for the 28-day old samples compares well with the results reported by Wainwright et. al. (2002). The results based on the basis of strength alone suggest

that the synthetic aggregate would be suitable as the natural aggregate replacement in normal strength structural concrete.

The stress-strain curves of all of the mixes have a similar curvilinear shape. The stress-strain relationship for both 28-day old Lytag and synthetic aggregate concrete look slightly more linear than the concrete containing natural aggregate and this behavior is consistent with the findings of other researchers which indicated the linear relationship approaching about 90 percent of the failure strength (Holm et al., 1984; Zhang and Gjørv, 1991[b] and Newman, 1993). The relative compatible of the stiffness between the aggregate and the cement paste which results in the reduction of microcracking that generally occurs at the interface region were given as an explanation for this phenomenon. In addition, the rough surface texture of the Lytag and synthetic aggregate provide a good mechanical interlock between the aggregate and the cement paste matrix and a consequence of this is that a very good bond between aggregate and cement paste is expected. Therefore, the early development of bond microcracking is reduced (FIP manual, 1983).

The results as shown in Figure 7.32 and 7.33 also clearly indicate that the ultimate strain of both Lytag and synthetic aggregate concretes are typically greater than that of the natural aggregate concrete. This could be attributed mainly to the lower stiffness of the Lytag and synthetic aggregate particles which result in a larger deformation of the composite.

The most damaged part of the samples tested were manually separated after testing. The failure surface of the remaining part for 28-day old sample are shown in Figures 7.34 to 7.36. A distinct difference in the mode of failure was noted between the Lyatg and quartz aggregate concrete. For quartz aggregate concrete, most of the fracture went around the aggregate particles, i.e. the aggregate-cement paste debonding is clearly seen on the fractured surface as shown in Figure 7.34. This reinforces the view that this aggregate is much stronger than the interfacial transition zone and bulk paste matrix. However, very little evidence on aggregate-cement paste debonding was observed in the case of concrete containing Lytag coarse aggregate. In this case, it is obvious that most of the cracks tend to run through the aggregate particles.

The fracture surface of the synthetic aggregate concrete shows the transgranular type of fracture (defined by Aïtcin and Mehta, 1990), i.e. cracks run through the

particles, typically occurs in the aggregate having orange and brown color but for the dark grey particle, which has a very dense microstructure, the cracks tend to pass around it.

The relatively undamaged cone of the dry synthetic and Lytag aggregate concrete suggest that these samples are significantly affected by the boundary friction effect which normally happens when the concrete sample is loaded between rigid loading platens. Because of the friction force, the platens act to restrain the lateral expansion of the ends of the tested sample and, therefore, cause a lateral confining pressure near the ends of the sample (Van Mier,1997).

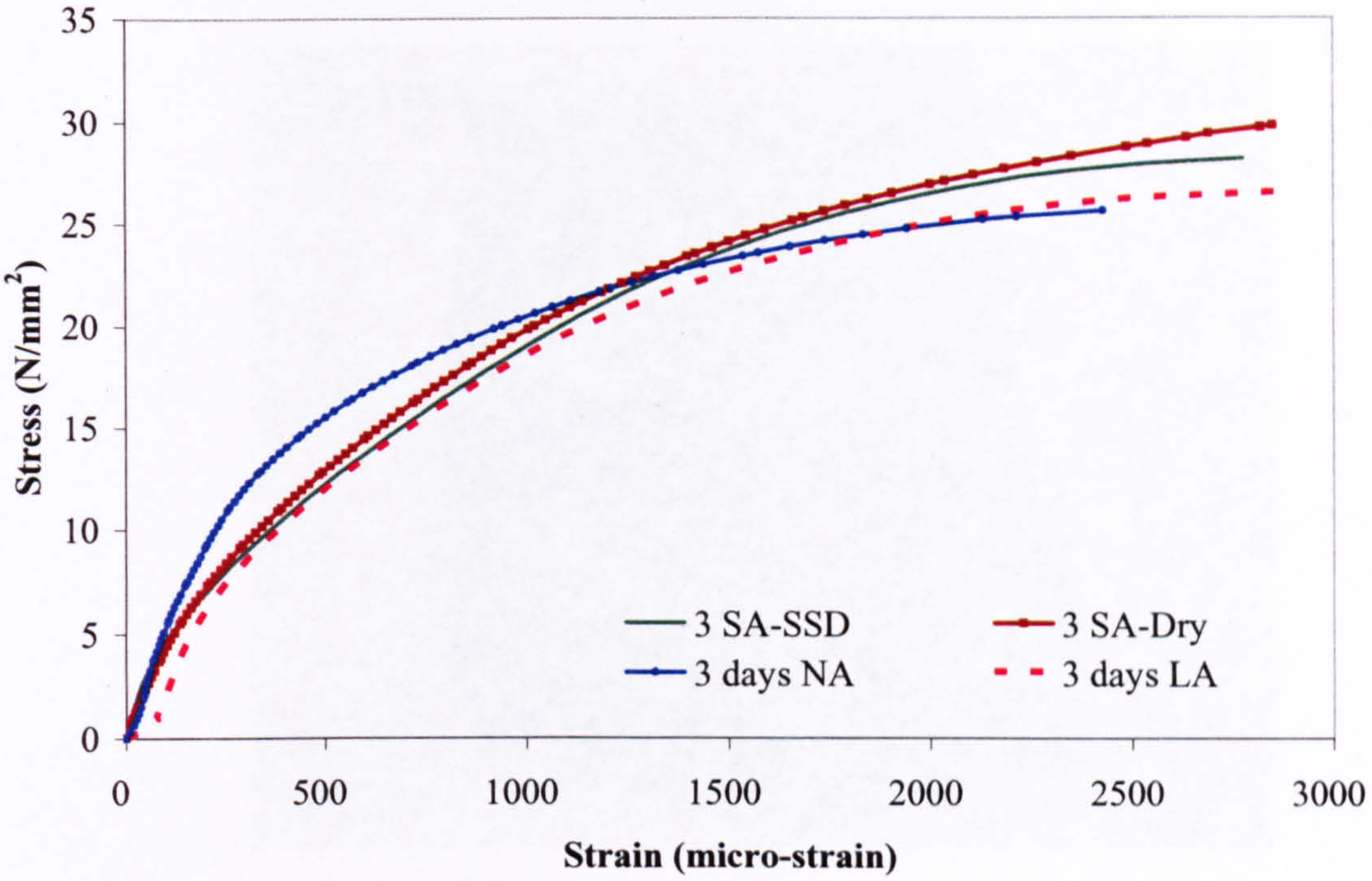

Figure 7.32 Stress-strain curves of 3-day old (w/c = 0.53) concrete containing various types of aggregate.

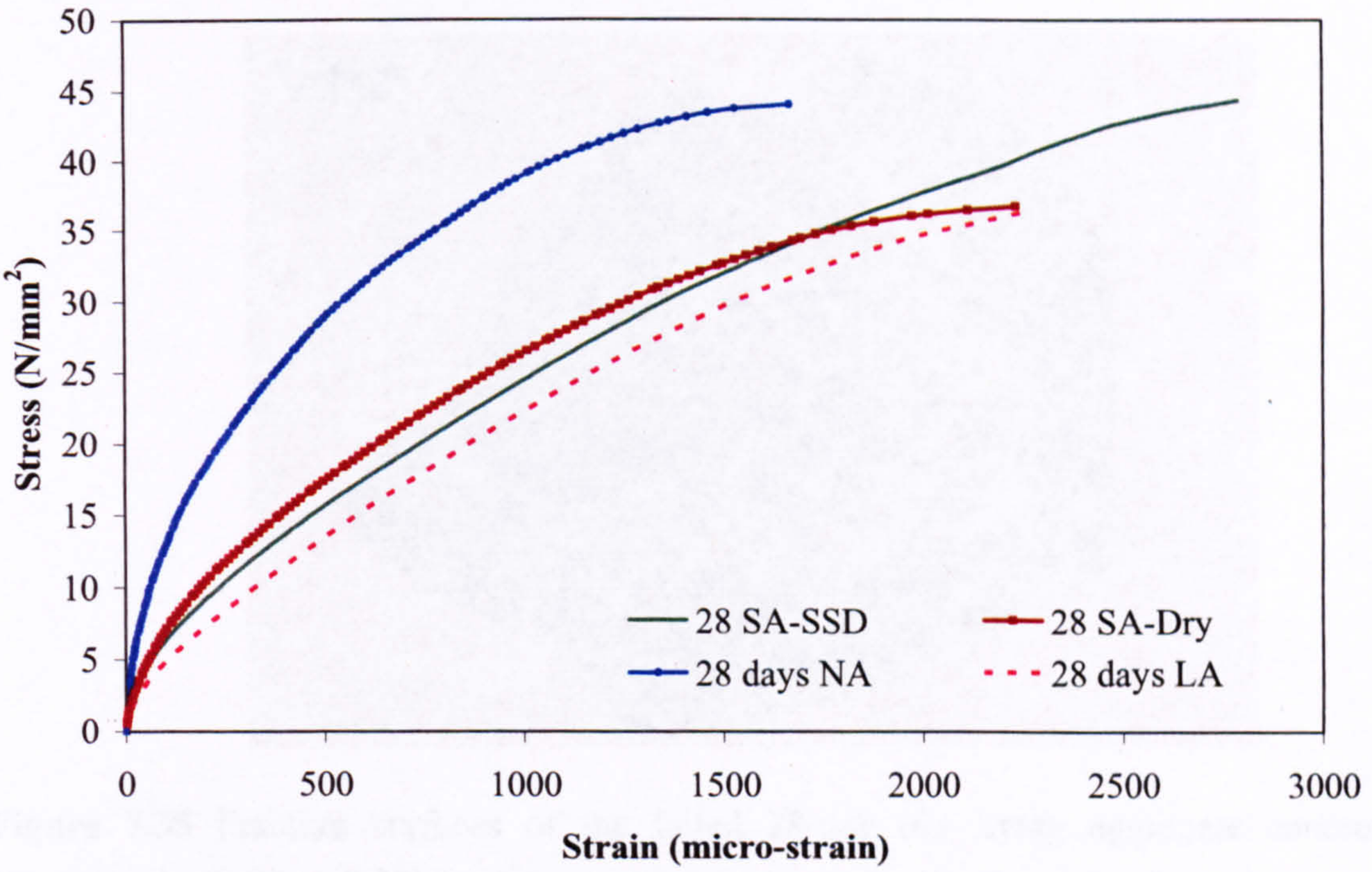

Figure 7.33 Stress-strain curves of 28-day old (w/c = 0.53) concrete containing various types of aggregate.

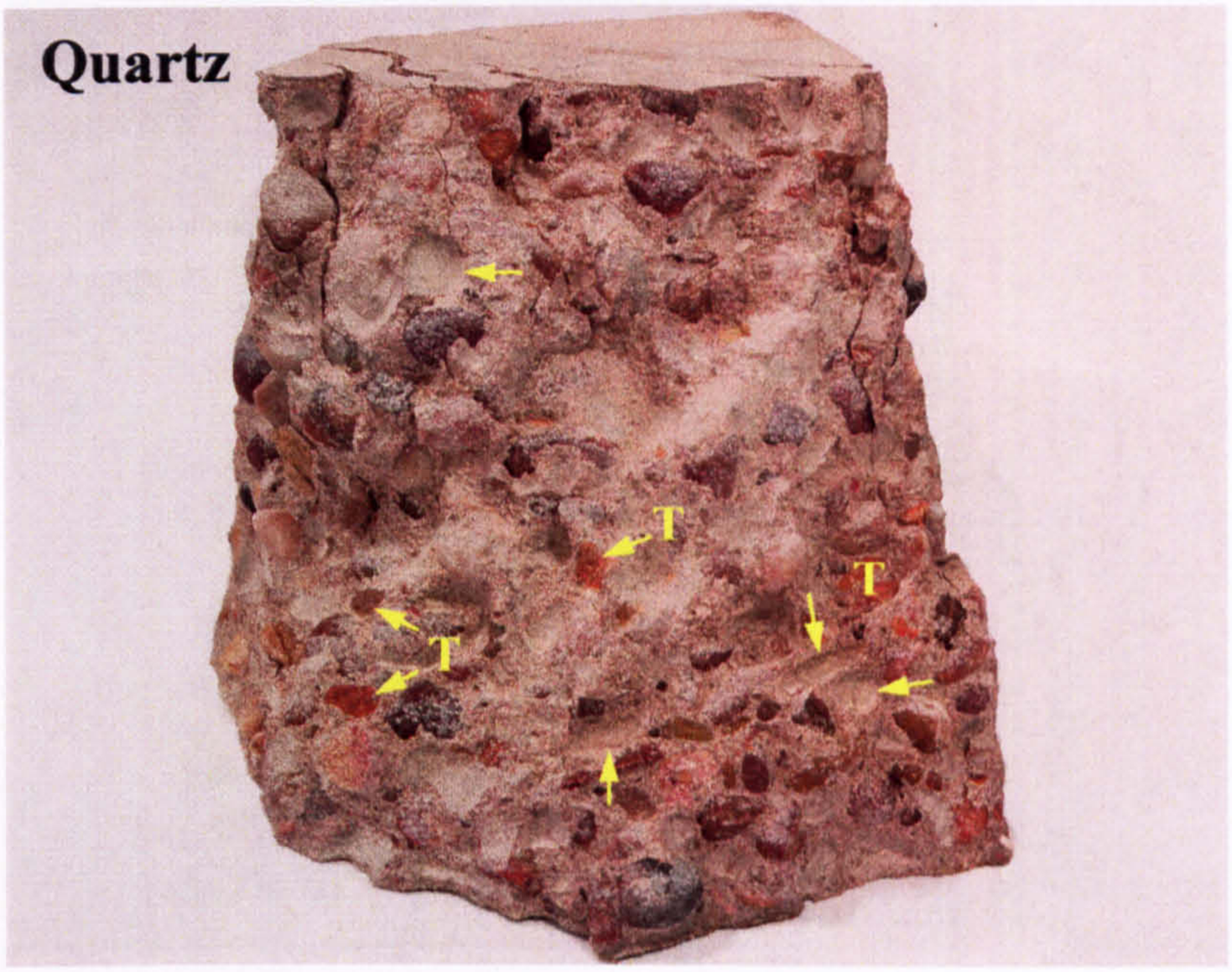

Figure 7.34 Fracture surfaces of the failed 28-day old natural aggregate concrete (water/cement ratio = 0.53). T, trans-granular fracture; yellow arrow, debonding.

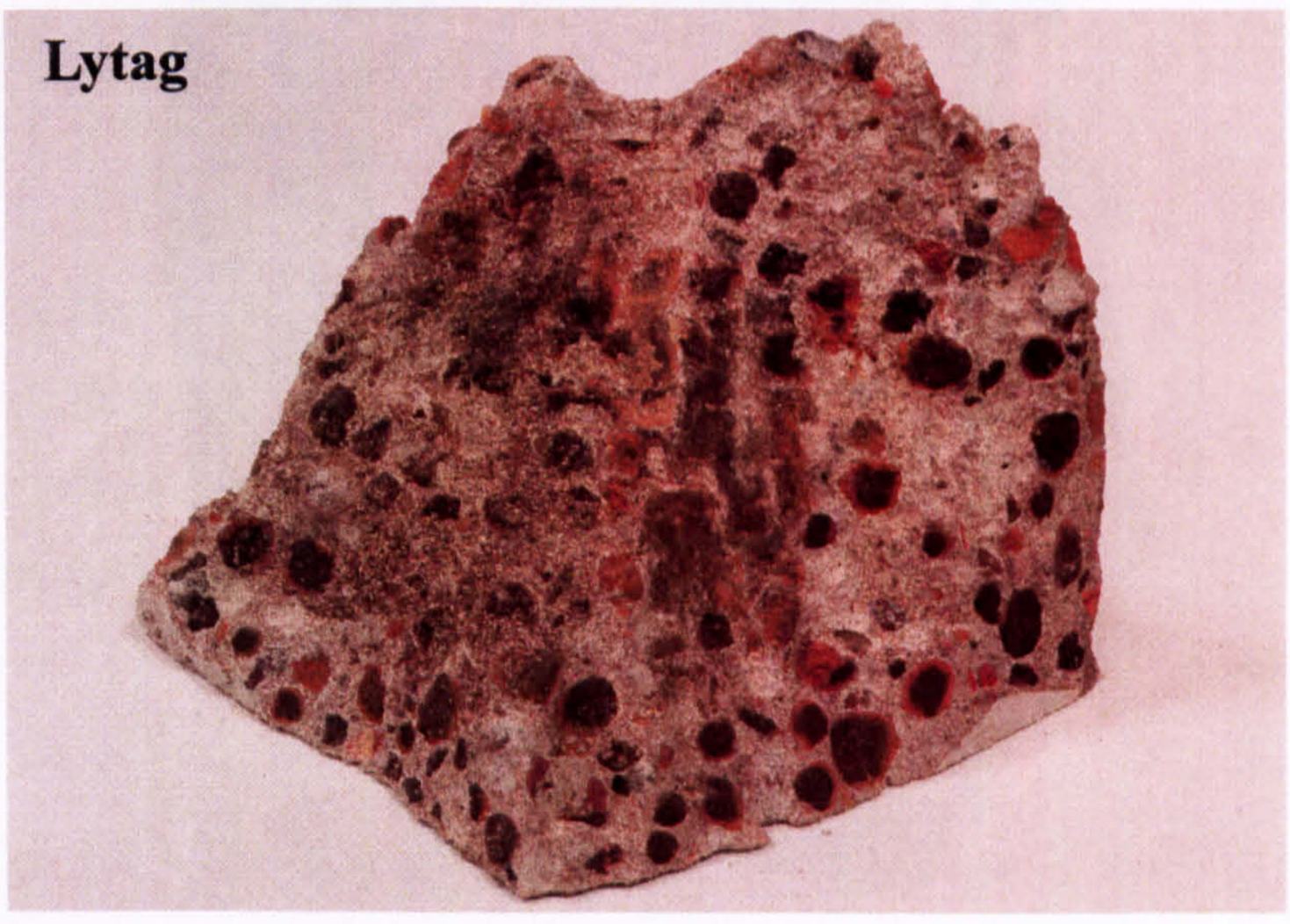

Figure 7.35 Fracture surfaces of the failed 28-day old Lytag aggregate concrete (water/cement ratio = 0.53).

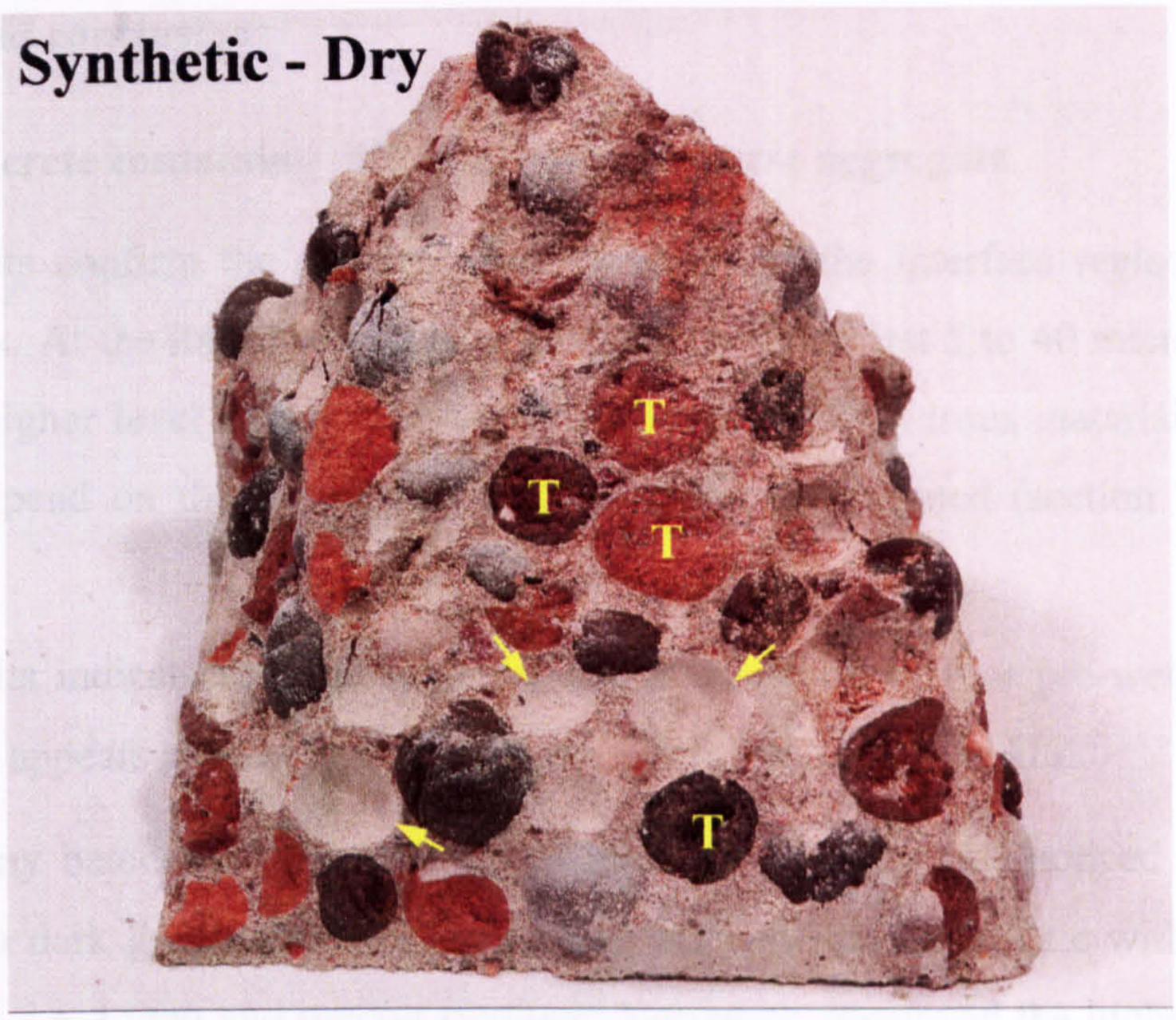

Figure 7.36 Fracture surfaces of the failed 28-day old synthetic aggregate (mixed in dry and SSD condition) concrete (water/cement ratio = 0.53). S, shear cones on the top and below the aggregate particle; T, trans-granular fracture; yellow arrow, debonding.

7.5 Summary and conclusions

7.5.1 ITZ of concrete containing different types of coarse aggregate

1. The results confirm the different microstructure of the interface region to the bulk paste matrix. At the interface region, especially over the first 5 to 40 microns, the interface has a higher level of porosity and lower levels of anhydrous material. These levels clearly depend on the age of the concrete being investigated (section 7.2.3 to 7.2.6).

2. The results indicate that the type and initial condition (dry or pre-wet) of the coarse aggregate appears to have an effect on the microstructure of the ITZ.

3. Within any batches of fired pellet, a difference in color was noticed ranging from orange to a dark grey color. For the 28-day old concrete, aggregate with higher water absorption, i.e. Lytag and orange synthetic aggregate, displayed the higher levels of porosity when compared to the natural or the dark grey synthetic aggregate. The ITZ of concrete made with the orange synthetic aggregate that was mixed in the dry condition has the highest porosity for both 3 and 28-day old samples; a lot of air bubbles were also observed at the aggregate interface region (Figure 7.30). For the Lytag and the orange synthetic aggregate that were mixed in the saturated surface dry (SSD) condition, a fairly dense microstructure with a lot of isolated pores filled with the low density hydration product was visually observed in the SEM images.

4. The results obtained indicate that the porous nature of the aggregate can affect the amount of water that tends to accumulate at the aggregate interface. The absorption of water from the surrounding paste into the aggregate particle influences the packing of the anhydrous particles leading to a reduction of porosity of the ITZ. However, too much and/or too rapid absorption of the water by the dry porous aggregate can have an adverse effect on the ITZ microstructure.

5. The 28-day old quartz aggregate concrete showed the lowest levels of porosity, followed by the dry dark grey synthetic aggregate and then pre-wetted dark grey synthetic aggregate. Therefore, in principle, the dark grey synthetic aggregate is recommended to be used in dry condition.

6. The porosity of the aggregate that was mixed in the pre-wetted condition seems to be related to the occurrence of the hollow pore and low density hydration product.

7. Calcium hydroxide tends to develop at the quartz and dark grey synthetic aggregate interface. There is very little deposition or build up of calcium hydroxide around the orange synthetic aggregate (in both dry and pre-wetted condition) interface. The lack of calcium hydroxide may be due to the penetration of the calcium ion (Ca^{2+}) into the porous orange synthetic aggregate.

8. There was little change in the amount of calcium hydroxide between 3 and 28-day old concrete which indicates that most of the calcium hydroxide developed within the first few days.

7.5.2 Permeability of concrete containing different types of coarse aggregate

1. Concrete with pre-wetted Lytag lightweight coarse aggregate displayed the highest permeability for both 3 and 28-day old sample. Quartz aggregate concrete showed the lowest permeability except for the 3-day old concrete which has a permeability slightly greater than the synthetic aggregate concrete.

2. It is possible that the oven-drying technique used in the sample preparation generated microcracking and provided an easy pathway for the oxygen to access the aggregate particles and led to the higher permeability in the lightweight aggregate concrete despite it having good quality cement paste matrix. Therefore, the drying regime for the permeability samples in the laboratory is very important and should simulate the actual condition of concrete on the actual situation.

3. The ITZ microstructure and the amount of aggregate seems to influence the concrete permeability. However, based on the results obtained, it is very difficult to give any conclusions on how significant these factors are on the transportation properties of the concrete.

7.5.3 Compressive strength and modulus of elasticity

1. The elastic modulus of the synthetic and Lyatg lightweight aggregate concrete are approximately 30 to 40 percent less than the natural aggregate concrete.

2. There is little difference in the 3 and 28-day compressive strength between the synthetic aggregate concrete and the control concrete using natural and Lytag aggregate. The strength of 3 and 28-day old concrete ranges from about 26 to 31 N/mm^2 and 37 to 45 N/mm^2, respectively. The results obtained indicate that the impact of coarse

aggregate type is not significant on the strength of concrete. The strength of the concrete was found to be mainly controlled by the strength of the cement paste matrix.

3. The ultimate strain of both 28-day old Lytag and synthetic aggregate concretes is typically greater than that of the natural aggregate concrete (Figure 7.33).

Chapter 8

Conclusions and recommendations for further research

The aims of this research, as already mentioned in the introductory chapter, were to get a better understanding about the effect of firing conditions on the properties of the synthetic aggregate and investigate the effect of using synthetic aggregate as the coarse aggregate replacement on the properties of concrete. The synthetic aggregate was manufactured from a mixture of granite quarry fine waste with the low grade ball clay and fired in a rotary kiln. As regards the properties of synthetic aggregate due to the effect of firing conditions, attempts were made to study in terms of the mineralogy, microstructure and engineering properties of the synthetic aggregate. Work was also carried out to investigate the effect of synthetic aggregate on the microstructure of the interfacial transition zone (ITZ). Permeability and compressive strength tests were performed to access the potential for using the synthetic aggregate in structural concrete. The following conclusions and recommendations are based solely on the main findings from the research carried out by the author.

8.1 Conclusions

8.1.1 Influence of firing conditions

1. For the *pre-set* sintering temperature of 1,110°C, sintering time of 10 minutes was found to be enough to give a suitable synthetic aggregate to use as a natural aggregate replacement. The amount of bloating pores of the pellets fired at this firing regime was about 6 percent.

2. Increasing of firing temperature and/or sintering time results in a reduction of the water absorption and an increase in the relative density of the synthetic aggregate.

3. The mineral components of the synthetic aggregate's raw material were quartz, feldspar, mica, kaolinite, chlorite and calcite. At 900°C, kaolinite, chlorite and calcite were found to decompose while the dehydration of mica occurred at temperature between 900° and 1,110°C. Melting of feldspar mineral occurred at temperature of about 1,110°C which lead to the densification of the fired pellet bodies. Only the transformation between the low-temperature form of quartz and high-temperature form occurred.

4. An increase in pore size was observed at the initial stage of sintering, i.e. at the pre-set temperature between 900° and 1,110°C. The densification of the fired pellet bodies began when a sufficient amount of the melting phase was formed.

8.1.2 ITZ of concrete containing synthetic aggregate

1. Types and initial conditions of the coarse aggregate were found to have an effect on the microstructure of the ITZ. The 28 day old concrete made with dark grey synthetic aggregate displayed slightly higher levels of porosity at the ITZ when compared to concretes containing natural quartz aggregate. The porosity of the Lytag and orange synthetic aggregate concrete was shown to be higher than that of the natural quartz and dark grey synthetic aggregate concrete.

2. The results indicate that too much and/or too rapid water absorption by the porous synthetic aggregate can have an adverse effect on the ITZ microstructure. This conclusion also apply to other porous aggregate.

3. The level of calcium hydroxide tended to increase at the ITZ surrounding the quartz and dark grey synthetic aggregate but very little build up was found for the orange synthetic aggregate.

4. A new porosity segmentation technique for the backscattered electron image of cement-based materials was proposed (section 5.3.3.2.2). It was successfully used to obtain reproducible and reliable results for the porosity analysis of the ITZ.

5. The ITZ microstructure of all concrete samples displays increased levels of porosity and decreased levels of anhydrous material. These levels vary with age of the concrete sample.

8.1.3 Macroproperties of concrete

1. The inclusion of the synthetic aggregate in concrete when compared to the concrete made with natural quartz aggregate lead to an increase in permeability and reduction of the modulus of elasticity. There was little difference in the compressive strength of the 3 and 28-day old concrete.

8.2 Recommendation for further research

Although a significant amount of valuable information about the effect of firing regime on the nature of synthetic aggregate and its influence on the performance of concrete was generated in this research, there are many areas where further research is still required. The following is a list of the suggested possible research work.

1. Even though it is possible to successfully produce green pellets by using the processes presented in this research (section 3.4), these techniques, however, are time consuming and not the automatic process that is normally required for production on an industrial scale. Moreover, rolling of blended material inside the rotary drum creates a big flaw inside the green pellet particles. It is a weaker part and has an adverse effect on the strength of the synthetic aggregate. The disc pelletization technique involves the agglomeration of moisturized fines in a rotating disc and it would be useful to make a comparison between the two techniques.

2. The effect of particle size distribution of the starting materials should be investigated.

3. There was only one waste material that was investigated in this research because of the time constraint. It would be of interest to investigate other kinds of waste materials, e.g. sewage sludge, paper making sludge and municipal solid waste incinerator, and other binders by using the testing framework developed here.

4. It would be of interest to investigate the effect of blending starting materials with the bloating substances on the properties and microstructure of the synthetic aggregate.

5. Quartz is one of the major mineral components of the starting material and the transformation between the low temperature form (α) and the high temperature form (β) of quartz at temperature of about 573°C results in an expansion on heating and contraction on cooling. Depending on the amount of quartz within the raw materials, too rapid a preheating and/or cooling, which were done in this research, can result in a number of cracks inside the synthetic aggregate. At present, it is not possible to control the temperature profile inside the kiln under 800°C due to the limitation of the pyrometer used. Therefore, thermocouples or pyrometers that can measure all temperature ranges required for synthetic aggregate production should be installed.

6. It is impossible to make all of the coarse aggregate particles reach the saturated surface dry (SSD) condition before casting concrete and this, therefore, can create a lot of variation in the ITZ microstructure. Soaking of coarse aggregates directly in the mixing water for 24 hours prior mixing is recommended.

7. It would be of interest to investigate the effect of drying methods on the permeability of concrete with different types of aggregate and therefore identify the exact influence of drying techniques.

8. Larger quantities of synthetic aggregate must be produced in order to get enough concrete specimens to obtain a representative result for the mechanical properties (short and long term properties) and the durability of concrete.

9. Leaching behaviour of the synthetic aggregate produced from various kinds of waste materials should be investigated in order to ensure its environmental compatibility.

References

Aligizaki, K. K. (2006) Pore structure of cement-based materials: testing, interpretation and requirements (modern concrete technology 12), Taylor & Francis, ISBN 0-419-22800-4.

Barlow, S. G. and Manning, D. A. C. (1999) Influence of time and temperature on reactions and transformations of muscovite mica, British Ceramic Transactions, Vol. 98, No. 3, pp. 122-126.

Barnes, M. S., Diamond, S. and Dolch, W. L. (1978) The contact zone between Portland cement paste and glass aggregate surfaces, Cement and Concrete Research, Vol. 8, pp. 233-244.

Barnes, M. S., Diamond, S. and Dolch, W. L. (1978) Hollow shell hydration of cement particles in bulk cement paste, Cement and Concrete Research, Vol. 8, pp. 263-272.

Baykal, G. and Döven, A. G. (2000) Utilization of fly ash by pelletization process; theory, application areas and research results, Resources, Conservation and Recycling, Vol. 30, pp. 59-77.

Bentur, A., Igarashi, S. and Kovler, K. (2001) Prevention of autogenous shrinkage in high-strength concrete by internal curing using wet lightweight aggregates, Cement and Concrete Research, Vol. 31, pp. 1587-1591.

Bentz, D. P., Garboczi, E. J. and Stutzman, P. E. (1992) Computer modelling of the interfacial zone in concrete, in: J. C. Maso (Ed.), Interfaces in Cementitious Composites, RILEM Proceedings, Vol. 18, E & FN Spon, London, ISBN 0-419-18230-6, pp. 107-116.

Bentz, D. P. and Snyder, K. A. (1999) Protected paste volume in concrete extension to internal curing using saturated lightweight fine aggregate, Cement and Concrete Research, Vol. 29, pp. 1863-1867.

Bonen, D. (1994) Calcium hydroxide deposition in the near interfacial zone in plain concrete, Journal of the American Ceramic Society, Vol. 77, No. 1, pp. 193-196.

Boni, S. P. K. (1980) Use of sintered pelletised domestic refuse as an aggregate in concrete, PhD Thesis, University of Leeds.

British Standards Institute (1983) Test concrete – Part 121: Method for determination of static modulus of elasticity in compression, BSI, London, BS1881-121

British Standards Institute (1996) Specification for Portland Cement, BSI, London, BS12.

British Standards Institute (1992) Specification for aggregate from natural sources for concrete, BSI, London, BS882.

British Standards Institute (2000) Test sieves – technical requirements and testing, BSI, London, BS410.

Brough, A. R. and Atkinson, A. (2000) Automated identification of the aggregate-paste interfacial transition zone in mortars of silica sand with Portland or alkali-activated slag cement paste, Cement and Concrete Research, Vol. 30, pp. 849-854.

Brown, P. W., Franz, E., Frohnsdorff, G. and Taylor, H. F. W. (1984) Analyses of the aqueous phase during early C_3S hydration, Cement and Concrete Research, Vol. 14, pp. 257-262.

Cabrera, J. G. and Lynsdale, C. J. (1988) A new gas permeameter for measuring the permeability of mortar and concrete, Magazine of Concrete Research, vol. 40, No. 144, pp. 177-182.

Carrier, R. E. and Cady, P. D. (1970) Evaluating effectiveness of concrete curing compounds, Vol. 5, No. 2, pp. 294-302.

Chon, C. M., Kim, S. A. and Moon, H. S. (2003) Crystal structures of biotite at high temperatures and of heat-treated biotite using neutron powder diffraction, Clays and clay minerals, Vol. 51, No. 5, pp. 519-528.

Crockett, R. N. (1975) Mica, Mineral Resources Consultative Committee, Mineral Dossier No. 15, ISBN 0-11-510839-4.

Crumbie, A. K. (1994) Chracterisation of the microstructure of concrete, PhD Thesis, University of London, UK.

Crumbie, A. K. (2001) SEM microstructural studies of cementitious materials: sample preparation of polished sections and microstructural observations with backscattered images – artifacts and practical considerations, Proceedings of the 23rd International Conference on Cement Microscopy, Albuquerque, pp. 320-341.

Cullity, B. D. and Stock, S. R. (2001) Elements of X-ray diffraction, 3rd Edition, Prentice Hall, Inc., ISBN 0-13-178818-3.

Cultrone, G., Rodriguez Navarro, C., Sebastian, E., Cazalla, O. and de la Torre, M. J. (2001) Carbonate and silicate phase reactions during ceramic firing, European Journal of Mineralogy, Vol. 13, No. 3, pp. 621-634.

Cultrone, G., Sebastian, E., Elert, K., de la Torre, M. J., Cazalla, O. and Rodriguez Navarro, C. (2004) Influence of mineralogy and firing temperature on the porosity of bricks, Journal of the European Ceramic Society, Vol. 24, pp. 547-564.

Dalgleish, B. J., Pratt, P. L. and Toulson, E. (1982) Fractographic studies of microstructural development in hydrated Portland cement, Journal of Materials Science, Vol. 17, No. 8, pp. 2199-2207.

de Gennaro, R., Cappelletti, P., Cerri, G., de' Gennaro, M., Dondi, M. and Langella, A. (2004) Zeolitic tuffs as raw materials for lightweight aggregates, Applied Clay Science, Vol. 25, pp. 71-81.

Delagrave, A., Bigas, J. P., Olivier, J. P., Marchand, J. and Pigeon, M. (1997) Influence of the interfacial zone on the chloride diffusivity of mortars, Advanced Cement Based Materials, Vol. 5, Issues 3-4, pp. 86-92.

DETR (1998) Digest of environmental statistics number 20, London, HMSO.

Detwiler, R. J., Powers, L. J., Jakobsen, U. H., Ahmed, W. U., Scrivener, K. L. and Kjellsen, K. O. (2001) Preparing specimens for microscopy, Concrete International, pp. 51-58.

Diamond, S. (2000) Mercury porosimetry an inappropriate method for the measurement of pore size distributions in cement-based materials, Cement and Concrete Research, Vol. 30, pp. 1517-1525.

Diamond, S. (2001[a]) Considerations in image analysis as applied to investigates of the ITZ in concrete, Cement and Concrete Composites, Vol. 23, pp. 171-178.

Diamond, S. (2001[b]) Calcium hydroxide in cement paste and concrete – a microstructural appraisal, in: Skalny, J., Gebauer, J. and Odler, I. (Eds.), Material Science of Concrete, Special volume: Calcium hydroxide in concrete, The American ceramic Society, Westerville, pp. 37-58.

Diamond, S. (2004) The microstructure of cement paste and concrete-a visual primer, Cement and Concrete Composites, Vol. 26, pp. 919-933.

Diamond, S. and Huang, J. (2001) The ITZ in concrete – a different view based on image analysis and SEM observations, Cement and Concrete Composites, Vol. 23, pp. 179-188.

Diamond, S. and Leeman, M. E. (1995) Pore size distributions in hardened cement paste by SEM image analysis, Materials Research Society Symposium Proceedings, Vol. 370, pp. 217-226.

DoE (Department of the Environment and the Welsh Office) (1995) Making waste work – A strategy for sustainable waste management in England and Wales, London, HMSO.

EEA (European Environment Agency) (1998) Europe's environment: The second assessment, Office for official publications of the European communities, Luxembourg, Elsevier Science Ltd.

Elsharief, A., Cohen, M. D. and Olek, J. (2003) Influence of aggregate size, water cement ratio and age on the microstructure of the interfacial transition zone, Cement and Concrete Research, Vol. 33, pp. 1837-1849.

Elsharief, A., Cohen, M. D. and Olek, J. (2005) Influence of lightweight aggregate on the microstructure and durability of mortar, Cement and Concrete Research, Vol. 35, pp. 1368-1376.

Fagerlund, G. (1978) Frost resistance of concrete with porous aggregate, Report of Cement and Concrete Institute in Sweden.

Fens, T. W. F. (2000) Petrophysical properties from small rock samples using image analysis techniques, Delft University Press, Netherlands, ISBN 90-9014-338-6.

FIP State of Art Report (1982) Lightweight aggregate concrete for marine structures.

FIP (1983) Manual of lightweight aggregate concrete, 2nd Ed., Surrey University Press.

French, W. J. (1991) Concrete petrography: a review, Quarterly Journal of Engineering Geology, Vol. 24, pp. 17-48.

Gallucci, E. and Scrivener, K. L. (2007) Crystallisation of calcium hydroxide in early age model and ordinary cementitious systems, Cement and Concrete Research, Vol. 37, pp. 492-501.

Giese, R. F. and van Oss, C. J. (2002) Colloid and surface properties of clays and related minerals, Surfactant science series, Vol. 105, ISBN 0-8247-9527-X.

Goldstein, J., Newbury, D., Joy, D., Lyman, C., Echlin, P., Lifshin, E., Sawyer, L. and Michael,J. (2003) Scanning electron microscopy and X-ray microanalysis, 3rd Edition, Kluwer Academic/Plenum Publishers, New York, ISBN 0-306-47292-9.

Goodhew, P. J. and Humphreys, F. J. (1997) Electron microscopy and analysis, 2nd Edition, Taylor & Francis Ltd., London, ISBN 0-85066-414-4.

Grandet, J. and Ollivier, J. P. (1980) Nouvelle methode d'etude des interface ciments-granulats, Proceedings of the 7th International Congress on the Chemistry of Cement, Paris, France, Vol. 3, Sub-Theme VII, pp. 85-89.

Groves, G. W. (1987) TEM studies of cement hydration, Materials Research Society Symposium Proceedings, Vol. 85, pp. 3-12.

Hadley, D. (1972) The nature of the paste-aggregate interface, PhD thesis, Purdue University, West Lafayette, IN.

Hadley, D. W., Dolch, W. L. and Diamond, S. (2000) On the occurrence of hollow-shell hydration grains in hydrated cement paste, Cement and Concrete Research, Vol. 30, pp. 1-6.

Hall, M. G. and Lloyd, G. E. (1981) The SEM examination of geological samples with a semi-conductor back-scattered electron detector, American Mineralogist, Vol. 66, pp. 362-368.

Head, M. K. (2001) Influence of the interfacial transition zone (ITZ) on the properties of concrete, PhD Thesis, University of Leeds, UK.

Hill, A. R., Dawson, A. R. and Mundy, M. (2001) Utilisation of aggregate materials in road construction and bulk fill, Resources, Conservative and Recycling, Vol. 32, pp. 305-320.

Hilliard, J. E. (1968) Measurement of volume in volume, in: Quantitative microscopy, Edited by Dehoff, R. T. and Rhines, F. N., McGraw Hill, pp. 45-76.

Holm, T. A., Bremner, T. W. and Newman, J. (1984) Lightweight aggregate concrete subject to severe weathering, Concrete International, Vol. 6, pp. 49-54.

Horne, A. T. (2004) Microstructure of interfaces in steel reinforced concrete, PhD Thesis, University of Leeds, UK.

Hostetter, J. C. and Roberts, H. S. (1921) Note on the dissociation of ferric oxide dissolved in glass and its relation to the color of iron-bearing glasses, Journal of the American Ceramic Society, Vol. 4, pp. 927-928.

Iqbal, Y. and Lee, W. E. (2000) Microstructural evolution in triaxial porcelain, Journal of the American Ceramic Society, Vol. 83, No. 12, pp. 3121-3127.

JOEL Ltd. A Guide to scanning microscope observation.

Kellam, D. and Nicholson, P. S. (1971) Pore shape changes during the initial stages of sintering, Journal of the American Ceramic Society, Vol. 54, No. 2, pp. 127-128.

Kjellsen, K. O., Detwiler, R. J. and Gjørv, O. E. (1991) Backscattered electron image analysis of cement paste specimens: specimen preparation and analytical methods, Cement and Concrete Research, Vol. 21, pp. 388-390.

Kjellsen, K. O. and Helsing Atlassi, E. (1999) Pore structure of cement silica fume systems; presence of hollow pores, Cement and Concrete Research, Vol.29, pp. 133-142.

Kjellsen, K. O., Jennings, H. M. and Lagerblad, B. (1996) Evidence of hollow shells in the microstructure of cement paste, Cement and Concrete Research, Vol. 26, No. 4, pp. 593-599.

Kjellsen, K. O. and Monsøy, A. (1996) Preparation of flat-polished specimens of high-performance concrete for SEM-backscattered electron imaging and microanalysis,

Proceedings of the 18th international conference on cement microscopy, Houston, pp. 356-364.

Kjellsen, K. O., Monsøy, A., Isachsen, K. and Detwiler, R. J. (2003) Preparation of flat-polished specimens for SEM-backscattered electron imaging and X-ray microanalysis—importance of epoxy impregnation, Cement and Concrete Research, Vol. 33, pp. 611-616.

Krinsley, D. H., Pye, K., Boggs Jr., S. and Tovey, N. K. (1998) Backscattered scanning electron microscopy and image analysis of sediments and sedimentary rocks, Cambridge University Press, Cambridge, ISBN 0-521-45346-1.

Konecny, L. and Naqvi, S. J. (1993) The effect of different drying techniques on the pore size distribution of blended cement mortars, Cement and Concrete Research, Vol. 23, pp. 1223-1228.

Kumar, A. and Roy, D. M. (1986) The effect of desiccation on the porosity and pore structure of freeze dried hardened Portland cement and slag-blended pastes, Cement and Concrete Research, Vol. 6, pp. 74-78.

Lange, D. A., Jennings, H. M. and Shah, S. P. (1994) Image analysis techniques for characterization of pore structure of cement-based materials, Cement and Concrete Research, Vol. 24, No. 5, pp. 841-853.

Langton, C. A. and Roy, D. M. (1980) Morphology and microstructure of cement paste/rock interface regions, Proceeding of 7th International Congress on the Chemistry of Cement, Paris, France, Sub-Theme VII, pp. 127-132.

Laskar, A. I., Kumar, K. and Bhattacharjee, B. (1997) Some aspects of evaluation of concrete through mercury intrusion porosimetry, Cement and Concrete Research, Vol. 27, No. 1, pp. 93-105.

Lee W. E. and Rainforth, W. M. (1994) Ceramic microstructures: property control by processing, 1st Ed., Chapman & Hall, London , ISBN 0-412-43140-8.

Lo, Y. Gao, X. F. and Jeary, A. P. (1999) Microstructure of pre-wetted aggregate on lightweight concrete, Building and Environment, Vol. 34, pp. 759-764.

Lundin, S. T. (1964) Microstructure of porcelain, in: Microstructure of Ceramic Materials, Proceedings of the American Ceramic Society Symposium, National Bureau

of Standards Miscellaneous Publications No. 257, Natural Bureau of standards, Gaithersburg, MD, pp. 93-106.

Lydon, F. D. (1995) Effect of coarse aggregate and water/cement ratio on intrinsic permeability of concrete subject to drying, Cement and Concrete Research, Vol. 25, No. 8, pp. 1737-1746.

Lytag Ltd., www.lytag.co.uk.

Maso, J. C. (1980) The bond between aggregates and hydrated cement paste, Proceeding of 7th International Congress on the Chemistry of Cement, Paris, France, Vol. 3, Sub-Theme VII-1, pp. 3-15.

Mattyasovszky-zsolnay, L. (1957) Mechanical strength of porcelain, Journal of the American Ceramic Society, Vol. 40, No. 9, pp. 299-306.

Mazzucato, E., Artioli, G. and Gualtieri, A. (1999) High temperature dehydroxylation of muscovite-2M_1: a kinetic study by in situ XRPD, Physics and Chemistry of Minerals, Vol. 26, No. 5, pp. 375-381.

McConville, C. J., Lee, W. E. and Sharp, J. H. (1998) Microstructural evolution in fired kaolinite, British Ceramic Transactions, Vol. 97, No. 4, pp. 162-168.

Monteiro, P. J. M. (1986) Improvement of the aggregate-cement paste transition zone by grain refinement of hydration products, Proceeding of 8th International Congress on the Chemistry of Cement, Rio, Brasilia, Vol. 3, pp. 433-437.

Monteiro, P. J. M. and Mehta, P. K. (1985) Ettringite formation on the aggregate-cement paste interface, Cement and Concrete Research, Vol. 15, pp. 378-380.

Monteiro, P. J. M., Maso, J. C. and Ollivier, J. P. (1985) The aggregate-mortar interface, Cement and Concrete Research, Vol. 15, pp. 953-958.

Moukwa, M. and Aïtcin, P. –C. (1988) The effect of drying on cement pastes pore structure as determined by mercury porosimetry, Cement and Concrete Research, Vol. 18, pp. 745-752.

Mouret, M., Ringot, E. and Bascoul, A. (2001) Image analysis: a tool for the characterization of hydration of cement in concrete – metrological aspects of

magnification on measurement, Cement and Concrete Composites, Vol. 23, pp. 201-206.

Neville, A. M. (1995) Properties of concrete, Longman Scientific & Technical, New York.

Newman J. B. (1993) Properties of structural lightweight aggregate concrete, in: Clarke, J. L. (Ed.), Structural lightweight aggregate concrete, 1993.

Nyame, B. K. (1985) Permeability of normal and lightweight mortars, Magazine of Concrete Research, Vol. 37, No. 130, pp.44-48.

Ollivier, J. P., Massat, M. and Parrott, L. (1995) Parameters influencing transport characteristics, in: Kropp, J. and Hilsdorf, H. K. (Eds.), Performance criteria for concrete durability, RILEM Report 12, E & FN Spon, London, ISBN 0419198806, pp. 33-96.

Osada, M. (1997) Direct melting process for MSW recycling, In: Waste materials in construction: putting the theory into practice, Gaumans, J. J. J. M. et. al. (Eds.), Amsterdam, Elsevier, pp. 73-78.

Owens, P. L. (1993) Lightweight Aggregates for Structural Concrete, in: Clarke J L (Eds.), Structural Lightweight Aggregate Concrete, London, UK, Blackie Academic and Professional, pp. 1-18.

Pietsch, W. (1991) Size enlargement by agglomeration, John Wiley & Son Inc., ISBN 0471929913.

Pope, A. W. and Jennings, H. M. (1992) The influence of mixing on the microstructure of the cement paste/aggregate interfacial zone and on the strength of mortar, Journal of Materials Science, Vol. 27, pp. 6452-6462.

Powers, T. C., Copeland, L. E., Hayes, J. C. and Mann, H. M. (1954) Permeability of Portland cement paste, Journal of the American Concrete Institute, Proceedings, Vol. 51, No. 3, pp. 285-298.

Pratt, P. L. and Ghose, A. (1983) Electron microscope studies of Portland cement microstructures during setting and hardening, Philosophical Transactions of the Royal Society of London, Series A, Vol. 310, pp. 93-102.

Puscas, T. M., Signorini, M., Molinari, A. and Straffelini, G. (2003) Image analysis investigation of the effect of the process variables on the porosity of sintered chromium steels, Materials Characterization, Vol. 50, pp. 1-10.

Pye, K. and Krinsley, D. H. (1984) Petrographic examination of sedimentary rocks in the SEM using backscattered electron detectors, Journal of Sedimentary Petrology, Vol. 54, No. 3, pp. 877-888.

Ramachandran, V. S., Paroli, R. M., Beaudoin, J. J. and Delgado, A. H. (2003) Handbook of thermal analysis of construction materials, Norwich, N. Y., ISBN 0-8155-1487-5.

Richardson, I. G. and Groves, G. W. (1993) Microstructure and microanalysis of hardened ordinary Portland cement pastes, Journal of Materials Science, Vol. 28, pp. 265-277.

Richardson, I. G. (2002) Electron microscopy of cements, in: Structure and performance of cements, 2nd ed., Edited by J. Bensted and P. Barnes, Spon Press, pp. 500-556.

Riley, C. M. (1951) Relation of chemical properties to the bloating of clays, Journal of the American Ceramic Society, Vol. 34, No. 4, pp. 121-128.

Rodriguez Navarro, C., Cultrone, G., Sanchez Navas, A. and Sebastian E. (2003) TEM study of mullite growth after muscovite breakdown, American Mineralogist, Vol. 88, pp. 713-724.

Roy, R. (1949) Decomposition and resynthesis of the micas, Journal of the American Ceramic Society, Vol. 32, No. 6, pp. 202-209.

Russ, J. C. (2002) The image processing handbook, 4th Ed., CRC Press, Inc., ISBN 0-8493-1142-X.

Ryan, W. (1978) Properties of ceramics raw materials, 2nd Ed. in SI/Metric units, Pergamon Press, ISBN 0-08-022113-0.

Sandrolini, F. and Palmonari, P. (1976) Role of iron oxides in the bloating of vitrified ceramic materials, Transactions of the British Ceramic Society, Vol. 75, No. 2, pp. 25-32.

Sanz, J., González-Carreño, T. and Gancedo, R. (1983) On dehydroxylation mechanisms of a biotite in vacuo and in oxygen, Physics and Chemistry of Minerals, Vol. 9, No. 1, pp. 14-18.

Sarkar, S. L., Chandra, S. and Berntsson, L. (1992) Interdependence of microstructure and strength of structural lightweight aggregate concrete, Cement and Concrete Composites, Vol. 14, pp. 239-248.

Sastry, K. V. S. and Fuerstenau, D. W. (1973) Mechanisms of agglomerate growth in green pelletization, Powder Technology, Vol. 7, pp. 97-105.

Scrivener, K. L. (1987) The microstructure of the anhydrous cement and its effect on hydration, Materials Research Society Symposium Proceedings, Vol. 85, pp. 39-46.

Scrivener, K. L. (1989[a]) The use of backscattered electron microscopy and image analysis to study the porosity of cement paste, Materials Research Society Symposium Proceedings, Vol. 137, pp. 129-140.

Scrivener, K. L. (1989[b]) The microstructure of concrete, in: Materials science of concrete, Edited by Skalny, J. P., American Ceramic Society, Westerville, OH, pp. 127-161.

Scrivener, K. L. (1997) Microscopy methods in cement and concrete science, World Cement, Vol. 28, pp. 92-112.

Scrivener, K. L. (2004) Backscattered electron imaging of cementitious microstructures: understanding and quantification, Cement and Concrete Composites, Vol. 26, pp. 935-945.

Scrivener, K. L., Baldie, K. D., Halse, Y. and Pratt, P. L. (1985) Characterisation of microstructure as a systematic approach to high strength cements, Materials Research Society Symposium Proceedings, Vol. 42, pp. 39-43.

Scrivener, K. L., Bentur, A. and Pratt, P. L. (1988[a]) Quantitative characterization of the transition zone in high strength concretes, Advances in Cement Research, Vol. 1, No.4, pp. 230-237.

Scrivener, K. L., Crumbie, A. K. and Laugesen, P. (2004) The interfacial transition zone (ITZ) between cement paste and aggregate in concrete, Interface Science, Vol. 12, pp. 411-421.

Scrivener, K. L., Crumbie, A. K. and Pratt, P. L. (1988[b]) A study of interfacial region between cement paste and aggregate in concrete, Materials Research Society Symposium Proceedings, Vol. 114, pp. 87-88.

Scrivener, K. L. and Gartner, E. M. (1988) Microstructural gradients in cement paste around aggregate particles, Materials Research Society Symposium Proceedings, Vol. 114, pp. 77-85.

Scrivener, K. L., Patel, H. H., Pratt, P. L. and Parrott, L. J. (1987) Analysis of phases in cement paste using backscattered electron images, methanol adsorption and thermogravimetric analysis, Materials Research Society Symposium Proceedings, Vol. 85, pp. 67-76.

Scrivener, K. L. and Pratt, P. L. (1984[a]) Backscattered electron images of polished cement sections in the scanning electron microscope, Proceeding of 6th international conference on cement microscopy, Albuquerque, USA, pp. 145-155.

Scrivener, K. L. and Pratt, P. L. (1984[b]) Characterisation of Portland cement hydration by electron optical techniques, Materials Research Society Symposium Proceedings, Vol. 31, pp. 351-356.

Scrivener, K. L. and Pratt, P. L. (1987) The characterization and quantification of cement and concrete microstructures, in: J. C. Maso (Ed.), Pore structure and construction materials properties, RILEM, Vol. 1, Chapman and Hall Ltd., ISBN 0-412-30140-7, pp. 61-68.

Scrivener, K. L. and Pratt, P. L. (1996) Characterisation of interfacial microstructure, in: J. C. Maso (Ed.), Interfacial Transition Zone in Concrete, RILEM Report, Vol. 11, E & FN Spon, London, ISBN 0-419-20010-x, pp. 3-17.

Sosman, R. B. (1965) The phases of silica, Rutgers University Press, New Brunswick, NJ.

Srb, J. and Ruzickova, Z. (1988) Pelletization of fines, Elsevier Science Publishing Company, NY.

Struble, L. and Stutzmn, P. (1989) Epoxy impregnation of hardened cement for microstructural characterization, Journal of Materials Science Letters, Vol. 8, pp. 632-634.

Stutzman, P. E. and Clifton, J. R. (1999) Specimen preparation for scanning electron microscopy, Proceedings of 21st International Conference on Cement Microscopy, Las Vegas, pp. 10-22.

Stutzman, P. (2004) Scanning electron microscopy imaging of hydraulic cement microstructure, Cement and Concrete Composites, Vol. 26, pp. 957-966.

Sundius, N. and Byström, A. M. (1953) Decomposition products of muscovite at temperatures between 1,000° and 1,260°C, Transactions of the British Ceramic Society, Vol. 52, pp. 632-642.

Swamy, R. N. and Lambert, G. H. (1981) The microstructure of Lytag aggregate, The International Journal of Cement Composites and Lightweight Concrete, Vol. 3, No. 4, pp. 273-282.

Taylor, H. F. W. and Turner, A. B. (1987) Reactions of tricalcium silicate paste with organic liquids, Cement and Concrete Research, Vol. 17, pp. 613-623.

Till, R. (1974) Statistical methods for the earth scientist – an introduction, The Macmillan Press Ltd., ISBN 0-333-14800-2.

Underwood, E. E. (1968) Particle-size distribution, in: Quantitative microscopy, Edited by Dehoff, R. T. and Rhines, F. N., McGraw Hill, pp. 149-200.

Van der Sloot, H. A., Hoede, D., Cresswell, D. J. F. and Barton, J. R. (2001) Leaching behaviour of synthetic aggregates, Waste Management, Vol. 21, pp. 221-228.

Van Mier, J. G. M. (1997) Fracture process of concrete : assessment of material parameters for fracture models, CRC Press, Inc., ISBN 0-8493-9123-7.

Vassányi, I. and Szabó, A. (1993) Thermic dehydroxylation of muscovite-2M1, Materials Science Forum, Vol. 133-136, pp. 655-658.

Wainwright, P. J. (1981) Artificial aggregate from domestic refuse, Concrete, Vol. 15, pp. 25-29.

Wainwright, P. J. and Boni, S. P. K. (1983) Some properties of concrete containing sintered domestic refuse as a coarse aggregate, Magazine of Concrete Research, Vol. 35, pp. 75-85.

Wainwright, P. J. and Robery, P. (1991) Production and properties of sintered incinerator residues as aggregate for concrete, in: Gaumans J J J M et. al. (Eds.), Waste Materials in Construction – Proceedings of the International Conference on the Environmental Implications of Construction with Waste, Elesvier, Amsterdam, pp. 425-432.

Wainwright, P. J., Barton, J., Cresswell, D. J. F., Schneider, A., van der Sloot, H. A., Hayes, R. and Mckeever, M. (2001) Final report: Utilization innovative rotary kiln technology to recycle waste into synthetic aggregate, BRST-CT98-5234.

Wainwright, P. J., Cresswell, D. J. F. (2001) Synthetic aggregate from combustion ashes using an innovative rotary kiln, Waste Management, Vol. 21, pp. 241-246.

Wainwright, P. J., Cresswell, D. J. F. and van der Sloot, H. A. (2002) The production of synthetic aggregate from a quarry waste using an innovative style rotary kiln, Waste Management & Research, Vol. 20, pp. 279-289.

Wainwright, P. J. and Cresswell, D. J. F. (2003) Longer term properties of concrete containing synthetic aggregate made from waste materials, Proceedings of the 5th International Conference on the Science and Engineering of Recycling for Environmental Protection, *WASCON 2003*, Spain, 4-6 June.

Wang, Y. and Diamond, S. (1995) An approach to quantitative image analysis for cement pastes, Materials Research Society Symposium Proceedings, Vol. 370, pp. 23-32.

WASCON 91 (1991) Proceedings International Conference Environmental Implications of Construction with Waste materials, Maastrict, Netherlands.

WASCON 94 (1994) Proceedings International Conference Environmental Aspects of Construction with Waste Materials, Maastrict, Netherlands.

WASCON 97 (1997) Proceedings International Conference Environmental Aspects of Construction with Waste Materials, Maastrict, Netherlands.

WASCON 2000 (2000) Proceedings International Conference Science & Engineering of Recycling for Environmental Protection, Harrogate, England.

Wasserman, R. and Bentur, A. (1996) Interfacial interactions in lightweight aggregate concretes and their influence on the concrete strength, Cement and Concrete Composites, Vol. 18, pp. 67-76.

Wasserman, R. and Bentur, A. (1997) Effect of lightweight fly ash aggregate microstructure on the strength of concretes, Cement and Concrete Research, Vol. 27, pp. 525-537.

Werner, A. M. and Lange, D. A. (1999) Quantitative image analysis of masonary mortar microstructure, Journal of Computing in Civil Engineering, Vol. 13, No. 2, pp. 110-115.

Whittemore Jr., O. J. and Sipe, J. J. (1974) Pore growth during the initial stages of sintering ceramics, Powder Technology, Vol. 9, pp. 159-164.

Winslow, D. N., Cohen, M. D., Bentz, D. P., Snyder, K. A. and Garboczi, E. J. (1994) Percolation and pore structure in mortars and concrete, Cement and Concrete Research, Vol. 24, pp. 25-37.

Wong, H. S. and Buenfeld, N. R. (2006) Monte Carlo simulation of electron-solid interactions in cement-based materials, Cement and Concrete Research, Vol. 36, pp. 1076-1082.

Wong, H. S. and Buenfeld, N. R. (2006) Euclidean distance mapping for computing microstructural gradients at interfaces in composite materials, Cement and Concrete Research, Vol. 36, Issue 6, pp. 1091-1097.

Wong, H. S., Head, M. K. and Buenfeld, N. R. (2006) Pore segmentation of cement-based materials from backscattered electron images, Cement and Concrete Research, Vol. 36, Issue 6, pp. 1083-1090.

Yang, R. and Buenfeld, N. R. (2001) Binary segmentation of aggregate in SEM image analysis of concrete, Cement and Concrete Research, Vol. 31, pp. 437-441.

Yasuda, Y. (1991) Sewage sludge utilization technology in Tokyo, Water Science Technology, Vol. 23, pp. 1743-1752.

Zhang, M. H. and Gjørv, O. E. (1990) Microstructure of the interfacial zone between lightweight aggregate and cement paste, Cement and Concrete Research, Vol. 20, pp. 610-618.

Zhang, M. H. and Gjørv, O. E. (1991[a]) Characteristics of lightweight aggregates for high-strength concrete, ACI Materials Journal, Vol. 88, No. 2, pp. 150-158.

Zhang, M. H. and Gjørv, O. E. (1991[b]) Mechanical properties of high-strength lightweight concrete, ACI Materials Journal, Vol. 88, No. 3, pp. 240-247.

Zhang, M. H. and Gjørv, O. E. (1991[c]) Permeability of high-strength lightweight concrete, ACI Materials Journal, Vol. 88, No. 5, pp. 463-469.

Zhao, H. and Darwin, D. (1992) Quantitative backscattered electron analysis of cement paste, Cement and Concrete Research, Vol. 22, pp. 695-706.

Zimbelman, R. (1985) A contribution to the problem of cement-aggregate bond, Cement and Concrete Research, Vol. 15, pp. 801-808.

Appendix A

Temperature control curve of kiln for the in-batch variation test

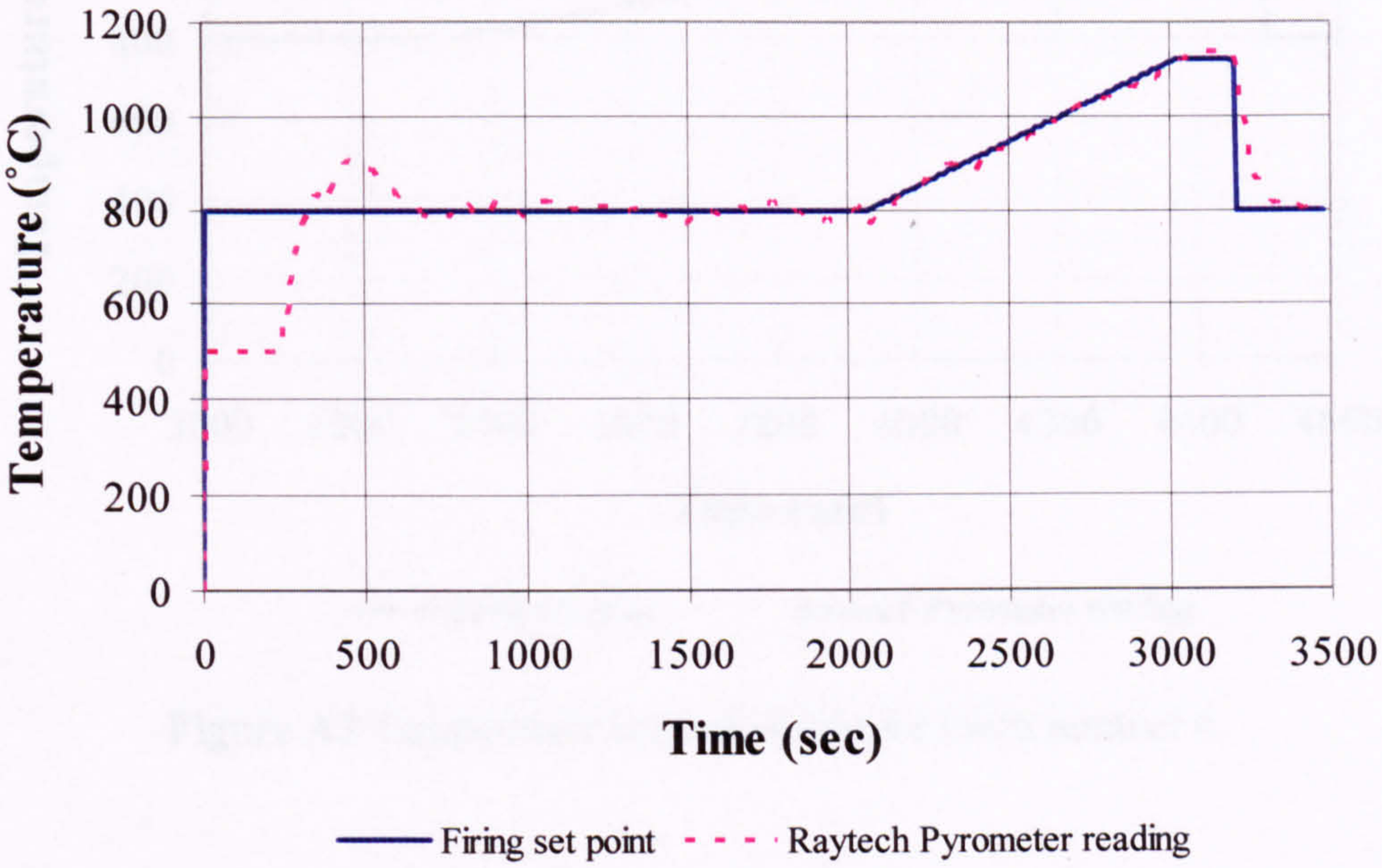

Figure A1 Temperature control of kiln for batch number 1.

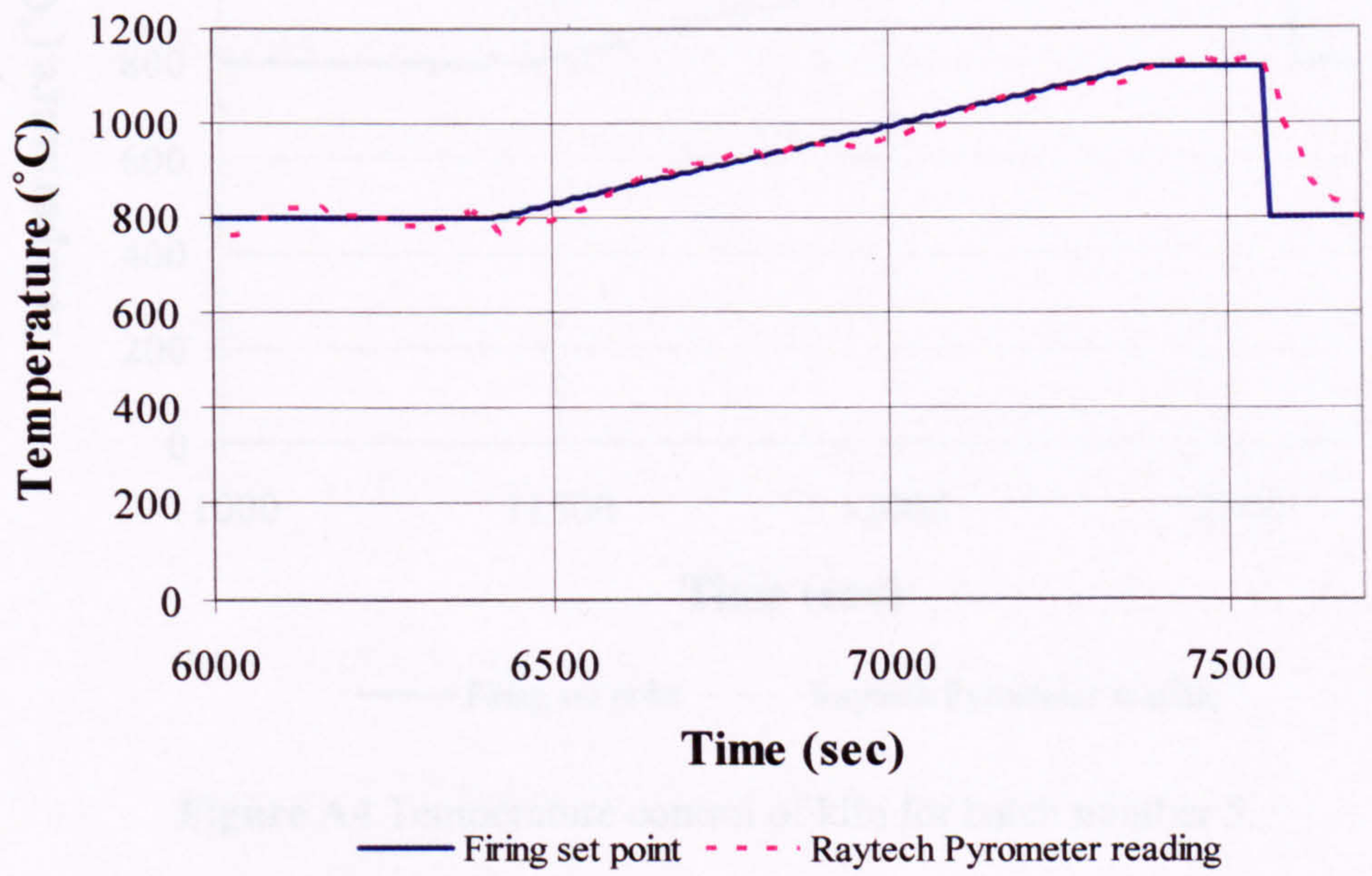

Figure A2 Temperature control of kiln for batch number 3.

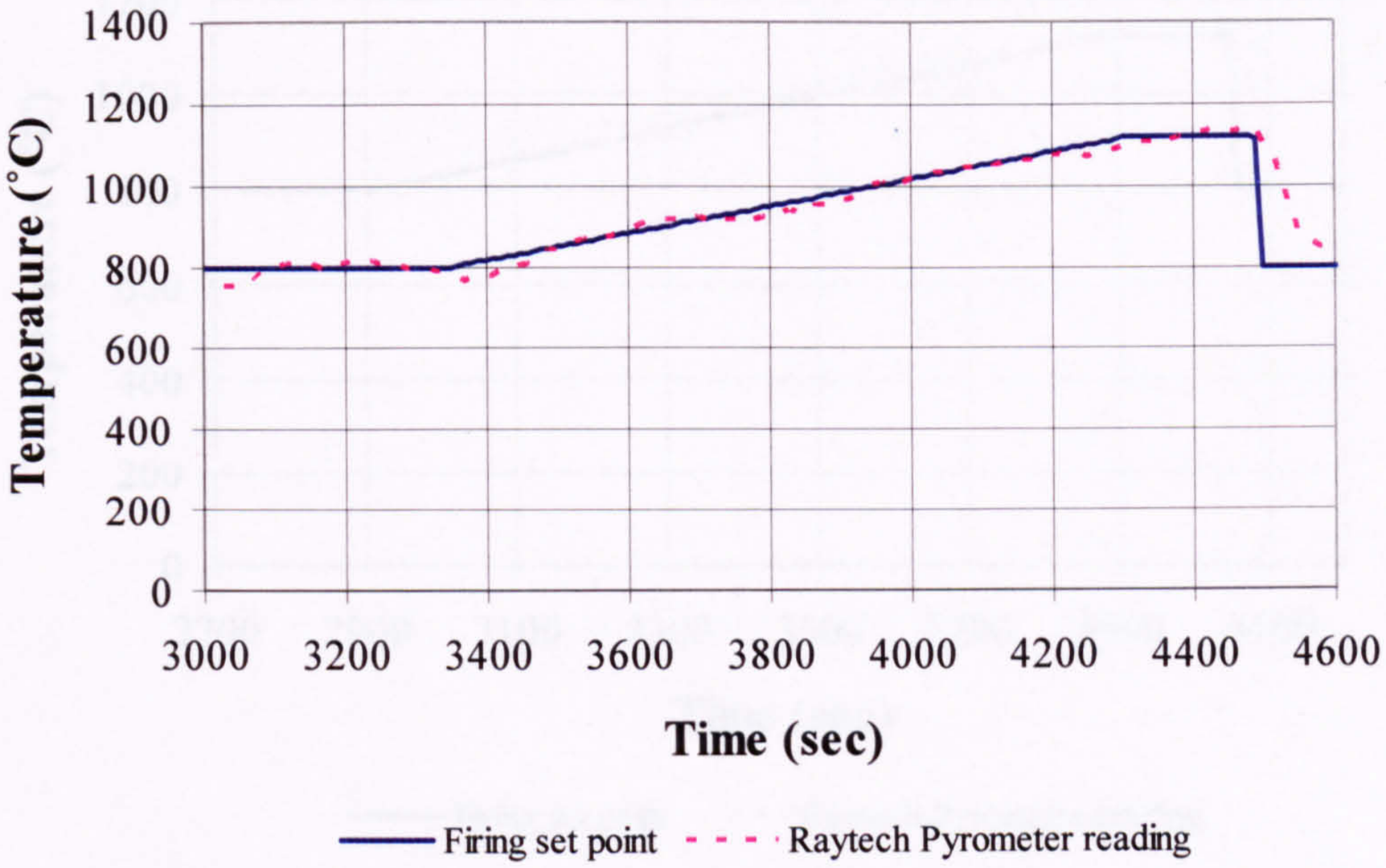

Figure A3 Temperature control of kiln for batch number 4.

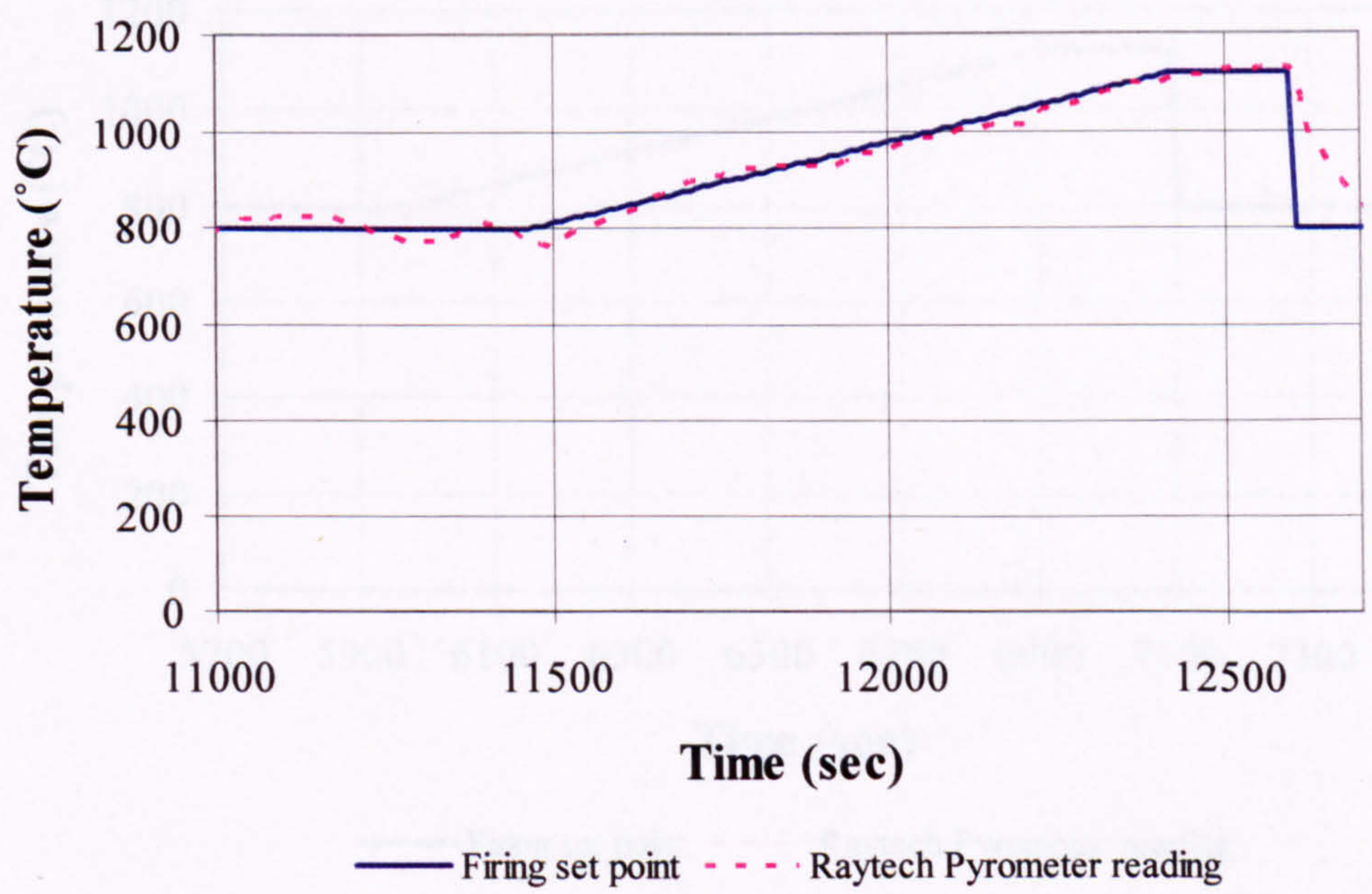

Figure A4 Temperature control of kiln for batch number 5.

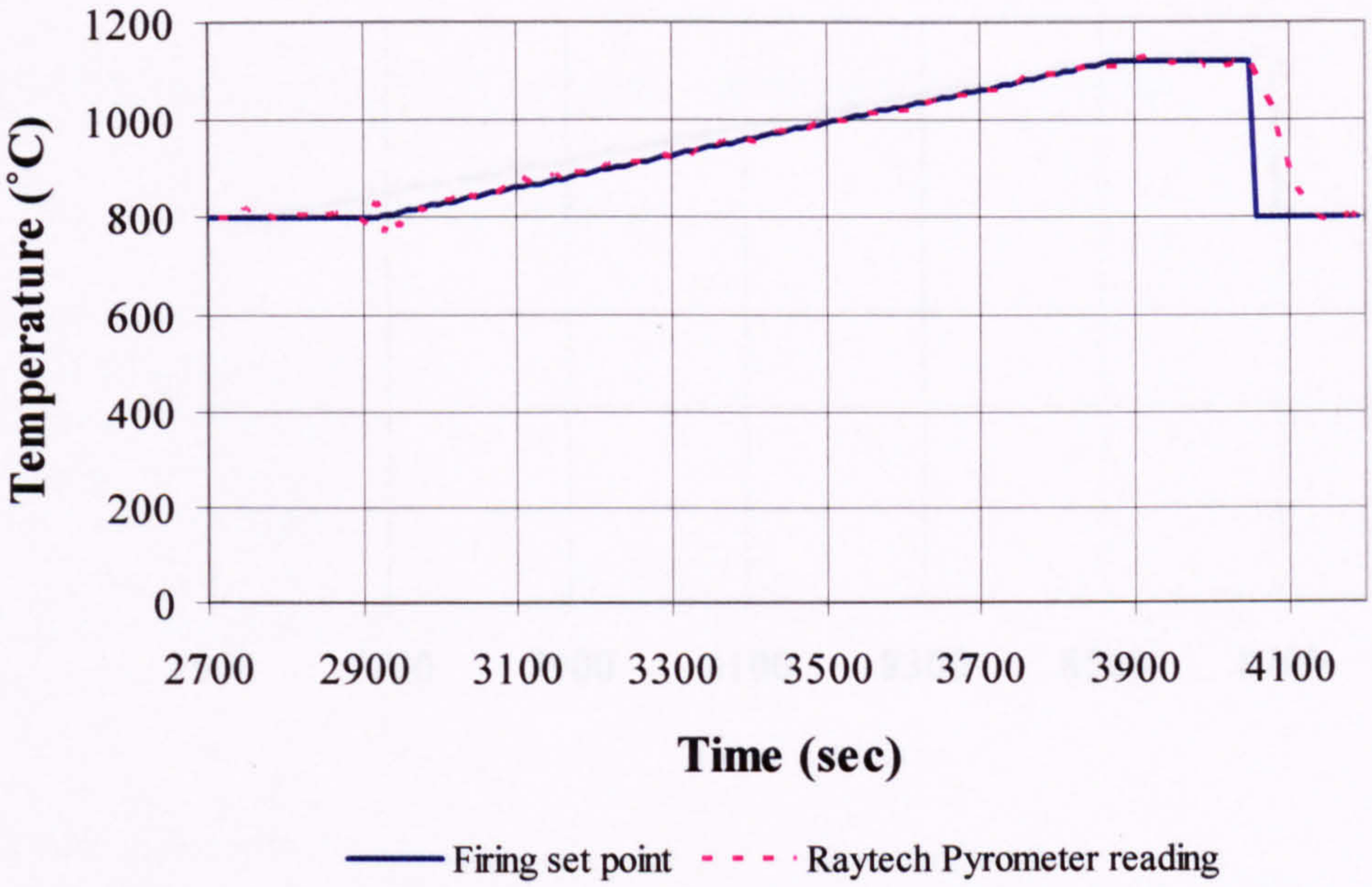

Figure A5 Temperature control of kiln for batch number 6.

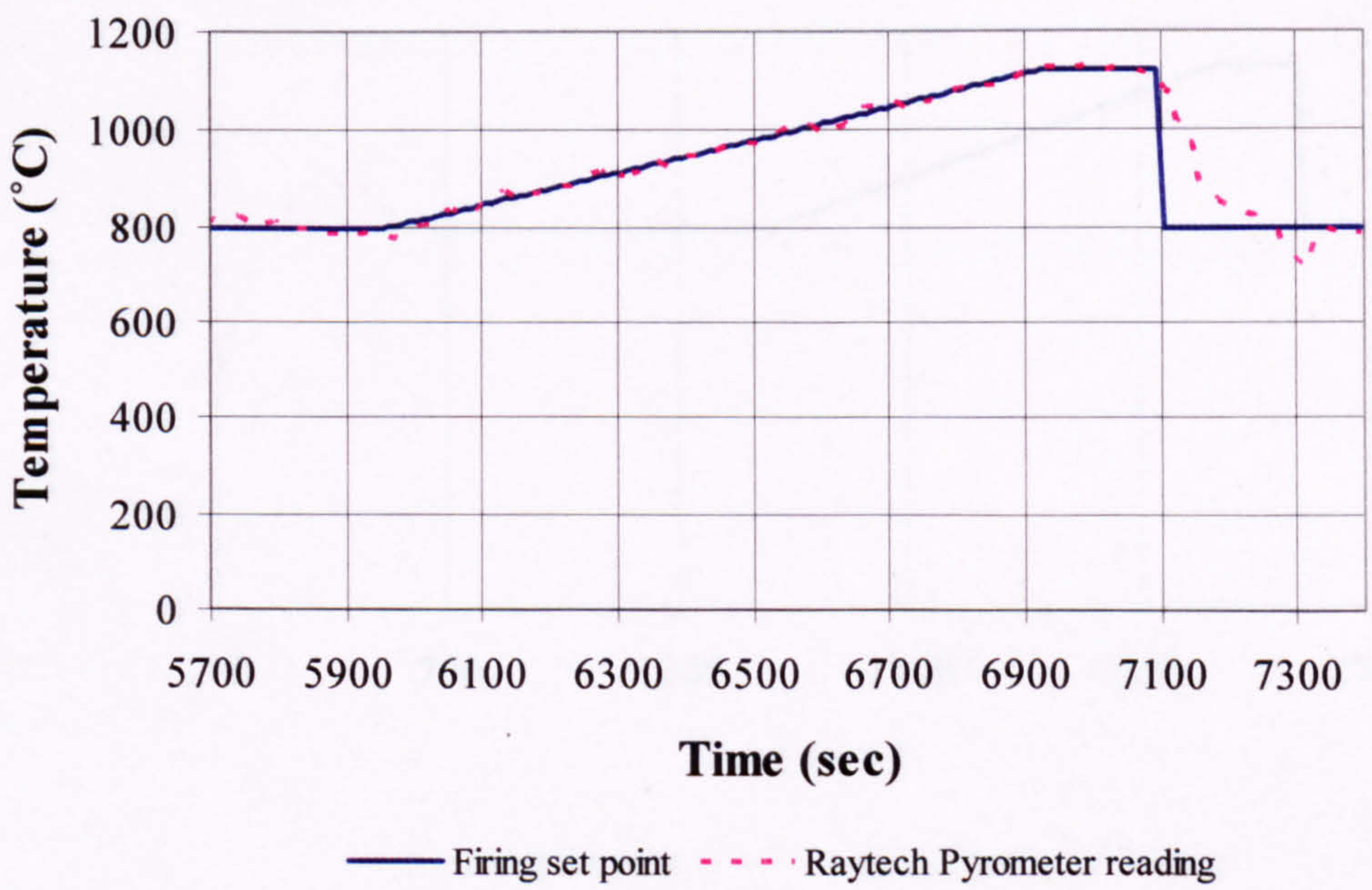

Figure A6 Temperature control of kiln for batch number 8.

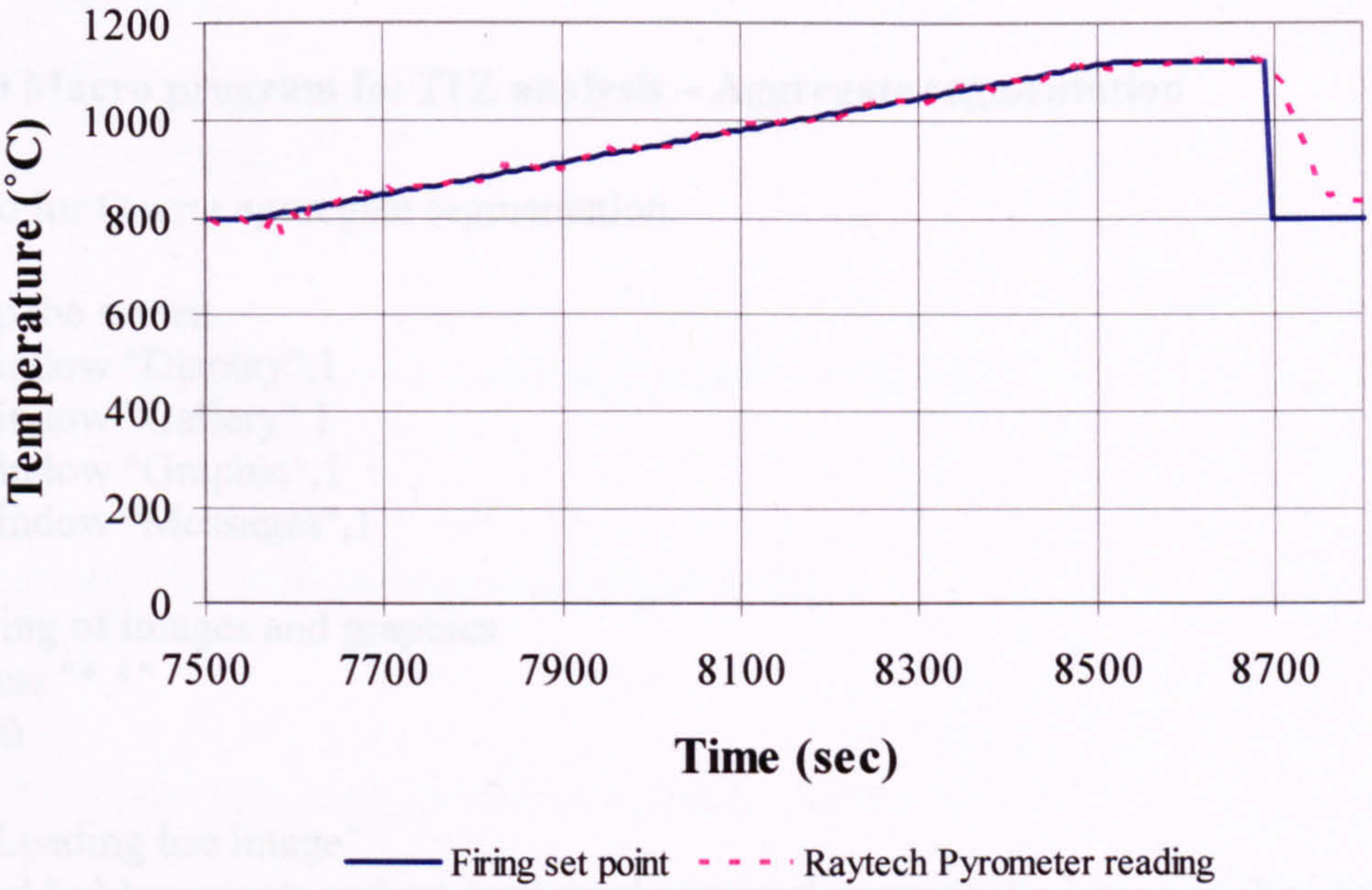

Figure A7 Temperature control of kiln for batch number 9.

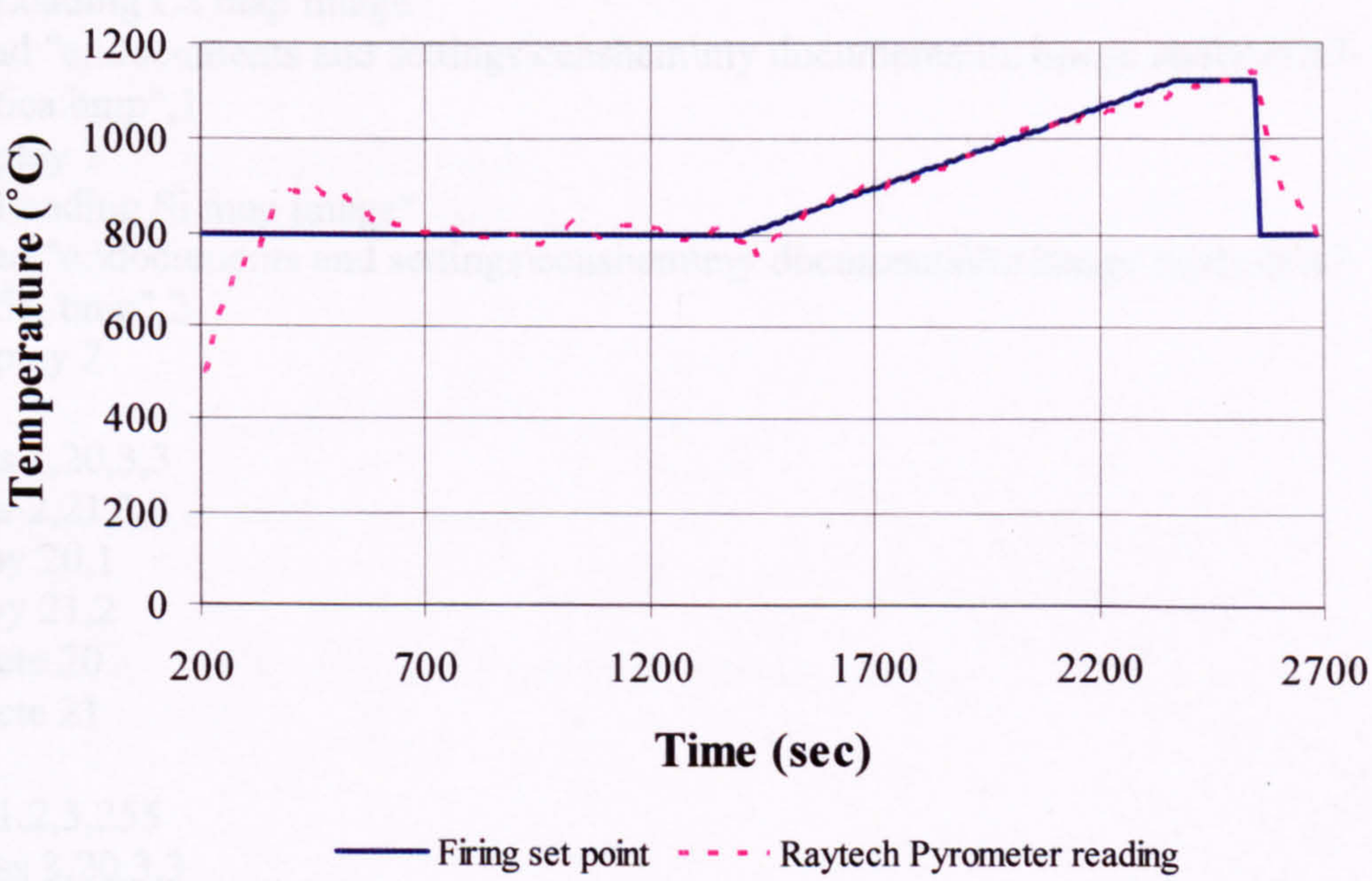

Figure A8 Temperature control of kiln for batch number 10.

Appendix B

KS-300 Macro program for ITZ analysis – Aggregate segmentation

```
# Macro for Quartz aggregate segmentation.

# Set up the screen
showwindow "Display",1
showwindow "Gallery",1
showwindow "Graphic",1
showwindow "Messages",1

# Clearing of images and graphics
imgdelete "*.*"
Gclear 0

write "Loading bse image"
!imgload "c:\documents and settings\censhem\my documents\itz image analysis\n7-
1\n71_6a.bmp",4
imgcopy 4,22
imgdisplay 22

# Quartz coarse aggregate binary mask production
write "Loading Ca map image"
!imgload "c:\documents and settings\censhem\my documents\itz image analysis\n7-
1\n71_6ca.bmp",1
imgdisplay 1
write "Loading Si map image"
!imgload "c:\documents and settings\censhem\my documents\itz image analysis\n7-
1\n71_5si.bmp",2
imgdisplay 2

lowpass 1,20,3,3
lowpass 2,21,3,3
imgcopy 20,1
imgcopy 21,2
imgdelete 20
imgdelete 21

divide 1,2,3,255
!lowpass 3,20,3,3
imgcopy 20,3
imgdelete 20

# Produce porosity mask
write "porosity segmentation"
! dislev 4,5,0,por1,1

# Produce coarse aggregate mask
```

```
write "Coarse aggregate mask production"
! dislev 3,6,0,169,1
imgcopy 6,20
write "Removing fine aggregate and noise"
!binscrap 6,7,0,90000,0
imgcopy 7,6
imgdelete 7
binnot 6,6
write "Removing hole inside the coarse aggregate boundary."
! binscrap 6,6,0,1000,0
binnot 6,6

# Subtract porosity from the coarse aggregate mask.
subtract 6,5,6,2

binnot 6,6
write "Removing hole inside the coarse aggregate boundary."
!binscrap 6,7,0,20000,0
imgcopy 7,6
imgdelete 7
binnot 6,6
write "Removing noise outside the coarse aggregate boundary."
! binscrap 6,6,0,1000,0
! median 6,7,9
imgcopy 7,6
imgdelete 7

# Producing the fine aggregate mask.
write "Fine aggregate mask production"
imgcopy 20,7
imgdelete 20

# Removing coarse aggregate from the image.
subtract 7,6,7,2
# Removing porosity from the image.
subtract 7,5,7,2

write "Removing noise outside the fine aggregate boundaries."
!binscrap 7,8,0,3000,0
imgcopy 8,7
imgdelete 8
binnot 7,7
write "Removing hole inside the fine aggregate boundaries."
!binscrap 7,8,0,1000,0
imgcopy 8,7
imgdelete 8
binnot 7,7
! median 7,8,9
imgcopy 8,7
imgdelete 8
```

```
# Convert the BSE image to the colour for graphic overlay
imgpal2RGB 4,4

# Show the coarse aggregate outline
imgcopy 6,10
binerode 10,10,5,1
subtract 6,10,11,2
Gextract 11,128,255,2
Gmerge 4,255
Gclear 0
imgdelete 10

# Show the fine or another coarse aggregate outline.
imgcopy 7,14
binerode 14,14,5,1
subtract 7,14,15,2
Gextract 15,128,255,2
Gmerge 4,255
Gclear 0
imgdelete 14
binor 11,15,16

# Checking the coarse aggregate boundary mask.

imgdisplay 4
add 22,6,20,2
add 20,7,20,2
imgdisplay 20
stop

write "Saving Coarse aggregate mask"
!imgsave 6,"g:\itz analysis\n7-1\analysis results\n-1-7-m3-cm-4.bmp"
write "Saving fine aggregate mask"
!imgsave 7,"g:\itz analysis\n7-1\analysis results\n-1-7-m3-fm-4.bmp"
write "saving Bse image for image analysis"
!imgsave 20,"g:\itz analysis\n7-1\analysis results\n-1-7-m3-bse-4.bmp"
```